THE PHYSICAL REVIEW

VOLUME 92 Second Series NUMBER 3

NOVEMBER 1, 1953

Published for the

AMERICAN PHYSICAL SOCIETY

by the

AMERICAN INSTITUTE OF PHYSICS

LANCASTER, PA., AND NEW YORK, N. Y.

THE
PHYSICAL REVIEW

A journal of experimental and theoretical physics established by E. L. Nichols in 1893

SECOND SERIES, VOL. 92, NO. 3 NOVEMBER 1, 1953

The Nonparticipation of He^6 in the Superfluidity of He^4

LESTER GUTTMAN AND JAMES R. ARNOLD
Institute for the Study of Metals and Institute for Nuclear Studies, University of Chicago, Chicago, Illinois
(Received July 27, 1953)

In a steady-state experiment, a stream of He^4 containing an extremely small concentration of He^6 has been cooled below the lambda point and passed through a narrow slit as superfluid. If the He^6 atoms had passed through the slit, most of them would have been detected by their radioactive decay in the gas stream leaving the cryostat. The fraction actually found was 0.04 ± 0.07 (standard deviation) of those expected if there had been no separation of the isotopes. This result is consistent with the Bose-Einstein condensation model for the superfluidity of He^4. A new type of generator for He^6 is described.

INTRODUCTION

THE striking differences in properties[1] between liquid He^3 and liquid He^4 have been widely interpreted as evidence that the superfluidity of the latter is essentially the result of Bose-Einstein condensation. However, the relatively large mass difference and the importance of zero-point energy in these systems make it desirable to attempt some independent confirmation of this hypothesis. The isotope of mass 6 has a half-life[2] of 0.82 sec, which, though short, allows the possibility of determining its behavior in the presence of superfluid He^4. We chose to measure the fraction of He^6 carried with He^4 through narrow channels below the λ point, because only a flow-type experiment seemed to have much chance of success, and because a critical property was thus being investigated.

One would predict that He^6 in dilute solution, like He^3, would not be transported with superfluid He^4, if superfluidity is basically a property of a system of identical atoms consisting of an even number of fundamental particles. On the other hand, if the only relevant properties are the interatomic forces and the atomic mass, then He^6, unlike He^3, should participate in the superflow of He^4 and be found unchanged in concentration (except for radioactive decay) in the material emerging from the channel. However, we should remark that Landau and Pomeranchuk[3] have predicted that He^3, He^6, and any other dilute impurities would not participate in superflow of He^4, from a model which does not invoke Bose-Einstein statistics.

METHOD AND APPARATUS

The experiment consists of establishing a steady state in which He^6, generated by the reaction $Be^9(n,\alpha)$-He^6, is carried by a stream of ordinary helium to a narrow slit kept at about 2°K. The He^4 liquefies, passes through the slit as superfluid, evaporates, and is warmed again to room temperature. The rate of He^6 generation is monitored continuously by passing the gas stream through an annular Geiger counter between the generator and the cryostat. Another annular counter of large volume after the cryostat records the decay (to Li^6, with the emission of betas of maximum

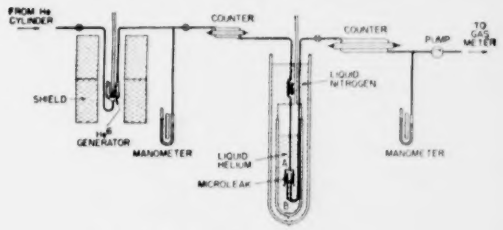

FIG. 1. Schematic diagram of apparatus.

[1] Abraham, Osborne, and Weinstock, Science **117**, 121 (1953); J. G. Daunt, Advances in Phys. (Phil. Mag. Supplement) **1**, 209 (1952).
[2] Hollander, Perlman, and Seaborg, Revs. Modern Phys. **25**, 469 (1953).
[3] L. Landau and I. Pomeranchuk, Doklady Akad. Nauk S.S.S.R. **59**, 669–70 (1948).

energy 3.5 Mev) of a large fraction of those He^6 atoms which have survived passage through the slit.

The apparatus design was dictated by several conflicting requirements. A large rate of gas flow is obviously desirable to shorten the transit time between counters. However, the rate is limited by the slit cross-sectional area. Slits greater in width than about 1 micron would permit flow not typical of true superfluidity,[4] while increasing the slit circumference requires a large volume at low temperature and a correspondingly long hold-up time. There is also a limitation on the rate imposed by the need to transfer to or from the bath the heat content of the gas in heating or cooling, the heat of vaporization, and the thermomechanical heat. The pressure in the parts of the system in the helium bath cannot greatly exceed the bath pressure without causing accumulation of liquid, yet the pressure at the exit counter must be large enough to allow a major fraction of the He^6 to decay there. The volumes of all parts of the system must be kept small to reduce the transit time. The dimensions of the microleak, of the connecting tubing, and of the Geiger counters are all determined within narrow limits by the foregoing requirements, together with such other "boundary conditions" as pump capacity, counter shielding, available neutron intensity, etc.

The apparatus is shown schematically in Fig. 1. The neutron source, a hollow sphere of beryllium coated internally with polonium and covered with nickel, was loaned to us by the Los Alamos Scientific Laboratory. During the measurements reported, its strength was about 3 curies, and it emitted about 3.5×10^6 neutrons/sec. Its great advantage over a radium-beryllium

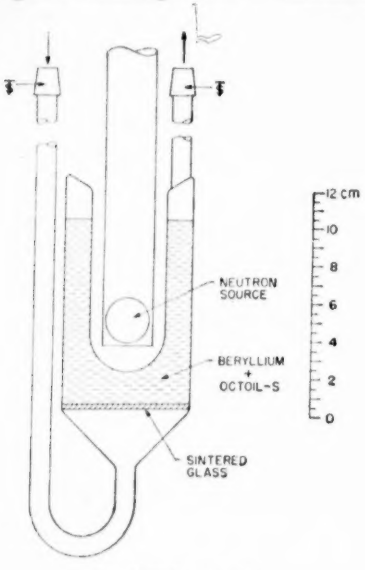

FIG. 2. He^6 generator.

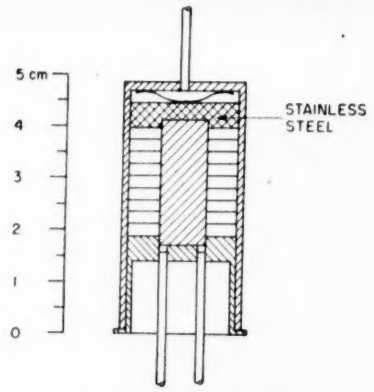

FIG. 3. Microleak assembly.

source is, of course, the freedom from gamma radiation, which enables an adequately shielded counter to be placed within four feet of the source with little rise in background. The decision against using a cyclotron source was based on the great inconvenience of transporting the cryogenic apparatus from the low-temperature facilities, as well as the greater steadiness of the radioactive source. The source was shielded for health purposes with an array of square 5-gallon cans filled with saturated sodium metaborate solution; this simple and inexpensive shield proved quite adequate.

The He^6 generator is based on the fast-neutron reaction $Be^9(n,\alpha)He^6$. The cross section of this reaction as a function of energy is given by Allen, Burcham, and Wilkinson;[5] its value is about 4×10^{-26} cm^2 from 2 to 4 Mev. A generator arrangement based on that of Allen, Paneth, and Morrish[6] was first tried. In this arrangement 100 g of beryllium powder (-200 mesh) was placed in an annular space surrounding the source and resting on a fritted disk. The He^6 nuclei formed in the reaction recoil and are carried into the gas space. If the average neutron energy is 6 Mev, the recoiling He^6 nucleus carries 2.2 Mev and has a range of approximately 1.8 mg/cm^2 or 10 microns. Thus most of the He^6 atoms are carried out of the particles in which they originate, but in the great majority of cases they re-enter and are stopped in other particles. A stream of helium carries those remaining in the gas phase into the system. The yield of this type of generator was disappointingly small.

A new technique was then tried, in which the beryllium powder was immersed in a nonvolatile liquid (Octoil-S or dibutyl-phthalate), and the helium gas was bubbled through the slurry. In this case most of the He^6 atoms are stopped in the liquid, while the gas volume in the generator is greatly decreased. The rate-determining step is now the transfer of He^6 from liquid to gas. Some data of Sugarman[7] on short-lived fission

[4] R. Bowers and K. Mendelssohn, Proc. Roy. Soc. (London) **A213**, 158 (1952), and references cited there.

[5] Allen, Burcham, and Wilkinson, Nature **159**, 473 (1947).

[6] Allen, Paneth, and Morrish, Phys. Rev. **75**, 570 (1949).

[7] N. Sugarman (private communication).

products indicated that this might be rapid enough to be useful. After suitable adjustment of conditions, it was found that the addition of liquid improved the yield of He^6 fivefold. The final form of the apparatus is shown in Fig. 2.

The calculation of the fraction of He^6 atoms produced which are recovered in the gas phase is a difficult matter, the chief uncertainties being the energy distribution of the neutrons and the source geometry. A rough value of 0.7 percent was obtained, uncertain by perhaps a factor two.

The Geiger counters used are thin-walled jacketed tubes of "Eck and Krebs" design, the monitor counter having an annular volume of 10.0 cc. The exit counter, designed to provide sufficient time for most of the remaining He^6 nuclei to decay in it, has a counter volume of 500 cc and an annular volume of 800 cc. Its wall thickness was not measured directly, but comparison of counting rates with the small counter in series led to a correction factor of 0.52 ± 0.02 for the difference in wall thickness (and geometry, although this effect was small), suggesting a wall thickness of about 275 mg/cm^2 for the large counter.

In preliminary studies, the half-life was approximately verified, and it was shown that the fraction of longer-lived activities (such as O^{15}) at the monitor counter was negligible.

The cryostat, of the design standard in this laboratory, consists of a helium Dewar, 7 cm i.d. by 65 cm long, surrounded by a liquid nitrogen bath. The helium bath pressure is regulated by manual adjustment of a needle valve and is measured by a mercury manometer and a manometer filled with Octoil-S. The helium stream leaving the monitor counter passes through 75 cm of copper tubing, 0.48 cm o.d., 0.30 cm i.d., immersed in the liquid nitrogen, through the cap of the inner Dewar, and then through stainless steel tubing, 0.16 cm o.d., 0.13 cm i.d., to the microleak, which is near the bottom of the helium bath. The exit tube in the helium space is also 0.16 cm o.d., but is larger in the parts expected to be at higher temperatures.

The helium, specially purified by passing it at 2000 lb/in.^{2} over charcoal at liquid nitrogen temperature, is supplied through a pressure regulator and needle valve, the settings of which determine the rate of gas flow. Mercury manometers measure the absolute pressure near each of the counters. Octoil-S manometers connected to the system close to the microleak (points A and B, Fig. 1) can be arranged to show either the absolute pressure or the difference from the helium bath pressure. A mechanical pump (capacity 33 l/min) is connected to the exit counter through a rubber tube. By constricting the tube it is possible to adjust the pressure in the counter to a suitable value. The pump discharge leads to a wet-test gas meter.

The microleak design as finally evolved is shown in Fig. 3. A pile of 9 copper washers and a stainless steel cap are centered by a copper cylinder. The assembly is contained in a closely fitting copper case soldered together with Rose's metal at a joint far from the washers. Moderate pressure is applied to the pile by a phosphor-bronze leaf spring. The plane surfaces of the washers and cap and the face of the case on which the end washer rests were polished flat to about $\frac{1}{4}$ wavelength of visible light (0.1 to 0.2 micron), and the superflow takes place in the narrow gap between these surfaces. By measuring the rate of gas flow through the leak at known pressures and temperature, an average slit gap can be calculated from the formula for flow between parallel plates, which applies approximately:

$$\dot{v}_2 = wh^3(p_1^2 - p_2^2)/(24\eta L p_2).$$

Here w, L, and h are the total width, length, and gap of the slit, η is the gas viscosity, p_1 and p_2 are the pressures at the ends of the slit, and $\dot{v}_2$ is the volume rate of flow, measured at p_2. For L, we took the difference between the inner and outer radii of a washer and for w the inner circumference of a washer multiplied by the number of gaps, namely 10. The value of $[\langle h^3\rangle_{Av}]^{\frac{1}{3}}$ obtained this way was always in the range 1 to 2μ, based on measurements at room temperature and at the boiling points of nitrogen and helium.

RESULTS

It was found that the apparatus could be operated successfully only in the temperature range from about 1.88 to 2.00°K. At higher temperatures the transit time was too great due to the higher vapor pressure

TABLE I. Summary of results.

Average temperature, °K	Total duration of flow, min	Average flow rate, cc/sec (STP)	Average transit time, sec	Exit counting rate: Expected min^{-1}	Exit counting rate: Observed min^{-1}	Ratio observed/expected
1.98	100	2.75	3.2	15.0±0.6	1.4±1.6	0.09±0.11
1.93	20	2.9	2.9	21.4±1.2	4.0±3.9	0.19±0.18
1.91	60	2.1	3.4	11.5±0.5	8.6±2.2	0.75±0.19*
1.90	41	2.2	3.2	13.1±0.6	0.3±2.4	0.02±0.18
1.89	100	2.2	3.1	15.0±0.7	−0.8±1.7	−0.05±0.11
			Weighted mean {all results			0.12±0.06
			Weighted mean {excluding the run marked*			0.04±0.07

and hence greater gas density. At lower temperatures, the pressure drop necessary to force the gas through the connecting tubing was excessive compared to the bath pressure. The results of five series of measurements at various temperatures in this range are given in Table I. Usually, once steady conditions were established, counting periods with flow were taken alternately with background measurements. The decay of He^6 in the monitor counter gave 50 counts/min above a background of 25–30 counts/min; the helium pressure at this counter was 2.5 to 3.0 cm Hg. The background of the exit counter was about 225 counts/min, and the decay of He^6 there could have given an additional 12–21 counts/min, as shown in Table I; the operating pressure was 6 to 10 mm Hg. The method of calculation is described in the next paragraph. The pressure at the slit entrance was between 0.3 mm of oil greater and 0.5 mm less than the bath pressure. The pressure drop across the slit was 1 to 8 cm of oil, and hence the *maximum* flow of gas, as calculated from the performance at 4.2°K, was about 1 percent of that due to the flow of superfluid. Operation with the pressure *less* than the bath pressure was probably possible due to capillary condensation in the narrower parts of the slit; this is confirmed by the fact that the observed flow was only about $\frac{1}{5}$ of the superflow which should occur in a slit of these dimensions. Under these conditions, one is assured that no liquid is present except in the slit and that the amount of gas adsorbed on the walls of the system is negligible.

Let t_1, t_2, and t be the times required for the gas to traverse the first counter, the second counter, and the system between the counters. Then, if $\dot{C}_1$ is the observed counting rate at the first counter, it is easy to show that the counting rate at the second counter, assuming no separation of He^6 and He^4, will be

$$\dot{C}_2=\dot{C}_1 e^{-\lambda t}\frac{1-e^{-\lambda t_2}}{e^{\lambda t_1}-1},$$

where λ is the decay constant of He^6. The times t_1 and t_2 can be obtained simply from the known volumes of the counters, the observed flow rate and the pressures at the counters. To calculate the values of t given in Table I, the connecting tubing was divided into 6 regions of known volumes: two at room temperature (one on each side of the leak), two assumed to be at 78°K, and two at the helium bath temperature. The pressure in each region was assumed to be uniform and equal to that shown by the nearest manometer, or, for each region at 78°K, to be the mean of the values on the two manometers on the same side of the leak. The microleak itself had a small volume, calculable with sufficient accuracy from its dimensions, and assumed to contain gas at the bath temperature. The time spent by the superfluid in traversing the slit is certainly less (since the liquid must evaporate before going the entire length) than the value obtained by dividing the slit length (0.6 cm) by the critical flow velocity[8] at these temperatures (~6 cm/sec). The total time t is then just the quantity of He^4 in the system between the counters divided by the rate of flow as measured by the gas meter and a timer.

A check on the amount of gas in the system under the operating conditions was obtained as follows. At the end of a flow period, the oil manometers were cut off from the system by closing stopcocks, and two stopcocks, one just before each counter, were turned off as nearly simultaneously as possible (probably within 0.1 to 0.2 sec). The remainder of the system was pumped to a good vacuum, and the gas trapped between the stopcocks was then pumped out and collected over water in an inverted graduated cylinder. Except for small known quantities of gas at room temperature, the volume measured in this way was that between the counters plus that of the first counter plus that in the leads to the manometers. The correction for the last contribution was unfortunately not at all negligible and was also subject to some uncertainty, since we do not know the temperature distribution above the bath. Since the heat leak down each tube can be calculated[9] to be only about 1 percent of the observed total heat leak into the bath, it seems likely that essentially the entire lengths of the manometer leads in the double-walled portion of the inner Dewar were cooled nearly to the bath temperature by the evaporated gas even when the Dewar was only half-filled with liquid. When the measured volume exceeded that calculated on the preceding assumptions by more than 1 cc (STP) (out of about 15 to 20), the corresponding run was rejected.

Earlier experiments with a different design of microleak, a disk fabricated by pressing, sintering, and rolling copper powder (−325 mesh), gave anomalous results. Below the λ point no He^6 was observed to pass the microleak, in agreement with the result using the slit. Above the λ point, however, a leak of the same design but pressed and rolled less, so that a large gas flow was possible, allowed no He^6 to reach the exit counter at 2.5°K. At higher temperatures there was an increased passage of He^6, and at 4.2°K the expected amount was observed. Attempts to explain this effect as due to adsorption, with concentration of He^6 in the adsorbed phase resulting in a long transit time, were not very successful, and the behavior with this type of leak remains obscure.

Experiments in which the microleak assembly was replaced with an open tube gave the expected exit counting rate both above and below the λ point.

The errors assigned in Table I are the standard deviations due to counting statistics. It is difficult to estimate the error in the transit time. If we have overlooked as much as about 2.5 cc (STP) of gas (which

[8] L. Meyer and W. Band, Naturwiss. **36**, 5–16 (1949); L. Meyer and J. H. Mellink, Physica **13**, 197 (1947).
[9] R. Berman, Phil. Mag. [7] **42**, 642 (1951).

seems unlikely), the ratios in Table I would all be approximately doubled, and so would their standard deviations.

DISCUSSION

It appears that He^6 behaves like He^3 in dilute solution,[10] in that the concentration of He^6 in material emerging from a fine channel is only a few percent at most of the concentration at the entrance. This is just what would be expected on the Bose-Einstein gas model for liquid He^4. The He^6, although it obeys Bose-Einstein statistics, is present at such a low concentration ($\sim 10^{-19}$ atom fraction) that its degeneracy temperature ($\sim 10^{-12}$ °K) is far below the temperature of the experiment. Since it is distinguishable from He^4, it cannot participate in the condensation of the latter. Hence it behaves like any other foreign solute in being excluded from the superfluid state.

In the present state of theoretical knowledge of liquid helium, it is perhaps still possible to imagine that the conditions for superfluidity are so stringent that there exist both *upper* and *lower* limits for the atomic mass, and that He^4 satisfies these conditions while He^3 and He^6 do not. However, the most natural interpretation of our results, taken together with the extensive work on He^3, is that superfluidity is connected essentially only with the symmetry properties of the wave function of a system with respect to the interchange of identical atoms, and not with the atomic mass.

[10] Abraham, Weinstock, and Osborne, Phys. Rev. **76**, 864 (1949).

ACKNOWLEDGMENTS

We are deeply indebted to the Los Alamos Laboratory and the Argonne National Laboratory for their cooperation in supplying us with the polonium-beryllium neutron source used in this work. The microleak was constructed by Mr. Paul Dolmer, under the supervision of Mr. Joseph Getzholtz. The support of the industrial sponsors of the Research Institutes is gratefully acknowledged.

PHYSICAL REVIEW VOLUME 92, NUMBER 3 NOVEMBER 1, 1953

Exchange Coupling in $CuK_2Cl_4 \cdot 2H_2O$ by Paramagnetic Resonance Absorption

KAZUO ŌNO, HIDETARŌ ABE, AND JUNJI SHIMADA
Institute of Science and Technology, University of Tokyo, Tokyo, Japan

(Received June 22, 1953)

$CuK_2Cl_4 \cdot 2H_2O$ contains two inequivalent Cu^{++} ions in each unit cell. At $\lambda = 5.4$ mm two peaks are obviously found corresponding to two different g values, whereas only one peak is found at longer wavelengths. From these facts the exchange frequency between these dissimilar ions is estimated to be about 0.1 cm^{-1}. For the crystal orientation relative to the magnetic field at which the two types of ions are similar, the line width decreases with decreasing wavelength. This may be the result of the "10/3 effect" discussed by Anderson and Weiss.

MEASUREMENTS of microwave paramagnetic resonance absorption in $CuK_2Cl_4 \cdot 2H_2O$ at $\lambda = 10$ cm, $\lambda = 3$ cm, and $\lambda = 1.5$ cm have already been reported.[1,2] As the crystal has two inequivalent ions we can expect to observe two absorption maxima. We found only one maximum at these wavelengths, with, however, a remarkable frequency dependence of the line width. This may be ascribed to exchange coupling. We have recently investigated this salt at $\lambda = 7.7$ mm and $\lambda = 5.4$ mm, and two maxima were found at $\lambda = 5.4$ mm.

The crystal structure of $CuK_2Cl_4 \cdot 2H_2O$ is tetragonal and each unit cell contains two inequivalent Cu^{++} ions situated at the points (0 0 0) $(\frac{1}{2}, \frac{1}{2}, \frac{1}{2})$.[2,3] Both ions are surrounded by four chlorine atoms and two water molecules. The chlorine atoms are on a rhomb in the a-a plane, the two rhombs in the unit cell being rotated relative to each other by 90° about the c axis. Thus the electric field acting on the Cu^{++} ion has rhombic symmetry, and two different g values would be expected at those orientations of the cyrstal at which the

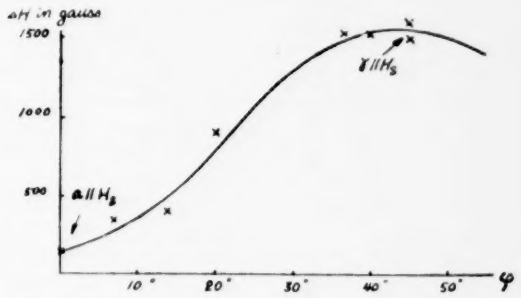

FIG. 1. Variation of line width with orientation for H_s in the a-a plane at $\lambda = 7.7$ mm, where φ is the angle between H_s and the a axis.

[1] Itoh, Fujimoto, and Ibamoto, Phys. Rev. **83**, 852 (1951).
[2] H. Kumagai *et al.*, J. Phys. Soc. Japan **7**, 535 (1952).
[3] L. Chrobak, Z. Krist. **88**, 35 (1934).

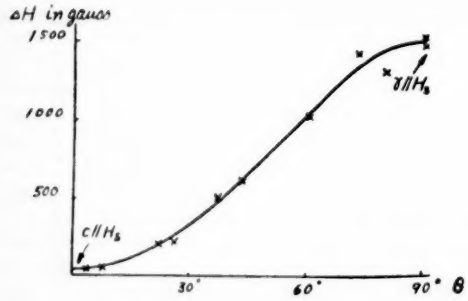

FIG. 2. Variation of line width with orientation for H_s in the γ-c plane at $\lambda=7.7$ mm, where θ is the angle between H_s and the c axis.

directions between the external field and the symmetry axes of the two ions are dissimilar.

The observed half-value widths at $\lambda=7.7$ mm in the a-a plane are shown in Fig. 1 and those in the γ-c plane in Fig. 2, where the γ axis is the bisector of the two a axes. The line width is narrowest ($\sim$40 gauss) when the static magnetic field H_s is parallel to the c axis and broadest ($\sim$1500 gauss) along the γ axis. This may be ascribed to the exchange interaction between the dissimilar ions. That is, with H_s along the c axis the precessional frequencies of the two types of ions are the same and the width is narrowest, while with H_s along the γ axis the greatest difference of the frequencies gives the broadest width.[4]

The line widths with H_s along the γ axis and the c axis at the wavelengths of 10 cm, 3 cm, 1.6 cm, 7.7 mm, and 5.4 mm are shown in Table I. For the γ axis, where the g values of the two types of ions should be different,

TABLE I. Frequency dependence of line widths.

λ (cm)	ΔH (gauss) with H_s along γ	ΔH (gauss) with H_s along c
10	200	150
3.01	250	115
1.65	480	80
0.77	1500	40±10
0.54	~800 (two maxima)	40±10

[4] J. H. Van Vleck, Phys. Rev. **74**, 1168 (1948).

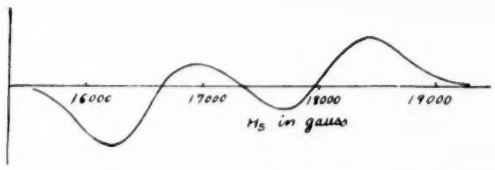

FIG. 3. Derivative curve of the paramagnetic resonance line with H_s along γ in $CuK_2Cl_4\cdot 2H_2O$ at $\lambda=5.4$ mm.

the width increases rapidly with decreasing wavelength until the two lines are separated at $\lambda=5.4$ mm (the absorption curve being shown in Fig. 3). Even at $\lambda=7.7$ mm there is some indication of two lines, since the top of the absorption curve is very flat. At this orientation of H_s, the precessional frequencies of the two types of ions are different and the line width obtained will depend on whether the exchange frequency is greater or smaller than the difference in the two precessional frequencies. In the latter case, absorption by each type of ion should be observed separately and two maxima should appear. If we assume that the difference of the precessional frequencies of the two types of ions at $\lambda=7.7$ mm is equal to the exchange frequency, the exchange frequency $2J$ is given by

$$2J=\beta H\times\Delta g\geqq\beta H\times(\Delta g')=12\,000\beta(2.30-2.14)$$
$$=0.09\ \text{cm}^{-1},$$

where H is the resonance magnetic field at $\lambda=7.7$ mm and $\Delta g'$ is the difference of the g values obtained at $\lambda=5.4$ mm.

On the other hand, for H_s along the c axis, where the g values of the two types of ions are similar, the width decreases remarkably with decreasing wavelength. The width at the longest wavelength is three or four times as broad as that at the shortest wavelength. This behavior of the line widths may be due to the "10/3 effect" discussed by Anderson and Weiss.[5]

Our thanks are due Professor Hiroo Kumagai for his continuous guidance and encouragement throughout this work. A more detailed report will appear in the *Journal of the Physical Society of Japan*.

[5] P. W. Anderson and P. R. Weiss, Revs. Modern Phys. **25**, 269 (1953).

Spin-Wave Theory of Antiferromagnetism for Simple Cubic Lattices

M. R. SCHAFROTH*
Swiss Federal Institute of Technology, Zürich, Switzerland
(Received June 19, 1953)

The transcendental functions which arise in a variational treatment of the spin-wave theory of antiferromagnetism are calculated for the case of the simple cubic lattice.

WE wish to give some numerical results of a calculation which was undertaken with the purpose of obtaining a variational approach to the theory of antiferromagnetism. Since then a similar approach was published by Kubo.[1] As we had specialized on the simple cubic lattice whereas Kubo considers body-centered lattices, we think it worth while to give a brief account of our results. We follow the notation of Kubo's paper to which the reader is referred for details.

The functions $A(\alpha)$ and $C(\alpha)$ can be defined by

$$2A+1=(2\pi)^{-3}\int d^3\lambda(1-\alpha^2\gamma_\lambda^2)^{-\frac{1}{2}},$$

$$C^2=\tfrac{1}{4}\alpha^2(2\pi)^{-6}\int d^3\lambda\int d^3\lambda'\gamma_\lambda\gamma_{\lambda-\lambda'}\gamma_{\lambda'}\times(1-\alpha^2\gamma_\lambda^2)^{-\frac{1}{2}}(1-\alpha^2\gamma_{\lambda'}^2)^{-\frac{1}{2}}, \quad (1)$$

$$C<0.$$

This definition of C can easily be seen to be equivalent to Kubo's by expressing the ground-state average of $a_j^*a_jb_{j+\rho}^*b_{j+\rho}$ once through Kubo's formula (A.6) and once by direct calculation. We choose this definition because of its symmetry, and because it allows A and C to be reduced in an analogous way to simple integrals in the case of the simple cubic lattice. This reduction runs as follows.

TABLE I. The functions $A(\alpha)$ and $C(\alpha)$ for the simple cubic lattice.

α	$2A+1$	$-C$
1.000	1.149	0.122
0.968	1.132	0.117
0.938	1.117	0.106
0.909	1.106	0.098
0.857	1.082	0.086
0.789	1.068	0.072
0.667	1.044	0.061
0.500	1.020	0.045

For the simple cubic lattice

$$\gamma_\lambda=\tfrac{1}{3}(\cos\lambda_1+\cos\lambda_2+\cos\lambda_3)$$

so that, with $\xi_i=\cos\lambda_i$,

$$\begin{aligned}2A+1&=\pi^{-3}\int_{-1}^{+1}d\xi_1\int_{-1}^{+1}d\xi_2\int_{-1}^{+1}d\xi_3\prod_{i=1}^{3}(1-\xi_i^2)^{-\frac{1}{2}}\\&\quad\times[1-\tfrac{1}{9}\alpha^2(\xi_1+\xi_2+\xi_3)^2]^{-\frac{1}{2}}\\&=\pi^{-3}\int_{-1}^{+1}d\xi_1\int_{-1}^{+1}d\xi_2\int_{-1}^{+1}d\xi_3\int_{-1}^{+1}d\xi_4\prod_{i=1}^{4}(1-\xi_i^2)^{-\frac{1}{2}}\\&\quad\times\delta(\xi_4-\tfrac{1}{3}\alpha(\xi_1+\xi_2+\xi_3))\\&=\frac{1}{2\pi^4}\int_{-\infty}^{+\infty}d\omega\int_{-1}^{+1}d^4\xi\prod_{i=1}^{4}(1-\xi_i^2)^{-\frac{1}{2}}\\&\quad\times\exp[i\omega(\xi_4-\tfrac{1}{3}\alpha(\xi_1+\xi_2+\xi_3))].\end{aligned}$$

If we use

$$J_0(\omega)=\frac{1}{\pi}\int_{-1}^{+1}d\xi e^{i\omega\xi}(1-\xi^2)^{-\frac{1}{2}}, \quad (2)$$

[$J_0(\omega)$ being the Bessel function of order 0], we get

$$2A+1=\int_0^\infty d\omega J_0(\omega)[J_0(\tfrac{1}{3}\alpha\omega)]^3. \quad (3)$$

Similarly, C^2 can be reduced to

$$C^2=\frac{1}{4}\left(\int_0^\infty d\omega J_1(\omega)J_1(\tfrac{1}{3}\alpha\omega)[J_0(\tfrac{1}{3}\alpha\omega)]^2\right)^2,$$

so that

$$C=-\frac{1}{2}\int_0^\infty d\omega J_1(\omega)J_1(\tfrac{1}{3}\alpha\omega)[J_0(\tfrac{1}{3}\alpha\omega)]^2. \quad (4)$$

These integrals have been computed with the aid of the digital computer in the Department of Applied Mathematics of the Swiss Federal Institute of Technology to which I am deeply indebted for its help. Numerical values are listed in Table I.

* Now at the Department of Theoretical Physics, University of Liverpool, Liverpool, England.
[1] R. Kubo, Revs. Modern Phys. **25**, 344 (1953).

Photoelectric Studies of Iron*

ALVIN B. CARDWELL
Kansas State College, Manhattan, Kansas
(Received June 15, 1953)

Studies of the photoelectric properties of spectroscopically pure, carefully outgassed iron were made through a wide temperature range, including the $\alpha \rightarrow \beta$ and $\beta \rightarrow \gamma$ transformation points. Interesting changes in the slope of the temperature-photoelectric current curves for the various monochromatic radiations are shown. Analyses of the data by Fowler's method at different temperatures indicate that the change in photoelectric sensitivity, to be associated with the allotropic states of iron, is explainable more on a change in the number density of free electrons and the transition-probability factor than on a change in the surface work function. The work function of iron at room temperature was found to be 4.70 electron-volts. The variation of the work function for the three allotropic forms α, β, and γ is only 0.10 electron-volt.

I. INTRODUCTION

INTERESTING changes, associated with crystallographic and/or magnetic transformation temperatures, have been observed in the photoelectric and thermionic properties of several metals.[1–5] This paper is a report on the photoelectric properties of iron at temperatures ranging from 300°K to 1243°K. Thus, the changes associated with the $\alpha \rightarrow \beta$ and $\beta \rightarrow \gamma$ transitions are observed.

II. APPARATUS AND METHOD

The experimental tube was essentially like that used by the author in studies on tantalum[6] and nickel.[5] The spectroscopically pure iron from which the specimens were fabricated was obtained from Adam Hilgar. The specimen, which in every case was 0.03 millimeter thick, 4 millimeters wide, and 14 centimeters long, was suspended in the form of a loop in a molybdenum collecting cylinder. Iron tabs on the collecting cylinder made possible the rotation of the cylinder by means of an external magnetic field. Thus, the evaporation of iron onto the windows of the glass envelope could be prevented during long outgassing periods.

Photoelectric currents were produced by the radiation from a quartz-enclosed mercury arc dispersed by a Bausch and Lomb quartz monochromator. A quartz lens was used to focus the radiation, through a thin quartz window and a hole in the collecting cylinder, onto the iron specimen. Relative intensities of the spectral lines were determined by use of an eight-junction bismuth-silver vacuum thermopile.

Photoelectric currents were determined by measuring the potential drop across a fixed high resistor. A circuit utilizing a Western Electric D-96475 tube was used for this measurement. Proper electrostatic shielding was provided for the experimental and electrometer tubes.

Temperatures in the upper range were determined by an optical pyrometer of the disappearing filament type focused onto the specimen through a thin optically flat Pyrex window and a hole in the collecting cylinder. Temperature observations were corrected for emissivity according to the data of Wahlin and Wright.[7] Lower temperatures were determined graphically by interpolation between room temperature and temperatures in the optical pyrometer range. A curve of temperature *versus* heating current through the specimen made this possible.

The vacuum system used in connection with the experimental tube consisted of a three-stage silicone fluid water-cooled diffusion pump, a liquid-air trap, a type VG-1A ionization manometer, and a mechanical pump. With this system final pressures of the order of 10^{-8} millimeter of mercury were obtained.

Each sample studied was subjected to essentially the same long tedious outgassing process. First, the entire tube and ionization manometer were baked at 500°C

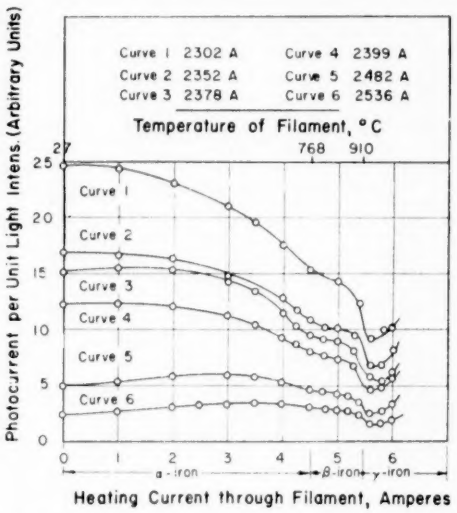

FIG. 1. Variation of photocurrent from iron with temperature.

* This work was generously supported by a Frederick Cottrell grant from the Research Corporation.

[1] Alvin B. Cardwell, Proc. Natl. Acad. Sci. U. S. **14**, 438 (1928)
[2] A. Goetz, Phys. Rev. **33**, 373 (1929).
[3] Alvin B. Cardwell, Phys. Rev. **38**, 2032 (1931).
[4] H. B. Wahlin, Phys. Rev. **61**, 509 (1942).
[5] Alvin B. Cardwell, Phys. Rev. **76**, 125 (1949).
[6] Alvin B. Cardwell, Phys. Rev. **38**, 2041 (1931).
[7] H. B. Wahlin and R. Wright, J. Appl. Phys. **13**, 40 (1942).

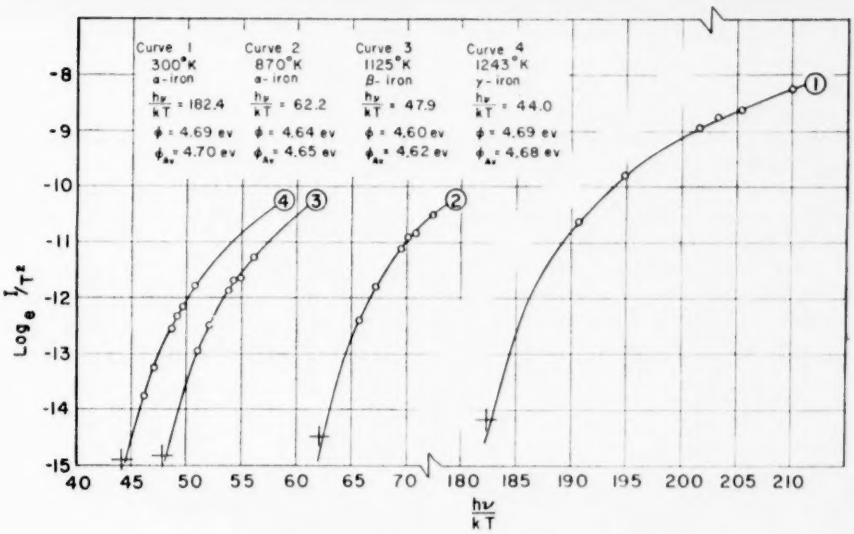

FIG. 2. Analysis of photoelectric observations by Fowler's method.

for several days. During the latter part of this period the specimen was heated by a conduction current to a temperature of approximately 800°C. Following this the iron sample was heated at temperatures which were slowly increased to 1200°C. Periodically the collecting cylinder was heated by high-frequency induction to a temperature of about 900°C. Heat treatment of this nature for 40 to 60 days produced iron samples which yielded stable reproducible results. It is therefore hoped that data presented below are characteristic of pure gas-free iron.

III. RESULTS

The variation of the photoelectric current per unit light intensity with temperature for various monochromatic wavelengths is shown in Fig. 1. As it was impossible to use the optical pyrometer for determining temperatures below 875°C, the photocurrent in Fig. 1 has been plotted as a function of the heating current through the iron specimen at the time the observation was made. The temperatures corresponding to three heating currents are indicated in the figure. Because of the large background thermionic emission, measurements of the photocurrent at temperatures higher than those indicated in the curves have not been made.

It is seen from Fig. 1 that the variation of the photocurrent with temperature for each of the monochromatic radiations is quite complex and does not follow the pattern required for a given metal by Fowler's theory.[8] It seems natural to consider associating this unique variation in photoelectric sensitivity with the transition from α to β iron at 768°C (Curie temperature), which involves a slight increase in the edge of unit cube but no change in crystal form, and the change at 910°C, where the crystal structure changes from a body-centered cubic to a face-centered cubic type. Such an association is reasonable in view of the discontinuities of electrical conductivity, thermal expansion, and secondary emission observed by Masumoto[9] and Hayakawa[10] at allotropic points in both nickel and iron. Changes analogous to those reported in this paper have been observed in the thermionic and/or photoelectric properties of tin,[2] cobalt,[3] and nickel[5] as these metals pass through temperatures at which allotropic changes occur.

Further interesting studies of these data may be made from their analysis by the Fowler method.[8] For any fixed temperature one is justified in making Fowler plots, and such sample plots for four temperatures are shown in Fig. 2. The choice of these temperatures provides for comparison two curves for α iron, one for β iron, and one for γ iron. The origin of the theoretical curve required to bring the experimental curve into coincidence with the theoretical curve is indicated by the large plus sign in each case. The work functions Φ shown on the figure were computed from the horizontal shifts $h\nu/kT$ required to bring the experimental and theoretical curves into coincidence. The average value of the work function Φ_{Au}, determined from 32 runs at each temperature on 4 different samples, is also shown in each case.

The percentage change in the value of the work function for iron in the α, β, and γ forms is small and only partially accounts for the change in the photoelectric sensitivity. The value 4.70 ± 0.01 (standard deviation) electron volts for the photoelectric work function ob-

[8] R. H. Fowler, Phys. Rev. **38**, 45 (1931).

[9] H. Masumoto, Sci. Repts. Tôhoku Univ. **15**, 449 (1926).

[10] K. Hayakawa, Sci. Repts. Tôhoku Univ. **22**, 934 (1933).

tained at room temperature agrees well with the value 4.77 and 4.72 electron volts obtained by Glasoe[11] and Cardwell,[1] respectively, at room temperature. Wahlin's[4] values 4.21 and 4.48 ev, determined thermionically for β and γ iron, respectively, do not agree with the corresponding values 4.62 and 4.68 ev reported in this work. No satisfactory explanation of this disagreement is evident.

As in the case of nickel,[5] it should be noted that the magnitudes of the vertical shifts required to bring the experimental curves into coincidence with the theoretical curve are not the same for all temperatures. The photocurrent in each case was measured in the same units. In a normal case with no allotropic change involved, no vertical shift occurs. According to Fowler's theory, such a shift indicates a change in the probability factor. Hence, the vertical shift in the case of iron indicates a change in both the number density of free electrons and the transition probability factor for these electrons. Whether the latter is characteristic of the metal itself or is produced by a changed equilibrium condition of a gaseous layer on the surface is a question which can be answered only when marked advances in present vacuum techniques are developed.

The writer wishes to express his indebtedness to Mr. Robert St. John whose services were valuable during the first year of the experimental work.

[11] G. N. Glasoe, Phys. Rev. **38**, 1490 (1931).

PHYSICAL REVIEW VOLUME 92, NUMBER 3 NOVEMBER 1, 1953

Solid-State Absorption Spectra of Mg and MgO †

JOHN R. TOWNSEND*
Department of Physics, Cornell University, Ithaca, New York
(Received June 24, 1953)

Linear absorption coefficients have been determined for Mg and MgO for wavelengths from 80A to 350A. The results for Mg have indicated values range from 1.8×10^4 to 12×10^4 cm^{-1}. These values are in reasonable agreement with those extrapolated from the region of the K absorption edge. Surface effects were eliminated by plotting transmission against foil thickness. MgO exhibits three absorption bands in this spectral region. These bands have been tentatively identified and discussed in relation to earlier emission data of O'Bryan and Skinner. A gap of about 4 ev is found to exist between the top filled level and the proposed conduction band.

INTRODUCTION

USING a method similar to that described by Tomboulian and Pell,[1] the photon absorption by magnesium and magnesium oxide has been studied experimentally in the wavelength region near the magnesium $L_{2,3}$ edges. The electronic configuration of Mg, which results in two $3s$ electrons, makes the distribution of electronic energy states in the metal of particular interest. This arises from the prediction based on a nonoverlapping band structure that this metal should be an insulator. Since the energy band arising from the $3s$ atomic states is filled, no electronic conduction would be expected.

The absorption by the metal in this wavelength region (from 80A to 350A) has been measured by O'Bryan and Skinner.[2] Apparent trouble with surface contaminants, however, made absolute measurement of the absorption coefficients very difficult. The present work on Mg was therefore undertaken to eliminate or correct for surface effects and to seek absolute values for the absorption coefficients. The work on MgO absorption was intended as a supplement to emission work done by O'Bryan and Skinner.[3] Also it enabled a comparison to be made between the absorption spectrum for Mg when in a conductor and in an insulator. Since MgO contamination of the Mg films was anticipated, it was hoped a means of correcting for this would also come from the MgO study.

EXPERIMENTAL

The source of radiation was of the condensed spark discharge type described by Tomboulian and Pell.[1] A concave glass grating with a 1.5-meter radius of curvature was used at an angle of incidence of about 85°. Slit widths of 0.05 to 0.10 mm were used.

Absorber foils of Mg were formed by evaporation in a vacuum of less than 10^{-5} mm Hg as determined by a McLeod gauge. A liquid N_2 trap was used between the gauge and evaporation bell jar. A small disk of Mg was heated in an open graphite crucible on which was wound a tungsten heater coil. The evaporated Mg was condensed on a microscope slide coated with zapon plastic. To minimize the absorption effects of the zapon, the slide then was immersed in amyl acetate to free

† Based on the authors thesis presented in partial fulfillment of the requirements for the Ph.D. degree at Cornell University, September, 1951.

* Present address: Hanford Atomic Products Operation, General Electric Company, Richland, Washington.

[1] D. H. Tomboulian and E. M. Pell, Phys. Rev. **83**, 1196 (1951).

[2] H. M. O'Bryan and H. W. B. Skinner, Proc. Roy. Soc. (London) **A162**, 49 (1937).

[3] H. M. O'Bryan and H. W. B. Skinner, Proc. Roy. Soc. (London) **A176**, 229 (1940).

the evaporated film from its backing. The resulting films were bright and metallic showing no discolorations. The unbacked Mg foils were then mounted on fine-wire open-mesh nickel screening.

Absorber thicknesses were determined by assuming the foil density to be that of bulk Mg. Determination of weight/cm² of foils for a given amount of evaporated Mg gave the foil thickness per gram of evaporated Mg. When this ratio was measured for films of thickness 3×10^{-4} cm or more, values agreed to within 5 percent. When attempted for foils thinner than this, weighing from 50 to 100 micrograms, the scatter was greater but the average value was consistent with that obtained from the thick foils. This indicated that the use of a single ratio for all thicknesses was justified, provided the evaporation geometry remained fixed. The measured foil thicknesses were in agreement with values calculated for a point source evaporating over a solid angle determined by the crucible depth and diameter.

MgO foils were prepared by heating the unbacked Mg foils supported on the nickel screen to 600°C for 5 minutes in a hydrogen furnace with a small amount of water vapor. If the furnace was left on for several hours prior to treatment, the residual water vapor was removed and the Mg foil passed the treatment apparently unchanged. If then a few drops of water were introduced along with the sample, the foil was rapidly converted to a transparent, brittle material. Since heats of combustion predict that Mg will replace the hydrogen in water with a large evolution of heat, this film is undoubtedly MgO. The formation of the hydroxide is prevented by the high temperature. Use of a desiccator and prompt mounting in the vacuum spectrometer, at pressures of 10^{-4} mm Hg or less, also served to prevent formation of the hydroxide.

The photographic methods were similar to those of the earlier paper[1] with the exception that each plate consisted of three spectra. Two of these were taken with no absorber and were used to calibrate the plate as described by Skinner and Johnston.[4] Each plate was

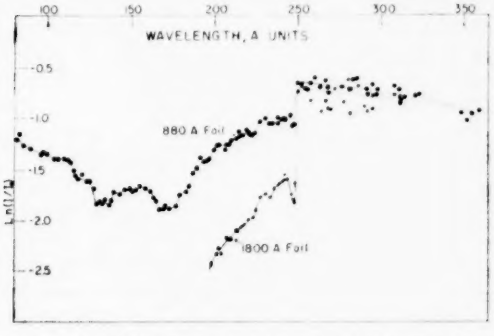

FIG. 1. $\ln(I/I_0)$ as a function of wavelength for two Mg foils of thickness 880A and 1800A.

[4] H. W. B. Skinner and J. E. Johnston, Proc. Roy. Soc. (London) **A161**, 420 (1937).

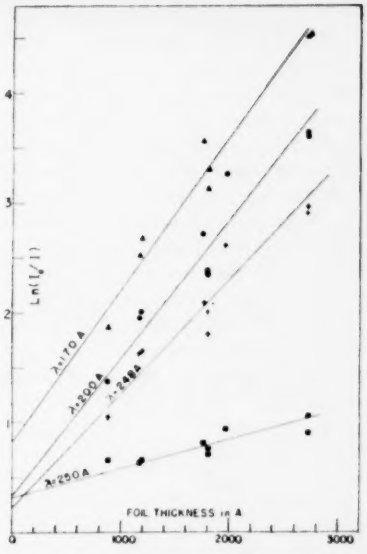

FIG. 2. $\ln(I_0/I)$ as a function of Mg foil thickness at several wavelengths.

internally calibrated and a third spectrum was that transmitted by the absorber. Appreciable changes in the calibration curves were recorded and seem to indicate the presence of the Eberhard effect.[5] These plates were not utilized for the data given in the following.

The location of the L absorption edges in Mg can be predicted in the following way. The $L_{2,3}$ edges can be found from the relation: $\nu_K=\nu_{K_\alpha}+\nu_L$, where ν_K is the K absorption-edge frequency, ν_{K_α} is the K_α emission frequency, and ν_L is the $L_{2,3}$ absorption-edge frequency. Data obtained by Wetterblad and Ase[6] for Mg give the result $\lambda_L=251$A. The separation of L_2 and L_3 absorption edges can be found from the usual spin doublet formula. This gives $\lambda_{L_3}-\lambda_{L_2}=1.19$A. The position of the L_1 edge can be predicted on the basis of observations made on the $L_{2,3}\rightarrow L_1$ transition in Mg.[7] This data places the L_1 absorption edge at 140A.

RESULTS

Magnesium

Figure 1 gives the $\ln(I/I_0)$ curves for two typical samples with thicknesses of 880A and 1800A. I_0 is the incident intensity and I is the intensity transmitted by the absorber. One such curve is obtained from each photographic plate; the curves shown are averages of two and four plates for the 880A- and the 1800A-foil, respectively. To check on the consistency of such curves

[5] Harrison, Lord, and Loofbourow, *Practical Spectroscopy* (Prentice-Hall, Inc., New York, 1948).

[6] T. Wetterblad (Mg. K emission), Z. Physik. **42**, 603 (1927); Ase (Mg K absorption edge), Reported in Siegbahn, *Spektroskopie der Röntgenstrahlen* (1931).

[7] D. H. Tomboulian and W. M. Cady, Phys. Rev. **59**, 422 (1941).

for various thicknesses and to eliminate surface effects, the curves shown in Fig. 2 were plotted giving $\ln(I_0/I)$ *versus* thickness for several wavelengths. If a fraction C of the incident radiation is absorbed or reflected by the surface layers, then the data should follow the relation $\ln(I_0/I)=\mu x-\ln C$. This linear relation is borne out to within the rather appreciable experimental error. The ordinates are averages of from two to four plates while the foil thicknesses were determined but once. As individual ordinate determinations were good to within 5 percent while foil thickness was determined to within 10 percent, the ordinate values were used as the independent variable in determining the least square lines for the various wavelengths.

Figure 3 shows values of μ calculated from the slopes of curves similar to those in Fig. 2 for 12 different wavelengths.

As a further check on the data's consistency, the magnitude of the change in $\ln(I_0/I)$ at the $L_{2,3}$ edge was plotted against foil thickness as shown in Fig. 4. This change was measured between wavelengths of 250A and 248A. The presence of this sudden increase in the absorption coefficient depends upon the Mg being

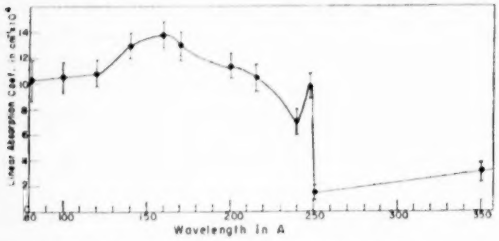

FIG. 3. Linear absorption coefficient for Mg as a function of wavelength.

in a metallic state with a Fermi level having a large density of empty energy levels just above it. If a thickness d of the deposited Mg was converted to a nonmetallic state such as MgO, then the data of Fig. 4 should yield a straight line whose slope is the change in the absorption coefficient between 250A and 248A and whose x axis intercept is equal to d. As for Fig. 2 the ordinate of Fig. 4 should be more reliable than the sample thickness. Thus a least-squares line was drawn using the ordinate values as the independent variable. The slope of the line gives a value for the change in μ of $(8.26\pm0.65)\times10^4$ cm^{-1}, while d was found to be 218 $\pm$134A. The errors quoted are probable errors calculated from the data.

As a final check on surface contamination, a foil was prepared and left on the zapon backing. Aside from a general increase in absorption, this had the effect of increasing the dip observed in Fig. 1 at a wavelength of 170A.

Magnesium Oxide

Magnesium oxide absorption was measured for three films. These were formed by oxidizing Mg foils whose

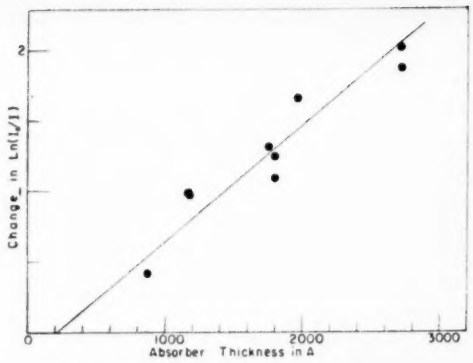

FIG. 4. The change in absorption of Mg foils at the $L_{2,3}$ absorption edge as a function of measured foil thickness.

measured thicknesses were 1450A, 2200A, and 2670A. No evidence of surface effects or surface contamination was found, for $\ln(I_0/I)$ was directly proportional to the thickness in the three cases. Figure 5 gives the values of $\ln(I_0/I)$ for the MgO film formed from the 2200A Mg foil. By assuming the densities of the Mg and MgO foils to be the same as for the bulk materials, one can find the thickness of the MgO film formed by oxidizing a Mg film of known thickness. This gives a thickness of 1710A for the MgO absorber considered in Fig. 5. Values of the linear absorption coefficient can be obtained from Fig. 5 by multiplying the ordinate by 6.15 $\times10^4$ cm^{-1}. All prominent features of the curve were found on all three foils. This includes the almost atomic-like absorption at 215A, the details of the band structure, and the absorption band of smaller magnitude near 100A.

DISCUSSION

Magnesium

The present study confirms the general properties of Mg absorption observed by O'Bryan and Skinner,[2] but differs in some details. The absorption maximum near 170A exhibits more fine structure and is not so large as reported in the earlier work. There is a clear indication that this maximum arises from some type of zapon-Mg interface as described by Tomboulian and Pell in the case of aluminum. Figure 2 shows the slopes of the curves for the 200A and 170A data to be nearly identical indicating equal Mg absorption coefficients even though the 170A absorption is always greater at any thickness. The 170A absorption must therefore contain an appreciable contribution from a surface layer. Also, leaving the zapon backing on increased the magnitude of this absorption maximum. The earlier report estimated that the change in μ at the $L_{2,3}$ edge was 1.8×10^4 cm^{-1}. This disagrees with the present value of 8.3×10^4 cm^{-1}. The discrepancy could arise if the earlier work was done with absorbers having a larger amount of Mg converted to some nonmetallic state.

The 880A curve in Fig. 1 shows a marked increase in absorption at a wavelength of 140A where the L_1 edge should be observed. The magnitude of the absorption change there is about $\frac{1}{3}$ that of the $L_{2,3}$ edge which is what would be expected on the basis of the statistical weights. Though five foils gave an indication of this edge, it remains doubtful as to whether it is a surface effect, fine structure from the $L_{2,3}$ edge or the L_1 edge.

The x intercept of Fig. 4 represents how much of the measured foil thickness has been converted to some nonmetallic state. As given above, the least square value obtained was 218A but it was found to have a large probable error of 134A. The large uncertainty in the intercept is felt to arise almost entirely from insufficient accuracy in the foil thickness determinations. Using more precise thickness measurements this method should be useful in the study of the formation of nonmetallic compounds on metals. As an example, the change in the absorption edge jump would enable one to study the surface oxidation of a metallic foil as a function of time and temperature.

In Fig. 6 are shown the available data on the K and L absorption coefficients for Mg metal. For wavelengths less than the K edge, Allen's data is plotted.[8] For wavelengths above the K edge Stobbe's theory[9] agreed well with data available for aluminum absorption just above the K edge, so good agreement would be expected here as well. As was the case for aluminum L absorption,[1] the extrapolation of the shorter wavelength curve falls somewhat above the observed L absorption in the case of Mg.

Magnesium Oxide

Magnesium oxide has a crystal structure similar to that of NaCl with a Mg-O separation of 2.10A. From the normal chemical valences of Mg and O one would anticipate that the compound consisted of doubly charged ions. Calculation of the electron affinity of O^{--} in the MgO lattice by the Born ionic model or the Born-Mayer equation for ionic solids assuming the metal ion to be doubly charged yields a value in fair agreement with values calculated similarly from CaO, SrO, and BaO.[10] However, an indication that other than ionic bonding is also present comes from the failure in the Cauchy relation between the elastic constants.[11] Thus the lattice most likely consists of ions nearly doubly charged with a small amount of nonradial interaction.

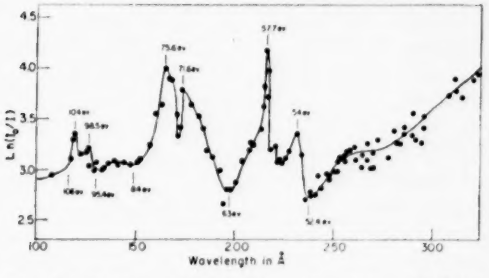

FIG. 5. $\ln(I_0/I)$ as a function of wavelength for a MgO foil formed by oxidizing a 2200A-Mg foil.

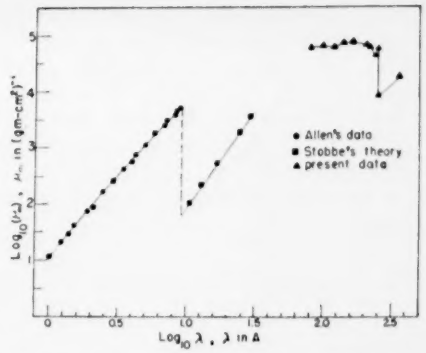

FIG. 6. Mg mass absorption coefficient as a function of wavelength near the K and L absorption edges.

The absorption spectrum of MgO as shown in Fig. 5 consists of three absorption bands for the wavelength region studied. The band with a threshold energy at 52 ev is believed to arise from the electronic transition from the $L_{2,3}$ shell to the conduction band. The band whose threshold is near 95 ev is then identified as arising from an L_1 shell electron being excited to the conduction band. The observed difference in the threshold energies of about 43 ev agrees within the uncertainty of the threshold determinations with the $L_{2,3}-L_1$ energy separation found by Tomboulian and Cady. The band widths appear comparable and absorption magnitudes differ by a factor of about 3 as expected from the statistical weights of the two shells. If one ascribes the structure seen between 52 ev and 82 ev to the density of conduction band energy levels alone, it is seen that a nearly forbidden range of energies is present at 12 ev above the lowest empty level. Also there is an indication of splitting each of the wider bands into two by a depression in the density of states.

These interpretations of the absorption spectrum are in conflict with the emission spectrum as obtained by O'Bryan and Skinner[3] and interpreted by Mott and Gurney.[12] The emission data as interpreted would place the top filled band of levels (the O^{--} $2p$ states) in the energy range from 50 ev to 60 ev above the Mg^{++} $L_{2,3}$ (or $2p$) states. This in turn implies the present absorption band with an average energy of 58 ev results in

[8] E. U. Compton and S. K. Allison, *X-Rays in Theory and Experiment* (D. Van Nostrand Company, Inc., New York, 1935), Appendix IX.

[9] H. Hall, Revs. Modern Phys. **8**, 358 (1936).

[10] F. Seitz, *Modern Theory of Solids* (McGraw-Hill Book Company, Inc., New York, 1942), p. 89.

[11] M. A. Durand, Phys. Rev. **50**, 449 (1936).

[12] N. F. Mott and R. W. Gurney, *Electronic Processes in Ionic Crystals* (Oxford University Press, London, 1940), p. 76.

the Mg^{++} $2p$ electrons being excited to levels already occupied by the O^{--} $2p$ electrons. This conflict arises from the double emission bands observed by O'Bryan and Skinner. If their lower energy peak is taken as arising from the direct transition from the filled band to the Mg^{++} $2p$ state, then the filled band occupies the energies from 38 ev to 48 ev above the Mg^{++} $2p$ state leaving a gap of about 4 ev between the filled and empty bands.

This interpretation of the emission data leaves unexplained the high-energy emission band observed by O'Bryan and Skinner. This, however, seems a smaller shortcoming than the overlap between filled and empty levels which results from Mott and Gurney's interpretation when applied to the present absorption data. It may be noted in this regard that the emission studies were carried out under conditions of electron bombardment which resulted in aluminum oxide being decomposed to

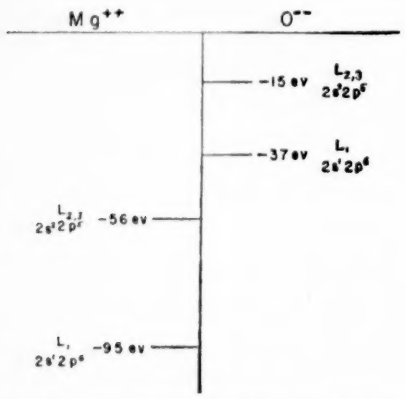

FIG. 7. An approximate electronic energy level scheme for MgO giving the levels of the isolated doubly charged ions after shifting them by an amount equal to the Madelung potential (see F. Seitz, reference 13).

leave a visible deposit of aluminum metal. If similar partial decomposition of the MgO occurred, the possibility of singly charged Mg ions being present would offer a lower lying energy level which would explain the high-energy emission band.

The absorption band interpretation given here gains support from the type of energy level diagram suggested by Seitz.[10] A purely ionic type of lattice is assumed and the energy levels of the Mg^{++} and O^{--} ions are found for the isolated states. Shifting these ionic levels by the Madelung potential, whose magnitude is 24 ev in MgO, we get an estimate of the positions of the energy bands in the solid. The levels are shown in Fig. 7 after shifting the Mg^{++} levels upward and the O^{--} levels downward by the Madelung potential.

The energy level of the O^{--} $2s2p^6$ excited ionic state was not known, so estimates were made which place it between -10.4 ev and -17.7 ev. The first estimate used the neon L_1 absorption edge[13] to determine an effective screening constant for the L shell of a 10 electron atom. The screening of the $2p$ electrons in the case of O^{--} will be smaller than in the case of neon and hence the use of neon's screening constant gives too large an energy. The other estimate utilized the ionization potential of neutral oxygen, *viz.*, 13.6 ev, and the extension of the screening doublet law down to oxygen. This predicts an L_1 ionization potential of 28.6 ev. To then estimate the screening of the two extra $2p$ electrons in O^{--}, a charge of $2e$ was considered as a spherical shell of 1.32A in radius as given by Goldschmidt.[14] This raises the electronic potential energy inside the sphere by 10.9 ev giving for the state in question an ionization potential of 17.7 ev. This is too low an estimate, for the $2p$ electrons will shield somewhat inside the L shell as well as outside it. An average value of -13 ev was thus taken for this level. The O^{--} $2s^22p^5$ level is given by Seitz[10] on the basis of the Born cycle. The Mg^{++} $2s^22p^5$ level is a spectroscopic one[15] and the Mg^{++} $2s^12p^6$ level is taken as 39 ev lower as found by Tomboulian and Cady for Mg metal. The Mg and O K levels are at -1300 ev and -500 ev, respectively, and do not concern us here.

The levels as plotted will be greatly broadened by perturbations from nearby atoms in the solid, but the levels should give approximately the mean energies of the bands involved. If the bottom of the conduction band is taken as the zero of energy, a negligible electron affinity is implied and this has been done. From this tentative level diagram one sees that a mean energy of 56 ev is expected for the Mg $L_{2,3}$→conduction band transition and 95 ev for the Mg L_1→conduction band. These numbers agree quite well with the observed values of 58 ev and 100 ev. Also a mean energy of 41 ev for the emission band O $L_{2,3}$→Mg $L_{2,3}$ is seen to agree with the mean energy of 43 ev given by the low-energy emission peak observed by O'Bryan and Skinner. It appears at present that photoconductivity experiments would be fruitful in identifying more clearly the absorption band corresponding to the conduction band and hence identifying which of the emission bands is to be the fundamental one.

The author wishes to express his deep gratitude for the continual guidance and encouragement given him by Professor D. H. Tomboulian who suggested the work on magnesium absorption. Also gratefully acknowledged are discussions with Professor J. A. Krumhansl regarding interpretation of the MgO results and the use of the microphotometer equipment made possible by Dr. G. W. Gartlein.

[13] R. F. Bacher and S. A. Goudsmit, *Atomic Energy States* (McGraw-Hill Book Company, Inc., New York, 1932).
[14] V. M. Goldschmidt, Chem. Ber. **60**, 1263 (1927).
[15] C. E. Moore, Natl. Bur. Standards (U. S.) Circular 467, U. S. Government Printing Office, Washington, D. C. (1949).

The Intermediate State of a Hollow Superconducting Tin Cylinder*†

J. GITTLEMAN‡
Rutgers University, New Brunswick, New Jersey
(Received July 8, 1953)

Small bismuth probes were used to measure the magnetic field inside and outside a long, hollow, thin-walled superconducting cylinder, both as a function of the applied field and as a function of the angular position of the probes. From the variation of the magnetic field the structure of the cylinder in the intermediate state was inferred. It would appear that with the onset of the intermediate state "windows" are formed at the poles of the cylinder. These "windows," through which the applied magnetic field can penetrate into the interior of the cylinder, probably consist of the usual rapidly alternating layers of normal and superconducting metal. The parts of the cylinder around the equator remain wholly superconducting until the applied field becomes equal to the critical field, at which time the entire cylinder becomes normal.

The intermediate state for the particular cylinder used in this experiment begins to appear at about $0.3H_c$ instead of at $0.5H_c$. It will be shown in a subsequent paper that this value is a function of the ratio of the inner and outside radii of the hollow cylinder.

1. INTRODUCTION

A LONG, solid metal cylinder in the superconducting state, when placed in a uniform magnetic field parallel to its axis, will remain in the superconducting state as long as the applied field is less than the critical value, H_c. When the applied field becomes equal to H_c the entire cylinder immediately goes into the normal state and remains in this state for all larger fields.[1] If, however, the cylinder is placed in a uniform magnetic field which is transverse to its axis, the transition from the superconducting state to the normal state becomes complicated. Instead of changing into the normal state at once, the cylinder first goes into the so-called intermediate state, since with the above geometry the magnetic field is not constant over the surface of the superconductor because of the magnetization of the cylinder.

A large amount of work has been done on the intermediate state of uniformly magnetized superconductors, particularly the solid sphere and the solid cylinder.[2–11] The results of this work may be summarized as follows: In the superconducting state, the magnetic field at the surface of the cylinder varies from zero at the two poles to a maximum at the two equators. (This statement specifies what we mean by the poles and equators.) As the applied field is increased the field at the equators reaches the critical value before the field at any other point. When this occurs the whole body goes into an intermediate state, breaking up into a uniform distribution of small regions of superconducting metal and normal metal, in such a way that the average field inside the metal is everywhere equal to the critical value and is in the direction of the applied field. The superconductor remains in this state until the applied field equals H_c. For applied fields equal to or greater than H_c the entire superconductor is in the normal state.

A further step in the understanding of the intermediate state would be to investigate the field distribution around a superconductor whose geometry is such that it is not uniformly magnetized when placed in a uniform magnetic field. The simplest geometry of this type, experimentally, is the hollow circular cylinder.

The experiment to be described consists of measurements of the magnetic field distribution around the outer and inner surfaces of a hollow tin cylinder placed in a uniform magnetic field transverse to the axis of the cylinder. The experimental results show that the structure of the intermediate state, in the case of the hollow cylinder, is by no means uniform; that while the regions around the poles are in the usual intermediate state, the regions around the equator remain superconducting until the entire body goes into the normal state.

We shall show that the assumption of a homogeneous intermediate state throughout the body is in contradiction to the magnetostatic boundary conditions at the inner and outer surfaces of the cylinder. We shall also demonstrate that the observed results are in accord with these boundary conditions.

The magnetic field begins to penetrate into the bulk of our sample at applied fields of about $0.3H_c$ instead of $0.5H_c$ as would be expected for the cylindrical symmetry. Serin, Gittleman, and Lynton[12] have demon-

* Based on a Ph.D. thesis submitted to the Graduate Faculty of Rutgers University.

† This work has been supported by a joint program of the U. S. Office of Naval Research, the Rutgers University Research Council, and the Radio Corporation of America.

‡ Present address: Franklin Institute, 20th and Parkway, Philadelphia, Pennsylvania.

[1] D. Shoenberg, *Superconductivity* (Cambridge University Press, Cambridge, 1938), Chaps. I and II.

[2] W. J. de Haas and M. J. Casimir-Jonker, Physica **1**, 291 (1933).

[3] C. J. Gorter and H. G. B. Casimir, Physica **1**, 305 (1933).

[4] W. J. de Haas and O. A. Guinau, Communs. Kamerlingh Onnes Lab. Univ. Leiden **241a**; **247e**.

[5] R. Peierls, Proc. Roy. Soc. (London) **A155**, 613 (1936).

[6] F. London, Physica **3**, 450 (1936).

[7] D. Shoenberg, Proc. Roy. Soc. (London) **A155**, 712 (1936).

[8] L. Landau, J. Phys. U.S.S.R. **7**, 99 (1943).

[9] E. R. Andrew, Proc. Roy. Soc. (London) **A194**, 98 (1948).

[10] A. Shalnikov, J. Phys. U.S.S.R. **9**, 202 (1945).

[11] A. Meshkovski and A. Shalnikov, J. Phys. U.S.S.R. **11**, 1 (1947).

[12] Serin, Gittleman, and Lynton, following paper, Phys. Rev. **92**, 566 (1953).

strated that this effect is a real one. They have shown that the value of magnetic field at which the penetration into the hollow cylinder takes place depends on the ratio of the inner diameter to the outer diameter.

2. EXPERIMENTAL DETAILS

The cylinder used in these experiments was made from spectroscopically pure tin (99.998 percent) supplied by Johnson-Matthey and Company. The sample was cast in a brass cylinder with a steel drill rod fitted through the center to form the inner surface. It was necessary to machine the inner and outer surfaces to obtain the proper dimensions. The cylinder was 4.79 inches long. The inside diameter was 0.580 inch and the outside diameter was 0.674 inch. No attempt was made to grow the sample into a single crystal.

A schematic representation of the arrangement inside the cryostat is shown in Fig. 1. *B* and *C* represent two sets of clamps which held the field measuring probes. The nature of these probes will be described later. A pair of leads was connected to each probe and brought up out of the cryostat through the shaft *G* to the detecting apparatus. This shaft also provided a means of positioning the probes or driving them at constant speed around the sample.

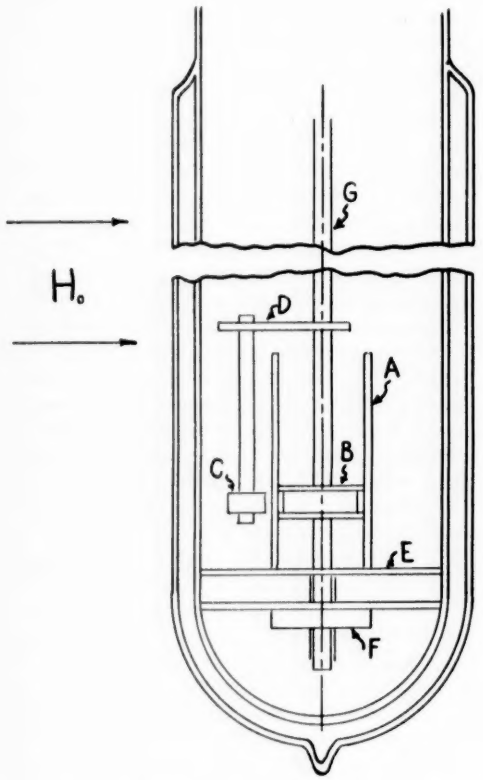

FIG. 1. The arrangement inside the cryostat. *A* = sample; *B* = inner probe; *C* = outer probe; *D* = clamp; *E* = sample mount; *F* = heater; *G* = driveshaft; H_0 = applied field direction.

The field measuring apparatus consisted of two bismuth probes, one for the inside surface of the cylinder and one for the outside surface. The effective dimensions of the probes were about 60 microns in length and 60 microns in diameter. The proper diameter was obtained by drawing the bismuth into wire while in soft glass. The glass was then etched off with hydrofluoric acid. The length was obtained in the following way. The clamps, which had the dual purpose of holding the bismuth in place and of providing electrical connections to the probes, were insulated by means of a single layer of Cellophane tape which also provided the proper spacing.

The strength of the magnetic field was obtained by measuring the electrical resistance of the bismuth probes in the field and calibrating the probes in known fields, making use of the well-known fact that at low temperatures the magnetoresistance in bismuth is very large.[2,4]

The detecting apparatus consisted of a Wheatstone bridge which was excited at 213 cps. The output of the bridge was amplified and detected, and the detected signal was measured by a Brown recording potentiometer. Figure 2 shows a block diagram of the apparatus. With this arrangement it was possible not only to measure the magnetic field at various points as a function of the applied field; but also, for a given applied field, to make continuous measurements of field as a function of the angular position of the probes around the cylinder.

The probes were calibrated at various temperatures. The results are plotted in Fig. 3. As can be seen from the figure, the sensitivity of the probes was independent of temperature in the helium range; thus it was possible to calibrate the probes at temperatures above the critical temperature of tin.

The magnetic field was provided by a large pair of Helmholtz coils, the field at the center of the coils being 27.6 oersted/amp.

The runs can be classified into two categories, static runs and dynamic runs. The static runs were made by placing a probe at the desired location and plotting the change in the probe resistance as a function of the applied magnetic field. The applied field was varied in convenient steps from zero up to a value greater than

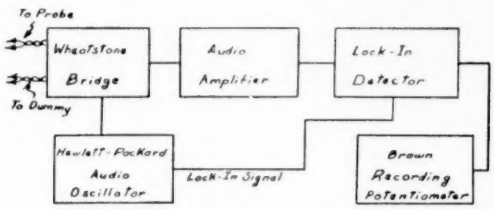

FIG. 2. The detecting apparatus.

the critical field value, H_c. Repetition of a run could not be made without first warming the sample to a temperature greater than the critical temperature because when the applied field was reduced to zero the cylinder retained a large magnetic moment. This "freezing in" of flux in multiply-connected bodies is well known.[1]

The procedure for the dynamic runs was the same as for the static runs with one exception. Instead of the probe being fixed at a single position, it was driven, by means of a synchronous motor, around the surface of the sample.

Since the chart of the Brown recording potentiometer is also run by a synchronous motor, we obtained in this way a plot of the magnetic field at the inner and outer surfaces as a function of the angular position of the probes.

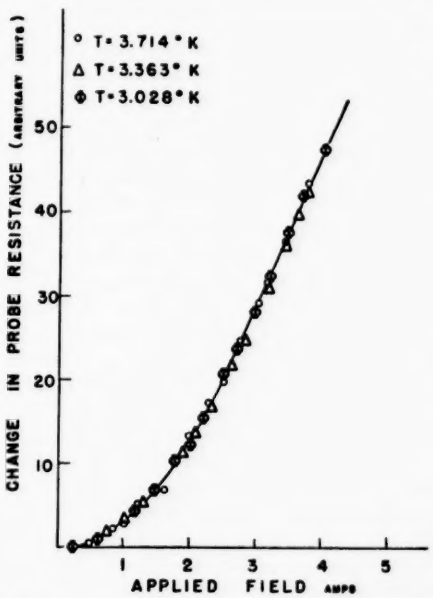

FIG. 3. Calibration of the bismuth probes at various temperatures.

3. EXPERIMENTAL RESULTS

Figure 4 shows typical results obtained from the dynamic runs. The superconducting state is characterized by an absence of magnetic field in the interior and a field at the outer surface whose magnitude varies as the sine of the polar angle.

When the cylinder goes into the intermediate state, the curves show that there is a broad region around the poles within which the magnitude of the magnetic field is constant and approximately equal to the applied field. We call this region the "window." For magnetic fields greater than about 1.8 amp[13] the angular width of this region was roughly constant and equal to about 110°. This corresponded quite closely to the angle subtended at the outer surface by a pair of parallel tangents to the inner surface of the cylinder.

[13] The critical field corresponded to 3.62 amp.

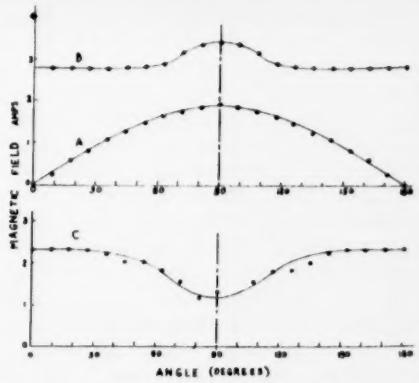

FIG. 4. Typical results of measurements of the magnetic field as a function of the angular position of the probe. A = outside probe; sample in the superconducting state. B = outside probe; sample in the intermediate state. C = inside probe; sample in the intermediate state.

At the outer equators the magnetic field is at all times greater than the applied field whereas, at the inner equators, the field is considerably less than the applied field. At high fields (approaching the critical value) the field at the inner equator becomes slightly greater than the applied magnetic field (see Fig. 5).

Figure 5 shows the magnetic field at the outer and inner equators as a function of the applied field. Figure 6 shows similar curves for the outer and inner poles.

The magnetic field distribution, before penetration, is clearly the same as that for a perfect diamagnet. The field at the inner and the outer poles is zero, whereas the field at the outer equator increases linearly with the applied magnetic field. The slope of this part of the curve is 1.94 rather than the expected 2.00 because the probe was located not at the surface of the cylinder but about 0.01 inch from it.

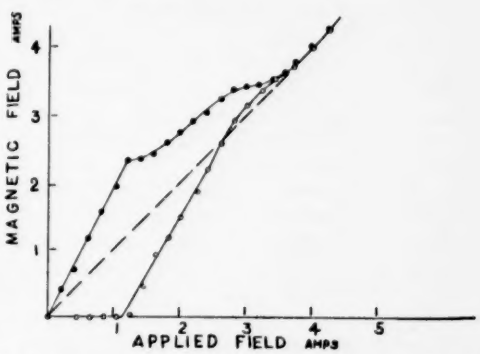

FIG. 5. The magnetic field at the equator as a function of the applied field. Open circles = inside cylinder. Solid circles = outside cylinder.

Time effects were observed throughout the intermediate state. That is to say, measurable times were required for the magnetic fields at the surfaces of the sample to stop changing when the applied field was changed. The longest observed times were of the order of ten minutes; these occurred when the applied field was in the neighborhood of those values for which penetration first begins to take place.

When the applied field was reduced in steps from values greater than H_c to zero, pronounced hysteresis was observed at all positions. In fact, hysteresis curves were obtained by cycling the applied field from H_c to $-H_c$ and back. This state of affairs is due to the setting up of persistent currents around isolated regions of normal conductor as the applied field is reduced from H_c, thus "freezing in" flux and giving rise to a residual magnetic moment. Experimental studies of time effects and hysteresis were made by Babiskin[14] for the hollow sphere. In this paper we make no attempt to interpret the time effects or hysteresis but concern ourselves only with the initial transition from the virgin superconducting phase to the normal phase in increasing magnetic field.

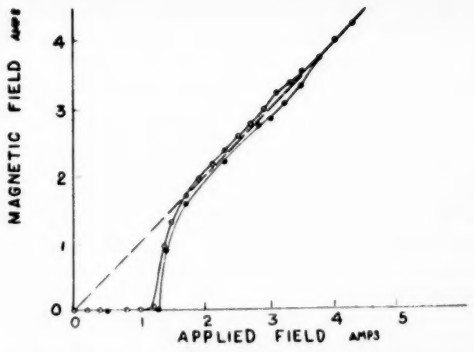

FIG. 6. The magnetic field at the pole as a function of the applied field. Open circles = inside cylinder. Solid circles = outside cylinder.

4. THE STRUCTURE OF THE INTERMEDIATE STATE

We shall now attempt to infer the structure of the intermediate state of the sample by studying the field distribution after penetration takes place. We note that when the field penetrates into the cylinder, a window is formed around the poles. The magnetic fields adjacent to the inner and outer surfaces of the window are approximately equal to the applied field. A hasty guess as to the structure of the tin composing the window would be that it is in the normal state. This is both unsatisfactory and unnecessary. It is unsatisfactory because it requires that a large amount of tin be in the normal state in the presence of a magnetic field which is much less than the critical value. That it is unnecessary can be seen in the following way. Since the wall thickness of the cylinder is small compared with the diameter,[15] the windows will appear to the field as a wall which is long compared to its thickness. In the case of such a wall, one obtains for the magnetic field distribution in the intermediate state: $B=H=H_0$ outside the wall, and $H=H_c$, $B=H_0$ within the walls for H_0 less than H_c, H_0 being the applied field. Thus we conclude that the structure in the window is that of the ordinary intermediate state.

There are several facts which lead us to believe that the regions around the equators, not included in the windows, remain substantially in the superconducting state until the applied field attains the value H_c. First, the field at the outside equator remains greater than the applied field for all values less than H_c. Second, in contrast to the field at the inside pole, the field at the inside equators remains appreciably less than the applied field for a large fraction of the transition. This indicates that this point is being shielded by a large concentration of superconducting metal near the equator. The fact that the field eventually exceeds the applied field indicates that the superconducting region is shrinking about the equator with increasing applied field. The third indication is that the magnetic field at the outside pole is slightly less than the applied field whereas the magnetic field at the inside pole is slightly greater than the applied field. If the regions at the equators are truly superconducting, then their induced magnetic moments would contribute a field which is superimposed on the applied field. This field, equivalent to the field of two line dipoles oriented antiparallel to the applied field and situated at the equators, would add to the applied field in such a way as to account for the slight deviations at the poles.

The structure of the intermediate state of a hollow superconducting cylinder, as described above, is thus quite inhomogeneous. This result is in sharp contrast to the structures observed in uniformly magnetized solid bodies. For example, H equals H_c throughout the body of a solid superconductor in the intermediate state, and it is supposed to consist of a homogeneous mixture of superconducting and normal regions. We shall now show that such a structure is not possible for a hollow cylinder.

We shall use a two-dimensional polar coordinate system, r and θ being the coordinates. Let a and b be the outer and inner radii of the cylinder; and let the applied field H_0 be in the x direction. Then the field outside the cylinder will be equal to the applied field plus a dipole term due to the magnetization of the cylinder. Thus,

$$B_r=H_r=[H_0-M/r^2]\cos\theta,$$
$$B_\theta=H_\theta=-[H_0+M/r^2]\sin\theta, \quad \text{for} \quad r\geqslant a;$$
$$B_r=H_r=H_1\cos\theta,$$
$$B_\theta=H_\theta=-H_1\sin\theta, \quad \text{for} \quad r\leqslant b;$$

[14] J. Babiskin, Phys. Rev. **85**, 104 (1952).
[15] The ratio of the wall thickness to the outer diameter is 0.07.

and

$$H_r = H_c \cos\theta,$$
$$H_\theta = -H_c \sin\theta, \quad \text{for} \quad a \gtrsim r \gtrsim b.$$

B in the walls of the cylinder must be determined so that div$B$ vanishes. Also H_1 and M must be determined from the usual boundary conditions that the tangential component of H and the normal component of B be continuous on all boundaries. Applying the boundary condition for the tangential component of H on the inner boundary, we obtain $H_1 = H_c$. Similarly, on the outer boundary, $-[H_0 + M/a^2] = -H_c$, or

$$M = [H_c - H_0]a^2.$$

Applying the boundary conditions to B, we have at $r = b$, $B_r = H_c$ and at $r = a$, $B_r = 2H_0 - H_c$.

Inside the cylinder walls B is parallel to H and thus is everywhere in the x direction. Thus, the condition div$B = 0$ reduces to $\partial B_x/\partial x = 0$, and we see that B must be independent of x. This is in obvious contradiction to the boundary conditions. Along the x axis, where it is wholly normal to the boundaries, B varies from $(2H_0 - H_c)$ on the outer boundary to H_c on the inner boundary. Thus it cannot be independent of x. The converse must also be true, that if div$B$ vanishes, the boundary conditions cannot be met. Thus we cannot expect the intermediate state of a hollow cylinder to be the same as for a solid body.

In order to determine the proper model for the intermediate state, one must calculate the Gibbs free energy for every possible magnetostatically sound model. That model which yields the least free energy is, then, the correct one. It is, however, impossible to carry out this calculation unless the precise way in which the normal regions grow is determined. Therefore, we shall not attempt to show that the suggested model of the intermediate state of a hollow cylinder is unique, but rather that it is a reasonable one.

Let us assume that the field has penetrated into the cylinder so that the cylinder is in the intermediate state. Further, to simplify the problem, we shall put the effective permeability of the sample equal to a constant μ. Then the solution of the field inside this cylinder in a uniform magnetic field H_0 for the case in which the ratio of the inner radius to the outer radius, b/a, is of the order of unity, is

$$H \simeq H_0/\mu, \quad B \simeq H_0, \text{ at the poles;}$$

and

$$H \simeq H_0, \quad B \simeq \mu H_0, \text{ at the equator.}$$

Peierls[5] has determined the conditions for the existence of the intermediate state of uniformly magnetized bodies. For these bodies B, H, and H_0 are related by $H(1-n) + Bn = H_0$, where $4\pi n$ is the demagnetizing coefficient. For the long cylinder in a longitudinal field, $n = 0$ and $H = H_0$. Peierls shows that in this case the body remains in the superconducting state until $H_0 = H_c$ and then becomes normal without an intermediate state. Comparing this with the observations at the equators, we see that it is reasonable that the equators remain in the superconducting state until the applied field reaches the critical value.

For a flat wall transverse to the field, $n = 1$ and $B = H_0$. Peierls has shown that in this case the body goes into the intermediate state for any H_0, however small, and that $H = H_c$ inside. Here, again, comparing this with the results at the poles, we see that the model based on our observations is a reasonable one.

Thus Fig. 7 gives a rough sketch of the inferred structure. This sketch should not, of course, be taken too literally since the determination of the normal-superconducting boundaries was, of course, impossible. We must also remark that the above structure probably only appears in hollow cylinders for which the wall thickness is small compared with the diameter. As the wall gets thicker, the structure undoubtedly approaches the usual structure for a solid cylinder.

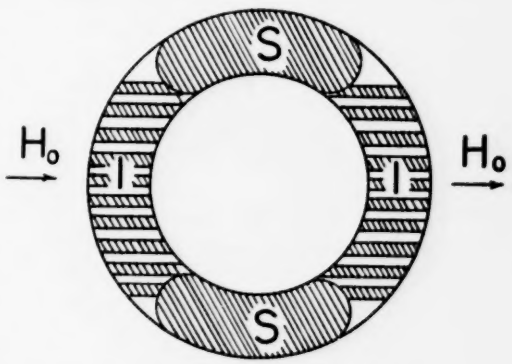

FIG. 7. The schematic representation of the inferred structure of the intermediate state of a hollow cylinder.

An interesting, but unexpected, result of the experiment was that the transition from the superconducting state to the intermediate state took place not when the applied field was one-half of the critical value but rather when it was approximately one-third of the critical value. This effect is discussed in the paper[12] following this one.

I would like to take this opportunity to thank those members of the Rutgers University Physics Department who have given me invaluable aid in this work. I would like to thank Dr. B. Serin, who suggested this problem and who advised me throughout this work, and Dr. P. R. Weiss, Dr. C. A. Reynolds, and Mr. S. Brooks for their interesting and inspiring discussions. I would also like to thank Mr. R. Campbell, Mr. J. Teza, and Mr. A. Siemons for their aid and advice in the design and construction of the apparatus.

The Transition into the Intermediate State of Hollow Superconducting Cylinders*

B. SERIN, J. GITTLEMAN,† AND E. A. LYNTON
Rutgers University, New Brunswick, New Jersey
(Received July 8, 1953)

The transition from the superconducting to the intermediate state has been investigated for hollow tin cylinders with various ratios of inner to outer radii. Thermodynamic arguments show that for values of this ratio greater than $(2^{\frac{1}{2}}/2)$ the free energy in the normal state becomes less than that in the superconducting state at applied fields less than one half the critical field. The experimental results indeed show that for ratios of inner to outer radii greater than $(2^{\frac{1}{2}}/2)$ the intermediate state begins to appear at less than one-half the critical field, whereas for smaller ratios the intermediate field appears at one-half the critical field.

1. INTRODUCTION

IT has been pointed out in the previous paper by Gittleman[1] that according to Peierls[2] the transition from the superconducting to the intermediate state for a cylinder should occur at an applied field H_0 equal to one-half the critical field H_c. In the work described in the previous paper, however, it was found that for the particular hollow cylinder used, this transition occurred at $H_0=0.34H_c$ rather than $H_0=0.50H_c$. In the present paper we shall show that this behavior follows from requirements of thermodynamic equilibrium, and shall report on further measurements in support of this theory.

2. THERMODYNAMIC CONSIDERATIONS

In order to work out a complete thermodynamic theory, at a given temperature, one should compare at each field value the free energies of the superconducting state, the intermediate state, and the normal state. The most stable state will be that one which has the smallest free energy. However, the calculation of the free energy of the intermediate state is very difficult, and depends somewhat on the details of the model one uses. We shall show that it is possible to gain considerable insight into the behavior of the hollow cylinder by considering only the free energies of the superconducting state and the normal state, and that one can in fact account qualitatively for Gittleman's result and our more extensive experiments. We now proceed with this more restricted program.

One can write the first law of thermodynamics for the body as follows:

$$TdS=dU+IdH_0,$$

where T is the absolute temperature, S the entropy, U the internal energy, H_0 the applied field, and I the *total* magnetic moment of the sample.[3] Then the Helmholtz free energy becomes

$$F=f_0(T)V-\int_0^{H_0} IdH_0,$$

where $f_0(T)$ is the free energy per unit volume in the absence of a magnetic field, and V is the volume of the superconductor.

Denoting by the subscripts n and s, respectively, the normal and the superconducting states, and putting

$$f_{0n}-f_{0s}=H_c^2/8\pi,$$

where H_c is the critical field value at temperature T, the difference between the total free energy in the normal state and that in the superconducting state for a *solid* cylinder of volume V becomes

$$F_n-F_s=[H_c^2/8\pi-H_0^2/4\pi]V,$$

when H_0 is transverse to the axis of the cylinder. Accordingly, $F_n=F_s$ when

$$H_0=H_c/\sqrt{2}>H_c/2.$$

For H_0 less than $H_c/\sqrt{2}$, F_n is greater than F_s, and for H_0 greater than $H_c/\sqrt{2}$, F_n is less than F_s. As at any value of the applied field H_0 the equilibrium state of the sample is that for which the free energy has its smallest value, the transition from the superconducting to the normal state *in the absence of an intermediate state* would occur at $H_0=H_c/\sqrt{2}$. The intermediate state does exist, however, indicating that the free energy of this intermediate state must become less than that of the superconducting state at an applied field less than $H_c/\sqrt{2}$. For the solid cylinder this occurs at $H_c/2$.[2]

For a *hollow* cylinder of volume V_H the difference in free energies between the normal and superconducting states is

$$F_n-F_s=[H_c^2V_H/8\pi-H_0^2V_s/4\pi], \quad (1)$$

where V_s is the volume of a solid cylinder having the same outer radius as the hollow one. Thus, it can be seen that the magnetic part of the free energy difference $(H_0^2V_s/4\pi)$ is independent of the size of the hole,

* This work has been supported by the joint program of the U. S. Office of Naval Research and the Rutgers University Research Council, and by the Radio Corporation of America.
† Present address: Franklin Institute, 20th and Parkway, Philadelphia, Pennsylvania.
[1] J. Gittleman, preceding paper [Phys. Rev. **92**, 561 (1953)].
[2] R. Peierls, Proc. Roy. Soc. (London) **A155**, 613 (1936).
[3] Considerable confusion exists in the literature concerning the proper expression for the magnetic part of the free energy. The thermodynamic variables used above are the proper ones for our problem, and we use the expression for the free energy given by E. C. Stoner, Phil. Mag. **23**, 833 (1937), which we have convinced ourselves is correct.

whereas the temperature dependent part $(H_c^2V_H/8\pi)$ becomes smaller with increasing inner radius. Hence, at a given temperature, the larger the inside radius, the smaller will be that H_0 for which $F_n=F_s$, and for all value of this inside radius $F_n=F_s$ for $H_0<H_c/\sqrt{2}$.

For sufficiently small values of the inner radius, however, $F_n=F_s$ for values of the applied field still greater than $H_c/2$, the value at which the intermediate state begins to occur. For such thick-walled hollow cylinders, therefore, the transition to the intermediate state still occurs at $H_0=H_c/2$. But beyond a certain value of the inner radius, the value of the applied field at which $F_n=F_s$ becomes less than $H_c/2$, and so one can expect that for such thin-walled cylinders the intermediate state should begin to appear at $H_0<H_c/2$, the critical value of H_0 being dependent on the size of the inner radius.

To show this dependence more clearly one can rewrite Eq. (1) in the form

$$F_n-F_s=\left[\frac{H_c^2}{8\pi}-\frac{H_0^2}{4\pi}\left(\frac{a^2}{a^2-b^2}\right)\right]V_H,$$

where a and b are respectively the outer and inner radii of the hollow cylinder.

When $F_n=F_s$, one sees that

$$2(H_{0e}/H_c)^2=1-(b/a)^2,$$

where H_{0e} is the applied field for which $F_n=F_s$. Figure 1 is a plot of $\sqrt{2}H_0/H_c$ *vs* b/a. ABC is the locus of points for which $F_n=F_s$. When the cylinder is solid, i.e., $b=0$, $\sqrt{2}H_{0e}/H_c=1$, when $b\to a$, $\sqrt{2}H_{0e}/H_c\to 0$. For $b/a<\sqrt{2}/2$, $\sqrt{2}H_{0e}/H_c>\sqrt{2}/2$; in other words, $H_{0e}>H_c/2$. For cylinders with $b/a<0.707$, hence, one would expect the inception of the intermediate state to occur for $H_0=H_c/2$, and the point for such cylinders should be along DB. For $b/a>\sqrt{2}/2$, $H_{0e}<H_c/2$, and for these ratios one would expect the points to fall a little below the curve BC. That is to say, we reason that if at a given applied field less than $H_c/2$, the normal state has a lower free energy than the superconducting state, then we expect that an intermediate state can almost certainly exist at a somewhat smaller field value.

3. EXPERIMENTAL DETAILS AND RESULTS

As in the experiments described by Gittleman,[1] bismuth probes were used to measure the magnetic field. As we were primarily interested only in the value of the field at which it begins to penetrate into the superconducting cylinder, only one probe was used and this was placed at the outer equator of the cylinder. This probe consisted of a bismuth wire about 3 cm long, held closely to the surface of the cylinder by being placed in a groove scratched in a lucite holder which fitted snugly around the cylinder. Thin copper wires were brought to the ends of the probe by means of additional grooves and these wires, as well as the probe, were kept in place by small drops of Duco cement. Electrical contact between the wires and the probe was obtained by painting their points of contact with conducting silver paint.

The detecting apparatus was that described by Gittleman,[1] and the same method was used to calibrate the bismuth probes. Similar also was the preparation of the hollow cylinders. They were cast from spectroscopically pure tin obtained from Johnson-Matthey and Company. The thickest cylinder (Sample I) was made simply by machining off the casing of the mold, leaving in place its brass core. For the next three wall thicknesses (Samples II, III, and IV) the brass core was pushed out, and the inside diameter of the tin cylinder was successively reamed out to the required value. A new casting was made for the thinnest cylinder (Sample V), and in this case again the core of the mold (here made of copper) was kept inside the cylinder, and the outside diameter machined to the required value.

For each cylinder, the general variation of the magnetic field at the outer equator is the same. As the applied field is increased (all measurements were performed with increasing field), the measured field initially increases linearly with the applied field. The slope of this increase should be two; since the probes were some small distance from the cylinder surface, the observed slopes are about 1.9. At a certain value of the applied field this linear increase of the equator field changes abruptly. At this point the magnetic field begins to penetrate into the hollow cylinder through the 'window' at the poles,[1] so that the field at the outside equator no longer increases twice as fast as the applied field. The manner of the further variation of the equator field will be discussed presently.

The points on Fig. 1 show the observed values of $\sqrt{2}H_0/H_c$ as a function of b/a, the ratio of inner to outer radii of the cylinder. H_0 is the applied field at which the increase of the equator field changes abruptly, and hence also the field at which penetration of the cylinder first occurs and the intermediate state begins. H_c is the

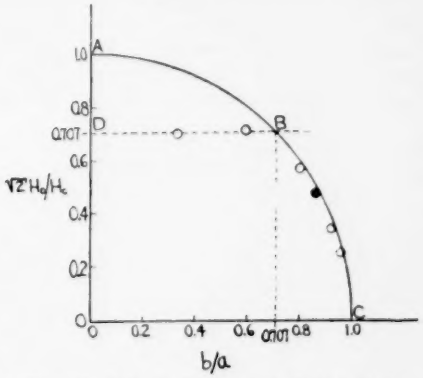

FIG. 1. The ratio of the applied magnetic field at which penetration begins to the critical field is plotted as a function of the ratio of inner to outer radii. The solid point was measured by Gittleman.

critical field at the temperature of the measurement; in all cases this temperature was about 2.61°K with a critical field corresponding to 5.3 amperes of coil current.

The points in Fig. 1 show that, as predicted above, the intermediate state begins at $H_0=H_c/2$, i.e., $\sqrt{2}H_0/H_c=\sqrt{2}/2$, for $b/a<\sqrt{2}/2$. For $b/a>\sqrt{2}/2$, the free energies of the normal and superconducting states become equal at smaller applied fields, and here, as expected, the experimental points fall just below curve *BC*.

Figure 2 is a composite of the variation of equator field with applied field for the different samples. In all cases there is an initial increase in the observed field with slope nearly equal to two, followed by a sharp break. The subsequent behavior, however, varies in different samples.

In Sample I (largest wall thickness), while the sample was in the intermediate state, the observed field at the equator remained constant even though the applied field was changed, until the latter reached the critical value after which the observed field was equal to the applied field for all large field values. In this sample all time effects were negligible, in the sense that when the applied field was changed, the observed field followed (or did not follow) in a time comparable to the time constant of our detecting apparatus, which was a few seconds. Thus, as far as we can tell, this sample behaved in all respects like a solid cylinder, at least in increasing field. Beginning with Sample II, upon reaching the intermediate state, the time effects became of the order of minutes, and the observed field showed a characteristic "overshoot" behavior. That is to say, when the applied field was increased, the observed field initially increased also, and then slowly decayed to an equilibrium value. Generally speaking in the subsequent samples, this irreversible behavior became more pronounced and occurred over a larger range of values of the applied field, with the resulting more complicated form of the curves in Fig. 2. In Fig. 2 we have plotted the equilibrium values of the observed field.

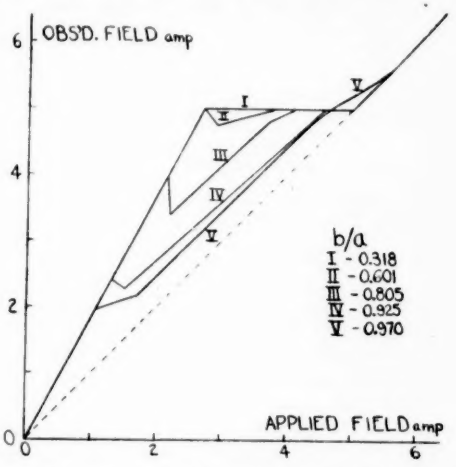

FIG. 2. The magnetic field observed at the equator is plotted as a function of the applied field for the various samples. The dashed line has a slope of one.

4. DISCUSSION

It should be noted that in Sec. 2, we have compared the *total* free energies of the body in the normal and superconducting phases. However, Gorter and Casimir[4] have proved that if one considers an infinitesimal volume in the superconducting phase, then this volume will become normal only if the field at its surface equals the critical value. In the case of an infinitely long cylinder, this will occur when the applied field is equal to or greater than half of the critical value, independently of whether the cylinder is solid or hollow. However, despite the proof just quoted, the cylinders in these experiments do attain the state of lowest total free energy, in which normal regions are present in applied fields appreciably less than $H_c/2$. The question raised by this contradiction can be broken into two separate parts. We may first ask how nuclei of normal metal[5] form in fields less than the critical value; secondly, given some nuclei, we may inquire how they grow into the final equilibrium state. The first question is easily answered; in our experiments we had finite cylinders which therefore had sharp corners at their ends, so that the field at the ends most probably exceeded the critical value and thus provided a source of nuclei. The second question we cannot at present answer.

We must remark, however, that we would expect that in a hollow sphere at the surface of which there are no places where the field can be locally quite large, there would be great likelihood of superheating because of the difficulty of nucleation. That is to say, one can show using the methods of Sec. 2, that in a hollow sphere, when $b/a>0.69$, the normal state has a lower free energy than the superconducting state for applied fields less than $\frac{2}{3}H_c$, corresponding to a field at the equator less than H_c. However, due to the difficulty of nucleation, we think it most probable that the spherical sample would not attain the state of lowest total free energy, but would superheat until the applied field was equal to $\frac{2}{3}H_c$. This conclusion is supported by the work of Babiskin[6] on a hollow lead sphere, for which $b/a=0.814$. Babiskin did not observe penetration until the applied field slightly exceeded $\frac{2}{3}H_c$.

In conclusion, it gives us great pleasure to thank Mr. A. Siemons for his technical assistance and Dr. P. R. Weiss for many helpful discussions.

[4] C. J. Gorter and H. G. B. Casimir, Physica **1**, 305 (1933).

[5] The problem involved in nucleation above should not be confused with recent examples in which nucleation was governed by surface energy, e.g., M. Garfunkel and B. Serin, Phys. Rev. **85**, 834 (1952). Here, nuclei are unstable because their volume free energy is too large.

[6] J. Babiskin, Phys. Rev. **85**, 104 (1952).

The Evaluation of Lattice Sums for Cubic Crystals

J. HOVE* AND J. A. KRUMHANSL
Cornell University, Ithaca, New York

(Received May 8, 1953; revised manuscript received August 3, 1953)

A method is presented of evaluating the sums which arise in calculating the total long-range interaction energy between a semi-infinite crystal and a particle placed above its surface. For example, if the particle is an ion and the crystal is polarizable, this method facilitates the calculation of the polarization and Van der Waal's energies. It is pointed out that many calculations within a solid can be reduced to a combination of cases each of which is of the above type. As an illustration, we obtain the total interaction at an interior lattice point for a simple-cubic structure with an individual atom-pair interaction of λr^{-n}.

I. INTRODUCTION

IN many problems which occur in the physics of solids, it is necessary to perform sums over the lattice sites of long-range central force interactions. One such problem is that of calculating the binding energy per ion pair of an ionic crystal, which can be assumed to be three-dimensionally infinite. In this case, the point at which the interaction energy is desired is located at a lattice site and the procedure is somewhat simplified. These sums have been worked out by Madelung and Ewald[1] for the Coulomb interaction energy using a potential method and by Jones and Ingham[2] for any interactions which can be represented by inverse powers (greater than 3) of the center distance. It is of some interest to note from the results of Jones and Ingham that a direct summation over the lattice sites becomes very inconvenient if good accuracy is desired. For example, for an inverse power of 4, a direct summation over the nearest 500 atom sites is in error by about 25 percent, while an error of 6 percent or less requires a sum over at least 4000 of the nearest atom sites.

If the point at which the interaction energy is to be evaluated is not a lattice site, the evaluation of such sums does not appear to have been so thoughly treated, except for the Coulomb potential. These calculations within a solid can be reduced to a combination of cases for each of which the point where the interaction energy is desired is an arbitrary distance above a principal surface of a semi-infinite crystal, so we shall discuss this latter problem, which is, of course, interesting in its own right. The Coulomb interaction between an ion above the (100) surface of an ionic crystal was first evaluated by Lennard-Jones and Dent,[3] using the potential method of Madelung. However, interactions involving higher inverse powers of the distance seem to have been evaluated by direct summation over a large number of sites and integration over the remainder of the crystal, a rather tedious and often unsatisfactory method. Since such interactions are frequently quite important, especially for highly polarizable materials, it appears that a better method of treating these sums would be useful.

In this note, the authors propose to outline a rather simple transformation whereby series of λr^{-n} (and other central force) interactions can usually be made to converge more rapidly. For illustration of the application of our method some of the results of Jones and Ingham[2] are obtained.

II. SUMMING METHOD

We consider a semi-infinite perfect single crystal and, although we will soon specialize to a cubic crystal, we will be more general at first. We define the crystal space vectors as

$$\mathbf{r}=x_1\mathbf{a}_1+x_2\mathbf{a}_2+x_3\mathbf{a}_3=\mathbf{y}+x_3\mathbf{a}_3,$$

where $\mathbf{y}$ is in the plane of the surface and $\mathbf{a}_3$ pointing inward (not necessarily normal to the surface plane). The position vector of any unit cell is

$$\mathbf{r}_l=l_1\mathbf{a}_1+l_2\mathbf{a}_2+l_3\mathbf{a}_3=\mathbf{y}_\lambda+l_3\mathbf{a}_3,$$

where $l_1l_2l_3$ are integers, and the position vector of an atom within the unit cell is

$$\mathbf{r}_s=x_1{}^s\mathbf{a}_1+x_2{}^s\mathbf{a}_2+x_3{}^s\mathbf{a}_3=\mathbf{y}_\sigma+x_3{}^s\mathbf{a}_3.$$

The crystal space vector of the kth atom is thus $\mathbf{r}_k=\mathbf{r}_l+\mathbf{r}_s$.

We also define the general reciprocal space vector as

$$\mathbf{h}=p_1\mathbf{b}_1+p_2\mathbf{b}_2+p_3\mathbf{b}_3=\mathbf{p}+p_3\mathbf{b}_3,$$

and the reciprocal lattice vector as

$$\mathbf{h}_m=m_1\mathbf{b}_1+m_2\mathbf{b}_2+m_3\mathbf{b}_3=\mathbf{p}_\mu+m_3\mathbf{b}_3,$$

where $m_1m_2m_3$ are integers. From its definition, $\mathbf{b}_3$ is normal to the crystal surface, but the plane formed by $\mathbf{b}_1$ and $\mathbf{b}_2$ is, in general, inclined to the crystal surface.

Let the interaction energy between a particle at the position $\mathbf{r}$ (above the surface) and the kth atom at $\mathbf{r}_k$ in a crystal be $\epsilon(|\mathbf{r}-\mathbf{r}_k|)$, i.e., an arbitrary function but with no angular dependence. The total interaction

* Now at Atomic Energy Research Department, North American Aviation, Inc., Downey, California.

[1] E. Madelung, Physik. Z. Sowjetunion **19**, 524 (1918); P. P. Ewald, Ann. Physik **64**, 253 (1921). For a review see, for example, M. Born and M. Göppert-Mayer, *Handbuch der Physik* (Verlag. Julius Springer, Berlin, 1933), Vol. 24, p. 623.

[2] J. E. Jones and A. E. Ingham, Proc. Roy. Soc. (London) **A107**, 636 (1925).

[3] J. E. Lennard-Jones and B. M. Dent, Trans. Faraday Soc. **24**, 92 (1928).

energy between this atom and the crystal is then

$$\phi(\mathbf{r})=\sum_k \epsilon(|\mathbf{r}-\mathbf{r}_k|)=\sum_l \sum_s \epsilon(|\mathbf{r}-\mathbf{r}_l-\mathbf{r}_s|). \quad (1)$$

The sum over l means all values of l_1 and l_2 but only $l_3 \geq 0$. Thus $\phi(r)$ is periodic in x_1 and x_2 with period unity and may be expanded in the double Fourier series

$$\phi(\mathbf{r})=\sigma_A^{-1} \sum_\mu \psi_{\mathbf{p}_\mu}(x_3) \exp(2\pi i \mathbf{p}_\mu \cdot \mathbf{y}), \quad (2)$$

where σ_A is the unit cell surface area $|\mathbf{a}_1 \times \mathbf{a}_2|$ in a plane $x_3=$ constant. Then

$$\psi_{\mathbf{p}_\mu}(x_3)=\int_{\sigma_A} d_2\mathbf{y}\phi(\mathbf{r}) \exp(-2\pi i \mathbf{p}_\mu \cdot \mathbf{y}), \quad (3)$$

where $d_2\mathbf{y}=|\mathbf{a}_1 \times \mathbf{a}_2| dx_1 dx_2$ is the element of surface area. Substituting from (1),

$$\psi_{\mathbf{p}_\mu}(x_3)=\sum_{\lambda,l_3} \sum_s \int_{\sigma_A} d_2\mathbf{y}[\exp(-2\pi i \mathbf{p}_\mu \cdot \mathbf{y})] \times \epsilon\{|\mathbf{y}-\mathbf{y}_\lambda-\mathbf{y}_\sigma+\mathbf{a}_3(x_3-l_3-x_3^s)|\}$$

$$=\sum_{l_3} \sum_s \sum_\lambda \{\exp[-2\pi i \mathbf{p}_\mu \cdot (\mathbf{y}_\lambda+\mathbf{y}_\sigma)]\} \times \int_{\sigma_A} d_2\mathbf{y}\{\exp[-2\pi i \mathbf{p}_\mu \cdot (\mathbf{y}-\mathbf{y}_\lambda-\mathbf{y}_\sigma)]\} \times \epsilon\{|\mathbf{y}-\mathbf{y}_\lambda-\mathbf{y}_\sigma+\mathbf{a}_3(x_3-l_3-x_3^s)|\}.$$

Noting that $\exp(-2\pi i \mathbf{p}_\mu \cdot \mathbf{y}_\lambda)=1$ and that summing over λ is then equivalent to extending the integration over the entire surface $x_3=$ constant, we finally obtain

$$\phi(\mathbf{r})=\sigma_A^{-1} \sum_\mu [\exp(2\pi i \mathbf{p}_\mu \cdot \mathbf{y})] \sum_{l_3} \sum_s [\exp(-2\pi i \mathbf{p}_\mu \cdot \mathbf{y}_\sigma)] \times \int_A d_2\mathbf{t}\epsilon\{|\mathbf{t}+\mathbf{a}_3(x_3-l_3-x_3^s)|\} \exp(-2\pi i \mathbf{p}_\mu \cdot \mathbf{t}), \quad (4)$$

where $\mathbf{t}=\mathbf{a}_1\xi_1+\mathbf{a}_2\xi_2$ is a dummy variable and the integration is over the entire surface A. In the particular case of the Coulomb potential, the ψ_{00} term diverges and must be considered separately by a limiting technique such as that of Ewald and Juretschke.[4] This term is the average Coulomb potential and is zero in a neutral cubic structure. It may be noted in passing that the above is a logical extension to two dimensions of the usual Poisson sum formula.[5]

For cubic lattices with $|\mathbf{a}_1|=|\mathbf{a}_2|=|\mathbf{a}_3|=a$ and with a (100) surface, we obtain (where μ stands for the pair of integers $m_1 m_2$), for a simple cubic,

$$\phi(\mathbf{r})=\sum_\mu \{\exp[2\pi i(m_1 x_1+m_2 x_2)]\} \sum_{l_3=0}^{\infty} E_{\mu, l_3}(0); \quad (5)$$

and for a face-centered cubic with basis

$$\left[0\,0\,0;\ \frac{a}{2}\frac{a}{2}0;\ \frac{a}{2}0\frac{a}{2};\ 0\frac{a}{2}\frac{a}{2}\right],$$

we obtain

$$\phi(\mathbf{r})=2\sum_{l_3=0}^{\infty}\Bigg\{\sum_{\substack{m_1 m_2 \\ \text{even}}} \{\exp[2\pi i(m_1 x_1+m_2 x_2)]\} \times [E_{\mu, l_3}(0)+E_{\mu, l_3}(\tfrac{1}{2})] + \sum_{\substack{m_1 m_2 \\ \text{odd}}} \{\exp[2\pi i(m_1 x_1+m_2 x_2)]\} \times [E_{\mu, l_3}(0)-E_{\mu, l_3}(\tfrac{1}{2})]\Bigg\}, \quad (6)$$

where

$$E_{\mu, l_3}(x_3^s)=\int_{-\infty}^{\infty}\int_{-\infty}^{\infty} d\xi_1 d\xi_2 \epsilon\{a[\xi_1^2+\xi_2^2+(z+l_3+x_3^s)^2]^{\frac{1}{2}}\} \times \exp[-2\pi i(m_1\xi_1+m_2\xi_2)].$$

Here $z=-x_3$ is the normal distance of the particle above the surface and this is valid only for $z \geq 0$. Note that $E_{\mu, 0}(0)$ is the double Fourier transform of the individual energy and can frequently be obtained from tables such as those of Foster and Campbell.[6] An important case is that in which $\epsilon=\lambda r^{-n}$ with n integral. For convenience we shall list in Table I some values of $E_{\mu, 0}(0)$ for such cases. To get $E_{\mu, l_3}(x_3^s)$ from these, one merely replaces z by $(z+l_3+x_3^s)$.

In Table I, K_ν is the Bessel function of the second kind for imaginary argument. For large z, K_ν is exponentially decreasing, so that the leading term in the series is the term which falls off algebraically. When z is replaced by $(z+l_3+x_3^s)$ and the sum over l_3 performed (these sums are generalized Riemann zeta functions and

TABLE I. The double Fourier transform, $E_{\mu, 0}(1)$, for an individual interaction energy $\epsilon=\lambda r^{-n}$.

n	$E_{000}(0)$	$E_{\mu, 0}(0)$
4	$\lambda a^{-4}\pi z^{-2}$	$\lambda a^{-4} 2\pi^2 (m_1^2+m_2^2)^{\frac{1}{2}} z^{-1} K_1[2\pi z(m_1^2+m_2^2)^{\frac{1}{2}}]$
5	$\lambda a^{-5} \frac{2}{3}\pi z^{-3}$	$\lambda a^{-5} \frac{2}{3}\pi z^{-3}[1+2\pi z(m_1^2+m_2^2)^{\frac{1}{2}}] \times \exp[-2\pi z(m_1^2+m_2^2)^{\frac{1}{2}}]$
6	$\lambda a^{-6} \frac{1}{2}\pi z^{-4}$	$\lambda a^{-6} \pi^3 z^{-2} (m_1^2+m_2^2) K_2[2\pi z(m_1^2+m_2^2)^{\frac{1}{2}}]$
7	$\lambda a^{-7} \frac{2}{3}\pi z^{-5}$	$\lambda a^{-7} \frac{2}{3}\pi z^{-5}[1+2\pi z(m_1^2+m_2^2)^{\frac{1}{2}} + (4/3)\pi^2 z^2 (m_1^2+m_2^2)] \times \exp[-2\pi z(m_1^2+m_2^2)^{\frac{1}{2}}]$
8	$\lambda a^{-8} \frac{1}{3}\pi z^{-6}$	$\lambda a^{-8} \frac{1}{3}\pi^4 z^{-3} (m_1^2+m_2^2)^{\frac{1}{2}} K_3[2\pi z(m_1^2+m_2^2)^{\frac{1}{2}}]$

[4] P. P. Ewald and H. Juretschke, paper presented at the National Research Council Conference on the Structure and Properties of Solid Surfaces, Lake Geneva, Wisconsin, September, 1952 (unpublished).

[5] The Poisson summation formula says that, for $f(x)$ a decent function,

$$\sum_{n=-\infty}^{\infty} f(x+n)=\sum_{m=-\infty}^{\infty} \int_{-\infty}^{\infty} f(y) \exp[2\pi i m(x-y)] dy.$$

By letting $f(x)=\exp(-\pi t x^2)$, the "Poisson identity" is obtained [see, for example, H. Bateman, *Partial Differential Equations* (Dover Publications, New York, 1944)]. It may be noted that the method presented here for a λr^{-n} interaction is analogous, in one-dimension, to Lerch's theorem given there (p. 405).

[6] G. A. Foster and R. M. Campbell, Bell Telephone System, Tech. Publs. (1942). Monograph B 584.

can be evaluated exactly; this is briefly discussed at the end of this section), this term is, of course, just the asymptotic value of ϕ for large z and essentially includes the contribution of a continuous distribution of force centers in the crystal. The advantage of the present formulation lies in the rapid decay of the coefficients E_μ with increasing μ; thus series of the form (5) and (6) converge rapidly, even if z is as small as half a lattice constant.

III. SUMMATION OVER A HALF-PLANE

In passing, we note that the same method can be applied to calculate the interaction energy at a point near the edge of a semi-infinite plane of atoms if this point is also in the plane. Consider a plane of atoms located at $x_2=0$ and extending from $x_3=0$ to infinity. In a similar fashion to the above treatment for a semi-infinite solid, we can find the interaction enery with an atom at the point x_1, $x_2=0$, $z=-x_3$. For a λr^{-n} interaction, the normal lattice sum for a square lattice with $|\mathbf{a}_1|=|\mathbf{a}_2|=a$ is

$$\phi_n(x_1, z)=\lambda a^{-n}\sum_{l=0}^{\infty}\sum_{k=-\infty}^{\infty}[(x_1-k)^2+(z+l)^2]^{-\frac{1}{2}n}, \quad (7)$$

and by the use of the present method, this may be expressed as

$$\phi_3(x_1, z)=\lambda a^{-3}\{2\sum_{l=0}^{\infty}(z+l)^{-2}+8\pi\sum_{l=0}^{\infty}\sum_{m=1}^{\infty}m(z+l)^{-1} \times\cos(2\pi m x_1)K_1[2\pi m(z+l)]\}, \quad (8)$$

$$\phi_4(x_1, z)=\lambda a^{-4}\left\{\frac{\pi}{2}\sum_{l=0}^{\infty}(z+l)^3 +\pi\sum_{l=0}^{\infty}\sum_{m=1}^{\infty}[1+2\pi m(z+l)](z+l)^{-3} \times\cos(2\pi m x_1)\exp[-2\pi m(z+l)]\right\}, \quad (9)$$

where z and x_1 are defined as before. Higher powers of n may be obtained as follows:

If we define $\phi_n{}^l$ such that

$$\phi_n(x_1, z)=\sum_{l=0}^{\infty}\phi_n{}^l,$$

we see from Eq. (7) that

$$\phi_{n+2}=-n^{-1}a^{-2}(z+l)^{-1}\partial\phi_n{}^l/\partial z,$$

and thus

$$\phi_{n+2}(x_1, z)=-n^{-1}a^{-2}\sum_{l=0}^{\infty}(z+l)^{-1}\partial\phi_n{}^l/\partial z.$$

The summation over m in (9) can be performed to give a closed form, but this is not usually convenient for computations. It should be noted that the first series in (8) and (9) are tabulated functions. The generalized Riemann zeta function

$$\zeta(z, n)=\sum_{l=0}^{\infty}(z+l)^{-n}$$

can be expressed in terms of the logarithmic derivative of the gamma function for non-negative integer values of n greater than unity.[6] Thus, if

$$\psi(z)=(d/dz)\ln\Gamma(z),$$

then

$$\zeta(z, n)=\frac{(-1)^n}{(n-1)!}\frac{d^{n-1}}{dz^{n-1}}\psi(z)$$

and the first few derivatives of ψ are tabulated.[7]

IV. EXAMPLES

1. The Coulomb interaction with a semi-infinite ionic crystal having the NaCl structure can be readily obtained from (6) since such a structure can be considered as two interlaced face-centered cubic lattices. The result is the same as that given in reference 3.

2. Lattice potentials at a lattice site in the interior of an infinite crystal.

Here we want to show briefly how sums of the type evaluated by Jones and Ingham[2] can be found by the above method. Principally this is intended to show the rate of convergence of the various series used above, since the numerical results of reference 2 are exact to within specified limits. We will consider, for simplicity, only the case of a simple cubic lattice and we want to sum terms like λr^{-n} over a three-dimensionally unbounded crystal to find the total interaction at a lattice point. For any value of n, this total interaction can be expressed as

$$\phi_n=a^{-n}A_n,$$

where A_n is a pure number. To use the above method, we break A_n up into two parts:

$$A_n=2B_n+C_n,$$

where B_n is the contribution of a semi-infinite crystal whose (100) face is a distance $z=1$ away from the lattice point in question, and C_n is the contribution from the 100 plane containing the lattice point. B_n is obtained from (5), and C_n is further broken up into

$$C_n=2D_n+F_n,$$

where D_n is from the semi-infinite plane a distance $z=1$ away [and obtained from Eqs. (7) or (8) or one of their derivatives] and F_n is from the (1,0) line contain-

[7] See E. Jahnke and F. Emde, *Tables of Functions* (Dover Publications, New York, 1945), and references therein, particularly H. T. Davis, *Tables of Higher Mathematical Functions* (Principia Press, Bloomington, 1935), Vol. 2. Note that Jahnke and Emde define ψ somewhat differently.

TABLE II. Terms in the evaluation of the total interaction at a lattice point inside an infinite crystal, for an individual interaction energy $\epsilon=\lambda r^{-n}$.

n	F_n	D_n	C_n	B_n	A_n	A_n (reference 2)
4	2.165	1.931	6.027	5.253	16.53	16.5323
5	2.074	1.510	5.094	2.643	10.38	10.3775
6	2.035	1.311	4.657	1.871	8.40	8.4019
7	2.017	1.203	4.422	1.420	7.46	7.4671
8	2.008	1.134	4.276	1.330	6.94	6.9458

ing the lattice point, F_n simply equals

$$F_n=2\sum_{s=1}^{\infty}s^{-n},$$

which is tabulated in Jahnke and Emde.[7] The results of the calculations are presented in Table II, which also includes the values given in reference 2.

All the values calculated above were obtained by using only the zero and first order terms of our series. The values given by Jahnke and Emde[7] for F_n are carried to three decimal places only. Since in addition the numerical work was done with a slide rule, the above calculated numbers are only good to two decimal places. To this accuracy, our values agree with the values of reference 2. It may be mentioned that the computations take little time to perform; for the above, the value for each n required about twenty minutes to obtain.

V. SUMMARY

A method of increasing the rate of convergence of sums of central-force interactions over a rigid cubic lattice is presented. We feel that the example considered in Sec. 3 shows that the method is convenient and practical to employ. Since the point at which the interaction energy is to be found need not necessarily be at a lattice point, it is possible, for example, to use this procedure conveniently to obtain the long-range contributions to the energy of an interstitial ion. Probably its greatest usefulness lies in the problem of evaluating the energy of atoms above the surfaces of solids, since the distance of the atom above the surface is usually great enough (about one lattice spacing) so that only the first periodic term in the series of Sec. 2 need be retained.

The Internal Friction of Rock Salt Single Crystals*

D. R. FRANKL†
Columbia University, New York, New York
(Received May 20, 1953)

The internal friction of rock salt crystals is markedly decreased by mild x-irradiation. This is interpreted as the pinning of dislocations by cation vacancies liberated from vacancy pairs on the trapping of photoelectrons. Very small applied stresses are capable of breaking the pinning points. Under some conditions, such breakage under the vibrational stress of measurement may lead to a doubly valued dependence of internal friction on strain amplitude. A variety of other phenomena occur, most of them being qualitatively explainable on the basis of damping by moving dislocations.

I. INTRODUCTION

THIS paper presents some results of a survey of the amplitude-dependent internal friction of rock salt single crystals, carried out for the purpose of comparing the mechanical dissipation in this ionic solid with that in metallic crystals.

Read[1] first proposed, based on a study of zinc crystals, that the amplitude-dependent part of the internal friction of single crystals arises from the motion of dislocations in the lattice. Numerous investigations[2] on other metals have given strong support to this hypothesis, and Koehler[3] has presented a phenomenological theory which correctly predicts the usually observed form of amplitude dependence. However, the evidence is not entirely conclusive, since the existing theoretical calculations[4] of energy dissipation by moving dislocations fail to account for the magnitude of the observed damping. For this reason, it was felt that additional experimental results would be of interest.

Previous work on mechanical dissipation in ionic crystals includes the measurements by Chatelet and Cabarat[5] on rock salt crystals of various origins and the investigation by Breckenridge[6] of the temperature dependence of the anelastic relaxation. However, these authors give no results in the higher range of strain amplitudes, which is of principal interest in the present paper.

The plastic properties, on the other hand, have been extensively investigated, and a comprehensive review is given by Schmid and Boas.[7] Of particular interest in connection with the present work are the observations that the critical shear stress for slip is markedly increased by the introduction of F centers[8] or divalent substitutional foreign cations.[9]

II. EXPERIMENTAL METHODS

A. Specimens

The specimens used in this work were synthetic single crystals obtained from the Harshaw Chemical Company, Cleveland, Ohio. Checks of the lattice perfection by back-reflection Laue patterns disclosed no discernible asterism, mosaic structure, or lineage structure. However, spectrographic analyses of crystals from the same source, reported by Duerig and Markham,[10] indicate that they may contain as much as 0.2 percent of impurity, mainly Al and Fe.

The crystals were received in rough-cut form, and were reduced to appropriate size, *viz.*, about 3 cm in length and about 3 to 5 mm square in cross section, by cutting with a fine jewelers' saw and dry grinding on abrasive paper from No. 1 through 4-0 grit. Measurements were made on eight specimens, six of them cut from a single growth at a cylinder axis orientation of about 20, 76, 76 degrees, and the other two cut from a second growth at about 29, 65, 75 degrees.

In some cases, further reduction in cross section was accomplished by etching with water, usually while the crystal was cemented to a transducer, as described below, with its ends protected by a paraffin coating which was subsequently dissolved off with benzene. The paraffin and benzene were found to have no effect on the internal friction.

When not in use, the crystals were stored in the vacuum chamber of the measuring apparatus or in a desiccator over calcium chloride, calcium sulfate, or phosphorus pentoxide. No effects of adsorbed moisture were found.

* Submitted in partial fulfillment of the requirements for the degree of Ph.D. at Columbia University. The work was supported by the Office of Ordnance Research, U. S. Army.

† Present address: Sylvania Electric Products, Inc., Physics Laboratories, Bayside, New York.

[1] T. A. Read, Phys. Rev. **58**, 371 (1940).

[2] T. A. Read, Trans. Am. Inst. Mining Met. Engrs. **143**, 30 (1941); T. A. Read and E. P. T. Tyndall, J. Appl. Phys. **17**, 713 (1946); I. H. Swift and J. E. Richardson, J. Appl. Phys. **18**, 417 (1947); C. A. Wert, J. Appl. Phys. **20**, 29 (1949); A. S. Nowick, Phys. Rev. **80**, 249 (1950); *Pittsburgh Symposium on Plastic Deformation of Crystalline Solids* (Mellon Institute, 1950); J. Marx and J. S. Koehler, *Pittsburgh Symposium*.

[3] J. S. Koehler, Chap. VII of *Imperfections in Nearly Perfect Crystals* (John Wiley and Sons, Inc., New York, 1952).

[4] G. Leibfried, Z. Physik **127**, 344 (1950); J. D. Eshelby, Proc. Roy. Soc. (London) **A197**, 396 (1950).

[5] J. Chatelet and R. Cabarat, Comp. rend. **23**, 2111 (1951).

[6] R. G. Breckenridge, Chap. VIII of reference 3.

[7] E. Schmid and W. Boas, *Plasticity of Crystals* (1935); (English translation published by F. A. Hughes and Company, Ltd., London, 1950).

[8] M. N. Podaschewsky, Phys. Z. Sowjetunion **8**, 81 (1935).

[9] W. Metag, Z. Physik **78**, 363 (1932).

[10] W. H. Duerig and J. J. Markham, Phys. Rev. **88**, 1043 (1952).

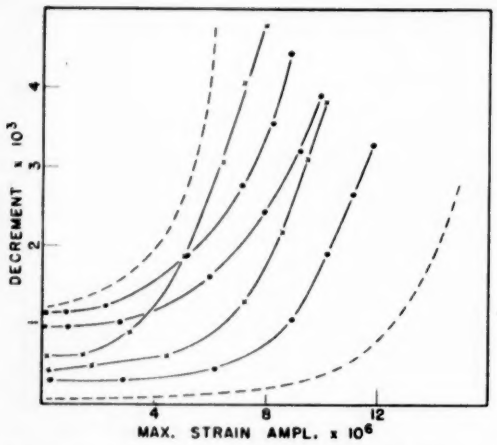

FIG. 1. Normal internal friction curves, showing the usually observed dependence of Δ on U. The solid lines are typical runs on one specimen, and the broken lines give roughly the range covered by seventy-eight runs on the eight specimens.

B. Measurements

The internal friction measurements were made by the composite piezoelectric oscillator method,[1] the transducer being a Straubel-cut quartz rod having contacting electrodes. The specimen and transducer were cemented together under light finger pressure with either phenyl salicylate ("salol") or a beeswax-rosin mixture. Despite all precautions, the cementing operation was found to produce an appreciable increase in the internal friction. The salol bond tended to be less objectionable in this respect but had the disadvantage of relatively high volatility, so that it could not be used for assemblies which were to be left undisturbed for more than a few days.

Each specimen was adjusted in length to have, within a few tenths of a percent in most cases, the same resonant frequency as its transducer. These frequencies, about 70 kc/sec, agreed within a few tenths of one percent with the values calculated from the elastic constants of rocksalt given by Durand.[11]

The measure of internal friction used throughout the present paper is the *decrement* Δ, defined as the ratio of the energy dissipated per half-cycle to the vibrational energy in the specimen. This quantity corresponds to the logarithmic decrement of amplitude in the case of small linear damping. The measure of the amplitude of vibration is the *maximum strain amplitude* U in the specimen. Under the present conditions of good frequency matching and small damping, the local strain amplitude is very nearly $U\sin(\pi x/L)$, where x is the position along the specimen rod, measured from either end, and L is the length of the rod.

C. Coloration

Introduction of F centers was accomplished by placing the specimen directly before the 0.0005-in. mica[12] window of an x-ray tube operating at 40 kv and about 20 ma for a few minutes at each of a number of spots covering one entire longitudinal face. At room temperature this dosage was sufficient to impart an amber coloration throughout the volume of the crystal, with some decrease of intensity in the direction of incidence. For low-temperature coloration, the specimen was held in a groove in a copper block which formed one face of a liquid nitrogen reservoir, the temperature being measured by a thermocouple embedded in a dummy crystal, and moisture being excluded by a cellophane tape window. The resulting coloration was considerably less intense than that at room temperature.

III. RESULTS

A. Amplitude Dependence

As would be expected for a structure sensitive property, the internal friction of rock salt crystals was found to be extremely sensitive to all details of their previous history. Consequently, conclusions can be based only upon fairly broad patterns of behavior, and small differences must be ignored.

Under most conditions of previous history, Δ is a monotonically increasing function of U as shown in Fig. 1; curves having about this shape and magnitude will henceforth be designated as "normal."

Along with the increase of Δ corresponding to an increase of U, there is a decrease in the Young's modulus

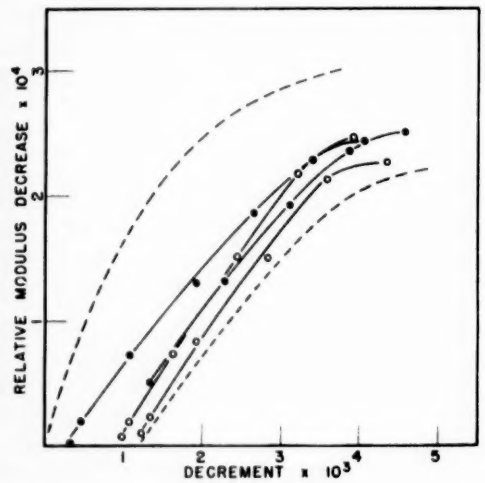

FIG. 2. Decrease in Young's modulus with increasing amplitude, plotted as function of the decrement. The solid lines are some of the runs shown in Fig. 1, and the broken lines give roughly the range covered by all runs.

[11] M. A. Durand, Phys. Rev. **50**, 449 (1936).

[12] D. R. Frankl and T. A. Read, Phys. Rev. **89**, 663 (1953). In this note it was erroneously stated that the x-ray tube had a beryllium window. However, the manufacturer's literature indicates that the transmission spectra of these two windows are essentially identical.

E of the specimen, detected as a small but measurable shift in the resonant frequency of the composite oscillator. The fractional decrease $-\delta E/E$ in the modulus is shown as a function of Δ in Fig. 2. When plotted in this manner the $\delta E/E$ curves observed under a wide variety of conditions all tend to cluster together in a fairly narrow band, even when Δ is far outside the normal range. Thus, $\delta E/E$ is, roughly, a function of Δ alone, suggesting that the modulus shift and the damping arise through the same mechanism.

In contrast to the normal internal friction, several other forms of dependence of Δ on U were observed. For example, five of the specimens behaved, at times, in the manner shown in Fig. 3, i.e., at the higher values of driving voltage applied to the transducer, an increase in voltage brought about such a large increase in

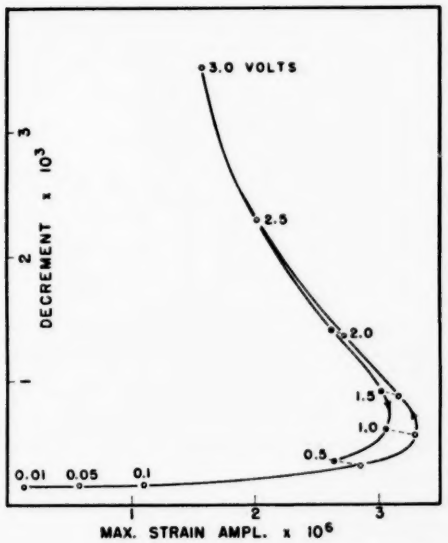

FIG. 3. Example of doubly-valued dependence of Δ on U.

damping that the amplitude of vibration was reduced. Under such conditions, Δ is a doubly valued function of U. Unfortunately, all attempts to determine the conditions under which a specimen would display this behavior failed. Indeed, all specimens in which it was observed at any time subsequently reverted to normal behavior. It seemed, however, that cold-working was part of the required treatment.

Still another type of amplitude dependence observed is a nearly discontinuous increase in Δ with increasing driving voltage, as shown in Fig. 4. At intermediate voltages in the discontinuity region, Δ changed with time so rapidly that measurements were impossible. However, with decreasing voltage, the corresponding decrease in Δ was continuous and reproducible. This behavior was displayed by one specimen after x-irradia-

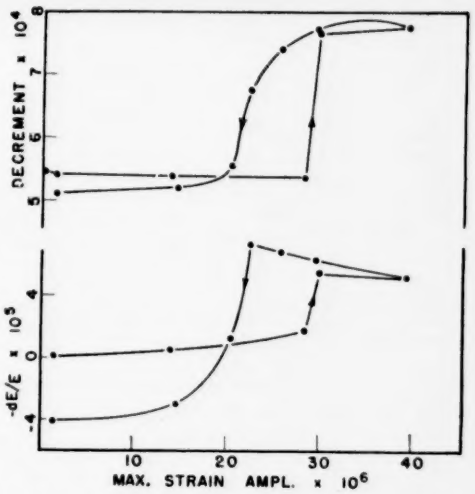

FIG. 4. Example of discontinuous dependence of Δ and $\delta E/E$ on U.

tion; other x-irradiated specimens sometimes behaved similarly, but with a more gradual increase in Δ.

B. Effects of Photochemical Coloration

The effects of introduction and subsequent removal of F centers were briefly described in reference 12. The salient observations, here presented in Figs. 5 and 6, are as follows. (a) On mild coloration by x-rays at room temperature, the internal friction is drastically reduced. Concurrently, E increases by about 0.1 percent. (b) On subsequent bleaching with visible and infrared radiation, Δ *remains small.* (c) On mild annealing, *viz.*, 30 min at 200°C in the case shown and somewhat longer at this temperature in other cases, Δ is increased considerably toward its initial magnitude. (d) On coloration at liquid nitrogen temperature, there is no reduction of internal friction if the crystal is subsequently bleached while still cold; however, if the

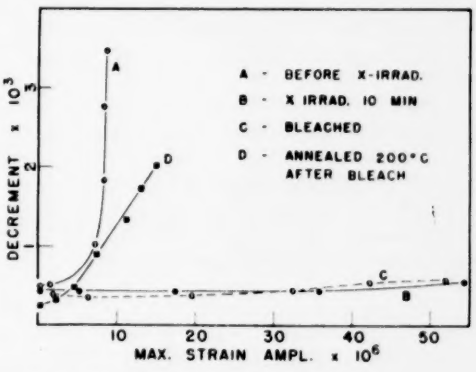

FIG. 5. Effects of x-irradiation at room temperature.

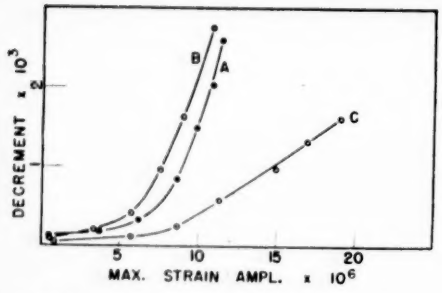

FIG. 6. Effects of x-irradiation at liquid nitrogen temperature. *A*—Before irradiation; *B*—cold irradiation, cold bleach; *C*—cold irradiation, room temperature bleach.

crystal is warmed to room temperature before bleaching, Δ is again markedly reduced.

The possibility that the reduction of Δ on x-irradiation is the result of some surface effect was investigated by etching off with water about 0.1 mm of the surface of a specimen after coloration and bleaching. The decrement remained extremely small, showing that the x-ray effect had taken place in bulk, or at least in appreciable depth. (Actually, the etching did result in a slight increase in Δ, but this occurred also in unirradiated specimens, as will be discussed below.)

Further details of the x-ray effect are shown in Fig. 7. It is particularly to be noted that after the extremely mild x-ray dosage of six minutes (per spot), the decrement of this specimen was nearly constant out to very large values of U, corresponding to stresses of about five times the static yield stress of annealed rock salt crystals.[7]

C. Effects of Mechanical Treatments

Application of static stress to the specimens was found always to increase their internal friction. The effects of the rather severe cold-working entailed in the grinding described above are illustrated in Fig. 8. Surface etching subsequent to the grinding was found also to produce an increase in Δ, showing that the plastic deformation on grinding is not confined to thin surface layers, but extends at least several tenths of a millimeter in depth. The amount of increase in Δ on etching was generally small compared to that on grinding.

As remarked above, even the mild handling of the specimen entailed in the cementing operation produced an appreciable increase in Δ. The amount of such increase, while extremely variable, was usually considerably less than that produced by grinding but appeared to be correlated with the initial magnitude of Δ; that is, the increase on handling was greater when Δ was initially large.

Finally, the vibrational stress applied in measurement also produced an increase in Δ, such that its value at a given driving voltage was increased after vibration under a higher voltage, as illustrated in Fig. 3.

D. Effects of Thermal Treatments

Heating a crystal to about 600°C and cooling it rapidly in air resulted always in high internal friction, in the neighborhood of the upper limit of the normal range. Furthermore, the Δ *vs* U curve was roughly the same for all specimens, regardless of the previous state; in other words, this high temperature treatment tends to obliterate all previous history.

Subsequent annealing for about 30 minutes at 200°C, with either slow (several hours) or rapid (few seconds) cooling, resulted in a considerable reduction in internal friction, particularly at high strain amplitudes, as shown in Fig. 9. Concurrently, there was an increase in the Young's modulus of about the same amount as occurs under coloration, *viz.*, about 0.1 percent.

Also shown in Fig. 9 and in more detail in Fig. 10 is the fact that considerable annealing takes place even at room temperature over a period of several days. Such annealing occurs after any increase in internal friction brought about by either cold-working or rapid cooling from high temperature. In numerous attempts to follow this annealing process over longer periods of time, the smooth decrease in internal friction was always interrupted, usually by small and variable increases probably resulting from accidental shock, but occasionally by a large increase and transition to the doubly valued type of Δ *vs* U curve. As remarked above, the reason for this behavior was not discovered.

After x-irradiation, when the internal friction is already very low, the room temperature annealing effect does not appear. Furthermore, in this case, the

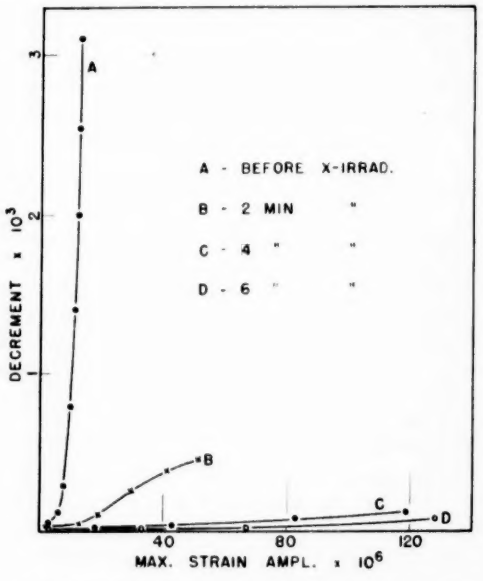

FIG. 7. Showing the rate of reduction of Δ by x-irradiation at room temperature. (This specimen had previously been heated to 600°C and cooled in a few seconds.)

200-degree anneal increases the decrement, though never to the magnitude it had had before the x-irradiation (see Fig. 5).

IV. DISCUSSION

A. The Dislocation Model

The normal internal friction (Fig. 1) and the change in the Young's modulus (Fig. 2) found for rock salt are similar to the corresponding properties of metallic crystals,[1–3] which suggests that the mechanism of damping is essentially the same in the two types of solids. We adopt here the currently accepted viewpoint that this mechanism consists of the oscillatory motion of dislocations.

The model, then, is a crystal containing some number of dislocation lines, as well as numbers of various "point" imperfections such as foreign ions and lattice vacancies. These point imperfections may interact with

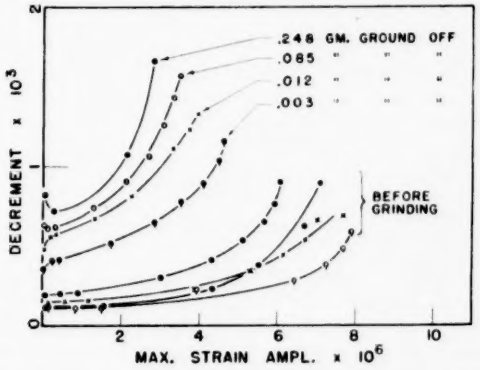

FIG. 8. Increase in Δ resulting from dry grinding on abrasive paper. The "before grinding" curves were obtained after many days of room temperature annealing.

the dislocations, in the manner described by Cottrell,[13] to form "pinning points" at which the dislocation line is immobilized under moderate stresses, but from which it may be "broken away" under sufficiently high stress. Then, as shown by Koehler,[3] the major contribution to the damping is given by the longer segments of dislocation lines lying between the more widely spaced pinning points.

In the following it will be shown that this model is adequate to account, at least qualitatively, for most of the observed phenomena. It should, however, be pointed out that other mechanisms, namely the relaxation of various thermodynamic potential differences, are also operative but give only linear damping and are therefore not important here.

B. The Abnormal Amplitude Dependences

The large increase in damping which leads to the doubly valued dependence of Δ on U (Fig. 3) can be

[13] A. H. Cottrell, *Bristol Conference on the Strength of Solids* (Physical Society, London, 1948), p. 30.

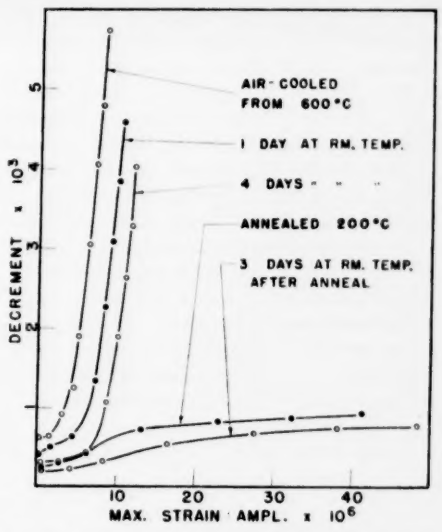
AIR-COOLED FROM 600°C
1 DAY AT RM. TEMP.
4 DAYS " "
ANNEALED 200°C
3 DAYS AT RM. TEMP. AFTER ANNEAL
DECREMENT x 10³
MAX. STRAIN AMPL. x 10⁶

FIG. 9. Effects of thermal treatments. (Curves are labeled in chronological order.)

accounted for by assuming the sudden breakage of large numbers of pinning points. Now, Koehler[3] has pointed out that a shear stress causes the exertion of stronger forces on widely spaced than on closely spaced pinning points. Hence, the initial breaking of only relatively few points under the increased stress may, for a suitable configuration of pinning points, give rise to an avalanche of unpinning, leading to the greatly increased decrement.

The fact that the points for decreasing driving voltage nearly duplicate those for increasing voltage shows that the time for repinning of dislocations is short compared to the few seconds required for a measurement. In this connection, it is essential to recognize that the points of the Δ *vs* U curves cannot be traversed truly in sequence. Rather, by virtue of the modulus shift described above, each change of driving voltage throws the system off resonance by an amount sufficient to reduce the amplitude of vibration

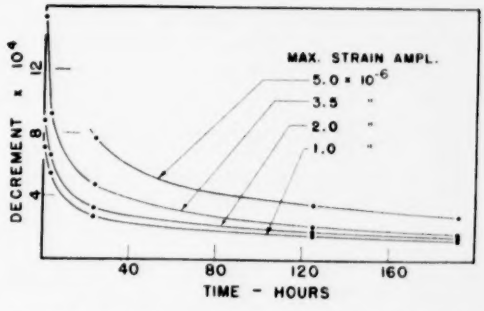

FIG. 10. Example of room temperature annealing following grinding of the specimen.

to a small fraction of its resonant value. The measurement is completed by tuning the driving signal to the new resonance and simultaneously balancing the bridge, these operations requiring several seconds to perform. Presumably the repinning of dislocations takes place during these intervals. While the method of measurement does not permit the determination of the path along which the system approaches the steady-state resonant vibration, this path must, for points on the upper branch of the curve, necessarily go through strain amplitudes at least as large as that at which the reversal occurs.

On the other hand, the fact that the high decrement persists at the reduced amplitude shows that repinning does not take place during the resonant vibration. We therefore postulate that when the dislocation moves at high velocity through the pinning point, repinning cannot occur; but when the dislocation is nearly stationary at the pinning point, repinning takes place very rapidly.

The phenomenon of doubly valued amplitude dependence, while not previously observed, is nevertheless, closely related to two well-known phenomena, the only essential difference being in the time scale. In the first instance, the cataclysmic breaking of pinning points occurs also in the yield-point phenomenon in static loading of metals, but the repinning time is much longer since the dislocations are permanently removed from their initial positions and the recovery process can occur only by diffusion of the pinning imperfections over appreciable distances. In the second instance, it has been observed that the decrement of some metallic crystals increases with time under vibration at a constant strain amplitude. Therefore, if the vibration were carried out under constant driving voltage, it would be found that the decrement would increase and the amplitude decrease with time. And, by waiting sufficiently long, it would be possible to obtain an amplitude smaller than that previously observed under a lower driving voltage. The present case differs only in that the required time is unobservably short under the experimental method employed.

The discontinuous amplitude dependence (Fig. 4) again suggests a cooperative breaking of pinning points. In this case, however, it is not clear why the breaking does not proceed further under the higher driving voltages.

C. The X-Irradiation Effects

In reference 12, a mechanism was proposed to account for the observed effects of coloration and bleaching (Figs. 5 and 6). Briefly, this consists of the liberation of cation vacancies from their association in pairs with anion vacancies by the trapping of electrons in the latter to form the F centers, and the diffusion of the liberated cation vacancies to dislocations, where they act as pinning points. This mechanism accounts not only for the reduction of internal friction on x-irradiation, but also for its independence of subsequent bleaching, and, especially, for the absence of the effect on low temperature coloration and bleaching, when the liberated vacancies cannot undergo the required diffusion.

Furthermore, this mechanism is plausible in the light of present knowledge of the properties of lattice vacancies in ionic crystals. Firstly, the work of Tubandt[14] has shown that, except at extremely high temperatures, the mobility of the cations is some 10^4 times that of the anions. Etzel and Maurer[15] have determined the activation energy for cation migration to be 0.85 ev, from which the jump rate of the cation vacancies may be estimated[16] as about one sec^{-1} at room temperature. Thus, it is not unreasonable to suppose that in an interval of a few minutes the cation vacancies may, in the presence of a stress field, migrate several hundred ion spacings, while the anion vacancies are essentially immobile. Secondly, Reitz and Gammel[17] have calculated the binding energy of a cation-anion vacancy pair to be 0.89 ev, which suggests that the existing vacancies will, at room temperature, be largely associated into pairs (or perhaps larger clusters). The binding energy of an F center, on the other hand, should be roughly comparable to the optical excitation energy, i.e., of the order of 2 ev, so that it is likely that an electron can, indeed, displace a cation vacancy from a vacancy pair.

It must be supposed that a cation vacancy is less strongly bound to a dislocation than to an anion vacancy, since otherwise the stable configuration would be that giving the extremely low internal friction. This supposition is further borne out by the fact (Fig. 5, curve D) that the vacancies are evaporated from the dislocations at only slightly elevated temperature.

Pinning of dislocations by vacancies may also occur in metals, as has been suggested by Seitz.[18] However, the situation in ionic crystals differs in one essential respect, owing to the fact that the Burgers vector must be twice the interionic distance, since otherwise the motion of the dislocation in the slip plane could not leave behind a perfect lattice. In metals, on the other hand, the fundamental slip vector may be a single interionic distance. In view of this difference, the interaction of edge dislocations with vacancies in the two types of crystals may be compared as follows: In metals (a) condensation of a single vacancy in the edge of a straight portion of the dislocation will leave the cross-section configuration unchanged, but merely moved to the adjacent slip plane; the resulting jog in the disloca-

[14] C. Tubandt, *Handbuch der Experimental Physik* (J. Springer, Berlin, 1932), Vol. 12, Part 1.
[15] H. W. Etzel and R. J. Maurer, J. Chem. Phys. **18**, 1003 (1950).
[16] F. Seitz, Revs. Modern Phys. **18**, 384 (1946).
[17] J. R. Reitz and J. L. Gammel, J. Chem. Phys. **19**, 894 (1951).
[18] F. Seitz, Advances in Physics (Supplement to Phil. Mag.) **1**, 43 (1952), see p. 73 ff.

tion line may act as a pinning point; (b) condensation of vacancies will actually occur most probably at preexisting jogs; this will merely move the jog one step along the dislocation line, leaving the same configuration, with no increase in pinning; (c) condensation of a complete row of vacancies will merely move the entire dislocation to the adjacent slip plane. In ionic crystals, on the other hand, (a) condensation of a single vacancy in the dislocation edge will result in an essential change in the cross-sectional configuration; (b) condensation of a single vacancy at a jog will also result in an essentially different configuration of the dislocation, with one additional pinning point; (c) condensation of a complete row of single vacancies will leave the dislocation completely pinned. This does not imply that such complete pinning is energetically possible; however, the results shown in Fig. 7 suggest that the pinning vacancies are, indeed, very closely spaced.

Finally, it may be remarked that pinning by cation vacancies provides a likely mechanism for the strong hardening effects of divalent substitutional impurity cations and of F centers in ionic crystals.

D. The Mechanical Effects

The increased internal friction observed after application of stress means, on the assumed model, that the number of long unpinned dislocation segments has been increased. This could come about either through multiplication of dislocations or through breaking of pinning points. The fact that appreciable increase in Δ occurs even under static stress far below that required to produce observable plastic deformation suggests that the latter mechanism predominates. Then, the observed correlation of the amount of increase in Δ with its initial magnitude is in general agreement with Koehler's aforementioned prediction of easier breakability of the more widely spaced pinning points. Finally, the increase in Δ on etching may be interpreted as the effect of plastic deformation under the unbalanced internal stresses.

E. The Thermal Effects

At the high temperature of 600°C, it is likely that the vacancies and impurity ions will be largely evaporated from the dislocations, so that the rapid cooling from this temperature will result in a large number of long unpinned dislocation segments, giving the observed high internal friction. The fact that the Δ *vs* U curves following such treatment are roughly independent of previous history suggests that the total length of dislocation line, pinned and unpinned, is essentially unchanged by the various other treatments.

At room temperature, on the other hand, the only imperfection which can give strong pinning and which also has appreciable mobility is the cation vacancy. (Theoretical calculations by Dienes[19] indicate that vacancy pairs also have appreciable mobility; however, as indicated above, these cannot give such pronounced pinning.) Thus, the room temperature annealing is probably also the result of diffusion of cation vacancies to the dislocations, the slow rate of this effect as compared to the x-irradiation effect being a statistical result of a smaller vacancy concentration.

The results of annealing at intermediate temperature (200°C) require the assumption that another type of pinning imperfection, presumably foreign ions, is also operative. Then the decrease in Δ when such annealing is carried out following the high temperature treatment and essential completion of the room temperature anneal (Fig. 9) is the result of the increased mobility of these ions. On the other hand, when the 200-degree anneal is carried out after x-irradiation, the impurity pinning process is overbalanced by the evaporation of vacancies, leading to the observed partial increase in Δ, as shown in Fig. 5.

V. ACKNOWLEDGMENT

The writer wishes to express his appreciation for the advice and encouragement of Professor Thomas A. Read, under whose guidance this investigation was conducted.

[19] G. J. Dienes, J. Chem. Phys. **16**, 620 (1948).

The Electrical Properties of Black Phosphorus*

ROBERT W. KEYES
Department of Physics and Institute for the Study of Metals, University of Chicago, Chicago, Illinois
(Received July 27, 1953)

The electrical conductivity of black phosphorus has been measured as a function of temperature and pressure up to 350°C and 8000 kg/cm². The Hall constant of the same material has been measured as a function of temperature at atmospheric pressure. At low temperatures *p*-type impurity conduction is observed; at high temperatures the phosphorus is an intrinsic semiconductor with a gap width of 0.33 ev. The mobilities at 27°C are 350 cm²/volt sec and 220 cm²/volt sec for the holes and electrons, respectively. Application of hydrostatic pressure decreases the gap at a rate $VdW/dV=8.3$ ev. The results are also interpreted in terms of a two-dimensional semiconductor model.

INTRODUCTION

PHOSPHORUS is an element of the fifth group of the periodic table which exists in a number of allotropic modifications. The most stable form,[1] black phosphorus, can be prepared only under high hydrostatic pressure, and was discovered by Bridgman[2] in 1914. Bridgman has measured the density[2] (2.69 gm/cm³) and the compressibility[3] of black phosphorus, and its electrical resistivity as a function of pressure over a limited range of temperature.[2,4] These measurements have shown that this type of phosphorus is a semiconductor, and that it apparently becomes more metallic with increasing hydrostatic pressure, the temperature coefficient of resistivity between 30°C and 75°C reversing sign at 12 000 kg/cm².

The crystal structure of black phosphorus has been determined,[5] the lattice is orthorhombic with eight atoms per unit cell and lattice parameters $a=3.31$A, $b=4.38$A, $c=10.50$A. The atoms are arranged in puckered layers; in a layer each atom is joined by covalent bonds to three neighbors at the same distance as the interatomic distance observed in the P_4 molecule, while the layers are held together at a distance about 50 percent greater by van der Waals forces.[6]

In view of the limited number of elementary semiconductors and the unusual structure of black phosphorus, further measurements of the electrical propties of this material have been made in order to provide a better understanding of the electronic processes involved. The following quantities have been measured: 1. Electrical conductivity from −195°C to 350°C; 2. Hall coefficient from −195°C to 350°C; 3. Electrical conductivity at pressures up to 8000 kg/cm² in the temperature range 27°C to 350°C; 4. Magnetoresistance coefficients at −195°C and −80°C; 5. Infrared absorption from 2μ to 30μ.

PREPARATION OF SAMPLES

The black phosphorus was prepared from white phosphorus by the method described by Bridgman.[2] Hydrostatic pressure of 13 000 kg/cm² is applied to the white phosphorus in high-pressure apparatus of a type which has been described elsewhere.[7] The vessel containing the phosphorus is heated to 200°C; after several minutes at this temperature the transition to black phosphorus takes place abruptly, accompanied by a marked change in volume (0.18 cm³/gm). After cooling of the high-pressure bomb the ingot of black phosphorus was washed in carbon disulfide to remove any untransformed white phosphorus. As a result of the large volume change and the violent nature of the transition, the ingot was polycrystalline and contained numerous cracks. Metallographic polishing of a sample disclosed grains of roughly 0.1-mm diameter. Dow-Corning silicone oil and hexane have both been used as pressure transmitting fluids in the preparation of black phosphorus. Small silica inclusions were found in the cracks in the material made in silicone oil; electrically both materials were the same. When black phosphorus is melted or vaporized, P_4 molecules are formed which crystallize into white or red phosphorus; thus it does not appear possible to prepare single crystal samples.

For the electrical measurements, pieces of phosphorus were sawed from the ingot and machined to rectangular shapes. The samples were cut as long and narrow as was consistent with the cracks in the ingot and the fragility of the material; cross-sectional dimensions of the samples veried from 0.1 to 0.2 cm and lengths from 0.5 to 1 cm. After machining, the samples were washed in acetone, and nickel electrode surfaces were electroplated onto the ends.

ELECTRICAL MEASUREMENTS

Sample holders for the electrical measurements were machined from lavite. The samples were held in place by forces transmitted through the electrodes. A copper plate was mounted beneath the samples, and separated

* A thesis submitted in partial fulfillment of the requirements for the Ph.D. degree at the University of Chicago.
[1] R. B. Jacobs, J. Chem. Phys. **5**, 945 (1937).
[2] P. W. Bridgman, J. Am. Chem. Soc. **36**, 1344 (1914).
[3] P. W. Bridgman, Proc. Am. Acad. Arts Sci. **62**, 207 (1927).
[4] P. W. Bridgman, Proc. Am. Acad. Arts Sci. **70**, 71 (1935).
[5] Hultgren, Gingrich, and Warren, J. Chem. Phys. **3**, 351 (1935).
[6] L. Pauling and M. Simonetta, J. Chem. Phys. **20**, 29 (1952).
[7] P. W. Bridgman, *Physics of High Pressure* (G. Bell and Sons, London, 1939), Chap. 2.

from them by a thin sheet of mica, to reduce thermal gradients. The electrodes were made of Nichrome wire and ribbon. During the measurements above room temperature the samples were in an atmosphere of helium. Between room temperature and $-80°$ the samples were immersed in acetone. Below the latter temperature, data were taken by cooling the sample in liquid nitrogen and taking data while the sample and holder were gradually warming up.

The Hall constant and conductivity were measured in a sample holder designed for use with a large electromagnet. With a 4-inch gap between the pole faces, which was large enough to contain the furnace used for the high-temperature measurements and the Dewar flask for the low-temperature measurements, fields up to 5600 gauss were obtainable. At this field strength the field was uniform within one percent over a region $1\frac{1}{2}$ inches in diameter. The field strength as a function of magnet current was determined with a G.E. fluxmeter, and the magnet current was read with a Sensitive Research Instrument Corporation DC Polyranger, appropriately shunted. The current corresponding to maximum field, at which most readings were taken, was 40 amperes, and the meter could be read with an accuracy of 0.2 ampere. An electronic current controller regulated the current, and no fluctuation could be detected in the time necessary to take data at a single temperature (about 10 minutes).

The conductivity was measured by the direct current potential probe method. Thermocouple emf, potential drop in the sample, potential across a standard resistor in series with the sample, and Hall emf were measured with a Leeds and Northrup Type K potentiometer. The directions of the sample current and the magnetic field could be reversed, and in order to eliminate thermal emf's conductivity measurements were made for both directions of current, and Hall voltage measurements for all combinations of directions of current and magnetic field.

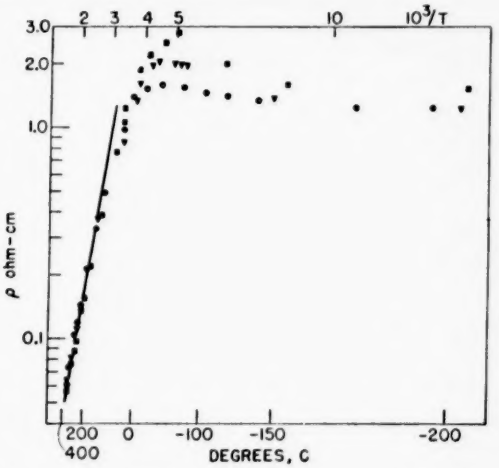

FIG. 1. The resistivity of three different specimens of phosphorus as a function of the reciprocal of the temperature in °K.

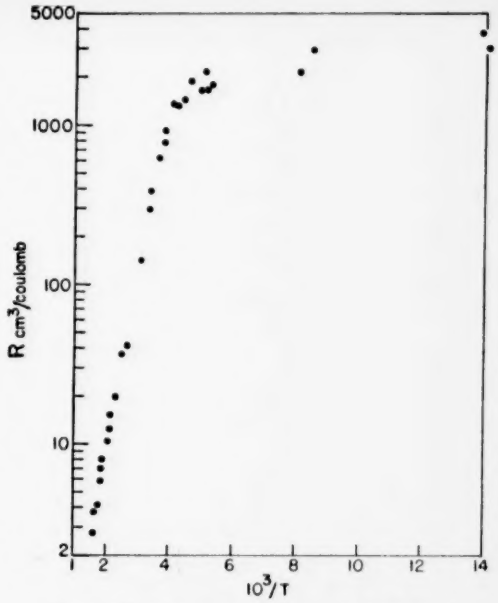

FIG. 2. The Hall constants of several samples as a function of the reciprocal of the temperature.

The conductivity at high pressures was measured by the same method in an apparatus of the type described by Bridgman[7] and modified for high temperatures by Kurnick.[8]

RESULTS AND DISCUSSION

The results of the resistivity measurements on several samples are shown in Fig. 1. At high temperatures the resistivity varies as

$$\rho = Ae^{W/2kT}, \tag{1}$$

with $W = 0.33$ ev and $A = 0.0030$ ohm cm. T is the absolute temperature, k is the Boltzmann constant, and A is a constant independent of temperature.

In Fig. 2 the Hall constant, R, is plotted as a function of temperature. The sign of the Hall voltage indicates that the charge carriers are positive. The direction of the thermoelectric effect confirmed this conclusion. The Hall constant was found to be independent of magnetic field up to 5600 gauss.

The logarithm of the product $(8/3\pi)R\sigma$ is plotted against the logarithm of the temperature in Fig. 3. Over most of the temperature range the points are well represented by the two lines of slope $-\frac{3}{2}$.

These results can be interpreted in terms of the conventional theory of an isotropic semiconductor.[9,10] At

[8] S. Kurnick, J. Chem. Phys. **20**, 218 (1952).
[9] G. L. Pearson and J. Bardeen, Phys. Rev. **75**, 865 (1949).
[10] W. Shockley, *Electrons and Holes in Semiconductors* (D. van Nostrand Company, Inc., New York, 1950).

low temperatures the conductivity is entirely due to holes. The concentration of holes, calculated from the Hall constant by the formula $p=3\pi/8Re$ is about 2×10^{-15} cm^{-3}. The mobility of the holes, found from $\mu_p=(8/3\pi)R\sigma$, is represented by the upper line in Fig. 3, the equation of which is $\mu_p=1.86\times10^6T^{-\frac{3}{2}}$ cm^2 sec^{-1} volt^{-1}. This temperature dependence is in agreement with theoretical expectation for scattering by lattice vibrations.[10] The low value of the mobility for the point at -200°C is probably due to the effect of impurity scattering.

At high temperatures (above 150°C) the conductivity is essentially intrinsic, holes and electrons being present in equal numbers. The energy gap between the conduction and valence bands, derived from the conductivity as mentioned above, is 0.33 ev. This picture explains the shape of the $R\sigma$ curve; the contribution to the Hall coefficient of the electrons which appears at high temperature is of opposite sign to that of the holes and decreases the measured Hall voltage.

The mobility of the electrons can be derived from the data by extrapolating the $T^{-\frac{3}{2}}$ line which describes the mobility of the holes in the impurity region to higher temperatures, and using the values for μ_p thus obtained in the expressions for conductivity and Hall constant when both types of carriers are present. These expressions are:

$$\sigma=(n\mu_n+p\mu_p)e, \tag{2}$$

$$R=\frac{3\pi}{8e}\frac{p-nb^2}{(p+nb)^2}, \tag{3}$$

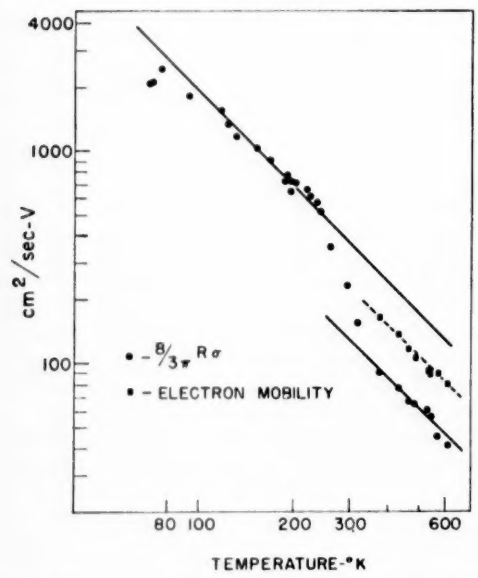

FIG. 3. The product $(8/3\pi)R\sigma$, which is equal to the mobility of the holes at low temperatures, and the mobilities of the electrons as calculated from Eq. (7). The lines drawn through the points have slope $-\frac{3}{2}$.

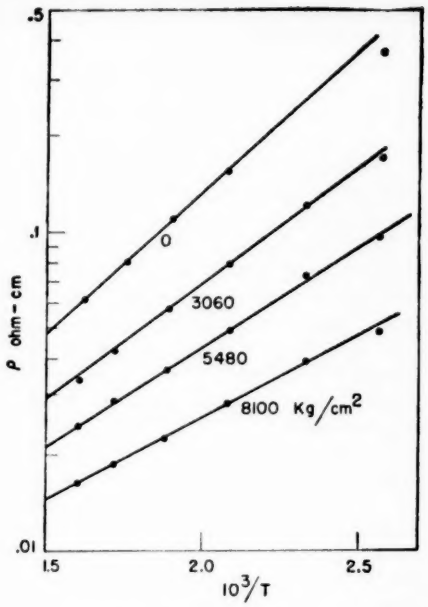

FIG. 4. Temperature dependence of the resistivity in the intrinsic range at various pressures.

where n and p are the concentrations and μ_n and μ_p the mobilities of the electrons and holes, respectively, and $b=\mu_n/\mu_p$. In the intrinsic range $n=p$ and these formulas reduce to

$$\sigma=pe(\mu_n+\mu_p), \tag{4}$$

$$R=\frac{3\pi}{8e}\frac{1}{p}\frac{1-b}{1+b}, \tag{5}$$

$$R\sigma=\tfrac{3}{8}\pi(\mu_p-\mu_n). \tag{6}$$

Values for μ_n in the intrinsic range were calculated from the formula:

$$\mu_n=\mu_p-(8/3\pi)R\sigma, \tag{7}$$

and are plotted in Fig. 3. These mobilities can be represented by $\mu_n=1.19\times10^6T^{-\frac{3}{2}}$. Thus $b=0.64$.

The magneto-resistance coefficient was measured at -195°C and -80°C. This coefficient is the constant f in the expression $\rho=\rho_0(1+fH^2)$ for resistivity as a function of transverse magnetic field. In the simple theory applied above, f has the value $0.378\mu_p^2$.[11] A calculation of μ_p from this data gives values 2.8 times those calculated from the Hall constant. This coefficient, however, is particularly sensitive to the details of the shape of the energy surfaces.

The conductivity as measured in the high-pressure apparatus is shown in Fig. 4. Values for the energy gap were derived from the slopes of the lines in the

[11] A. H. Wilson, *The Theory of Metals* (Cambridge Univeristy Press, Cambridge, 1936).

intrinsic region. These energies are plotted as a function of volume in Fig. 5, using the compressibility measured by Bridgman[3] to relate the pressure to the volume. Extrapolation of the lines of Fig. 4 to $1/T=0$ gives values for the term A of Eq. (1) at the pressures indicated. These values of A are independent of pressure within the accuracy of the extrapolation, about 25 percent. This indicates that there is no strong dependence of the mobility on pressure.

An interpretation of data of this type in terms of a simplified model of a semiconductor has been developed by Bardeen and Shockley.[12] The energy gap, regarded as a function of the volume of the crystal, may be written, to first-order terms as

$$W=W_0+E_1\Delta, \tag{8}$$

where E_1 is a constant, W_0 is the gap extrapolated to zero temperature and pressure, and $\Delta=(V-V_0)/V$ is the volume dilation. This Δ depends on both temperature and pressure, and, assuming a constant volume coefficient of thermal expansion, α, is $\Delta=\alpha T+\Delta_p$, Δ_p being the fractional change in volume due to applied pressure. Thus W becomes

$$W=W_0+E_1\alpha T+E_1\Delta_p. \tag{9}$$

If this expression is substituted into the exponential term in the conductivity $e^{-W/2kT}$, it is seen that the temperature-dependent part of W becomes part of the constant factor in the conductivity, and that the energy derived from the graph of conductivity *vs* $1/T$ is $(W_0+E_1\Delta_p)$. Thus W_0 has the value 0.33 ev derived from the atmospheric pressure measurements above, and E_1 is the slope of the line representing energy gap against volume in Fig. 5. This value for E_1 is 8.3 ev.

The mobilities of the charge carriers are related to the shifts in energy of the band edges with volume dilation:[12]

$$\mu T^{3/2}=\frac{(8\pi)^{\frac{1}{2}}eh^4C}{3m^{5/2}k^{3/2}E_1^2}, \tag{10}$$

where C is the elastic constant for longitudinal sound waves, m is the effective mass of the charge carriers, and k is the Boltzmann constant. There is one such equation for the holes, with E_{1c} referring to the bottom of the conduction band and E_{1v} to the top of the valence band. The constant $E_1=E_{1c}+E_{1v}$. In this way a value for E_1 can be obtained from the mobilities.

The only elastic constant known for black phosphorus is the compressibility (2.9×10^{-12} dyne^{-1} cm^2). By comparison of this with elastic constants for other materials, a value of the elastic constant for longitudinal waves was estimated to be 0.6×10^{12} dyne/cm^2. Using the free electron mass for m and the mobilities given above, the calculated values for $|E_{1c}|$ and $|E_{1v}|$ are 4.2 ev and 3.4 ev, respectively. The signs of these constants are not determined by the mobility formula; good agreement with the value of E_1 found from the pressure experiment is obtained by assuming that the bands shift in opposite directions and taking $E_1=+4.2+3.4=7.6$ ev.

The temperature dependence of the energy gap is given by the coefficient $(E_1\alpha)$ in the above equation. In order to calculate this term, the thermal expansion, α, was measured by determining the changes in the lattice parameters between room temperature and 434°C. Powder patterns were taken with a Unicam 19-cm diameter high-temperature camera at 24°C, 272°C, and 434°C. Values for the changes in lattice constants were derived from the changes in position of about ten lines by a least-squares fitting of the data. The values of the linear coefficients are: a direction, 22×10^{-6} deg^{-1}; b direction, 39×10^{-6} deg^{-1}; c direction, 38×10^{-6} deg^{-1}. This gives 99×10^{-6} deg^{-1} for the volume coefficient. Because of the broadening of the lines at high temperatures these values are accurate to only about 10 percent; however, this is sufficient for the present purpose. The rate of temperature variation of the energy gap $E_1\alpha$ is 8×10^{-4} ev/deg. The temperature variation of the energy gap can also be estimated from the data by comparing the number of carriers in the intrinsic range as calculated from Eq. (5) with the number derived from theory.[9,13] This gives $dW/dT=2.3\times10^{-4}$ ev/deg.

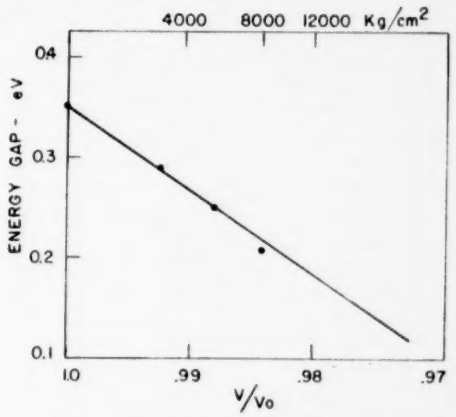

FIG. 5. Dependence of the activation energies derived from Fig. 4 on the dilation.

Although the picture just presented reproduces satisfactorily most of the observed electrical properties, because of the structural anisotropy and the polycrystallinity of the samples, the derived parameters must be considered as properties averaged over spatial direction. In fact, a comparison of the measured characteristics of the phosphorus with the theory of a two-dimensional semiconductor is also interesting. A statistical mechanical analysis of an electron gas

[12] J. Bardeen and W. Shockley, Phys. Rev. **80**, 72 (1950).

[13] V. A. Johnson and H. Y. Fan, Phys. Rev. **79**, 899 (1950).

constrained to move in a plane, with application of the Boltzmann equation to determine the transport properties, was carried out. Naturally the observed electrical characteristics depend on the orientation of the planes relative to the electric and magnetic fields, and for comparison with the properties of a polycrystalline aggregate the properties of the planar semiconductor were simply averaged over all possible directions of the planes. The relationships between the averaged electrical properties of such a polycrystalline aggregate differ from those of an isotropic conductor because of the altered distribution of the energy states of the electrons in the two-dimensional case and differences in the effect of the averaging process on the various electrical parameters. The mobility in the two-dimensional case may be characterized by a quantity v, the mobility of a charge carrier in a plane under the influence of an electric field parallel to the plane. The significant points of difference are as follows.

1. Because some grains are oriented so as to make only small contributions to the conductivity or Hall constant, the mobility calculated from $\mu=(8/3\pi)R\sigma$ is less than v by a factor 4.2. The mobilities shown in Fig. 3 must be multiplied by this factor to obtain the corresponding v's.

2. Because of the changed velocity distribution, the magnetoresistance coefficient for a magnetic field perpendicular to the planes is larger for a two-dimensional semiconductor; the decrease due to the averaging process almost exactly cancels this effect, so that the mobility calculated from the magnetoresistance coefficient in the usual way is equal to $0.99v$. This means that this mobility should be 4.1 times as large as that calculated from the Hall constant, which coincides qualitatively with the observation noted above of an anomalously large magnetoresistance effect.

3. The intrinsic conductivity varies with temperature as $T^{-\frac{1}{2}}\exp(-W/2kT)$. The two types of temperature dependence cannot be distinguished experimentally; in the two-dimensional case W comes out 0.02 ev higher.

4. The temperature dependence of the energy gap required to account for the density of charge carriers in the intrinsic range is $dW/dT=9\times10^{-4}$ ev/deg, in better agreement with that calculated from the thermal expansion and E_1.

Extrapolation of the line of Fig. 5 reperesenting the variation of energy gap with volume indicates that the bands will begin to overlap when the volume has been decreased by 4 percent, which corresponds to a pressure somewhat over 20 000 kg/cm². Bridgman[14] has observed a transition from black phosphorus to a denser form in the pressure range 25–50 000 kg/cm²; the possibility that these two phenomena are related was considered. An attempt was made to produce the high-pressure phase at pressures around 50 000 kg/cm² with a shearing apparatus described by Bridgman,[15] and to quench this phase in liquid nitrogen and determine its structure by x-ray diffraction methods.[16] Only lines attributable to black phosphorus could be found in powder patterns of the quenched samples.

For certain simple types of dependence of electron energy on wave number, an infrared absorption edge should occur at quantum energies corresponding to the thermal excitation energy, i.e., at a wavelength $\lambda=hc/W$. For $W=0.33$ ev, $\lambda=3.8$ microns; if the temperature dependence of energy gap $dW/dT=8\times10^{-4}$ ev/deg is accepted, at room temperature $W=0.57$ ev and $\lambda=2.2$ microns. The material was found to be transparent to wavelengths from 2 to 30 microns.

CONCLUSIONS

1. The black phosphorus studied is a semiconductor with an energy gap of 0.33 ev; the resistivity above 200°C is $\rho=0.0030\exp(0.33/2kT)$. At low temperatures p-type impurity semiconduction is observed.

2. The mobility of holes in this material is $1.9\times10^{6}\,T^{-\frac{1}{2}}$ cm²/volt sec, and that of the electrons is $1.2\times10^{6}\,T^{-\frac{1}{2}}$ cm²/volt sec. It appears that over most of the temperature range the mobility is limited by scattering by lattice vibrations.

3. At room temperature the values of the electrical properties for an intrinsic sample are: $\rho=1.5$ ohm cm, $\mu_p=350$ cm²/volt sec, $\mu_n=220$ cm²/volt sec. These values and the band separation are very similar to the corresponding properties of tellurium.

4. The energy gap decreases with decreasing volume of the crystal at a rate $VdW/dV=8.3$ ev.

5. It should be noted that the structure of black phosphorus is highly anisotropic and that the electrical properties may vary strongly with crystalline direction; certain data are more consistent with a model of a polycrystalline two-dimensional semiconductor than with the common, three-dimensional, isotropic model.

ACKNOWLEDGMENTS

The author wishes to thank Professor A. W. Lawson for advice and discussion concerning this investigation. The work was performed at the Institute for the Study of Metals, and the cooperation of many members of the Institute is gratefully acknowledged. This experiment was supported in part by the U. S. Office of Naval Research.

[14] P. W. Bridgman, Proc. Am. Acad. Arts Sci. **76**, 55 (1948).

[15] P. W. Bridgman, Phys. Rev. **48**, 825 (1935).

[16] The apparatus for quenching high pressure phases with liquid nitrogen was developed by I. S. Jacobs.

Annealing of Bombardment Damage in a Diamond-Type Lattice: Theoretical

R. C. Fletcher and W. L. Brown
Bell Telephone Laboratories, Inc., Murray Hill, New Jersey
(Received July 22, 1953)

The annealing of isolated interstitial-vacancy pairs presumably introduced by bombardment is considered theoretically with special attention paid to the diamond-type lattice. It is proposed that the annealing can be divided into three stages. First, those vacancy-interstitial pairs having a small initial separation will recombine under the influence of short-range elastic forces. Second, vacancies located initially farther from their companion interstitials will wander according to a random walk process, some of them wandering back within the range of the elastic forces and recombining but some escaping from the vicinity of their interstitials. Finally, vacancies which have escaped in the second stage will continue to wander until captured on surfaces or dislocations or by interstitials other than their own. Approximate analytic expressions are derived for these various stages. An outline is given of a more complete treatment with a quantitative solution for one particular phase of the annealing in the diamond-type lattice.

I. INTRODUCTION

WHEN crystals are bombarded with high-energy particles (neutrons, deuterons, alpha particles, electrons, etc.) the mechanical and electrical properties have been found to change.[1] Heating tends to restore the original properties of the crystal. These irradiation effects are believed to be caused by displacement of atoms from their normal lattice sites into interstitial positions. After bombardment the interstitial atoms tend to return to their original positions in the lattice, particularly if the crystal is heated.

In this paper we consider the annealing mechanism of the simplest type of irradiation damage. It is believed that many of the essential details of more complicated types of damage will be exhibited by this simple type. The case which we will consider is that of a single interstitial atom associated with each vacancy. In the case of heavy particle bombardment, clumps of such interstitial-vacancy pairs will undoubtedly be present, but the simplest case may actually be realizable in bombardment with electrons with energies near to the threshold for interstitial-vacancy production.

We have also given special attention to a particular crystal structure, the diamond-type lattice, so that annealing of germanium, silicon, and diamond can be analyzed directly. The same general procedures can be applied to other crystal structures.

II. DIFFUSION OF VACANCIES

We shall begin by assuming that the interstitial remains fixed and examine the behavior of a vacancy. In order for the vacancy to be stable each of its neighboring atoms must find itself in a potential energy trough. Each must therefore overcome a potential barrier E in order to jump into the vacancy. The average time τ required for one of them to make such a jump under thermal excitation is given by[2]

$$\tau = \nu_0^{-1} e^{E/kT}, \tag{1}$$

where ν_0 is interpreted as the average lattice frequency (*ca* 10^{13} cps), T is the absolute temperature, and k is Boltzmann's constant. When an adjacent atom jumps into the vacancy, the vacancy moves to the former position of the jumping atom. Hence the vacancy can be said to jump with an average jump time τ given by (1).

If the vacancy is close to an interstitial atom, the energy barrier and hence the jump time will be altered.

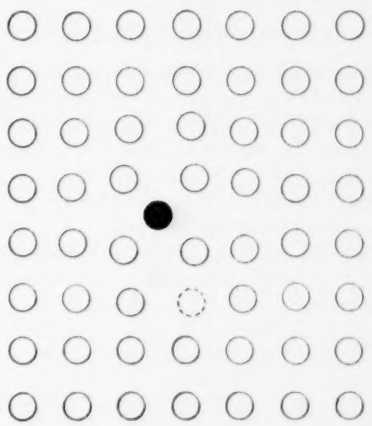

FIG. 1. Effect of elastic deformation around an interstitial on the nearest neighbor atoms of a vacancy. The distortion due to the vacancy has been neglected. Notice how the atom between the interstitial and the vacancy has been pushed toward the vacancy.

One reason for this is that the lattice is deformed by the interstitial. The atoms around the interstitial are forced away from the interstitial. This causes the lattice to be compressed in a direction radially outward from the interstitial and to be expanded in directions perpendicular to the radial direction. This effect is shown schematically in Fig. 1 for a two-dimensional simple cubic lattice. If a vacancy is located in this deformed region, its neighboring atoms which are located along the radial line from the interstitial are pushed toward

[1] For a review of the literature, see G. J. Dienes, "Radiation Effects in Solids," *Annual Reviews of Nuclear Science* (Annual Reviews, Inc., Stanford, 1952), Vol. II.

[2] N. F. Mott and R. W. Gurney, *Electronic Processes in Ionic Crystals* (Oxford University Press, London, 1940).

the vacancy, while those perpendicular to this line are pushed away. This lowers the potential barrier E for radial jumps and increases it for lateral jumps. Since the atoms closest to the interstitial are affected most, the jumps toward the interstitial have the lowest barrier. Thus a vacancy within a distorted lattice around the interstitial has a preference for jumping towards the interstitial and an average jump time which decreases the closer it is to the interstitial.

If we assume the vacancy to be fixed and the interstitial atom to move, in the undistorted lattice the average jump time is given by (1), where the barrier energy E is now interpreted as the energy required by an interstitial to squeeze between neighboring atoms to an adjacent interstitial site. Within the region distorted by the vacancy, however, the situation is more complicated than before. The germanium lattice surrounding the vacancy moves towards the vacancy, the radial distance between atoms increasing and the tangential distance decreasing. Thus interstitial jumps along the line to the vacancy are more difficult. Motion toward or away from the vacancy will therefore be accomplished by diagonal jumps. This possibility has not been fully explored, although we do not believe it will change our general conclusions significantly. We shall consider here only the vacancies as moving.

III. STAGES OF ANNEALING

For those vacancies located within the deformed lattice around the interstitial, the vacancy jumps mainly towards the interstitial with jump times which become progressively smaller as the vacancy approaches the interstitial. Thus, the time required for recombination of these vacancies is approximately the time in which the vacancy jumps from its initial position.

For those vacancies which are located outside this deformed region, the probability of jumping in any direction is the same. Thus these vacancies wander according to a random-walk process, some wandering back within the deformed region where they are subsequently captured, and the rest wandering off through the crystal. The vacancies which wander off are "liberated" from their original interstitials. These will eventually be captured on dislocations or on the surface or may recombine with other interstitials.

These different processes correspond to different stages of the annealing, since they occur at different times. First to recombine will be those vacancies initially located within the deformed lattice surrounding the interstitial, since the time of recombination is less than the average jump time in the undistorted lattice. Second to recombine will be those which are initially located outside of the deformed lattice around the original interstitial, but which wander back after a small number of jumps of time τ and are captured at their original interstitials. Finally, because they must wander throughout the crystal, those vacancies which were liberated from their original interstitials will recombine or be captured after a large number of jump times τ.

IV. APPROXIMATE TIME DEPENDENCE OF ANNEALING

We shall consider the functional dependence on time of these various stages of annealing. Let us designate N as the number of unrecombined vacancy-interstitial pairs per unit volume and number the vacancy sites in order of their distance from the interstitial. Let N_i be the number of vacancies which were originally in the ith site. The expression for the annealing will be obtained from the expression for a particular initial site i, multiplied by N_i, and summed over all the sites.

For a vacancy initially within the distorted region around the interstitial, the rate of recombination of vacancies in site i will be approximately proportional to the number of unrecombined pairs:

$$dN/dt = -N/\tau_i, \tag{2}$$

where τ_i is the average jump time from the site i towards the interstitial. This leads to an exponential dependence on time characteristic of a monomolecular law of recombination. We shall designate by subscript M this first stage of the annealing, which is thus given by

$$N_M = \sum_1 N_i e^{-t/\tau_i}, \tag{3}$$

where $\sum_1$ indicates summation over all of the sites within the region distorted by the interstitial.

A vacancy located initially outside this distorted region will be governed by a random-walk process. As a first approximation, we shall treat this as diffusion in an isotropic medium. Let $P(r_i, r, t)$ be the probability per unit volume of finding a vacancy at a distance r from the interstitial at a time t after it was initially located at r_i. There is spherical symmetry around the interstitial so that the differential equation governing the diffusion can be written

$$\frac{\partial P}{\partial t} + \frac{D}{r^2}\frac{\partial}{\partial r}\left(r^2\frac{\partial P}{\partial r}\right) = 0, \tag{4}$$

where D is the diffusion constant. This equation can be solved under the boundary conditions that P must vanish at infinity and also at $r = r_c$, where r_c is the radius of the deformed region around the interstitial:[3]

$$P(r_i, r, t) = \frac{1}{8\pi(Dt)^{\frac{1}{2}}}\frac{1}{rr_i}\left[\exp\left[-\frac{(r-r_i)^2}{4Dt}\right] - \exp\left[-\frac{(r+r_i-2r_c)^2}{4Dt}\right]\right]. \tag{5}$$

The integration of this expression over the volume gives

[3] H. S. Carslaw and J. C. Jaeger, *Conduction of Heat in Solids* (Oxford University Press, London, 1947).

the total probability of finding a vacancy unrecombined. The integrated expression contains two parts: one which vanishes with time and the other which does not. The vanishing part corresponds to the vacancies which recombine during this second stage and the constant part corresponds to the vacancies which are liberated, eventually to recombine in the final stage. By multiplying the time-dependent part by the initial number of vacancies in site i and summing over all the sites, we obtain the expression for the second stage of the annealing, indicated by a subscript L for liberation:

$$N_L=\sum_2 N_i\frac{r_c}{r_i}\operatorname{erf}\left[\frac{r_i-r_c}{(4Dt)^{\frac{1}{2}}}\right]. \tag{6}$$

Here $\sum_2$ indicates summation over all of the sites outside r_c and erf refers to the error function. The diffusion constant is related to the jump time by the expression[4]

$$D=\langle b^2\rangle/2\tau, \tag{7}$$

where b is the magnitude of the change in the radius r during a single jump, and the brackets indicate the average over all possible jumps. Equation (6) can be rewritten in terms of (7) to give

$$N_L=\sum_2 N_i\frac{r_c}{r_i}\operatorname{erf}\left[\frac{(r_i-r_c)}{(2\langle b^2\rangle)^{\frac{1}{2}}}\left(\frac{\tau}{t}\right)^{\frac{1}{2}}\right]. \tag{8}$$

For the diamond-type lattice it is not difficult to show that $\langle b^2\rangle=a^2/16$, where a is the cube edge of the unit cell.

The time dependence of the final stage of the annealing will depend on whether capture occurs at dislocations or on the surface or whether the liberated atom recombines with other interstitials besides the one with which it was originally associated. We shall present expressions for all three. Let us introduce N_F (F for final) for the number of vacancies which are still free during the final stage of the annealing. The initial number of such vacancies N_{F0} is found from the constant part of the integration of Eq. (5). By multiplying this by N_i and summing, we find

$$N_{F0}=\sum_2 N_i[1-(r_c/r_i)]. \tag{9}$$

We shall assume that these are initially distributed uniformly through the volume of the crystal.

If these vacancies are captured on the surface, we must solve the transient diffusion equation.[3] For a rectangular parallelepiped of dimensions of u, v, w, this leads to

$$N_F=N_{F0}\frac{2^9}{\pi^6}\sum_{l=0}^{\infty}\sum_{m=0}^{\infty}\sum_{n=0}^{\infty}\frac{e^{-\alpha_{lmn}t}}{(2l+1)^2(2m+1)^2(2n+1)^2}, \tag{10}$$

where

$$\alpha_{lmn}=\pi^2D\left[\frac{(2l+1)^2}{u^2}+\frac{(2m+1)^2}{v^2}+\frac{(2n+1)^2}{w^2}\right]. \tag{11}$$

[4] M. C. Wang and C. E. Uhlenbeck, Revs. Modern Phys. **17**, 333 (1945).

A fair approximation to (10) is obtained by taking only the first term of the summation, so that if $w\ll u$, v, (10) can be rewritten

$$N_F\doteq N_{F0}\exp\left[-\frac{\pi^2\langle b^2\rangle}{2w^2}\left(\frac{t}{\tau}\right)\right], \tag{10a}$$

where expression (7) for the diffusion constant has been used. The approximate expression (10a) is correct at $t=0$, but becomes 20 percent too high at long times.

For capture at dislocations we shall solve the same equation with the requirement that the vacancy density vanish at a distance r_d from each dislocation. Inside r_d we assume that the lattice is distorted in such a way that capture is certain to follow. By symmetry the flow of vacancies vanishes midway between adjacent dislocations. We shall simplify this problem by assuming that cylindrical symmetry exists around each dislocation. The boundary conditions are then (a) the vacancy density vanishes at $r=r_d$, and (b) the vacancy flow vanishes at $r=R_d$, where $2R_d$ is approximately the average distance between dislocations. With these simplifying assumptions, the annealing is given by[3]

$$N_F=4N_{F0}\sum_n\frac{1}{(\alpha_nR_d)^2}\frac{J_1^2(\alpha_nR_d)\exp(-D\alpha_n^2t)}{J_0^2(\alpha_nr_d)-J_1^2(\alpha_nR_d)}, \tag{12}$$

where the J's and Y's are the Bessel and Neuman functions, respectively, and the α_n's are the roots of

$$J_0(\alpha_nr_d)Y_1(\alpha_nR_d)-J_1(\alpha_nR_d)Y_0(\alpha_nr_d)=0. \tag{13}$$

An approximate expression can be obtained for (12) if we take only the first term of the summation and assume $R_d\gg r_d$. For this case, the smallest solution of (13) is obtained when $\alpha_0r_d\ll\alpha_0R_d\ll1$, so that we may expand the Bessel Functions around their arguments and obtain for the smallest root of (13):

$$\frac{1}{\alpha_0^2}\doteq\frac{R_d^2}{2}\left[-\gamma+\ln\frac{2}{\alpha_0r_d}\right]. \tag{13a}$$

Here γ is Euler's constant $=0.577$. With this approximation and the use of (7), Eq. (12) can be written

$$N_F\doteq N_{F0}\exp[-\tfrac{1}{2}\alpha_0^2\langle b^2\rangle(t/\tau)]. \tag{12a}$$

If the final stage consists of a direct recombination of vacancies with interstitials, we shall obtain a second-order or bimolecular process. This can be seen by the following consideration: The number of vacancies which recombine in a jump time will be equal to the number of vacancies multiplied by the fraction of lattice sites available to the vacancy from which recombination is practically certain. This fraction is equal to the density of interstitials N_F divided by the total density of lattice sites N_{atom} and multiplied by the number of sites within the deformed region surrounding each interstitial which can be reached in a single jump from a site outside the deformed region. On the average

the number of such sites will be equal to $4\pi r_c^2\langle b\rangle N_{\text{atom}}$, where r_c is the same capture radius previously introduced and $\langle b\rangle$ is the magnitude of the change in the separation of interstitial and vacancy during one jump averaged over all possible jumps. Thus the rate of change of vacancies with time is

$$\frac{dN_F}{dt}=-\frac{N_F}{\tau}\times\frac{N_F}{N_{\text{atoms}}}\times 4\pi r_c^2\langle b\rangle N_{\text{atoms}}, \tag{14}$$

giving a differential equation which is easily integrable:

$$N_F=\frac{N_{F0}}{1+4\pi r_c^2\langle b\rangle N_{F0}(t/\tau)}. \tag{15}$$

For a diamond-type lattice the indicated average can be performed to give $\langle b\rangle=(\sqrt{3}/16)a$.

The total number of vacancies present after an annealing time t is given by the summation

$$N=N_M+N_L+N_F. \tag{16}$$

It should be noted that the annealing time t in all the above expressions only appears in the ratio t/τ. By comparing the times at which the same degree of annealing occurs for different temperatures, the barrier energy can be determined without an actual fit of the theoretical expressions to experimental data. The barrier energy, so determined, will be constant in the stages of the annealing governed by N_L and N_F but will decrease with decreasing time (or temperature) in the stage governed by N_M.

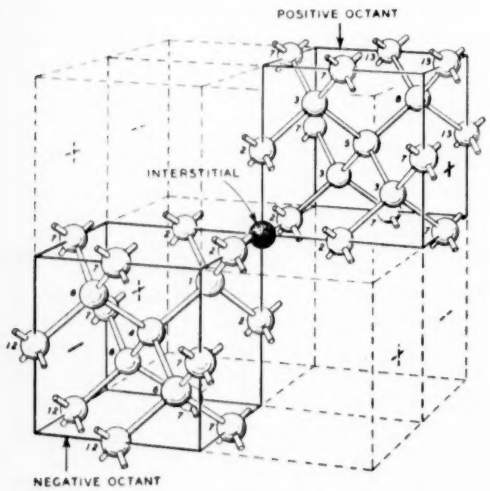

FIG. 2. The diamond lattice surrounding an interstitial site place at the origin. Only the details of the two essentially different octants are shown. All the octants with the same label (+ or −) have identical symmetry with respect to the interstitial. Numbers indicate site numbers (i) arranged in an increasing sequence with their distance from the interstitial.

V. ANNEALING IN A DISCRETE LATTICE

In the last section we developed expressions for the time dependence of the annealing by approximating the discrete lattice outside the capture radius r_c with a continuum in which diffusion takes place, and by idealizing the discrete lattice inside the capture radius by permitting vacancy jumps only toward the interstitial. In this section we shall present a set of differential equations which describe the annealing without using the above approximations.

To begin with, lattice symmetry enables us to reduce the number of sites which we must consider. Vacancies in sites which have the same symmetry with respect to the interstitial have exactly the same probability of escaping or recombining with the interstitial. Let us introduce P_i as the probability of finding the vacancy in any of these identical sites.

We next need to consider those sites of different symmetry which are adjacent to the ith site. Let us introduce b_{ji} for the number of j sites adjacent to the ith site. Also let $1/\tau_{ji}$ be the probability per unit time that a vacancy located in the ith site will jump to a particular one of the adjacent j sites. The total probability of a vacancy jumping from the ith site is thus $\sum_j b_{ji}/\tau_{ji}$. This leads us to the differential equation governing the rate of change of P_i with time,

$$\frac{dP_i}{dt}=-P_i\sum_j\frac{b_{ji}}{\tau_{ji}}+\sum_i\frac{b_{ij}}{\tau_{ij}}P_j. \tag{17}$$

This actually represents an infinite set of linear homogeneous differential equations for which the solution is

$$P_i=\sum_n A_n\Psi_{in}e^{-\gamma_n t}, \tag{18}$$

where γ_n are the eigenvalues of the matrix

$$\left\|\delta_{ij}\left(\gamma_n-\sum_k\frac{b_{ki}}{\tau_{ki}}\right)+\frac{b_{ij}}{\tau_{ij}}\right\|, \tag{19}$$

in which δ_{ij} is the Kronecker delta, Ψ_{in} are the eigenvectors of the matrix (19), and A_n are constants determined from the initial distribution of P_i. Equation (18) thus represents the general solution for the first two stages of the annealing, providing the b_{ij} and τ_{ij} are known, and the initial values of P_i are given.

VI. ANNEALING IN THE DIAMOND-TYPE LATTICE

To illustrate how this method works we have obtained the b_{ij} for a diamond-type lattice and solved the equations for the special case where τ_{ij} is constant independent of i, j. This corresponds to the liberation stage of the annealing.

In the diamond-type lattice there exist "natural" interstitial sites such that an atom located in such a site is the same distance from its four nearest neighbors as the separation between nearest neighbors in the normal lattice sites. If we place the interstitial at the

origin of the coordinate system and place one of its nearest neighboring interstitial sites at the (111) position (measured in units of one-fourth the cube edge of the unit cell), this will locate the germanium atoms or vacancy sites. Thus the four neighboring vacancy sites will be $(\bar{1}\bar{1}\bar{1})$, $(\bar{1}11)$, $(1\bar{1}1)$, and $(11\bar{1})$. The next six nearest neighbors will be (200), (020), (002), $(\bar{2}00)$, $(0\bar{2}0)$, and $(00\bar{2})$. All other sites can be obtained from these first two by adding or subtracting integral multiples of the fundamental translation vectors (022), (202), and (220). All sites in the nearest position to the interstitial and all progeny of these sites obtained by translation have neighboring vacancy sites in the same directions, namely $(\bar{1}\bar{1}\bar{1})$, $(\bar{1}11)$, $(1\bar{1}1)$, and $(11\bar{1})$. Similarly all sites in the next nearest position to the interstitial and their progeny will have their neighboring vacancy sites in the directions (111), $(1\bar{1}\bar{1})$, $(\bar{1}1\bar{1})$, and $(\bar{1}\bar{1}1)$. This enables us to locate easily the nearest neighbors and hence to determine the b_{ij}.

Since around each coordinate axis there is twofold rotational symmetry, of the eight octants around the origin only two will be essentially different (see Fig. 2). For instance, we may choose for the two octants those whose indices are all positive or all negative. Thus the four nearest sites to the interstitial have identical symmetry and are characterized by the $(\bar{1}\bar{1}\bar{1})$ position in the negative octant. In each octant there is a threefold rotational axis along the cube diagonal, so that all sites whose indices are related by a simple permutation have identical symmetry. Thus (200), (020), and (002) have the same symmetry. In fact since at least one of the indices is zero, they are on the edge of the octant and are common to the positive and negative quadrants, so that all six next nearest neighbors to the interstitial have the same symmetry. The four nearest neighbors thus represent site $i=1$, and six next nearest neighbors represent site $i=2$. The first few sites are shown in Fig. 2.

A scheme for representing all the vacancy sites in the vicinity of the interstitial is shown in Fig. 3. Here the nearest neighbors are connected by lines and the numbers on the lines indicate the b_{ij}. For convenience the sites are plotted with their distance from the interstitial on the vertical axis and their distance from the nearest coordinate plane on the horizontal axis. Position in the positive octant is plotted to the right and position in the negative octant to the left. The areas of the circles are drawn proportional to the number of sites with the same symmetry.

We have attempted the solution of Eqs. (19) with two different boundary conditions, capture at $i=1$ and $i=2$, and initial location of the vacancy successively at each of the nine closest sites. Because the determinations of γ_n, Ψ_{in}, and A_n are laborious if many sites are considered, we did not use this method. Instead we used three separate approximate methods whose regions of accuracy overlapped enough to determine the complete solution. For the early stages of the annealing we considered only the first twelve sites and permitted no return from sites outside these. The Eqs. (19) were then solved on an analog computer for P_1 and P_1+P_2 for the two stated boundary conditions, respectively. After enough time elapses (*ca* 5τ) these computed values will fall below the actual values because of the neglect of vacancies diffusing back from outside the first twelve positions. In order to correct this error, we would have to consider more sites than the computer could handle. To extend the solution to longer times we replaced the continuous differential equation of (19) by a discontinuous jump equation in which after a time τ the increase in P_i is given by

$$\Delta P_i = -P_i + \tfrac{1}{4}\textstyle\sum_j b_{ij} P_j. \qquad (19a)$$

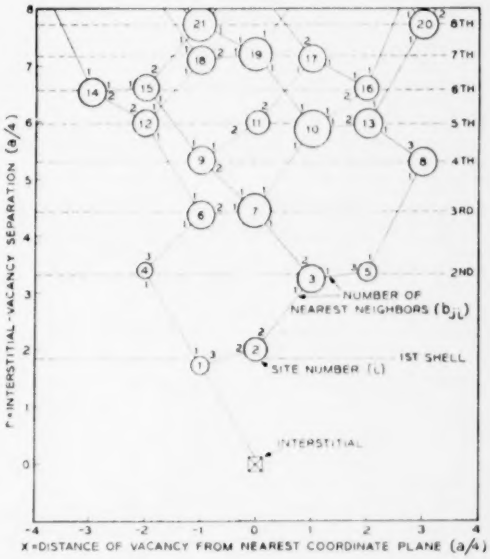

FIG. 3. Representation of the vacancy sites relative to an interstitial located at the origin. Sites with the same symmetry are lumped together, the area of each circle being arranged proportional to the number of individual sites. Lines connect nearest neighbors, and the number of these (b_{ij}) is indicated. Notice that the sites occur in shells of about the same radius.

The factor $\frac{1}{4}$ appears here because there are four sites to which a vacancy may jump; i.e., $\sum_j b_{ij}=4$ and $\tau_{ij}=4\tau$. It was not difficult to solve this equation taking into consideration the first one hundred sites. This allowed sixteen jump times τ before the influence of sites outside the first one hundred could be felt. For times longer than this enough sites were involved so that we felt the continuum differential equations should be applicable and we could use an equation of the type (8), where r_e and r_i were regarded as adjustable parameters to tie smoothly onto the solutions obtained from (19a).

The complete solutions for two particular initial conditions are shown in Fig. 4. Here on the vertical axis is plotted the probability that a vacancy has recombined

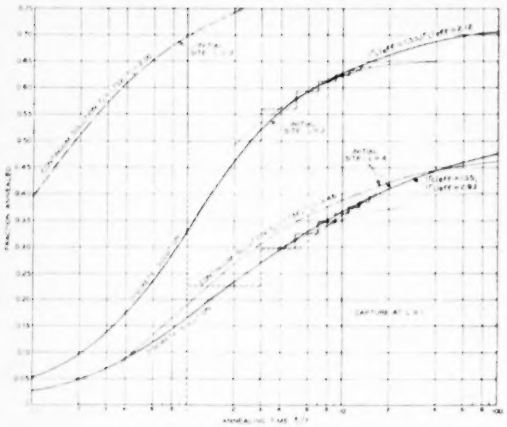

FIG. 4. The annealing in an undistorted discrete diamond-type lattice [Eq. (19)] compared with the annealing in an isotropic homogeneous medium [Eq. (6)] for two particular initial conditions. The light lines indicate how the three approximate curves used in solving Eq. (19) depart from the actual curve. The two cases shown represent the largest departures of the continuum solution from the discrete solution.

with an interstitial, $1-(N/N_i)$, at a time t after starting in position i. The heavy line for each curve represents the final solution and the light lines show the departure

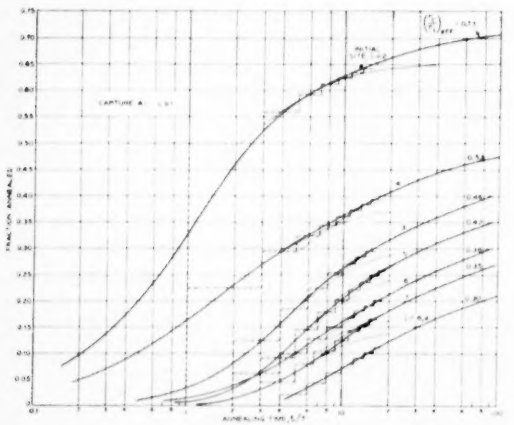

FIG. 5. The probability that a vacancy and interstitial have recombined a time t after starting in the ith site of a diamond-type lattice. The heavy line represents the complete solution for a lattice which is undeformed outside the first site ($i=1$). The light and the dashed lines indicate how the three approximate curves used in the solution depart from the actual curve.

of the approximate solutions from this in the range of time where the approximation begins to break down. The approximate solution of Sec. IV, Eq. (6), in which r_e and r_i were not adjusted is shown as a dashed curve. The two boundary conditions shown represent the largest departures of the approximate solution of Eq. (6) from the more complete solution of all the boundary conditions investigated. The approximate solutions of Eq. (6) can be made coincident with the complete solution for long times by adjustment of r_e and r_i. The effective values of these radii for coincidence for these two cases are marked on the curves. Even though the approximate solution departs considerably from the complete solution, only a small adjustment of r_e and r_i is required for coincidence of the curves.

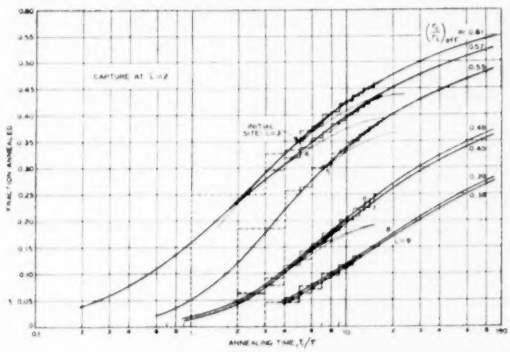

FIG. 6. Same as Fig. 3 except that the lattice is assumed to be deformed out to the second site ($i=2$).

The complete solutions for all of the boundary conditions investigated are shown in Figs. 5 and 6. The effective value of r_e/r_i is marked on the curves. This represents the asymptotic value for the annealing probability at long times. The value for $(r_e)_{\text{eff}}$ could be chosen the same for all curves with the same capture site. The value for $(r_i)_{\text{eff}}$ approached the true value as r_i increased. In no case did these radii have to be adjusted by more than 15 percent. Use will be made of the analysis in this section in the interpretation of the observed annealing of bombarded germanium in the following paper.

We should like to thank R. W. Hamming and other members of the analysis group for the numerical computations and S. Machlup, W. T. Read, and W. Shockley for their helpful suggestions.

Annealing of Bombardment Damage in Germanium: Experimental

W. L. BROWN AND R. C. FLETCHER, *Bell Telephone Laboratories, Murray Hill, New Jersey*
AND
K. A. WRIGHT, *High Voltage Research Laboratory, Massachusetts Institute of Technology, Cambridge, Massachusetts*
(Received July 22, 1953)

Experiments have been performed on the annealing of bombardment damage in germanium above room temperature. The damage was produced by 3-Mev electrons and consisted primarily of isolated vacancy-interstitial pairs. The extent of the damage was determined by measurement of the change in conductivity of *n*-type samples. From the annealing results, the activation energy for the diffusion of vacancies in germanium was found to be about 1.7 ev. The actual annealing curves have been fitted in terms of the model of the annealing process described in the preceding paper.

I. INTRODUCTION

EXPERIMENTS have been reported[1] on the bombardment of germanium with heavy particles (deuterons,[2] alpha particles,[3] neutrons[4]) and with electrons.[5] In all cases the bombardment has decreased the conductivity of *n*-type specimens. Since under continued bombardment it is possible to convert the samples to *p*-type, the principal effect is not due to a change in carrier mobility, but must be explained as a change in carrier concentration. The bombardment presumably displaces atoms from their normal lattice sites to interstitial positions in the crystal, i.e., creates vacancy-interstitial pairs, and the change in conductivity has been attributed to localized electron energy levels associated with the pairs. The crystal recovers from its damaged condition as evidenced by a recovery of the conductivity subsequent to bombardment. Part of the damage anneals in the order of minutes even at room temperature, but the original conductivity is not fully restored until annealing has been carried out at several hundred degrees centigrade. In this paper we shall be principally concerned with the characteristic features of this higher-temperature annealing.

It is experimentally feasible to produce a simple type of damage in germanium by bombardment with electrons. In a single collision between a germanium atom and an electron with an energy the order of 3 Mev, the energy transferred to the atom is so small that only a single vacancy-interstitial pair or at most a few pairs can be created. This is in contrast to the large amount of damage generally produced in a single encounter of a heavy particle with a germanium atom. Furthermore, an electron loses energy slowly enough (principally through ionization) for the damage to the lattice to be reasonably uniform through samples the order of a millimeter in thickness. For an equivalent uniformity samples must generally be much thinner with heavy charged-particle bombardment. Because of these two simplifying conditions we have confined our attention to electron bombardment in the experiments described in this paper.

II. EXPERIMENTAL PROCEDURE

The samples which were used were rods $\frac{1}{16}$ in. $\times\frac{1}{16}$ in. $\times\frac{1}{2}$ in. with sand blasted surfaces. During bombardment the samples were maintained at approximately room temperature by partially immersing them in running water. The bombarded surface of the samples remained dry. Three Mev electrons for the bombardments were obtained from one of the Van de Graaff generators of the High Voltage Research Laboratory at M.I.T. The samples were located 46 cm from a 0.009 inch thick aluminum exit window and approximately on the axis of the cone of high energy electrons from the machine. Measurements of the intensity distribution across the beam[6] indicate that at such a position the electron flux should be uniform within one percent over the area of our samples. Calibration measurements were made of the total beam current *versus* the current to a 3-in. diameter aluminum plate placed at the position of the samples. The total beam current was then used to monitor the flux during bombardment. For most of our runs the flux at the samples was approximately 4×10^{12} electrons/cm^2 sec. In this number there is no correction for back scattering from the 3-inch aluminum plate or from the germanium samples.

The conductivity of the samples was determined by four electrode resistance measurements: two plated contacts on the ends of the rod carried a current, and two tungsten points were used to measure a voltage difference along the rod's length. All resistance measurements, both before bombardment and at various stages in the annealing, were made at room temperature. No measurements were made during bombardment.

III. RESULTS OF THE ANNEALING—ACTIVATION ENERGY

Several samples with the same initial conductivity were given the same bombardment but were annealed

[1] For an extensive account of this work see K. Lark-Horovitz, *Nucleon Bombarded Semi-Conductors*, Reading Conference on Semi-Conducting Materials (Butterworths Scientific Publications, London, 1951), pp. 47–78.
[2] Lark-Horovitz, Bleuler, Davis, and Tendam, Phys. Rev. **73**, 1256 (1948).
[3] W. H. Brattain and G. L. Pearson, Phys. Rev. **80**, 846 (1950).
[4] Cleland, Crawford, Lark-Horovitz, Pigg, and Young, Jr., Phys. Rev. **83**, 312 (1951); **84**, 961 (1951).
[5] E. Klontz and K. Lark-Horovitz, Phys. Rev. **86**, 643 (1952).
[6] Trump, Wright, and Clarke, J. Appl. Phys. **21**, 345 (1950).

at different temperatures. The initial conductivity of one such group was 1.4 mho/cm n type and the conductivity after bombardment and room temperature annealing was about 0.8 mho/cm n type. Figure 1 shows the annealing curves obtained for this group. We have plotted f, the fraction of the conductivity which has annealed, as a function of time at different temperatures. The fraction f is defined as

$$f=(\sigma-\sigma_{AB})/(\sigma_0-\sigma_{AB}),$$

where σ is the conductivity at some stage in the annealing, σ_0 is the initial conductivity, and σ_{AB} is the conductivity after bombardment and room temperature annealing. This fraction is monotomically related to the fraction of the vacancy-interstitial pairs which have annealed,[7] and it thus provides a consistent measure of the extent of the annealing for all the samples in this group.

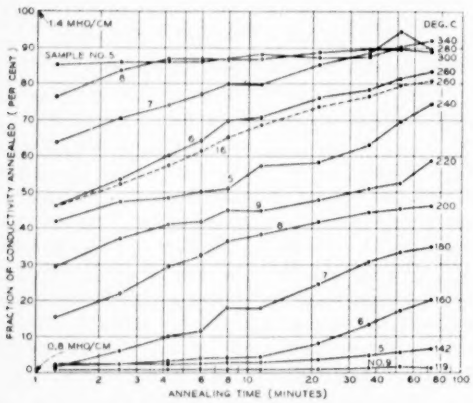

FIG. 1. Annealing curves at different temperatures for a group of samples having the same initial conductivity and given the same bombardment. The sample numbers appear above the curves, the annealing temperatures at the right end.

Samples 6 and 16 were both annealed at 260°C. Sample 6 had previously been annealed at 160°C while sample 16 had not. The fact that the two curves at the higher temperature agree fairly closely indicates that the annealing at one temperature is not affected by a previous annealing carried out at a temperature 100°C lower. That is, all of the annealing which took place in more than an hour at 160°C took place in less than a minute at 260°C. This observation has made it possible to cover a wide range of annealing temperatures in 20°C intervals using only five samples, each of which is annealed in 100°C intervals. This scheme has been carried out in the curves of Fig. 1.

It has been shown in the preceding paper that if a vacancy moves in the crystal by jumping to an adjacent atomic site the annealing should depend upon the average jump time for a vacancy τ and the annealing time t only in the combination t/τ. The temperature dependence of the annealing appears almost entirely through τ. Thus it should be possible to superimpose the annealing curves for different temperatures by adjusting the time scales by the proper factors. On our logarithmic plot, adjusting the time scale amounts to displacing the curves along the horizontal axis. The superposition has been carried out for all the curves of Fig. 1 and the result is shown in Fig. 2. The abscissa is now the equivalent annealing time at an arbitrarily chosen reference temperature of 220°C. The arrow above each curve indicates the annealing time at 220°C equivalent to ten minutes annealing at the temperature shown. The ratio of these two times is just equal to the ratio of the jump times at these two temperatures.

A plot of the relative jump time as a function of $1/T$ is shown in Fig. 3. Three different sets of points are shown in this figure. They correspond to three groups of samples having different initial conductivities and different bombardments as indicated in the legend.

The points in Fig. 3 can be represented fairly well by a single straight line, but a line with a slight curvature at the bottom, as shown, fits better. The slope of the line at high temperatures corresponds to an activation energy of about 1.8 ev. The slope at the lower temperatures ranges from 1.8 to about 1.6 ev. The observation that a lower activation energy is associated with the annealing at lower temperatures is significant in terms of the model of the annealing process described in the previous paper. This point will be brought out in Sec. V.

IV. THE LOCATION OF BOMBARDMENT ENERGY LEVELS

In order to analyze the composite annealing curve of Fig. 2 in terms of a model of the process, it is necessary to know the relationship between the conductivity, which is measured, and the density of vacancy-interstitial pairs. For this purpose the change in conductivity of a number of samples has been measured for different

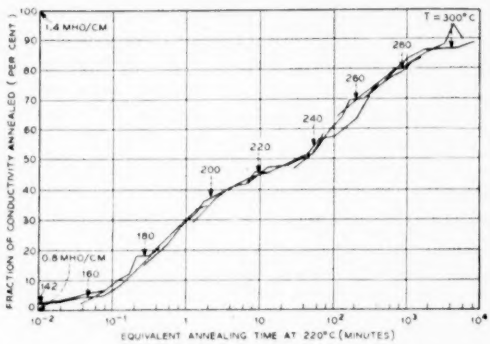

FIG. 2. Composite annealing curve obtained by adjusting the time scales for superposition of the curves of Fig. 1 with respect to the curve at 220°C. The arrows above the curves indicate the ten minute annealing points for the original curves.

[7] This, of course, does not apply if the bombardment is so long that the samples are converted to p type.

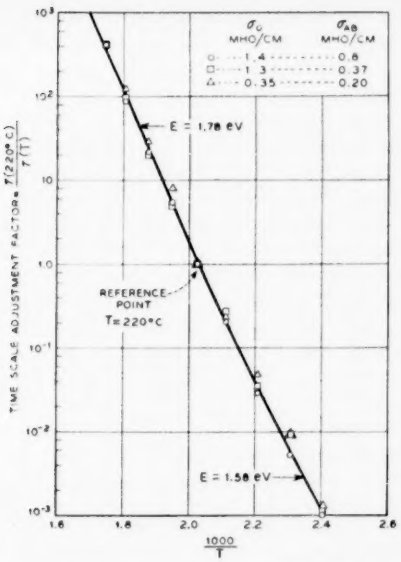

FIG. 3. Plot of the time scale adjustment factors used in obtaining a composite curve such as Fig. 2. The results for three different groups of samples are shown. σ_0 is the initial conductivity and σ_{AB} the conductivity after bombardment.

amounts of bombardment. The density of interstitial-vacancy pairs is presumably proportional to the bombardment but the conductivity change in general is not. The relationship between these two had only to be monotonic in order to permit determination of the activation energy for the annealing process as discussed in the preceding section. It must be known more specifically to fit the annealing curve.

Figure 4 shows the change in conductivity as a function of the integrated bombarding electron flux for two groups of *n*-type samples having different initial conductivities. Each point represents a different sample. For short bombardments on the higher conductivity samples the conductivity changes linearly with the bombardment. This is the result to be expected if none of the energy levels introduced by the bombardment lie close to the position of the Fermi level for these conductivities. The slope of this part of the curve corresponds to a cross section of 30×10^{-24} cm^2 for producing vacancy-interstitial pairs assuming each pair has the effect of a single acceptor-type center. McKinley and Feshbach[8] give the differential cross section for relativistic scattering of particles in a Coulomb field. This can readily be related to the total cross section for production of a vacancy-interstitial pair by a high-energy electron. Using Klontz's[5] experimental value for the threshold of the process (630 kev) we calculate a cross section of 56×10^{-24} cm^2 at 3 Mev. Correcting for the energy loss through the thickness of our samples reduces the effective cross section to 42×10^{-24} cm^2. Unless the fraction of pairs annealing at room temperature and below is large, the agreement between theoretical and experimental values of the cross section supports the assumption that each vacancy-interstitial pair has the effect of a single acceptor-type center. For incident electron fluxes greater than 10^{15}/cm^2 on the samples having $\sigma_0=1.4$ mho/cm the conductivity changes nonlinearly with bombardment. This nonlinearity occurs at too high a conductivity to be attributable to an approach to intrinsic. We can conclude that there are bombardment energy levels lying above the middle of the forbidden band and within 0.1 ev of it.

The change in conductivity on the samples having $\sigma_0=0.3$ mho/cm indicates nonlinearity even for the short bombardments. This is consistent with the interpretation of the results for the higher conductivity samples.

Several experiments were performed on the bombardment of low conductivity *p*-type samples (*ca* 0.04 mho/cm). The rate of change of conductivity with bombardment in this case was more than a hundred times smaller than for the *n*-type samples. This observation is quite different from that reported by Cleland *et al.*[4] in which a *p*-type sample under neutron bombardment increased in conductivity only about eight times more slowly than *n*-type samples decreased in conductivity. It was noted in Sec. I that electron bombardment would be expected to produce a simpler type of lattice disorder than the heavier particles. The difference between our results for electrons and that reported for neutrons may perhaps be ascribed to differences in the systems of bombardment energy levels.

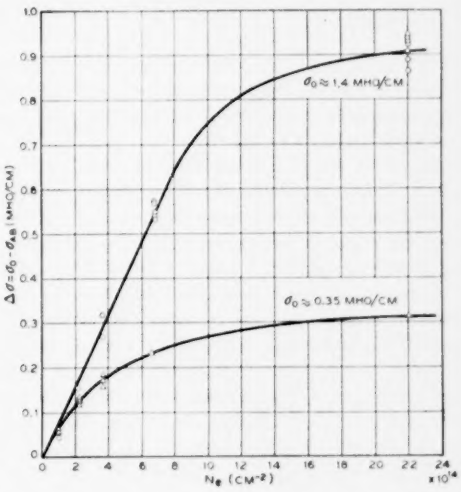

FIG. 4. The change in conductivity produced by bombardment. Results are shown for samples with two different initial conductivities. Each point is a single sample.

[8] W. A. McKinley and H. Feshbach, Phys. Rev. **74**, 1759 (1948).

V. THEORETICAL FIT OF THE COMPOSITE ANNEALING CURVE

The composite annealing curve of Fig. 2 has been made for samples with an initial conductivity of 1.4 mho/cm which had been bombarded with a flux of about 7×10^{14} electrons/cm^2. These samples fall in the range of linear dependence of conductivity on the density of interstitial-vacancy pairs. The fraction of the change in conductivity which has annealed, the ordinate of Fig. 2, is thus just equal to the fraction of the vacancy-interstitial pairs which has annealed.

Before proceeding to fit the annealing curve theoretically, we shall note several particularly significant features of the curve which will need to be explained. First of all, the annealing takes place over a very large range in time; second, the curve has two humps; and finally, at an equivalent annealing time of 10^4 minutes at 220°C ten percent of the vacancy-interstitial pairs have still not annealed. These features are prominent in the annealing curves obtained for each of the three groups of samples used in determining Fig. 3. The

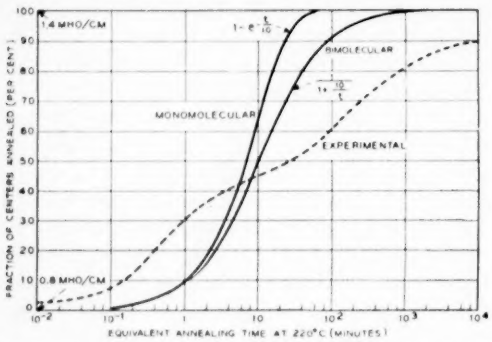

FIG. 5. Theoretical fit of the composite experimental annealing curve of Fig. 2 with a bimolecular or a single monomolecular recombination process.

relationship between the conductivity and the density of pairs is linear for only one of the groups, however, and for simplicity the curve for this group is the only one we shall attempt to fit.

Exponential or hyperbolic functions of time have previously been suggested for representing annealing phenomena.[1,5] These two possibilities are indicated in Fig. 5. The composite experimental annealing curve of Fig. 2 is represented by a smooth curve in this figure. The monomolecular—exponential—curve goes from its 10 percent to its 90 percent point in a factor of twenty in time. The bimolecular—hyperbolic—curve covers the same range of annealing in a factor of ninety in time. By different choice of the time constants these curves may be shifted along the time scale, but the factors of twenty and ninety are invariant to such changes. Neither the exponential nor the hyperbolic function anywhere near satisfies the experimental curve, which requires a factor of almost 10^5 in time to cover the 10 to 90 percent annealing range.

There are several possibilities for explaining the experimental annealing curves which depend upon the model of the annealing process discussed in the preceding paper. Let us briefly review the stages in the annealing according to that model. A vacancy which after bombardment is close to its original interstitial will recombine with it easily because of lattice distortion. The energy required for a vacancy to jump toward the interstitial is less than it would be if the interstitial were far removed. Vacancy-interstitial pairs having a small initial separation thus recombine monomolecularly. More than a single monomolecular time constant may arise from differences in the initial separation within the distorted region. Vacancies which initially are somewhat farther from their interstitials will wander about in the lattice. Some of them will recombine with their original vacancy in their wandering, but some will wander completely away from their interstitial and be "liberated." Vacancies which have been liberated will be captured on surfaces or dislocations or will recombine with other interstitials in a bimolecular process.

On the basis of this model we shall attempt to fit the experimental curve with three different possibilities: (A) a distribution of monomolecular processes;[9] (B) monomolecular processes plus recombination during liberation; (C) recombination during liberation plus bimolecular recombination. We shall consider these in detail in the following paragraphs.

(A) Distribution of Monomolecular Processes

We suppose that all of the vacancy-interstitial pairs recombine monomolecularly but that they have a distribution of time constants corresponding to differences in their initial separations in the elastically distorted region. The fraction of centers which have annealed in a time t in this case will be given by

$$f=\sum_i N_i(1-e^{-t/\tau_i})/\sum N_i,$$

where N_i is the density of pairs having a particular separation and τ_i is the time constant associated with that separation. We can assume a continuous distribution of τ_i and write this as

$$f(t)=\int_0^\infty \rho(\tau)(1-e^{-t/\tau})d\tau,$$

where $\rho(\tau)d\tau$ is the fraction of pairs with time constants in the range $d\tau$. This integral can be evaluated approximately by assuming

$$1-e^{-t/\tau}=\begin{cases}0 \text{ for } \tau>t\\ 1 \text{ for } \tau<t.\end{cases}$$

Then

$$f(t)=\int_0^t \rho(\tau)d\tau,$$

[9] This suggestion has previously appeared in the literature (see reference 4).

and

$$df(t)/dt=\rho(t).$$

It is apparent from this relationship and from the shape of the composite annealing curve that the distribution $\rho(t)$ will have two maxima. By approximating the exponential function with a step function we have artificially broadened the peaks in the distribution. Perhaps there are in fact only two different time constants. Figure 6 shows a theoretical curve drawn assuming two time constants $\tau_1=0.8$ min and $\tau_2=450$ min corresponding approximately to the maxima in the distribution. The ratio of the two time constants represents a difference of 0.27 ev in the annealing energy of the two groups of vacancy-interstitial pairs. This difference is consistent with the difference found from the $1/T$ plot of Fig. 3.

The curve drawn in Fig. 6 is not a particularly good fit to the data. It is poorest at the upper end since it does not predict the failure of the vacancy-interstitial

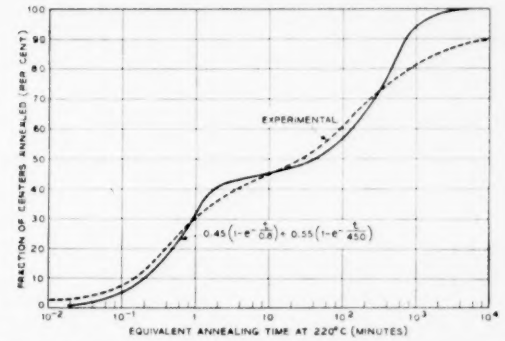

FIG. 6. Theoretical fit of the experimental annealing curve with two monomolecular recombination processes.

pairs to anneal completely in the times shown. The theoretical curve also has a much flatter region in the middle of the annealing range than is observed. One can conclude that two time constants are insufficient to fit the data. Two groups of time constants centered at the values we have chosen above are required for a good fit. These will give rise to the two humps in the annealing curve without as flat an intermediate region as there is in Fig. 6. To avoid the difficulty at long times we suggest there is still another group or perhaps another process (recombination during liberation, for example) which represents the 10 percent of the pairs beyond the range of these experiments.

By examining the lattice in detail we can get some idea as to which vacancies will be contributing to the monomolecular processes. We remarked earlier that some annealing takes place at room temperature. This has been reported by Klontz,[10] who also finds evidence of annealing at even lower temperatures. The annealing curve which we wish to explain applies after room temperature annealing is essentially complete. Thus, in fitting the composite annealing curve from a detailed picture of the lattice some allowance for the lower temperature effects must be made. From Fig. 2 of the preceding paper, vacancies initially in the two sites of the first shell will certainly be the first to anneal, and we shall suppose that these two contribute the annealing at room temperature and below.

The vacancies having the next shortest time constants will be those located in the next closest positions to their interstitials. The arrangement of these positions in shells at particular distances is suggestive of the grouping of time constants which we have seen will fit the experimental curve. The grouping tendency is more pronounced the smaller the separation of the vacancy and interstitial. Thus we are led to associate the two groups of time constants with vacancy sites in the second and third shells. This is not a unique association but involves the smallest shells which allow a consistent explanation of the low temperature annealing. In addition to the grouping tendency, there is another consideration which suggests low numbered shells are involved. If we identify the two humps of the experimental curve with vacancies initially in two adjacent shells, these two shells represent about 90 percent of all the vacancies left after room temperature annealing. This observation is not unreasonable for shells two and three, but if higher numbered shells are to be important the initial distribution must have a more abrupt cutoff than one would expect.

(B) Monomolecular Plus Liberation Processes

Figure 7 shows an attempt to fit the annealing curve with two monomolecular processes plus the recombination during liberation. We have associated the hump at longer times in the experimental curve with the recombination during liberation, the lower hump with monomolecular processes. The final mechanism (bimolecular recombination or capture at surfaces or dislocations) only represents the 10 percent of the vacancies not yet annealed at the longest times shown.

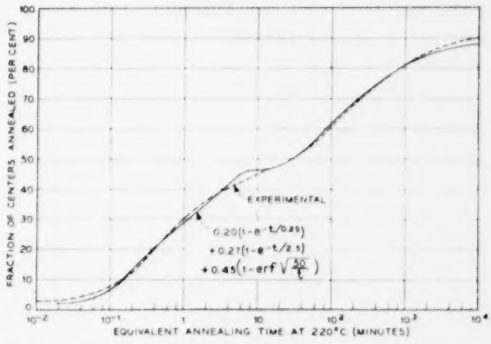

FIG. 7. Theoretical fit of the experimental annealing curve with two monomolecular recombination processes plus the recombination during liberation (see text).

[10] E. E. Klontz, Signal Corps Report, Purdue University, June 1952 (unpublished).

In looking at the lattice in detail again, we assume that the vacancies in the first shell (Fig. 2, preceding paper) have annealed at room temperature and below. The vacancies which anneal monomolecularly in the range of temperatures and times which we are considering will be those initially located next closest to their interstitials. There are sites at two slightly different distances, at approximately $0.9a$ (where a is the cube edge of the unit cell), and to these we attribute different time constants. The vacancies in these sites make up about 50 percent of the observed annealing.

With this picture of the early stages of the annealing we can fix the capture radius r_c for the liberation stage at $r_c=0.9a$. Figure 2 indicates that of those vacancies participating in the liberation process a large fraction must be captured. About 50 percent of the vacancies are left after the monomolecular processes are complete. Only 20 percent of these will actually be liberated. Thus about 80 percent of the vacancies having initial locations $r_i>0.9a$ will be captured during liberation.

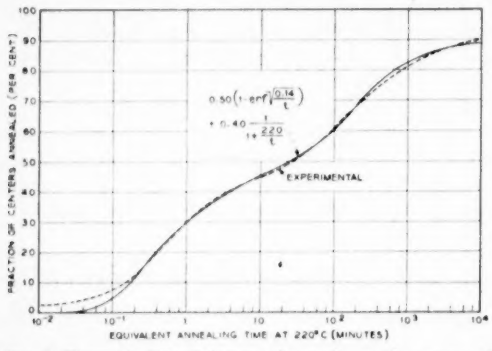

FIG. 8. Theoretical fit of the experimental annealing curve with the recombination during liberation and bimolecular recombination.

Since this fraction is just r_c/r_i we find $r_i \simeq 1.1a$. This suggests that most of the vacancies having $r_i>0.9a$ are in those sites at about $1.1a$ (see Fig. 2 of the preceding paper). We have assumed in drawing the curve of Fig. 7 that all of them are located there.

From the time constant associated with the theoretical curve in the liberation range and from the activation energy for the jump process determined in Sec. III we can compute a lattice vibration frequency. This turns out to be about 10^{13}/sec, an entirely reasonable value. The ratio of the jump time used in the first monomolecular process to that used in the liberation part of the curve represents a difference in activation energy of about 0.2 ev, consistent with the indications of Fig. 3. Apart from these consistencies the fit drawn in Fig. 7 is not exceptionally good. The predicted liberation range extends over a larger interval in time than is experimentally observed. The predicted monomolecular range is not as smooth as the experimental curve. It was assumed in the analysis of the preceding paper that a sharp distinction could be drawn between the monomolecular and liberation mechanisms. No account was taken of the transition from one to the other. Unfortunately, in the fit we are now considering the transition region plays its most prominent role. Thus the incompleteness of the analysis may be responsible for the discrepancies in the fit.

(C) Liberation and Bimolecular Processes

Figure 8 shows an attempt to fit the annealing curves with liberation and bimolecular processes. We now associate the hump in the experimental curve at short times with the liberation range, the hump at longer times with the bimolecular range. The 10 percent of the vacancy-interstitial pairs not yet annealed at the longest times shown may perhaps be attributed to capture on surfaces or dislocations. The monomolecular processes involving pairs initially in the elastically distorted region are complete before the start of these annealing experiments.

The theoretical curve is a good fit to the observed curve. From the time constants of the two parts of the theoretical curve we can calculate the capture radius r_c and the lattice vibration frequency ν_0. We find $r_c=20.7$A, rather larger than seems reasonable. It is about four times that chosen in the preceding section. The elastic deformation falls off so rapidly it seems unlikely that there can be any appreciable interaction between vacancies and interstitials out to this great a distance. For ν_0 we obtain about 10^{17}/sec, where the order of 10^{13} would be expected. The calculation of ν_0 involves the activation energy obtained from Fig. 3. This will be different from the actual jump energy if the actual energy has a temperature coefficient. However, it seems highly improbable that one can account for a discrepancy of 10^4 in this way.

The jump energy associated with the liberation and bimolecular ranges should be the same since only jumps in an undistorted lattice are involved. This implies a single slope to the curve of Fig. 3. As we have previously remarked, a straight line can be fitted to the points, but not as well as the curve drawn.

There is still another objection to fitting the annealing with (C). Trapping on dislocations or surfaces cannot account for the final 10 percent of the vacancy-interstitial pairs unless we assume that the interstitial diffuses or that the electron acceptor energy level is associated with the interstitial. Neither alternative is a desirable one.

The liberation and bimolecular processes do not seem to provide a satisfactory explanation for the observed annealing. Either of the other possibilities, *viz.*, a series of monomolecular processes or monomolecular processes plus the liberation process provides a reasonably consistent explanation. We believe the latter is the more probable of the two.

The authors wish to acknowledge the assistance of Mr. A. A. Studna who prepared the germanium samples and performed the resistance measurements on them.

Bleaching Properties of *F* Centers in KBr at 5°K†

JORDAN J. MARKHAM,* REUEL T. PLATT, JR., AND IRVING L. MADOR
Applied Physics Laboratory, Johns Hopkins University, Silver Spring, Maryland
(Received June 15, 1953)

The bleaching properties of *F* centers in KBr have been investigated experimentally at 5°K and 78°K. The stability of *F* centers towards bleaching is dependent on the temperature and mode of formation. Those produced by additive coloration are stable; those produced at room temperature by x-rays bleach slightly; those produced at 78°K by x-radiation show some bleaching; while those produced at 5°K by x-radiation show a large initial instability. Some tentative theoretical conclusions are made.

I. INTRODUCTION

THE nature of the *F* center which forms in alkali halide crystals is well established.[1] The *F* center results from the trapping of an electron in a negative-ion vacancy, and has a ground state and a single excited state. The gap between the excited state and the conduction band is small (about 0.15 ev in KBr) so that at room temperature the electron easily escapes from the excited level. However, at 5°K the thermal energy of the lattice is too small to produce the transition and the center should not be destroyed by light absorption.

These properties are observed in KBr additively colored with excess potassium. In KBr colored by x-rays, the *F* band bleaches when exposed to light. The extent and nature of this process depends on the temperature at which the crystal was x-rayed.

The paper begins by considering the explanation by Mott and Gurney[1] of Glaser's[2] photoconductivity data. This theory forms the basis of our interpretation. Next the experimental details will be described. Following this the bleaching data will be presented and finally, a summary of the results will be made.

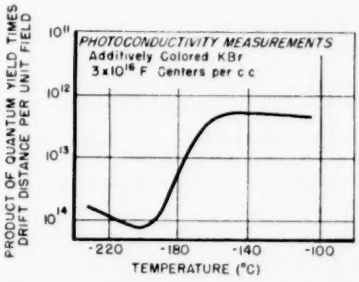

FIG. 1. Photoconductivity as a function of temperature in additively colored KBr. Curve taken from Glaser, reference 1. (The increased thermal range caused by thermal ionization of *F'* centers is not shown.)

II. ENERGY LEVEL DIAGRAM FOR AN *F* CENTER IN KBr

Glaser's[2] photoconductivity data on additively colored KBr is reproduced in Fig. 1. Two regions of $\eta\omega$ should be noted (η is the ejection probability per quantum absorbed and ω is the electron drift distance per unit electric field). Below −190°C this product decreases with increasing temperature. This is known as the colloidal range since the photoconductivity seems to be the result of colloidal particles which form in additively colored crystals. One would not expect this region to appear in the case where the coloration was produced by x-rays. The second region occurs at temperatures above −190°C where the product rises to a plateau. If we associate the change in the curve as being due to changes in η, (i.e., ω is independent of temperature), we may apply the theory of Mott and Gurney[3] to obtain the thermal activation energy ϵ_i to ionize an excited *F* center. A simplified energy level diagram is shown in

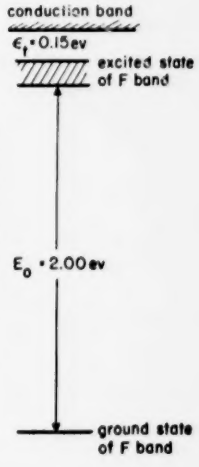

FIG. 2. Energy level diagram of an *F*-center in KBr. The energy at the half-height of the *F* band on the red side is taken as the lower level of the excited state; the energy on the violet side as the upper level. ϵ_i is the thermal ionization energy obtained from the theory of Mott and Gurney and the measurements shown in Fig. 1.

† This work was supported by the U. S. Navy, Bureau of Ordnance.
* Now at Zenith Radio Corporation, Research Div. 6001 W. Dickens Avenue, Chicago, Illinois.
[1] Some reviews of the field are R. W. Pohl, Proc. Phys. Soc. (London) **49** (extra part) 4 1937, or Physik. Z. **39**, 36 (1938); N. F. Mott and R. W. Gurney, *Electronic Processes in Ionic Crystals* (Oxford Press, New York, 1940), Chap. 4; and F. Seitz, Revs. Modern Phys. **18**, 384 (1946).
[2] G. Glaser, Nachr. Akad. Wiss. Göttingen, Math.-physik. Kl **3**, 31 (1937).
[3] See reference 1, pp. 133 and 160. η was assumed to have a value of unity at −150°C. This is sufficient to determine the thermal ionization energy.

Fig. 2. These two figures indicate that an electron cannot escape from the excited state at 5°K and that the fraction which escape at 78°K is very small.

Glaser has measured the photoconductivity in KCl crystals colored (1) by K vapor, (2) by the dissociation of KH molecules which have been built into the crystal, (3) by x-rays, and (4) by a pointed cathode. The general features of Fig. 1 hold in every case. The gap between the excited level and the conduction band seems to depend slightly on the mode of production, i.e., the thermal activation energy for additively colored KCl is 0.11 ev while for x-rayed KCl is 0.13 ev. Variations between samples of crystals are possible and we do not know what causes the change of 0.02 ev. Nevertheless Glaser's data indicate that the energy level diagram shown in Fig. 2 applies approximately to all F centers in KBr irrespective of their mode of formation.

From Figs. 1 and 2 one must conclude that F light creates excited F centers. At 5°K the thermal energy is insufficient to ionize this state so that no electrons are released to the conduction band. This indicates that the explanation of the data to be presented cannot be given in terms of the migration of electrons through the conduction band.

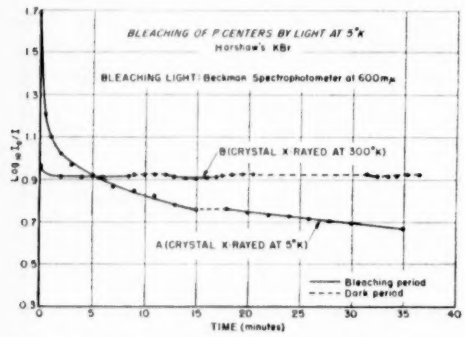

FIG. 3. Decay curves of the F band at 5°K when exposed to F light.

III. EXPERIMENTAL PROCEDURE

The experimental procedures were similar to those described previously.[4,5] The KBr crystals were obtained from three sources. One was from the Harshaw Chemical Company. The purity of this sample has been discussed previously.[5] The second specimen was a large single crystal grown by J. Schulman of the Naval Research Laboratory. The third sample were Harshaw crystals additively colored with potassium by A. B. Scott of the Oregon State College.

Qualitative spectroscopic analyses made by S. Zerfoss of the Naval Research Laboratory, of the Schulman and Harshaw samples did not indicate any major difference. (It will be recalled that the spectroscopic analyses are only approximate.) An absorption band at 285 mμ appears in the untreated Schulman crystal.

The ionic conductivity of Schulman's crystal however, is exceptionally low.[6] This indicates that the concentration of divalent impurities is smaller in Schulman's samples. This fact and the method of preparation leads us to believe that Schulman's samples are purer than the Harshaw samples in spite of the appearance of the 285 mμ-band.[7]

All the bleaching was done with the Beckman Model DU Spectrophotometer using a slit width of 2 mm. At 600 mμ, the peak of the F band at 5°K, this slit width corresponds to a band pass of about 20 mμ. At 750 mμ, the wavelength used for bleaching the F' centers, the band pass was about 30 mμ. Throughout these experiments no corrections were made for the variation of coloration with depth.

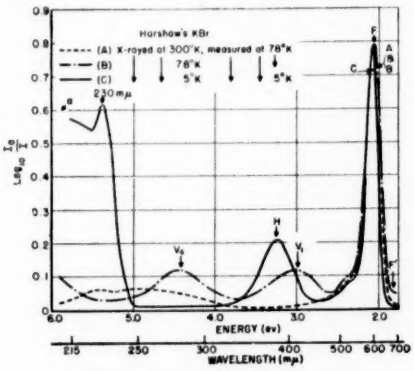

FIG. 4. Absorption spectra of Harshaw KBr crystal x-rayed at 300°, 78° and 5°K.

IV. RESULTS AND INTERPRETATIONS

1. The General Phenomena

Our experiments on additively colored KBr indicate that no bleaching occurs at 78°K and 5°K with our light source. This agrees with the model shown in Fig. 2. The F centers produced by x-radiation, however, bleach at both temperatures. Figure 3 shows the bleaching properties at 5°K of two Harshaw crystals, one x-rayed at 5°K and the other at 300°K.

The temperature of the irradiation is of great importance in determining the susceptibility to bleaching.

[4] W. H. Duerig and I. L. Mador, Rev. Sci. Instr. **23**, 421 (1952).
[5] W. H. Duerig and J. J. Markham, Phys. Rev. **88**, 1043 (1952).

[6] Private communication. The conductivity measurements were made by Dr. H. W. Etzel.
[7] Because of the uncertainty of the role that impurities play in coloration phenomena it was desirable to compare the crystals used in these experiments with those employed at Göttingen University. Crystals furnished by Prof. R. W. Pohl were analyzed spectroscopically. The crystals were not so pure as those used here. However, Prof. Pohl has stated that crystals of higher purity than those made available for analysis have been grown in Göttingen.

For convenience, the following abbreviations will be adopted: X-5 for the crystal x-rayed at 5°K, X-300 for the crystal x-rayed at 300°K, etc. In Fig. 3, X-5 shows a large amount of initial bleaching and no definite saturation. There is no recovery in the dark. The X-300, however, shows a much smaller amount of bleaching, a definite saturation, and a small but measurable amount of recovery in the dark. After the recovery, one may rebleach the crystal and again obtain a definite saturation. Evidently, there is a considerable difference between the X-300 and X-5 crystals which also shows up in the optical absorption spectra of these crystals.

The structure of the absorption bands formed during x-raying depends on the temperature of irradiation. Figure 4 shows the absorption spectra of Harshaw crystals for various irradiation temperatures. The difference in absorption measuring temperature is of little importance. The only structure observed to the red of the F band is the F' band in X-78. The radical changes occur to the violet. The X-300 crystal has a violet structure about which little is known. The structure has been partially resolved by Dorendorf.[8] The X-78 crystal has an F' band due to the association of two electrons with a negative-ion vacancy; a well-developed V_1 band, which is believed to be caused by a hole attached to a positive-ion vacancy;[9] and a V_4 band of unknown origin. From Martienssen's[10] measurements we know that an α and a β band occur beyond the wavelength range of the Beckman. The X-5 crystal has a prominent H band which Seitz[11] has suggested may be due to the trapping of a hole at a vacancy pair and a band at 230 mμ of unknown origin. Similarly to X-78 it has an α and a β band. According to Delbecq, Pringsheim and Yuster[12] an α band is associated with the creation of an exciton next to a negative-ion vacancy, and a β band arises from a similar process which occurs next to an F center.

Figure 5 shows the spectra of a Schulman X-5 measured at 5°K. The crystal was then warmed to 78°K and remeasured. Comparison of Fig. 5 with previous work done in a similar manner on Harshaw KBr[5] shows that the 230 mμ band (see Fig. 4) is not observed in the Schulman sample. The other essential features seem to be preserved. From these data it appears likely that the 230 mμ band is due to some impurity which occurs in the Harshaw but not in the Shulman sample.

A difference between the Harshaw and Schulman samples is found in NaCl as well as in KBr. Figure 6 shows the absorption of a Schulman NaCl which has been x-rayed and measured at 5°K. Previous work[6] indicates that with Harshaw NaCl a small F' band

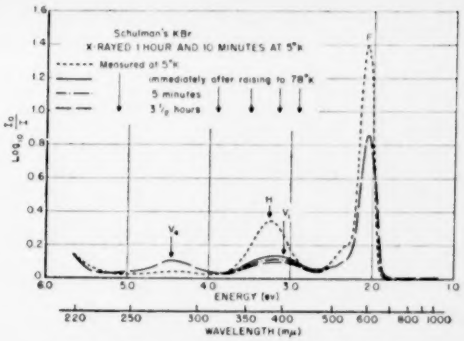

FIG. 5. Absorption spectra of KBr x-rayed at 5°K and subsequently raised to 78°K. The crystal was prepared by Dr. Schulman.

(hardly measurable) may form during x-radiation of NaCl at 5°K. The large F' band of Fig. 6 points to a distinct difference between the two materials. Speculations on the formation of lattice vacancies suggest that the production of F' centers occurs when the concentrations of α centers (negative-ion vacancies) is small.[13]

The data on NaCl suggest that the α centers are created less readily in Schulman's sample than in the Harshaw sample. The α band has not yet been studied in NaCl[10] so that its concentration cannot be measured directly. Two reasons for the lower concentration suggest themselves. If the Nabarro-Seitz mechanism[13,14] is responsible for the production of negative-ion vacancies, one must assume that there are less Seitz jogs in Schulman's crystals as a result of different growth techniques. If purity is a basic factor in the growth rates of F centers, then the difference in purity of these samples may account for the F' band. This problem has recently been reviewed by Schulman[15] and

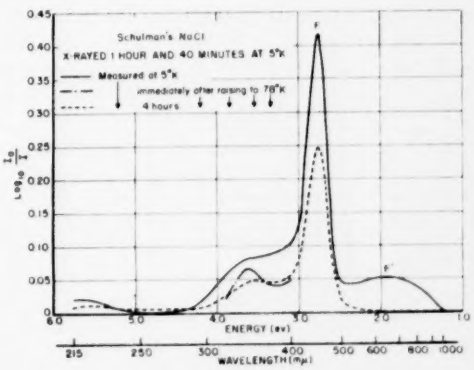

FIG. 6. Absorption spectra of NaCl x-rayed at 5°K and subsequently raised to 78°K. The crystal was prepared by Dr. Schulman.

[8] H. Dorendorf, Z. Physik **129**, 317 (1951).
[9] F. Seitz, Phys. Rev. **79**, 529 (1950).
[10] W. Martienssen, Nachr. Akad. Wiss. Göttingen, Math. physik. Kl. 111 (1952).
[11] F. Seitz, Phys. Rev. **89**, 1299 (1953).
[12] Delbecq, Pringsheim, and Yuster, J. Chem. Phys. **19**, 574 (1951).
[13] J. J. Markham, Phys. Rev. **88**, 500 (1952).
[14] F. Seitz, Phys. Rev. **80**, 239 (1950).
[15] J. H. Schulman (to be published).

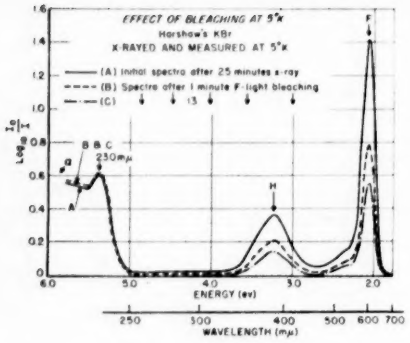

FIG. 7. Absorption spectra of Harshaw KBr x-rayed at 5°K and subsequently bleached with *F* light.

his study indicates that impurities have an effect on the coloration rate.

If one releases electrons to the conduction band during bleaching, the difference between the properties of *X*-5 and *X*-300 could be accounted for in terms of the variations in the hole centers shown in Fig. 4. Figure 2 indicates, however, that this explanation is questionable An alternate mechanism will be offered when the data are presented in detail.

2. X-Radiation at 5°K

Figure 7 shows what effect the bleaching of *F* centers in an *X*-5 crystal has on the other centers. The *H* band diminishes along with the *F* band but the 230 mμ and α bands increase. The overlap of the 230 mμ and α bands is such that one cannot be certain whether the increases are caused by a change in concentration of both centers or only one. No *F'* band was detected during these measurements. Further studies of these effects are shown in Figs. 8–10. Figures 8 and 9 show the percentage remaining centers in a Harshaw crystal.

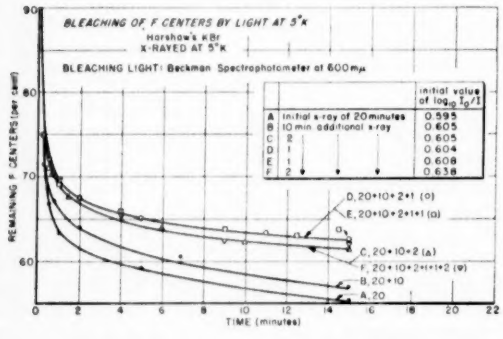

FIG. 8. Bleaching of the *F* band in Harshaw KBr after repeated x-ray exposures. Curve *C* represents a crystal that was initially x-rayed for 20 minutes, bleached for 15 minutes, exposed to x-rays for 10 minutes and again bleached for 15 minutes. Finally it was exposed to x-rays for 2 additional minutes, and Curve *C* describes the third bleaching.

In Fig. 8 the curves seem to depend on the length of the last x-raying interval. The shape of the curve which gives the percentage of the remaining *H* centers is similar; however, the fraction remaining is considerably larger.

Figure 10 shows that bleaching also occurs in a Schulman crystal. The percentage bleached is greater although the spectroscopic analysis and absence of the 230 mμ band indicate the Schulman crystal is more nearly perfect. In this case the curves do not depend on the last x-raying interval. Further tests are needed to show under which conditions, if any, the last x-raying

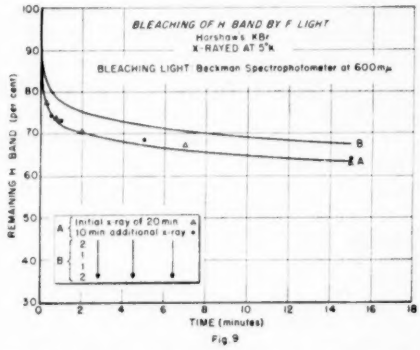
BLEACHING OF H BAND BY F LIGHT
Harshaw's KBr
X-RAYED AT 5°K
BLEACHING LIGHT: Beckman Spectrophotometer at 600mμ
A Initial x-ray of 20 min.
10 min additional x-ray
B 2 1 1 2
REMAINING H BAND (per cent)
TIME (minutes)
Fig. 9

FIG. 9. Decay of the *H* band in KBr as a function of time of bleaching of the *F* band.

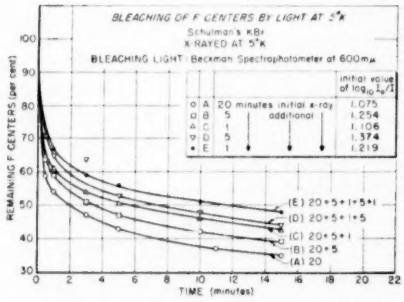

FIG. 10. Bleaching of the *F* band in KBr after repeated x-ray exposures. The crystal was prepared by Dr. Schulman.

interval determines the shape of the percentage curve.

Two additional observations have been made:

(a) After x-raying at 5°K, the decay rate in the dark of the *H* band is extremely small.

(b) Attempts were made to bleach the 230 mμ band and the *H* band. The 230 mμ band was not affected by a two-minute exposure in the Beckman. The band pass of the Beckman with a slit width of 2 mm at this wavelength is about 3 mμ. The *H* band seemed to bleach very slightly in an eight-minute exposure. In this case the band pass is 20 mμ wide.

It is impossible to interpret fully the above data. It seems, however, opportune to consider briefly what may

be happening. It is believed that the x-rays produce free electrons and holes as well as generate vacancies in the lattice. The generation of vacancies seems to be produced by a mechanism proposed by Nabarro and extended by Seitz.[13,14] In the simplest form of this theory one assumes that the "extra half plane" associated with a Taylor dislocation has a jog in it. This jog may capture an electron or a hole or even an exciton. This process generates a local thermal spike which results in some ionic diffusion.[11] It is believed that this may cause ions to diffuse into the jog, leaving vacant sites behind near the boundary of the "extra half plane." As this process continues the plane builds up but leaves many vacancies in a region around the boundary of the original "extra half plane."

Since the alkali halides have positive and negative charges, neutrality requires a pair of half-planes instead of single planes. Most probably the Nabarro-Seitz mechanism produces a high concentration of vacancy pairs along certain planes. Thus, the extra planes associated with a Taylor dislocation determine layers in the crystal where there is a high concentration of vacancy pairs as well as individual vacancies. The thickness of the layer and hence the vacancy concentration is determined by the ability of the imperfections to diffuse away from the "extra planes." It is estimated that when an α center captures an exciton the energy liberated produces a thermal spike of a temperature 400° above ambient.[11] Thus, the diffusion of the vacancies would be much greater when the crystal is x-rayed at 300°K than when x-rayed at a lower temperature. At 5°K the generated vacancy pairs can trap electrons to form F centers (the positive vacancy diffusing away) or holes to form H centers.

The photoconductivity data quoted previously[3] and the shape of the F band, which to a first approximation is independent of the method of production,[16] suggest that the model shown in Fig. 2 applies to X-5. We, therefore, do not release electrons from the excited state to the conduction band in these experiments. In bleaching, one excites F centers in regions where the concentration of hole centers is high. The electron may tunnel from the excited state to a neighboring H center, causing annihilation of both itself and the hole. This would explain the rise in the absorption in the far ultraviolet where the α band is located. The decrease in the bleaching efficiency occurs as the closest H and F centers are destroyed.

The above explanation is the simplest that can be given which preserves the fairly well established theory of the F center and the most reasonable mechanism for its generation during x-radiation. Further, the calculation of Simpson[17] shows that the Bohr radius of the excited state of the F center is 3A compared to 1.6A for the ground state. This lends support to the suggestion, since the electron in the excited state has a lower and narrower hill to go through.

3. X-Radiation at 300°K

Figure 11 shows the bleaching which occurs when one x-rays KBr (Schulman) at 300°K and lowers it to 5°K. We shall first describe the left-hand side of the curve. There a sizable initial bleaching occurs which seems to approach a saturation after 10 minutes. In the dark there is a measurable recovery which takes of the order of an hour to occur. These effects have been observed in both Harshaw and Shulman X-300 KBr at 78° and 5°K. The magnitude of the effect seems to be independent of the temperature or the source of the material. The only difference that has been noticed is that a very definite saturation occurs in the Harshaw sample after 2 minutes.

It was difficult to establish directly if any bands besides the F band were bleached or created during the

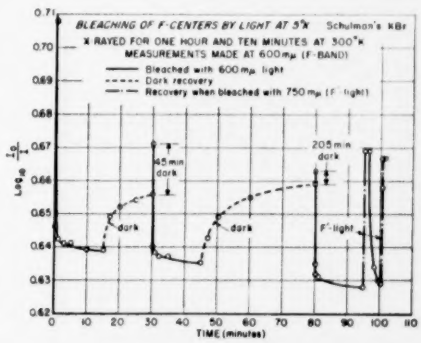

FIG. 11. Bleaching and recovery in dark of the F band in KBr. The crystal was prepared by Dr. Schulman.

experiments. If F' centers were formed, their concentration was too small to be determined by direct measurement although there was a small increase in absorption in the F' region.

It is to be stressed that X-300's recovery after bleaching eliminates the possibility that one is dealing with a thermal ionization process. The lifetime of this type of process should be determined by an equation of the type $A\exp(b/T)$, where A and b are constants. At 78°K the lifetime must be of the order of 100 sec (time for the F center to recover). If one assumes that A is as large as 10^{-8}, then $e^{b/T}$ is of the order of 10^{10}. At 5°K this would make the lifetime so long that no bleaching would be observed. This argument is based on classical statistics.

The dark recovery suggests that tunneling is again involved. If all the electrons were trapped at hole centers, one would expect annihilation and no recovery in the dark. The following explanation suggests itself. Consider two F centers which are close to each other,

[16] Mador, Markham, and Platt, Phys. Rev. **91**, 1277 (1953).
[17] J. H. Simpson, Proc. Roy. Soc. (London) **197**, 269 (1949).

perhaps several lattice sites apart.[18] We excite one of them and the following reaction occurs:

$$F_{ex}+F \xrightarrow[\text{(minutes)}]{\text{(by tunneling)}} F'+V_-, \qquad (1)$$

where F is an F center in the ground state, F_{ex} is an excited F center, F' is an F' center, and V_- is a negative-ion vacancy. We assume that this reaction occurs by tunneling, and Fig. 11 indicates that it takes a matter of minutes to approach completion. On the other hand, the dark recovery may be a result of the following reaction:

$$F'+V_- \xrightarrow[\text{(hours)}]{\text{(by tunneling)}} 2F. \qquad (2)$$

If the F' centers formed by (1) are anything like the F' centers studied by Pick,[19] they should be completely stable at 5°K relative to thermal dissociation of an electron to the conduction band. Figure 11 suggests that it takes about an hour for reaction (2) to occur. Since the ground state of the F' center is considerably

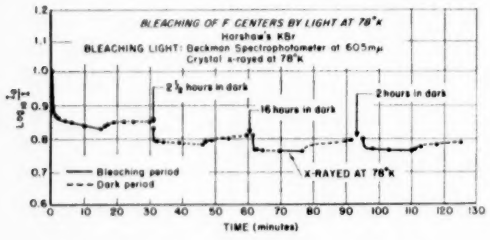

FIG. 12. Bleaching and recovery in dark of the F band in Harshaw KBr.

lower than that of the excited F center one would expect the barrier for reaction (2) to be greater than the barrier for reaction (1). This agrees with the observed relative rates of the reactions.

F' centers are readily subjected to optical bleaching at any temperature. This leads to the reaction

$$F'+V_- \xrightarrow[\text{(seconds)}]{\text{(by } F' \text{ light)}} 2F. \qquad (3)$$

The difference between (2) and (3) is in the rate. To study the above hypothesis the data shown on the right-hand side of Fig. 11 were taken. The difference in rates between (2) and (3) is clearly shown.

The optical recovery shown in Fig. 11 is as complete as the dark thermal recovery. This is a little surprising in view of Duerig's growth rate data at 78°K.[20] These data indicate that a sizable fraction of the electrons released optically from an F' center end up in hole centers, causing an annihilation of the hole. One may suggest two possible reasons for this difference: (a) The V centers formed at room temperature in KBr do not trap electrons as readily as the V bands formed at 78°K or (b) the proximity of F' centers and V_- centers is such that an electron released from an F' center does not wander through the lattice but is immediately retrapped by the neighboring negative-ion vacancy. Test, on X-78 could partially resolve this question.

The saturation to bleaching which is observed may be due to a combination of two effects: (a) the number of pairs of close F centers may diminish after the first minutes of F light irradiation, or (b) the F and F' bands overlap so that back reaction (3) occurs in addition to (1). Probably both effects enter into this problem.

Reaction (3) has been tested in Harshaw's X-300 at 78°K. The results are very similar to the one given in Fig. 11.

4. X-Radiation at 78°K

One bleaching run was made on an X-78 Harshaw crystal at 78°K. The results are shown in Fig. 12. The graph indicates that one has a combination of two effects. The lack of saturation during the first 15 minutes of bleaching is similar to the behavior of X-5. The dark recovery is similar to X-300 and the behavior after the second cycle resembles this crystal completely. This suggests that immediately after irradiation there is tunneling to both F and hole centers. There seems to be only a limited number of close hole centers, however, so that after a period of bleaching the properties of the X-78 crystal approach the properties of the X-300 crystal. The layers of vacancies at 78°K have a thickness between the values at 5° and 300°K.

V. SUMMARY

The summary will be divided into two parts. The first presents the actual data, while the second gives a tentative interpretation. The following experimental facts seem to be established for KBr.

1. The F band in additively colored KBr cannot be bleached at 5° and at 78°K.

2. The F band in crystals which have been colored by x-rays bleach at 5° and at 78°K. The stability depends on the temperature of x-radiation. Between the limits of 5° and 78°K it does not depend on the temperature of bleaching. The following statements can be made regarding the behavior.

(a) The F centers formed by x-raying KBr at 5°K bleach up to 65 percent. During this process a large fraction of the H centers disappear. No recovery is observed in the dark. A small amount of bleaching by H light has been observed. The 230 $m\mu$ band cannot be bleached.

[18] This may arise by a quartet of vacancies (two positive and two negative) capturing two electrons and dissociating into two F-centers and two positive-ion vacancies. Positive-ion vacancies have a high mobility at room temperature, a jump frequency of one per second in KCl. See Seitz, reference 1, pp. 402 and 404.

[19] H. Pick, Ann. Physik **31**, 365 (1938).

[20] W. H. Duerig, thesis, University of Maryland (1952).

(b) Ten percent of the F centers formed by x-raying KBr at 300°K can be bleached by F light at 5° or at 78°K. Over half of the bleached centers are rebuilt in the dark after several hours. After the dark recovery, one may bleach the F band again. If one shines F' light on a bleached crystal, it recovers in a few seconds. The changes in the F' absorption band were too small to directly establish its presence.

(c) About 20 percent of the F centers can be bleached in a crystal x-rayed at 78°K. There is a partial recovery in the dark, the fraction recovered being less than the previous case. After this crystal has been put through the cycle of bleaching and dark recovery several times, it behaves similarly to a crystal x-rayed at 300°K.

It is to be stressed that no qualitative calculations on tunneling have been made as yet. Some idea of the order of magnitude of the distance the electron can tunnel through would be very helpful in interpreting the above data. Photoconductivity measurements at 5°K would undoubtedly throw a great deal of light on the mechanisms of bleaching. Nevertheless, the following interpretation of the above data is offered: These data indicate the tunneling from one imperfection to another occurs if the distance is small. This tunneling can cause significant and readily measurable effects. These experiments suggest that the color centers are not distributed uniformly throughout the crystal but have a relatively high concentration in certain layers. The concentration of imperfections in these layers depends on the temperature at which the crystal is x-rayed. Higher concentrations are obtained at lower temperatures. If the Nabarro-Seitz production hypothesis is correct, the location of high concentrations is determined by the distributions of dislocations.

ACKNOWLEDGMENT

The authors would like to express their appreciation to Dr. J. H. Schulman and Professor A. B. Scott for their crystals and to Professor F. Seitz and Dr. W. H. Duerig for their helpful discussions of the theoretical problems of this paper.

PHYSICAL REVIEW VOLUME 92, NUMBER 3 NOVEMBER 1, 1953

An Augmented Plane Wave Method for the Periodic Potential Problem

J. C. SLATER*
Massachusetts Institute of Technology, Cambridge, Massachusetts

(Received July 13, 1953)

A new method is proposed for solving a periodic potential problem in which the potential can be approximated as a constant outside spheres surrounding the atoms, spherically symmetrical within the spheres. We set up unperturbed functions consisting of a plane wave outside the spheres, joined continuously and with continuous derivative to functions derived from the spherical problem within the spheres. These spherical solutions are linear combinations of eigenfunctions of Schrödinger's equation within the spheres, subject to the boundary conditions that the logarithmic derivative of the function of each l value at the surface equals the logarithmic derivative of the corresponding Bessel function in the expansion of the plane wave, thereby insuring continuity of the derivative of the wave function over the sphere if the function itself is continuous. The coefficients in the expansion within the spheres are determined by demanding that the expectation value of the energy of the wave function be stationary when the coefficients are varied. The secular equation connected with this variation problem can be solved exactly, leading to wave functions having the general character of orthogonalized plane waves. A linear combination of such functions is then used to build up an approximate solution of Schrödinger's equation. It is shown that the tightly-bound states are handled quite differently from the conduction band, and that the treatment of the conduction band can well resemble the free-electron approximation, thereby perhaps explaining the empirical success of the free-electron approximation for the conduction electrons in metals. The method can be extended to a case where the potential does not have the simple behavior postulated, by treating the difference between the actual potential and the postulated form as a perturbation.

1. GENERAL FORMULATION OF THE METHOD

THE solution of the wave-mechanical problem of an electron moving in a three-dimensional periodic potential of the type found in a crystal as treated by a self-consistent field method is an important part of the theory of solids. No existing approximate solution is completely satisfactory, and we present in this paper a new method having certain advantages over each of the existing approximations. The method is directly applicable to a problem in which the potential is spherically symmetrical within spheres surrounding the various nuclei, and is constant in the region between the spheres, which are assumed not to overlap, though we shall later show how to extend it to more general potentials.

For such a potential, it has been generally assumed that the wave function in the region between spheres could be well approximated by a superposition of a relatively small number of plane waves. On the other hand, such a wave function behaves very badly in the neighborhood of the atoms. Herring[1] has suggested the method of orthogonalized plane waves, by which one adds to each of these plane waves a set of atomic func-

* Assisted by the U. S. Office of Naval Research.

[1] C. Herring, Phys. Rev. **57**, 1169 (1940).

tions corresponding to the tightly bound states of the various atoms, with such coefficients that the resulting function is orthogonal to Bloch sums representing wave functions of all the tightly bound states. Herring and Hill[2] have applied this method with success to beryllium, Herring and Parmenter[3] to lithium, and Herman and Callaway[4] to diamond and germanium. Relatively few such orthogonalized or augmented plane waves suffice to give a rather good approximate wave function. The method has drawbacks, however, as Herman found in treating diamond. An energy band of $2p$-like symmetry in diamond has no lower, tightly-bound state to which it must be orthogonalized, and as a result the method merely uses ordinary plane waves to construct such a wave function, with rather poor convergence. Herman[5] has suggested that in such a case we could augment the plane wave by adding something which would make it behave more nearly like an atomic function near the nucleus, even though this was not required for orthogonalization, but this has not been carried out in an actual case.

The present method may be regarded as a straightforward procedure for augmenting a plane wave by adding to it a contribution near each nucleus such as to make the resulting wave function satisfy Schrödinger's equation as closely as possible. We set it up in a slightly different form, however: we use for an unperturbed wave function a plane wave of given $\mathbf{k}$ value, or propagation constant, in the region between the atomic spheres, but join this smoothly onto a function within each sphere which represents the best possible solution of Schrödinger's equation. We call such a function an augmented plane wave. Then to get the final result, we make a linear combination of a number of such augmented plane waves, with different $\mathbf{k}$ values, being led thereby to a secular equation as in the method of Herring. Since we start with the best approximate functions which we can set up, our method should converge as rapidly as any such augmented plane wave method can.

We set up these augmented plane waves in the following way. Outside an atom located at vector position $\mathbf{R}_i$, the wave function is assumed to be $a_0 \exp(i\mathbf{k}\cdot\mathbf{r})$, where a_0 is a constant. Let the atomic sphere have a radius r_i. Then the value of this wave function at points on the surface of the sphere is

$$a_0 \exp(i\mathbf{k}\cdot\mathbf{R}_i)\sum(l)\ (2l+1)i^l P_l(\cos\theta) j_l(kr), \qquad (1)$$

where r, θ are spherical coordinates with the origin at the nucleus of the atom, and the axis along the direction of the propagation vector $\mathbf{k}$. We now wish to set up a wave function within the sphere which joins continuously and with continuous derivative onto this plane wave. This cannot be a solution of Schrödinger's equation, for we know that a solution of Schrödinger's equation within a spherical atom cannot in general be joined smoothly onto a plane wave; scattering theory shows that it can only be joined to a plane wave plus scattered wavelets. We shall, however, try to make the solution inside as good an approximation to a solution of Schrödinger's equation as we can.

As a first step, we set up Schrödinger's equation within the sphere, separate variables in the usual way, and find that the radial function u associated with a given l value satisfies the equation

$$\left[\frac{-d^2}{dr^2}+V_i(r)+l(l+1)/r^2\right](ru)=Eru, \qquad (2)$$

where $V_i(r)$ is the potential within the sphere; we use the Bohr radius as unit of length, the Rydberg as unit of energy. We solve this Schrödinger equation for all energy values E, finding the solution regular at the origin, and find the logarithmic derivative $(1/u)du/dr$ at the surface of the sphere, or at $r=r_i$, as a function of E. We pick out those particular values of E for which this logarithmic derivative equals the logarithmic derivative of $j_l(kr)$ at $r=r_i$. The corresponding wave functions form a complete orthogonal set within the sphere. To prove the orthogonality, we set up Eq. (2) first for one eigenvalue and eigenfunction E_1 and u_1, then for another E_2 and u_2, and proceed by the usual method for showing orthogonality. We find

$$(E_2-E_1)\int_0^{r_i} r^2u_1u_2dr=r_i^2u_1(r_i)u_2(r_i) \times[(1/u_1)du_1/dr-(1/u_2)du_2/dr]|_{r_i}, \qquad (3)$$

where the expression on the right is to be computed when $r=r_i$. Since the two logarithmic derivatives are equal, each being equal to the logarithmic derivative of $j_l(kr)$, the orthogonality is proved. We normalize each of the wave functions $u(r)P_l(\cos\theta)$ over the sphere. Each of the wave functions and energy values should really carry three indices: one (i) to indicate which atom we are dealing with, a second (n) to indicate which of the eigenvalues we are dealing with, numbering up from the lowest energy, and finally the l value. Thus we shall call them u_{inl}, E_{inl}.

Now we build up within the sphere a linear combination of these wave functions, of the form

$$\sum(n,l)a_{inl}u_{inl}(r)P_l(\cos\theta). \qquad (4)$$

We choose the a's to obtain continuity with the plane wave outside. That is,

$$\sum(n)\ a_{inl}u_{inl}(r_i)=a_0\exp(i\mathbf{k}\cdot\mathbf{R}_i)(2l+1)i^l j_l(kr_i), \qquad (5)$$

for each l value. Since each of the u_{inl}'s has the same logarithmic derivative as $j_l(kr)$, this means that if we

[2] C. Herring and A. G. Hill, Phys. Rev. **58**, 132 (1940).
[3] C. Herring, Phys. Rev. **55**, 598 (1939); R. H. Parmenter, Phys. Rev. **86**, 552 (1952).
[4] F. Herman, Phys. Rev. **88**, 1210 (1952); F. Herman and J. Callaway, Phys. Rev. **89**, 518 (1953).
[5] F. Herman, Ph.D. Thesis, Columbia University, 1953 (unpublished).

make the wave function continuous, we shall also automatically make its derivative continuous. We must now determine the a's. We do this as follows. We set up the expectation value of the energy of our augmented plane wave, consisting of the function (4) within the ith sphere, and the plane wave outside the spheres. This expectation value is

$$E=\sum(inl)\, a_{inl}{}^{*}a_{inl}E_{inl}+a_0{}^{*}a_0E_0\Omega, \tag{6}$$

where E_0 is the kinetic energy of a plane wave of propagation vector k, and Ω is the volume of the space outside the spheres. We may carry our integrations over unit cell, in which case Ω is the volume of unit cell outside the spheres, and the summation over i goes over all atoms in the unit cell; but we may equally well use the whole crystal. We wish to have the wave function normalized over the same volume, and this leads to the condition

$$1=\sum(inl)\, a_{inl}{}^{*}a_{inl}+a_0{}^{*}a_0\Omega. \tag{7}$$

Now we demand that the a's be chosen so that the expectation value E of the energy is stationary with respect to variation of these parameters, consistent with always maintaining a normalized wave function, and always satisfying the condition (5) of continuity.

This variation problem can be handled by the method of undetermined multipliers; and by a great piece of good fortune, as shown in the Appendix, the solution of the resulting secular problem can be carried out explicitly. We find in the first place that the eigenvalues E are given by the equation

$$-\Omega^{-1}\sum(il)\,(2l+1)^2j_l^2(kr_i)(E_0-E)^{-1}\times\{\sum(n)\,[u_{inl}{}^2(r_i)/(E_{inl}-E)]\}^{-1}=1. \tag{8}$$

This equation can be handled by computing the function of E appearing on the left side of the equation, and finding the values of E for which it equals 1. We can show that there is an eigenvalue closely equal to each of the tightly bound energy levels of each of the atoms, and also an infinite number of higher eigenvalues; in fact, we can set up a one-to-one correspondence between the eigenvalues and the E_{inl}'s, one eigenvalue being found between each pair of E_{inl}'s.

Having found the E's from Eq. (8), we can next determine the a's. We find

$$a_{inl}=a_0\exp(i\mathbf{k}\cdot\mathbf{R}_i)(2l+1)i^lj_l(kr_i)u_{inl}(r_i)(E_{inl}-E)^{-1}\times\{\sum(n')\,[u_{in'l}{}^2(r_i)/(E_{in'l}-E)]\}^{-1}. \tag{9}$$

This equation determines the relation between the coefficients of the spherical functions and the coefficient a_0 of the plane wave. In Eq. (9) of course we are to insert one of the E values determined from Eq. (8). To find a_0, we use the normalization relation, which leads to

$$a_0{}^{*}a_0\Omega\{\Omega^{-1}\sum(il)\,(2l+1)^2j_l^2(kr_i)\sum(n)\times[u_{inl}{}^2(r_i)/(E_{inl}-E)^2]\times[\sum(n')\,u_{in'l}{}^2(r_i)/(E_{in'l}-E)]^{-2}+1\}=1. \tag{10}$$

We thus have completely determined our augmented plane waves. For tightly bound states, these functions are much like Bloch waves. We find an eigenvalue close to each of the tightly bound atomic levels of each of the atoms, as we have stated, and in such a case the wave function within the atoms of that type is approximately the corresponding atomic function, joined on to a plane wave of very small amplitude outside, and with very small contributions in the other types of atoms which do not have this eigenvalue. For the higher-energy values, however, such as we find in the valence and conduction bands, the eigenvalue E will no longer approach an atomic value, and the wave function will be of significant size in all the types of atoms, and in the region between.

The various wave functions for a given $\mathbf{k}$ value, being solutions of a secular problem, are orthogonal to each other, and have no nondiagonal matrix components of energy between them. These facts, which we expect from general principles, are explicitly proved in the Appendix. They thus form in a very real sense orthogonalized plane waves, but the wave functions of the tightly bound states are set up by the same method used for the higher energy levels, and we have a systematic procedure for finding all such functions. On the other hand, the wave functions for different $\mathbf{k}$ values are not orthogonal to each other, and will have nondiagonal matrix components of energy between them. The required nondiagonal matrix components of energy, and of unity, are easily computed, and are needed in setting up the secular problem involved in making a linear combination of a number of augmented plane waves.

These matrix components come from two contributions: integration over the spheres, and integration over the volumes outside the spheres. Within the ith sphere, the Hamiltonian operating on the wave function will give $\sum(nl)\, a_{inl}E_{inl}u_{inl}P_l(\cos\theta)$. We must now multiply this by another wave function, and integrate over the sphere. We integrate first over the spherical harmonics, getting nothing unless both terms are connected with the same l value; we note that the axes of the spherical harmonics will be different for the two functions. We are then left with the integral over the sphere of a u_{inl} connected with one $\mathbf{k}$ value, and a $u_{in'l}$ connected with another $\mathbf{k}$ value. These two functions have different logarithmic derivatives at r_i, and the integral of their product does not vanish; but by Eq. (3), we can reduce the integral to quantities on the surface of the sphere which are already known. For the integrations over the regions outside the spheres, we must merely integrate E_0 times the product of two plane waves, which itself is a plane wave. The integral of this product over a whole unit cell is zero. Thus the integral over the region outside the spheres is the negative of the integral over the interiors of the spheres. Within each sphere, the plane wave can be expanded in spherical harmonics of angle times spherical Bessel

functions; these can be integrated explicitly, so that we have the complete answer.

We thus see that the matrix components of energy are easily determined between two augmented plane waves of different $\mathbf{k}$'s. The integral of the product of the wave functions is equally simple, found merely by omitting the E_{inl}'s. We then set up a secular equation between the augmented plane waves which we wish to combine, and solve it in the standard way. We can handle the non-orthogonality of wave functions of different $\mathbf{k}$'s either by orthogonalizing them initially, or by carrying the overlap integrals in the secular equation. As in the orthogonalized plane wave method, if we are dealing with a symmetry point in the Brillouin zone, the coefficients of a number of orthogonalized plane waves will automatically be equal, so that the order of the required secular equation may be much less than the number of waves which we are superposing.

2. DISCUSSION AND CONCLUSIONS

For each $\mathbf{k}$ value, we have found an infinite number of augmented plane waves, corresponding to the various eigenvalues E. These eigenvalues depend on the magnitude of $\mathbf{k}$, but not on the direction, and will be continuous functions of $|\mathbf{k}|$. They depend on the number of atoms of each type in the volume, but not on their arrangement. All directional effects, and all effects of crystal structure, appear in the process of combining a number of augmented plane waves to get our final wave function. In this respect our method resembles the free-electron method, as well as Herring's orthogonalized plane wave method.

There is a feature which is present in our method, however, which is different from the other methods so far proposed: there is a great redundancy of wave functions, and we must use our judgment in deciding which ones to use. We can understand this redundancy from a simple case, the tight-binding wave function made up from the 1s atomic orbital on one of the atoms. One of the eigenvalues E will lie close to the atomic energy of this state, and the wave functions will be almost like Bloch combinations of the 1s atomic orbitals, but joined onto plane waves of very small amplitudes between the atoms. Now let us consider two $\mathbf{k}$ values, one differing from the other by one of the vectors of the reciprocal lattice. The plane wave of either of these $\mathbf{k}$ values will have the same phase at each of the atoms, so that the corresponding Bloch sums will be almost precisely the same, and the wave functions corresponding to these two $\mathbf{k}$'s will be practically identical within the atoms, where they are large, but will be quite different between the atoms, where they are small, being plane waves of different propagation constants. The integral of the product of the wave functions will mostly come from the interiors of the spheres, and will be practically unity, instead of zero as it would be if they were orthogonal. Clearly in our expansion we do not wish to use both of these wave functions. In fact, by analogy with the tight binding approximation, we know that we can get all the 1s-like wave functions which we need by taking just those values of $\mathbf{k}$ in the central Brillouin zone.

We might think that we could get all the wave functions we needed for any case if for each of the eigenvalues of E we chose only those $\mathbf{k}$'s in the central Brillouin zone; this would be closely analogous to the tight-binding approximation. Yet it clearly is not sufficient, for in this case we should have no secular problem, and the wave function between the atoms would be represented only by a single plane wave with a $\mathbf{k}$ vector in the central Brillouin zone. For the tightly bound states, for which the wave function is small between the atoms anyway, this is not a bad approximation, though we find that for p-like states we must have propagation vectors in three central Brillouin zones, for d-like states in five zones, and so on, to get the necessary number of functions. For valence and conduction bands, however, the wave function between the atoms is important, and we must certainly superpose waves with a number of $\mathbf{k}$ values to get a good approximation. The question remains whether these waves should all correspond to the same eigenvalue of E (that is, to the eigenvalues which join smoothly onto each other as $\mathbf{k}$ changes), or to different eigenvalues. It seems clear, from our information about wave functions from other sources, that in some cases we wish to use waves with $\mathbf{k}$'s in many Brillouin zones, but all corresponding to the same eigenvalue.

The most straightforward case of this would be sodium. There we know, mainly from the cellular method, that for energies in the conduction band, the wave function is well approximated by a single plane wave between the atoms, joining onto solutions of a spherical problem within the atoms. This means that a single augmented plane wave, with a $\mathbf{k}$ value which can range through many Brillouin zones, may well be a very good approximation to a solution, for this particular case. This would imply that we were working with a single eigenfunction, which would reduce for $\mathbf{k}=0$ essentially to a combination of 3s-like orbitals obeying the Wigner-Seitz boundary condition of zero slope at the boundary, in each unit cell. As $\mathbf{k}$ increases, we see from Eq. (9) that we shall also have contributions from p-like, then d-like, orbitals, and so on, coming in with gradually increasing coefficients (on account of the way in which $j_l(kr_i)$ increases with k, more slowly with high l values). We might well expect in this case that the energy of this state would be approximately proportional to k^2, as with a free-electron wave function, and that the wave functions corresponding to $\mathbf{k}$'s in different Brillouin zones might approach orthogonality, instead of being almost identical as with the bound states. If we found this type of behavior, as seems plausible, we might get a very good approximation by taking linear combinations of such augmented plane

waves. We should find very small nondiagonal matrix components of energy, since the unperturbed functions were so nearly solutions as they stood. Two wave functions connected with **k**'s in different unit cells in **k** space will be degenerate if their **k**'s satisfy the Bragg condition, so that along the planes where the Bragg condition is satisfied we shall have to introduce linear combinations of these plane waves. We shall have, in other words, an almost complete analogy to a free-electron calculation, and this may well prove to be the justification of the well-known fact that free-electron methods for the conduction electrons work much better than we should expect from any of the approximate methods usually in use.

We see, then, that we may have two quite different ways of choosing unperturbed wave functions, out of the great superfluity of functions which our method yields. For tightly bound states, we choose functions whose eigenvalues are close to the energies of the atomic states, and with **k**'s in the central Brillouin zone for *s* states, the central three zones for *p* states, and so on (it will be interesting to make a detailed study of the symmetry relations arising from these tightly bound *p* and *d* states, at some future time). For the conduction band, however, we are much more likely to want to choose functions all corresponding to the same eigenvalue, but to **k**'s in different Brillouin zones. This corresponds to the way we have been in the habit of handling such problems, treating the tightly bound states separately by the Bloch method, and the conduction band as if by the free-electron method, but disregarding the fact that these electrons are in fact far from free. The justification seems to come only from such an augmented plane wave method as described here.

We now note that there can be cases that are ambiguous, and presumably the first one of these which will appear in the periodic table comes with the iron group, where the 3*d* electrons are being incorporated into the interior of the atom. For potassium, calcium, and the elements following immediately after, the atomic 3*d* energy level lies above the 4*s*. We may presume that in these cases we wish to use a single eigenvalue, which reduces to something like the 4*s* atomic level for $\mathbf{k}=0$, and to follow continuously along to higher **k** values, using wave functions in many Brillouin zones. On the other hand, when we have gone through iron, cobalt, and nickel, to copper and zinc, the 3*d* level in the atom has become rather tightly bound. In this case presumably we wish to treat the appropriate wave functions in central Brillouin zones (we remember that we must use five such zones), and to start again with a higher eigenvalue and a continuous set of **k** values, to represent the conduction band of the elements starting with copper. The change in the method of treatment which will arise in this way would be a very interesting thing to study, and may well explain many of the paradoxes associated with the energy bands of the transition elements, and the question as to which electrons are to be treated as free electrons, which as bound or atomic electrons.

We may note two generalizations of the method which follow easily. In the first place, we have noted that the setting up of the augmented plane waves does not demand a regular crystalline arrangement of the atoms. Thus we have an equally valid starting point for a treatment of perturbed or irregular lattices. Secondly, the potential function in a real crystal does not have the properties postulated here, of being spherically symmetrical within each atomic sphere, and constant outside. If we wish to take account of the deviations of the real potential function from such a behavior, we may first set up as good an approximation to the real potential as possible which has the behavior we have postulated, and set up the wave functions using this potential. When we come to compute the diagonal and nondiagonal matrix components of energy, however, and to solve the secular problem, we may include the deviations of the real potential from this simplified value as perturbations, computing their contributions to the matrix components of energy numerically, if no analytic method is available. This possibility of taking into account deviations from this simplified potential is found in the orthogonalized plane wave method, but not in the cellular method, and it results in considerable shortcomings in the applications of the latter method.

We may observe in closing that our method is really a form of cellular method in which we have transferred the problem of satisfying boundary conditions from the surfaces of the polyhedral cells, to the surfaces of the inscribed spheres; we may regard the regions where we expand the wave functions in plane waves as matching regions, extending the wave functions smoothly from one spherical cell to another. The writer[6] attempted in 1937 to avoid the difficulties of the cellular method by a method somewhat like the present one. That suggestion, however, suffered from mathematical complications so severe that it has never proved useful. It is hoped that these mathematical difficulties have been overcome by the present method, sufficiently so that it may be better adapted for application to real crystals than the hitherto available methods.

APPENDIX

To find the required wave functions, we wish to vary the a_{inl}'s and a_0 so as to make the energy in Eq. (6) stationary, while maintaining the conditions (5) and (7). To do this by the method of undetermined multipliers, we may add the derivative of Eq. (6) with respect to one of the a_{inl}^*'s (formally treating this as independent of the corresponding a_{inl}), plus appropriate constants times the derivative of Eq. (7), and of the conjugates of each of Eqs. (5), with respect to the same quantity, and set this equal to zero; we do the same for

[6] J. C. Slater, Phys. Rev. **51**, 846 (1937).

derivatives with respect to a_0^*. We thus have

$$a_{inl}(E_{inl}-E)-\lambda_{il}u_{inl}(r_i)=0, \tag{11}$$

$$a_0\Omega(E_0-E)+\sum(il)\,\lambda_{il}\times\exp(-i\mathbf{k}\cdot\mathbf{R}_i)(2l+1)(-i)^l j_l(kr_i)=0. \tag{12}$$

Here we have chosen the undetermined multiplier for Eq. (6) to be $-E$ [we shall shortly prove that this E is the same as the expectation value appearing in Eq. (6)], and that connected with Eq. (5) for a particular i and l to be $-\lambda_{il}$. We can now solve Eqs. (11) and (12) very simply. We have at once

$$a_{inl}=\lambda_{il}u_{inl}(r_i)/(E_{inl}-E); \tag{13}$$

$$a_0\Omega=-\sum(il)\,\lambda_{il}\exp(-i\mathbf{k}\cdot\mathbf{R}_i)\times(2l+1)(-i)^l j_l(kr_i)/(E_0-E). \tag{14}$$

We must next determine the multipliers λ_{il} and E. First we eliminate the λ_{il}'s, and get an equation for E. We substitute Eqs. (13) and (14) in Eq. (5), obtaining

$$\lambda_{il}\sum(n)\,[u_{inl}^2(r_i)/(E_{inl}-E)]=-\Omega^{-1}\exp(i\mathbf{k}\cdot\mathbf{R}_i)(2l+1)i^l j_l(kr_i)\times\sum(i'l')\,\lambda_{i'l'}\exp(-i\mathbf{k}\cdot\mathbf{R}_{i'})(2l'+1)(-i)^{l'}\times j_{l'}(kr_{i'})/(E_0-E). \tag{15}$$

We multiply both sides by

$$\{\sum(n)\,[u_{inl}^2(r_i)/(E_{inl}-E)]\}^{-1}\exp(-i\mathbf{k}\cdot\mathbf{R}_i)(2l+1)(-i)^l j_l(kr_i),$$

and add terms for all i and l values. We then can cancel terms from both sides of the equation, and are led at once to Eq. (8). Now that E has been determined, we see at once from Eq. (15) that

$$\lambda_{il}=b\exp(i\mathbf{k}\cdot\mathbf{R}_i)(2l+1)i^l j_l(kr_i)\times\{\sum(n)\,[u_{inl}^2(r_i)/(E_{inl}-E)]\}^{-1}, \tag{16}$$

where b is a constant. By substituting Eq. (16) in Eq. (12), and using Eq. (8), we find at once that $b=a_0$. Thus we are led to Eq. (9). Substitution in Eq. (7) leads at once to Eq. (10).

We can now prove the three theorems we desire about our wave functions: the quantity introduced as an undetermined multiplier E is the same as the expectation value of energy defined in Eq. (6); and the functions are orthogonal, and have no nondiagonal matrix components of energy between them. To prove the first, we start with Eq. (15), multiply by λ_{il}^*, and sum over i and l. We have

$$\sum(inl)\,\lambda_{il}^*\lambda_{il}u_{inl}^2(r_i)/(E_{inl}-E)=-\Omega^{-1}[\sum(il)\,\lambda_{il}^*\exp(i\mathbf{k}\cdot\mathbf{R}_i)(2l+1)i^l j_l(kr_i)]\times[\sum(i'l')\,\lambda_{i'l'}\exp(-i\mathbf{k}\cdot\mathbf{R}_{i'})(2l'+1)(-i)^{l'}\times j_{l'}(kr_{i'})/(E_0-E)]. \tag{17}$$

We multiply and divide each term on the left by $E_{inl}-E$, and multiply and divide on the right by E_0-E. We may then rewrite the result, using Eqs. (11) and (12), as

$$\sum(inl)\,a_{inl}^*a_{inl}(E_{inl}-E)+a_0^*a_0\Omega(E_0-E)=0,$$

from which it follows at once, from Eqs. (6) and (7), that E is the expectation value of the energy.

To prove the other theorems, we must use two energy values, E_1 and E_2, with corresponding coefficients λ_{il1}, λ_{il2}, a_{01}, a_{02}, etc. We then set up Eq. (15) for the state 2, multiply it by λ_{il1}^*, and by a coefficient A, and sum over i and l; we also set up Eq. (15) for the state 1, take its conjugate, multiply by λ_{il2}, and by a coefficient B, and sum over i and l; and subtract this from the first equation. The result of this is

$$\begin{aligned}\sum(inl)\,\lambda_{il1}^*\lambda_{il2}u_{inl}^2(r_i)[A/(E_{inl}-E_2)-B/(E_{inl}-E_1)]&=-\Omega^{-1}[\sum(il)\,\lambda_{il1}^*\exp(i\mathbf{k}\cdot\mathbf{R}_i)(2l+1)i^l j_l(kr_i)]\\&\times[\sum(i'l')\,\lambda_{i'l'2}\exp(-i\mathbf{k}\cdot\mathbf{R}_{i'})(2l'+1)(-i)^{l'}\\&\times j_{l'}(kr_{i'})]A/(E_0-E_2)+\Omega^{-1}[\sum(il)\,\lambda_{il2}\\&\times\exp(-i\mathbf{k}\cdot\mathbf{R}_i)(2l+1)(-i)^l j_l(kr_i)][\sum(i'l')\,\lambda_{i'l'1}\\&\times\exp(i\mathbf{k}\cdot\mathbf{R}_{i'})(2l'+1)i^{l'}j_{l'}(kr_{i'})]B/(E_0-E_1).\end{aligned} \tag{18}$$

We reduce the fractions on the left to a common denominator, use Eqs. (13) and (14), and have

$$\sum(inl)\,a_{inl1}^*a_{inl2}[(A-B)E_{inl}+(-AE_1+BE_2)]+a_{01}^*a_{02}\Omega[(A-B)E_0+(-AE_1+BE_2)]=0. \tag{19}$$

The two constants A and B are at our disposal. First let us chose them so that $A-B=0$, $-AE_1+BE_2=1$. Then we have

$$\sum(inl)\,a_{inl1}^*a_{inl2}+a_{01}^*a_{02}\Omega=0, \tag{20}$$

which is the expression of the fact that the two wave functions are orthogonal to each other. Next let $A-B=1$, $-AE_1+BE_2=0$. Then

$$\sum(inl)\,a_{inl1}^*a_{inl2}E_{inl}+a_{01}^*a_{02}\Omega E_0=0, \tag{21}$$

showing that the nondiagonal matrix component of energy between the two states is zero.

PHYSICAL REVIEW VOLUME 92, NUMBER 3 NOVEMBER 1, 1953

A Collective Description of Electron Interactions: III. Coulomb Interactions in a Degenerate Electron Gas

DAVID BOHM, *Faculdade de Filosofia, Ciencias e Letras, Universidade de Sao Paulo, Sao Paulo, Brazil*

AND

DAVID PINES, *Department of Physics, University of Illinois, Urbana, Illinois*

(Received May 21, 1953)

The behavior of the electrons in a dense electron gas is analyzed quantum-mechanically by a series of canonical transformations. The usual Hamiltonian corresponding to a system of individual electrons with Coulomb interactions is first re-expressed in such a way that the long-range part of the Coulomb interactions between the electrons is described in terms of collective fields, representing organized "plasma" oscillation of the system as a whole. The Hamiltonian then describes these collective fields plus a set of individual electrons which interact with the collective fields and with one another via short-range screened Coulomb interactions. There is, in addition, a set of subsidiary conditions on the system wave function which relate the field and particle variables. The field-particle interaction is eliminated to a high degree of approximation by a further canonical transformation to a new representation in which the Hamiltonian describes independent collective fields, with n' degrees of freedom, plus the system of electrons interacting via screened Coulomb forces with a range of the order of the inter electronic distance. The new subsidiary conditions act only on the electronic wave functions; they strongly inhibit long wavelength electronic density fluctuations and act to reduce the number of individual electronic degrees of freedom by n'. The general properties of this system are discussed, and the methods and results obtained are related to the classical density fluctuation approach and Tomonaga's one-dimensional treatment of the degenerate Fermi gas.

I.

IN this paper we wish to develop a collective description of the behavior of the electrons in a dense electron gas which will be appropriate when a quantum-mechanical treatment of the electronic motion is required, as is the case for the electrons in a metal. Our collective description is based on the organized behavior of the electrons brought about by their long-range Coulomb interactions, which act to couple together the motion of many electrons. In the first paper of this series[1] hereafter referred to as I, we developed a collective description of the organized behavior in an electron gas due to the transverse electromagnetic interactions between the electrons. This was done by means of a canonical transformation to a set of transverse collective coordinates which were appropriate for a description of this organized behavior. Here we shall develop an analogous canonical transformation to a set of longitudinal collective coordinates which are appropriate for a description of the organization brought about by the Coulomb interactions.

In the preceding paper[2] hereafter referred to as II, we developed a detailed physical picture of the electronic behavior (due to the Coulomb interactions). Although the electron gas was treated classically, we shall see that most of the conclusions reached there are also appropriate (with certain modifications) in the quantum domain. Let us review briefly the physical picture we developed in II, since we shall have occasion to make frequent use of it in this paper.

We found that, in general, the electron gas displays both collective and individual particle aspects. The primary manifestations of the collective behavior are organized oscillation of the system as a whole, the so-called "plasma" oscillation, and the screening of the field of any individual electron within a Debye length by the remainder of the electron gas. In a collective oscillation, each individual electron suffers a small periodic perturbation of its velocity and position due to the combined potential of all the other particles. The cumulative potential of all the electrons may be quite large since the long range of the Coulomb interaction permits a very large number of electrons to contribute to the potential at a given point. The screening of the electronic fields may be viewed as arising from the Coulomb repulsion, which causes the electrons to stay apart, and so leads to a deficiency of negative charge in the immediate neighborhood of a given electron. The collective behavior of the electron gas is decisive for phenomena involving distances greater than the Debye length, while for smaller distances the electron gas is best considered as a collection of individual particles which interact weakly by means of a screened Coulomb force.

These conclusions were reached by analyzing the behavior of the electrons in terms of their density fluctuations. It was found that these density fluctuations could be split into two approximately independent components, associated with collective and individual particle aspects of the electronic motion. The collective component is present only for wavelengths greater than the Debye length and represents the "plasma" oscillation. It may be regarded as including the effects of the long range of the Coulomb force which leads to the simultaneous interaction of many particles. The individual particles component is associated with the random thermal motion of the electrons and shows no collective behavior; it represents a collection of individual electrons surrounded by co-moving clouds of

[1] D. Bohm and D. Pines, Phys. Rev. **82**, 625 (1951).
[2] D. Pines and D. Bohm, Phys. Rev. **85**, 338 (1952).

charge which act to screen their fields as described above. The individual particles component thus includes the effects of the residual short-range screened Coulomb force, which leads only to two-body collisions.

A quantum-mechanical generalization of the density fluctuation method is quite straightforward and is sketched briefly in Appendix I. However, we do not choose to adopt this point of view, because although it is quite useful in establishing the existence of collective oscillations and describing certain related phenomena, it does not enable one to obtain a satisfactory over-all description of the electron gas. Quantum-mechanical calculations aimed at solving for the wave functions and the energy levels of the system are much more conveniently done in terms of a Hamiltonian formalism through the use of appropriate canonical transformations.

Our general approach in this series of papers has been to analyze the collective oscillatory motion first, since this is associated with the long-range aspects of the interaction which, in a sense, are responsible for the major complications in the many-electron problem. Once the collective motion is accounted for, we then investigate the aspects of the electronic behavior which are independent of the collective behavior, and which, if our method is successful, should turn out to be simple. Thus we are led to seek a canonical transformation to a representation in which the existence of the collective oscillations is explicitly recognized, and in which these oscillations are independent of the individual electronic behavior. In this representation, which we shall call the collective representation, we do not expect that the electron gas can be described entirely in terms of the collective coordinates which describe the organized oscillations, since we know that the gas also displays individual particle behavior. We shall see that in the collective representation, the individual electronic coordinates correspond to the electrons plus their associated screening fields, and that as might be anticipated from II, these screened electrons interact rather weakly via a screened Coulomb force.

In this paper we shall be primarily concerned with obtaining the canonical transformation to the collective representation. We shall discuss the approximations involved and, in a general way, the resultant wave functions of our electron system in the collective representation. Our development of a quantum-mechanical description of the electron assembly makes possible a treatment of the effects of electron interaction in metallic phenomena which utilizes at the outset the simplicity brought about by the organized oscillatory behavior. The detailed application of the collective description to the electrons in a metal is given in the following paper,[3] hereafter referred to as IV.

Historically, the first utilization of the 'plasma' aspects of the electron gas in a metal is due to Kronig and Korringa,[4] who treated the effect of electron-electron interaction on the stopping power of a metal for fast charged particles. However, their treatment is open to objection, in that they describe the electron gas as a classical fluid, with an artificially introduced coefficient of internal friction. A more satisfactory treatment of electron-electron interaction in the stopping power problem is due to Kramers[4] and Bohr.[4] The quantum treatment of this problem from the viewpoint of the collective description is given in Paper IV.

Tomonaga[5] has independently investigated the extent to which a degenerate Fermi gas can be described in terms of longitudinal oscillations. Tomonaga's treatment is, however, confined to a one-dimensional system, and as we shall see, there are certain essential difficulties associated with its generalization to a three-dimensional system which make the direct extension of this approach to three dimensions impossible. The relationship between our approach and that of Tomonaga is discussed in Appendix II.

II.

We consider an aggregate of electrons embedded in a background of uniform positive charge, whose density is equal to that of the electrons. The Hamiltonian for our system may be written

$$\sum_i \frac{p_i^2}{2m} + 2\pi e^2 \sum_{kij}{}' \frac{e^{i\mathbf{k}\cdot(\mathbf{x}_i-\mathbf{x}_j)}}{k^2} - 2\pi n e^2 \sum_k{}' \frac{1}{k^2}, \qquad (1)$$

where the first term corresponds to the kinetic energy of the electrons, the second to their Coulomb interaction and the third to a subtraction of their self energy. The prime in the summations over k denotes a sum in which $k=0$ is excluded, and this takes into account the uniform background of positive charge, and hence the over-all charge neutrality of our system.[6] In obtaining (1) we have used the fact that the Coulomb interaction between the ith and jth electrons may be expanded as a Fourier series in a box of unit volume, and is $(e^2/|\mathbf{x}_i-\mathbf{x}_j|)=4\pi e^2\sum_k (1/k^2)e^{i\mathbf{k}\cdot(\mathbf{x}_i-\mathbf{x}_j)}$. n is the total number of electrons and is numerically equal to the mean density (since we are working in a box of unit volume).

Instead of working directly with the Hamiltonian of Eq. (1), we shall find it convenient to introduce an equivalent Hamiltonian which is expressed in terms of the longitudinal vector potential of the electromagnetic field, $\mathbf{A}(\mathbf{x})$, where $\mathbf{A}(\mathbf{x})$ may be Fourier-analyzed as

$$\mathbf{A}(\mathbf{x})=(4\pi c^2)^{\frac{1}{2}}\sum_k q_k \boldsymbol{\varepsilon}_k e^{i\mathbf{k}\cdot\mathbf{x}}, \qquad (2)$$

[3] D. Pines, following paper [Phys. Rev. **92**, 626 (1953)].

[4] R. Kronig and J. Korringa, Physica **10**, 406 (1943). See also H. A. Kramers, Physica **13**, 401 (1947); A. Bohr, Kgl. Danske Videnskab. Selskab, Mat.-fys. Medd. **24**, No. 19 (1948); and R. Kronig, Physica **14**, 667 (1949).

[5] S. Tomonaga, Prog. Theor. Phys. **5**, 544 (1950).

[6] We shall drop this prime in the remainder of this paper since we have no further occasion to make explicit use of the fact that the term with $k=0$ is excluded.

and $\boldsymbol{\varepsilon}_k$ denotes a unit vector in the $\mathbf{k}$ direction. The electric field intensity, $\mathbf{E}(\mathbf{x})$ is

$$\begin{aligned}\mathbf{E}(\mathbf{x}) &= -(4\pi)^{\frac{1}{2}}\textstyle\sum_k \dot{q}_k \boldsymbol{\varepsilon}_k e^{+i\mathbf{k}\cdot\mathbf{x}} \\ &= (4\pi)^{\frac{1}{2}}\textstyle\sum_k p_{-k}\boldsymbol{\varepsilon}_k e^{i\mathbf{k}\cdot\mathbf{x}}.\end{aligned} \tag{3}$$

To ensure that $\mathbf{A}(\mathbf{x})$ and $\mathbf{E}(\mathbf{x})$ are real, we take

$$q_k = -q_{-k}^*, \quad p_k = -p_{-k}^*. \tag{4}$$

Our equivalent Hamiltonian is then given by

$$H = \sum_i \left[\mathbf{p}_i + \frac{e}{c}\mathbf{A}(\mathbf{x}_i)\right]^2 \Big/ 2m + \int [E^2(\mathbf{x})/8\pi]d\mathbf{x} - 2\pi n e^2 \sum_k \frac{1}{k^2}, \tag{5}$$

which using (2) and (3) may be shown to become

$$\begin{aligned}H = \sum_i \frac{p_i^2}{2m} + \frac{e}{m}(4\pi)^{\frac{1}{2}} \sum_{ik} \boldsymbol{\varepsilon}_k \cdot (\mathbf{p}_i - \hbar\mathbf{k}/2) q_k e^{i\mathbf{k}\cdot\mathbf{x}_i} \\ + (2\pi e^2/m) \sum_{ikl} \boldsymbol{\varepsilon}_k \cdot \boldsymbol{\varepsilon}_l q_k q_l e^{i(\mathbf{k}+\mathbf{l})\cdot\mathbf{x}_i} - \textstyle\sum_k \frac{1}{2} p_k p_{-k} \\ - 2\pi n e^2 \textstyle\sum_k 1/k^2.\end{aligned} \tag{6}$$

This Hamiltonian, when used in conjunction with a set of subsidiary conditions acting on the wave function of our system,

$$\Omega_k \Phi = 0 \quad \text{(for all } k\text{)}, \tag{7}$$

where

$$\Omega_k = p_{-k} - i\left(\frac{4\pi e^2}{k^2}\right)^{\frac{1}{2}} \sum_i e^{-i\mathbf{k}\cdot\mathbf{x}_i} \tag{8}$$

will lead to the correct electron equations of motion. Ω_k is proportional to the kth fourier component of $\operatorname{div}\mathbf{E}(\mathbf{x}) - 4\pi\rho(\mathbf{x})$, and hence these subsidiary conditions guarantee that Maxwell's equations are satisfied. It may easily be verified that the subsidiary condition operator Ω_k commutes with the Hamiltonian (6), so that if the subsidiary condition (7) is satisfied at some initial time, it will be true at all subsequent times.[7]

The equivalence of our Hamiltonian (6) with the Hamiltonian expressed by (1) may be seen by applying the unitary transformation[8] $\Phi = S\psi$, where,

$$S = \exp\left[-(1/h)\sum_{ki}(4\pi e^2/k^2)^{\frac{1}{2}} q_k e^{i\mathbf{k}\cdot\mathbf{x}_i}\right]. \tag{9}$$

With this transformation, we find

$$\begin{aligned}p_i &\to S^{-1}p_i S = p_i - (4\pi e^2)^{\frac{1}{2}}\textstyle\sum_k q_k \boldsymbol{\varepsilon}_k e^{i\mathbf{k}\cdot\mathbf{x}_i} \\ p_k &\to S^{-1}p_k S = p_k + i(4\pi e^2/k^2)^{\frac{1}{2}}\textstyle\sum_i e^{i\mathbf{k}\cdot\mathbf{x}_i},\end{aligned}$$

and

$$H \to \mathcal{H} = S^{-1}HS = \sum_i \frac{p_i^2}{2m} + 2\pi e^2 \sum_{ij} \frac{e^{i\mathbf{k}\cdot(\mathbf{x}_i - \mathbf{x}_j)}}{k^2} - \sum_k \frac{p_k p_{-k}}{2} - i\sum_{ki}\left(\frac{4\pi e^2}{k^2}\right)^{\frac{1}{2}} p_k e^{-i\mathbf{k}\cdot\mathbf{x}_i} - 2\pi n e^2 \sum_k \left(\frac{1}{k^2}\right).$$

The subsidiary condition (8) becomes

$$p_{-k}\psi = 0 \quad \text{(for all } k\text{)}.$$

If we choose a ψ which is independent of q_k, we may satisfy the new subsidiary condition identically, the terms involving p_k in the Hamiltonian will drop out, and $\mathcal{H}$ is seen to be equivalent to (1). We note that the term $-2\pi n e^2 \sum_k (1/k^2)$ was included in (6) so that this Hamiltonian might be numerically equivalent to (1), as well as leading to equivalent equations of motion, since this term is just what is needed to cancel the terms with $i = j$ in the Coulomb energy.

The introduction of the longitudinal decrees of freedom, q_k, and the subsidiary conditions (7) provides a convenient means of introducing the concept of independent collective oscillation within the framework of the Hamiltonian formalism. The utility of this representation lies in the fact that (7) introduces in a simple way a relationship between the fourier components of the electronic density, $\rho_k = \sum_i e^{-i\mathbf{k}\cdot\mathbf{x}_i}$, and a set of field variables p_k. We shall see that there is, in consequence, a very close parallel between the behavior of the ρ_k, as analyzed in II, and the behavior of our field coordinates. In this representation we find that the field variables (just as did the ρ_k) oscillate with a frequency equal to the plasma frequency, provided we neglect a small coupling between the collective motion and the individual electronic behavior (characterized by their random thermal motion). Furthermore, just as we found it possible in II to find a purely oscillatory component of the density fluctuations, which is approximately independent of the individual electronic behavior, so we shall here be able to carry out a canonical transformation to a new set of field variables, which describe pure collective behavior and do not interact with the individual electrons to a good degree of approximation. In this section we shall analyze the approximate oscillatory behavior of the (q_k, p_k), while in the next section we carry out the canonical transformation to the pure collective coordinates.

Before beginning our analysis, we find it desirable to modify somewhat our Hamiltonian (6). We found in Paper II that in the classical theory there is a minimum wavelength λ_c (which classically is the Debye length), and hence a maximum wave vector k_c, beyond which organized oscillation is not possible. We may anticipate that in the quantum theory a similar (but not identical) limit arises, so that there is a corresponding limit on the extent to which we can introduce collective coordinates to describe the electron gas.

[7] This may be contrasted with the customary gauge [corresponding to $\operatorname{div}\mathbf{A} = (1/c)\partial\varphi/\partial t$], in which the commutator of the subsidiary condition with H is proportional to the subsidiary condition itself, and is therefore zero only when the subsidiary condition is satisfied.

[8] See G. Wentzel, *Quantum Theory of Wave Fields* (Interscience Publishers, New York, 1949), p. 131.

Since this is the case, rather than introduce the full spectrum of longitudinal field coordinates (and associated subsidiary conditions) as we do in (6), we might as well confine our attention to only as many p_k and q_k as we expect to display collective behavior, i.e., (p_k, q_k) for $k<k_c$. The number of collective coordinates, n', will then correspond to the number of k values lying between $k=0$ and $k=k_c$, and so will be given by

$$n'=\frac{4\pi}{3}\frac{k_c^3}{(2\pi)^3}=\frac{k_c^3}{6\pi^2}. \tag{10}$$

One might expect that there is a natural upper limit to n', *viz.*, the total number of longitudinal degrees of freedom n (for a system of n electrons), since at most n independent longitudinal degrees of freedom may be introduced. In practice we find that n' is considerably less than this theoretical maximum.

The modification of (6) to include only terms involving (p_k, q_k) with $k<k_c$ may be conveniently carried out by applying a unitary transformation similar to (9), but involving only q_k for which $k>k_c$. Thus we take $\Phi=S\psi$ where,

$$S=\exp[-(1/\hbar)\sum_{i,k>k_c}(4\pi e^2/k^2)^{\frac{1}{2}}q_k e^{i\mathbf{k}\cdot\mathbf{x}_i}], \tag{9a}$$

and where ψ is chosen to be independent of all q_k with wave numbers greater than k_c. We then obtain for our Hamiltonian

$$H=\sum_i\frac{p_i^2}{2m}+(4\pi)^{\frac{1}{2}}\frac{e}{m}\sum_{ik<k_c}\boldsymbol{\varepsilon}_k\cdot(\mathbf{p}_i-\hbar\mathbf{k}/2)q_k e^{i\mathbf{k}\cdot\mathbf{x}_i}$$
$$+(2\pi e^2/m)\sum_{\substack{ik<k_c\\ l<k_c}}\boldsymbol{\varepsilon}_k\cdot\boldsymbol{\varepsilon}_l q_k q_l e^{i(\mathbf{k}+\mathbf{l})\cdot\mathbf{x}_i}-\sum_{k<k_c}\frac{p_k p_{-k}}{2}$$
$$+2\pi e^2\sum_{\substack{k>k_c\\ i\neq j}}\frac{e^{i\mathbf{k}\cdot(\mathbf{x}_i-\mathbf{x}_j)}}{k^2}-2\pi ne^2\sum_{k<k_c}\frac{1}{k^2}, \tag{11}$$

with the associated set of subsidiary conditions:

$$\Omega_k\psi=0 \quad (k<k_c). \tag{12}$$

We shall find it convenient, in dealing with this Hamiltonian, to split up the third term into two parts. That part for which $\mathbf{k}+\mathbf{l}=0$ is independent of the electron coordinates and is given by

$$\frac{2\pi ne^2}{m}\sum_{k<k_c}q_k q_{-k}=\frac{\omega_p^2}{2}\sum_{k<k_c}q_k q_{-k}, \tag{13}$$

where we have introduced ω_p, the so-called plasma frequency, defined by

$$\omega_p=(4\pi ne^2/m)^{\frac{1}{2}}. \tag{14}$$

The remaining part, for which $\mathbf{k}+\mathbf{l}\neq 0$, we shall denote by U where,

$$U=\frac{2\pi e^2}{m}\sum_{\substack{ik<k_c\\ l<k_c\\ l\neq -k}}\boldsymbol{\varepsilon}_k\cdot\boldsymbol{\varepsilon}_l q_k q_l e^{i(\mathbf{k}+\mathbf{l})\cdot\mathbf{x}_i}. \tag{15}$$

U is much smaller than (13), for it always depends on the electron coordinates, and since these are distributed over a wide variety of positions, there is a strong tendency for the various terms entering into U to cancel. Let us for the time being neglect U, a procedure which we have called the random phase approximation in our earlier papers, and which we shall presently justify.

With this approximation we see that the third and fourth terms in our Hamiltonian (11) reduce to

$$H_{\text{osc}}=-\tfrac{1}{2}\sum_{k<k_c}(p_k p_{-k}+\omega_p^2 q_k q_{-k}) \tag{16}$$

the Hamiltonian appropriate to a set of harmonic oscillators, representing collective fields, with a frequency ω_p. The first term in (11) represents the kinetic energy of the electrons, while the second term,

$$H_1=(4\pi)^{\frac{1}{2}}\frac{e}{m}\sum_{ik<k_c}\boldsymbol{\varepsilon}_k\cdot\left(\mathbf{p}_i-\frac{\hbar\mathbf{k}}{2}\right)q_k e^{i\mathbf{k}\cdot\mathbf{x}_i}, \tag{17}$$

represents a simple interaction between the electrons and the collective fields, which is linear in the field variables. The fifth term,

$$H_{\text{s.r.}}=2\pi e^2\sum_{\substack{k>k_c\\ i\neq j}}\frac{e^{i\mathbf{k}\cdot(\mathbf{x}_i-\mathbf{x}_j)}}{k^2}, \tag{18}$$

represents the short-range part of the Coulomb interaction between the electrons. If we carry out the indicated summation, we find

$$H_{\text{s.r.}}=\tfrac{1}{2}\sum_{i\neq j}\frac{e^2}{|\mathbf{x}_i-\mathbf{x}_j|}\left\{1-\frac{2}{\pi}\operatorname{Si}(k_c|\mathbf{x}_i-\mathbf{x}_j|)\right\}, \tag{19}$$

where

$$\operatorname{Si}(y)=\int_0^y dx\frac{\sin x}{x}.$$

$\operatorname{Si}(y)=\pi/2$ for $y=2$ and oscillates near $\pi/2$ for larger values of y, so that $H_{\text{s.r.}}$ describes screened electron interaction with a range $\sim k_c$. A plot of $H_{\text{s.r.}}$ is given in Fig. 1.

Thus we see that in using (11) we have redescribed the long-range part of the Coulomb interactions between the electrons in terms of the collective oscillations (16), which interact with the electrons via H_1, (17). Our problem has now been reduced to one quite analogous to that encountered in I, *viz.*, a set of particles interacting with collective fields; the only new complications are the short-range interaction $H_{\text{s.r.}}$, and the subsidiary conditions on the system wave function. We shall see that as was the case in I with the trans-

verse collective oscillations, the coupling between the fields and particles described by H_I is not very strong, so that it is possible to obtain a good qualitative understanding of the behavior of the system by neglecting this term. In this section, we shall make this approximation, and then investigate to what extent it applies, while in Sec. III we will give a more accurate treatment which includes the effects of the electron-field interaction.

If we neglect H_I, we may write the stationary state wave function as

$$\psi=\psi_{osc}\chi(\mathbf{x}_1\cdots\mathbf{x}_n). \tag{20}$$

ψ_{osc} represents the wave functions of the collective fields, and may be written as a product of harmonic oscillator wave functions like

$$h_n(p_k)\exp[-(|p_k|^2/2\hbar\omega_p)],$$

where h_n is the nth Hermite polynomial, and we are using the *momentum* representation of the oscillator wave functions. $\chi(x_i\cdots x_n)$ represents the eigenfunction for a set of particles interacting through $H_{s.r.}$ For the lowest state, we then get

$$\psi_0=[\exp-\{\sum_{k<k_c}|p_k|^2/2\hbar\omega_p\}]\chi_0(\mathbf{x}_1\cdots\mathbf{x}_n), \tag{21}$$

where $\chi_0(\mathbf{x}_1\cdots\mathbf{x}_n)$ is the lowest state electron wave function.

In general χ_0 will be quite complex. However, just because the long-range part of the Coulomb potential is included in the oscillator energy, the remaining part $H_{s.r.}$ is considerably reduced in effectiveness. In fact it will often be of so short a range that for many purposes the free particle wave functions will constitute an adequate approximation. In this case, the lowest state wave function is

$$\psi_0=\{\exp[-\sum_{k<k_c}|p_k|^2/2\hbar\omega_p]\}D_0(\mathbf{x}_1\cdots\mathbf{x}_n), \tag{22}$$

where D_0 is the usual Slater determinantal wave function composed of the free electron wave functions appropriate to the ground state of the individual electrons. Our wave function ψ_0 then satisfies the exclusion principle.

Let us now consider the effects of the subsidiary conditions (12). In the representation in which p_k and $\mathbf{x}_i$ are diagonal these reduce to n' algebraic relations. We can view these relations in either of the following ways:

(a) They permit us to eliminate the p_k in terms of the $\mathbf{x}_i$.

(b) They permit us to eliminate n' of the $\mathbf{x}_i$ in terms of the p_k.

Let us begin with the first way. Our wave function (22) then becomes

$$\psi_0=\exp[-\tfrac{1}{2}(\sum_{ij}F(\mathbf{x}_i-\mathbf{x}_j)/\hbar\omega_p)D_0(\mathbf{x}_1\cdots\mathbf{x}_n), \tag{23}$$

where

$$F(\mathbf{x}_i-\mathbf{x}_j)=2\pi e^2\sum_{k<k_c}e^{i\mathbf{k}\cdot(\mathbf{x}_i-\mathbf{x}_j)}/k^2 \tag{24}$$

represents the long-range part of the Coulomb potential. $F(\mathbf{x}_i-\mathbf{x}_j)=e^2/|\mathbf{x}_i-\mathbf{x}_j|$ for $|\mathbf{x}_i-\mathbf{x}_j|\gg 1/k_c$ but approaches a constant $4\pi e^2\sum_{k<k_c}(1/k^2)$, when $|\mathbf{x}_i-\mathbf{x}_j|\ll 1/k_c$. Thus in (23) we have the usual free electron wave function D_0 modified by a factor which describes long-range electron correlation, such that the probability that two electrons are found a given distance apart is less than that calculated by neglecting the Coulomb interactions or by including the short-range interaction $H_{s.r.}$ In fact in consequence of this correlation term, each electron tends to keep apart from the others, in a manner quite similar to that obtained in the classical treatment of II. A similar result has been

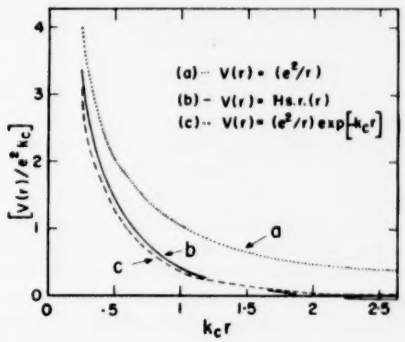

FIG. 1. $H_{s.r.}(r)$ compared with (e^2/r) and $(e^2/r)\exp(-k_cr)$.

obtained by Tomonaga in his one-dimensional treatment.

Let us now consider method (b), in which we seek to eliminate n' of the particle variables in terms of the field variables p_k. As is clear from the form of (12), this is a much more formidable task, one which we are not able to carry out explicitly. However, as we shall see throughout this paper, we can still draw a number of useful conclusions concerning the effect of such an elimination without actually solving for the $\mathbf{x}_i$ in terms of the p_k. In particular, we shall see in Sec. III how one may use a canonical transformation to replace (to lowest order in the field-particle coupling constant) n' of the individual particle degrees of freedom by as many collective degrees of freedom.

We now wish to justify our neglect of U and to investigate to what extent corrections arising from the inclusion of H_I will be of importance. In the remainder of this section we confine our attention to the lowest state of the system. We first show that the exact lowest state eigenfunction ψ_0 of our Hamiltonian (11) auto-

matically satisfies the subsidiary conditions (12). For as we have noted the subsidiary condition operators Ω_k commute with the Hamiltonian H, so that the wave function ψ_0 can, in general, be expressed in terms of a series of simultaneous eigenfunctions of H and the Ω_k. The lowest state of the system is nondegenerate and hence corresponds to a single eigenvalue of the operator Ω_k, which we may call α_k. To determine the value of α_k, we consider a space displacement of the entire system (field plus electrons) through a distance $\Delta\mathbf{x}$, so that

$$\mathbf{x}\rightarrow\mathbf{x}'+\Delta\mathbf{x}, \quad \mathbf{p}_i\rightarrow\mathbf{p}_i',$$
$$\mathbf{x}_i\rightarrow\mathbf{x}_i'+\Delta\mathbf{x}.$$

From Eqs. (2) and (3) we see that the effect of this displacement on the field coordinates is given by

$$p_k\rightarrow p_k' e^{-i\mathbf{k}\cdot\Delta\mathbf{x}},$$
$$q_k\rightarrow q_k' e^{i\mathbf{k}\cdot\Delta\mathbf{x}}.$$

The Hamiltonian is thus invariant under this displacement, while the subsidiary condition applied to our lowest state wave function becomes

$$e^{-i\mathbf{k}\cdot\Delta\mathbf{x}}\Omega_k'\psi_0=\alpha_k\psi_0.$$

However, since the lowest state is nondegenerate, it is not changed by this displacement, and we must have $\Omega_k'\psi_0=\alpha_k\psi_0$. Thus we find $\alpha_k=\alpha_k e^{i\mathbf{k}\cdot\Delta\mathbf{x}}$, which can only be satisfied if $\alpha_k=0$.

Thus, if we could obtain an exact solution for the lowest state eigenfunction ψ_0, we would automatically satisfy the subsidiary condition $\Omega_k\psi_0=0$. We may, in general, expect that if we obtain an approximate solution for ψ_0, we will not be able to satisfy the subsidiary condition, but that any error we make in determining the energy of the lowest state will not be increased by our failure to satisfy this subsidiary condition, since an exact solution satisfies the subsidiary condition and leads to the lowest possible energy state. The situation with regard to the excited states of the system will be somewhat different, and we will return to this question later.

Let us take as our approximate ψ_0, the wave function (22). In this approximation the energy of the lowest state is given by

$$\begin{aligned} E&=\tfrac{3}{5}E_0+\sum_{k<k_c}\frac{\hbar\omega_p}{2}-\frac{2\pi ne^2}{k^2}+\langle H_{s.r.}\rangle_{\text{Av}} \\ &=\tfrac{3}{5}E_0+n'\frac{\hbar\omega_p}{2}-\frac{ne^2}{\pi}k_c+\langle H_{s.r.}\rangle_{\text{Av}}, \end{aligned} \tag{25}$$

where E_0 is the energy of an electron at the top of the Fermi distribution, and $\langle H_{s.r.}\rangle_{\text{Av}}$ is the exchange energy arising from the screened Coulomb interaction term, $H_{s.r.}$, Eq. (18). We will not be concerned with evaluating $\langle H_{s.r.}\rangle_{\text{Av}}$ at present (reserving this for Paper IV), as we are here primarily interested in evaluating the corrections arising from U and H_I. We estimate these terms using perturbation theory. With the wave function (22) the average values of U and H_I vanish. U, in fact, has non-vanishing matrix elements only between the lowest state (with zero quanta) and a two-quantum state, while H_I connects the lowest state and a one-quantum state. From second-order perturbation theory, we have

$$\Delta U=-\sum_n\frac{|U_{0n}|^2}{E_n-E_0}, \tag{26}$$

where

$$U_{0n}=\frac{2\pi e^2}{m}\frac{\hbar}{2\omega_p}\boldsymbol{\varepsilon}_k\cdot\boldsymbol{\varepsilon}_l, \tag{27}$$

if the state n has two quanta of momentum $\mathbf{k}$ and $\mathbf{l}$, respectively; and

$$E_n-E_0=2\hbar\omega_p+\frac{\hbar(\mathbf{k}+\mathbf{l})^2}{2m}-\frac{\hbar(\mathbf{k}+\mathbf{l})}{m}\cdot\mathbf{p}_i, \tag{28}$$

if the electron in the initial state has momentum $\mathbf{p}_i$. In (28) we may, for the purpose of this rough estimate, approximate $E_n-E_0=2\hbar\omega_p$ since, as we shall see in Paper IV, $\hbar(\mathbf{k}+\mathbf{l})^2/2m-[\hbar(\mathbf{k}+\mathbf{l})/m]\cdot\mathbf{p}_i$ is always appreciably less than $2\hbar\omega_p$ as long as $k, l<k_c$. We then find

$$\begin{aligned} \Delta U&=-\left(\frac{\pi e^2\hbar}{m\omega_p}\right)^2 n\sum_{\substack{k<k_c\\ l<k_c}}\frac{(\boldsymbol{\varepsilon}_k\cdot\boldsymbol{\varepsilon}_l)^2}{2\hbar\omega_p} \\ &=-\left(\frac{\hbar\omega_p}{4}\right)^2\frac{1}{n}\frac{(n')^2}{6\hbar\omega_p}=-\frac{1}{48}\left(\frac{n'}{n}\right)\frac{n'\hbar\omega_p}{2}. \end{aligned} \tag{29}$$

Thus ΔU introduces a fractional change in the zero point energy, per oscillator, of $(1/48)(n'/n)$, and since n' is never greater than n (and is, in fact, often quite a bit smaller), this change is negligible. Thus, we are justified in neglecting completely the term U.

We may estimate the corrections arising from H_I in similar fashion. We have

$$\Delta H_I=-\sum_n\frac{|H_{I0n}|^2}{E_n-E_0}, \tag{30}$$

where

$$(H_I)_{n0}=(2\pi\hbar/\omega_p)^{\frac{1}{2}}(e/m)\boldsymbol{\varepsilon}_k\cdot(\mathbf{p}_i-\hbar\mathbf{k}/2), \tag{31}$$

if the state n has one quantum of momentum $\mathbf{k}$ present, and

$$E_n-E_0=\hbar\omega_p+\frac{\hbar k^2}{2m}-\frac{\hbar\mathbf{k}\cdot\mathbf{p}_i}{m}\cong\hbar\omega_p. \tag{32}$$

We then find

$$\begin{aligned} \Delta H_I&=-\frac{2\pi\hbar}{\omega_p}\frac{e^2}{m^2}\sum_{i,k<k_c}\frac{[\boldsymbol{\varepsilon}_k\cdot(\mathbf{p}_i-\hbar\mathbf{k}/2)]^2}{\hbar\omega_p} \\ &=-\frac{n'}{3n}\left\{\sum_i\frac{p_i^2}{2m}-\frac{9n}{40}\frac{\hbar^2k_c^2}{m}\right\}. \end{aligned} \tag{33}$$

Since, as we shall see, $k_c \lesssim k_0$, the wave vector of an electron at the top of the Fermi distribution, we see that the second term in the parenthesis in (33) is generally somewhat smaller than the first, and the first term corresponds to a fractional correction in the kinetic energy per electron (and thus in its effective mass) of $\sim n'/3n$. This may be appreciable if $n' \sim n$ but otherwise is small. This term implies a similar order of magnitude correction for the frequency of the collective oscillations, since $\sum_i p_i^2/2m$ and $n'\hbar\omega_p/2$ are roughly of the same order of magnitude. Thus we find that we are justified in neglecting H_1 in order to obtain a qualitative and rough quantitative understanding of the behavior of our system, but that the effects arising from H_1 should definitely be taken into account in a careful quantitative treatment. This we shall give in Sec. III.

Thus far we have not specified the value of k_c, and hence the number of collective degrees of freedom we find it desirable to introduce in our treatment. We may obtain a rough qualitative estimate of n' by minimizing our approximate expression for the lowest state energy (25) with respect to k_c (or n'). For the purpose of this rough estimate, let us neglect the dependence of $\langle H_{s.r.}\rangle_{Av}$ on k_c. We then note that the second term in (25) will be negative for those k for which $(2\pi ne^2/k^2) > \hbar\omega_p/2$. Hence we obtain the minimum value for (25) if we include in this summation, only those k for which this inequality is satisfied. This criterion yields

$$k_c^2 = \frac{4\pi ne^2}{\hbar\omega_p} = \frac{k_0^2}{2.14}\left(\frac{r_0}{a_0}\right)^{\frac{1}{2}}, \tag{34}$$

where r_0 is the interelectronic spacing, defined by

$$n = (4\pi r_0^3/3)^{-1}, \tag{35}$$

and a_0 is the Bohr radius. For a typical metal like Na, we have $(r_s/a_0) \sim 4$ and hence $k_c \sim k_0$. From (10) we see that in this case $n' \sim n/2$. In Paper IV where we give a more detailed treatment of that choice of k_c which minimizes the energy, including the effects of H_1, and $\langle H_{s.r.}\rangle_{Av}$, we find for Na, $k_c \sim 0.68 k_0$, and $n' \sim n/8$ in fair agreement with this rough estimate.

Finally we may remark that with the choice of k_c(34), the energy of the lowest state is

$$\begin{aligned} E &= \tfrac{3}{5}E_0 + \frac{n'\hbar\omega_p}{2} - \frac{ne^2k_c}{\pi} + \langle H_{s.r.}\rangle_{Av} \\ &= \tfrac{3}{5}E_0 - \frac{2}{3}\frac{ne^2}{\pi}k_c + \langle H_{s.r.}\rangle_{Av}. \end{aligned} \tag{36}$$

The energy $-\frac{2}{3}(ne^2/\pi)k_c$ represents a long-range correlation energy, i.e., that energy associated with the long-range correlations in electronic positions described by the wave function (23). In contrast to the exchange energy, this term represents Coulomb correlations between electrons of both kinds of spin. For Na it is, per electron,

$$-\frac{2}{3\pi}e^2k_c \cong -\frac{2}{3\pi}e^2k_0 \cong -0.4\frac{e^2}{r_0}, \tag{37}$$

a not inconsiderable energy. In Paper IV we return to a more careful estimate of the long-range correlation energy.

III.

In this section we wish to consider the effect of the field particle interaction term H_1 on the motion of the electrons and the collective oscillations. We do this with the aid of a canonical transformation which is chosen to eliminate H_1 in first approximation. Thus we seek a canonical transformation to a new representation in which the coupling between the fields and the electrons is described by a term H_{11}, which is appreciably smaller than H_1, and may consequently be neglected to a good degree of approximation (comparable, say, with our neglect of U). We shall then see that the effects of the coupling between the electrons and the collective field variables, as described by H_1, are threefold: there is an increase in the electronic effective mass, the frequency of the collective oscillations is increased and becomes k dependent, and the effective electron-electron interaction is modified. As we anticipated on the basis of our perturbation-theoretic estimate of H_1 in the preceding section, none of these effects is so large as to destroy the qualitative conclusions we reached there, although the quantitative estimates of the energy and wave functions of our system are somewhat altered.

The measure of the smallness of H_{11}, and hence the extent to which we are successful in carrying out our canonical transformation, is the expansion parameter

$$\alpha = \left\langle\left(\frac{\mathbf{k}\cdot\mathbf{p}_i}{m\omega}\right)^2\right\rangle_{Av}, \tag{38}$$

where we average over the particle momenta and the collective field wave vectors, and ω is the frequency of the collective oscillations. We find

$$\alpha \cong \frac{9}{25}\times\frac{1}{3}\frac{k_c^2p_0^2}{m^2\omega_p^2} \cong \tfrac{1}{2}\beta^2\frac{a_0}{r_s}, \tag{39}$$

where we have replaced ω by its approximate value ω_p and

$$\beta = k_c/k_0. \tag{40}$$

It is clear that by choosing β or k_c small enough, our expansion parameter α may be made as small as we like. We shall assume throughout the remainder of this paper that such a choice has been made, i.e., that $\alpha \ll 1$. In Paper IV we show that this criterion is satisfied in that $\alpha \sim 1/16$ for the electronic densities encountered in metals, if we take for β that value which minimizes the total energy. Another parameter of whose smallness

we shall have occasion to make use is the ratio of the number of collective degrees of freedom, n', to the total number of degrees of freedom, $3n$. For most metals, with the above choice of β, we find $(n'/3n)\sim 1/25$.

We shall make the further approximation of neglecting the effects of our canonical transformation on $H_{s.r.}$, the short-range Coulomb interaction between the electrons. From Eq. (11), we see that if we neglect H_1, the collective oscillations are not affected at all by $H_{s.r.}$. Thus $H_{s.r.}$ can influence the q_k only indirectly through H_1. But, as we shall see, the *direct* effects of H_1 on the collective oscillations are small. Thus, it may be expected that the *indirect* effects of $H_{s.r.}$ on the q_k through H_1 are an order of magnitude smaller and may be neglected in our treatment which is aimed at approximating the effects of H_1. We will justify this procedure in greater detail in the following section.

With regard to the subsidiary conditions (11), we shall find that to order α, the subsidiary conditions in our new representation involve only the new particle coordinates $(\mathbf{X}_i, \mathbf{P}_i)$. Thus we may write our new wave function in terms of products like

$$\Phi_{\text{field}}\chi(\mathbf{X}_1\cdots\mathbf{X}_n),$$

and the subsidiary conditions will only act on the $\chi(X_i)$. The n' subsidiary conditions may thus be viewed as consisting of n' relationships among the particle variables, which effectively reduce the number of individual electronic degrees of freedom from $3n$ to $3n-n'$. This reduction is necessary, since in this new representation the n' collective degrees of freedom must be regarded as independent. For the field coordinates no longer appear in the subsidiary conditions, and hence describe real collective oscillation, which is independent of the electronic motion in this new representation.

There is a close resemblance between our Hamiltonian (11), which describes a collection of electrons interacting via longitudinal fields, and the Hamiltonian we considered in I, which described a collection of electrons interacting via the transverse electromagnetic fields. In fact, we shall see that our desired canonical transformation is just the longitudinal analog of that used in Paper I to treat the organized aspects of the transverse magnetic interactions in an electron gas. In order to point up this similarity and to simplify the commutator calculus, we introduce the creation and destruction operators for our longitudinal photon field, a_k and a_k^*, which are defined by[9]

$$\begin{aligned} q_k &= (\hbar/2\omega)^{\frac{1}{2}}(a_k - a_{-k}^*), \\ p_k &= i(\hbar\omega/2)^{\frac{1}{2}}(a_k^* + a_{-k}), \end{aligned} \tag{41}$$

and which possess the commutation properties

$$\begin{aligned} [a_k, a_{k'}] &= [a_k^*, a_{k'}^*] = 0, \\ [a_k, a_{k'}^*] &= \delta_{kk'}, \end{aligned} \tag{42}$$

in virtue of (41). In terms of these variables, we then write our Hamiltonian and supplementary conditions schematically as

$$\begin{aligned} H &= H_{\text{part}} + H_1 + H_{\text{field}} + H_{s.r.}, \\ \Omega_k\Phi &= 0 \quad (k<k_c), \end{aligned} \tag{43}$$

where, using (11), (12), and (41) and neglecting U (Eq. 15),

$$H_{\text{part}} = \sum_i \frac{p_i^2}{2m} - \sum_{k<k_c} \frac{2\pi e^2 n}{k^2}, \tag{44a}$$

$$H_1 = (e/m)\sum_{i,k<k_c} (2\pi\hbar/\omega)^{\frac{1}{2}}\{\boldsymbol{\varepsilon}_k\cdot(\mathbf{p}_i - \hbar\mathbf{k}/2)a_k e^{i\mathbf{k}\cdot\mathbf{x}_i} + e^{-i\mathbf{k}\cdot\mathbf{x}_i}a_k^*\boldsymbol{\varepsilon}_k\cdot(\mathbf{p}_i - \hbar\mathbf{k}/2)\}, \tag{44b}$$

$$H_{\text{field}} = \sum_{k<k_c} \frac{\hbar\omega}{2}(a_k^* a_k + a_k a_k^*) + \frac{\hbar\omega}{4}(\omega_p^2 - \omega^2) \times (a_k^* a_k + a_k a_k^* - a_k a_{-k} - a_{-k}^* a_k^*), \tag{44c}$$

$$H_{s.r.} = 2\pi e^2 \sum_{\substack{k>k_c \\ i\neq j}} \frac{e^{i\mathbf{k}\cdot(\mathbf{x}_i - \mathbf{x}_j)}}{k^2}, \tag{44d}$$

$$\Omega_k = a_k^* + a_{-k} - \left(\frac{8\pi e^2}{k^2\hbar}\right)^{\frac{1}{2}} \sum_i e^{+i\mathbf{k}\cdot\mathbf{x}_i}. \tag{44e}$$

We note that H_{field} takes the form (44c), because we have expanded in terms of creation operators of frequency ω rather than ω_p.

We now consider a transformation from our operators $(\mathbf{x}_i, \mathbf{p}_i, a_k, a_k^*)$ to a new set of operators $(\mathbf{X}_i, \mathbf{P}_i, A_k, A_k^*)$, which possess the same eigenvalues and satisfy the same commutation rules as our original set.[10] The relation between these two sets may be written as

$$\mathbf{x}_i = e^{-iS/\hbar}\mathbf{X}_i e^{+iS/\hbar} \tag{45}$$

(with similar equations for $\mathbf{p}_i$, a_k, and a_k^*); (45) may be viewed as an operator equation, and we may take S the generating function of our canonical transformation to be a function of the new operators $(\mathbf{X}_i, \mathbf{P}_i, A_k, A_k^*)$ only. The operator relationship between the old and new Hamiltonians is

$$H = e^{-iS/\hbar}\mathfrak{K}e^{iS/\hbar} = H_{\text{new}}, \tag{46}$$

where $\mathfrak{K}$ represents that Hamiltonian which is the same function of the new coordinates as H is of the old, and H_{new} denotes the Hamiltonian expressed in terms of the new coordinates.

[9] ω is here unspecified, but will later be chosen to be the frequency of the collective oscillations.

[10] Quantum mechanical transformation theory is developed in, for instance, P. A. M. Dirac, *Principles of Quantum Mechanics* (Oxford University Press, London, 1935), second edition.

The problem of finding the proper form of S to realize our program was solved by a systematic study of the equations of motion. We do not have space to go into the details of this study here but confine ourselves to giving the correct transformation below. We shall then demonstrate that it leads to the desired results. Our canonical transformation is generated by

$$S=-(ei/m)\sum_{ik<k_c}(2\pi\hbar/\omega)^{\frac{1}{2}}\left\{\frac{\boldsymbol{\epsilon}_k\cdot(\mathbf{P}_i-\hbar\mathbf{k}/2)A_k}{\omega-\mathbf{k}\cdot\mathbf{P}_i/m+\hbar k^2/2m}\times\exp(i\mathbf{k}\cdot\mathbf{X}_i)-\exp(-i\mathbf{k}\cdot\mathbf{X}_i)A_k^*\times\frac{\boldsymbol{\epsilon}_k\cdot(\mathbf{P}_i-\hbar\mathbf{k}/2)}{\omega-\mathbf{k}\cdot\mathbf{P}_i/m+\hbar k^2/2m}\right\}. \quad (47)$$

On comparison with Eq. (45) of I, this generating function may be seen to be just the longitudinal analog of the "transverse" generating function given there. [The additional term in $\hbar k/2$ arises because $\mathbf{k}\cdot\mathbf{P}_i$ does not commute with $\exp(i\mathbf{k}\cdot\mathbf{X}_i)$.] Since H_{inter} and H_{field} are also analogous to the transverse terms encountered in I, we may expect that many of the results obtained there may be directly transposed to this longitudinal case. The differences in the treatments will arise from a consideration of $H_{\text{short-range}}$ and the subsidiary conditions.

We find it convenient to write the relationship between any old operator, O_{old} and the corresponding new operator O_{new} as

$$O_{\text{old}}=\exp(-iS/\hbar)O_{\text{new}}\exp(iS/\hbar)=O_{\text{new}}+(i/\hbar)[O_{\text{new}},S]-(1/2\hbar^2)[[O_{\text{new}},S],S]+\cdots, \quad (48)$$

and we will classify terms in this series according to the power of S they contain; i.e., $[O,S]$ is the first-order commutator of O and S. We then find, keeping only first-order commutators, that

$$\mathbf{p}_i=\mathbf{P}_i+(e/m)\sum_{k<k_c}\left(\frac{2\pi\hbar}{\omega}\right)^{\frac{1}{2}}\mathbf{k}\left\{\frac{\boldsymbol{\epsilon}_k\cdot(\mathbf{P}_i-\hbar\mathbf{k}/2)}{\omega-\mathbf{k}\cdot\mathbf{P}_i/m+\hbar k^2/2m}\times A_k\exp(i\mathbf{k}\cdot\mathbf{X}_i)+\exp(-i\mathbf{k}\cdot\mathbf{X}_i)A_k^*\times\frac{\boldsymbol{\epsilon}_k\cdot(\mathbf{P}_i-\hbar\mathbf{k}/2)}{\omega-\mathbf{k}\cdot\mathbf{P}_i/m+\hbar k^2/2m}\right\}+\cdots, \quad (49)$$

$$a_k=A_k-(e/m)\sum_i\left(\frac{2\pi}{\hbar\omega}\right)^{\frac{1}{2}}\times\exp(-i\mathbf{k}\cdot\mathbf{X}_i)\frac{\boldsymbol{\epsilon}_k\cdot(\mathbf{P}_i-(\hbar\mathbf{k})/2)}{\omega-\mathbf{k}\cdot\mathbf{P}_i/m+\hbar k^2/2m}+\cdots, \quad (50)$$

$$e^{i\mathbf{k}\cdot\mathbf{x}_i}=\exp(i\mathbf{k}\cdot\mathbf{X}_i)+\sum_{l<l_c}\left(\frac{2\pi e^2\omega}{\hbar l^2}\right)^{\frac{1}{2}}\times\left\{\frac{1}{\omega-\mathbf{l}\cdot\mathbf{P}_i/m+\hbar l^2/2m+\hbar\mathbf{l}\cdot\mathbf{k}/m}-\frac{1}{\omega-\mathbf{l}\cdot\mathbf{P}_i/m+\hbar l^2/2m}\right\}A_l\exp[i(\mathbf{l}+\mathbf{k})\cdot\mathbf{X}_i]-\sum_{l<l_c}\left(\frac{2\pi e^2\omega}{\hbar l^2}\right)^{\frac{1}{2}}\exp(-i\mathbf{l}\cdot\mathbf{X}_i)A_l^*\times\left\{\frac{1}{\omega-\mathbf{l}\cdot\mathbf{P}_i/m+\hbar l^2/2m+\hbar\mathbf{l}\cdot\mathbf{k}/m}-\frac{1}{\omega-\mathbf{l}\cdot\mathbf{P}_i/m+\hbar l^2/2m}\right\}\exp(i\mathbf{k}\cdot\mathbf{X}_i)+\cdots, \quad (51)$$

and we shall use these relationships in determining H_{new}.

We now proceed in a manner directly analogous to that of Paper I. We classify terms in H_{new} by considering the corresponding schematic terms in H [Eq. (44a)–(44d)] from which they may be considered to arise. Every term, $\mathcal{T}$, in H, leads to a zero-order (commutator) term, $\mathcal{T}$, which is the same function of the new variables as it was of the old variables, and in addition, a first order commutator, $+(i/\hbar)[\mathcal{T},S]$, a second-order term, $-(1/2\hbar^2)[\mathcal{T},[\mathcal{T},S]]$, etc. A convenient grouping of the terms in H exists which considerably simplifies the calculation of H_{new}. To demonstrate this grouping, we consider

$$H_a=\textstyle\sum_i P_i^2/2m+\sum_{k<k_c}(\hbar\omega/2)(a_k^*a_k+a_ka_k^*).$$

The first-order commutator arising from H_a is

$$+(i/\hbar)[\mathcal{H}_a,S]=-(e/m)\sum_{i,k<k_c}(2\pi\hbar/\omega)^{\frac{1}{2}}\times\{\boldsymbol{\epsilon}_k\cdot(\mathbf{P}_i-\hbar\mathbf{k}/2)A_k\exp(i\mathbf{k}\cdot\mathbf{X}_i)+\exp(-i\mathbf{k}\cdot\mathbf{X}_i)A_k^*\boldsymbol{\epsilon}_k\cdot(\mathbf{P}_i-\hbar\mathbf{k}/2)\}. \quad (52)$$

By Eq. (44c) we see that the above term is just the negative of H_{I}, expressed in terms of the new variables. Thus, the first-order commutator of $\mathcal{H}_a$ with S cancels the term arising from the zero-order commutator of $\mathcal{H}_{\text{I}}$. $\mathcal{H}_{\text{I}}$ and $\mathcal{H}_a$ are thus "connected" in that a simple relationship exists between the various order commutators arising from these terms; in fact, the nth order commutator of $\mathcal{H}_a$ with S is equal to the negative of the $(n-1)$th-order commutator of $\mathcal{H}_{\text{I}}$ with S. The terms in H_{new} arising from the connected terms H_a+H_{I}, may consequently be written in the following series:

$$H'=\mathcal{H}_a+\sum_{n=1}^{\infty}[\mathcal{H}_{\text{I}},S]_n\left\{\frac{1}{n!}-\frac{1}{(n+1)!}\right\}(i/\hbar)^n, \quad (53)$$

where $[\mathcal{H}_I, S]_n$ is the nth-order commutator of $\mathcal{H}_I$ with S.

We shall see that the effects of the field-particle interaction (up to order α) are contained in the first correction term to $\mathcal{H}_a$, $[(i/2\hbar)S, \mathcal{H}_I]$. The higher-order commutators will be shown to lead to effects of order α^2 or $\alpha(n'/3n)$ and may hence be neglected. The evaluation of our lowest-order term, $(i/2\hbar)[S, \mathcal{H}_I]$ is lengthy, but straightforward. We find, after some rearrangement of terms, that

$$
\begin{aligned}
(i/2\hbar)[\mathcal{H}_I, S] = & \frac{4\pi e^2}{m}\sum_{ki}\left(\frac{\hbar}{4\omega}\right) \\
& \times\left\{\frac{2\omega(\mathbf{k}\cdot\mathbf{P}_i/m)-(\mathbf{k}\cdot\mathbf{P}_i/m)^2+(\hbar^2k^4/4m^2)}{(\omega-\mathbf{k}\cdot\mathbf{P}_i/m)^2-(\hbar^2k^4/4m^2)}\right\} \\
& \times(A_kA_k^*+A_k^*A_k)+\frac{4\pi e^2}{m}\sum_{ki}\left(\frac{\hbar}{4\omega}\right) \\
& \times\left\{\frac{2\omega(\mathbf{k}\cdot\mathbf{P}_i/m)+(\mathbf{k}\cdot\mathbf{P}_i/m)^2-(\hbar^2k^4/4m^2)}{(\omega+\mathbf{k}\cdot\mathbf{P}_i/m)^2-(\hbar^2k^4/4m^2)}\right\} \\
& \times(A_kA_{-k}+A_k^*A_{-k}^*)-(\pi e^2/m^2) \\
& \times\sum_{\substack{k<k_c \\ i,j;i\neq j}}\frac{[\boldsymbol{\varepsilon}_k\cdot(\mathbf{P}_i-\hbar\mathbf{k}/2)][\boldsymbol{\varepsilon}_k\cdot(\mathbf{P}_j+\hbar\mathbf{k}/2)]}{\omega[\omega-\mathbf{k}\cdot\mathbf{P}_j/m-\hbar k^2/2m]} \\
& \times\exp[i\mathbf{k}\cdot(\mathbf{X}_i-\mathbf{X}_j)]+\exp[-i\mathbf{k}\cdot(\mathbf{X}_i-\mathbf{X}_j)] \\
& \times\frac{\boldsymbol{\varepsilon}_k\cdot(\mathbf{P}_i-\hbar\mathbf{k}/2)\boldsymbol{\varepsilon}_k\cdot(\mathbf{P}_j+\hbar\mathbf{k}/2)}{\omega(\omega-\mathbf{k}\cdot\mathbf{P}_j/m-\hbar k^2/2m)} \\
& -\frac{2\pi e^2}{m^2}\sum_{ik<k_c}\frac{(\boldsymbol{\varepsilon}_k\cdot\mathbf{P}_i)^2}{(\omega-\hbar k^2/2m)^2-(\mathbf{k}\cdot\mathbf{P}_i/m)^2}. \qquad (54)
\end{aligned}
$$

In obtaining (54) we have neglected a number of terms which are quadratic in the field variables and are multiplied by a phase factor with a nonvanishing argument, $\exp[i(\mathbf{k}+\mathbf{l})\cdot\mathbf{X}_i]$. These are terms like

$$
\begin{aligned}
\frac{4\pi e^2}{m^2}\sum_{\substack{k<k_c,i \\ l<k_c \\ l\neq -k}}\left(\frac{\hbar}{4\omega}\right)\frac{\boldsymbol{\varepsilon}_l\cdot(\mathbf{P}_i-\hbar\mathbf{l}/2)A_lA_k}{\omega-\mathbf{l}\cdot\mathbf{P}_i/m+\hbar l^2/2m} \\
\times\exp[i(\mathbf{k}+\mathbf{l})\cdot\mathbf{X}_i]. \qquad (55)
\end{aligned}
$$

Such terms are of exactly the same character as those we considered earlier in U [Eq. (15)], except that they are smaller by a factor of $\sim(\mathbf{l}\cdot\mathbf{P}_i/m\omega)$. Exactly the same arguments that we applied in showing that U could be neglected may be applied to terms like (55), with the result that we find that these terms are also completely negligible, leading in fact, to an energy correction which is smaller than that arising from U by a factor of α [Eq. (39)].

The remaining lowest-order term in H_{new} is just the zero-order term from $H_{\text{field}}-\sum_{k<k_c}(\hbar\omega/2)(a_k^*a_k+a_ka_k^*)$,

$$
\begin{aligned}
\mathcal{H}_{\text{field}}-\tfrac{1}{2}\sum_{k<k_c}(\hbar\omega/2)(A_k^*A_k+A_kA_k^*) = & \sum_{k<k_c}(\hbar/4\omega) \\
\times(\omega_p^2-\omega^2)[A_k^*A_k+A_kA_k^*-A_kA_{-k}-A_{-k}^*A_k^*]. & \qquad (56)
\end{aligned}
$$

We will now show that if we define ω by the dispersion relation,

$$
1=\frac{4\pi e^2}{m}\sum_i\frac{1}{(\omega-(\mathbf{k}\cdot\mathbf{P}_i/m))^2-\hbar^2k^4/4m^2}, \qquad (57)
$$

then the sum of (56) and the first two terms of (54) vanishes. To see this we note that multiplying (57) by $\omega^2-\omega_p^2$ on both sides, and rearranging terms on the right-hand side, yields

$$
\begin{aligned}
\omega^2-\omega_p^2 &= \frac{4\pi e^2}{m}\sum_i\frac{\omega^2-[\omega-(\mathbf{k}\cdot\mathbf{P}_i/m)]^2+\hbar^2k^4/4m^2}{[\omega-(\mathbf{k}\cdot\mathbf{P}_i/m)]^2-\hbar^2k^4/4m^2} \\
&= \frac{4\pi e^2}{m}\sum_i\frac{2\omega(\mathbf{k}\cdot\mathbf{P}_i/m)+(\hbar^2k^4/4m^2)-(\mathbf{k}\cdot\mathbf{P}_i/m)^2}{[\omega-(\mathbf{k}\cdot\mathbf{P}_i/m)]^2-\hbar^2k^4/4m^2}, \qquad (58)
\end{aligned}
$$

from which the above statement follows for the $(A_k^*A_k+A_kA_k^*)$ terms in (54). The $(A_kA_{-k}$ and $A_k^*A_{-k}^*)$ terms likewise go out when we replace $\mathbf{k}$ by $-\mathbf{k}$ in (57) and (58) and use the resulting relations to compare (56) and (54).

The results in lowest order of our canonical transformation on the Hamiltonian may thus be expressed schematically as follows:

$$
H_{\text{new}}{}^{(0)}=H_{\text{electron}}+H_{\text{coll.}}+H_{\text{res part}}, \qquad (59)
$$

where

$$
\begin{aligned}
H_{\text{electron}} = & \sum_i\frac{P_i^2}{2m}-\frac{2\pi e^2}{m^2}\sum_{ik<k_c}\frac{(\boldsymbol{\varepsilon}_k\cdot\mathbf{P}_i)^2}{(\omega-\hbar k^2/2m)^2-(\mathbf{k}\cdot\mathbf{P}_i/m)^2} \\
& +2\pi e^2\sum_{\substack{i,jk>k_c \\ i\neq j}}\frac{\exp[i\mathbf{k}\cdot(\mathbf{X}_i-\mathbf{X}_j)]}{k^2}-2\pi ne^2\sum_{k<k_c}\frac{1}{k^2}, \qquad (60)
\end{aligned}
$$

$$
H_{\text{coll.}}=\tfrac{1}{2}\sum_{k<k_c}(\hbar\omega)(A_k^*A_k+A_kA_k^*), \qquad (61)
$$

and

$$
\begin{aligned}
H_{\text{res part}} = & -\frac{\pi e^2}{m^2}\sum_{\substack{k<k_c \\ ij;i\neq j}}\frac{[\boldsymbol{\varepsilon}_k\cdot(\mathbf{P}_i-\hbar\mathbf{k}/2)][\boldsymbol{\varepsilon}_k\cdot(\mathbf{P}_j+\hbar\mathbf{k}/2)]}{\omega[\omega-\mathbf{k}\cdot\mathbf{P}_j/m-\hbar k^2/2m]} \\
& \times\exp[i\mathbf{k}\cdot(\mathbf{X}_i-\mathbf{X}_j)]+\exp[-i\mathbf{k}\cdot(\mathbf{X}_i-\mathbf{X}_j)] \\
& \times\frac{[\boldsymbol{\varepsilon}_k\cdot(\mathbf{P}_i-\hbar\mathbf{k}/2)][\boldsymbol{\varepsilon}_k\cdot(\mathbf{P}_j+\hbar\mathbf{k}/2)]}{\omega[\omega-(\mathbf{k}\cdot\mathbf{P}_j/m)-(\hbar k^2/2m)]}. \qquad (62)
\end{aligned}
$$

The effect of our transformation on the subsidiary conditions may be obtained in similar fashion. Our new

subsidiary conditions are given by

$$(\Omega_k)_{\text{new}}\psi=\exp(-iS/\hbar)\Omega_k'\exp(iS/\hbar)\psi$$
$$=\left\{\Omega_k'-\frac{i}{\hbar}[S,\Omega_k']-\frac{1}{2\hbar^2}[S,[S,\Omega_k']]+\cdots\right\}$$
$$\times\psi=0,\quad (k<k_c),\quad (63)$$

where ψ is our new system wave function, and Ω_k' is the same function of the new variables that Ω_k was of the old variables. We find

$$(\Omega_k)_{\text{new}}=A_k^*\left(1-\frac{4\pi e^2}{m}\sum_i\frac{1}{[\omega-(\mathbf{k}\cdot\mathbf{P}_i/m)]^2-\hbar^2k^4/4m^2}\right)$$
$$+A_{-k}\left(1-\frac{4\pi e^2}{m}\sum_i\frac{1}{[\omega+(\mathbf{k}\cdot\mathbf{P}_i/m)]^2-\hbar^2k^4/4m^2}\right)$$
$$-\left(\frac{8\pi e^2}{k^2\hbar\omega}\right)^{\frac{1}{2}}\sum_i\frac{\omega^2}{\omega^2-(\mathbf{k}\cdot\mathbf{P}_i/m-\hbar k^2/2m)^2}$$
$$\times\exp(i\mathbf{k}\cdot\mathbf{X}_i)-\left(\frac{8\pi e^2}{k^2\hbar\omega}\right)^{\frac{1}{2}}\sum_{\substack{l<l_c,i\\ l\neq k}}\left(\frac{2\pi e^2\omega}{\hbar l^2m^2}\right)^{\frac{1}{2}}$$
$$\times\left\{\left[\frac{1}{\omega+(\mathbf{l}\cdot\mathbf{P}_i/m)+\hbar l^2/2m-\hbar\mathbf{l}\cdot\mathbf{k}/m}\right.\right.$$
$$\left.-\frac{1}{\omega+\mathbf{l}\cdot\mathbf{P}_i/m+\hbar l^2/2m}\right]A_{-l}\exp[+i(\mathbf{k}-\mathbf{l})\cdot\mathbf{X}_i]$$
$$-\exp(-i\mathbf{l}\cdot\mathbf{X}_i)A_1^*\left[\frac{1}{\omega-\mathbf{l}\cdot\mathbf{P}_i/m+\hbar l^2/2m+\hbar\mathbf{l}\cdot\mathbf{k}/m}\right.$$
$$\left.\left.-\frac{1}{\omega-\mathbf{l}\cdot\mathbf{P}_i+\hbar l^2/2m}\right]\exp(i\mathbf{k}\cdot\mathbf{X}_i)\right\}$$
$$-\frac{1}{2\hbar^2}[S,[S,\Omega_k']]+\cdots.\quad (64)$$

$(\Omega_k)_{\text{new}}$ is considerably simplified when we note that the first two terms vanish when we apply the dispersion relation [Eq. (57)] for both plus and minus k. The fourth term consists of a linear term in the field coordinates multiplied by a nonvanishing phase factor, and the effect of such a term in the subsidiary condition is the same as that of a term like (55) in the Hamiltonian. Since there is no point in obtaining the subsidiary condition to a higher order of accuracy than is maintained in our Hamiltonian, we may neglect this term. With this approximation, our subsidiary condition reduces to one which does not involve (in lowest orders) the field variables, and is given by

$$(\Omega_k)_{\text{new}}\psi=\sum_i\frac{\omega^2}{\omega^2-[(\mathbf{k}\cdot\mathbf{P}_i/m)-\hbar k^2/2m]^2}$$
$$\times\exp(i\mathbf{k}\cdot\mathbf{X}_i)\psi=0,\quad (k<k_c).\quad (65)$$

IV.

The physical consequences of our canonical transformation follow from the lowest-order Hamiltonian, $H_{\text{new}}^{(0)}$ [Eq. (59)] and the associated set of subsidiary conditions on our system wave function [Eq. (65)]. We discuss these briefly and then show that the higher-order terms in H_{new} and $(\Omega_k)_{\text{new}}$ are actually negligible. We first note that our field coordinates occur only in H_{coll}, and thus describe a set of uncoupled fields which carry out real independent longitudinal oscillations, since the subsidiary conditions no longer relate field and particle variables, and since there are no field-particle interaction terms in H_{new}. The frequency of these collective oscillations is given by the dispersion relation [Eq. (57)], which is the appropriate quantum-mechanical generalization of the classical dispersion relation derived in II, as well as being the longitudinal analog of the quantum-dispersion relation for organized transverse oscillation, which we obtained in I.

This dispersion relation plays a key role in our collective description, since it is only for $\omega(k)$ which satisfy it that we can eliminate the unwanted terms in the Hamiltonian [Eq. (54)] and the unwanted field terms in the subsidiary condition. For sufficiently small k, we may expand (57) in powers of $(\mathbf{k}\cdot\mathbf{P}_i/m\omega)$ and $(\hbar k^2/m\omega)$ and so always obtain a solution for $\omega(k)$. If we do this, and assume an isotropic distribution of $\mathbf{P}_i$, we find

$$\omega^2=\omega_p^2+\frac{k^2}{nm^2}\sum_i P_i^2+\frac{\hbar^2k^4}{4m^2},\quad (66)$$

and hence

$$\omega=\omega_p\left(1+\frac{k^2}{2nm^2}\sum_i\frac{P_i^2}{\omega_p^2}+\frac{\hbar^2k^4}{8m^2\omega_p^2}\right).\quad (67)$$

These appropriate dispersion relations are, in fact, quite sufficient for our purpose, since the expansions involved in obtaining them are the same that we have used in obtaining H_{new}.

We have treated ω as a pure number thus far, although we see from (57) or (67) that ω is, in fact, an operator, since it contains $\mathbf{P}_i$. We have ignored this fact, for instance, in working out our commutation relations and obtaining H_{new}. This treatment of ω as a pure number is only strictly justified if our system wave function is an eigenfunction of $\mathbf{P}_i$, which is not the case. Thus ω contains and, in turn, can contribute to the Hamiltonian, off-diagonal terms which cause transitions between states of different energy. These terms could then, in principle, be eliminated from the

Hamiltonian by a further canonical transformation. However because the dependence of ω on P_i is already or order α, this elimination would produce terms of order α^2 which are truly negligible. We are justified in neglecting the off-diagonal elements of the operator ω.

According to (67), in consequence of the electron-field interaction the frequency of the collective oscillations has become k dependent. We may obtain an order-of-magnitude estimate of the fractional change in this frequency by averaging the dispersion relation (67) over all $k<k_c$ and carrying out the indicated sum over particle momenta. In obtaining this mean value of $\sum_i P_i^2$, we should use the appropriate eigenfunctions of our new Hamiltonian (59). However, as we shall see later, the correct particle eigenfunctions can be replaced for many applications by plane waves, so that $\sum_i P_i^2$ may be approximately evaluated by assuming a Fermi distribution of electrons at absolute zero. We then find

$$\langle\omega\rangle_{\text{Av}}=\omega_p\left(1+\frac{3}{10}\frac{\langle k^2\rangle_{\text{Av}}P_0^2}{m^2\omega_p^2}+\frac{\hbar^2\langle k^4\rangle_{\text{Av}}}{8m^2\omega_p^2}\right)$$
$$=\omega_p(1+3\alpha[1+(3/10)\beta^2]), \quad (68)$$

where α is given by (39) and β by (40). Since $\beta\lesssim 1$, we see that the effect of the k^4 term is small compared to the k^2 term. This result holds true quite generally, in that where an expansion in powers of $\alpha=\langle(\mathbf{k}\cdot\mathbf{P}_i/m\omega)^2\rangle_{\text{Av}}$ is justified, the terms of order $(\hbar^2k^4/4m^2\omega^2)$ are negligible. The average fractional increase in the frequency is thus of order 3α. As we have remarked, for the electronic densities encountered in metals, α turns out to be $\sim 1/16$, so that this constitutes at most a 20 percent correction in the collective oscillation frequency.

The effect on the electrons of the elimination (in lowest order) of the electron-field interaction may be seen by considering the second term in H_{electron} and $H_{\text{res part}}$. We first note that in the approximation of small α, the second term in H_{electron} becomes

$$E_{\text{red}}=-\frac{k_c^3}{18\pi^2 n}\sum_i\frac{P_i^2}{2m}=-\frac{n'}{3n}\sum_i\frac{P_i^2}{2m}.$$

If we combine this with the first term, $\sum_i P_i^2/2m$, we obtain

$$E_{\text{red}}+\sum_i\frac{P_i^2}{2m}\left(\frac{3n-n'}{3n}\right)=\sum_i\frac{P_i^2}{2m^*},$$

where

$$m^*=m\times 3n/(3n-n'). \quad (69)$$

Thus the "new" electrons behave as if they had an effective mass m^*, which is given by (69), and which is slightly greater than the "bare" electron mass m. This increase in the effective electronic mass has a simple physical interpretation. For we note that according to Eqs. (47) and (48),

$$\mathbf{X}_i=\mathbf{x}_i-\frac{ei}{m}\sum_{k<k_c}\left(\frac{2\pi\hbar}{\omega}\right)^{\frac{1}{2}}\left\{\frac{\boldsymbol{\varepsilon}_k\omega A_k}{\omega-\mathbf{k}\cdot\mathbf{P}_i/m+\hbar k^2/2m}\right.$$
$$\times\exp(i\mathbf{k}\cdot\mathbf{x}_i)-\exp(-i\mathbf{k}\cdot\mathbf{x}_i)$$
$$\left.\times\frac{\boldsymbol{\varepsilon}_k\omega A_k^*}{\omega-\mathbf{k}\cdot\mathbf{P}_i/m+\hbar k^2/2m}\right\}. \quad (70)$$

The $\mathbf{X}_i$ thus represents the "bare" electron plus an associated cloud of collective oscillation; the increased effective mass may be regarded as an inertial effect resulting from the fact that these electrons carry such a cloud along with them.

$H_{\text{res part}}$, in the approximation of small α, may be written as

$$H_{\text{r.p.}}=\frac{-2\pi e^2}{m^2}\sum_{\substack{k<k_c\\ i,j;i\neq j}}\frac{(\boldsymbol{\varepsilon}_k\cdot P_i)(\boldsymbol{\varepsilon}_k\cdot P_j)}{\omega_p^2+k^2\langle V^2\rangle_{\text{Av}}}\exp[i\mathbf{k}\cdot(\mathbf{X}_i-\mathbf{X}_j)]$$
$$=-2\pi e^2\sum_{\substack{k<k_c\\ i,j;i\neq j}}\frac{(\boldsymbol{\varepsilon}_k\cdot\mathbf{P}_i)(\boldsymbol{\varepsilon}_k\cdot\mathbf{P}_j)/(m^2\langle V^2\rangle_{\text{Av}})}{k^2+K^2}$$
$$\times\exp[i\mathbf{k}\cdot(\mathbf{X}_i-\mathbf{X}_j)], \quad (71)$$

where $\langle V^2\rangle_{\text{Av}}=\sum_i P_i^2/m^2n$ and $K^2=\omega_p^2/\langle V^2\rangle_{\text{Av}}$. If we assume that the electrons form a completely degenerate gas, then for most metals,

$$K^2=(5/3)(\omega_p^2/v_0^2)\cong k_0^2. \quad (72)$$

Thus

$$H_{\text{r.p.}}\cong-2\pi e^2\sum_{\substack{i\neq j\\ k<k_c}}\frac{(\boldsymbol{\varepsilon}_k\cdot\mathbf{P}_i)(\boldsymbol{\varepsilon}_k\cdot\mathbf{P}_j)/(m^2\langle V^2\rangle_{\text{Av}})}{k^2+k_0^2}$$
$$\times\exp[i\mathbf{k}\cdot(\mathbf{X}_i-\mathbf{X}_j)]. \quad (73)$$

$H_{\text{res part}}$ thus describes an extremely weak attractive velocity dependent electron-electron interaction. For if the summation in (73) were over all k, it would correspond to a screened interaction of range $\sim(1/k_0)$; however, the summation is only for $k<k_c$, where $k_c<k_0$, so that we are describing here that part of a screened interaction beyond the screening length. A more detailed analysis confirms that this qualitative estimate, and justifies our neglecting $H_{\text{r.p.}}$ in comparison with $H_{\text{s.r.}}$ in considering the effects of electron-electron interaction.

Let us now consider the effect of the higher-order terms, such as $[S,[S,\mathcal{H}_{\text{I}}]]$. {The higher-order commutators arising from $\mathcal{H}_{\text{field}}-\sum_{k<k_c}(\hbar\omega/2)(A_k^*A_k+A_kA_k^*)$ will be of this same type, since the zero-order commutator from this term cancelled part of $[S,\mathcal{H}_{\text{I}}]$.} The calculation of $[S,[S,\mathcal{H}_{\text{I}}]]$ is quite straightforward, but scarcely worth going into here, since by comparison of Eqs. (49), (50), (51), and (44), it may easily be seen that the lowest order non-negligible terms terms will resemble H_{I} but will be at least of order $(\mathbf{k}\cdot\mathbf{P}_i/m\omega)$ smaller. These terms which we earlier de-

noted by H_{II} could be eliminated by a further transformation. However, since as we have seen, the elimination of H_I led to effects of order α (or $n'/3n$), the effects so obtained would then be of order α^2, and we may neglect them entirely in our approximation of small α. Exactly the same conclusions apply with respect to the higher-order commutators of the subsidiary condition operator, $(\Omega_k)_{\text{new}}$, since it is not fruitful for us to evaluate $(\Omega_k)_{\text{new}}$ to any greater accuracy than that obtaining for H_{new}.

It is interesting to note that included in these higher-order terms is the influence of our effective mass correction, Eq. (69), on the frequency of the collective oscillations. Thus, on evaluating these terms, one finds

$$\omega^2=\omega_p{}^2+\frac{k^2}{n(m^*)^2}\sum_i P_i{}^2+\frac{\hbar^2k^4}{4(m^*)^2},$$

instead of the dispersion relation (66). This is, of course, just what might be expected, since the successive elimination of the field-particle interaction terms leads to a mass renormalization, familiar from quantum electrodynamics, in that everywhere m appears, it should properly be replaced by m^*.[11] This correction is here quite negligible, usually leading to a fractional change in the collective oscillation frequency of less than 1 percent. For this change is $\sim(\alpha n'/n)$, and for the electronic densities encountered in metals,

$$\alpha(n'/n)\cong(1/16)(3/25)=(3/400).$$

Our only other approximation has been to neglect the effect of the canonical transformation on $H_{s.r.}$, which will lead, indirectly, to the effect of $H_{s.r.}$ on the collective oscillations. Suppose we consider a typical first-order term arising from $[S, H_{s.r.}]$. This will be like

$$2\pi e^2\sum_{\substack{k>k_c\\ l<k_c\\ i,j}}\left(\frac{2\pi e^2}{\hbar l^2}\right)^{\frac{1}{2}}\frac{\exp(-i\mathbf{l}\cdot\mathbf{X}_j)}{k^2}\frac{(\hbar\mathbf{l}\cdot\mathbf{k}/m)A_l{}^*\exp(i\mathbf{k}\cdot\mathbf{X}_i)\exp(-i\mathbf{k}\cdot\mathbf{X}_j)}{(\omega-\mathbf{l}\cdot\mathbf{P}_i/m+\hbar l^2/2m)(\omega-\mathbf{l}\cdot\mathbf{P}_i/m+\hbar l^2/2m+\hbar\mathbf{l}\cdot\mathbf{k}/m)}. \tag{74}$$

These terms thus consist of a nonvanishing phase factor multiplying a field variable and a short-wavelength density fluctuation. The structure of (74) is quite similar to that of U [Eq. (15)], the difference being that the short-wavelength density fluctuation $\sum_j\exp(-i\mathbf{k}\cdot\mathbf{X}_j)$ here plays the same role as the collective field variable (which is essentially a long-wavelength density fluctuation) did in U. If we had a term for which $\mathbf{k}=\mathbf{l}$, (74) would reduce to a term like H_I, just as the third term in (11) reduced to $\omega_p{}^2\sum_k\times(q_kq_{-k}/2)$. Thus we might expect that (74) bears about the same relationship to H_I, as U does to $(\omega_p{}^2/2)\times\sum_kq_kq_{-k}$. However, it is quite a bit more difficult to establish the smallness of (74) mathematically than it was for U, since a perturbation theoretic estimate involves the consideration of intermediate states in which two electrons are excited. We note that the main effect of $H_{s.r.}$ is to produce short-range correlations in particle positions, analogous to the long-range correlations produced by the long-range part of the Coulomb potential, in the sense that the particles tend to keep apart and thus tend to reduce the effectiveness of $H_{s.r.}$. Because of the analytical difficulties involved in a justification along these lines we prefer to justify our neglect of (74) in a more qualitative and physical fashion.

We see that (74) describes the effect of the collective oscillations on the short range collisions between the electrons, and conversely, the effect of the short-range collisions on the collective oscillations. We may expect that these effects will be quite small, since $H_{s.r.}$ is itself a comparatively weak interaction. The short-range electron-electron collisions arising from $H_{s.r.}$ will act to damp the collective oscillations, a phenomenon which has been treated in some detail classically by Bohm and Gross.[12] A test for the validity of our approximation in neglecting terms like (74) is that the damping time from the collisions be small compared with the period of a collective oscillation. In this connection we may make the following remarks:

(1) Electron-electron collisions are comparatively ineffective in damping the oscillations, since momentum is conserved in such collisions, so that to a first approximation such collisions produce no damping. [Such collisions produce damping only in powers of $(\mathbf{k}\cdot\mathbf{P}_i/m\omega)$ higher than the first.]

(2) The exclusion principle will further reduce the cross section for electron-electron collision.

(3) If H_I is neglected, collisions have no effect on the collective oscillations. This means that the major part of the collective energy is unaffected by these short-range collisions, since only that part coming from H_I, (which is of order α relative to $\hbar\omega_p$) can possibly be influenced. Thus at most 20 percent of the collective energy can be damped in a collision process.

All of these factors combine to reduce the rate of damping, so that we believe this rate is not more than 1 percent per period of an oscillation and probably is quite a bit less. A correspondingly small broadening of the levels of collective oscillation is to be expected. It is for these reasons that we feel justified in neglecting the effects of our canonical transformation on $H_{s.r.}$.

[11] Note, however, that m is not replaced by m^* in our expression for ω_p, Eq. (14), since the collective oscillations are not affected by the field-electron interaction in this order.

[12] D. Bohm and E. P. Gross, Phys. Rev. **75**, 1864 (1949).

V.

The motion of the electrons in our new representation is considerably more complicated than that of the collective fields. The major reason for this complication is our set of subsidiary conditions (65), which essentially act to reduce the number of individual electron degrees of freedom from $3n$ to $3n-n'$, where n' is the number of collective degrees of freedom and is given by

$$n'=\frac{k_c^3}{6\pi^2}=\frac{\beta^3k_0^3}{6\pi^2}=\frac{\beta^3 n}{2}. \tag{75}$$

We may obtain a better understanding of the role of these subsidiary conditions by making use of the density fluctuation concept which we developed in Paper II. There we saw that classically the collective component of the density fluctuation ρ_k was proportional to

$$R_k{}^c=\sum_i \frac{1}{\omega^2-(\mathbf{k}\cdot\mathbf{P}_i/m)^2}e^{i\mathbf{k}\cdot\mathbf{x}_i}.$$

In a quantum-theoretical treatment of the density fluctuations, the collective component is found to be proportional to

$$R_k{}^q=\sum_i \frac{1}{\omega^2-[(\mathbf{k}\cdot\mathbf{P}_i/m)-\hbar k^2/2m]^2}e^{i\mathbf{k}\cdot\mathbf{x}_i}. \tag{76}$$

This result may be seen to follow directly from the quantum generalization of the methods of II given in Appendix I. In the preceding expressions, $\mathbf{x}_i$ and $\mathbf{p}_i$ of course refer to the "original" position and momentum of the electron, i.e., the Hamiltonian in terms of these variables is given by Eq. (1). On the other hand, our "new" electron variables (X_i, P_i) describe electron motion in the absence of any collective oscillation, since there are no terms in our Hamiltonian (59) which couple the electrons and the collective oscillation. Consequently we should expect that the collective component of the density fluctuation when expressed in terms of these "new" variables should vanish, since these variables are chosen to describe "pure" individual electron motion and are incapable of describing, or taking part in, collective oscillation. But this is just what our subsidiary conditions assert, as may be seen by comparing (76) and (65). Thus, if we carry out a transformation to "individual" electron variables, we must expect a set of subsidiary conditions given by (65), since these guarantee that we have developed a consistent description of the state of the electron gas in the absence of collective oscillation.

The physical content of the subsidiary condition also follows from the density fluctuation concept. For we may rewrite the subsidiary condition, Eq. (65) as

$$\sum_i \exp(+i\mathbf{k}\cdot\mathbf{X}_i)\psi = \sum_i \frac{(\mathbf{k}\cdot\mathbf{P}_i/m-\hbar k^2/2m)^2\exp(i\mathbf{k}\cdot\mathbf{X}_i)}{\omega^2-[(\mathbf{k}\cdot\mathbf{P}_i/m)-\hbar k^2/2m]^2}. \tag{77}$$

Since we are dealing with $k<k_c$, for which $(\mathbf{k}\cdot\mathbf{P}_i/m\omega)^2 \ll 1$, we see that the subsidiary condition asserts that in terms of our new coordinates and momenta, the density fluctuations of long wavelength are greatly reduced. This reduction is due to the fact that the major portion of the long-wavelength density fluctuations is associated with the collective oscillations, and described in terms of these in our collective description.

In our new representation, the subsidiary conditions (65) continue to commute with the Hamiltonian (59). This follows since the commutation relations are unchanged by a canonical transformation; it may easily be directly verified from (65) and (59) that these commute within the approximations we have made. Consequently, just as was the case with (11) and (12), if we correctly solved for the exact lowest state eigenfunction of our Hamiltonian H_{new}, we would automatically satisfy the subsidiary conditions (65), since the ground state of our system is nondegenerate. For this reason, the energy of the lowest state of our system is relatively insensitive to whether we satisfy the subsidiary conditions or not. For since the lowest state wave function does satisfy the subsidiary condition, moderate changes in this wave function, involving corresponding failures to satisfy the subsidiary conditions, will provide quite small changes in the energy. Conversely, because of this insensitivity of the ground state energy to the degree of satisfaction of the subsidiary condition, it will take a quite good approximation to the lowest eigenfunction of H_{new} to satisfy the subsidiary conditions to a fair degree of approximation.

It should be noted that the lowest state wave function satisfies the subsidiary condition because of the effects of the term $H_{\text{r.p.}}$ in the Hamiltonian. For as we have seen, the subsidiary condition describes a long range correlation in the particle positions, which is independent of the amplitude of collective oscillation. In the approximation that we are using, this correlation has to be due to the residual interaction between the particles, since the subsidiary conditions will automatically be satisfied if we solve for the lowest state wave function. At first sight, it might be thought that the short-range potential $H_{\text{s.r.}}$ might also play an important role in establishing these correlations, since it corresponds to a fairly strong interaction potential when the particles are close to each other. However, from the definition of $H_{\text{s.r.}}$ in Eq. (18), we see that it has no Fourier components corresponding to $k<k_c$. As a simple perturbation theoretical calculation shows, the only effect of $H_{\text{s.r.}}$ in the first approximation is to turn a plane wave function.

$$\psi_0=\exp(i\sum_n \mathbf{k}_n\cdot\mathbf{x}_n),$$

into the function

$$\psi=\psi_0(1+\sum_{\substack{m,n\\ k>k_c}} C_{mn}\exp[i\mathbf{k}\cdot(\mathbf{x}_m-\mathbf{x}_n)]),$$

where C_{mn} is a suitable expansion coefficient, which can be obtained by a detailed calculation.[13] But since the sum is restricted to $k>k_c$, $H_{s.r.}$ introduces only *short-range* correlations, which have nothing to do with the subsidiary conditions. On the other hand, $H_{r.p.}$ which has only *long-range* fourier components (i.e., $k<k_c$) introduces only corresponding long-range correlations. Thus, in the present approximation, it is $H_{r.p.}$ that is responsible for the long-range correlations implied by the subsidiary condition.

On the basis of the above conclusions, we may deduce the following physical picture. The long range Coulomb forces produce a tendency for electrons to keep apart, as a result of which the Coulomb force itself tends to be neutralized. But this neutralization could not be perfect; for if it were, then there would be no force left to produce the necessary correlations in particle positions. Our calculations show that $H_{r.p.}$ is the small residual part of the Coulomb force which must remain unneutralized in order to produce the long-range correlations needed for agreeing. Because this force is so small, it will produce only correspondingly small changes in the particle momenta, so that in most applications a set of plane waves will provide a good approximation to the particle wave function (in the new representation, of course).

All of the above applies rigorously only in the ground state. In the excited states, similar conclusions apply; but the application of the subsidiary conditions is more difficult, because the wave functions of the excited states are no longer now degenerate. Here, we could in general expand an arbitrary eigenfunction of $H_{\text{new}}{}^{(0)}$ as a series of eigenfunctions of $(\Omega_k)_{\text{new}}$. To satisfy the subsidiary conditions, we then retain only those terms in this series for which $(\Omega_k)_{\text{new}}=0$. This reduction in the number of possible eigenfunctions corresponds to the reduction in the number of individual electron degrees of freedom implied by (65). The exact treatment of the problem of the excited states is quite complex and will be reserved for a later paper by one of us. However, we may expect that if the reduction in the number of individual electron degrees of freedom is comparatively small [i.e., $(n'/n)\ll 1$], then their effect on the energy spectrum of the electron gas will be correspondingly reduced.

We conclude this section by summing up the results of our canonical transformation to the collective description. We have obtained a Hamiltonian describing collective oscillation plus a system of individual electrons interacting via a screened Coulomb force, with a screening radius of the order of the inner-electronic distance. Although the individual electron wave functions are restricted by a set of n' subsidiary conditions, which act to reduce the number of individual electron degrees of freedom and to inhibit the long-range density fluctuations associated with the individual electron motion, for many purposes the effect of these subsidiary conditions may be neglected. In Paper IV we examine the physical conclusions we are led to by the use of the collective description for the motion of electrons in metals. We shall see that these are in good agreement with experiment and enable us to resolve a number of hitherto puzzling features of the usual one-electron theory.

One of us (D.P.) would like to acknowledge the support of the Office of Ordnance Research, U. S. Army, during the writing of this paper.

APPENDIX I

In this appendix we treat the collective fluctuations in charge density by finding the equations of motion of the associated operators, thus developing a direct quantum-mechanical extension of the methods used in Paper II. We use the electron field second-quantization formalism, in order to facilitate comparison with the work of Tomonaga and to take into account explicitly the fact that the electrons obey Fermi statistics.

Following the usual treatments,[14] we describe the electrons by the field quantities $\psi_\sigma(\mathbf{x})$ which satisfy the anti-commutation relations $[\psi_\sigma(\mathbf{x}), \psi_\sigma(\mathbf{x}')]_+=[\psi_\sigma{}^*(\mathbf{x}), \psi_{\sigma'}{}^*(\mathbf{x}')]_+=0$ and $[\psi_\sigma(\mathbf{x}), \psi_{\sigma'}{}^*(\mathbf{x}')]_+=\delta(\mathbf{x}-\mathbf{x}')\delta_{\sigma\sigma'}$. σ refers to the electron spin and takes on two values corresponding to the two orientations of the electron spin. We work in the Heisenberg representation. The Hamiltonian which determines the equation of motion of the ψ's is

$$H=-\int\psi^*(\mathbf{x})\frac{\hbar^2}{2m}\Delta\psi(\mathbf{x})d\mathbf{x}+\frac{e^2}{2}\int\int\frac{\rho(\mathbf{x})\rho(\mathbf{x}')}{|\mathbf{x}-\mathbf{x}'|}d\mathbf{x}d\mathbf{x}', \quad \text{(A1)}$$

where

$$\rho(\mathbf{x})=\textstyle\sum_\sigma\psi_\sigma{}^*(\mathbf{x})\psi_\sigma(\mathbf{x}). \quad \text{(A2)}$$

It is convenient to Fourier-analyze $\psi_\sigma(\mathbf{x})$ and $\psi_\sigma{}^*(\mathbf{x})$ by

$$\psi_\sigma(\mathbf{x})=\sum_k c_{k\sigma}e^{i\mathbf{k}\cdot\mathbf{x}},\qquad \psi_\sigma{}^*(\mathbf{x})=\sum_k c_{k\sigma}{}^*e^{-i\mathbf{k}\cdot\mathbf{x}}, \quad \text{(A3)}$$

where the $c_{k\sigma}$ and $c_{k\sigma}{}^*$ obey the anticommutation relations

$$[c_k\sigma, c_{k'\sigma'}]_+=[c_{k\sigma}{}^*, c_{k'\sigma'}{}^*]_+=0,\qquad [c_{k\sigma}, c_{k'\sigma'}{}^*]_+=\delta_{kk'}\delta_{\sigma\sigma'}, \quad \text{(A4)}$$

in virtue of the anticommutation relations satisfied by the $\psi_\sigma(x)$. We also find

$$\rho(x)=\textstyle\sum_k\rho_k e^{i\mathbf{k}\cdot\mathbf{x}}, \quad \text{(A5)}$$

where, using (A2) and (A3),

$$\rho_K=\textstyle\sum_k c_{k\sigma}{}^*c_{k+K\sigma}. \quad \text{(A6)}$$

In terms of $c_{k\sigma}$ and ρ_K, our Hamiltonian (A1) becomes

$$H=\sum_k c_{k\sigma}{}^*c_{k\sigma}\frac{\hbar^2k^2}{2m}+2\pi e^2\sum_k\frac{\rho_k\rho_{-k}}{k^2}. \quad \text{(A7)}$$

[13] The additional terms describe correlations in particle positions.

[14] See, for instance, G. Wentzel, *Quantum Theory of Wave Fields* (Interscience Publishers, New York, 1949).

The second quantization formalism we are using here is of course equivalent to the use of an antisymmetrized many-electron wave function in the usual configuration-space representation (which we use elsewhere in this paper). For instance, the density fluctuation operator ρ_k is equivalent to the configuration space operator $\sum_i \exp(-i\mathbf{k}\cdot\mathbf{X}_i)$ we introduce earlier. Thus the results obtained in this appendix may be directly compared to those obtained in the previous sections of this paper, and in Paper II.

In Paper II, we saw that classically ρ_k could be split into an oscillatory part q_k, and an additional part which represented the charge density of a set of screened electrons moving at random. We shall now show that a similar q_k can be introduced quantum mechanically, and is proportional to

$$q_K=\sum_{k\sigma}\frac{c_{k\sigma}^*c_{k+K\sigma}}{\omega^2-(\hbar\mathbf{k}\cdot\mathbf{K}-\hbar^2K^2/2m)^2}. \tag{A8}$$

In the usual coordinate representation, this operator is

$$q_K=\sum_i\frac{1}{\omega^2-(\mathbf{K}\cdot\mathbf{P}_i/m-\hbar K^2/2m)^2}\exp(-i\mathbf{K}\cdot\mathbf{X}_i). \tag{A8a}$$

In the limit of $\hbar\to 0$, this reduces to the q_k of Paper II (Eq. 16).

As in Paper II, Eq. (17) we find it convenient to introduce the quantities $\xi_{K,\omega}$, which are, quantum mechanically

$$\xi_{K,\omega}=\sum_k\frac{c_{k\sigma}^*c_{k+K\sigma}}{\omega-(\hbar\mathbf{k}\cdot\mathbf{K}-\hbar K^2/2m)}, \tag{A9}$$

and are related to q_K by

$$q_K=(1/2)[(\xi_{K,\omega}-\xi_{K,-\omega})/\omega]. \tag{A10}$$

If the $\xi_{K,\omega}$ satisfy

$$\dot{\xi}_{K,\omega}+i\omega\xi_{K,\omega}=0, \tag{A11}$$

then it immediately follows on differentiation of (A10) that

$$\ddot{q}_K+\omega^2q_K=0.$$

We have $\dot{\xi}_{K,\omega}=(1/i\hbar)[\xi_{K,\omega},H]$. If we use the commutation properties [Eq. (A4)], we find that

$$\begin{aligned}\dot{\xi}_{K,\omega}+i\omega\xi_{K,\omega}=&\sum_{k\sigma}c_{k\sigma}^*c_{k+K\sigma}\\&+2\pi e^2\sum_{\alpha k\sigma}c_{k\sigma}^*\frac{c_{k+K-\alpha,\sigma}\rho_{-\alpha}}{\alpha^2}\left\{\frac{1}{\omega-\hbar\mathbf{k}\cdot\mathbf{K}+\hbar K^2/2m}\right.\\&\left.-\frac{1}{\omega-\hbar(\mathbf{k}-\boldsymbol{\alpha})\cdot\mathbf{K}+\hbar K^2/2m}\right\}+2\pi e^2\sum_{\alpha k\sigma}\\&\times\frac{\rho_\alpha c_{k\sigma}^*c_{k+K+\alpha,\sigma}}{\alpha^2}\frac{1}{\omega-\hbar\mathbf{k}\cdot\mathbf{K}+\hbar K^2/2m}\\&-\frac{1}{\omega-\hbar(\mathbf{k}+\boldsymbol{\alpha})\cdot\mathbf{K}+\hbar K^2/2m}.\end{aligned} \tag{A12}$$

We now split the sums over $\boldsymbol{\alpha}$ and $\mathbf{K}$ into two parts. In the second term on the right hand side of (A12), we see that those terms for which $\boldsymbol{\alpha}=\mathbf{K}$ give us a factor of n, the total number of particles, while the remaining terms, with $\alpha\neq K$ lead to nonlinear contributions, since there appear here effectively two factors, each of order ρ_K. It can be shown that the neglect of those terms for which $\alpha\neq K$ is equivalent to the "random phase approximation," as applied for instance in the neglect of U Eq. (15). Similarly, in the third term on the right-hand side of (A12) we find the terms for which $\boldsymbol{\alpha}=-\mathbf{K}$ give us a factor of n, while those with $\boldsymbol{\alpha}\neq-\mathbf{K}$ may be neglected in the random phase approximation.

With these approximations, we then obtain

$$\begin{aligned}&\xi_{K,\omega}+i\omega\xi_{K,\omega}\\&=\rho_K\left\{1-\sum_{k\sigma}\frac{4\pi e^2}{m}\frac{c_{k\sigma}^*c_{k\sigma}}{(\omega-\mathbf{k}\cdot\mathbf{K}\hbar)^2-\hbar^2K^4/4m}\right\}.\end{aligned} \tag{A13}$$

Thus we see that $\xi_{K,\omega}$ and hence q_K, oscillates harmonically provided ω satisfies the dispersion relation

$$1=\frac{4\pi e^2}{m}\sum_k{}'\frac{1}{(\omega-\hbar\mathbf{k}\cdot\mathbf{K})^2-\hbar^2K^4/4m^2}, \tag{A14}$$

where $\sum_k'$ here denotes the sum over all occupied electronic states. This dispersion relation is, however, identical with that we found in Sec. II Eq. (57). Thus we see that the same results can be obtained by solving for the operator equations of motion as can be obtained by the canonical transformation method.

However, a word of caution should be injected at this point. For if one naively diagonalizes the terms on the right-hand side on (A12), assuming the electrons occupy a Fermi distribution at $T=0$, one obtains additional "exchange" terms which apparently contribute to order k^2 in the dispersion relation (A14). This in turn introduces an apparent contradiction between the results herein obtained and the dispersion relation (57). The resolution of this contradiction lies in the fact that the electrons in consequence of the Coulomb interactions do not behave like a gas of free particles (as is tacitly assumed in diagonalizing A12), but rather exhibit long-range correlations in positions which act to reduce the long-wavelength density fluctuations. This reduction in the long-wavelength density fluctuations has the result that no "exchange" contributions to the dispersion relation appear up to order k^4. Physically this result follows from the fact that the long-range correlations act to keep the particles far apart, so that they have less chance to feel the effects of the exclusion principle. This result follows quite simply in our treatment in the body of this paper where we take into account the exclusion principle by antisymmetrizing the individual electronic wave functions. However, it is rather difficult to establish the equivalent result in the above second-quantization formalism, so we do not enter on this question farther here.

APPENDIX II

Tomonaga[5] has developed a very interesting one-dimensional treatment of the degenerate gas of Fermi particles in which the excitations are described in terms of a Bose field, and in which he obtains plasma oscillations for the degenerate electron gas. His method, however, appears to be intrinsically restricted to this one-dimensional case. It also involves the approximation that the wave function of the electron gas is not very different from that of a collection of free electrons with a Fermi distribution at absolute zero. In this appendix we shall exhibit the relationship between Tomonaga's methods and ours.

To do this let us first find the equation of motion of the operator ρ_K. We find it convenient to make the simple transformation[15]

$$\rho_K=\sum_k c_k^* c_{k+K}=\sum_k c_{k-K/2}^* c_{k+K/2}. \tag{A15}$$

The equations of motion of ρ_K may be obtained by commuting it with the Hamiltonian (A7). We find

$$\dot{\rho}_K=-i\sum_k (\hbar k\cdot K/m)c_{k-K/2}^* c_{k+K/2}, \tag{A16}$$

$$d^2\rho_K/dt^2=-\sum_k (\hbar k\cdot K/m)^2 c_{k-K/2}^* c_{k+K/2}-\omega_p^2\rho_K - \sum_{K'\neq K}\frac{(\mathbf{K}\cdot\mathbf{K}')}{(K')^2}\rho_{K'}\rho_{K-K'}. \tag{A17}$$

If we neglect the nonlinear terms on the right-hand side of the above equation, we see that ρ_K still does not quite oscillate harmonically. This is because of the term $-\sum_k(\hbar\mathbf{k}\cdot\mathbf{K}/m)^2 c_{k-K/2}^* C_{k+K/2}$, which is the quantum-analog of the term $\sum_i(\mathbf{k}\cdot\mathbf{V}_i)^2 e^{-i\mathbf{k}\cdot\mathbf{x}_i}$ appearing in Paper II, Eq. (9). As in the classical treatment, this term arises from the fact that we have a collection of different electrons, each moving with a different velocity and each therefore contributing differently to ρ_K. Hence, for the same reasons given in Paper II, it is necessary to seek the function q_K [given in (A8)] which oscillates harmonically in spite of the random motions of the individual electrons.

However in the *one-dimensional* case a considerable simplification is possible when the wave function is approximately that associated with a Fermi distribution of electrons at absolute zero. For in this case, either the operator $c_{k-K/2}^*$ or the operator $c_{k+K/2}$ will be zero except in a small region of width K at the top of the distribution. If K is small, then the term $(K\cdot k)^2 = K^2k^2$ can be approximated as $K^2k_0^2$, where k_0 is the wave vector of an electron at the top of the distribution. We then get

$$d^2\rho_K/dt^2=-(\hbar^2K^2k_0^2/m^2+\omega_p^2)\rho_K, \tag{A18}$$

and we see that ρ_K oscillates harmonically, which is the result of Tomonaga.

In the three-dimensional case, such a simplification is not possible. For the Fermi distribution is now spherical, and the factor $\mathbf{k}\cdot\mathbf{K}\cong k_0K\cos\vartheta$, where ϑ is the angle between $\mathbf{k}$ and $\mathbf{K}$ for the electrons at the top of the Fermi distribution. Thus the various terms $c_{k-K/2}^* \times c_{k+K/2}$ can no longer be given a common factor, and the simple result (A18) can no longer be obtained. The reason for this change may be given a simple physical interpretation. In a one-dimensional problem, the electrons at the top of the Fermi distribution have only one velocity, and therefore all electrons contribute approximately in unison to ρ_K. In the three-dimensional case, each electron contributes differently, so that the function ρ_K is altered in time, and a new function is introduced which cannot be expressed as a simple function of ρ_K.

It should also be noted that our criterion for the validity of the collective approximation is different from that of Tomonaga. For we require the smallness of $\alpha=\langle(\mathbf{k}\cdot\mathbf{P}_i/m\omega)^2\rangle_{\mathrm{Av}}$, while Tomonaga requires the smallness of $(\Delta W/\hbar\omega)$ where ΔW is the mean excitation energy of the electron distribution over the ground state Fermi energy.

Finally, we shall demonstrate explicitly the relationship between Tomonaga's variables and ours. From (A8), (A9), and (A10) we may write for our collective variables in the one-dimensional case:

$$q_K=\sum_k \frac{c_{k-K/2}^* c_{k+K/2}\omega_p^2}{\omega^2-(\hbar kK/m)^2}, \tag{A19}$$

$$p_K=\frac{i}{\omega(K)}\sum_k \frac{c_{k-K/2}^* c_{k+K/2}}{\omega^2-(\hbar kK/m)^2}(\hbar kK/2m\omega)\omega_p^2. \tag{A20}$$

Now Tomonaga breaks his sums over k into two parts, corresponding to positive and negative values of k. We shall do the same, noting that the only nonzero contributions are in a small region of width K near the top of the distribution. We get

$$q_K=q_K^+ + q_K^- = \left\{\frac{\omega_p^2}{2[\omega^2-(\hbar k_0K/m)^2]}\right\} \times\sum_{+k} c_{k-K/2}^* c_{k+K/2}+\sum_{-k} c_{k-K/2}^* c_{k+K/2},$$

$$p_K=p_K^+ + p_K^- = \left\{\frac{\omega_p^2 i}{2[\omega^2-(\hbar k_0K/m)^2]}\right\} \times\sum_{+k} c_{k-K/2}^* c_{k+K/2}+\sum_{-k} c_{k-K/2}^* c_{k+K/2}.$$

If we note from (A18) that $\omega^2-(\hbar k_0K/m)^2=\omega_p^2$, we then obtain for the operators

$$a_k=q_K-i\omega P_K=\sum_{+k} c_{k-K/2}^* c_{k+K/2},$$

$$a_k^*=q_K+i\omega P_K=\sum_{-k} c_{k-K/2}^* c_{k+K/2}.$$

These are just the Eqs. (2.5) of Tomonaga.

Thus, in the one-dimensional case, with Tomonaga's assumption of an approximate Fermi distribution of free electron momenta, we obtain the same results as Tomonaga.

[15] We here suppress the spin index, since this will play no role in what follows.

A Collective Description of Electron Interactions: IV. Electron Interaction in Metals

DAVID PINES
Department of Physics, University of Illinois, Urabna, Illinois
(Received May 21, 1953)

The effects of the Coulomb interaction between free electrons in an electron gas are considered for a variety of phenomena. The analysis is based on the collective description, which describes the long-range correlations in electronic positions (due to the Coulomb force) in terms of the collective oscillations of the system as a whole. It is shown that an independent electron model should provide a good description of the electrons in a metal in many cases of interest. The ground state energy of the free electron gas is determined, and an estimate of the correlation energy is obtained, with results in good agreement with those of Wigner. The exchange energy is shown to be greatly reduced by the long-range correlations, so that its effect on the level density and the specific heat is comparatively slight, leading to an electronic specific heat for Na which is approximately 80 percent of the free-electron value. The possible ferromagnetism of a free-electron gas is investigated, and it is found that the long-range Coulomb correlations are such that a free-electron gas will never become ferromagnetic (no matter how low the density). The excitation of the collective oscillations by a fast charged particle is studied, and the semiclassical results obtained by Bohm and Pines are verified by a quantum-mechanical calculation. The results are applied to the experiments of Ruthermann and Lang on the scattering of electrons by thin metallic films and to experiments on the stopping power of light metals for fast charged particles, with resulting good agreement between theory and experiment.

I.

IN the preceding paper,[1] a quantum-mechanical collective description of the electrons in a dense-electron gas has been developed. In this paper we wish to apply this collective description to the motion of the conduction electrons in metals. In so doing, we shall assume that the effect of the positive ions in the metal may be represented by a smeared out uniform background of positive charge. This assumption should be quite a good one for the alkali metals (in which the electronic wave functions are almost plane waves), and we may expect it to apply generally for any metallic phenomenon in which the periodicity of the lattice plays no important role. In assuming a uniform positive charge, we are also neglecting the ionic charge density fluctuations and so cannot consider the interaction of the electrons with the lattice vibrations. Actually, a collective description of the ionic motion is also possible and offers a promising approach to the treatment of problems in which the electron-lattice interaction plays an important role.[2,3]

We also assume that the only interactions of importance for the conduction electrons in a metal are those with the other conduction electrons. If this is not true, as might be the case if, for instance, the exchange interaction with the core electrons is large, then the collective description may well become inapplicable. For the validity of the collective description requires that the mean collision time for electron collisions which tend to disrupt the collective motion should be large compared to the period of a collective oscillation. This follows from the fact that the effect of these disruptive collisions is to cause damping of the collective oscillation, and the criterion,

$$\tau_{\text{coll}} \gg 2\pi/\omega_p, \tag{1}$$

is just the criterion that such damping be small.[4] If (1) is not valid then the damping is large, and the whole concept of collective oscillation loses its significance in a description of electron interaction.

The criterion (1) will be satisfied for a free-electron gas, since as was shown in Paper III, the only collisions which act to disrupt organized motion are via the short-range screened Coulomb force, and for an almost degenerate Fermi gas these lead to a collision time considerably larger than $2\pi/\omega_p$. This will also be the case for the collisions between the electrons and the lattice vibrations in metals, since the mean free time between such collisions is $\gtrsim 10^{-12}$ sec, which is long compared to the period of a collective oscillation. Whether the criterion (1) is satisfied for other disruptive effects requires detailed investigation for the metal in consideration, and we shall not enter on such questions here.

We first apply the collective description to a consideration of the widespread success of the independent electron model for the motion of electrons in metals. In this model, the motion of a given electron is assumed, in first approximation, to be independent of the motion of all the other electrons. The effect of the other electrons on this electron is then represented by a smeared-out potential, which can be determined by using the self-consistent field methods of Hartree and Fock. In this one-electron approximation, the correlations in the position and energy of the electrons due to their Coulomb interactions are treated as small perturbations, and often entirely neglected. It is rather puzzling that such an independent electron model should have been so successful qualitatively, and in many cases, quantitatively, since the Coulomb inter-

[1] D. Bohm and D. Pines, preceding paper [Phys. Rev. **92**, 609 (1953)]. This paper will hereafter be referred to as Paper III. The earlier papers in this series, hereafter referred to as I and II, respectively, are D. Bohm and D. Pines, Phys. Rev. **82**, 625 (1951) and D. Pines and D. Bohm, Phys. Rev. **85**, 338 (1952).

[2] D. Bohm and T. Staver, Phys. Rev. **84**, 836 (1951).

[3] T. Staver, Ph.D. thesis, Princeton University, 1952 (unpublished).

[4] D. Bohm and E. P. Gross, Phys. Rev. **75**, 1864 (1949).

action is a long-range interaction and might be expected to affect profoundly the electron motion in metals. In fact, as we have seen, it does bring about long-range correlations in the electron positions and so leads to organized oscillation of the electron system as a whole, a phenomenon which cannot be described in terms of an independent electron model.

The introduction of the collective description enables us to investigate in some detail just what physical phenomena are associated with the long-range aspects of the Coulomb force. We may sum up the mathematical results obtained in Paper III by writing down our Hamiltonian in the collective description. If we use Eqs. (59), (60), and (61) of III, we find

$$H = H_{\text{part}} + H_{\text{coll}} + H_{\text{s.r.}}, \tag{2}$$

where

$$H_{\text{part}} = \sum_i \frac{P_i^2}{2m}\left(1 - \frac{n'}{3n}\right) - 2\pi n e^2 \sum_{k<k_c} \frac{1}{k^2}, \tag{3}$$

$$H_{\text{coll}} = \sum_{k<k_c} (\hbar\omega/2)(A_k^* A_k + A_k A_k^*), \tag{4}$$

$$H_{\text{s.r.}} = 2\pi e^2 \sum_{\substack{i \neq j \\ k > k_c}} \frac{\exp[i\mathbf{k}\cdot(\mathbf{X}_i - \mathbf{X}_j)]}{k^2}. \tag{5}$$

We also have a set of subsidiary conditions on our electronic wave functions which are [Eq. (65), III]

$$\sum_i \frac{\omega^2}{\omega^2 - (\mathbf{k}\cdot\mathbf{P}_i/m - \hbar k^2/2m)^2} \exp(i\mathbf{k}\cdot\mathbf{X}_i)\Psi = 0. \tag{6}$$

The above Hamiltonian and subsidiary conditions are accurate to order

$$\alpha = (\mathbf{k}\cdot\mathbf{P}_i/m\omega)^2_{\text{Av}} \tag{7}$$

or $(n'/3n)$ with respect to the electronic kinetic energy and the zero-point energy of the collective oscillations. As we shall see, this constitutes quite an accurate approximation. We have also neglected $H_{\text{r.p.}}$ [Eq. (73), III] since as pointed out in III, it will produce negligible effects when compared with $H_{\text{s.r.}}$, and this latter term itself is small.

We see from (2)–(5) that the long-range part of the Coulomb interactions has been effectively redescribed in terms of the collective oscillations of the system as a whole. The frequency of these oscillations is, from [Eq. (67), III],

$$\omega = \omega_p\left(1 + \frac{k^2}{2nm^2}\sum_i \frac{P_i^2}{\omega_p^2} + \frac{\hbar^2 k^4}{8m^2\omega_p^2}\right). \tag{8}$$

It may easily be seen that the energy of a quantum of collective oscillation is so high (being greater than the energy of an electron at the top of the Fermi distribution) that these will not be excited in metals at ordinary temperatures, and hence may not be expected to play an important role in our description of a metal under ordinary conditions. (We discuss the excitation of these oscillations by an external fast charged particle in Sec. V.)

The remainder of our Hamiltonian corresponds to a collection of individual electrons interacting via a comparatively weak short-range force $H_{\text{s.r.}}$. These electrons differ from the usual "free" electrons in that they possess a slightly larger effective mass,

$$m^* = (m/[1 - (n'/3n)]), \tag{9}$$

and their wave functions are subject to a set of n' restrictions, as given by the subsidiary conditions (6). However, in the limit of small $n'/3n$, we may expect that both of these changes are unimportant qualitatively (and in some cases quantitatively). Furthermore, since the effective electron-electron interaction is so greatly reduced in our collective description, we should expect that it is quite a good approximation to neglect it for many applications. Thus we are led directly to the independent electron model for a metal.

The use of the collective description not only enables us to understand qualitatively the general success of the independent electron model, but it also enables us to clear up a number of quantitative difficulties arising from the application of this model to problems in which the electron-electron interaction is taken into account. We consider these questions in Sec. III.

II.

In this section we calculate, on the basis of the collective description, the ground-state energy for our free-electron gas. In so doing, we shall determine the maximum collective oscillation wave vector k_c (and hence the number of collective degrees of freedom n'), by minimizing the resultant energy with respect to this hitherto arbitrary parameter. We then apply our results to a consideration of the correlation energy correction to the calculation of the cohesive energies of the alkali metals.

Our wave equation for the ground state is

$$H\psi_0 = \epsilon_0\psi_0, \tag{10}$$

where ψ_0 and ϵ_0 are the ground-state eigenfunction and energy, respectively. We will also have a set of subsidiary conditions on our wave function,

$$\sum_i \frac{\omega^2 \exp(i\mathbf{k}\cdot\mathbf{X}_i)}{\omega^2 - (\mathbf{k}\cdot\mathbf{P}_i - \hbar k^2/2m)^2}\psi_0 - \psi_0 = 0 \quad (k<k_c) \tag{11}$$

but, as was emphasized in III, for the ground state the exact eigenfunction ψ_0 which satisfies (10) will automatically satisfy (11). Thus, we may concentrate on obtaining the best possible solution of our eigenvalue equation (10). In doing so, we may expect that an approximate ψ_0 will not satisfy the subsidiary conditions, but that any errors we make in determining the energy of the lowest state will not be increased by our failure to satisfy this subsidiary condition, since an

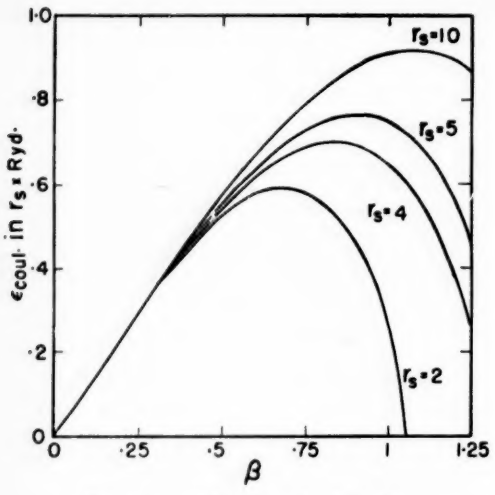

FIG. 1. ϵ_{Coul} *vs* β for several values of r_s.

exact solution satisfies it and leads to the lowest possible energy state.

We may obtain an approximate solution for ψ_0 by treating the comparatively weak short-range electron-electron interaction term $H_{s.r.}$ as a small perturbation in our expression for H, Eq. (2). In this case, we have as a first approximation,

$$\psi_0=\psi_0^{\text{osc}}\chi_0, \tag{12}$$

where ψ_0^{osc} represents a product of simple harmonic oscillator lowest-state wave functions, one for each collective oscillation wave-vector up to $k=k_c$, and χ_0 is the usual Slater determinant made up of the free-electron wave functions appropriate to the ground state of our system. The foregoing treatment may then be improved by taking into account the short-range correlations in electronic positions brought about by $H_{s.r.}$. We return to this question later.

In using the wave function (12), we are describing to a high degree of approximation the long-range correlations in electronic positions brought about by the Coulomb interactions. The great virtue of the collective description is that these quite complex correlations may be simply described in terms of the collective oscillations of the electron gas, and for the ground state of our system, are for the most part contained in ψ_0^{osc}. We note that if we attempted to express (12) in terms of our original "bare" electron coordinates $(\mathbf{x}_i\mathbf{p}_i)$, in a manner similar to that used in obtaining Eq. (23, III), we find that ψ_0 would be a complicated many-electron wave function, which would bear no simple resemblance to a determinant composed of single particle wave-functions and would not easily lend itself to a computation of the system energy.

Before evaluating the lowest-state energy ϵ_0, we find it convenient to re-express our Hamiltonian (2) by introducing the dimensionless parameter β, where

$$\beta=k_c/k_0. \tag{13}$$

We obtain

$$H=\sum_i P_i^2/2m(1-\beta^3/6)-(ne^2/\pi)\beta k_0 + \tfrac{1}{2}\sum_{k<\beta k_0}\hbar\omega(A_k^*A_k+A_kA_k^*) + 2\pi e^2\sum_{\substack{i\neq j\\ k>\beta k_0}}\frac{\exp[i\mathbf{k}\cdot(\mathbf{X}_i-\mathbf{X}_j)]}{k^2}. \tag{14}$$

If we now evaluate ϵ_0 using (14) and ψ_0 as given in (12), we find that the ground-state energy per electron is given by

$$\epsilon_0'=(\epsilon_0/n)=\epsilon_F+\epsilon_{\text{Coul}}+\epsilon_{\text{exch}}, \tag{15}$$

where

$$\epsilon_F=E_F(1-\beta^3/6)=\tfrac{3}{10}(\hbar^2k_0^2/m)(1-\beta^3/6), \tag{16}$$

$$\epsilon_{\text{Coul}}=-(e^2/\pi)\beta k_0+(n'/n)\left\langle\frac{\hbar\omega}{2}\right\rangle_{Av}, \tag{17}$$

$$\epsilon_{\text{exch}}=-2\pi e^2\sum_{\substack{k,\,k'<k_0\\ |\mathbf{k}-\mathbf{k}'|>\beta k_0}}\frac{1}{|\mathbf{k}-\mathbf{k}'|^2}. \tag{18}$$

In Eq. (15), ϵ_F represents the average Fermi energy, differing from the usual expression in that our electrons have the effective mass m^*. ϵ_{Coul} represents the difference in energy (per electron) between the zero-point energy of the collective oscillations $(n'/n)(\langle\hbar\omega\rangle_{Av}/2)$ and the usual self-energy of the charge distribution the oscillations here describe $-e^2/\pi\beta k_0$. It may be regarded as arising from the reduction in the long-range density fluctuations of the electron gas, as described, for instance, by Eq. (77, III). $\langle\omega\rangle_{Av}$ is the average frequency of collective oscillation, obtained by averaging our dispersion relation over all $k<k_c$. One finds, from (68, III) that

$$\langle\omega\rangle_{Av}=\omega_p(1+3\alpha[1+(3/10)\beta^2]). \tag{19}$$

In Fig. 1 we give a plot of ϵ_{Coul} (in units of $r_s\times$rydbergs) *vs* β for several values of

$$r_s=r_0/a_0=(3/4\pi)^{\frac{1}{3}}(me^2/\hbar^2), \tag{20}$$

the interelectron spacing measured in units of the Bohr radius.

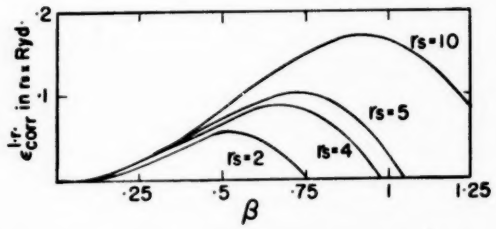

FIG. 2. $\epsilon_{\text{corr}}^{\text{l.r.}}(=-\epsilon_0'+E_F+E_{\text{exch}})$ *vs* β for several values of r_s.

ϵ_{exch} is the exchange energy arising from $H_{s.r.}$, the short-range electron interaction energy. The sums over $\mathbf{k}$ and $\mathbf{k}'$ in (18) are to be carried out for all electrons of parallel spin in the Fermi distribution (i.e., $k<k_0$, $k'<k_0$) such that $|\mathbf{k}'-\mathbf{k}|>\beta k_0$. This latter restriction arises from the short-range character of the interaction, as expressed by the restriction of k values in (5) to $k>\beta k_0$. We evaluate ϵ_{exch} in Appendix I, and there show that

$$\epsilon_{exch}=-(0.916/r_s)(1-(4/3)\beta+\beta^2/2-\beta^4/48) \text{ ry}. \quad (21)$$

The results of our calculation of the ground-state energy are given in Figs. 2 and 3. In Fig. 2 we plot ϵ_0' (actually $\epsilon_{corr}^{l.r.}=\epsilon_0'-E_{exch}-E_F$ [see Eq. (24)] as a function of β for various values of r_s. From this we may easily obtain β_{min}, that value of β for which the ground-state energy is a minimum. In Fig. 3 we plot β_{min} as a function of r_s.

On the basis of these calculations we see that for the electronic densities encountered in metals (r_s roughly between 2 and 5), β_{min} runs between 0.5 and 0.75. We may now verify the validity of our perturbation theory expansions in powers of α and $(n'/3n)$. In terms of β these are given by

$$\alpha\cong\beta^2/2r_s, \quad (22)$$

and

$$n'/3n=\beta^3/6. \quad (23)$$

We find from (22), and Fig. 4, that $\alpha\sim 1/16$ for $r_s=2$ and $\alpha\sim 1/20$ for $r_s=5$, so that expansions in powers of α should be quite accurate. Similarly, we find $(n'/3n)$ is $(1/48)$ for $r_s=2$ and $\sim(1/17)$ for $r_s=5$, so that it constitutes an equally valid expansion parameter.

The preceding results are conveniently analyzed by the introduction of the concept of the correlation energy of the free-electron gas. This energy may be defined as the difference between the energy calculated by means of suitable many-electron wave functions and the energy calculated in the Hartree-Fock one-electron approximation. The latter energy is[5]

$$E=E_F+E_{exch}, \quad (24)$$

TABLE I. Correlation energy in the free-electron gas model for the alkali metals.
Units: Rows (c), (d), and (e), r_s×ry;
Rows (f) and (g), kcal/mole.

Metal	Li	Na	K	Rb	Cs
(a) r_s	3.22	3.96	4.87	5.18	5.57
(b) β_{min}	0.63	0.68	0.73	0.75	0.77
(c) $\epsilon_{corr}^{l.r.}$	−0.076	−0.086	−0.100	−0.106	−0.112
(d) $\epsilon_{corr}^{s.r.}$	−0.164	−0.183	−0.206	−0.213	−0.221
(e) ϵ_{corr}	−0.240	−0.269	−0.308	−0.319	−0.333
(f) $\epsilon_{corr}\frac{\text{kcal}}{\text{mole}}$	23.3	21.1	19.5	19.1	18.6
(g) ϵ_{corr}(Wigner)	21.7	19.7	17.9	17.4	16.8

[5] F. Seitz, *The Modern Theory of Solids* (McGraw-Hill Book Company, Inc., New York, 1940), p. 341.

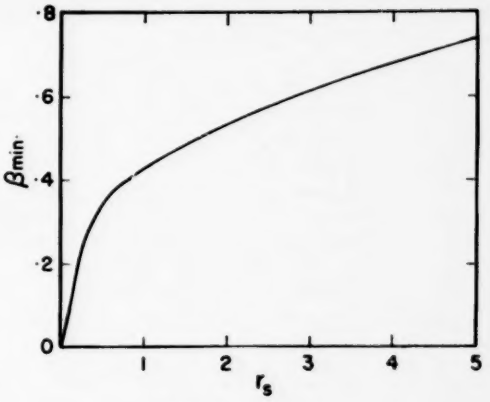

FIG. 3. β_{min} vs r_s.

where

$$E_F=\tfrac{3}{5}(\hbar^2k_0^2/2m)=(2.21/r_s^2) \text{ ry}. \quad (25)$$

and

$$E_{exch}=-(0.916/r_s) \text{ ry}. \quad (26)$$

The correlation energy for the free-electron gas was first calculated by Wigner,[6] who used a perturbation theory method in which the wave function of the electron of a given spin was assumed to depend on the positions of all the electrons of opposite spin. Wigner extended the results of his calculation, which was only valid for very high electronic densities ($r_s\lesssim 1$), to lower densities in such a way as to approach the correct value of the correlation energy for very low densities ($r_s\gg 1$). He obtained the result,

$$E_{corr}=-0.576/(r_s+5.1) \text{ ry}, \quad (27)$$

which he estimated to be accurate to within 20 percent.

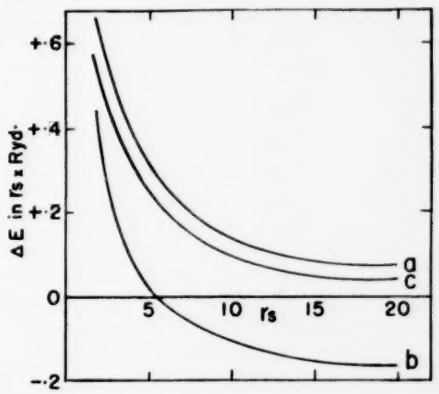

FIG. 4. Energy difference between ferromagnetic and nonferromagnetic states of free electron gas on three different models: (a) Simple theory ($E=E_F$); (b) Hartree-Fock theory ($E=E_F+E_{exch}$); (c) Hartree-Fock theory, with inclusion of long-range correlation effects.

[6] E. P. Wigner Phys. Rev. **46**, 1002 (1934).

We shall regard the correlation energy, when calculated in the collective description, as split into two parts, representing long-range and short-range effects. The long-range correlation energy is associated with the long-range correlations in the electronic positions which are essentially described by our introduction of the collective degrees of freedom. This is therefore given by the difference between the ground-state energy we calculated above and the expression (24). The short-range correlation energy then arises from the modification in electronic wave functions brought about by $H_{s.r.}$, an effect we consider below.

The long-range correlation energy is thus from (24) and (15),

$$\epsilon_{\text{corr}}^{l.r.} = -(\beta^3/6)E_F + \epsilon_{\text{Coul}} + [\epsilon_{\text{exch}} - E_{\text{exch}}]. \quad (28)$$

The first two terms in (28) are both negative and represent the energy gain arising from the long-range Coulombic correlations we have considered above. The third term is positive, and represents the difference between the effect of the exclusion principle in a gas of *interacting* electrons and in a gas of *free* electrons. In Table I we give the calculated values of $\epsilon_{\text{corr}}^{l.r.}$ for electron gases of the same density as those found in alkali metals.

We may understand the origin of the terms contributing to $\epsilon_{\text{corr}}^{l.r.}$ in the following way. In the collective description we consider *ab initio* the correlations brought about by the Coulomb interactions. We find that the electrons tend to stay out of one another's way, and that in fact these long-range Coulomb correlations are such that the effective electron interaction is given by $H_{s.r.}$. The energy gain from such Coulombic correlations is $\epsilon_{\text{Coul}} - (\beta^3/6)E_F$. We then put in the exclusion principle in the usual way and find an additional energy gain coming from the "accidental" correlations due to the exclusion principle in our gas of *interacting electrons*, which is ϵ_{exch}. On the other hand, E_{exch} represents the exchange energy for a gas of *free electrons*, in which Coulombic effects are otherwise neglected. The use of this term represents an overestimate of the role of the exclusion principle, since the long-range Coulomb forces tend to keep the electrons apart, and would do so even if the electrons had integral spin. In consequence the exclusion principle should properly play no role in such long-range correlations, and we see that this is properly accounted for by our correction to the exchange energy $(\epsilon_{\text{exch}} - E_{\text{exch}})$. Other effects associated with the different role of the exclusion principle in a gas of interacting electrons are considered in the following section.

The short-range electron-electron interaction term, $H_{s.r.}$ may be consistently treated as a perturbation in the Hamiltonian (2), since it is of such a short-range and weak strength that it does not affect the individual electronic motion appreciably. The short-range correlation energy may then be calculated according to perturbation-theoretic techniques. When this is done one finds that the short-range correlation energy is associated almost entirely with correlations between electrons of antiparallel spin, and it is this latter energy which we list in Table I. The details of this calculation, together with a more extensive investigation of correlation phenomena, will be published in the near future.

We have summarized the results of our correlation-energy calculations in Table I, where we give those values corresponding to the electron densities encountered in the alkali metals. It may be seen that our results are in quite close agreement with those of Wigner, an agreement which is well within the accuracy of the two methods. The major source of error in our calculation lies in our perturbation theoretic estimate of the effects of $H_{s.r.}$, and a rough estimate indicates that the use of perturbation theory, together with certain other approximations, may be responsible for errors of as much as 20 percent in $\epsilon_{\text{corr}}^{s.r.}$. Our expansion parameters α and $(n'/3n)$ are both quite small, so that the errors introduced by our neglect of higher-order terms in these parameters will be less than 10 percent of $\epsilon_{\text{corr}}^{l.r.}$. An order of magnitude estimate of the exchange energy associated with $H_{r.p.}$ (a term we neglected in comparison to $H_{s.r.}$) shows that this is less than $(0.01/r_s)$ ry for Na, so that the neglect of this term is justified within the accuracy of the present treatment. If we combine the above estimates, we are led to estimate the over-all accuracy of our calculated correlation energy as approximately 15 percent.

III.

In this section we consider briefly the result of including electron-electron interactions in a description of certain metallic phenomena. In general, the most simple form of the theory of metals, in which the electron-electron interactions are entirely neglected, has led to qualitative, and in many cases, quantitative agreement with experiment. If the electron-electron interactions are then included in the one-electron picture, the corrections to the simple theory arise from the exchange energy contributions to the phenomenon under consideration. These corrections, far from improving the agreement with experiment, tend to worsen it, both qualitatively and quantitatively. Wigner[7] suggested that correlations brought about by the Coulomb interactions may counteract the difficulties arising from these exchange contributions. We here wish to show that the long-range correlations we have considered in the collective description have just this property.

In the one-electron approximation, the exchange energy contribution to the Coulomb interaction energy of two electrons of wave vectors k_1 and k_2 is

$$W_{1,2} = -4\pi e^2/|\mathbf{k}_1 - \mathbf{k}_2|^2. \quad (29)$$

For a given electron, the total energy of interaction

[7] E. P. Wigner, Trans. Faraday Soc. **34**, 678 (1938).

with all the other electrons is then

$$W_i=\sum_{j\neq i}W_{i,j}=-\frac{e^2k_0}{2\pi}\left(2+\frac{k_0^2-k^2}{k_0k}\ln\frac{k+k_0}{k-k_0}\right), \quad (30)$$

if we assume the electrons form a completely degenerate gas. As a consequence of (30) the *E versus k* curve for a given electron becomes very steep as k approaches k_0, so that the density-in-energy of electron levels at low temperatures will be greatly reduced. Bardeen[8] and Wohlfarth[9] calculated the modification in the specific heat of a free-electron gas due to the inclusion of the exchange energy (30) and found that at low temperatures the specific heat should vary as $T/\ln T$. This result is in contradiction with the experimental results, which show a linear dependence on T—a result that follows from theory if exchange effects are entirely ignored. This large reduction in the density of electron energy levels might also be expected to affect profoundly other metallic phenomena which are sensitive to its magnitude, such as paramagnetism, conductivity, and the optical properties of metals; such an effect on these phenomena has also not been found experimentally.

The origin of these difficulties lies in the long-range of the Coulomb interaction which leads to a very large exchange energy for electrons of nearly equal momentum; this, in turn, is responsible for the undesirable behavior of (30). If we have, instead, an effective short-range, screened Coulomb interaction between the electrons, these large exchange energy contributions are greatly reduced, and the energy term corresponding to (30) takes a more satisfactory form.

Actually, a screened Coulomb interaction between electrons was proposed empirically by Landsberg,[10] who found it necessary to introduce such an effective interaction in order to obtain agreement between theory and experiment for the width of the tail of the soft x-ray emission spectrum of sodium. Wohlfarth[9] then showed that the effect of the exchange energy on the specific heat of the electron gas is greatly reduced, provided the electron-electron interaction potential is empirically taken as $(e^2/r_{ij})\exp[-(r_{ij}/\lambda)]$, with a screening radius λ of the order of 10^{-8} cm, the value introduced by Landsberg.

In the collective description, the exchange energy contribution to the Coulomb interaction energy of two electrons of wave vectors k_1 and k_2 arises from $H_{s.r.}$, and is given by

$$\begin{aligned} W_{1,2}&=-4\pi e^2/|\mathbf{k}_1-\mathbf{k}_2|^2, && (|\mathbf{k}_1-\mathbf{k}_2|>k_c);\\ W_{1,2}&=0, && (|\mathbf{k}_1-\mathbf{k}_2|<k_c). \end{aligned} \quad (31)$$

In Appendix I, we show that for a given electron of wave vector $\mathbf{k}$, the total energy of interaction with all the other electrons is

$$W_i=-\frac{e^2k_0}{2\pi}\left\{1+\frac{k_0^2-k^2}{kk_0}\ln\left(\frac{k+k_0}{\beta k_0}\right)+\frac{3k^2-k_0^2}{2kk_0}-2\beta+\frac{\beta^2k_0}{2k}\right\}, \quad (32a)$$

when $(k_0-k_c)<k<k_0$, and

$$W_i=-\frac{e^2k_0}{2\pi}\left\{2+\frac{k_0^2-k^2}{kk_0}\ln\left(\frac{k+k_0}{k_0-k}\right)-4\beta\right\}, \quad (32b)$$

when $k<(k_0-k_c)$. It may easily be verified that the *E versus k* curve given by (32) no longer displays singular behavior as k approaches k_0.

With the aid of (32), we may now obtain an estimate of the exchange-energy contributions to the electronic specific heat in metals. We are limited in the accuracy of our estimate, because in considering the specific heat we should properly take into account the effect of our subsidiary conditions (6) on the excited states of the electron gas. As was pointed out in Paper III, this effect is in the direction of reducing the effective number of degrees of freedom of the electron gas from $3n$ to $3n-n'$. Since, as we have seen, $(n'/3n)\ll 1$ for electrons in metals, we might expect that the neglect of the subsidiary conditions should be a reasonably good approximation, and it is this approximation we adopt in what follows.

We may obtain the influence of the exchange energy on the specific heat of the electron gas by considering its effect on the density of levels at the top of the Fermi distribution. Lidiard[11] has shown by the use of a variational Fermi-Dirac distribution function, that provided the free energy may be sensibly expanded in powers of (KT/E_0) near $T=0$ according to the method of Sommerfeld and Bethe,[12] the specific heat per electron may be written as

$$C_e=\frac{\pi^2K^2T}{3n}\left(\frac{dn}{d\epsilon}\right)_{\epsilon=E_0}, \quad (33)$$

where $(dn/d\epsilon)_{\epsilon=E_0}$ is the density of electronic levels at the top of the Fermi distribution, and K is Boltzmann's constant. We may write

$$\frac{dn}{n}=\frac{k^2}{\pi^2}\frac{3\pi^2}{k_0^3}dk=\frac{3k^2}{k_0^3}\frac{d\epsilon}{(d\epsilon/dk)}, \quad (34)$$

so that

$$C_e=\frac{\pi^2K^2T}{k_0}\frac{1}{(\partial\epsilon/\partial k)_{k=k_0}}. \quad (35)$$

Now, from (32) we find that near the top of the Fermi

[8] J. Bardeen, Phys. Rev. **50**, 1098 (1936).
[9] E. P. Wohlfarth, Phil. Mag. **41**, 534 (1950).
[10] P. T. Landsberg, Proc. Phys. Soc. (London) **A162**, 49 (1949).
[11] A. B. Lidiard, Phil. Mag. **42**, 1325 (1951) and private communication. We should like to thank Dr. Lidiard for communicating his results to us.
[12] A. Sommerfeld and H. Bethe, *Handbuch der Physik* (J. Springer, Berlin, 1934), Vol. 24, p. 12.

distribution ($k>k_c$),

$$\epsilon=\frac{\hbar^2k_0^2}{2m}-\frac{e^2k_0}{2\pi}\left\{1+\frac{k_0^2-k^2}{kk_0}\ln\left(\frac{k+k_0}{\beta k_0}\right)+\frac{3(k^2-k_0^2)}{2kk_0}-2\beta+\frac{\beta^2k_0}{2k}\right\}, \quad (36)$$

and hence

$$C_e=\frac{\pi^2K^2T}{2E_0}\frac{1}{1+\frac{me^2}{2\pi\hbar^2k_0}\left[2\ln\left(\frac{2}{\beta}\right)+\frac{\beta^2}{2}-2\right]}. \quad (37)$$

Thus the ratio of the above electronic specific heat to the usual electronic specific heat $C_0=(\pi^2K^2T/2E_0)$ is

$$\frac{C_e}{C_0}=\left[1+\frac{r_s}{12}\left\{2\ln\frac{2}{\beta}+\frac{\beta^2}{2}-2\right\}\right]^{-1}. \quad (38)$$

For Na, for which $r_s=4$ and $\beta=0.65$, we find

$$C_e/C_0=1/1.22=0.82. \quad (39)$$

Thus the effect of taking the exchange energy into account is to reduce the electronic specific heat to about 80 percent of its free electron value for Na. We note from (38) that our calculated reduction in the density of energy levels at the top of the Fermi distribution is now comparatively small, so that the influence of the exchange effects on other metallic phenomena may be expected to be correspondingly small. The experimental accuracy in the determination of electronic specific heats does not at present appear to be sufficiently great to check the validity of the above formulas.

There is probably a slight further reduction in the electronic specific heat arising from the effect of the subsidiary conditions in reducing the number of individual electronic degrees of freedom. In addition, we may expect the short-range correlations produced by $H_{s.r.}$ to affect the density of energy levels and the electronic specific heats. This effect will be considered in a later paper.

We may also use our results on the long-range correlation energy to investigate the possible ferromagnetism of a free electron gas. If the energy of an electron in the gas in the nonmagnetic state is given by the expression (24)

$$E=+E_F+E_{\text{exch}}=2.21/r_s^2-0.916/r_s,$$

then it is clear that for sufficiently large r_s, the electron gas should become ferromagnetic. For the cost in kinetic energy which results from lining the spins up (an increase in k_0 to $k_0\sqrt[3]{2}$) will eventually be more than compensated by the gain in the exchange energy. Thus the energy for the magnetic state is given by

$$E=3.52/r_s^2-1.156/r_s,$$

and one finds that electron gases for which $r_s>5.47$ should be ferromagnetic. This is not the case (e.g., Cs), and the reason that it is not lies in the Coulomb correlation energy, as Wigner[7] has pointed out. We will now show that the long-range correlation energy is actually sufficient to prevent the free-electron gas from becoming ferromagnetic.

Qualitatively it is easy to understand why this is so. We have seen that the Coulomb interaction keeps the electrons sufficiently far apart so that the exchange-energy attraction which acts to line up the electron spins is greatly reduced, even for $r_s\sim4$. Then as we go to higher r_s and lower electronic density, the screening cloud around each electron due to long-range correlations becomes even more efficient (corresponding to a higher value of β), so that the exchange energy is, in fact, further reduced, rather than having its relative strength increase. In Fig. 4 we give r_s times the energy difference between the ferromagnetic and nonferromagnetic states using our energy expression (15). This result has been obtained by calculating ϵ_0' as a function of β for both the nonmagnetic and ferromagnetic states, and choosing an optimum value of β (for which ϵ_0' is a minimum) in each case. For comparison we have plotted this energy difference as calculated using the simple theory, $E=E_F$, and using the Hartree-Fock approximation, $E=E_F+E_{\text{exch}}$. A result similar to this has been obtained by Wigner[7] on the basis of a somewhat different model for the free-electron gas.

The above results are subject to corrections arising from the effect of the subsidiary conditions (6) on our lowest-state wave function, since the lowest-state wave function is no longer nondegenerate and hence will no longer satisfy the subsidiary conditions automatically. However this should not alter our results appreciably, since the relative number of subsidiary conditions is small even for very low densities ($n'/3n\sim15$ percent for $r_s\sim10$), and since the subsidiary conditions involve only long-wavelength density fluctuations ($k<k_c$) while the exchange energy depends primarily on short-wavelength density fluctuations ($k>k_c$). Further corrections, which are in the direction of making ferromagnetism even less likely, will come from the short-range correlation energy. This follows from the fact that our energy $\epsilon_{\text{corr}}^{s.r.}$ will be absent in the magnetized state. We have not included these corrections here, because in the region of possible ferromagnetism ($r_s>5.47$), our perturbation theoretic estimates are beginning to become unreliable.

IV.

In the preceding sections we have considered the low-lying states of electrons in metals in the collective description. We have seen that at ordinary temperatures we should not expect the collective oscillations to be excited, since $\hbar\omega_p$ lies several electron volts higher than E_F for all metals, so that no electron in the metal will have sufficient energy to excite a collective oscillation. (Temperature excitation is clearly out of the question.) Thus, the only way that collective oscillations can be

excited in a metal is by bombardment of the metal with charged particles of sufficient energy to excite the oscillations. In this section, we will apply our canonical transformation to the investigation of the interaction of a charged particle with the electron gas.

This problem was treated classically in II by the density fluctuation method. There it was shown that a fast charged particle would excite collective oscillation, and the results for this excitation, together with some semiclassical arguments, were applied to the experiments of Ruthemann[13] and Lang[14] on the scattering of kilovolt electrons by thin metallic films. By so doing, excellent agreement was obtained between theory and experiment. The density fluctuation method has also been applied to a determination of the contribution of the conduction electrons in a metal to its stopping power for a fast charged particle.[15] In this section, we shall obtain the appropriate quantum-mechanical results and verify the validity of the results obtained by the semiclassical application of the density fluctuation method.[16]

Let us consider a charged particle of mass M, charge Ze, position and momentum $(\mathbf{r}_0, \mathbf{P}_0)$. We can describe its motion and interaction with our electron gas by adding the following terms to the original Hamiltonian of Paper III, Eq. (43, III):

$$\frac{P_0^2}{2M}+-4\pi Ze^2\sum_{ik}\frac{e^{i\mathbf{k}\cdot(\mathbf{x}_i-\mathbf{r}_0)}}{k^2}. \tag{40}$$

The effect of the canonical transformation to the collective description on these terms may then be obtained by using Eq. (51, III) and applying the random phase approximation and the dispersion relation [Eq. (57, III)] to the resulting terms. We find that the above terms then become

$$H_{\text{add}}=-4\pi Ze^2\sum_{ik>k_c}\frac{\exp[i\mathbf{k}\cdot(\mathbf{X}_i-\mathbf{r}_0)]}{k^2}$$
$$-Ze\sum_{k<k_c}\left(\frac{2\pi\hbar\omega}{k^2}\right)^{\frac{1}{2}}(A_{-k}+A_k^*)e^{-i\mathbf{k}\cdot\mathbf{r}_0}+\frac{P_0^2}{2m}$$
$$-4\pi Ze^2\sum_{ik<k_c}\frac{\exp[i\mathbf{k}\cdot(\mathbf{X}_i-\mathbf{r}_0)]}{k^2}. \tag{41}$$

The first term in H_{add} describes a short-range screened Coulomb interaction between the charged particle and the individual electrons in our electron gas. This interaction is of the same form as that found for the interaction between the individual electrons $H_{s.r.}$ [Eq. (5)]. The second term describes the interaction between the charged particle and the collective oscillations of the system and may lead to the excitation of collective oscillations by the particle. The last term in H_{add} will be the only term affected by the subsidiary conditions on our system wave function. We see that when (6) is applied, this term reduces to

$$-4\pi Ze^2\sum_{ik<k_c}\frac{(\mathbf{k}\cdot\mathbf{P}_i/m)-(\hbar k^2/2m)^2}{\omega^2-(\mathbf{k}\cdot\mathbf{P}_i/m-\hbar k^2/2m)^2}$$
$$\times\exp[i\mathbf{k}\cdot(\mathbf{X}_i-\mathbf{r}_0)], \tag{42}$$

which may be neglected in the approximation of small $(\mathbf{k}\cdot\mathbf{P}_i/m\omega)$.

Thus, we see that the use of our canonical transformation to the collective description provides us with a simple, natural splitup of the interaction between a charged particle and the electron gas into two parts: a short-range interaction with the individual electrons, and the interaction with the collective oscillations of the system as a whole (which has its origin in the long-range electron-electron and electron-particle interactions). This splitup is analogous to the splitup of the density fluctuations into individual particle and collective components, which was carried out in II.

Let us now consider the interaction between the charged particle and the collective oscillations. For this purpose, it is convenient to introduce the canonical collective variables, P_k and Q_k, defined by

$$Q_k=(\hbar/2\omega)^{\frac{1}{2}}(A_k-A_k^*),$$
$$P_k=i(\hbar\omega/2)^{\frac{1}{2}}(A_k^*+A_{-k}). \tag{43}$$

In terms of these variables, the collective interaction term in (4) becomes

$$iZe\sum_{k<k_c}(4\pi/k^2)^{\frac{1}{2}}P_ke^{-i\mathbf{k}\cdot\mathbf{r}_0}, \tag{44}$$

and

$$H_{\text{coll.}}=\tfrac{1}{2}\sum_{k<k_c}(P_k^2+\omega^2Q_k^2).$$

The equations of motion of our charged particle and the collective field are then given by

$$M\ddot{\mathbf{r}}_0=\mathbf{P}_0=-Ze\sum_{k<k_c}(4\pi)^{\frac{1}{2}}\boldsymbol{\epsilon}_kP_ke^{-i\mathbf{k}\cdot\mathbf{r}_0} \tag{45}$$

and

$$\ddot{P}_k+\omega^2P_k=+Zei\omega^2(4\pi/k^2)^{\frac{1}{2}}e^{+i\mathbf{k}\cdot\mathbf{r}_0}. \tag{46}$$

Equation (46) describes forced harmonic oscillation of the collective fields and is directly analogous to Eq. (47) of II. Because of the similarity between these equations, and because the latter equation was analyzed in some detail in II, we will merely quote the results of our solutions for (46) here.

We can obtain a straightforward solution of (46) provided the velocity of the charged particle $\mathbf{V}_0=\mathbf{P}_0/M$ may be taken as constant. (This will be a good approxi-

[13] G. Ruthemann, Ann. Phys. **2**, 113 (1948).
[14] W. Lang, Optik **3**, 233 (1948).
[15] D. Pines, Phys. Rev. **85**, 931 (1952). For earlier work on this subject, see references 18–21.
[16] D. Gabor [Phil. Mag. (to be published)], has obtained results in substantial agreement with ours by the use of a somewhat different method. We should like to thank Dr. Gabor for communicating his results to us prior to publication.

mation as long as the change in velocity of the charged particle during the period of oscillation is small compared to V_0, which will be true for all applications of interest to us here.) Then if $\mathbf{k}\cdot\mathbf{V}_0$ is not equal to ω, Eq. (46) has the steady-state solution

$$P_k=\left(\frac{4\pi}{k^2}\right)^{\frac{1}{2}}\frac{Ze i\omega^2}{\omega^2-(\mathbf{k}\cdot\mathbf{V}_0)^2}e^{i\mathbf{k}\cdot\mathbf{r}_0}. \tag{47}$$

This solution corresponds to the particle moving through the electron gas accompanied by a co-moving cloud of collective oscillation. This co-moving cloud leads only to a somewhat larger effective mass for the charged particle, which may be calculated by substituting (47) into (44).

The more physically interesting case occurs when $\mathbf{k}\cdot\mathbf{V}_0=\omega$. In this case the steady-state solution (47) is no longer appropriate, and the correct solution corresponds to resonant excitation of the collective oscillation. This oscillation, which was discussed in some detail in II, will take the form of a wake of collective oscillation trailing behind the particle, a phenomenon which resembles closely the Čerenkov radiation produced by fast electrons in passing through dielectric materials. We calculate the energy loss per unit length to the collective oscillations by obtaining the force due to the wake at the position of the particle, under the boundary condition that the energy loss occurs behind the charged particle. We find

$$\left(\frac{dT}{dX}\right)_{\text{coll}}=\frac{2\pi nZ^2e^4}{MV_0^2}\left\{\ln\left[\frac{\beta^2k_0^2(V_0^2-\langle V^2\rangle_{\text{Av}})}{\omega_p^2}\right]+\frac{\langle V^2\rangle_{\text{Av}}}{V_0^2}\beta^2k_0^2(V_0^2-\langle V^2\rangle_{\text{Av}})\right\}, \tag{48}$$

where $\langle V^2\rangle_{\text{Av}}$ is the mean-square velocity of the electrons in the metal, and we have used $k_c=\beta k_0$. This result differs slightly in two respects from that obtained in II [Eq. (59a, II)]. The logarithmic term is slightly altered because in obtaining (48) we have chosen as the maximum value of the collective oscillation wave vector perpendicular to V_0 a more accurate value than that used in II, *viz.* $[\beta^2k_0^2(1-\langle V^2\rangle_{\text{Av}}/V_0^2)-\omega_p^2/V_0^2]^{\frac{1}{2}}$. The appearance of the second term in the brackets (multiplying $2\pi nZ^2e^4/MV_0^2$) is due to the fact that in (48) we have ω^2 as a factor on the right-hand side of the equation, as compared to the factor ω_p^2 appearing in the similar position in the analogous equation of II. Both of these differences become negligible in the limit of $V_0^2\gg\langle V^2\rangle_{\text{Av}}$.

As pointed out in II, our picture of collective oscillations of the electrons in a metal and the excitation of collective oscillations by a fast charged particle finds experimental confirmation in the experiments of Ruthemann[12] and Lang[13] on the scattering of kilovolt electrons by thin metallic films. They found that for Be and Al the electrons lose energy in integral multiples of a well-defined basic quantum. Theoretically we should expect this quantum to be very nearly $\hbar\omega_p$, since as we saw in II, the long-wavelength quanta play a major role in the stopping power if V_0 is considerably greater the mean velocity of the metallic electrons, as is the case in these experiments. The experimental values of this quantum of energy loss are 14.7 ev for Al and 19.0 ev for Be, and these agree very well with our calculated $\hbar\omega_p$ (under the assumption that all the valence electrons are free) of 15.9 ev for Al and 18.8 ev for Be.

We may also calculate the mean free path for the emission of a quantum of collective oscillation. In the limit of $V_0^2\gg\langle V^2\rangle_{\text{Av}}$, this is

$$\lambda=\frac{\hbar\omega_p}{(dT/dx)_{\text{coll}}}=\frac{\hbar\omega_pMV_0^2}{4\pi nZ^2e^4\ln(\beta k_0V_0/\omega_p)}. \tag{49}$$

From the data given by Lang on the thickness of his Al films, one may obtain an experimental estimate for λ. This turns out to be somewhat less than 185A. The theoretical value of λ is, from (49), $\sim$160A (for the 7.6-kev electrons used by Lang) and is in good agreement with the above experimental estimate.

Lang and Ruthemann did not find a similar set of discrete energy losses in Ag, Cu, and Ni. This is probably due to the fact that the valence electrons in these metals are not sufficiently free (in the sense of Sec. IV) to take part in undamped collective motion. In the cases of Cu and Ag there is some evidence for a large exchange interaction with the core electrons, which is probably responsible for the damping of the collective oscillation.[17] Experiments have not yet been performed on the alkali metals, where we should expect to find collective oscillation and the appearance of discrete energy losses.

The interaction between the charged particle and the individual electrons in our electron gas, which is described by the term

$$-4\pi Ze^2\sum_{ik>k_c}(1/k^2)\exp[i\mathbf{k}\cdot(\mathbf{X}_i-\mathbf{r}_0)],$$

in our Hamiltonian (41), provides an alternate mechanism for the energy loss of the particle in traversing the gas. This term is not appreciably affected by our subsidiary condition (6), since the latter involves only long-wavelength density fluctuations ($k<k_c$). Thus the energy loss per unit length due to these individual electron collisions may be obtained by the usual methods of collision theory and is, in the nonrelativistic limit,

$$\left(\frac{dT}{dx}\right)_{\text{i.p.}}=\frac{4\pi nZ^2e^4}{MV_0^2}\ln\left(\frac{1}{b\beta k_0}\right) \tag{50}$$

[17] See reference 5. Recently P. Wolff [Bull. Am. Phys. Soc. **28**, No. 2, 35 (1953)] has used the Hartree approximation to investigate the effect of the binding of the electrons in the lattice on collective oscillation. He finds that this may account for the single line of rather considerable width found in these metals.

for collisions involving impact parameters greater than b. The appropriate choice of a minimum impact parameter depends on the details of the collision considered (through Z, M, and V_0), but in general the energy loss to the individual electrons is roughly comparable to that given up to the collective oscillations. The total energy loss per unit path length of the charged particle is the sum of (48) and (50) and is

$$\frac{dT}{dx}=\frac{4\pi nZ^2e^4}{MV_0^2}\left\{\left(\ln\frac{V_0}{\omega_p b}\left[1-\frac{\langle V^2\rangle_{Av}}{V_0^2}\right]^{\frac{1}{2}}\right)+\frac{\beta^2k_0^2\langle V^2\rangle_{Av}}{2\omega_p^2}\left(1-\frac{\langle V^2\rangle_{Av}}{V_0^2}\right)\right\}. \quad (51)$$

We see that, in the limit of $V_0^2\gg\langle V^2\rangle_{Av}$, this expression essentially is independent of our choice of screening parameter β.

It is of some interest to compare our description of the energy loss of a charged particle traversing a free-electron gas with those due to Kramers[18] and Bohr.[19] Both Kramers and Bohr take into account the effects of electron-electron interaction in determining this energy loss, and although their methods are rather different from ours, as we shall see their results are essentially equivalent to (51). Kramers[18] used a macroscopic description in which the electrons were treated as a continuum characterized by an effective dielectric constant. His method of treating the polarization effects associated with electron interaction is closely related to that used by Fermi in treating the analogous polarization effects for very fast particles interacting with bound electrons (the "density effect"). Bohr[19] has given a very interesting microscopic description of the collisions between the charged particle and the individual electrons (both free and bound) in which the influence of the electron-electron interactions is taken into account explicitly. Bohr has shown that the energy loss of a fast charged particle to a system of bound electrons may be considered to take place in two different modes. One mode corresponds to the Čerenkov radiation, which may be regarded as corresponding to the organized behavior of the system brought about by the electron-electron interaction. The other essentially corresponds to the interaction of the particle with the individual electrons, and displays no collective aspect. This microscopic separation of the mechanisms of energy loss of the charged particle to the bound electrons is directly analogous to that we have given above for the free-electron gas. We might add that, as is the case with the Čerenkov radiation for bound electrons, the energy given up by the particle to the collective oscillations does not constitute an additional source of energy loss from a microscopic viewpoint; for a collective oscillation is due to the cumulative contributions arising from the displacement of the individual electrons by the charged particle and represents the organized motion associated with these displacements.

A somewhat different method of treating this problem, which is in some respects similar to that used in the collective description, is due to Kronig and Korringa.[20] They have given a treatment by the methods of classical hydrodynamics in which the effects of electron-electron interactions are described in part in terms of an artificially introduced internal friction of the conduction electron fluid. Kronig[21] has suggested that this theory bears a relationship to that of Kramers which is similar to that obtaining between hydrodynamics and a kinetic theory of fluids.

For the free electron gas, both Kramers and Bohr find, in the nonrelativistic limit,

$$\frac{dT}{dx}=\frac{4\pi nZ^2e^4}{MV_0^2}\ln\left(\frac{V_0}{\omega_p b}\right). \quad (42)$$

Our expression (41) differs from (42) due to the fact that we have taken into account the dependence of the frequency of organized oscillation on the electron kinetic energy. This correction is rather small and may be neglected in the limit of high particle velocity $V_0^2\gg\langle V^2\rangle_{Av}$.

The total stopping power of a metal for a fast charged particle is the sum of that due to the conduction electrons and to the core electrons. Thus, in order to obtain experimental verification of our expression (41) as applied to the conduction electrons, we must consider metals in which the number of core and valence electrons is roughly comparable, e.g., Li and Be. Bohr has used the expression (42) together with the appropriate theoretical expression for the core electrons to obtain a theoretical average excitation potential of 45 ev for Li and 60 ev for Be. (The corresponding excitation potentials using (41) are 44 ev and 57 ev, respectively.) These values are in good agreement with the experimental values of Bakker and Segrè, who found excitation potentials of 34 ev for Li and 60 ev for Be, when one considers the fact that an experimental uncertainty of $\sim$10 percent in the stopping power for Li corresponds to an uncertainty in the Li excitation potential of $\sim$50 percent.[19]

The author wishes to thank Professor D. Bohm, Professor J. Bardeen, Professor J. Blatt, Professor F. Low, and Dr. A. B. Lidiard for stimulating discussions of subjects related to this paper. He would like to acknowledge the partial support of the Office of Ordnance Research, U. S. Army, during this work.

[18] H. A. Kramers, Physica **13**, 401 (1947).
[19] A. Bohr, Kgl. Danske Videnskab. Selskab, Mat.-fys. Medd. **24**, No. 19 (1948).
[20] R. Kronig and J. Korringa, Physica **10**, 406 (1943).
[21] R. Kronig, Physica **15**, 667 (1949).

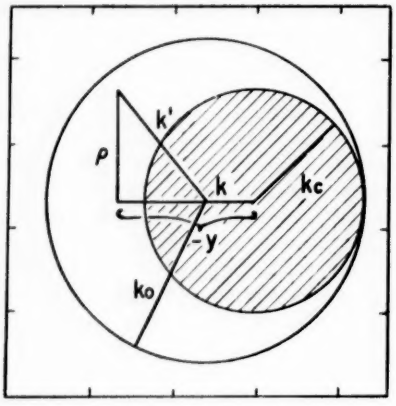

FIG. 5. Allowed regions for $\mathbf{k}'$ integration.

APPENDIX I

In this appendix we wish to evaluate ϵ_{exch} which may be written, according to (18), as

$$\epsilon_{\text{exch}}=-2\pi e^2 \sum_{\substack{k,\,k'<k_0 \\ |\mathbf{k}'-\mathbf{k}|>k_c}} \frac{1}{|\mathbf{k}'-\mathbf{k}|^2}, \tag{A1}$$

where the sum is to be carried out for all electrons of parallel spin in the Fermi distribution, such that $|\mathbf{k}'-\mathbf{k}|>k_c$, this latter restriction arising from the short-range character of the interaction $H_{s.r.}$. Let us first obtain the exchange energy of interaction with all the other electrons for a given electron of wave vector k. This is, on changing our sum over $\mathbf{k}'$ to an integral,

$$W_i=-\frac{4\pi e^2}{(2\pi)^3}\int d\mathbf{k}'\frac{1}{|\mathbf{k}'-\mathbf{k}|^2}, \tag{A2}$$

where the integration must be carried out in such a way as to exclude the shaded portion of the k_0 sphere (corresponding to $|\mathbf{k}'-\mathbf{k}|<k_c$) as illustrated in Fig. 5.

It is convenient to introduce for our $\mathbf{k}'$ coordinate system, cylindrical coordinates (ρ, y, φ) centered at k, as shown in Fig. 5, for we then find that

$$(\mathbf{k}'-\mathbf{k})^2=\rho^2+y^2. \tag{A3}$$

The requirement that $|\mathbf{k}'-\mathbf{k}|$ be greater than k_c then leads to the following regions of integration for our $\mathbf{k}'$ integration:

$k>k_0-k_c$

$$\int d\mathbf{k}'=\int_{-(k+k_0)}^{-k_c} dy\int_0^{[k_0^2-(y+k)^2]^{\frac{1}{2}}}\rho d\rho\int_0^{2\pi} d\varphi + \int_{-k_c}^{[k_0^2-k_c^2-k^2]/2k} dy\int_{[k_c^2-y^2]^{\frac{1}{2}}}^{[k_0^2-(y+k)^2]^{\frac{1}{2}}}\rho d\rho\int_0^{2\pi} d\varphi,$$

$k<k_0-k_c$

$$\int d\mathbf{k}'=\int_{-(k+k_0)}^{-k_c} dy\int_0^{[k_0^2-(y+k)^2]^{\frac{1}{2}}}\rho d\rho\int_0^{2\pi} d\varphi + \int_{-k_c}^{k_c} dy\int_{[k_c^2-y^2]^{\frac{1}{2}}}^{[k_0^2-(y+k)^2]^{\frac{1}{2}}}\rho d\rho\int_0^{2\pi} d\varphi + \int_{k_c}^{k_0-k} dy\int_0^{[k_0^2-(y+k)^2]^{\frac{1}{2}}}\rho d\rho\int_0^{2\pi} d\varphi.$$

The integrations for W_i are quite straightforward and yield for $k_0-k_c<k<k_0$

$$W_i=-\frac{e^2k_0}{2\pi}\left\{1+\frac{k_0^2-k^2}{kk_0}\ln\left(\frac{k+k_0}{\beta k_0}\right)+\frac{3k^2-k_0^2}{2kk_0}-2\beta+\frac{\beta^2k_0}{2k}\right\},$$

$k<(k_0-k_c)$

$$W_i=-\frac{e^2k_0}{2\pi}\left\{2+\frac{k_0^2-k^2}{kk_0}\ln\left(\frac{k+k_0}{k_0-k}\right)-4\beta\right\}.$$

We may then evaluate ϵ_{exch} by summing over all $\mathbf{k}$ within the Fermi distribution (and dividing by two so that no interactions are counted twice). We find

$$\epsilon_{\text{exch}}=\tfrac{1}{2}\sum_k W_i=\frac{1}{(2\pi)^3}\int d\mathbf{k}W_i$$

$$=-\frac{3e^2k_0n}{4\pi}\left\{1-\frac{4}{3}\beta+\frac{\beta^2}{2}+\frac{\beta^4}{48}\right\},$$

where $\beta=k_c/k_0$. The exchange energy per electron may then be written as

$$\epsilon_{\text{exch}}'=-\frac{0.916}{r_s}\left\{1-\frac{4}{3}\beta+\frac{\beta^2}{2}-\frac{\beta^4}{48}\right\}\text{ry}.$$

The Quenching of Mercury Resonance Radiation (2537A) by Nitrogen

C. G. MATLAND
Westinghouse Research Laboratories, East Pittsburgh, Pennsylvania
(Received July 20, 1953)

When a mercury atom in the resonance 6^3P_1 state collides with a nitrogen molecule, it may be transferred to the metastable 6^3P_0 state. The cross section for this reaction has been measured by a new method. Mercury vapor, in the presence of a known pressure of nitrogen gas, is excited by 2537A radiation. After the source of the excitation is cut off, the decay time of the imprisoned radiation is observed. The quenching collision cross section σ_Q is calculated from the measured decay time and the known value of the imprisonment time in the absence of the quenching gas. Measurements have been taken over the temperature range 325–525°K; σ_Q is found to increase from 5.0×10^{-17} cm² at the lower temperature to 1.0×10^{-16} cm² at the upper temperature.

I. INTRODUCTION

WHEN an atom in an excited state undergoes an optical transition to the ground state, the light emitted is called resonance radiation. If a beam of such light is incident on an enclosure containing normal atoms, the incident quanta may be absorbed by some of these atoms, exciting them to a resonance state. After the natural lifetime of the excited state, the quanta are re-emitted with the atoms returning to the ground state. If the density of the absorbing vapor is sufficiently high, the quanta may be repeatedly emitted and absorbed before finally escaping the enclosure; the resonance radiation is then said to be "imprisoned."[1]

In the event that certain foreign gases are present in the enclosure containing the absorbing vapor, a mechanism is available for the destruction of the resonance states. An excited atom may collide with a foreign gas molecule and transfer some or all of its energy to the latter. The excited atom is thereby reduced to a lower state of excitation while the foreign gas molecule may be raised to a higher vibrational state or in some cases may be completely dissociated. This collision process is referred to as a "quenching" collision since the resonance radiation is thus effectively "quenched."

An example of a quenching mechanism that may occur between excited mercury atoms and nitrogen molecules is given by the reaction[2]

$$Hg(6^3P_1)+N_2 \rightarrow Hg(6^3P_0)+N_2^*-0.07 \text{ ev}. \quad (1)$$

The nitrogen is thought to be excited to its first vibrational level which requires an additional energy of 0.070 ev. It has been shown by optical absorption experiments[3] that as a result of the collision the excited mercury atom is lowered to the metastable $^3P_0$ state.

An early investigation of the quenching of mercury resonance radiation was carried out by Zemansky in 1930.[4] In his experiment he observed the reduction (quenching) of scattered resonance radiation from a tube containing mercury vapor when a foreign gas was introduced to known pressures. By an extension of the existing theory of imprisonment,[5] he was able to derive a relationship between the amount of quenching and the collision frequency of the excited atoms. However, it has since been shown[1] that the early theory of imprisonment is incorrect. Hence the quenching cross sections obtained by Zemansky and other early workers[6,7] who used this theory to evaluate imprisonment effects are in error.

The recent theoretical work of Holstein[1,8] on the imprisonment of resonance radiation has been experimentally verified by Alpert, McCoubrey, and Holstein.[9] Therefore, it is now possible to make quenching measurements in which the imprisonment effects can be correctly evaluated. Furthermore, with the modern gas-handling techniques now available it is felt that gas impurities can be kept at a lower level than ever before. In the present paper we describe a new method with which measurements were obtained of the cross section for the quenching of the 2537A resonance radiation of mercury by nitrogen over the temperature range 325–525°K.

II. PRINCIPLE OF THE EXPERIMENT

Alpert, McCoubrey, and Holstein measured the decay time of imprisoned resonance radiation in the following way. They irradiated a sealed-off vessel (resonance tube) containing mercury vapor with the 2537A resonance line. At the time t_0 they turned off the incident light and observed the decay in intensity of the scattered light from the resonance tube. In the absence of quenching, the rate of decay of excited atoms is[1]

$$dn/dt=-n/T_i, \quad (2)$$

where n is the density of excited atoms, and T_i is the decay time for the imprisoned resonance radiation.

[1] T. Holstein, Phys. Rev. **72**, 1212 (1947).
[2] A. C. G. Mitchell and M. W. Zemansky, *Resonance Radiation and Excited Atoms* (Cambridge University Press, Cambridge, 1934), Chap. IV.
[3] Reference 2, pp. 250–252.
[4] M. W. Zemansky, Phys. Rev. **36**, 919 (1930).
[5] E. A. Milne, J. London Math. Soc. **1**, 1 (1926).
[6] E. W. Samson, Phys. Rev. **40**, 940 (1932).
[7] V. S. Duffendack and J. S. Owens, Phys. Rev. **46**, 417 (1934).
[8] T. Holstein, Phys. Rev. **83**, 1159 (1951).
[9] Alpert, McCoubrey and Holstein, Phys. Rev. **76**, 1257 (1949).

Equation (2) has the solution

$$n=n_0\exp(-t/T_i). \tag{3}$$

Experimentally one observes the intensity of the escaping radiation which, since it is proportional to dn/dt, has the same exponential variation as Eq. (3).

The present experiment is based on the fact that the introduction of known quantities of a foreign "quenching" gas into the resonance tube reduces the decay time of the imprisoned radiation by destroying resonance states. Another term must be added to Eq. (2) to account for this loss of excited atoms brought about by the quenching collisions. The rate of destruction of excited atoms is equal to the product of the density of the excited atoms and the quenching collision frequency $1/T_Q$. Under these circumstances Eq. (2) becomes

$$dn/dt=-n/T_i-n/T_Q, \tag{4}$$

which has the solution

$$n=n_0\exp[-(1/T_i+1/T_Q)t]. \tag{5}$$

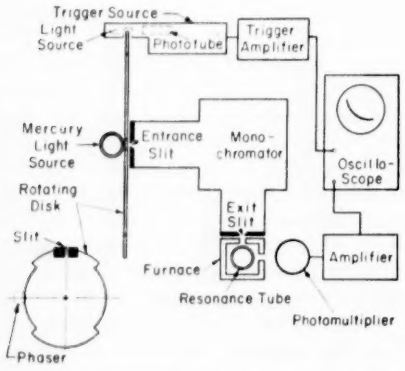

FIG. 1. Schematic diagram of apparatus.

The new decay time T is then given by the relation

$$1/T=1/T_i+1/T_Q. \tag{6}$$

From kinetic theory the expression for the quenching collision frequency is given by[10]

$$1/T_Q=N\sigma_Q\bar{v}, \tag{7}$$

where N is the density of the quenching gas, σ_Q is the cross section for the quenching collision process, and $\bar{v}$ is the mean relative speed.

The value of the imprisonment time in pure mercury is given by the experimentally verified relation[11]

$$T_i=\tfrac{5}{8}k_0R(\pi\ln k_0R)^{\frac{1}{2}}\tau, \tag{8}$$

where k_0 is the absorption coefficient at the center of the Doppler-broadened resonance line, R is the radius of the resonance tube, and τ the natural lifetime of the 6^3P_1 state of mercury. The presence of the nitrogen gas modifies T_i due to the pressure broadening of the mercury absorption line. This has the effect of reducing T_i according to the relation

$$1/T_i'\cong 1/T_i+\Delta\beta_p, \tag{9}$$

where T_i' is the imprisonment time corrected for pressure broadening. The quantity $\Delta\beta_p$ is given by[12]

$$\Delta\beta_p=0.5a_N\gamma_p/(\ln k_0R)^{\frac{1}{2}}, \tag{10}$$

where $a_N=\lambda_0/(4\pi v_0\tau)$, in which λ_0 is the wavelength of the radiation and v_0 the most probable speed. The factor γ_p is equal to twice the pressure-broadening collision frequency and is calculated using the broadening cross section measured by Zemansky.[13] Under our experimental conditions T_i is reduced approximately 10–20 percent by the addition of the nitrogen. From the corrected imprisonment time T_i' and the measured decay time T, the quenching cross section may be calculated from Eqs. (6) and (7).

III. APPARATUS

The apparatus for measuring resonance radiation decay times in the presence of a foreign gas is identical to that used by Alpert *et al.*[9] A schematic diagram of their apparatus is shown in Fig. 1. Light from a mercury discharge source is periodically interrupted by a disk rotating at about 10 000 rpm and directed into the resonance tube through a monochrometer which selects the 2537A line. The radiation escaping from the resonance tube is detected by the photomultiplier and amplified. The output of the amplifier is fed onto the vertical axis of the oscilloscope. The horizontal trace of the oscilloscope is initiated by the trigger source. Timing markers on the oscilloscope trace are obtained from a calibrated oscillator. The oven surrounding the resonance tube is composed of two independent sections so that the mercury vapor temperature and density can be controlled independently. The decay times are obtained from analysis of photographs of the decay trace taken at various vapor densities and temperature.

Temperature control of the ovens surrounding the resonance tube was obtained by operating them on a 110-volt ac regulated source. For every run the upper section of the oven was maintained at a higher temperature than the lower section to insure that no mercury condensed on the walls of the upper part of the resonance tube. A temperature constant within ± 0.1°C was maintained for a minimum period of fifteen minutes before any data for a given point was taken.

IV. PREPARATION OF RESONANCE TUBES

An important requirement for the measurement of quenching is the elimination of all contaminating gases.

[10] Earle H. Kennard, *Kinetic Theory of Gases* (McGraw-Hill Book Company, Inc., New York, 1938), p. 112.
[11] Holstein, Alpert, and McCoubrey, Phys. Rev. **85**, 985 (1952), Eq. (1).
[12] Reference 1, Eq. (5.15) and following text.
[13] Reference 2, Table XIX, p. 171.

The gas-handling techniques are therefore of paramount importance; hence, we describe in some detail the preparation of the resonance tubes used in our experiment.[14]

The nitrogen used in the present experiment was obtained from Air Reduction Company, Inc. and supplied with the following mass spectrographic analysis: argon, 2 parts in 10^5; neon, 6 parts in 10^5; all other gases not greater than 2 parts in 10^4. The mercury was chemically pure (99.98 percent) triply distilled mercury. This material was again triply distilled at 200°C in our own vacuum system. The pressure of noncondensible gases during the final distillation of the mercury into a glass break-off capsule was $\sim 10^{-8}$ mm Hg.

The resonance tubes are formed of Vycor[15] tubing 13 mm i.d., with 1-mm thick walls and an over-all length of 15 cm. The tubing is closed at one end and to the other end is joined a quartz-to-Pyrex transition seal for attachment to the Pyrex glass of the vacuum manifold. The tubes are sealed off in the softer glass to minimize the contaminating gases driven out of the glass.

A schematic diagram of the vacuum system used for the preparation of the resonance tubes is shown in Fig. 2. The three valves in the figure are of all metal construction.[14] The manometer shown is a null-reading balance type with a movable metal diaphragm that separates the clean side of the vacuum system from a liquid manometer.[16] Both the vacuum valves and manometer are designed to withstand high-temperature (400–500°C) bakeout.

The vacuum and gas handling procedure used in the preparation of the resonance tubes is as follows. The entire vacuum system is baked out for 12 hours at 400–450°C. After the bakeout both ion gauges are outgassed concurrently for two to four hours. When normal operating voltages are applied to the ion gauges, a pressure of $\sim 10^{-8}$ mm Hg is observed, and in a few minutes the ion gauges pump down the system to a pressure of 5×10^{-9} mm Hg or less. With the manifold isolated from all pumping action, one observes a typical rate of rise of pressure in the system of 2×10^{-10} mm Hg/min.

When filling at low pressures, the expansion volume of the system (see Fig. 2) is filled to the proper pressure, the mercury distilled into the resonance tube, the expansion valve opened, and the tube sealed off. By this method, mercury resonance tubes containing various nitrogen pressures were prepared.

V. ANALYSIS OF DATA

A typical photograph of the oscilloscope trace is shown in Fig. 3. The width of the decay trace is due to the large random fluctuations which occur because the intensity of the radiation being detected is very low. Some smoothing of these fluctuations is accomplished by making photographic exposures of 8- to 16-seconds duration. Under these circumstances the photographic record represents an average over several thousand separate decay traces. The positive prints made for data analysis are overexposed to facilitate the visual selection of the most dense area of the decay trace. Measurements are made from the most dense region between timing markers to the baseline. The results obtained from the trace of Fig. 3 are shown on Fig. 4.

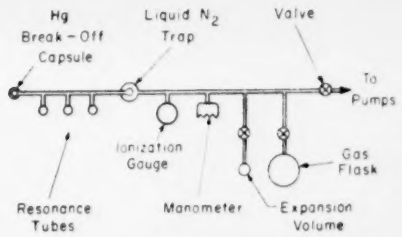

FIG. 2. Schematic diagram of the vacuum manifold used for the preparation of gas-filled resonance tubes.

In these measurements there is a small correction for background intensity which arises from the persistent band fluorescence of mercury molecules.[17] The correction is made by extrapolating the intensity at late times in the decay (due entirely to band fluorescence) back to early times when the resonance radiation predominates.

Since the mean free path for the mercury and nitrogen is small compared to the diameter of the resonance tube, the density in the upper portion of the tube is obtained by equating the pressures of the two temperature regions. The mercury vapor pressure as a function

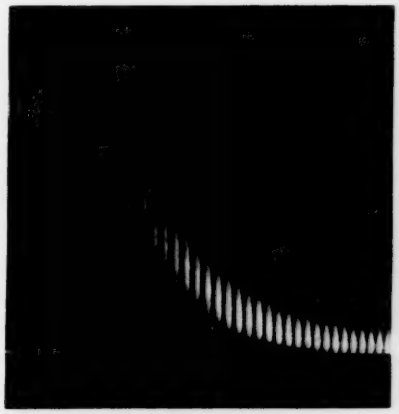

FIG. 3. Photograph of an oscilloscope trace for a nitrogen density of 2.4×10^{16} atoms/cc and a mercury vapor density of 5.7×10^{14} atoms/cc. The blanks in the trace have a 1μsec separation.

[14] For a fuller account of the vacuum techniques employed, see D. Alpert, J. Appl. Phys. **24**, 860 (1953).

[15] An ultraviolet transmitting glass obtained from Corning Glass Company, Corning, New York.

[16] Alpert, Matland, and McCoubrey, Rev. Sci. Instr. **22**, 370 (1951).

[17] A. O. McCoubrey, Phys. Rev. **84**, 1073 (1951).

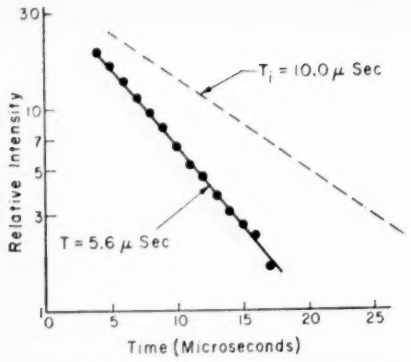

FIG. 4. Experimental results derived from the oscilloscope trace of Fig. 3. The dotted line represents the decay characteristic obtained in the absence of a quenching gas for the same mercury vapor density.

of temperature is taken from tables as given in Landolt-Bornstein.[18]

VI. DISCUSSION OF RESULTS

A plot of the measured quenching cross section *versus* the temperature is shown on Fig. 5. The quenching cross section σ_Q varies from 5.0×10^{-17} cm² at 325°K to 1.0×10^{-16} cm² at 525°K. The solid curve of the figure is obtained in the following way. As indicated in Eq. (1), if the nitrogen molecule is assumed to be excited to its first vibrational level, an energy of 0.07 ev must be supplied by the kinetic energy of the colliding particles. It is assumed that the cross section for the reaction is constant above this threshold energy. The observed cross section is then equal to this constant cross section times the fractional number of molecules with energies in excess of 0.07 ev. From kinetic theory the fraction of molecules with energies greater than ϵ is given by[19]

$$(1+\epsilon/k\theta)e^{-\epsilon/k\theta},$$

where k is the Boltzmann constant, and θ is the temperature of the upper portion of the resonance tube. With the assumption that this function determines the temperature variation of the cross section, a curve is plotted which is fitted to the data at the temperature 340°K. The curve so obtained is close to the best one which could be drawn through the data.

Direct comparison of the measured value of σ_Q with the experiment of Zemansky is not possible because of the temperature difference of the two experiments. He obtained a value of $\sigma_Q=8.5\times10^{-17}$ cm² at 298°K. Our extrapolated value is some 50 percent lower. In view of uncertainties in the earlier experiment and theory, it is thought the value obtained by Zemansky is in error. Other measurements of the quenching cross section are those of Sampson[6] giving $\sigma_Q=9.7\times10^{-17}$ cm² for $\theta=301$, 374, and 486°K, and the results (obtained by a similar method) of Duffendack and Owens[7] yielding $\sigma_Q=1.92$, 2.48, and 2.62×10^{-16} cm² at $\theta=473$, 673, and 873°K, respectively. In both the above experiments, the early theory was used to evaluate the effect of imprisonment. Furthermore, the pressure-broadening effect of the nitrogen was neglected even though the nitrogen pressure was as large as 100-mm Hg. Consequently, these results are also considered to be in doubt.

Although resonance tubes were prepared containing various nitrogen pressures, the measurements reported here are for $p(N_2)=0.74$-mm Hg only. At higher and lower nitrogen pressures, the measurements become difficult. At higher pressures the amplitude of the band fluorescence becomes quite large (as much as $\frac{1}{3}$ of the total amplitude), tending to obscure the resonance radiation decay. In addition, the shorter decay times encountered at higher pressures are more difficult to measure with accuracy. At low foreign gas pressures,

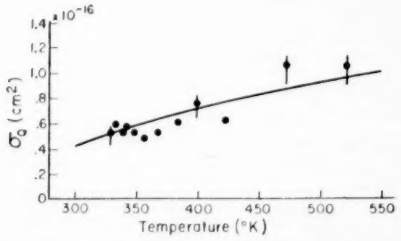

FIG. 5. The quenching cross section σ_Q *versus* temperature. The solid curve is obtained from theory and is fitted to the data at the temperature 340°C. The vertical lines on four data points indicate the variation of the estimated experimental error with temperature.

where T is nearly equal to T_i, the quenching effect becomes too small to measure accurately.

VII. CONCLUSIONS

When a mercury atom in the resonance 6^3P_1 state collides with a nitrogen molecule, it may be transferred to the metastable 6^3P_0 state. The cross section for this reaction has been obtained from measurements of the decay of resonance radiation following excitation of a resonance tube. The imprisonment effects are taken into account by use of a theoretical formula which has been experimentally verified. A correction has been included for the pressure broadening of the absorption line by the nitrogen gas.

The resonance tubes were prepared using improved vacuum and gas handling techniques. Consequently, it is felt that the impurity contaminations in these tubes is lower than has been achieved before, so that the experimental results may have greater significance than earlier measurements.

The method used for the measurements, while applied to studies of nitrogen, may be used for measuring the

[18] *Landolt-Bornstein Tables* (Verlag Julius Springer, Berlin, 1923), fifth edition, Vol. II, p. 1335.

[19] R. C. Tolman, *Statistical Mechanics with Application to Physics and Chemistry* (The Chemical Catalog Company, Inc., New York, 1927), pp. 67–70.

quenching cross section of such gases as CO, NO, H_2, or O_2. With these gases, the pressure broadening correction would be negligible since a measurable quenching effect is produced at much lower gas pressures. Moreover, for the gases H_2 and O_2 the difficulty arising from the presence of the band fluorescence would be very much reduced. In these cases the quenching processes do not produce metastable mercury atoms, which are the source of the band fluorescence.

The author wishes to express his thanks to M. A. Biondi, T. Holstein, and A. V. Phelps for many helpful discussions; to A. O. McCoubrey for his aid during the course of the experiment, and to D. Alpert for his active interest and advice.

PHYSICAL REVIEW VOLUME 92, NUMBER 3 NOVEMBER 1, 1953

Hyperfine Structures of Silver and Gold by the Atomic Beam Magnetic Resonance Method*

GÜNTER WESSEL† AND HIN LEW
Division of Physics, National Research Council, Ottawa, Canada
(Received July 24, 1953)

An ionizer of the electron bombardment type has been applied to a beam of atoms in a magnetic resonance apparatus. The ionization efficiency for potassium atoms has been found to be 1 part in 3000. The new ionizer has made it possible to study the hyperfine structures and the g factors of the ground states of silver and gold, two elements which cannot be detected by the surface ionization method commonly used heretofore. The measurements yield the following results:

$$|\Delta\nu(\mathrm{Ag}^{107})| = 1712.56 \pm 0.04 \text{ Mc/sec},$$
$$|\Delta\nu(\mathrm{Ag}^{109})| = 1976.94 \pm 0.04 \text{ Mc/sec},$$
$$g_J(\mathrm{Ag})/g_J(\mathrm{Cs}) = 0.99987 \pm 0.00010,$$
$$|\Delta\nu(\mathrm{Au}^{197})| = 6107.1 \pm 1.0 \text{ Mc/sec},$$
$$g_J(\mathrm{Au})/g_J(\mathrm{Cs}) = 1.00081 \pm 0.00005.$$

I. INTRODUCTION

A SERIOUS limitation to the scope of the molecular or atomic beam method of radio-frequency spectroscopy has been the difficulty of detecting the neutral atoms or molecules after they have passed through the various deflecting fields of the apparatus. Hitherto there have been two main types of detectors in use. They are the Pirani gauge, which can be used for gases only, and the surface ionization detector. The latter consists of a heated filament on which the atoms to be detected impinge. If the ionization potential of the atom is lower than the work function of the filament, or at most slightly higher, the atom has a high probability of being re-emitted as a positive ion. Thus far, aside from the halogens, only atoms with ionization potentials of 6 volts or less have been detected by this technique. In the case of the halogens,[1] negative ions are formed by electron attachment. Other detectors, as for example one which makes use of the radioactivity[2] of radioactive isotopes, are limited in their applicability to special groups of elements. In an attempt to make a detector that would be applicable to all atoms, we have constructed an ionizer which depends on electron bombardment. The design is based on an ion source developed by Heil[3] and applied to mass spectrometry by Paul.[4] Estimates from Paul's work indicated that the efficiency of such an ionizer should be sufficient even for the low intensities usually encountered in atomic beam work where the density of atoms in the beam may be less than that in the vacuum of the apparatus. Our experiments have confirmed these estimates. However, although the ionizer is probably capable of ionizing any atom or molecule, it cannot be claimed that all detection problems in the field of molecular beams have been overcome. Because of the relatively low efficiency (about 1 part in 3000) and because of the inevitable background resulting from the ionization of the residual gases in the vacuum, a strong source of atoms is required at the source end of the resonance apparatus. The source strength needed is such that the ionizer will probably be restricted to atoms which can be obtained in quantities of appreciable fractions of a gram. The exact amount, of course, will depend on the geometry of the apparatus and the complexity of the spectrum.

Tests of the electron bombardment ionizer have been made with the stable isotopes of silver and gold. These elements are particularly suited for the tests because they cannot be detected by the surface ionization

* First reported as an abstract in Bull. Am. Phys. Soc. **28**, No. 3, 52 (1953).
† National Research Laboratories Postdoctorate Fellow.
[1] Davis, Feld, Zabel, and Zacharias, Phys. Rev. **76**, 1076 (1949).
[2] E. H. Bellamy and K. F. Smith, Phil. Mag. **44**, 33 (1953).
[3] H. Heil, Z. Physik **120**, 212 (1943).
[4] W. Paul, Z. Physik **124**, 244 (1948).

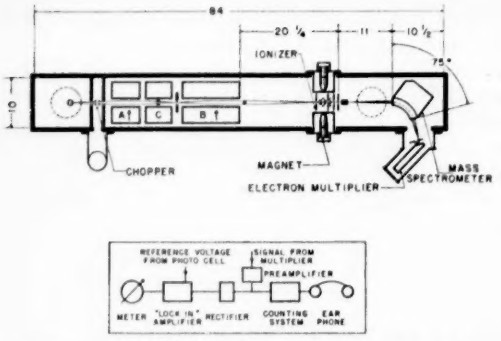

FIG. 1. The atomic beam apparatus (all dimensions in inches) and the amplification system for the electron multiplier signal.

method (ionization potentials 7.57 and 9.22 electron volts, respectively), they are readily available in sufficiently large quantities, and they are relatively easy to vaporize. Furthermore, their ground-state hyperfine structures are simple, consisting of only one interval ($\Delta\nu$) arising from the interaction of a nuclear moment with a $^2S_{\frac{1}{2}}$ electronic state. The $\Delta\nu$'s have, in fact, been determined optically to precisions of a few percent. Brix, Kopfermann, Martin, and Walcher[5] found for the silver isotopes,

$$\Delta\nu(\mathrm{Ag}^{107}) = -(57\pm2)10^{-3}\ \mathrm{cm}^{-1} = -(1710\pm60)\ \mathrm{Mc/sec},$$
$$\Delta\nu(\mathrm{Ag}^{109}) = -(66\pm2)10^{-3}\ \mathrm{cm}^{-1} = -(1980\pm60)\ \mathrm{Mc/sec}.$$

Kelly[6] found for gold

$$\Delta\nu(\mathrm{Au}^{197}) = 0.210\ \mathrm{cm}^{-1} = 6300\ \mathrm{Mc/sec},$$

with an estimated error of 6 percent. Using the Goudsmit-Fermi-Segrè relation, these authors calculated the magnetic dipole moments of the respective nuclei and found

$$\mu(\mathrm{Ag}^{107}) = -0.111\ \mathrm{n.m.},$$
$$\mu(\mathrm{Ag}^{109}) = -0.129\ \mathrm{n.m.},$$
$$\mu(\mathrm{Au}^{197}) = +0.136\ \mathrm{n.m.}$$

In addition to being suitable for tests of the ionizer, the silver isotopes are of interest from the point of view of the hyperfine structure anomaly.[7,8] For this relatively heavy pair of isotopes, it has been estimated that the anomaly may be of the order of 0.5 percent. A precise measurement of the $\Delta\nu$'s will permit a check of the theory when the nuclear g values are precisely known at some future time.‡

II. THE EXPERIMENTAL ARRANGEMENT

(a) The Atomic Beam Apparatus

The atomic beam apparatus in which the present experiments were carried out is shown diagrammatically in Fig. 1. Except for the ionizer and its associated components, this apparatus is identical with that used by Lew[9] in the study of praseodymium and already described in conjunction with that work. Associated with the electron bombardment ionizer are a rotating chopper, for interrupting the beam at 10 cycles per second (for reasons given below), and a mass spectrometer system that is behind the ionizer instead of being in front of it. The magnet for the mass spectrometer is a 75° sector with a 1.27-cm gap and a radius of curvature of 12.4 cm. The exciting winding consists of 40 turns of $\frac{3}{16}$-inch outside diameter copper tubing insulated with Teflon tape. The beam chopper consists of a vertical tube with four vertical slots cut in it equally spaced around the circumference. It is driven by an external motor through a shaft which enters the vacuum chamber through a Garlock "Klozure" seal.

The oven for the generation of beams of silver and gold differs from that used for praseodymium only in that graphite is substituted for molybdenum as the material for the heating jacket. A thoria crucible is used to contain the metal as before but is kept from

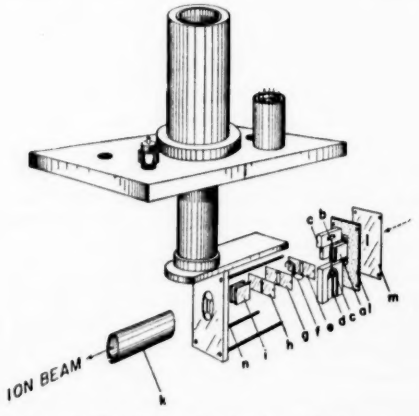

FIG. 2. The electron bombardment ionizer.

[5] Brix, Kopfermann, Martin, and Walcher, Z. Physik **130**, 88 (1951). The same lines had been measured previously in absorption by D. A. Jackson and H. Kuhn [Proc. Roy. Soc. (London) **A158**, 372 (1937)] and in emission by Crawford, Schawlow, Gray, and Kelly [Can. J. Research **A28**, 558 (1950)], but the assignment of the hfs components to the isotopes had been either uncertain or in error. It should be pointed out, however, that in the evaluation of the $\Delta\nu$'s, Brix, Kopfermann, Martin, and Walcher used the more precise measurements of Crawford, Schawlow, Gray, and Kelly with the proper assignment.

[6] F. M. Kelley, Proc. Phys. Soc. (London) **A65**, 250 (1952). See also earlier work by R. Ritschl [Naturwiss. **19**, 690 (1931)]; R. M. Elliot and J. Wulff [Phys. Rev. **55**, 170 (1939)]; and L. Sibaiya [Proc. Indian Acad. Sci. **2**, 313 (1935)].

[7] A. Bohr and V. F. Weisskopf, Phys. Rev. **77**, 94 (1950).

[8] A. Bohr, Phys. Rev. **81**, 331 (1951).

‡ *Note added in proof.*—Recent measurements by C. D. Jeffries and P. B. Sogo using the method of nuclear induction yielded the following results for the nuclear moments of silver: $\mu(\mathrm{Ag}^{107}) = -0.113024\pm0.000013$ n.m., $\mu(\mathrm{Ag}^{109}) = -0.129936\pm0.000013$ n.m. Combining these measurements with the present measurements of $\Delta\nu$ the hfs anomaly turns out to be $\Delta = -(0.416\pm0.008)$ percent. We are indebted to Dr. Jeffries and Dr. Sogo for informing us of their results prior to publication.

[9] H. Lew, Phys. Rev. **91**, 619 (1953).

direct contact with the graphite jacket by means of some tantalum foil.

(b) The Ionizer

Ionization of the atoms in the beam is accomplished by means of electrons oscillating back and forth transversely across the beam. The electrons are guided in their oscillations by a magnetic field of a few hundred gauss directed parallel to the oscillations. An exploded view of the device is shown in Fig. 2. The permanent magnet which supplies the guide field is not shown. The ionizer assembly is mounted on the end of a tubular liquid air trap which extends into the vacuum envelope of the apparatus and the seal is made vacuum tight by means of Apiezon "*Q*" wax. All electrical leads go through the plate.

Ionization of the atoms takes place in the chamber *a* through which the atomic beam passes. This chamber is a rectangular box which is open at both ends and which has a vertical slit in each of the broad faces. Tungsten filaments, measuring 0.005 cm×0.038 cm in cross section, are mounted opposite these slits. One of these filaments *b* is shown stretched between two stainless steel clamps *c*. The lower of these two clamps can slide up and down in a groove. A coil spring *d* attached to the lower clamp keeps the tungsten filament taut. All these parts are mounted on a fired lava piece *l*.

Electrons emitted by the heated tungsten filaments are accelerated into the chamber *a* to an energy of from 30 to 100 electron volts. The total current is usually between 3 and 15 milliamperes. The ions that are formed are pulled out of the ionization region by an electrode *e* and further accelerated by electrodes *g* and *h*. The potential of *e* relative to the chamber *a* is from 0 to 20 volts. The potential of the chamber *a* relative to *h*, which is necessarily at ground potential, depends on the mass of the ion and the strength of the magnetic field in the mass spectrometer magnet. For the silver isotopes it is usually around +1300 volts. The electrode *g* is at some intermediate potential adjusted experimentally for maximum ion intensity. The exit slit in *h* as well as the entrance slit in *m* measures 0.038 cm×1.27 cm. The electrostatic deflecting plates *i* permit the ion beam to be directed more accurately at the mass spectrometer magnet. The copper tube *k* is merely a shield between the ions and the stray fields of lead-in wires.

Located between the electrodes *e* and *g* and at the same potential as *e* is a tungsten grid *f* which can be heated electrically. Its purpose is to serve as a surface ionization detector for the alkalis. Although it intercepts only about 8 percent of the incident beam, its efficiency of ionization for alkali atoms which do strike it is so high (substantially 100 percent) that the net efficiency for alkalis is much higher than that of the electron bombardment ionizer. In fact, on ionizing a beam of potassium atoms first with the tungsten grid and then with electron bombardment ionizer and assuming that the tungsten grid is 100 percent efficient, we have estimated that the electron bombardment ionizer ionizes 1 out of every 3000 K^{39} atoms. In the present experiment, the tungsten grid is used mainly for the detection of the Cs atoms used in the calibration of the *C* field.

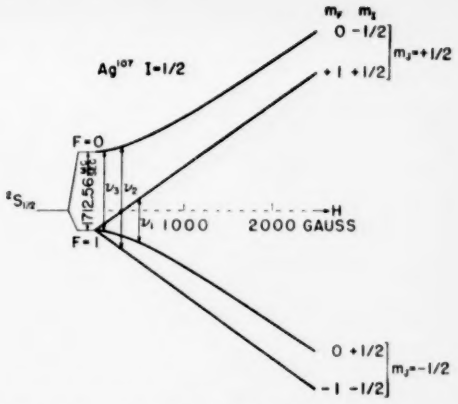

FIG. 3. Energy levels of Ag^{107} in the $5s\ ^2S_{\frac{1}{2}}$ state in an external magnetic field.

The entire ionizer assembly is easily demountable for such repairs as the replacement of the filaments. In operation the pole pieces of the external magnet supplying the guide field are adjusted for the best signal-to-noise ratio.

(c) The Electrical System

As shown in the lower part of Fig. 1 the signal from the electron multiplier may be fed either into a conventional counting system with aural monitoring or into a rectifier and a narrow-band 10 cycle/sec amplifier with the final indication given on a meter. The pulse counting system may be used when the background from the ionizer at the mass number under study is small compared with the desired signal. In this case it is not necessary to modulate the atomic beam. In most cases, however, despite the selectivity of the mass spectrometer, the background is so large that the 10-cps system is necessary to improve the signal-to-noise ratio. The background, being unmodulated, does not get through the amplification system. The improvement in signal-to-noise ratio may be as high as a hundred-fold. The narrow-band amplifier employed is of the "lock-in" type[10] which requires a reference signal of the same frequency as the signal under measurement and of constant phase relative to the latter. This reference signal is generated by a photoelectric cell actuated by a modulated light beam. The modulation is accomplished by a rotating disk with sectors cut out and driven by the same motor as that which drives the atomic beam chopper.

[10] Amplifier for Golay infrared detector, the Eppley Laboratory, Inc., Newport, Rhode Island.

TABLE I. Observed $\Delta F=\pm 1$ transitions in $Ag^{107,109}$.

(a) Field-dependent transition ν_1 and ν_2 in Ag (in Mc/sec).

Ag^{107}			Ag^{109}		
ν_1	ν_2	$\nu_2-\nu_1=-\Delta\nu$	ν_1	ν_2	$\nu_2-\nu_1=-\Delta\nu$
4.52	1717.06	1712.54	17.68	1995.01	1977.33
6.84	1719.41	1712.57	21.06	1998.00	1976.94
25.28	1738.05	1712.77	21.31	1998.31	1977.00
			22.83	1999.67	1976.84
			25.58	2002.38	1976.80
			46.38	2023.20	1976.82
			71.40	2048.44	1977.04
Average: 1712.6±0.1			Average: 1976.97±0.10		

(b) Field-independent transition ν_3 in Ag (in Mc/sec).

Ag^{107}			Ag^{109}		
ν_3	ν_1	$-\Delta\nu$	ν_3	ν_1	$-\Delta\nu$
1712.55	4.52	1712.53	1976.92	3.15	1976.91
1712.61	6.84	1712.56	1976.99	4.39	1976.97
1712.75	12.27	1712.57	1976.98	5.98	1976.95
1713.32	25.28	1712.57	1976.99	9.01	1976.91
			1977.03	9.30	1976.95
Average: 1712.56±0.04			Average: 1976.94±0.04		

The electronic instruments of the pulse counting system are of standard commercial manufacture. The frequency generating and measuring instruments are the same as those used by Lew.[9]

III. THE HYPERFINE STRUCTURE OF THE GROUND STATE OF SILVER

The two silver isotopes 107 and 109 both have nuclear spins of $\frac{1}{2}$ and negative magnetic dipole moments.[5] Their ground-state hyperfine structures consist of two levels $F=0$ and $F=1$ with the former lying higher. In the presence of a magnetic field, these levels split up in the manner shown in Fig. 3. Although the figure is drawn to scale for Ag^{107}, it holds very closely for Ag^{109} whose $\Delta\nu$ differs from that of Ag^{107} by only about 15 percent. In each of these isotopes, three transitions,

$$\nu_1(F=1,\ m_F=1\rightarrow F=1,\ m_F=0),$$

$$\nu_2(F=0,\ m_F=0\rightarrow F=1,\ m_F=-1),$$

and

$$\nu_3(F=0,\ m_F=0\rightarrow F=1,\ m_F=0),$$

are observable in the present atomic beam apparatus. The Breit-Rabi formula yields for these transitions the following expressions:

$$\begin{aligned}\nu_1&=g_I\mu_0H-\tfrac{1}{2}\Delta\nu\{(1+x^2)^{\frac{1}{2}}-1-x\},\\ \nu_2&=g_I\mu_0H-\tfrac{1}{2}\Delta\nu\{(1+x^2)^{\frac{1}{2}}+1-x\},\\ \nu_3&=-\Delta\nu(1+x^2)^{\frac{1}{2}},\end{aligned}\qquad(1)$$

where

$$x=(g_J-g_I)\mu_0H/\Delta\nu.\qquad(2)$$

It is to be noted that in these expressions, because of the inverted order of the hyperfine structure levels, $\Delta\nu$ is a negative quantity. At any given field strength H, a very simple relation exists between ν_1, ν_2, and $\Delta\nu$, namely,

$$\nu_2-\nu_1=-\Delta\nu.\qquad(3)$$

Hence by measuring the frequencies ν_1 and ν_2 at the same field H, the hyperfine structure interval may be obtained by simple subtraction. In Table I(a) are shown some measurements of these two transitions together with their differences. The differences agree to within 1 part in 10 000. The precision of this method of measurement is limited by the width of the lines due to the inhomogeneity of the C field and by the drift of the C field. The transition ν_3, however, is less subject to these limitations because at low fields it is, in first-order approximation, independent of field. Its narrower line and the small correction owing to a finite field permits a more accurate value of $\Delta\nu$ to be found. The small field correction is accomplished by measuring ν_1 at the same time as ν_3.

Measurements of ν_3[11] are shown in Table I(b). The $\Delta\nu$ obtained by means of ν_3 is seen to be more accurate than that obtained by means of ν_1 and ν_2. As final values for the hyperfine structure separations of the ground states of the silver isotopes, we find

$$\Delta\nu(Ag^{107})=-(1712.56\pm0.04)\text{ Mc/sec},$$

$$\Delta\nu(Ag^{109})=-(1976.94\pm0.04)\text{ Mc/sec},$$

where the sign, as previously mentioned, is taken from optical spectroscopy.

A comparison of ν_1 with the low-frequency line ($F=4,\ m_F=-3\rightarrow F=4,\ m_F=-4$) of Cs^{133} at the same field H yields the ratio $g_J(\text{Ag})/g_J(Cs^{133})$ of the g factors of the ground states of these elements. The low-frequency line of Cs is given by

$$\nu(\text{Cs})=g_I(\text{Cs})\mu_0H+\tfrac{1}{2}\Delta\nu(\text{Cs})\{(1-\tfrac{3}{2}x+x^2)^{\frac{1}{2}}-1+x\},\quad(4)$$

where x is defined by Eq. (2) with constants appropriate to Cs^{133}. In this expression and in that for ν_1 given in

TABLE II. $\Delta F=0$ transition in $Ag^{107,109}$, with "C" field calibration by Cs frequency.

Isotope	ν_1(Mc/sec)	ν(Cs) (Mc/sec)	$g_J(\text{Ag})/g_J(\text{Cs})$
Ag^{107}	575.470	125.685	0.99982
	575.575	125.658	1.00018
	575.800	125.708	1.00017
	848.822	180.761	0.99972
	848.939	180.761	0.99984
	849.066	180.800	0.99974
Ag^{109}	827.309	181.141	0.99989
	827.433	181.187	0.99980
	827.510	181.207	0.99977
	827.609	181.230	0.99978
	827.860	181.270	0.99982
		Average:	0.99987±0.00010

[11] The transition ν_3 requires an rf field which is parallel to the steady C field. In the present experiments, the rf loop is so oriented that the resulting rf magnetic field is mainly perpendicular to the C field with only a weak component parallel to the field. The observed ν_3 transitions are therefore much weaker than ν_1 or ν_2 but adequate for accurate measurements.

Eq. (1), the g_J's appear, of course, through the x's. Since the ratio of the g_J's cannot be obtained in explicit form from Eqs. (1) and (4), it is arrived at by successive approximations. Of the various terms appearing in these expressions, those involving the nuclear g factors g_I, of the respective atoms are of the order of a thousandth of the other terms. Hence, although the g_I of the silver isotopes are known only to 3 percent from optical spectroscopy,[12] the resulting uncertainty in the calculated g_J is less than the uncertainties in the measurements. The constants used in the calculation of g_J are, then, for Ag

$$g_I(\mathrm{Ag}^{107})=+0.000121, \quad g_I(\mathrm{Ag}^{109})=+0.000141;$$

and, for Cs (Lyons,[13] Kusch and Taub[14]),

$$\Delta\nu(\mathrm{Cs}^{133})=9192.632\pm0.002 \text{ Mc/sec},$$
$$g_I(\mathrm{Cs}^{133})=-0.0003991.$$

In Table II are shown the silver transitions ν_1 with the corresponding cesium transitions at the same field. The calculated ratio of the g_J's is shown in the last column. Within the accuracy of the measurements, this ratio is the same for the two isotopes. This is also to be expected on theoretical grounds. The average of all the measurements is

$$g_J(\mathrm{Ag})/g_J(\mathrm{Cs}^{133})=0.99987\pm0.00010.$$

From the work of various authors,[15] it has been found that the g_J of Cs is

$$g_J(\mathrm{Cs})=2(1.00125\pm0.00003).$$

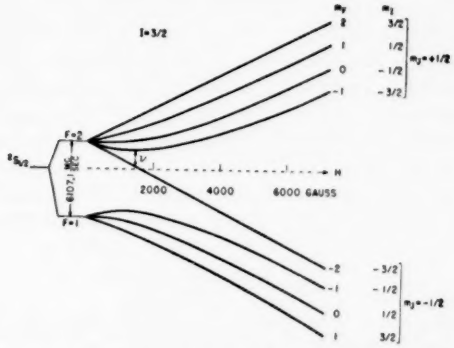

FIG. 4. Energy levels of Au^{197} in the $6s\ ^2S_{\frac{1}{2}}$ state in an external magnetic field.

[12] The uncertainty of 6 percent in the magnetic moments of silver stated by Brix, Kopfermann, Martin, and Walcher (reference 5) includes a 3 percent uncertainty in their $\Delta\nu$'s. The present work has shown, however, that the latter are accurate to better than 0.2 percent, and hence the only uncertainty in the magnetic moments arises from the application of the Goudsmit-Fermi-Segrè formula. This uncertainty has been estimated by the aforementioned authors to be at most 3 percent.

[13] H. Lyons, Ann. N. Y. Acad. Sci. **55**, 831 (1952).

[14] P. Kusch and H. Taub, Phys. Rev. **75**, 1477 (1949).

[15] The exact manner in which g_J(Cs) has been deduced is given in Brix, Eisinger, Lew, and Wessel (following paper), Phys. Rev. **92**, 647 (1953).

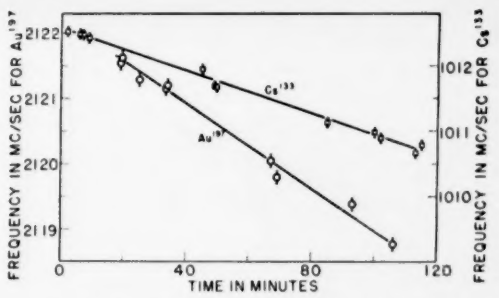

FIG. 5. Observed "low frequency" transitions in Au^{197} and Cs^{133} as function of time, "C" field drifting.

Hence,

$$g_J(\mathrm{Ag})=2(1.00112\pm0.00010).$$

To within the stated precision, this agrees with the anomalous gyromagnetic ratio of the free electron $[2(1.001146\pm0.000012)]$. The low precision of the measurements arises mainly from the width of the lines and the drift of the C field.

IV. THE HYPERFINE STRUCTURE OF THE GROUND STATE OF Au^{197}

With a nuclear spin $I=\frac{3}{2}$ and a $^2S_{\frac{1}{2}}$ electronic ground state, the hyperfine structure of Au^{197} in a magnetic field is as shown in Fig. 4. Only the low-frequency line ($F=2$, $m_F=-1\rightarrow F=2$, $m_F=-2$) has been measured in the present experiments and the zero-field separation $\Delta\nu$ calculated by means of the Breit-Rabi formula. A direct measurement of a transition between $F=2$ and $F=1$ was not done because oscillators in the region of 6000 Mc/sec were not on hand. The low-frequency line is given by the expression

$$\nu=g_I\mu_0 H+\tfrac{1}{2}\Delta\nu\{(1-x+x^2)^{\frac{1}{2}}-1+x\}, \qquad (5)$$

where x is defined by Eq. (2) with constants appropriate to Au. As in the case of silver, the optical value of g_I of gold may be used here. According to Kelly's[6] value of the nuclear magnetic dipole moment of gold, we have

$$g_I(\mathrm{Au})=-0.0000494.$$

Using the low-frequency transition of Cs^{133} [Eq. (4)] to eliminate H for any given value of H there remain two unknowns in Eq. (5), namely $\Delta\nu$ and $g_J(\mathrm{Au})/g_J(\mathrm{Cs})$. For any given measurement of ν, an arbitrary value may be assigned to either of these two unknowns and the other one calculated. However, since the relation between $\Delta\nu$ and the ratio of the g_J's varies with H, only for one pair of values, the correct pair, will the equation be satisfied for different magnetic fields.

When a series of measurements is taken over a period of several hours in the present experiments, no attempt is made to keep the C field constant, but it is allowed to drift. The time of making each observation is noted and the results plotted against a time scale. A typical run taken at a field of about 1705 gauss is shown in Fig. 5

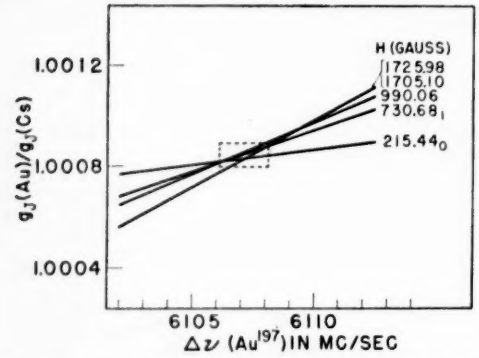

FIG. 6. g_J(Au)/g_J(Cs) as function of $\Delta\nu$(Au^{197}), evaluated from the Breit-Rabi formula using sets of observed values ν(Au) and ν(Cs) at various field strengths H.

where the gold transition frequencies are shown on the left and those of Cs on the right. Any pair of values corresponding to the same time may be used in Eq. (5) for the calculation of $\Delta\nu$ and g_J(Au)/g_J(Cs). Since one of these may be chosen of arbitrary value, and the other calculated, a range of reasonable values has been chosen for g_J(Au)/g_J(Cs) and the $\Delta\nu$ calculated. The pairs of values so obtained are plotted against each other in the manner shown in Fig. 6. The different straight lines correspond to measurements at different field settings. These should all intersect at one point. The dotted rectangle gives the estimated point of intersection and probable error. The values of $\Delta\nu$ and g_J(Au)/g_J(Cs) found are

$$\Delta\nu(\text{Au}) = 6107.1 \pm 1.0 \text{ Mc/sec},$$

$$g_J(\text{Au})/g_J(\text{Cs}) = 1.00081 \pm 0.00005.$$

If again we take g_J(Cs) = 2(1.00125), we get

$$g_J(\text{Au}) = 2(1.00206 \pm 0.00006).$$

This is larger than the gyromagnetic ratio of the free electron by 1 part in 10^3. It is of interest to note that a similar, though smaller, excess has been observed in the case of the $^2S_{\frac{1}{2}}$ ground states of Rb and Cs by Kusch and Taub.[14]

V. THE NUCLEAR MAGNETIC DIPOLE MOMENTS

The present measurements are not sufficiently accurate to permit the extraction of an accurate value of g_I directly from the Breit-Rabi formula and the observations. It is possible, however, to obtain approximate values of g_I from the observed hfs separation by means of the Goudsmit-Fermi-Segrè formula. This has been done for silver by Brix, Kopfermann, Martin, and Walcher[5] and for gold by Kelly,[6] with spectroscopic values of the hfs separations being used in both cases. In the case of silver, the present work has shown that the errors in the spectroscopic values of the hfs separations are less than 0.2 percent. Since this is much less than the uncertainties in the application of the Goudsmit-Fermi-Segrè formula, no change in the values of the nuclear moments of silver from the spectroscopic values is warranted. They remain as previously quoted

$$\mu(\text{Ag}^{107}) = -0.111 \text{ nm}, \quad \mu(\text{Ag}^{109}) = -0.129 \text{ nm}.$$

In the case of gold, however, the value of the hfs separation used by Kelly is 3.2 percent higher than our more accurate value. Adjusting his value of $\mu = 0.136$ n.m. to take this error into account, we find $\mu = 0.132$ n.m.

A large source of uncertainty in the application of the Goudsmit-Fermi-Segrè formula lies in the evaluation of the Fermi-Segrè factor $1 - d\sigma/dn$, where σ is the quantum defect and n the principal quantum number. It has been pointed out by von Siemens[16] that, for the $6s\ ^2S_{\frac{1}{2}}$ ground state of Au, the value of $1 - d\sigma/dn$ is sensitive to the assumed functional relationship between σ and the term value T. The relationship assumed by Kelly, following Crawford and Schawlow,[17] is $\sigma = \alpha + \beta T$, and the value found for the Fermi-Segrè factor is 1.424. Von Siemens, assuming $\sigma = \alpha_0 + \alpha_1 T + \alpha_2 T^2$, finds for this factor the value 1.481. With the present value of $\Delta\nu$, the calculated magnetic moment then becomes 0.127 n.m. Spectroscopic work[6,16] on the $5d^{10}7s\ ^2S_{\frac{1}{2}}$ and the $5d^9 6s^2\ ^2D_{\frac{5}{2}}$ states of Au yields values of 0.135 ± 0.003 and 0.14 ± 0.02 n.m., respectively, for the magnetic moment. For the $^2S_{\frac{1}{2}}$ terms, in addition to the uncertainty in $d\sigma/dn$, there exists an uncertainty in the Bohr-Weisskopf correction[7] which is much larger in the case of Au (about 10 percent) than in the case of Ag (about 1 percent). In view of these considerations, it is felt that the best value of the magnetic moment of Au that can be given at present is

$$\mu = 0.13 \pm 0.01 \text{ n.m.}$$

The authors wish to thank Dr. P. Brix and Dr. J. T. Eisinger for helpful discussions.

[16] W. von Siemens, dissertation, Göttingen, 1952 (unpublished).
[17] M. F. Crawford and A. L. Schawlow, Phys. Rev. **76**, 1310 (1949).

The Zeeman Effect of the Cr Ground State

P. Brix,* J. T. Eisinger, H. Lew, and G. Wessel*
Division of Physics, National Research Council, Ottawa, Canada
(Received July 24, 1953)

The linear Zeeman effect of the ground state of Cr^{52} has been studied using the atomic beam magnetic resonance method at magnetic fields up to 850 gauss. The Cr atoms were detected by means of an electron-bombardment type ionizer. Using the known g factors for the ground states of K^{39} and Cs^{133}, the g factor of the $^7S_3$ ground state of neutral Cr was determined to be $g_J=2(1.00081\pm0.00005)$.

INTRODUCTION

THE Zeeman effect of atomic hyperfine structure has been investigated for the ground and metastable states of various elements by the atomic beam magnetic resonance technique. Thus far, however, this technique has not been applied to the study of the Zeeman effect of a ground state without hyperfine structure. The reason for this is that those elements to which the familiar methods of detecting atomic beams are applicable either do show hyperfine structure ($I\neq0$) or have a $^1S_0$ ground state ($J=0$). The construction in this laboratory of an electron-bombardment type of ionizer[1] has increased the variety of elements that can be detected and made possible the study of elements with $I=0$ and $J\neq0$. Though a large amount of experimental material on the Zeeman effect of fine structure levels is available from optical investigations, there remains a need for precise data. As an example of the information that may be obtained by the atomic beam method along these lines, we have studied the ground state of Cr^{52}.

Chromium is of interest because its ground state is an S state of high multiplicity ($3d^54s\ ^7S_3$), and because it is a light element for which Russell-Saunders coupling is expected to hold. In the absence of perturbations, an S state should have a g factor close to the anomalous spin g factor of the electron[2] $g_s=2(1.001146\pm0.000012)$. It can be reasonably expected in the case of chromium that the terms mainly effective in perturbing the g factor originate from the six valence electrons and not from a breaking up of lower closed shells. Such perturbations can arise only from states with $J=3$ and even parity. All atomic levels with $J=3$ resulting from six electrons have Landé g factors which are not larger than 2. Landé g factors larger than 2 can come about only when, in the language of the vector model, the total spin angular momentum **S** and the total orbital angular momentum **L** are antiparallel, and when, in addition, **S** is larger than **L**. This cannot happen for $S\leq3$, $J=3$. An admixture of higher states to the ground state of Cr should, therefore, cause $g_J(\mathrm{Cr})$ to be less than g_s. Since the published optical value[3] $g_J(\mathrm{Cr})=2.007$ suggested that g_J exceeded g_s, it was thought worth while to obtain an accurate value for $g_J(\mathrm{Cr})$ by comparing it with the well-known g factors of the ground states of K^{39} and Cs^{133}.

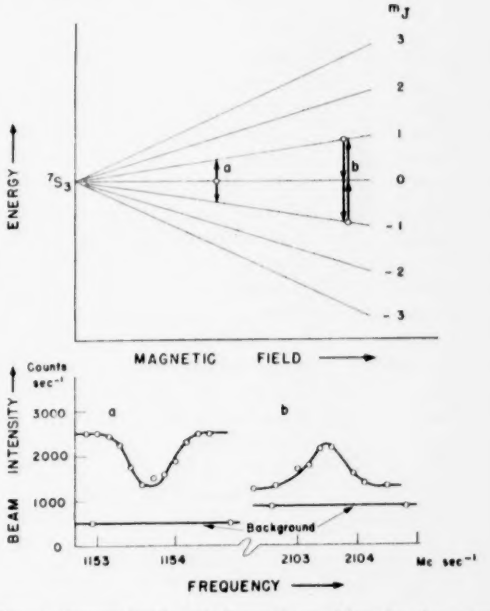

FIG. 1. Zeeman levels and observed transitions for the ground state of chromium. The upper part of the figure shows the energy levels as a function of an external magnetic field. The transitions referred to in the text as "flop-out" and "flop-in" are marked (a) and (b), respectively, in the figure and are set at arbitrary values of the abscissa. In the lower part of the figure the observed changes in beam intensity near the resonances are shown for two typical runs.

EXPERIMENTAL METHOD AND RESULTS

The atomic beam apparatus used in the present experiment has been described previously.[1,4] A beam of Cr atoms was produced by evaporating chromium powder from a thoria crucible inside a graphite oven at about 1500°C. It was found necessary to use oven

* National Research Laboratories Postdoctorate Fellow.
[1] G. Wessel and H. Lew, preceding paper [Phys. Rev. **92**, 641 (1953)].
[2] Koenig, Prodell, and Kusch, Phys. Rev. **88**, 191 (1952).
[3] *Atomic Energy Levels*, National Bureau Standards Circular 467 (U. S. Department of Commerce, Washington, D. C., 1952), Vol. II. No experimental error is quoted.
[4] H. Lew, Phys. Rev. **91**, 619 (1953).

TABLE I. Individual data for the run taken at $H=849$ gauss. The frequencies in ordinary type are averages of four individual settings, the decimal places printed in italics have been interpolated.

Time	Frequency (mc/sec) Cr	Cs	$\frac{g_J(\mathrm{Cr})}{g_J(\mathrm{Cs})}$
19.03	2378.44		
13	*0.32*	379.724	0.99952
31	2378.11	*0.681*	53
38	*0.04*	379.664	53
49	2377.94	*0.637*	55
59	*0.79*	379.613	53
20.07	2377.67	*0.582*	55
16	*0.61*	379.547	59
24	2377.56	*0.529*	61
28	*0.48*	379.520	60
33	2377.38	*0.510*	58
38	*0.35*	379.500	58
49	2377.30	*0.490*	58
21.03		379.478	
		Mean	0.99956 ±0.00005

slits of the order of 0.4 mm which is somewhat wider than the slit widths usually used. Narrower slits had a tendency to become clogged.

The Cr beam was detected by means of the universal ionizer described in the preceding paper.[1]

The upper part of Fig. 1 shows the energy levels of an atomic state with $J=3$, $I=0$ as a function of the magnetic field H. The atoms in the beam are distributed equally between the seven magnetic substates. The atoms in one of these ($m_J=0$) have zero magnetic moment and are therefore not affected by the inhomogeneous A and B fields of the apparatus. The remaining atoms of the beam have nonvanishing magnetic moments, and since the field gradients in the A and B fields are parallel in our arrangement, they will fail to reach the detector when the deflecting fields are on. A rough measurement of the ratio of beam intensities with the deflecting fields on and off gave $1:(7.0\pm0.2)$. The ratio remained unchanged when the B field alone was used.

An atom originally in the substate $m_J=0$ may undergo transitions to the states $m_J=\pm1$ in the C-field region when a radio-frequency field of the appropriate frequency is superimposed on the C field. With both deflecting fields on, these transitions manifest themselves by a decrease in beam intensity at the detector, and such "flop-out" transitions are readily observed with low rf power. By increasing the rf power and intercepting the undeflected atoms in the state $m_J=0$ by means of an obstacle wire, it was also possible to observe the double transitions $m_J=\pm1\rightarrow m_J=0\rightarrow m_J=\mp1$. Atoms undergoing such transitions are refocused on the detector after being deflected in opposite directions in the A and B fields, so that the beam intensity increases when such "flop-in" transitions are being induced. The two types of transitions have been schematically drawn at arbitrary fields in the upper part of Fig. 1. The lower part of the figure illustrates typical line widths, beam intensities, and ionizer backgrounds encountered in the present experiment.

The Cr resonance frequencies were compared with the transitions $\Delta F=0$, $m_F=-I-\frac{1}{2}\rightarrow m_F=-I+\frac{1}{2}$ of K^{39} or Cs^{133}. All frequency settings were made by listening to the intensity of the 10-cps signal from the detector without the use of the lock-in amplifier system described in reference.[1] A counting rate meter was used to obtain line shapes. Table I gives the results of the run taken at a field of 849 gauss. It will be noticed that H drifted slowly in the course of the run. The Cs frequency belonging to a given Cr frequency was obtained by linear interpolation between the two adjacent measured Cs frequencies and vice versa. The interpolated frequencies are shown in italics.

The Cr transition frequencies are given by $\nu(\mathrm{Cr})=g_J(\mathrm{Cr})\mu_0H/h$, where μ_0 is the Bohr magneton. The Breit-Rabi formula[5] gives the K and Cs frequencies as functions of μ_0H/h. By eliminating μ_0H/h, the ratios $g_J(\mathrm{Cr})/g_J(\mathrm{K})$ and $g_J(\mathrm{Cr})/g_J(\mathrm{Cs})$ can be evaluated. The following numerical data were used in this calculation:

K^{39}: $\Delta\nu=461.723$ Mc/sec,[6] $g_I/g_J=-0.0000708$.[6-8]

Cs^{133}: $\Delta\nu=9192.632$ Mc/sec,[9] $g_I/g_J=-0.0001993$.[6]

To check the linearity of the Zeeman effect of the state under study, observations were made at various values of H. These results are shown in Table II. Columns 1 and 2 give the magnetic field and Cr resonance frequency for each run. Since these values changed slightly in the course of a run, nominal values are quoted. The uncertainties given in column 5 were conservatively estimated from the scatter of individual evaluations for each run. In calculating $g_J(\mathrm{Cr})$ (column 6 of Table II) we used the values $g_J(\mathrm{K})$ and $g_J(\mathrm{Cs})$ listed in Table III. It can be seen that no variation in $g_J(\mathrm{Cr})$ with H is apparent. A weighted average was obtained by weighing the different runs according to

TABLE II. Measured ratios of g factors.

Nominal field (gauss)	Cr frequency mc/sec	$\frac{g_J(\mathrm{Cr})}{g_J(\mathrm{K})}$	$\frac{g_J(\mathrm{Cr})}{g_J(\mathrm{Cs})}$	Error 10^{-5}	$g_J(\mathrm{Cr})$	Weight
170	476[a]	0.99946		50	2(1.00060)	0
318	892	0.99947		20	2(1.00061)	1
412	1154	0.99963		12	2(1.00077)	2
458	1284		0.99966	30	2(1.00091)	1
582	1632		0.99974	15	2(1.00099)	1
751	2104[a]		0.99954	10	2(1.00079)	2
849	2378		0.99956	5	2(1.00081)	5
					Weighted mean	2(1.00081)

[a] Measured as "flop-in," all others as "flop-out."

[5] G. Breit and I. I. Rabi, Phys. Rev. **38**, 2072 (1931).
[6] P. Kusch and H. Taub, Phys. Rev. **75**, 1477 (1949).
[7] T. L. Collins, Phys. Rev. **80**, 103 (1950).
[8] Eisinger, Bederson, and Feld, Phys. Rev. **86**, 73 (1952).
[9] H. Lyons, Ann. N. Y. Acad. Sci. **55**, 831 (1952).

their errors. Essentially the same weights were obtained independently from a consideration of the line widths and rates of drift in the various runs. If we take into account the small uncertainties of $g_J(\mathrm{K})$ and $g_J(\mathrm{Cs})$ we obtain

$$g_J(\mathrm{Cr}) = 2(1.00081 \pm 0.00005).$$

DISCUSSION AND CONCLUSION

Our measurements show that the ground state of Cr is a much "better" S state than was indicated by the less accurate optical value for g_J. However, $g_J(\mathrm{Cr})$ does differ by approximately 3 parts in 10^4 from g_s, the pure electron spin g factor. This discrepancy can be due to several factors: (a) interaction terms in the radiative correction,[10,11] (b) nonradiative relativistic correction,[12] (c) diamagnetic correction,[13] and (d) perturbations due to higher states. The effects (a) and (b) have been calculated for some spectra with one or two[11] valence electrons and have been found to be much smaller than 3×10^{-4}. No calculations are available for Cr which has six valence electrons. The diamagnetic correction (c) is negligible[13] (-2×10^{-6} for Cr). The deviation of $g_J(\mathrm{Cr})$ from g_s that has been found is indeed in the direction to be expected from a perturbation (d), but no quantitative conclusions can be drawn until the corrections (a) and (b) are known.

[10] G. Breit, Phys. Rev. **39**, 616 (1932).
[11] W. Perl and V. Hughes, Phys. Rev. **89**, 886 (1953).
[12] G. Breit, Nature **122**, 649 (1928); H. Margenau, Phys. Rev. **57**, 383 (1940).
[13] W. E. Lamb, Phys. Rev. **60**, 817 (1941).

TABLE III. Experimental results used in the derivation of $g_J(\mathrm{K})$ and $g_J(\mathrm{Cs})$. The quantities designated A to E are experimental results obtained by various investigators. Values for $g_J(\mathrm{K})/g_I$ and $g_J(\mathrm{Cs})/g_I$ are derived from these in the manner shown in the last two rows. Throughout the text of the present paper, wherever the g_J's of K and Cs have been used, g_I has been set equal to 1, as is done in optical spectroscopy.

Symbol	Quantity	Value
A	$2g_I/g_p$	-657.475 ± 0.008[a]
B	$g_J(\mathrm{K})/g_p$	-658.2274 ± 0.0023[b]
C	$g_p/g_J(\mathrm{Cs})$	$-(15.1911 \pm 0.0003)\times10^4$[c]
D	$g_J(\mathrm{Cs})/g_J(\mathrm{Na})$	1.000134 ± 0.000007[d]
E	$g_J(\mathrm{Na})/g_J(\mathrm{K})$	1.00000 ± 0.00002[d]
$2B/A$	$g_J(\mathrm{K})/g_I$	$2(1.00114 \pm 0.00001)$
Av of $2/CA$ and $2BDE/A$	$g_J(\mathrm{Cs})/g_I$	$2(1.00125 \pm 0.00003)$

[a] J. H. Gardner and E. M. Purcell, Phys. Rev. **76**, 1262 (1949); J. H. Gardner, Phys. Rev. **83**, 996 (1951).
[b] P. Franken and S. Koenig, Phys. Rev. **88**, 199 (1952).
[c] H. Taub and P. Kusch, Phys. Rev. **75**, 1481 (1949).
[d] See reference 6.

Apart from these theoretical considerations, it should be mentioned that, with the accurately known g_J of the ground state, the Zeeman splittings of the resonance lines of Cr I (e.g., of the transitions $^7S_3 - {}^7P^\circ_{2,3,4}$ at 4290A, 4275A, and 4254A) are now very suitable for the calibration of magnetic fields in optical Zeeman spectroscopy.[14]

We are much indebted to Dr. G. Herzberg for helpful criticism.

[14] See, e.g., the pattern of λ4254A as reproduced in A. Sommerfeld, *Atombau und Spektrallinien* (F. Vieweg & Sohn, Braunschweig, 1931), fifth edition, Vol. I, p. 523.

PHYSICAL REVIEW VOLUME 92, NUMBER 3 NOVEMBER 1, 1953

The 7.68-Mev State in C^{12}

D. N. F. DUNBAR,* R. E. PIXLEY, W. A. WENZEL, AND W. WHALING
Kellogg Radiation Laboratory, California Institute of Technology, Pasadena, California
(Received July 21, 1953)

Magnetic analysis of the alpha-particle spectrum from $N^{14}(d,\alpha)C^{12}$ covering the excitation energy range from 4.4 to 9.2 Mev in C^{12} shows a level at 7.68 ± 0.03 Mev. At $E_d = 620$ kev, $\theta_{\mathrm{lab}} = 90°$, transitions to this state are only 6 percent of those to the level at 4.43 Mev.

SALPETER[1] and Öpic[2] have pointed out the importance of the $Be^8(\alpha,\gamma)C^{12}$ reaction in hot stars which have largely exhausted their central hydrogen. Hoyle[3] explains the original formation of elements heavier than helium by this process and concludes from the observed cosmic abundance ratios of $O^{16}:C^{12}:He^4$ that this reaction should have a resonance at 0.31 Mev or at 7.68 Mev in C^{12}.

An early measurement of the range of the alpha particles from $N^{14}(d,\alpha)C^{12}$ indicated a level in C^{12} at 7.62 Mev.[4] However, a recent magnetic analysis of this reaction failed to detect a transition to any level in this region of excitation,[5] nor did the level show up in the neutron spectrum[6] from $B^{11}(d,n)C^{12}$. From the

* On leave from the University of Melbourne, Melbourne, Australia.
[1] E. E. Salpeter, *Annual Review of Nuclear Science* (Annual Reviews, Inc., Stanford, 1953), Vol. 2, p. 41.
[2] E. J. Öpic, Proc. Roy. Irish Acad. **A54**, 49 (1952).
[3] F. Hoyle (private communication).
[4] M. G. Holloway and B. L. Moore, Phys. Rev. **58**, 847 (1940).
[5] R. Malm and W. W. Buechner, Phys. Rev. **81**, 519 (1951).
[6] W. M. Gibson, Proc. Phys. Soc. (London) **A62**, 586 (1949); V. R. Johnson, Phys. Rev. **86**, 302 (1952).

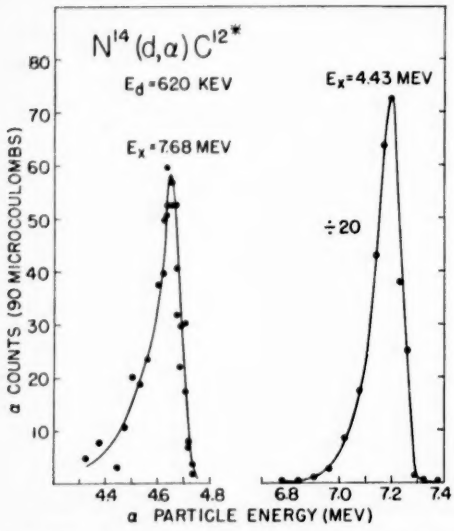

FIG. 1. Alpha spectrum from $N^{14}(d,\alpha)C^{12}$ obtained with a thick NH_3 target. No other groups were observed in the range $E_\alpha = 3.7 - 7.4$ Mev of magnitude 1 percent of the group to the 4.43-Mev state. The spectrometer was set at $\theta_{lab} = 90°$.

$Be^9(\alpha,n)C^{12}$ neutron spectrum there is evidence for a level near 7.5 Mev,[7] and inelastic proton scattering from carbon also gives a level at 7.5 ± 0.4 Mev.[8] Gamma rays accompanying the $Be^9(\alpha,n)C^{12}$ reaction have been interpreted as a cascade from a state at 7.59 ± 0.07 Mev; direct transitions to the ground state of C^{12} are not observed.[9]

We have determined the position of this level by observing the spectrum of alpha particles from the $N^{14}(d,\alpha)C^{12}$ reaction with a double-focusing magnetic spectrometer. Because of its large aperture of 0.007 steradian, this spectrometer is particularly suited to the measurement of very weak groups. A thick target of NH_3 frozen on a copper target cooled with liquid nitrogen was bombarded with 620-kev deuterons from the electrostatic generator. The energy spectrum of the alpha particles emitted at 90° is shown in Fig. 1. The higher energy group is from the transition to the state in C^{12} at 4.43 Mev. No other groups were observed between 7.4 and 3.7 Mev; a group 1 percent as strong as the transition to the 4.43-Mev level could have been detected.

[7] Guier, Bertini, and Roberts, Phys. Rev. **85**, 426 (1952).
[8] R. Britten, Princeton University Report, NYO-971, June 1951 (unpublished).
[9] Beghian, Halban, Husain, and Sanders, Phys. Rev. **90**, 1129 (1953).

Identification of this group as alpha particles was made by placing nuclear track plates in the focal plane of the spectrometer and measuring the range of these particles of known mv/e. To make certain that this weak group does not come from any likely contamination in the target, the measurements were repeated with targets of ice, carbon, and with the target warm. This group did not appear. It did appear with targets prepared from two different samples of ammonia, one of 99.98 percent purity according to the Mathiesson Company.

The energy of each group is taken to be that of the half-maximum point on the leading edge with an assigned uncertainity of ±one quarter of the full width of the rise. A more exact determination of the energy of these groups by fitting the curves to the theoretical thick-target spectrum shape is not worth while because of the poor statistical accuracy of the low-energy group. The energy scale was calibrated against the energy of the group to the 4.43-Mev state which was calculated from the MIT value[5] for the Q of this transition. The difference in energy of the two groups is 2.438 ± 0.025 Mev, and using the value[10] 4.431 ± 0.013 for the first-excited state, we find the energy of excitation in C^{12} to be 7.68 ± 0.03 Mev.

A limit can be set on the width of this state by an examination of the spectrum. The slope of the leading edge of the thick target spectrum is determined by the natural line width, the resolution of the spectrometer, and the energy spread $(dE_2/d\theta)\Delta\theta$ introduced by the finite aperture $\Delta\theta$. The results in Fig. 1 were taken with very low resolution, $E/\Delta E = 117$, in order to obtain the maximum counting rate for the weak group. With nuclear plates as detector it was possible to increase the resolution of the spectrometer so that it made a negligible contribution to the width of the leading edge. The width of the edge was then found to be 33 kev; the value calculated from $(dE_2/d\theta)$ and the observed width of the edge for the high-energy group is 31 kev. This discrepancy is well within the limits of our experimental accuracy, and we conclude that this state has a natural width not noticeably greater than the width of the 4.43-Mev state. A width of 25 kev could have been detected. Thus the decay into Be^8 and He^4 with an energy of 0.31 Mev is apparently slowed down by the penetration factor which is indeed expected to be small.

We are indebted to Professor Hoyle for pointing out to us the astrophysical significance of this level.

[10] F. Ajzenberg and T. Lauritsen, Revs. Modern Phys. **24**, 321 (1952).

The Reaction $C^{12}(\gamma,3p)Li^9$†

DARYL REAGAN
Department of Physics and W. W. Hansen Laboratories, Stanford University, Stanford, California
(Received July 3, 1953)

A carbon target was bombarded in a partially-converted 270-Mev electron beam. The 0.168-second Li^9 delayed neutron activity produced in the block was compared with the β activity produced in a polystyrene foil bombarded in the same beam. The measured integrated cross section for $C^{12}(\gamma,3p)Li^9$ is $(6.9\pm2)\times10^{-5}$ Mev barn.

THE integrated cross section for the reaction $C^{12}(\gamma,3p)Li^9$ has been measured to be $(6.9\pm2)\times10^{-5}$ Mev barn. The Li^9 was identified and measured by its characteristic delayed neutrons, which have an apparent half-life of 0.168 second.[1] They were counted in a water moderator $B^{10}F_3$ proportional counter system which partially enclosed the carbon target. The counts were separated in a 5-channel delay gate, each channel counting for 0.167 second. The system was calibrated with a radium beryllium source.

The carbon target, $3\frac{1}{2}$ inches in diameter by 7 inches long, was bombarded in the direct beam of the Stanford Mark III linear electron accelerator, operating near 270 Mev. A tungsten converter, 0.04 inch thick, was placed ahead of the target to convert the beam. The bombardment was monitored by counting the 20.5-minute C^{11} activity[2,3] produced in a 2.5-mil polystyrene foil sandwiched between the converter and the target. Marshall's value, 0.086 Mev barn, was used for the $C^{12}(\gamma,n)C^{11}$ integrated cross section.

In the bombardment, the beam was pulsed for 0.735 second, a 0.1-second pause allowed the short half-lived activities to die out, the delay gate counted for 0.833 second, and the cycle was repeated; the data here (Fig. 1) represent a 10-minute run. A previous experiment, done with a different neutron counting system and at 170-Mev electron beam energy gave a result equal, within probable error, to the one quoted.

In the earlier run, the background resulting from the substitution of copper for the carbon target was very small and exhibited no decay. In the later run, a large neutron count was noted when aluminum and sodium nitrate were substituted for the target. The activity had a measured half-life of about 4.2 seconds and has been attributed to N^{17} from the reactions $Al^{27}(\gamma;2\alpha,2p)N^{17}$ and $Na^{23}(\gamma;\alpha,2p)N^{17}$. The integrated cross section for the $Al^{27}(\gamma;2\alpha,2p)N^{17}$ reaction is estimated on this basis at roughly 5×10^{-4} Mev barn.

The background subtraction for the data presented has been chosen to give the best fit with the known half-life of Li^9. The integrated cross section quoted is an approximation, computed from

$$\left[\int\sigma(E)dE\right]_{Li^9}=\frac{I(C^{11})}{I(Li^9)}\frac{N(Li^9)}{N(C^{11})}\frac{D_f}{D_t}\left[\int\sigma(E)dE\right]_{C^{11}},$$

where $I(C^{11})$ is the photon intensity of the bremsstrahlung radiation at the center of gravity of the plot of $I(E)\sigma(E)$ *vs* energy for the reaction $C^{12}(\gamma,n)C^{11}$. $I(Li^9)$ is the equivalent intensity for the $C^{12}(\gamma,3p)Li^9$ reaction. $N(Li^9)$ and $N(C^{11})$ are the total numbers of Li^9 and C^{11} atoms produced, D_f and D_t are the densities in atoms of C^{12} per square centimeter, of the monitor foil and the target, respectively, and $[\int\sigma(E)dE]_{C^{11}}$ is the integrated cross section for the $C^{12}(\gamma,n)C^{11}$ reaction.

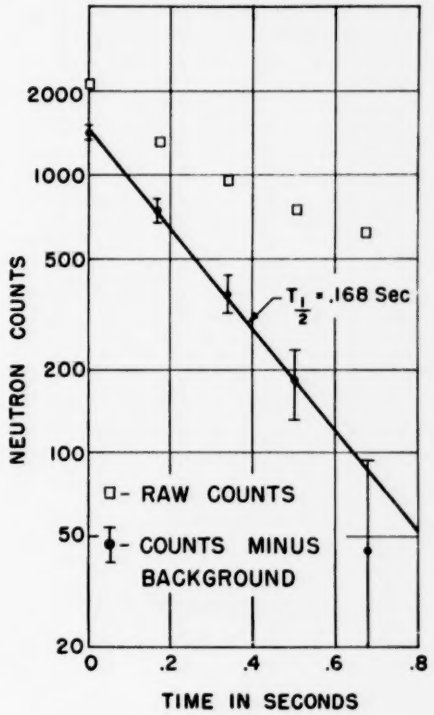

FIG. 1. Delayed neutron activity from carbon target as function of time.

† The research reported in this document was supported jointly by the U. S. Navy (Office of Naval Research) and the U. S. Atomic Energy Commission.

[1] Gardner, Knable, and Moyer, Phys. Rev. **83**, 1054 (1951).
[2] L. Marshall, Phys. Rev. **83**, 345 (1951).
[3] L. Katz and A. G. W. Cameron, Can. J. Phys. **29**, 518 (1951).

The intensity ratio is estimated using Heitler's[4] curves for the bremsstrahlung in the case of screening. The center of gravity of the C^{11} excitation curve, weighted by the Bethe-Heitler bremsstrahlung curve, is taken to be 24 Mev.[3] The corresponding point for Li^9 is estimated to be 62 Mev, making the intensity ratio 2.96:1.

It is a pleasure to give due thanks to W. K. H. Panofsky, who suggested the problem and gave invaluable encouragement and advice and identified the N^{17} decay. Thanks are also due Phyllis Hanson, George Masek, and Donald Hagerman, who provided 10^{14} electrons.

[4] W. Heitler, *Quantum Theory of Radiation* (Oxford University Press, London, 1944), p. 179.

PHYSICAL REVIEW VOLUME 92, NUMBER 3 NOVEMBER 1, 1953

Total Neutron Cross Section of Phosphorus*

K. F. Hansen, R. M. Kiehn, and Clark Goodman
Department of Physics and Laboratory for Nuclear Science, Massachusetts Institute of Technology, Cambridge, Massachusetts
(Received July 20, 1953)

The total cross section of phosphorus for neutrons has been measured in good geometry by the transmission method with a resolution of 2 kev. The energy range is from 125 kev to 850 kev, the neutrons being produced by the $Li^7(p,n)Be^7$ reaction. Red phosphorus contained in a thin steel cylinder was used as scatterer. The neutrons were detected by a hydrogen recoil counter. The neutron beam was monitored by a BF_3 long counter. The average cross section is 3 barns with an average level spacing of about 25 kev.

INTRODUCTION

SPOT measurements on the total cross section of phosphorus have been made at Argonne over an energy range of 0.024 to 0.83 Mev.[1] With a resolution of approximately 80 kev, Ricamo[2] found an average total cross section of 3 barns in an energy range from 2.0 to 3.5 Mev using a $D(d,n)$ reaction. Snowdon and Whitehead[3] have recently reported measurements from 100 to 700 kev with a resolution of 40 kev. However, this is insufficient to resolve even the major resonances.

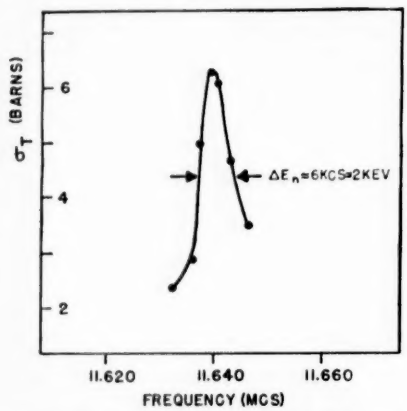

FIG. 1. Total cross section of sulfur near 588 kev. A target thickness of about 2 kev is estimated from the observed width of this resonance since the natural width $\Gamma_n \lesssim \sim 1$ kev. This target thickness agrees with that obtained from measurements of the geometric peak near the $Li(p,n)$ threshold. The scale of abscissas indicates the proton resonance frequency on the magnet control.

Preparation of Scatterer

Yellow phosphorus burns spontaneously in air and is extremely poisonous. Red phosphorus shows none of these characteristics at normal temperatures and pressures and was used throughout this experiment.

To avoid even the small corrections for scattering and absorption by containers, attempts were made to press red phosphorus into slugs of the desired size (length 2 inches, diameter 1 inch). Slugs were pressed up to 2000 psi but were found to be too soft for practical use. Rather than try higher pressures, the phosphorus was packed into a steel cylinder, 5 mils in wall thickness, and the necessary corrections made.

Neutron Source

Neutrons were obtained from the $Li^7(p,n)Be^7$ reaction using the Rockefeller electrostatic generator as the proton source.[4]

The energy resolution is primarily limited by the finite thickness of the lithium target. Measurements of this energy spread were accomplished by two methods: (a) the geometric peak of the neutron yield[5] in the

* This work was supported by the Bureau of Ships and the U. S. Office of Naval Research.
[1] Fields, Russell, Sachs, and Wattenberg, Phys. Rev. **71**, 508 (1947).
[2] R. Ricamo, Nuov cimento **8**, 383 (1951).
[3] S. C. Snowdon and W. D. Whitehead, Phys. Rev. **90**, 617 (1953).
[4] W. M. Preston and Clark Goodman, Phys. Rev. **82**, 316 (1951).
[5] Willard, Preston, and Goodman, U. S. Office of Naval Research Technical Report No. 45, Laboratory for Nuclear Science and Engineering, Massachusetts Institute of Technology, September 27, 1950 (unpublished).

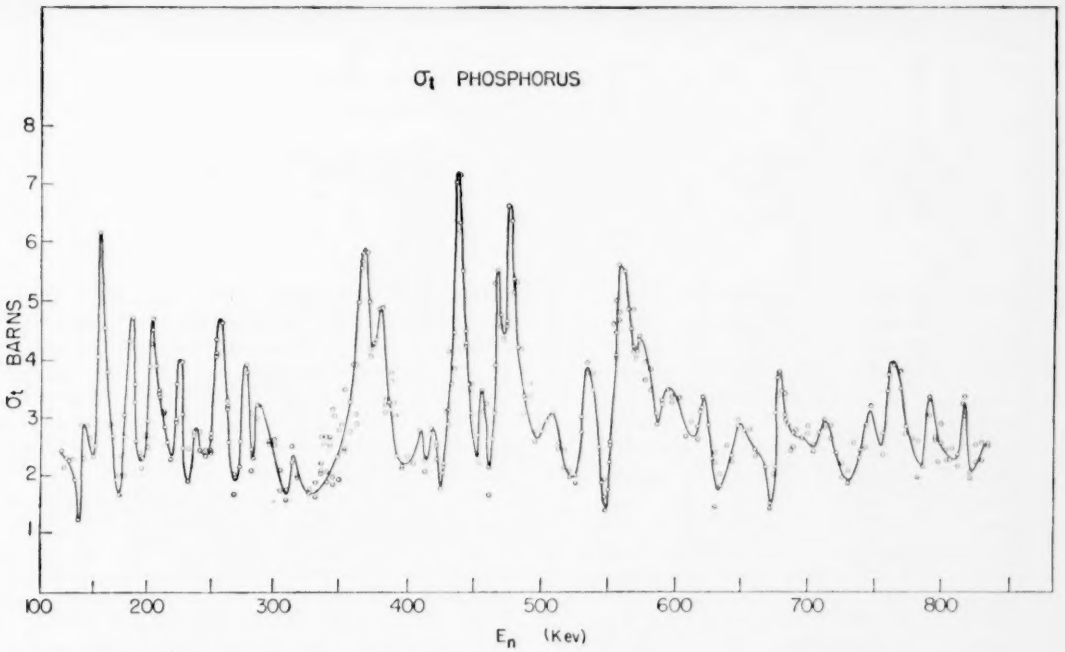

FIG. 2. Total neutron cross section of phosphorus energy resolution about 2 kev. Average total level spacing about 25 kev.

forward direction above the threshold energy (1.882 Mev), and (b) the width of the narrow resonance in sulfur at 588 kev; see Fig. 1.

EXPERIMENTAL PROCEDURE

All measurements were made in good geometry at intervals of 2.0 kev. The targets used varied from 2.0 to 5.0 kev in thickness. The detector in the forward direction was a hydrogen recoil counter of variable bias.[6] The bias was continually adjusted to eliminate background neutrons. Two BF_3 long counters were used as monitors. These were set outside the solid angle subtended by the scatterer, one at 15° from the forward direction and the other at 90°. The monitors not only serve as neutron yield integrators but give two simultaneous values of the cross section. At any point where the two values of the cross section differed by more than 10 percent the point was checked again. (Some difference is to be expected due to the anisotropy in the scattered neutron distribution.)

The container cross section was measured empty by the same method and corrections for its cross section applied. For this geometry and assuming isotropic scattering in the center-of-mass coordinates, scattering-in corrections are negligible. The background was measured by placing a paraffin shadow cone in front of the beam and measuring the counting rate. At all energies background was less than 1 percent of the total count.

RESULTS

The cross section as a function of energy is shown in Fig. 2. The average level spacing over the energy range studied was approximately 25 kev. This high level density is not unexpected for an odd-odd compound nucleus ($_{16}P^{32}$) of this mass. Several of the peaks are larger than those found in neighboring nuclei. The total cross section has an average value near 3 barns in agreement with previous investigations.

[6] F. S. Replogle, Servomechanisms Engineering Memo No. 29, Massachusetts Institute of Technology, March 18, 1952 (unpublished).

The Inelastic Scattering of Fast Neutrons in Carbon and Lead

B. G. WHITMORE
University of Manitoba, Winnipeg, Manitoba, Canada
(Received July 27, 1953)

The inelastic scattering of 14-Mev neutrons in carbon and lead has been investigated by the photographic emulsion method. In carbon, evidence of the excitation of the first-excited level is found, as well as excitation corresponding to Weisskopf's evaporation theory. Comparison with previous results for lead gives no evidence for double inelastic scattering in a thick scatterer.

MEASUREMENTS of the energy distribution of originally monoenergetic neutrons, which have been inelastically scattered by the nuclei of a material, allow the energy taken up by the scattering nucleus to be determined. Such measurements have been used in particular to test the Weisskopf "evaporation" theory for the emission of the scattered neutron from the compound nucleus. It might also be expected that in certain cases, with light elements, evidence of discrete nuclear energy levels could be obtained. In line with previous experiments,[1] measurements have been carried out by the photographic emulsion method using carbon and lead as scattering elements.

CARBON

Recently Graves and Rosen[2] have published the results of inelastic scattering experiments with a number of elements, including both carbon and lead. In their experiments, the scattering substance was, as is usual, in the form of a sphere surrounding the neutron source. This introduces a spread in energy in the laboratory system for neutrons emitted from the compound nucleus with definite energy, owing to the recoil of the compound nucleus. This spread is inappreciable for heavy elements, but considerable for carbon, and might mask any weak monoenergetic scattered neutron group. The carbon scatterer was therefore made in the form of a double cone, the apexes being at the neutron source and photographic plate, respectively, of such proportions that the maximum angle of scattering for a neutron reaching the plate was 70°. Elastically scattered 14.0-Mev neutrons will then reach the plate with an energy range from 12.6 to 14.0 Mev; those which have given, e.g., 10 Mev as internal energy to the scattering nucleus will have a range of energies from 3.1 to 3.7 Mev.

The neutron source was a tritium target bombarded with a 150-kev deuteron beam in the Chalk River accelerator. Exposures were made with and without the scattering substance in position to correct for background. The source and plates were as far as possible from surrounding materials, about 5 ft above a concrete floor. Ilford C2 emulsions, 400μ thick were used, and the developed plates scanned using a Leitz Ortholux microscope, with 90× objective and 6× eyepieces. Tracks making initial angles up to 20° with the original neutron direction were accepted, and neutron energies calculated assuming all neutrons to have been traveling in this original direction. Since they actually reach the plate in all directions within a cone of semivertical angle 10°, a small error is made in this assumption. Number of tracks measured was 1300.

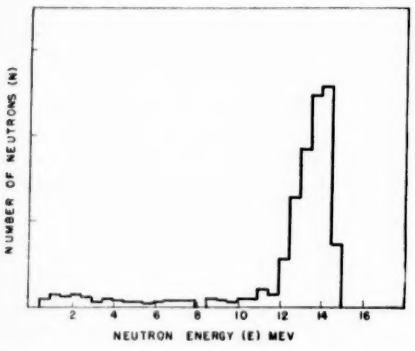

FIG. 1. Energy distribution of neutrons from a d-T source. "Background" without scatterer; number of tracks, 408.

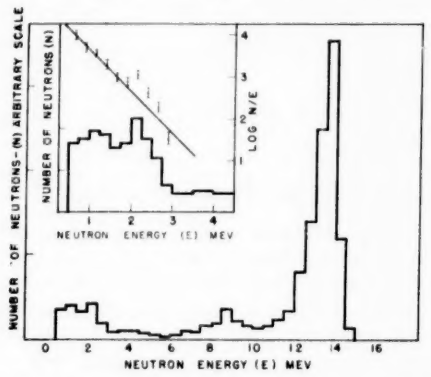

FIG. 2. Energy distribution of neutrons from a d-T source, scattered by carbon. Number of tracks, 1300; inset—region below 3.0 Mev in 0.25-Mev intervals; 800 tracks.

The results, corrected for neutron-proton cross section and loss of tracks in the usual way, are shown in Figs. 1 and 2.

The curve with scatterer shows the usual low-

[1] B. G. Whitmore and G. E. Dennis, Phys. Rev. **84**, 296 (1951).
[2] E. R. Graves and L. Rosen, Phys. Rev. **89**, 343 (1953).

energy group of neutrons, but also a clearly marked group at about 8.75 Mev.

This must correspond to the excitation of the well-known first-excited state of the C^{12} nucleus at 4.5 Mev though the position of the peak corresponds to an absorption of nearer 5.0 Mev.

In the low-energy region there is also a rather strong indication of a discrete group at about 2.1 Mev, as is shown in the inset of Fig. 2. This would correspond to the preferential absorption of about 11.5 Mev. Statistical variations between partial counts were rather larger than average in this region, and the magnitude of the peak at 2.1 Mev is subject to considerable uncertainity, but its existence seems fairly well-established.

These features would not appear but for the limitation of the scattering angle. This limitation, however, has the disadvantage that only a fraction, calculated in this case to be 0.16, of the scattered flux reaches the plate. This in turn means that the scattered flux is comparable with background. In fact, as was found by Mandeville and Swan[3] in a similar experiment, the total flux of low-energy neutrons with scatterer in position is actually slightly less than background, implying that most of the background came from a direction now screened by the scatterer. The proportion of background so screened is, however, unknown, and any accurate comparison of the observations with Weisskopf's formula is therefore impossible. If one assumes, however, that all the background has been screened off, a plot of $\log(N/E)$ against E (Fig. 2) shows a general slope corresponding to a nuclear temperature of 1.0 Mev. Assuming half the background to have been screened does not greatly affect the results, though statistical errors are increased. These results agree, within the rather large experimental errors, with those of Graves and Rosen,[2] though the plot of Fig. 2 indicates that the evaporation theory may not apply accurately for a nucleus as light as carbon.

LEAD

Results have previously been reported[1] of measurements using a sphere of lead of radius 6 cm surrounding the neutron source. In this case the proportion of neutrons inelastically scattered (about 40 percent) suggested that a considerable fraction of them might be twice so scattered, if the once-scattered neutron had sufficient energy. This it may not in fact have, since there is evidence that the lower excited states of all lead isotopes are widely spaced.[4] There was also a question whether the $(n,2n)$ reaction occurred to any extent.

[3] C. E. Mandeville and C. P. Swann, Phys. Rev. **84**, 214 (1951).
[4] Kinsey, Bartholomew, and Walker, Phys. Rev. **82**, 380 (1951).

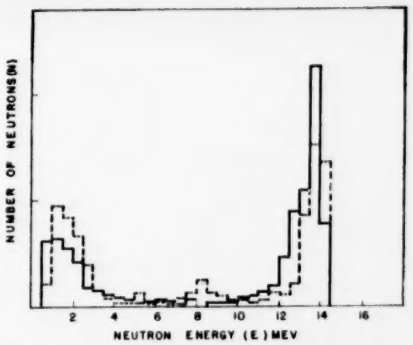

FIG. 3. Energy distribution of neutrons from a d,T source, scattered by lead. Full line—4-cm lead sphere, 1140 tracks; broken line—6-cm lead sphere, 300 tracks.

In an attempt to get further evidence bearing on the first point, these measurements have been repeated using a lead sphere of 4-cm radius around the source. Results of measurements on 1140 tracks, after the usual corrections, are shown in Fig. 3 together with the previous results for 300 tracks using the 6-cm sphere. The exposures were made with the same apparatus and in a similar manner as those with carbon, and separate, "background" plates, though exposed, have not been measured. It is unlikely that they would differ sufficiently from those previously obtained to affect any general conclusions concerning the low-energy region.

It will be seen that the total inelastic scattering has been decreased by about 30 percent, as would be expected from the decreased thickness of scatterer. The doubtful group at 8 Mev in the previous results does not show up, otherwise the low-energy regions are closely similar.[5] The Weisskopf formula again fits approximately, giving a nuclear "temperature" of 0.8 Mev, agreeing with the previous results and with those of Graves and Rosen. There is thus no evidence here of double inelastic scattering.

It was not found possible to measure the absolute neutron flux from the photographic plates sufficiently accurately to determine whether or not the $(n,2n)$ reaction occurred with frequency comparable with that of the (n,n) reaction.

This work was assisted by a grant from the National Research Council of Canada. I wish to thank Dr. E. B. Paul of Atomic Energy of Canada, Ltd. for carrying out the exposures. Most of the measurements were made by Mr. G. W. Langtry and Mr. G. A. Kerr-Wilson.

[5] It might appear at first sight that this group is as prominent as the similar one in carbon. The total count was, however, much lower in the 6-cm lead experiment, and the statistical error consequently greater.

Slow Neutron Resonances in Holmium, Thulium, and Lutetium*

H. L. Foote, Jr.,† H. H. Landon, and V. L. Sailor
Brookhaven National Laboratory, Upton, New York

(Received July 30, 1953)

The total cross sections of holmium, thulium, and lutetium have been measured over the neutron energy range from 0.1 to ~30 ev. Resonances were found in Ho^{165} at 3.96, 12.8, 19, 22, and 39 ev; in Tm^{169} at 3.92 14.8, and 17.6 ev. Of the many resonances found in lutetium, the following tentative isotopic assignments have been made: Lu^{175}—resonances at 5.30, 11.4, 14.4, 20.6, 24, and 31 ev; Lu^{176}—resonances at 0.142, 1.57 2.62, and 4.80. It is probable that many additional resonances are present at higher energies in Lu^{176} but were not observed. The average spacing between resonances in Ho^{165}, Tm^{169}, and Lu^{175} (odd-even isotopes) is estimated to be of the same order of magnitude; i.e., respectively 10, 10, and 6 ev; while the spacing in Lu^{176} (odd-odd) appears to be much smaller, of the order of 1 to 2 ev. Parameters for several of the resonances have been obtained.

INTRODUCTION

THE rare earth elements occupy more than half of that region of the nuclear periodic table lying between the closed shells of 82 and 126 neutrons. Neutron cross-section data for these interesting elements are incomplete, largely because of the difficulty in obtaining specimens of adequate quantity and purity.

The three elements reported in this paper are the three heaviest odd-Z elements of the rare earth group. Preliminary results have been reported previously.[1] Other cross-section measurements on these elements have been limited to the thermal cross sections,[2,3] and to a measurement of the holmium cross section from 0.025 to 0.5 ev by Stephenson.[4,5] Holmium and thulium each occur as single isotopes,[6] Ho^{165} and Tm^{169} (both odd-even); while lutetium occurs as two isotopes,[7] Lu^{175} (odd-even) and Lu^{176} (odd-odd). Isotopic abundances, spins, and thermal absorption cross sections are summarized in Table I.

The thermal cross sections of all four isotopes concerned are relatively large, indicating the existence of resonances at neutron energies of a few electron volts. Level spacings obtained from fast neutron activation cross sections[8] furnish information pertaining to expected differences between the resonance structure in the odd-even and the odd-odd isotopes. Spacing between resonances in Lu^{176} would be expected to be significantly smaller according to those measurements.

EXPERIMENTAL DETAILS

Specimens

As previously indicated, the greatest difficulty encountered in these measurements is the problem of obtaining adequate specimens. These measurements were made possible by Dr. F. H. Spedding and his colleagues at the U. S. Atomic Energy Commission's Ames Laboratory, who generously made available excellent specimens of the sesquioxides of these elements. The purity of the samples exceeded 99.9 percent. Thick samples were made by mounting the oxides in precision quartz cells. The thickness of each sample was determined from the weight of the material and the dimensions of the cell. An additional thin sample of thulium was prepared from a solution of accurately measured concentration of $Tm(NO_3)_3$ in D_2O. In measuring the transmissions, comparisons were made between the samples and empty identical quartz cells, and in the case of the solution, with an identical cell filled with D_2O. In general, the samples were not thick enough to obtain reliable measurements in regions where the cross section was less than 20 barns.

Spectrometer

The measurements were made with the BNL crystal spectrometer which has previously been described in detail.[9] Monochromatic neutrons were obtained from the $(12\bar{3}1)$ planes of a single crystal of Be, except below 0.3 ev where the (200) planes of NaCl were used.

RESULTS

Holmium

The total cross section observed for holmium in the energy range from 0.3 to 50 ev is shown in Fig. 1. Resonances were observed at 3.96, 12.8, 19, 22, and 39 ev. An additional resonance observed at 8.2 ev is

* Research performed under contract with the U. S. Atomic Energy Commission.

† Doctoral candidate from the University of Utah.

[1] Foote, Sailor, and Landon, Phys. Rev. **90**, 362 (1953).

[2] H. Pomerance, Phys. Rev. **83**, 641 (1951).

[3] H. Bomke and H. Reddemann, Z. Physik **120**, 56 (1943); W. Riezler, Ann. Phys. **41**, 476 (1942); Atterling, Bohr, and Sigurgeirsson, Arkiv Mat. Astron. Fysik **32A**, No. 2 (1946); W. Bothe, Z. Naturforsch **1**, 179 (1946); Seren, Friedlander, and Turkel, Phys. Rev. **72**, 888 (1947); H. Pomerance, Oak Ridge National Laboratory Reports ORNL-577, 33, 1949 and ORNL-366, 47, 1949 (unpublished).

[4] T. E. Stephenson, Oak Ridge National Laboratory Report ORNL-1068, 1951 (unpublished).

[5] Bernstein, Borst, Stanford, Stephenson, and Dial, Phys. Rev. **87**, 487 (1952).

[6] F. W. Aston, Proc. Roy. Soc. (London) **A146**, 46 (1934); W. T. Leland, Phys. Rev. **77**, 634 (1950).

[7] J. Mattauch and H. Lichtblau, Z. Physik **111**, 514 (1939).

[8] Hughes, Garth, and Levin, Phys. Rev. **91**, 1423 (1953).

[9] L. B. Borst and V. L. Sailor, Rev. Sci. Instr. **24**, 141 (1953).

believed due to Sm impurity. The possibility that the 3.96-ev resonance found in this specimen is due to thulium impurity (see next section) has been considered but discounted for the following reasons: The resonant energy for the two cases is significantly different; the other thulium resonances could not be detected in this specimen; and a spectroscopic analysis of the material showed no measurable trace of thulium.[10]

A rough estimate of the level spacing[11] in the compound nucleus at an excitation energy equal to the binding energy of the last neutron can be made from the number of resonances observed in the 50-ev interval. The spacing is seen to be of the order of 10 ev.

A detailed analysis of the observed resonances in order to obtain the Breit-Wigner parameters has not yet been completed; however, some preliminary estimates of the "strength," $\sigma_0\Gamma^2$ of the 3.96- and the 12.8-ev resonances have been obtained. A least-squares fit to the wings[12] of the 3.96-ev resonance gave $\sigma_0\Gamma^2=77\pm10\times10^{-24}$, and an area analysis[13] of the 12.8-ev resonance gave $\sigma_0\Gamma^2=300\pm100\times10^{-24}$ cm^2 ev^2.

It is interesting to examine the relationship of the 3.96- and 12.8-ev resonances to the thermal absorption cross section. In particlular, one would like to see what evidence this information would furnish in regard to the possible occurrence of a resonance at slightly negative neutron energy, i.e., a level in the compound nucleus at an excitation slightly below the binding energy. Such a level was suggested by Wigner as a possible explanation of the anomalously large thermal scattering cross section in Ho found by Stephenson.[4]

There are two possible ways for combining the two resonances to obtain the resultant contribution to the thermal cross section. The first of these methods of combination would be valid if the levels were of different total angular momentum, in which case the cross section contributions to thermal would be additive. From the single-level dispersion formula one obtains a contribution of 15.5 ± 2.0 barns from the 3.96-ev resonance and 10.3 ± 3.0 barns from the 12.8-ev resonance; both effectively are entirely absorption. Thus, the total of the two would give a thermal absorption cross section of 26 ± 5 barns. Additive cross section contributions from the higher resonances would amount at most to 1 or 2 barns. Thus, on the above assumption, it is seen that the observed resonances do not fully account for the thermal cross section of 64 barns found by Pomerance.[2]

The second method of combination probably must be used when the two levels have the same total angular momentum. For this case, according to the Wigner many-level dispersion formula,[14] it is not valid to add the cross-section contributions of the two resonances, but instead one must add the "absorption amplitudes" to account for interference effects between the two resonances. As far as is presently known, these amplitudes can be both of the same sign or of opposite sign. The two possible combinations of signs give, respectively, 50 barns or 4 barns for the resultant thermal contribution. These numbers serve merely to illustrate the possible importance of interference effects and, of course, could be in serious error because the effects of other resonances cannot be taken properly into account.

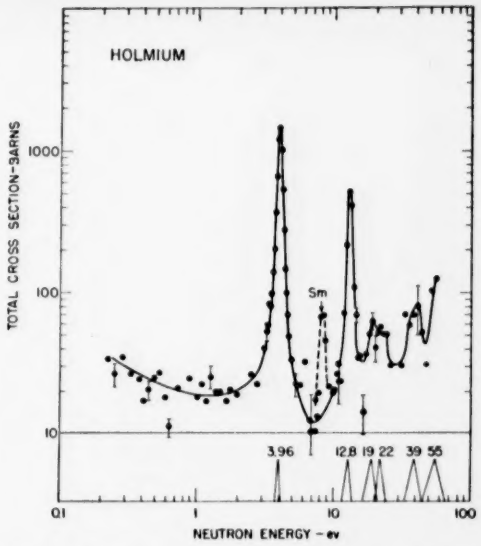

FIG. 1. The observed total cross section of holmium. The resonance at 8.2 ev is at the same energy as an unusually strong resonance in Sm^{152}. The observed peak could be accounted for by about 0.1 percent Sm impurity in the specimen. The statistical error is smaller than the diameter of the points for cross sections greater than 100 barns.

TABLE I. Nuclear properties of Ho, Tm, and Lu isotopes.

Isotope	Abundance (percent)	Spin	Thermal absorption cross section (barns)
Ho^{165}	100[a]	7/2[b]	64[c]
Tm^{169}	100[d]	1/2[e]	118[c]
Lu (element)			108[c]
Lu^{175}	97.4[f]	7/2[g]	16[h]
Lu^{176}	2.6[f]	7[i]	3640[h]

[a] Reference 6.
[b] H. Schüler and T. Schmidt, Naturwiss. **23**, 69 (1935).
[c] Reference 2.
[d] F. W. Aston, reference 6, and C. R. Lagergren and M. E. Kettner, Phys. Rev. **80**, 102 (1950).
[e] H. Schüler and T. Schmidt, Naturwiss. **22**, 838 (1934).
[f] Hayden, Hess, and Inghram, Phys. Rev. **77**, 299 (1950); see also reference 7.
[g] H. Schüler and T. Schmidt, Z. Physik **95**, 265 (1935).
[h] Seren, Friedlander, and Turkel, Phys. Rev. **72**, 888 (1947); see also reference 3.
[i] H. Schüler and H. Gollnow, Z. Physik **113**, 1 (1939).

[10] F. H. Spedding (private communication).
[11] The level spacing here refers to only those levels which can be excited by slow neutrons, i.e., levels having the same parity as the ground state of the target nucleus and having total angular momentum of $I+\frac{1}{2}$, or $I-\frac{1}{2}$, where I is the spin of the target nucleus.
[12] For method, see V. L. Sailor, Phys. Rev. **91**, 53 (1953).
[13] E. Melkonian, Phys. Rev. **90**, 362 (1953).
[14] E. P. Wigner, Phys. Rev. **70**, 606 (1946).

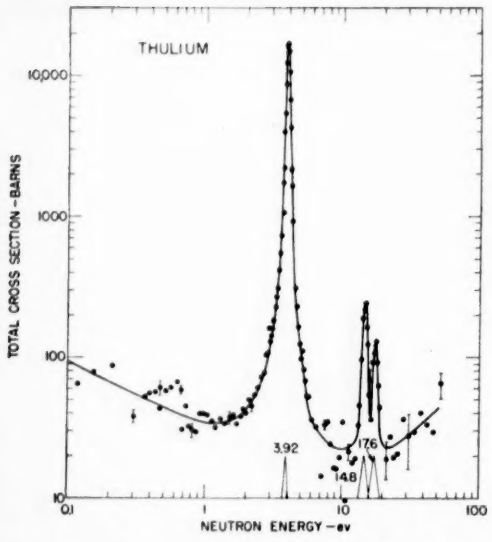

FIG. 2. The observed total cross section of thulium. The statistical errors are smaller than the diameter of the points for cross sections greater than 100 barns.

From the above discussion, it is seen that the question of a negative energy resonance in Ho close to zero energy remains unsettled. It is possible that the shape of the total cross-section curve in the thermal region could give a conclusive answer provided that a sample (e.g., a solution) could be used which eliminated the crystalline coherent scattering effects observed by Stephenson.

Thulium

The total cross section observed for thulium is presented in Fig. 2. Resonances are present at 3.92, 14.8, and 17.6 ev. Data above 30 ev are inconclusive and cannot be considered. The level spacing for this compound nucleus is of the order of 10 ev.

The 3.92-ev resonance has a "strength" $\sigma_0\Gamma^2=380\pm40\times10^{-24}$ cm² ev², obtained by fitting the wings of the resonance. It should be noted that this resonance is about five times as strong as the corresponding resonance in holmium. Asymmetry in the wings of the thulium resonance indicates that the scattering component is relatively large, although more detailed analysis will be required before a quantitative estimate of $g\Gamma_n$ can be made. This resonance by itself would give a thermal absorption cross section of 78 ± 7 barns, compared with the observed 118 barns.[2]

Lutetium

The total cross section of lutetium over the energy range from 0.3 to 35 ev is presented in Fig. 3. The peak observed at 0.035 ev is the second order of the 0.142-ev resonance. For this spectrometer, second-order contamination becomes serious below 0.08 ev. The resonances observed in lutetium are listed in Table II. The values of $\sigma_0\Gamma^2$ were obtained by the area analysis method.[13] A more detailed analysis was made of the 0.142-ev resonance by fitting the data to the single-level formula. At such a low energy Doppler broadening and instrument resolution could be neglected. The parameters obtained for the resonance were $E_0=0.142\pm0.002$ ev, $\sigma_0=350\pm20\times10^{-24}$ cm², and $\Gamma=0.063\pm0.005$ ev. If we assume that this resonance is in Lu^{176} (see discussion below), then several additional combinations of the parameters can be computed.[11] For the isotope, $\sigma_0=13\,500\times10^{-24}$ cm²; $\sigma_0\Gamma^2=54\pm12\times10^{-24}$ cm² ev²; $g\Gamma_n=(0.925\pm0.090)\times10^{-4}$ ev; and $\sum_a=(9400\pm660)\times10^{-24}$ cm². Since the spin of Lu^{176} is $\geqslant7$, g can have the values $0.533\geqslant g\geqslant0.467$, or $g\approx\frac{1}{2}$. Thus Γ_n can be estimated as 1.8×10^{-4} ev.

Tentative isotopic assignments of several of the resonances can be made from the observed values of $\sigma_0\Gamma^2$. Normally within this energy range, values of $\sigma_0\Gamma^2$ (corrected for isotopic abundance) lie within the limits[15] from 50 to 1000×10^{-24} cm² ev². Examination of Table II shows that the first three resonances are unusually weak and that assignment to Lu^{176} gives more normal values of $\sigma_0\Gamma^2$. The thermal activation cross section of Lu^{176} (Table I) adds further support for the assignment of the 0.142-ev resonance to this isotope. The 4.80-ev resonance is more difficult to assign since the strength would be larger than normal if assigned to 176 and smaller than normal if assigned to 175; however, the weight of the evidence would favor assignment to 176. The 5.30- and the 11.4-ev resonances appear to belong to Lu^{175}. The shape, the observed width, and the very large $\sigma_0\Gamma^2$ of the 14.4-ev resonance strongly

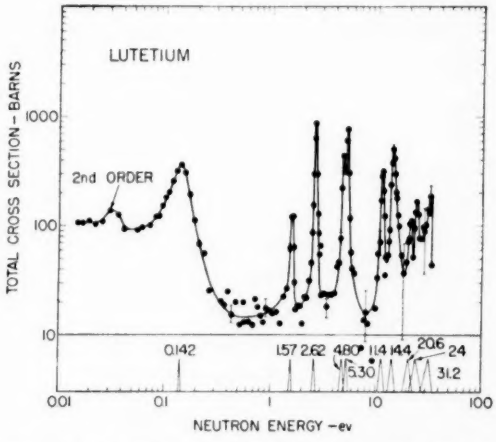

FIG. 3. The observed total cross section of lutetium. The peak at 0.035 ev is the second order of the 0.142-ev resonance. Second-order effects become negligible (<1 percent) above 0.1 ev. Statistical errors are smaller than the diameter of the points for cross sections greater than 100 barns except at very high energies.

[15] W. W. Havens, Jr. and T. I. Taylor, Nucleonics **6**, No. 2, 66 (1950) (see Fig. 2).

indicate that this is two or more unresolved resonances. At least one of these belongs to Lu^{175}.

The spacing between the observed resonances must be carefully considered before attempting to estimate the level spacing in the two compound nuclei. Assuming the isotopic assignments to be correct, we see that four resonances occur in Lu^{176} below 5 ev, but none above 5 ev. Calculations show that resonances having a strength of the order of 1 to 5×10^{-24} cm^2 ev^2 would be difficult to observe above 4 or 5 ev with the resolution of this spectrometer. This would be particularly true if other stronger resonances were present to mask the weak ones. It is reasonable to assume, therefore that more resonances were present in Lu^{176} but were unobservable above 5 ev. The only hope of observing Lu^{176} resonances above 5 ev would be to use a specimen enriched in this isotope. If we consider only the range 0 to 5 ev, then the spacing of the Lu^{176} resonances is of the order of 1.2 ev. If all the remaining resonances are in Lu^{175}, the spacing for this target isotope would be of the order of 5 or 6 ev. The 0.142-ev resonance does not fully account for the thermal activation cross section of Lu^{176}; however, the 5.30-ev resonance, if the isotopic assignment is correct, will account for most of the Lu^{175} thermal activation cross section.

CONCLUSIONS

The isotopes Ho^{165} and Tm^{169} have slow neutron resonances spaced at intervals of about 10 ev; while the spacing in Lu^{175} is approximately 6 ev, and in Lu^{176} 1.2 ev. The smaller spacing in Lu^{176} is consistent with qualitative expectations. At the present, it is not possible to account unambiguously for the thermal absorption cross sections of these isotopes except possibly Lu^{175}. There is need for further study at higher energies of all these isotopes, and need for a study over the entire energy range with enriched samples of Lu^{176}.

TABLE II. Summary of lutetium resonances. The strengths $\sigma_0\Gamma^2$ were obtained by method of area analysis, except for the 0.142-ev resonance, which was obtained by fitting the data to a Breit-Wigner curve. The isotopic strength is obtained by dividing $\sigma_0\Gamma^2$ by the abundance, F.

E_0 (ev)	$\sigma_0\Gamma^2$ (barn ev^2)	Tentative isotopic assignment	Isotopic strength $\sigma_0\Gamma^2/F$
0.142	1.4± 0.3	176	54±12
1.57	0.9± 0.3	176	35±12
2.62	5.5± 2.0	176	210±77
4.80	21. ± 7.	(176?)	810±270
5.30	45. ±15.	175	46±15
11.4	58. ±20.	175	60±20
14.4	(560.)	(175)[a]	...
20.6	...[b]	(175?)	...
24.	...[b]	(175?)	...
31.	...[b]	(175?)	...

[a] This is apparently two or more unresolved resonances, one of which belongs to Lu^{175}.
[b] Data inadequate for analysis.

The authors are grateful to Dr. F. H. Spedding for furnishing the excellent rare earth specimens which made these measurements possible. It is a pleasure to acknowledge the valuable assistance of Mr. Ronald Smith in the operation and maintenance of the spectrometer.

Alpha-Alpha Scattering from 12.88 to 21.62 Mev

F. E. Steigert* and M. B. Sampson
Indiana University, Bloomington, Indiana†
(Received July 15, 1953)

The differential scattering cross section of alpha particles on helium has been investigated as a function of energy in the range from 12.88 to 21.62 Mev. The data obtained indicate a very strong angular dependence. This further appears to be a fairly sensitive function of energy. At the lower excitations there is a rather singular interference between the Coulomb and nuclear interactions. Above 20 Mev, interferences among the various components of the nuclear phase shifts again give rise to marked singularities. These data have been analyzed with respect to the phase shifts arising from the angular momentum components of the interaction. This decomposition indicated resonances at 7.55 and 10.8 Mev with widths, Γ of 1.2 Mev in each case and state assignments of 0 and 4, respectively.

INTRODUCTION

A STUDY of the high-energy interaction of two alpha particles encompasses two basic aspects. There is the fundamental concept of the type of potential to be associated with the alpha particle itself. This gives rise to the nonresonant or potential scattering. The interaction will also be influenced by the virtual energy states of the barely unstable compound nucleus of Be^8. This will result in the superposition upon the potential scattering of a resonant behavior characteristic of the angular momenta involved.

Until about 1950 this problem had been investigated only over the range of energies available from naturally radioactive substances. This early work has been thoroughly discussed by Wheeler[1] and more recently by Haefner.[2] It is perhaps sufficient to say that these experiments were plagued by all the difficulties attendant upon the low intensities of the sources then available. Taking these experimental limitations into consideration, Wheeler treated the data analytically and gave an apparently reasonable interpretation to it. The reported analysis showed one rather undesirable aspect, however. The resonance structure is observed in the S wave in direct contradiction of the results of other data. On the theoretical side of the problem, an encouraging point has been Haefner's success in obtaining Wheeler's nonresonant phase angles using a rather simple model.

More recently, attempts to extend the data to higher energies have been made by Mather[3] and Graves[4] at 20 and 30 Mev, respectively. These will be discussed more fully below. The work of Heydenburg and Temmer[5] in the lower-energy region is not as yet definitive.

The present research was undertaken in an attempt to obtain better resolution and with the use of better techniques to extend the data to cover a greater range of energies. It was found, however, that the method of reducing the cyclotron beam energy by the use of absorbing foils was impracticable below about 12 Mev, owing to the loss in beam intensity. No information could be obtained, therefore, on the question of the angular momentum of the 3-Mev resonance. Data were taken, however, covering the region from 12.88 to 21.62 Mev. This made it possible to obtain information regarding the two known states at 7.5 and 10 Mev in Be^8.

EXPERIMENTAL PROCEDURE

Apparatus

The external ion beam of the Indiana University cyclotron was passed through a double-sector inhomogeneous-field focusing magnet and a 32° homogeneous-field analyzer magnet into the scattering chamber. The focal properties of this lens system were adjusted to give an image point at the center of the scattering chamber. The resolution of the system was measured by observation of the alpha particle, deuteron doublet with a constant magnetic field. This was calculated to be about 45 kev/mm for 22-Mev alpha particles. The field of the analyzer magnet was maintained at predetermined values by means of an electronic stabilizer circuit utilizing a Brown converter and a phase-sensitive detector. The magnitude and constancy of the field were determined by the use of a calibrated search coil.

The analyzed beam was defined by a $\frac{1}{8}$-in. diameter circular slit of tungsten backed by lead and entered the scattering chamber through a $\frac{1}{4}$-in. cylindrical tube to within $\frac{1}{4}$ in. of the actual scattering center. At the terminus of this tube final definition was given by a $\frac{1}{16}$-in. diameter brass slit. The scattering chamber was isolated from the main cyclotron vacuum system by a 0.2-mil aluminum foil window covering this last slit. Visual observation of the beam image on a Willemite screen, as well as on photographic plates, showed no evidence of beam spread as a result of slit scattering.

* Now at Yale University, New Haven, Connecticut.
† Supported by the U. S. Office of Naval Research and the U. S. Atomic Energy Commission.
[1] J. A. Wheeler, Phys. Rev. **59**, 16 (1941).
[2] R. R. Haefner, Revs. Modern Phys. **23**, 228 (1951).
[3] K. B. Mather, Phys. Rev. **82**, 126 (1951).
[4] E. Graves, Phys. Rev. **84**, 1250 (1951).
[5] Cowie, Heydenburg, Temmer, and Little, Phys. Rev. **86**, 593 (1952); G. M. Temmer and N. P. Heydenburg, Phys. Rev. **90**, 340 (1953).

The range in energies used was obtained by interposing aluminum absorbing foils at the cyclotron exit, approximately at the effective object point of the lens system. The energy was then defined by momentum analysis. Energies of 21.62, 20.95, 20.38, 19.62, 19.47, 18.82, 18.32, 16.55, 14.86, and 12.88±0.06 Mev were so obtained.

The actual scattering volume was defined by means of the slit system illustrated schematically in Fig. 1. A number of $\frac{1}{16}$-in. wide slits were machined in each of two brass cylinders concentric with the scattering center. These slits were aligned radially as shown at each of the angles 15°, 30°, 45°, etc., spaced every 15° up to 165° counterclockwise with respect to the incoming beam and 22½°, 37½°, 52½°, 67½°, 82½°, 90°, and 97½° clockwise. Kodak NTA emulsions of 50 and 60 micron thickness were used as detectors. These were centered vertically with regard to the beam axis and radially along the slit axes. They were further oriented so as to form an angle of 7° between the vertical plane of the emulsion and the plane of the slits. For the

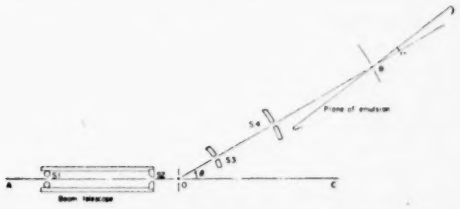

FIG. 1. Schematic drawing of slit system. *S1* and *S2* are circular beam apertures of tungsten and brass, respectively. *S3* and *S4* are rectangular brass slits oriented every 15° for θ 15° to 165° counterclockwise and 22½° to 97½° clockwise. $\angle AOC$ defines the incident beam direction. Point *O* is the scattering center and point *B* the center of the detecting plate.

scattering experiments the entire chamber was filled with helium gas to pressures of 5 to 8 centimeters of mercury as measured on a mercury manometer before and after each run. The chamber was evacuated and flushed with helium twice before each filling. Both high purity and commercial grade helium were used in different exposures.

The beam left the chamber through a second aluminum foil window and was monitored by means of a Faraday cage and an integrating circuit of the type developed at Wisconsin.[6] Secondary electron emission from the Faraday cup, and the aluminum window was eliminated by the use of a guard ring maintained at −300 volts. Beam currents from 0.01 to 0.3 microampere were used. Exposures were from one to fifteen minutes.

Control Experiments

Several control experiments were performed to check the apparatus used. A complete set of plates, including

[6] G. M. B. Bouricious and F. C. Shoemaker, Rev. Sci. Instr. **22**, 183 (1951).

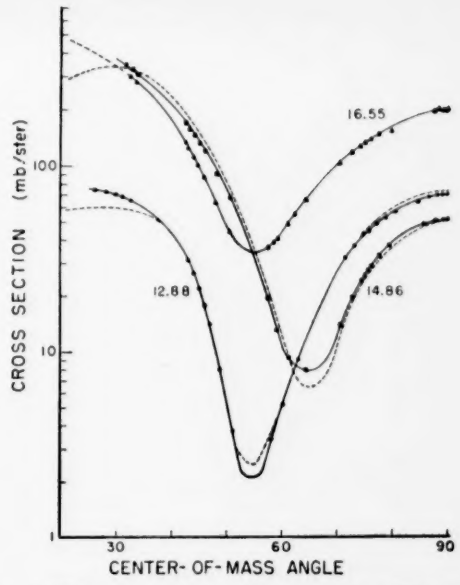

FIG. 2. Differential scattering cross section in millibarns per steradian for incident energies of 12.88, 14.86, and 16.55 Mev. Dashed curves indicate best fit using only *S*- and *D*-wave interaction.

those at angles greater than 90° not accessible to alpha-alpha scattering, were exposed with the chamber evacuated to determine the background scattering of the incoming beam at the slits and the aluminum windows. A search was also made for contaminant groups of

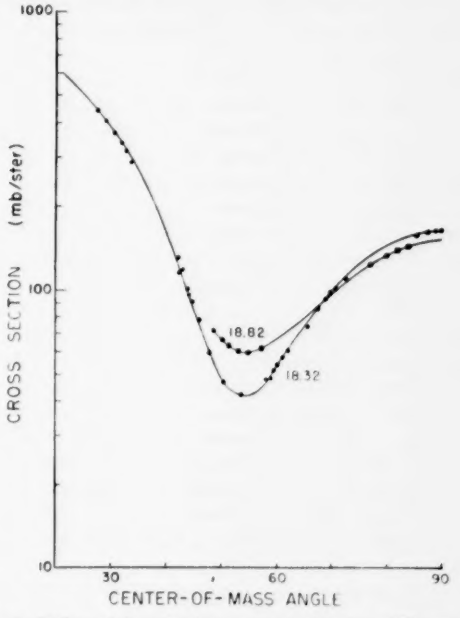

FIG. 3. Differential scattering cross section in millibarns per steradian for incident energies of 18.32 and 18.82 Mev.

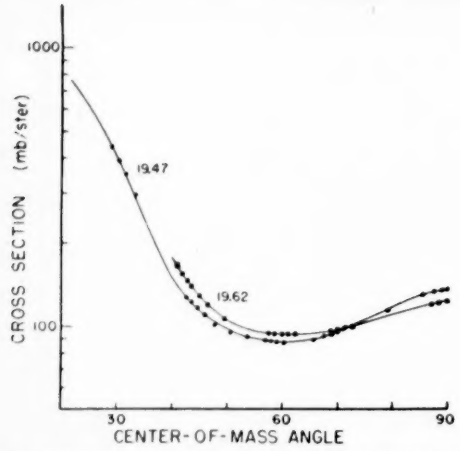

FIG. 4. Differential scattering cross section in millibarns per steradian for incident energies of 19.47 and 19.62 Mev.

elastically scattered particles from pump oil and other vapors which might be present in the scattering chamber. An exposure of one hour—about 500 microcoulombs of charge—was made, but no tracks other than thorium alphas and a few random protons were observed. None of these latter could possibly have come from the scattering volume seen by the plates. This suggested they were recoils from neutrons, possibly from the first beam slits. The low-energy spectrum of alpha particles normally observed on plates several months old has been successfully eliminated in this laboratory by the storage of the plates in cadmium containers.

Another set of plates was exposed to a source constructed of a $\frac{1}{16}$-in. diameter polished stainless steel cylinder uniformly coated with thorium-active deposit. This experiment simulated the cylinder of scattering centers across the chamber seen by the cylindrical beam. This gave a direct check on the alignment of the slit system, since the expected density of tracks at each angle was calculable. It also served as a check on the geometrically calculated corrections which were applied to the data from those portions of the plates situated a small distance from the slit axes. In all cases the calculations and direct measurements agreed to within 0.5 percent.

A third set of plates was exposed to a source of thorium active deposit with 0.2 atmosphere of helium gas in the chamber. Since the exposure could be quite accurately timed so as to correspond to a similar set using an evacuated chamber, this would provide a measure of the effects of straggling and the amount of secondary scattering to be expected at the two energies, 6.06 and 8.78 Mev. The relative density of tracks observed indicated that the secondary scattering was less than 0.5 percent.

These direct checks upon the apparatus demonstrate that the experimental data are limited by integration problems and by statistics rather than by any of the factors here considered. The first set of plates indicates that essentially all tracks observed originated in the target gas itself. No alpha-particle tracks scattered from either the apparatus or any apparatus contaminant were observed. The second set indicates that the alignment of the apparatus is certainly as good as the statistics available. The density of tracks as calculated from the geometry of the apparatus agreed with that observed to within 0.5 percent on the basis of about 10 000 tracks per plate. The third set of plates demonstrated quite clearly that the effect of secondary scattering either in the gas or from the slits was entirely negligible. No systematic difference in track densities was observed, the maximum effect being about 0.5 percent.

Scattering Experiment

The exposed plates were processed in the usual manner. Scanning was done on a Spencer binocular research microscope. The ranges of about 1000 tracks were measured on each plate preliminary to actual counting. In this manner a measure of the energy and a check on the impurities in the target were obtained. No contaminant tracks were observed on plates using high purity helium. A plot of the data obtained using the commercial grade helium indicated the impurities present were hydrocarbons. These gave rise to peaks well resolved from the helium and of less than 1 percent of the intensity. All tracks within the range limits thus prescribed by the helium peak were counted. Corrections were then applied to the track densities

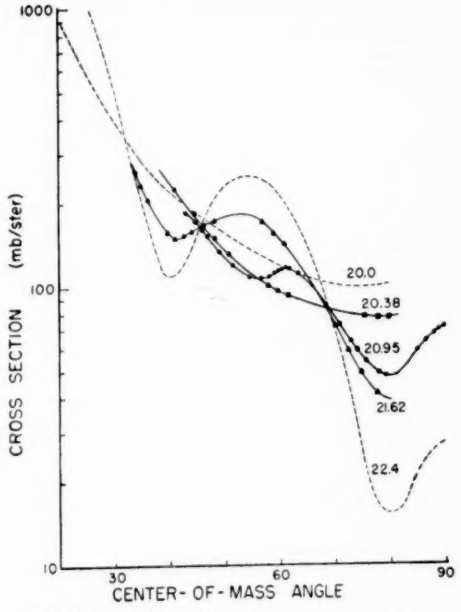

FIG. 5. Differential scattering cross section in millibarns per steradian for incident energies of 20.38, 20.95, and 21.62 Mev. Dashed curves are from Mather (reference 3), and Kerman, Nilson, and Jentschke (reference 8).

measured away from the center of the plate. The range measurements also gave an additional check on both the incident beam energy and on the angle of observation. In all cases the incident energies agreed to within 0.3 percent with the values obtained by magnetic analysis. On several plates additional range measurements were made to check the shift in angle occurring for the off center sections of the plate. The calculated energy shifts were within 2 percent of those measured.

After each exposure an additional plate was exposed at 45° to the incident beam at the same energy using a gold foil target. The elastic scattering from gold had been reported not to deviate from Coulomb scattering at 30 Mev for angles back to 50°.[4] This experiment was repeated here at 22 Mev and corroborated for the range of angles 22½° to 60°. These plates were then used to give an additional check on the absolute value of the cross section. In all cases where applicable the normalization to the gold cross section gave results which agreed to within 3 percent with the direct measurements using the integrator data.

The corrected data are given in Figs. 2–5. The absolute values are considered accurate to about 5 percent for the energies above 18 Mev and about 10 percent for those below. The relative values are considered to be better than 2 percent. This latter is primarily a function of the statistics, since the number of spurious tracks has been shown to be negligible, and the accuracy of the geometry was experimentally checked. The error in the absolute values is essentially that of the integration of the beam current, since the gas pressures were readable to better than 1 percent. Each curve represents a total of more than 30 000 tracks.

ANALYSIS

The data represented by the solid curves in Figs. 2–5 were analyzed in accordance with the Legendre polynomial expansion suggested by Taylor[7] and used successfully by Wheeler and Haefner. Several minor changes were made for simplicity. The expression used is essentially that for a modified Coulomb field with point charges and identical particles. If we write the center-of-mass cross section as

$$\sigma(\theta)=R^2(2e^2/mv^2),$$

then

$$R=Ae^{-i\alpha}+Be^{-i\beta}+\Sigma A_L e^{i\gamma}(1-e^{2i\delta_L}),$$

where the summation is over even values of L because of the symmetry. The various coefficients are defined by

$$A=\csc^2\tfrac{1}{2}\theta \quad \alpha=n\ln(\sin^2\tfrac{1}{2}\theta),$$

$$B=\sec^2\tfrac{1}{2}\theta \quad \beta=n\ln(\cos^2\tfrac{1}{2}\theta),$$

$$A_L=2(2L+1)P_L(\cos\theta)/n,$$

$$\gamma_L=2[\arctan n+\arctan(n/2)+\cdots+\arctan(n/L)]-\pi/2,$$

$$n=4e^2/hv,$$

[7] H. M. Taylor, Proc. Roy. Soc. (London) **A136**, 605 (1932).

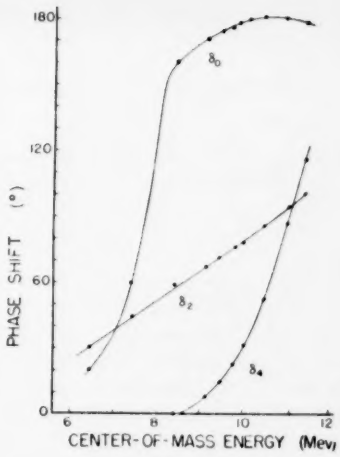

FIG. 6. The nuclear phase shift δ_L in degrees as a function of the center-of-mass energy in Mev. Data above 10.5 Mev are tentative.

where θ is the center-of-mass angle and δ_L is the nuclear phase shift of angular momentum L. It should be noted that in the summation γ_L is $-\pi/2$ for the S wave.

The complexity of these equations precludes any attempt at a simple analytical solution. Instead, a solution was sought by means of geometrical constructions. For simplicity the angles 15.3°, 27.3°, and 35.0° were chosen, the coefficients A_4, A_2, and A_4 vanishing, respectively, at these angles. Briefly, the procedure consists of adding the terms vectorially for one assumed phase angle, say δ_2, and determining what simultaneous values of δ_0 will give the observed cross section. This is repeated over the complete range of compatible variables, obtaining a locus of values which would satisfy the 15.3° cross section, for example. Similar loci may be found for the other two angles. Using the 15.3° and 35.0° data, simultaneous solutions for δ_0 and δ_2 are obtained from the intersection of the loci. The 27.3° data then determine acceptable values of δ_4. Up to eight such triads of solutions are possible. These are then individually checked to determine which of them gives the best fit to the rest of the experimental curve. Usually no unique solution is found for the limited range of angles available. A modification of this procedure is actually employed because of the experimental limitations. Solutions were sought using the observed cross section plus and minus the estimated experimental error. This resulted in areas of intersection rather than points as obtained in principle. The agreement between the solutions chosen and the experimental data is shown in Fig. 2. In cases where alternative solutions were available, a choice was based upon physical simplicity. For example, the solution requiring the smaller number of interacting orders was preferred. More important, however, was the restriction that the energy dependence of the respective orders be continuous and not arbi-

TABLE I. Comparison of levels and widths of excited states in Be^8.

$Li^7(d,n)$ Level energy Mev	$Li^7(d,n)$ Level width Mev	$\alpha+\alpha$ Level energy Mev	$\alpha+\alpha$ Level width Mev	State
7.5	1.7	7.55±0.08	1.2±0.4	$J=0$
10	~1.5	10.8 ±0.4	1.2±0.4	$=4$

trarily irregular. The best set of values so obtained is given in Fig. 6.

With reference to the data it should be noted that in the reconstructed curves shown in Fig. 2, no fourth-order phase shift has been used. None appears to be necessary for the 16.55-Mev data. For the 12.88- and 14.86-Mev data small admixtures of negative fourth-order phase shift will improve the fit, but it is believed the correspondence shown is within the experimental accuracy. The higher-energy data may likewise be fitted to within the errors quoted. In Fig. 5 the data presented by Mather,[8] and a typical curve obtained by Kerman, Nilson, and Jentschke,[8] are shown for comparison.[9] The data obtained at Illinois agree very closely both in general shape and magnitude with that presented here. Mather's results are also in rough agreement, although a slight lowering of the right-hand portion of the curve would improve the agreement. There is no agreement with the results of Braden, Carter, and Ford.[10] This is undoubtedly because of their poor statistics.

DISCUSSION

The steep rise in the S-wave phase shift indicated in Fig. 6 can be accounted for by the assumption of a resonance level at 7.65±0.08-Mev excitation energy and a width Γ, of 1.2±0.4 Mev. The large error assigned the width measurement arises from the few points available to give the resonant shape. The values are obtained from fitting an $\arctan\frac{1}{2}\Gamma(E_0-E)^{-1}$ curve to the data at three energies.

The sharp rise in the G wave may similarly be accounted for. Fitting only the forward slope of this resonance, one obtains a level at 10.9±0.4-Mev excitation and a width Γ, of 1.2±0.4 Mev. These values do not take into account the Illinois data previously mentioned and will undoubtedly need revision when this analysis is complete.

The D wave shows no evidence of any resonance behavior in the energy region covered. In fact, irrespective of the choice made among the individually acceptable solutions, the value of δ_2 does not change by more than about 10°. The values indicated all fall within 2° of a straight line.

These facts are in good agreement with present knowledge concerning the Be^8 compound nucleus. Only two 2-alpha-particle states of sufficient width to be observed in this experiment are observed in the energy region covered. These would be an S state at 7.55 Mev and a G state at about 10.8 Mev, assuming the ground state to be unstable to 2-alpha particle breakup by 96 kev. These values compare favorably with the broad levels observed in the $Li^7(d,n)$ experiments.[11] A comparison is given in Table I.

The assignment also agrees with the available data on the beta decay of Li^8 [12] and on the $C^{12}(\gamma,\alpha)$ reaction[13] predicting a unique configuration for the 3-Mev state. If one temporarily disregards Wheeler's analysis, the weight of the experimental evidence favors the assumption of $J=2$ for this level.[14] The proposed assignments would still leave this D state unique as required.

A possible explanation for the inconsistency of Wheeler's assignment of $J=0$ to this first excitation level may be seen from Fig. 2. The minima are becoming narrower and more pronounced with decreasing energy. The observed energy dependence of δ_2 further suggests that this tendency may be extrapolated. Thus, it may well be that the relatively poor resolution of the early experiments would cause such an effect to have been missed. This would suggest that the original data rather than Wheeler's analysis are at fault. This point is further strengthened by the fact that the present experiments require only two orders of interaction—S and D wave—for an incident energy of 17 Mev, while the most reasonable analysis of the early data required admixtures of G wave at 6 Mev.

[8] Kerman, Nilson, and Jentschke (to be published).

[9] The authors wish to express their appreciation to Professor Jentschke and his group at the University of Illinois for making their data available prior to publication and also for many very helpful discussions on the problems involved in the analysis and interpretation of the data.

[10] Braden, Carter, and Ford, Phys. Rev. **84**, 837 (1951).

[11] K. T. Richards, Phys. Rev. **59**, 796 (1941); L. L. Green and W. M. Gibson, Proc. Phys. Soc. (London) **62**, 407 (1949).

[12] W. F. Hornyak and T. Lauritsen, Phys. Rev. **77**, 160 (1950); C. W. Li and W. Whaling, Phys. Rev. **81**, 661 (1951).

[13] V. L. Tegledi and W. Zunti, Helv. Phys. Acta **23**, 745 (1950).

[14] J. W. Gardner, Phys. Rev. **82**, 283 (1951); M. Eder and V. L. Tegledi, Helv. Phys. Acta **25**, 55 (1952); J. J. Wilkins and F. K. Goward, Proc. Phys. Soc. (London) **A64**, 1056 (1951).

PHYSICAL REVIEW VOLUME 92, NUMBER 3 NOVEMBER 1, 1953

Inelastic Scattering of Protons and Deuterons from B^{10} and N^{14}†

C. K. Bockelman, C. P. Browne, W. W. Buechner, and A. Sperduto
Physics Department and Laboratory for Nuclear Science, Massachusetts Institute of Technology, Cambridge, Massachusetts

(Received July 30, 1953)

Proton and deuteron groups scattered from B^{10} and N^{14} targets were measured with a magnetic spectrograph. Accurate values for the level positions up to approximately 5-Mev excitation were obtained. One level in each nucleus failed to scatter deuterons. The operation of an isobaric spin-selection rule seems to be the most reasonable explanation of this behavior.

I. INTRODUCTION

THE systematics of the binding energies of light mirror nuclei and the close correspondence of their excited states seem to establish the charge-symmetry of nuclear forces in the "classical" energy region. Moreover, the level structures of light isobars of even atomic weight support the hypothesis that nuclear forces are charge-independent. The evidence that certain states in such isobars have similar characteristics is, however, not extensive.

In B^{10}, the 1.74-Mev level is near the position expected for the analog to the ground state of Be^{10}. The intensities of the gamma rays[1] and the angular distribution of the neutron groups[2] from $Be^9(d,n)B^{10}$ suggest that this state has the required zero spin and even parity. In the isobaric-spin formalism, it is the $T_z=0$ member of the $T=1$ charge triplet, of which the Be^{10} and C^{10} ground states are the $T_z=+1$ and -1 components, respectively. Similarly, for $A=14$, a $T=1$ state would be expected in N^{14}, corresponding to the ground states of C^{14} and O^{14}. Adair[3] has pointed out that this may explain the lack of alpha particles to the 2.31-Mev level in the $O^{16}(d,\alpha)N^{14}$ reaction.[4–6] The reaction would be prohibited by the requirement of conservation of isobaric spin.

Such a selection rule would also prohibit the inelastic scattering of deuterons and alpha particles, which are characterized by $T=0$, from a state which differs in T from the ground state. The present report compares the inelastic scattering of deuterons with that of protons for the nuclei B^{10} and N^{14}. In the course of the work, an accurate measure of the positions of the levels was obtained. A preliminary report of this work has been published.[7,8]

II. METHOD

Protons or deuterons were accelerated by the MIT-ONR electrostatic generator to energies between 4 and 8 Mev. A magnet deflected the monatomic beam through 90 degrees and focused it in a horizontal line at the energy-defining exit slits, which had an opening of $\frac{1}{2}$ mm and were approximately 1 foot from the target. A $\frac{1}{4}$-inch vertical slit limited the length of the beam to prevent it from striking the target frame. The scattered particles leaving the target at 90 degrees to the incident beam were analyzed in momentum by the 180-degree magnetic spectrograph and registered on Eastman NTA photographic plates. The magnetic field was measured with a nuclear induction fluxmeter and the position of the tracks on the plates, with a microscope. The range of the tracks of known momentum serves to distinguish between protons, deuterons, and alpha particles.

The combination of the field and position measurements allows a comparison of the momentum of the scattered particles with that of polonium alpha particles. The point on the high-energy side of a peak that lies $\frac{1}{3}$ of the peak height above background was used as a reference for both the scattered and the calibration groups, since experience had indicated that this point is most consistent for targets of different thickness.

During the period in which the experiment was performed, some motion of the beam in the accelerating tube occurred. The lack of a mechanism for deflecting the beam made it necessary to open the entrance slit of the deflecting magnet to $\frac{1}{4}$ inch. Therefore, the deflecting magnet could not be used for measuring the beam energy. The incident particle energy was determined from the momentum of elastic groups. This procedure introduced a possible error, since the open entrance slits could allow a different beam momentum during the exposure for the inelastic groups than during the elastic measurements.

Further details of the method have been given in a recent paper.[9]

Calculations show that the errors introduced by the uncertainties in the fundamental constants, in the magnetic field measurement, in the $H\rho$ of polonium alpha particles, and in the reaction angle are small compared with the 0.2-mm uncertainty in determining the position

† This work has been supported by the joint program of the U. S. Office of Naval Research and the U. S. Atomic Energy Commission.

[1] Rasmussen, Hornyak, and Lauritsen, Phys. Rev. **76**, 581 (1949).
[2] Fay Azjenberg, Phys. Rev. **88**, 298 (1952).
[3] R. K. Adair, Phys. Rev. **87**, 1041 (1952).
[4] A. Ashmore and J. Raffle, Proc. Phys. Soc. (London) **A64**, 754 (1951).
[5] Van de Graaff, Sperduto, Buechner, and Enge, Phys. Rev. **86**, 966 (1952).
[6] Craig, Donahue, and Jones, Phys. Rev. **88**, 808 (1952).
[7] Bockelman, Browne, Sperduto, and Buechner, Phys. Rev. **90**, 340 (1953).
[8] Browne, Bockelman, Sperduto, and Buechner, Phys. Rev. **90**, 340 (1953).
[9] Buechner, Sperduto, Browne, and Bockelman, Phys. Rev. **91**, 1502 (1953).

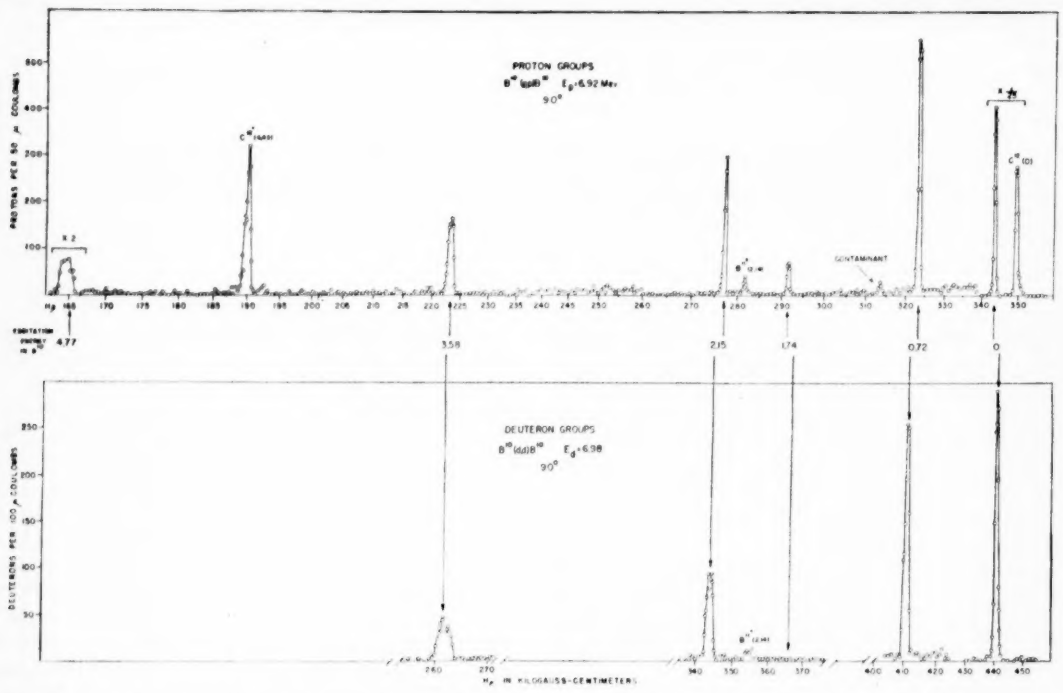

FIG. 1. Scattered proton and deuteron groups from B^{10} obtained at 90 degrees. Incident proton energy 6.92 Mev. Incident deuteron energy 6.98 Mev. Groups arising from B^{10} are labeled with the corresponding excitation energy. Other groups are identified with the contributing nucleus and its excitation. Note abscissa is not linear in $H\rho$ but in ρ. The B^{11} ground state observed with protons does not show on the reduced scale.

of the $\frac{1}{3}$ heights of the reaction peaks relative to the polonium alpha peaks. This factor alone contributes an uncertainty of approximately 2 kev to the total error. Although variations in incident trajectories which were geometrically possible with the open entrance slits could introduce larger errors, the over-all consistency of results leads to the belief that the errors quoted below are reasonable estimates.

For intensity comparisons between scattered groups, the integrated beam current incident on a catcher placed directly behind the target and biased to trap secondary electrons was used.[10]

III. RESULTS

A. Boron 10

Thin films of B^{10} were evaporated on Formvar films, supported on a wire frame. The enriched boron isotope was obtained from the Stable Isotopes Division of the U. S. Atomic Energy Commission, Oak Ridge.

A typical proton momentum spectrum obtained at a bombarding proton energy of 6.92 Mev is shown in the upper part of Fig. 1. Peaks appear which arise from B^{10}, B^{11}, and C^{12}. The mass of a light nucleus responsible for a peak was determined by observing the change in momentum of the group as the bombarding energy was varied. Groups arising from nuclei other than B^{10} are labeled on the graph and have been identified with well-known levels. The origin of the peak at $H\rho$=314 kilogauss-centimeters is not known, but energy shifts make it possible to assign it to a level in a nucleus of mass considerably greater than 10.

The unlabeled groups in Fig. 1 are produced by inelastic scattering from levels in B^{10}. A number of measurements of these peaks on different B^{10} targets at different energies, using deuterons as well as protons when possible, were used to calculate the excitation energies. These energies were derived by inserting the measured energy of the inelastic group and the bombarding energy calculated from an elastic group in the relativistic Q equation for 90 degrees. The excitation energies obtained from the proton measurements are listed in the first column of Table I, together with an estimate of the rms error. The deuteron data checked these numbers but with larger errors.

TABLE I. Levels of B^{10} and N^{14}.

B^{10} excitation (Mev)	N^{14} excitation (Mev)
0.717±0.005	2.313±0.005
1.739±0.005	3.945±0.005
2.152±0.005	4.910±0.010
3.583±0.005	5.104±0.010
4.771±0.005	

[10] H. Enge, Rev. Sci. Instr. **23**, 599 (1952).

TABLE II. Relative intensities of inelastic groups.

Levels in B^{10}	6 Mev		7 Mev		7.6 Mev	
	Proton	Deuteron	Proton	Deuteron	Proton	Deuteron
0	100	100	100	100	100	100
0.72	7	7	6	9	4	7
1.74	1	<0.4	1	<0.15	1	<0.15
2.15	6	2	5	4	3	4
3.58	4	···	5	4	7	7

The lower part of Fig. 1 shows sections of the spectrum of scattered deuterons with an incident energy of 6.98 Mev. Portions are shown which correspond to those excitation energies in B^{10} below 4 Mev at which proton peaks were seen. Groups are shown which correspond to the ground state, and excited levels at 0.72, 2.15, and 3.58 Mev. However, in the region where a group from the 1.74-Mev level would be expected, only a low uniform background of deuterons was seen even from bombardments some ten times greater than those necessary to bring out other peaks. This sort of background was common to all plates exposed in this momentum region and was presumed to be instrumental in origin. The measurements were repeated at energies of 7.3 and 7.6 Mev, but no deuteron peak was observed which could be associated with the 1.74-Mev level in B^{10}.

An estimate of the intensities of the inelastic scattering relative to the elastic scattering from B^{10} was obtained by comparing the number of tracks in each peak for a given incident charge on a particular target. The intensities, relative to the proton and deuteron elastic groups at the three energies, are listed in the appropriate column in Table II. Each of these numbers is the average of at least two runs, except in the case of deuteron scattering to the 1.74-Mev level, where the upper limit is derived from the longest exposure undertaken. The relative intensities so measured varied by as much as 30 percent. Errors in current integration may have contributed, but the most likely source of these variations was changes in the current distribution across the bombarded area of the target. Different portions of the target subtend different solid angles at the nuclear plate so that variations in current distribution amount to a change in the effective solid angle of the analyzer. This effect is increased if the targets are not uniform.

At a bombarding energy of 7.6 Mev, a deuteron peak resulting from inelastic scattering from the 4.77-Mev level was seen, but no measurements of its intensity were made. At lower bombarding energies, this group was not seen, presumably because of the Coulomb barrier.

B. Nitrogen 14

For measurements of the inelastic scattering from N^{14} targets of thin Nylon were used. The upper part of

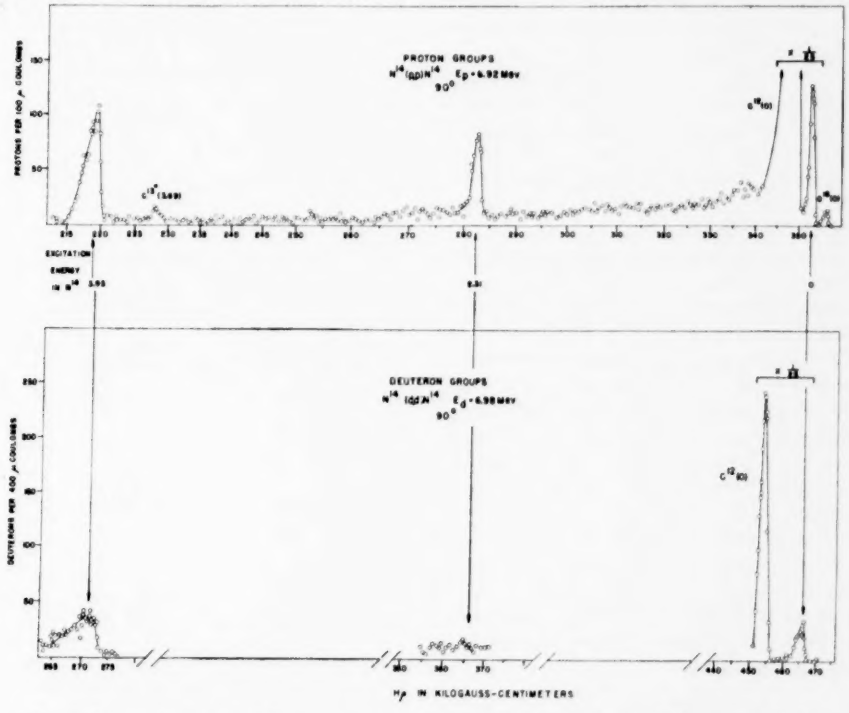

FIG. 2. Scattered proton and deuteron groups observed at 90 degrees from a Nylon target. Incident proton energy = 6.92 Mev. Incident deuteron energy = 6.98 Mev. Groups arising from N^{14} are labeled with the corresponding excitation energy.

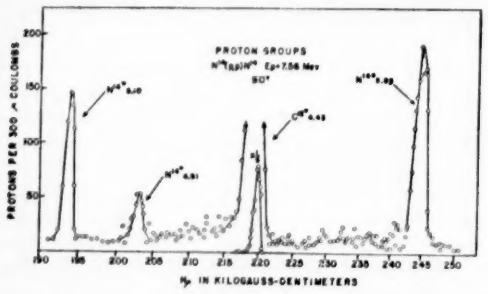

FIG. 3. Inelastic proton groups observed at 90 degrees from a Nylon target with 7.56-Mev bombarding energy.

Fig. 2 shows a momentum spectrum of scattered protons when the incident energy was 6.92 Mev. The ground-state groups from N^{14} and C^{12} appear, and a known level in C^{13}, as well as the first two excited states of N^{14}. A second level in C^{13}, at an excitation energy of 3.89 Mev, is buried under the front edge of the N^{14} 3.95 level at this energy. Because of the low intensity of the groups associated with higher nitrogen levels at this bombarding energy, the next two levels were measured at higher energies. The results with 7.6-Mev incident protons are graphed in Fig. 3. The N^{14} level at 3.95 Mev is shown again, and the C^{12} level at 4.43 Mev appears. Two peaks ascribed to levels in N^{14} at 4.91 and 5.10 Mev also are seen. The measured excitation energies for the four N^{14} levels are given in the second column of Table I with estimated rms errors.

The lower part of Fig. 2 shows portions of the momentum spectrum of scattered deuterons in regions of excitation of N^{14} where proton groups to the three lowest states were seen. A typical run at 6.98 Mev is shown. The ground state and the 3.95-Mev level appear, but nothing above background is seen in the region corresponding to the 2.31-Mev level.

Because the Nylon targets were somewhat unstable under bombardment, less reliance is placed in the nitrogen intensity measurements. Further complication is added by the presence of the C^{13} 3.89 level in the region of the N^{14} 3.95 group. However, exposures on polyethylene targets which contained at least as much carbon as did the Nylon targets showed that the C^{13} level contributes only a small amount to the peaks attributed to the N^{14} 3.95 level. From Fig. 2 for protons the intensity ratios to the ground state are 5 percent and 10 percent for the 2.31- and 3.95-Mev levels, respectively. For deuterons the ratio for the 3.95-Mev state is 10 percent, while an upper limit of about 0.5 percent is set for the 2.31-Mev level. Similar results were obtained at 7.6-Mev bombarding energy. No attempt was made to observe deuteron scattering to the 4.95- and 5.10-Mev states.

IV. DISCUSSION

The level scheme observed for B^{10} up to an excitation of 4.8 Mev agrees with that seen by other investigators.[2,6] The gamma-ray energies measured by Rasmussen[1] agree with the present results within the stated errors.

Thomas and Lauritsen[11] have observed gamma rays of 1.638 and 2.310 Mev, among others, which fit into the present level scheme of N^{14}.

In both B^{10} and N^{14}, a level that scatters protons fails to scatter deuterons at various bombarding energies. Although observations were made only at 90 degrees, it does not seem reasonable to account for this behavior in terms of an angular-momentum or parity-selection rule. Kroll and Foldy[12] have given a possible explanation based on charge-symmetry of nuclear forces. However, in each case here the level in question lies at the place expected for the analog to the ground state of the neighboring isobars. This is illustrated in Figs. 4 and 5 where the level structure for the isobar with $T=0$ ground state is shown, together with the ground states of the $T=1$ members of the triad. The position of these ground states has been drawn after the observed binding-energy differences were adjusted to account for the differences in the $n-H$ masses and Coulomb energy. A rough Coulomb energy difference

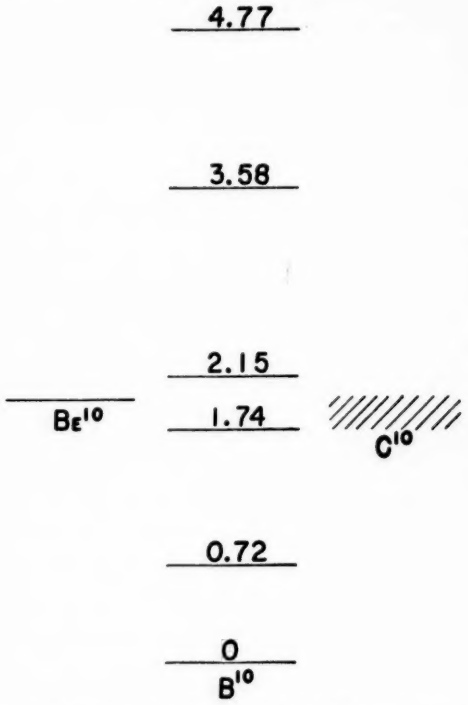

FIG. 4. Energy levels for the mass-10 triad. The positions of the Be^{10} and C^{10} ground states have been corrected for the $n-H$ mass difference and Coulomb energy difference.

[11] R. G. Thomas and T. Lauritsen, Phys. Rev. **88**, 969 (1952).
[12] N. Kroll and L. Foldy, Phys. Rev. **88**, 1177 (1952).

was computed from the relation

$$\Delta E_c = \frac{3}{5}\frac{e^2}{r_0 A^{\frac{1}{3}}}\{(Z+1)Z - Z'(Z'-1)\}. \qquad (1)$$

It is seen that, for both B^{10} and N^{14}, the level that has been observed not to scatter deuterons is close to the position expected for a member of a charge triplet. Since charge-symmetry would not account for the existence of charge triplets, the assumption of charge-independence of nuclear forces, giving rise to a selection rule for isobaric spin, seems a more nearly complete explanation of the present results.

Competition with neutron emission should reduce the intensity of inelastic proton scattering to the $T=1$ states relative to the $T=0$ states. Ignoring the effect of other factors which might govern the intensities, one would expect the intensity of the proton group to the 1.74-Mev level in B^{10} to be $\frac{1}{3}$ of the proton intensity to the $T=0$ levels. Although insufficient information is available to estimate the barrier penetrabilities, at 7.6-Mev incident energy, the energies of both the protons and deuterons emitted to the 1.74 and 2.15 states are nearly equal and greater than the Coulomb barrier, so that one might expect that the barrier penetrabilities do not differ greatly. It is interesting to note that the ratio of proton intensities for these two levels reaches its maximum value of $\frac{1}{3}$ in this case.

Again at 7.6 Mev, Table II shows that the upper limit for deuterons emitted to the 1.74-Mev state is 4 percent of those to the 2.15-Mev level. If the deuteron penetrabilities are approximately equal and if the difference in matrix elements for inelastic deuteron scattering to these two levels is attributed entirely to the isobaric spin-selection rule, the measurements indicate that a $T=0$ component in the wave function of the 1.74-Mev state must be less than 20 percent of the $T=1$ component. This upper limit is considerably greater than the impurity of a few percent estimated by Radicati[13] and quoted by Wilkinson[14] for other $T=1$ levels.

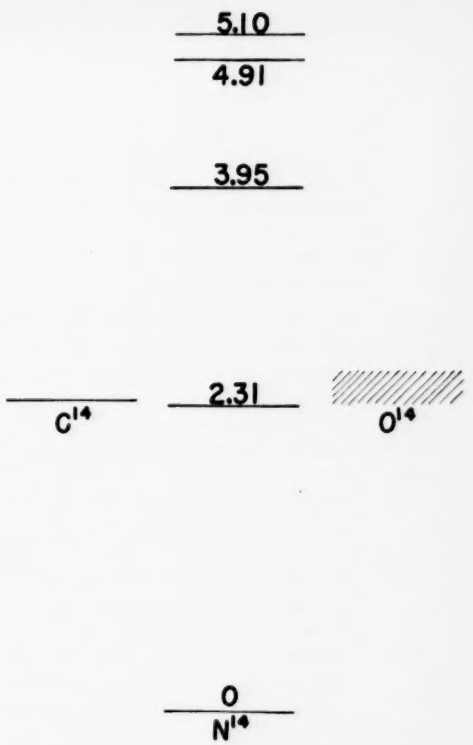

FIG. 5. Energy levels for the mass-14 triad. The positions of the C^{14} and O^{14} ground states have been corrected for the $n-H$ mass difference and Coulomb energy difference.

The authors are indebted to W. A. Tripp, Lee Stone, and Janet Frothingham for assistance in reading many of the plates. We are also grateful to Dr. M. M. Elkind for preparation of the boron targets.

[13] L. A. Radicati, Proc. Phys. Soc. (London) **A66**, 139 (1953).
[14] G. Jones and D. Wilkinson, Phys. Rev. **90**, 722 (1953).

Evaluation of the Interaction Effect in n-p Capture

N. AUSTERN
Cornell University, Ithaca, New York
(Received July 17, 1953)

It is found possible to establish by theoretical arguments that the recently measured thermal n-p capture cross section cannot all be ascribed to the neutron and proton magnetic moments, but that about 8 percent ±5 percent must be contributed by an "interaction" magnetic dipole moment.

I. INTRODUCTION

IT is generally recognized that when a nuclear system is in interaction with the electromagnetic field the nucleons do not merely act as individuals, possessing charges and magnetic moments, but rather their electromagnetic interaction is also somewhat influenced by their nuclear interaction. This influence has been named "interaction effect" (although also called "exchange effect"), because of its association with the mechanism of nuclear interaction, and it is expected to be important only for magnetic multipole radiation. Perhaps the best case from which to obtain some quantitative information about interaction effects is the well-known magnetic dipole transition in n-p capture. Here we would look for some "interaction" magnetic dipole moment, in addition to the neutron and proton moments. The thermal capture cross section is considered in this paper.

Until this year, considerations of n-p capture[1,2] were unable to draw conclusions from the experimental numbers which have been available. Accurate thermal n-p capture measurements have since been made,[3,4] supplementing those of Whitehouse and Graham,[5] and the n-p singlet effective range has been measured in precision scattering experiments.[6] With these new data the situation has been altered to the extent that the chief remaining uncertainties are now of theoretical origin.

The present paper was originally written as an analysis of the result of Hamermesh *et al.*[3] Harris *et al.*,[4] in a brief analysis of their own experiment, have since announced the existence of an interaction moment contribution in the capture cross section. Their analysis is based on the effective range discussion of Bethe and Longmire.[7] In actuality the n-p capture matrix element (assuming no interaction moment) receives such large contributions from regions within the range of nuclear forces that the precision to be expected of the Bethe-Longmire result is by no means obvious. The aim of the present paper is to present a careful study of the sensitivity of the n-p capture matrix element to whatever arbitrary assumptions one might make about the wave functions.

It is found that the limitations of our knowledge of the wave functions lead to an uncertainty of about $1\frac{1}{2}$ percent in the matrix element. In particular, it is very unlikely that the wave functions can be of such a sort that the matrix element is much bigger, for example, than for Hulthén functions. Thus, the existence and sign of the interaction effect are certain, although the magnitude is not known very well. The sign is that which was expected from studies[1,2] of the three-body moment anomaly, and the magnitude also is roughly as expected. Numerically, the effect is 8±5 percent of the cross section.

Interestingly, the new values for $\sigma_c(\text{exp})$ are just about 8 percent larger than the old values. This 8 percent is mostly a consequence of a recalibration[8] of the boron capture cross section, with which that of hydrogen is compared.

II. FORMAL ASPECTS OF THE CALCULATION

If there is no interaction moment contribution, the total n-p capture cross section is given by

$$\sigma_c=(\pi/2)(e^2/Mc^2)(\omega^3/k^3c^3)(\mu_N-\mu_P)^2\left(\int_0^\infty u_0u_s dr\right)^2. \quad (1)$$

Here k is the wave number for the incident system in center-of-mass coordinates, having the value 1.743×10^8 cm^{-1} at the standard neutron velocity, 2200 m/sec. For thermal energies the frequency of the emitted light is $\omega=\epsilon/\hbar$, ϵ being the deuteron binding energy. The wave functions u_0 and u_s are the usual "radial" wave functions for the ground state and for the continuum singlet s state, respectively. Here u_0 is normalized such that $\int_0^\infty(u_0^2+w_0^2)dr=1$, where w_0 is the corresponding D state function. The function u_s is normalized so as to go asymptotically to $\sin(kr+\delta_s)$ as r becomes very large.

The deuteron D state plays no role in Eq. (1). Indeed, the analysis which completely neglects the D state is almost exact, for the reduced amplitude which u_0 possesses by virtue of the presence of the D state is

[1] N. Austern and R. G. Sachs, Phys. Rev. **81**, 710 (1951).
[2] E. P. Gray, thesis, Cornell University, 1952 (unpublished).
[3] Hamermesh, Ringo, and Wexler, Phys. Rev. **90**, 603 (1953).
[4] Harris, Muehlhause, Rose, Schroeder, Thomas, and Wexler, Phys. Rev. **91**, 125 (1953).
[5] W. J. Whitehouse and G. A. R. Graham, Can. J. Research **A25**, 261 (1947)
[6] R. K. Adair (to be published). Hafner, Hornyak, Falk, Snow, and Coor, Phys. Rev. **89**, 204 (1953). The singlet range value which is used here is essentially that of Adair, and is fairly close to the p-p range.
[7] H. A. Bethe and C. Longmire, Phys. Rev. **77**, 647 (1950).
[8] Unpublished Argonne National Laboratory data.

counterbalanced by a corresponding correction to the triplet effective range. However, there is some D state influence on the shape of u_g, even if not on the amplitude, and this enters in the subsequent discussion. The rudiments of effective range theory with tensor forces are presented in the Appendix.

It is convenient to define the functions U_g, W_g, U_s, $\mathfrak{U}_g$, $\mathfrak{W}_g$, $\mathfrak{U}_s$. Here U_g, W_g, and U_s have the same shapes as u_g, w_g, and u_s, only being normalized differently. The relative normalization is given by $N_g=u_g/U_g=w_g/W_g$, so that N_g satisfies

$$N_g^{-2}=\int_0^\infty (U_g^2+W_g^2)dr. \tag{2}$$

The functions $\mathfrak{U}_g$, $\mathfrak{W}_g$, and $\mathfrak{U}_s$ agree asymptotically with U_g, W_g, and U_s, but satisfy differential equations in which the nuclear interaction and centrifugal repulsion terms have been dropped. The normalizations of $\mathfrak{U}_g$ and $\mathfrak{U}_s$, hence of U_g, W_g, and U_s, are given by $\mathfrak{U}_g(0)=\mathfrak{U}_s(0)=1$. Specific forms for the asymptotic functions are

$$\mathfrak{U}_g=e^{-\gamma r}, \tag{3a}$$

$$\mathfrak{U}_s=\sin(kr+\delta_s)/\sin\delta_s\approx 1-r/a_s, \tag{3b}$$

$$\mathfrak{W}_g=\eta e^{-\gamma r}. \tag{3c}$$

Here $\hbar^2\gamma^2/M=\epsilon$, the deuteron binding energy, and η is a parameter which is both defined and utilized only in the Appendix. In terms of U_g and U_s, Eq. (1) becomes

$$\sigma_c=(\pi/2k)(e^2/Mc^2)(\omega/c)^3(\mu_N-\mu_P)^2N_g^2a_s^2|\mathfrak{M}|^2, \tag{4}$$

where

$$\mathfrak{M}\equiv\int_0^\infty U_gU_s dr, \tag{5}$$

and a_s is the zero-energy singlet scattering length.

The calculation of N_g is given in terms of the effective range as

$$N_g^{-2}=1/2\gamma-\tfrac{1}{2}\rho_t(-\epsilon,-\epsilon),$$

where

$$\rho_t(E_1,E_2)=2\int_0^\infty(\mathfrak{U}_{g1}\mathfrak{U}_{g2}-U_{g1}U_{g2}-W_{g1}W_{g2})dr. \tag{A7}$$

As usual the quantity which is found experimentally is $\rho_t(0,-\epsilon)$, so some energy correction is needed in order to compute N_g. This correction is uncertain. It is customarily made with the aid of the "shape dependent parameter" of the effective range theory and amounts to about 1 percent of ρ_t. (Only in the Yukawa potential analysis has the correction been found to be much larger, and Biedenharn has shown this large result to be a spurious consequence of the neglect of tensor forces.[9]) Consistent with the spirit of the present calculation, which does not directly concern itself with the nuclear forces, it is only possible to ignore the energy variation of ρ_t and to tolerate the resulting uncertainty in N_g.

Aside from the calculation of N_g, the principal use made of the effective ranges will be in obtaining limitations on the forms of the wave functions, U_g and U_s. In each case the technique is to assume a form for the wave function, leaving one parameter undetermined, then to choose this parameter so that the wave function leads to a correct value for the effective range. For U_s the procedure is especially simple:

$$\rho_s(0,0)=2\int_0^\infty(\mathfrak{U}_s^2-U_s^2)dr. \tag{6}$$

For U_g the D state introduces some complication. We have

$$\rho_t(-\epsilon,-\epsilon)=2\int_0^\infty(\mathfrak{U}_g^2-U_g^2-W_g^2)dr. \tag{A7}$$

Then

$$\int_0^\infty W_g^2dr=N_g^{-2}\int_0^\infty w_g^2dr=N_g^{-2}P_D, \tag{7}$$

where $P_D=\int_0^\infty w_g^2dr$ is the quantity which is commonly called the "percent of D state" in the deuteron. In terms of P_D we can define

$$\rho_t'\equiv\rho_t(-\epsilon,-\epsilon)+2N_g^{-2}P_D, \tag{8}$$

and base the further calculations on the relation

$$\rho_t'=2\int_0^\infty(\mathfrak{U}_g^2-U_g^2)dr. \tag{9}$$

The quantity ρ_t', the effective range for the s state alone, is uncertain to just that extent that the percent D state is unknown. The uncertainty in the percent D state will lead to an uncertainty in the capture cross section which will be seen to be of about the same size as the other major uncertainties. A reasonable estimate for P_D is $P_D=0.04\pm0.02$.

A tabulation of relevant numbers is given in Table I.

TABLE I. Relevant data.

	Ref. No.
$\sigma_c=0.329\pm0.0046$ at 2200 m/sec	a
$\epsilon=2.225$ Mev, $\gamma=0.2315\times10^{13}$ cm^{-1}	b
$k=1.743\times10^{13}$ cm^{-1}	
$(\mu_N-\mu_P)=-4.7054$	c
$a_s=-23.67\times10^{-13}$ cm	b
$\rho_s=2.6\pm0.2\times10^{-13}$ cm	d
$\rho_t(0,-\epsilon)=1.703(1\pm0.02)\times10^{-13}$ cm	b
$\rho_t'=1.80\pm0.05\times10^{-13}$ cm	

[a] See references 3 and 4.
[b] E. E. Salpeter, unpublished tabulation of low-energy data.
[c] J. E. Mack, Revs. Modern Phys. **22**, 64 (1950).
[d] See reference 6.

[9] Private communication from J. Blatt Doctoral Thesis, Massachusetts Institute of Technology (unpublished). Other calculations also suggest that tensor forces tend to reduce the Yukawa "shape dependent parameter," although they do not seem to show so complete a reduction as is stated above. For the present calculation, however, this is not a major source of error.

TABLE II. Repulsive core parameters [case (*b*)].

R	ξ	ζ	$\mathfrak{M}$
0.3	1.635	1.552	4.032
0.6	2.396	2.480	4.036
0.9	4.525	5.50	4.045
1.1	11.10	23.4	4.022

III. DETAILED CALCULATIONS

It might be supposed impossible to estimate the overlap integral, $\mathfrak{M}=\int_0^\infty U_g U_s dr$, to the accuracy required for our application, i.e., about 2 percent. The corresponding integral for zero-range wave functions, $\mathfrak{M}_0=\int_0^\infty \mathfrak{U}_g \mathfrak{U}_s dr$ is easily computed and is seen to receive a 30 percent contribution from distances $r\leqslant 2\times10^{-13}$ cm. Even for wave functions with the correct ranges the contribution from $r\leqslant 2\times10^{-13}$ cm is still about 10 percent. Nevertheless $\mathfrak{M}$ can be estimated to the requisite accuracy, a result which is only suggested by the analysis of Bethe and Longmire. A particularly satisfying result for the present purpose is that the upper limit on $\mathfrak{M}$ is especially sharp and plausible.

A variational calculation for $\mathfrak{M}$ would be very pleasant, as the extrema found in such a way would be reliable. The effective ranges would appear as conditions on the variations. Unfortunately, we also want to limit the possible wave functions to the class of, what might be called, "reasonable" functions. This class seems not to have any very sharp mathematical definition. Essentially, a "reasonable" wave function is one for which the associated nuclear potential is reasonable. We can require, for example, that $U_g(0)=U_s(0)=0$; that U_g and U_s everywhere be bounded between zero and the asymptotic functions $\mathfrak{U}_g$ and $\mathfrak{U}_s$; that they go over monotonically to the asymptotic forms; that the associated potential have not too long a range. For a problem as ill-defined as this one, an empirical approach seems advised, even if the reliability of the answer is left uncertain.

Nearly all the functions which will be tested will satisfy all of the conditions just listed. The functions are made to satisfy Eqs. (6) and (9) and their overlap $\mathfrak{M}$ computed in each case. The choice of functions tested is designed to explore systematically the range between extreme localization at $r=0$, and extreme repulsion from $r=0$. Our requirement that the functions fit the effective ranges establishes a familiar connection. Namely, functions which are strongly localized at $r=0$ must become asymptotic more slowly than functions which are small near $r=0$, i.e., they must arise from "long-tailed" nuclear potentials.

TABLE III Damping parameters ζ and ξ as functions of α and β.

α	1	0.7	0.5	0.3	0
ζ	1.340	0.987	0.694	0.351	impossible
β	1	0.7	0.5	0.3	0
ξ	1.207	0.942	0.718	0.469	0

The cases which follow below are all fitted to $\rho_s=2.6\times10^{-13}$ cm and $\rho_t'=1.8\times10^{-13}$ cm, but with the effects of differential variations of the effective ranges being indicated in several typical cases. All the numbers below have dimensions 10^{-13} cm or 10^{13} cm^{-1}.

(a) *U_s and U_g of Hulthén shape*

$$U_s=1-r/a_s-e^{-\xi r},$$
$$U_g=e^{-\gamma r}-e^{-\xi r},$$
$$\xi=1.207,\quad \zeta=1.340,$$
$$\mathfrak{M}=4.031[1-0.036d\rho_s-0.102d\rho_t'].$$

(b) *Hard core types*

$$U_g=e^{-\gamma r}[1-e^{-\xi(r-R)}], \quad \text{for } r>R$$
$$=0, \quad \text{for } r<R$$
$$U_s=(1-r/a_s)[1-e^{-\xi(r-R)}], \quad \text{for } r>R$$
$$=0, \quad \text{for } r<R.$$

TABLE IV. $\mathfrak{M}$ as a function of α and β.

$\beta\backslash\alpha$	1	0.7	0.5	0.3
1	4.031	3.987	3.908	3.643
0.7	4.046	4.021	3.958	3.712
0.5	4.050	4.040	3.990	3.759
0.3	4.072	4.080	4.041	3.828
0	4.334	4.364	4.340	4.146

The values of ξ, ζ, and $\mathfrak{M}$ for this case are listed in Table II as functions of R.

For the case $R=0.6$ we also have

$$\mathfrak{M}=4.036[1-0.093d\rho_t'-0.042d\rho_s].$$

(c) *"Maximum" hard core*

$$U_g=e^{-\gamma r}, \quad \text{for } r>b_t$$
$$=0, \quad \text{for } r<b_t$$
$$U_s=(1-r/a_s), \quad \text{for } r>b_s$$
$$=0, \quad \text{for } r<b_s.$$

Interestingly, the quantities b_s and b_t are roughly equal.

$$b_s=1.235,\quad b_t=1.161.$$

To first approximation $\mathfrak{M}$ is independent of b_t here, hence of ρ_t'.

$$\mathfrak{M}=3.99[1-0.089d\rho_s].$$

(d) *U_g Hulthén—U_s maximum core*

$$\mathfrak{M}=3.85.$$

(e) *U_g maximum core—U_s Hulthén*

$$\mathfrak{M}=3.93.$$

(f) *Long-tailed functions*

The class of functions considered here has the property that the functions become asymptotic rather more

slowly than the ones considered above, so they must be closer to asymptotic in the region near $r=0$. An interesting analytical realization of the class envisaged can be achieved with a modified Hulthén type, where we do not require that $U_g(0)$ and $U_s(0)$ be zero. Thus, we now consider

$$U_g=e^{-\gamma r}-\alpha e^{-\xi r},$$
$$U_s=1-r/a_s-\beta e^{-\xi r},$$

and $\mathfrak{M}$ can be studied as a function of α and β. Values of the damping parameters ζ and ξ, and the overlap integral $\mathfrak{M}$ are given in Tables III and IV.

For the case $\beta=1$, $\alpha=0.5$, we also have

$$\mathfrak{M}=3.908[1-0.145d\rho_t'-0.037d\rho_s].$$

(g) *U_g long tail—U_s max core*

The case considered here is $\alpha=0.5$.

$$\mathfrak{M}=3.66.$$

(h) *U_g max core—U_s long tail*

Here $\beta=0.5$, $\mathfrak{M}=3.89$.

It was found above that it is only with difficulty, for the extreme cases of the long tailed functions, that $\mathfrak{M}$ can be made much bigger than about 4.05. The long-tailed functions, $\beta=0$ and 0.3 and $\alpha=0.3$, are limiting cases which are of interest chiefly because they show how unreasonable the wave functions have to become before $\mathfrak{M}$ can be made very large. In these cases the wave functions actually approach asymptotic so slowly that they would imply that a significant part of the n-p interaction would have a range of the order of or greater than the deuteron radius.

The reliability of the upper limit of $\mathfrak{M}$ can be made more plausible by considering a reordering of $\mathfrak{M}$, according to the method of Bethe and Longmire.[7] They find

$$\mathfrak{M}=\mathfrak{M}_0-\tfrac{1}{4}(\rho_s+\rho_t')+C, \tag{10}$$

where

$$C\equiv\tfrac{1}{2}\int_0^\infty[(\mathfrak{U}_g-\mathfrak{U}_s)^2-(U_g-U_s)^2]dr. \tag{11}$$

Their approximation for $\mathfrak{M}$ is obtained if $C=0$. Now C goes positive only if the first term of the integrand dominates the second. But also, to make C positive and large, the dominating must occur in a region where the first term is large enough to contribute strongly. Thus, it is interesting to study the function

$$C_0(R)\equiv\tfrac{1}{2}\int_0^R(\mathfrak{U}_g-\mathfrak{U}_s)^2dr. \tag{12}$$

This function is shown in the accompanying graph (Fig. 1). Clearly, to obtain $C\gtrsim 0.15$, say, it is necessary that U_g and/or U_s differ considerably from asymptotic for distances $r\gtrsim 3\times10^{-13}$ cm. Thus, the long tailed functions do provide a satisfactory study of large $\mathfrak{M}$.

IV. CONCLUSIONS

The theoretical value for σ_c is obtained merely by substituting $\mathfrak{M}$ into Eq. (4). Suppose we take $\mathfrak{M}$ for the Hulthén case. Then

$$\sigma_c(\text{theor})=0.303 \text{ b}.$$

Experimentally, σ_c is about

$$\sigma_c(\text{exp})=0.330 \text{ b}.$$

The difference between these two numbers, 0.027 b, is attributed to the interaction moment. It is 8 percent of 0.330 b.

Now the work in the preceding section shows that it takes quite unreasonable wave functions to make $\mathfrak{M}$ much larger than the value obtained for the Hulthén

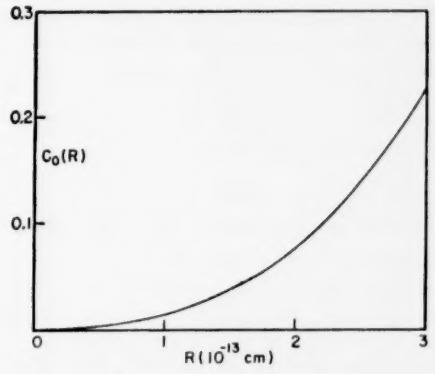

FIG. 1. The function $C_0(R)$.

case. To fit experiment, $\mathfrak{M}$ would actually have to be as large as $\mathfrak{M}(\text{"exp"})=4.20$, well above the range of values given by reasonable functions. For the Hulthén case, $\mathfrak{M}$ lies near the upper end of the range of reasonable values. Although certain of the repulsive core cases do give much smaller $\mathfrak{M}$ values, these are mostly interesting as indicating that U_g and U_s are probably not radically different in shape, as we do expect the interaction effect to be fairly small. (Thus, the calculation suggests as an incidental result that the assumption of a large respulsive core interaction in one of the s states probably requires a similar core for the other.) Altogether, from the set of calculations which are listed,[12] it seems plausible to claim about ±1–2 percent as the accuracy with which $\mathfrak{M}$ can be predicted, exclusive of variations of the effective ranges, and to take the Hulthén value as central.

The various errors which must be considered are (a) $\sigma_c(\text{exp})$ is ±1 percent; (b) $\mathfrak{M}$ is uncertain to ±1–2

[12] Additional calculations along the lines of those reported here were performed by W. A. Newcomb and E. E. Salpeter; see Salpeter, Phys. Rev. **82**, 60 (1951). Using the measured singlet effective range, their formulas for Yukawa, Gauss, and exponential potentials give results in complete agreement with the above material.

percent, by virtue of our not knowing the wave functions, so σ_c(theor) is uncertain to about ± 3 percent; (c) because ρ_s is uncertain by $\pm 0.2\times 10^{-13}$ cm, $\mathfrak{M}$ is uncertain by about 1 percent, so σ_c(theor) by ± 2 percent; (d) because P_D is uncertain by about ± 2 percent, ρ_t' is uncertain by $\pm 0.05\times 10^{-13}$ cm, so σ_c(theoret.) by about ± 2 percent; (e) ρ_t itself is uncertain, leading to about a ± 2 percent uncertainty in σ_c(theor). It is apparent that these uncertainties can be made to add up, and even to cancel the interaction moment effect, but the errors seem genuinely independent, the square root of the sum of their squares being 5 percent, so the effect would seem to be quite real.

With regard to the uncertainty in ρ_t, listed above as (e), we have both the energy correction from $\rho_t(0, -\epsilon)$ to $\rho_t(-\epsilon, -\epsilon)$, and also the experimental uncertainty in $\rho_t(0, -\epsilon)$. These enter into σ_c(theoret.) both through $N_{\mathfrak{s}}^{-2}$ and through $\mathfrak{M}$, these two appearances partially canceling. For the above this cancellation has been considered as about 50 percent complete.

I am grateful to R. Margulies for some assistance with the numerical work and to J. Blatt, E. E. Salpeter, and P. Morrison for useful discussions.*

APPENDIX

Effective Range Theory with Tensor Forces

Two eigenwaves[13] of the scattering matrix are α, γ and we label the S and D functions as $U^{\alpha,\gamma}$ and $W^{\alpha,\gamma}$. These eigenwaves have the property that U^α and W^α have the same phase shift δ^α, similarly for state γ. Define $\eta^{\alpha,\gamma}$ as $\eta^{\alpha,\gamma}=\lim_{r\to\infty}(W^{\alpha,\gamma}/U^{\alpha,\gamma})$. For state α we assume little D admixture, so this is the state which scatters strongly. We know η^α is very small, and η^α goes to zero as the energy goes to zero. Since $\eta^\alpha\eta^\gamma=-1$, state γ is mostly D wave, and scatters weakly. State γ can thus be ignored. The following discussion only applies to state α, so the superscript can be dropped.

Following the method of Bethe,[14] the coupled Schrödinger equations are written for two different energies, multiplied by appropriate functions, and added judiciously.

$$U'\left\{\frac{\partial^2 U}{\partial r^2}+\frac{M}{\hbar^2}[(E+V_c)U+2\sqrt{2}V_T W]\right\}=0,$$

$$W'\left\{\frac{\partial^2 W}{\partial r^2}-\frac{6W}{r^2}+\frac{M}{\hbar^2}[(E+V_c-2V_T)W+2\sqrt{2}V_T U]\right\}=0,$$

$$U\left\{\frac{\partial^2 U'}{\partial r^2}+\frac{M}{\hbar^2}[(E'+V_c)U'+2\sqrt{2}V_T W']\right\}=0,$$

$$W\left\{\frac{\partial^2 W'}{\partial r^2}-\frac{6W'}{r^2}+\frac{M}{\hbar^2}[(E'+V_c-2V_T)W''+2\sqrt{2}V_T U']\right\}=0.$$

Therefore,

$$U'\frac{\partial^2 U}{\partial r^2}+W'\frac{\partial^2 W}{\partial r^2}-U\frac{\partial^2 U'}{\partial r^2}-W\frac{\partial^2 W'}{\partial r^2}=(k'^2-k^2)(UU'+WW'). \quad \text{(A1)}$$

Now consider the comparison functions $\mathfrak{U}$, $\mathfrak{W}$.

$$U\underset{r\to\infty}{\longrightarrow}\mathfrak{U}, \quad W\underset{r\to\infty}{\longrightarrow}\mathfrak{W}.$$

Including normalizations, the explicit forms for $\mathfrak{U}$ and $\mathfrak{W}$ are

$$\mathfrak{U}=\sin(kr+\delta)/\sin\delta, \quad \mathfrak{W}=\eta\sin(kr+\delta)/\sin\delta. \quad \text{(A2)}$$

Then the equation corresponding to (A1) is

$$\mathfrak{U}'\frac{\partial^2\mathfrak{U}}{\partial r^2}+\mathfrak{W}'\frac{\partial^2\mathfrak{W}}{\partial r^2}-\mathfrak{U}\frac{\partial^2\mathfrak{U}'}{\partial r^2}-\mathfrak{W}\frac{\partial^2\mathfrak{W}'}{\partial r^2}=(k'^2-k^2)(\mathfrak{U}\mathfrak{U}'+\mathfrak{W}\mathfrak{W}'). \quad \text{(A3)}$$

Subtraction of (A1) from (A3) and integration yields the result

$$(k'^2-k^2)\int_0^\infty(\mathfrak{U}\mathfrak{U}'+\mathfrak{W}\mathfrak{W}'-UU'-WW'')dr=-\left[\mathfrak{U}'\frac{\partial\mathfrak{U}}{\partial r}+\mathfrak{W}'\frac{\partial\mathfrak{W}}{\partial r}-\mathfrak{U}\frac{\partial\mathfrak{U}'}{\partial r}-\mathfrak{W}\frac{\partial\mathfrak{W}'}{\partial r}\right]_{r=0}$$

$$=-(1+\eta\eta')(k\cot\delta-k'\cot\delta').$$

Thus,

$$k\cot\delta-k'\cot\delta'=\frac{k^2-k'^2}{1+\eta\eta'}\int_0^\infty[(1+\eta\eta')\mathfrak{U}\mathfrak{U}'-UU'-WW'']dr. \quad \text{(A4)}$$

Suppose E' is taken to be $E'=0$. Then $\eta'=0$, and

$$k\cot\delta=-1/a+\tfrac{1}{2}k^2\rho(0,E), \quad \text{(A5)}$$

where

$$\rho(0,E)=2\int_0^\infty(\mathfrak{U}\mathfrak{U}_0-UU_0-WW_0), \quad \text{(A6)}$$

and a is the scattering length.

Thus, η drops out when the effective range theory is referred to zero energy. Inasmuch as only the effective range $\rho(0, E)$ has been defined so far, we are still free to extend the definition and to set

$$\rho(E_1,E_2)\equiv 2\int_0^\infty dr(\mathfrak{U}_1\mathfrak{U}_2-U_1U_2-W_1W_2). \quad \text{(A7)}$$

This is not the integral which appears in (A4), but it is just as well not to have $\rho(E_1, E_2)$ cluttered up with η's.

* *Note added in proof.*—One further measurement of σ_c(exp) has since been published. G. von Dardel and A. W. Waltner [Phys. Rev. **91**, 1284 (1953)] give the value 0.321 ± 0.005 barns, which implies a 6 percent interaction moment contribution.

[13] For details of this formalism, consult F. Rohrlich and J. Eisenstein, Phys. Rev. **75**, 705 (1949); or J. Schwinger, lectures on nuclear physics.

[14] H. A. Bethe, Phys. Rev. **76**, 38 (1949).

Capture Gamma Rays from the Proton Bombardment of Be^9†

W. F. HORNYAK AND T. COOR
Brookhaven National Laboratory, Upton, New York
(Received July 28, 1953)

The gamma rays produced at the 0.993- and 1.085-Mev proton capture resonances in Be^9 were studied using a NaI scintillation spectrometer. Gamma rays of energies 0.41, 0.72, 1.02, 1.43, and 7.5 Mev, and energies 0.72, 1.43, 2.0–2.5, and 6.8$_9$ Mev were observed for the two levels, respectively. Absolute yields were determined, and the possible decay schemes are discussed.

1. INTRODUCTION

THE excitation function for proton capture radiation from Be^9 has been extensively studied,[1] with numerous resonances being evident. The radiative decay of the broad resonance observed at 998±4 kev (7.48-Mev excitation in B^{10}) was found to proceed mostly by the direct transition to the ground state of B^{10} giving a 7.38±0.07-Mev[2,3] gamma ray with a thick target (Be metal) yield of 17.8 $\gamma/10^9 p$.[4] The radiation from the narrow resonance at 1087±2 kev (7.56-Mev excitation in B^{10}) was found to consist predominantly of 6.8- and 0.72-Mev gamma rays of approximately equal intensity, indicating the major mode of decay to be a cascade through the first excited state in B^{10} at 0.72 Mev.[3,5] The thick target yield was observed to be 1.01 $\gamma/10^9 p$.[4]

The object of this experiment is to investigate further the nature of the capture radiation from these two resonances.

2. APPARATUS

The Brookhaven electrostatic accelerator was used to supply protons for the bombardment of various Be targets mounted in a thin wall (0.015 in.) brass target holder. The gamma-ray detector was a NaI scintillation crystal, 4 cm in diameter and 3 cm in height, used in conjunction with an electronic single-channel pulse-height analyser. The source to detector distance was 2.0 cm, measured from the center of the $\frac{3}{32}$-in. diameter collimated proton beam to the front flat face of the crystal, the cylindrical axis of the crystal being at 90° relative to the beam. Lead shielding was used to reduce the background, notably the x-rays from the several tantalum collimators used. This shielding was found necessary to reduce the electronic pile up of pulses and the resulting lowering of the resolution of the various lines observed in the scintillation pulse height spectrum.

3. DETECTOR CALIBRATION

The differential pulse-height spectrum for various gamma rays observed with the NaI crystal used in this experiment is shown in Fig. 1. The sources consisted of the 1.28-Mev γ ray from Na^{22}, the 3.08-Mev γ ray from $C^{12}(d,p\gamma)$, and the 6.13-Mev γ ray from $F^{19}(p,\alpha\gamma)$ at the 340-kev resonance. Only the total conversion line and the Compton electron peak are detected for the lowest energy γ ray, the pair production being relatively small. For the higher-energy γ rays, the annihilation quantum escape peaks are seen to gain in prominence as the incident gamma-ray energy is raised.

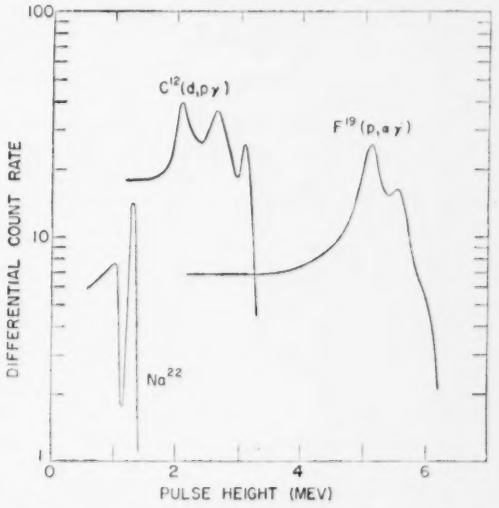

FIG. 1. The differential pulse-height spectrum for a NaI crystal (4 cm in diameter and 3 cm in height) irradiated by several γ-ray sources; Na^{22}—1.28 Mev, $C^{12}(d,p\gamma)$—3.08 Mev, and $F^{19}(p,\alpha\gamma)$ —6.13 Mev.

The counting rate observed at any of the line structures described above, with a unit strength source, will in general depend in a complicated way on the geometry and the various electro-magnetic cross sections, the division of the total effect into "solid angle" and "efficiency" being to a large extent arbitrary. For example, the attempt to define solid angle along conventional lines leads in general to efficiencies which are functions of source to detector distance as well as

† Research done at Brookhaven National Laboratory under contract with the U. S. Atomic Energy Commission.
[1] F. Ajzenberg and T. Lauritsen, Revs. Modern Phys. **24**, 231 (1952).
[2] R. L. Walker (private communication).
[3] Fowler, Lauritsen, and Lauritsen, Revs. Modern Phys. **20**, 236 (1948).
[4] W. A. Fowler and C. C. Lauritsen, Phys. Rev. **76**, 314 (1949).
[5] Lauritsen, Fowler, Lauritsen, and Rasmussen, Phys. Rev. **73**, 636 (1948).

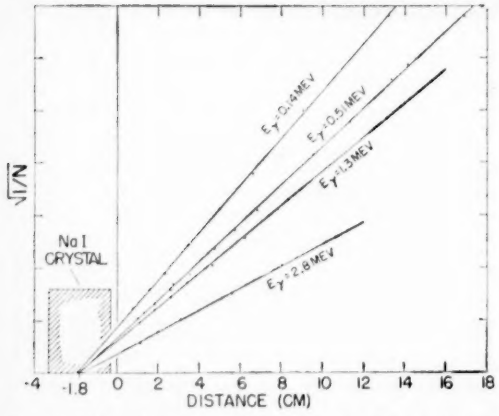

FIG. 2. The variation of $1/N^{\frac{1}{2}}$, where N is the counting rate at the total conversion line peak, with the source to detector distance for several γ-ray sources. The NaI crystal was mounted in a $\frac{1}{32}$-in. thick Al can packed with MgO as a reflector.

of gamma-ray energy. It was found (refer to Fig. 2) that the count rate with the channel discriminator set to the total conversion line peak could be empirically fitted with an "inverse square law,"

$$N \propto (d+x)^{-2},$$

with x the distance from the source to the front face of the crystal and with d a constant relatively independent of gamma-ray energy. Thin sources under $\frac{1}{4}$ in. in diameter were used and located on the axis of symmetry of the crystal. This law was found to hold to ± 5 percent for $x \geq 1.0$ cm, $E_\gamma \geq 140$ kev, and with $d=1.5$ cm. The entire variation of d with energy is within ± 0.1 cm. The area to be used with the inverse square law was arbitrarily taken as the cross-sectional area of the crystal used in this experiment, which was 4π cm^2. Thus, the "solid angle" for this particular crystal may be written as

$$\Omega = (x+1.5)^{-2} \text{ fraction of a sphere,} \qquad (1)$$

with x in cm.

Coincidence γ-γ and β-γ counting with Na^{22},[6] Na^{24}, Co^{60}, and Au^{198} were used to determine the efficiency from the area under the total conversion line, the effect of the electronic channel width being appropriately corrected for each time. The results are given in Fig. 3. An interesting check on the efficiency curve thus obtained was made using the single γ-ray emitting source Cs^{137}. The discriminator was set to count all pulses above tube noise (appropriate extrapolations to zero pulse height were made). The discriminator was then set to a narrow channel and the area under the total conversion line determined. After an experimental correction is made to the integral count rate, necessitated by the internal conversion x-ray in Cs^{137}, a comparison of this rate with the rate observed under the total conversion line gives the efficiency for the latter, since the efficiency for the former may be readily calculated. In this comparison it is also necessary to determine the appropriate d in the solid angle expression for the case of the integral pulse-height counting (this experiment was restricted to large source to detector distances).

The efficiency for counting all scintillation events is calculated from the total absorption coefficient, which for the Cs^{137} γ ray (0.662 Mev) is 0.276 cm^{-1}.[7,8] The calculation is simple when the variation of the solid angle over the crystal is kept small by using a large source to detector distance. The effect resulting from partial energy transfer to the scintillator by electrons or scattered γ rays escaping through the surface is negligible due to the high signal-to-noise ratio generally realized. A considerable simplification results from the fact that multiple processes in the interactions of the γ ray within the NaI crystal need not be considered since the phosphor decay time and amplifier response time are long compared to the time within which all such multiple interactions occur.

The resulting total conversion line efficiency for Cs^{137} is also given in Fig. 3. The point on this curve at 6.1 Mev was obtained from the $F^{19}(p,\alpha\gamma)$ reaction using a thick CaF_2 target and $E_p=370$ kev. The yield was taken as 16.4 $\gamma/10^6 p$, the average of the absolute γ-ray determination and the absolute α-particle deter-

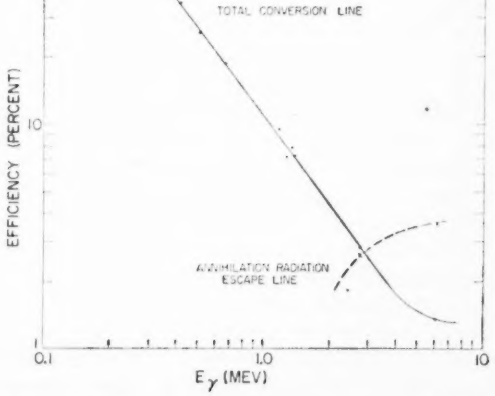

FIG. 3. The measured efficiency for a NaI crystal (4 cm in diameter and 3 cm in height) as determined by the area under the total conversion lines and the area under the two quantum annihilation radiation escape lines. The experimental errors on the points are ± 5 percent, except for the points at 6.1 Mev where the error is ± 15 percent.

[6] During the course of this work a K-capture branch in Na^{22} of 7.1 ± 2.0 percent was discovered.

[7] G. R. White, National Bureau of Standards Report 1003, 1952 (unpublished).

[8] C. M. Davisson and R. D. Evans, Revs. Modern Phys. 24, 79 (1952).

mination obtained by previous experimenters.[3,9] The part of the efficiency curve below 3.5 Mev can be fitted with the expression

$$\eta = 10.6 E_\gamma^{-1.31} \text{ percent}, \quad (2)$$

with E_γ in Mev. The two points on the annihilation radiation escape peak curve of Fig. 3 were obtained using Na^{24} and $F^{19}(p,\alpha\gamma)$ sources.

4. RESULTS

The differential pulse-height spectrum of γ rays, having energies below 2 Mev, obtained with a thick Be metal target bombarded at 0.860 and 1.060 Mev, and a thin (4-kev) evaporated Be metal target bombarded at 1.085 Mev are shown in Fig. 4. The beam current was limited to less than 1 μa with the thin

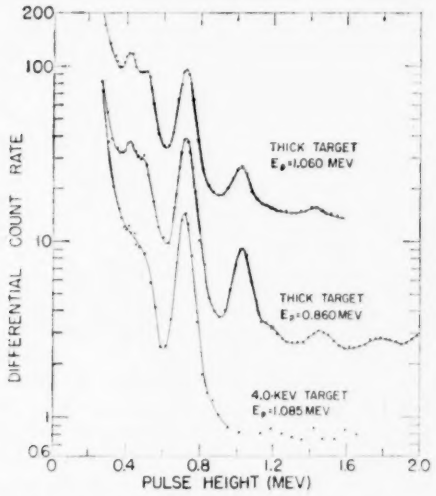

FIG. 4. The differential pulse-height spectrum for $Be^9(p,\gamma)$ γ rays below 2.0 Mev for several bombardment conditions.

target to prevent its deterioration. The energies of the prominent total conversion lines were determined by comparison with the lines produced by the 0.511- and 1.277-Mev radiations from Na^{22}. The resulting energies are $0.41_4 \pm 0.01$, $0.71_6 \pm 0.01$, 1.02 ± 0.01, 1.43 ± 0.01, and 1.78 ± 0.02 Mev. Only a continually rising background was observed below 0.4 Mev, with any possible structure being obscured by background not originating in the target reaction. The prominent edge at 0.51 Mev is due partly to the Compton line of the 0.72-Mev radiation and to annihilation radiation from the lead shield produced by energetic γ rays. This latter point was checked by varying the shield geometry. The interpretation of the anomaly at $\sim$1.2 Mev is not clear.

The differential pulse-height spectrum for the energetic γ rays under identical bombardment conditions

[9] Chao, Tollestrup, Fowler, and Lauritsen, Phys. Rev. **79**, 108 (1950).

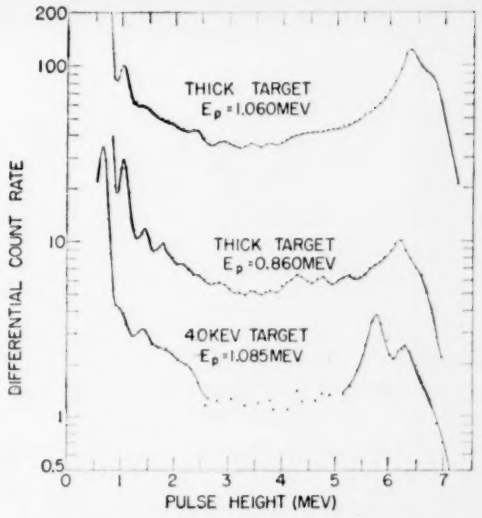

FIG. 5. The differential pulse-height spectrum for $Be^9(p,\gamma)$ γ rays for several bombardment conditions.

is shown in Fig. 5. In each case the strongest prominence near the high-energy end of the spectrum is interpreted as the two annihilation quanta escape peak, $E_\gamma - 1.02$ Mev, of the highest energy γ ray present (compare with Fig. 1). The γ-ray energies obtained for the thick target runs at $E_p = 0.860$ and 1.060 Mev are 7.1 and 7.4 Mev, respectively, and $6.8_9 \pm 0.1$ for the thin target run at $E_p = 1.085$ Mev. In addition, it is noted that the one-annihilation-quantum escape peak, $E_\gamma - 0.51$ Mev, is clearly resolved for the case of the thin-target run and is only barely evident for the thick-target runs because of the energy spread resulting from the reaction proceeding at all energies below the incident proton beam energy. Although the anomalies in

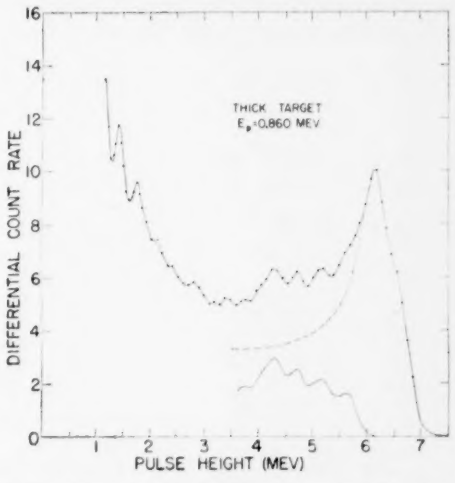

FIG. 6. The differential pulse-height spectrum for $Be^9(p,\gamma)$ γ rays, showing the resolving of the structure above 4 Mev.

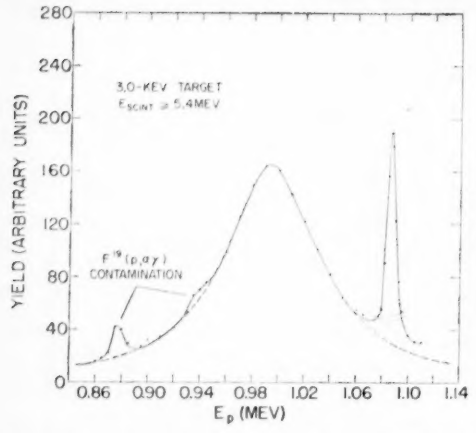

FIG. 7. The thin target $Be^9(p,\gamma)$ yield of energetic scintillation events. The fluorine contamination was introduced to establish the proton energy scale. The dashed curve represents a single-level dispersion formula fit of the experimental points.

the curves between scintillation energies of 2–4 Mev are reproducible, their interpretation is not clear except perhaps for the peak at 2.1_5 Mev which is probably a total conversion line. Figure 6 is a linear scale plot of the thick target data taken at $E_p=0.860$ Mev to emphasize the resolution of the structure above 4 Mev. The simplest interpretation of the four peaks at 4.2, 4.7, 5.1, and 5.6 Mev is that they are the two- and one-annihilation-quantum escape peaks of two γ rays of energy 5.2 and 6.1 Mev.

With the discriminator set to accept scintillation pulses greater than 5.3_5 Mev, the thin target (3-kev) yield curve of Fig. 7 was obtained. A small amount of fluorine contamination of the beryllium target was introduced to establish the voltage scale through the $F^{19}(p,\alpha\gamma)$ resonances at 874 and 935 kev. Resonance energies for the $Be^9(p,\gamma)$ reaction of 993 ± 2 and 1085 ± 2 were determined, correction for the target thickness having been made. It was found that the broad resonance could be fitted with a one-level dispersion formula (the dotted line extensions of the curve in Fig. 7). The total level width found was 88 ± 3 kev. No direct determination of the width of the narrow resonance was made although the value of 4 kev obtained by Fowler and Lauritsen[4] was found to be consistent with the present results.

Figure 8 shows the thin-target (3-kev) excitation function obtained when the discriminator channel was set on the 0.72-Mev line. The corresponding thick Be metal target yield is given in Fig. 9. The background of higher energy γ rays falling in the channel has been corrected for, the correction never exceeding 15 percent. In all cases the thickness of the thin targets was determined by a comparison of the resonant thin-target yield of 0.72-Mev radiation with the corresponding "step" in the thick-target yield. Also shown in Fig. 9 is the thick-target yield of 1.02-Mev radiation. In this case the aforementioned background correction varied from 20 to 48 percent. Note the absence of any prominent rise in the yield at the narrow resonance.

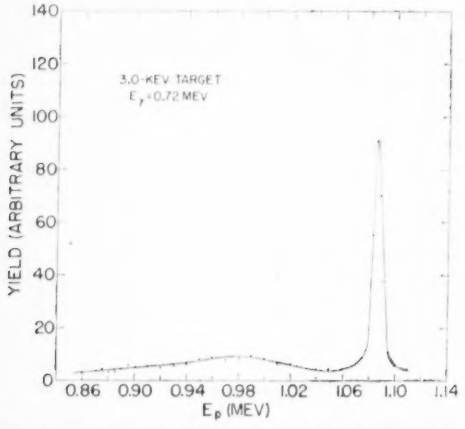

FIG. 8. The thin-target $Be^9(p,\gamma)$ yield of 0.72-Mev γ radiation.

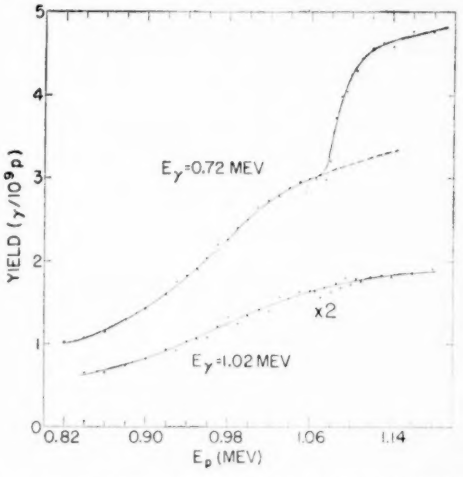

FIG. 9. The thick-target $Be^9(p,\gamma)$ yields of 0.72- and 1.02-Mev γ radiations.

The absolute thick (Be metal) target yield of the γ radiation found in this experiment is given in Table I. In these determinations absolute counting rates for $E_\gamma<3$ Mev were determined by measuring areas under the total conversion lines and using the appropriate NaI calibration of Fig. 3 and Eq. (1). In the case of the 5.2- and 6.2-Mev radiations the areas under the peaks ascribed to the two annihilation quantum escape lines were used. The estimate of the yield of 2.0–2.5 Mev radiation for the narrow resonance was made on the basis of a rough comparison with Na^{24}.

In each case of Table I the absolute count rate of the most energetic γ ray was determined by a comparison of the total area above a pulse height $0.92(E_{\gamma\,\max}-1.02)$

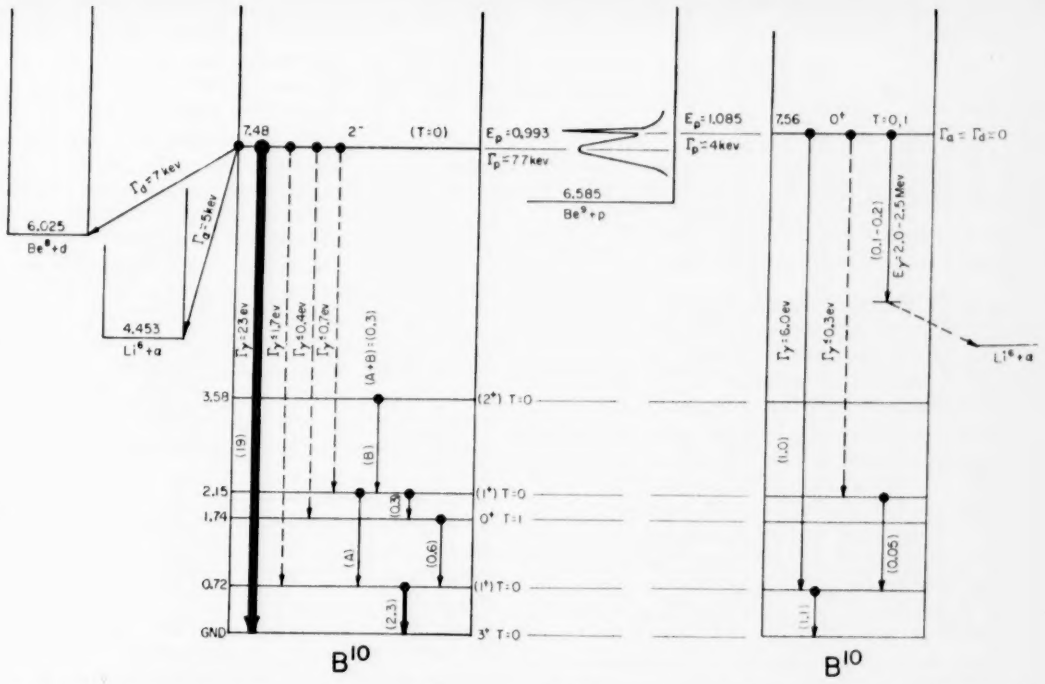

FIG. 10. The decay modes of the two prominent Be^9p resonances. All energy units are in Mev except where specifically otherwise noted. The quantities in parentheses labeling the γ-ray transitions are $\gamma/10^9p$. The sum of the transitions A and B is indicated, $A \gg B$. The other quantities in parentheses represent tentative spin and parity, or isotopic spin assignments. The dotted transitions are inferred and have not been experimentally observed.

Mev with the corresponding area for the $F^{19}(p,\alpha\gamma)$ radiation. Appropriate corrections for the variation of γ-ray cross sections with energy were made. The above procedure to a large extent avoids the problems arising from the use made of thick targets in some of the runs.

The yield of 0.72-Mev radiation originating from the narrow resonance was determined from the step in the thick target curve of Fig. 9. The yields of the other radiations from the narrow resonance were then determined from the absolute counting rates observed in Figs. 4 and 5, relative to the 0.72-Mev line. The yields of the 0.72- and 1.02-Mev radiations from the broad resonance were determined by fitting integrated dispersion formula yields to the thick-target curves of Fig. 9. The difference in absolute counting rates at 1.060 and 0.860 Mev for the other radiations relative to the corresponding difference for the 0.72- and 1.02-Mev lines was used to calculate the remaining absolute yields.

5. DISCUSSION OF RESULTS

The yield of the various γ radiations from the narrow resonance (refer to Table I, and Fig. 10) substantiate the results observed by previous investigators in that the principle mode of decay is through the first excited state in B^{10} at 0.72 Mev. It will be noted that the energy balance 0.72+6.89=7.61 Mev is within experimental error of the value 7.56 Mev calculated from the mass values. The agreement of the absolute yields for these two lines with one another is an indication of the internal consistency of the measurements and an indirect check of the $F^{19}(p,\alpha\gamma)$ yield. The small amount of 1.43-Mev radiation was assumed to also cascade through the 0.72-Mev state, thus giving rise to a 5 percent correction (see Table I, and Fig. 10). The average value of $1.0_0\pm0.1$ cascades per 10^9 protons agrees well with the value reported by Fowler and Lauritsen.[4] The simplest explanation for the 2.0–2.5 Mev radiation,

TABLE I. The absolute thick (Be metal) target yield of γ rays.[a]

Thick target 860 kev		993 kev resonance (7.48 Mev in B^{10}) Γ=88±3 kev		1085 kev resonance (7.56 Mev in B^{10}) Γ≃4 kev	
E_γ(Mev)	Yield $\gamma/10^9p$	E_γ(Mev)	Yield $\gamma/10^9p$	E_γ(Mev)	Yield $\gamma/10^9p$
0.41	0.05±0.01	0.41	0.2_6±0.06	0.41	≲0.008
0.72	1.0_5 ±0.2	0.72	2.3 ±0.4	0.72	1.0_8±0.2
1.02	0.3_9 ±0.1	1.02	0.6±0.2	1.02	≲0.04
1.43	0.12±0.03	1.43	≃0.3	1.43	≃0.05
1.78	0.07±0.02				
2.1_5	≲0.03			2.0–2.5	≃0.1–0.2
5.2	0.3_2±0.1				
6.2	≃0.2			6.8_9	0.9_8±0.2
7.1	1.5_4±0.4	7.5	18.9±5.0		

[a] The errors on the absolute yields are indicated; the relative errors are approximately one-half as large. The results given are in most cases the average of several runs.

TABLE II. Theorectical radiation widths.

Level (Mev)	Γ_γ(ev) $E1$	$E2$	$E3$	$M1$	$M2$	$M3$
ground	185	0.045	7.9×10^{-6}	8.8	2.2×10^{-3}	3.7×10^{-7}
0.72	130	0.026	3.9×10^{-6}	6.5	1.3×10^{-3}	1.8×10^{-7}
1.74	83	0.013	1.2×10^{-6}	3.9	6.0×10^{-4}	5.7×10^{-8}
2.15	67	8.5×10^{-3}	7.5×10^{-7}	3.2	4.3×10^{-4}	3.5×10^{-8}
3.58	26	1.8×10^{-3}	8.6×10^{-8}	1.2	9.0×10^{-5}	3.9×10^{-9}
5.11 } 5.17 }	5.5	1.4×10^{-4}	....	0.28	6.7×10^{-6}	....
~6	1.5	1.4×10^{-5}	....	0.08	8.0×10^{-7}	....

in view of the absence of any 5.0–5.5 Mev γ radiation of comparable yield and the agreement of the 0.72- and 6.89-Mev γ-ray intensities,[10] is that this radiation represents a transition to states at 5.0–5.5 Mev in B^{10} which then decay by α-particle emission to Li^6.

A cascade beginning by a transition from the narrow proton resonance level to a state in B^{10} above 4.5 Mev most likely would be arrested by α-particle decay to Li^6; hence, any intermediate cascade population of the state at 1.74 Mev in B^{10} would proceed mainly through the states at 3.58 and 2.15 Mev, principally through the latter with an accompanying 0.41-Mev γ ray. The absence of any 0.41-Mev γ radiation indicates that the above mode of population of the 1.74-Mev level does not occur. Since no 1.02-Mev γ ray is observed (the 1.74-Mev state decays principally to the 0.72-Mev state), the remaining mode of population of the 1.74-state, that is, a direct transition from the proton capture state, does not occur either, which is consistent with the assignment of a 0^+ character to both of these two states.

The predominant radiative decay of the broad resonance is by the direct transition to the ground state (see Table I, and Fig. 10). In addition to the radiative level widths, the particle widths estimated from the experiments of Thomas *et al.*[11] are also indicated in Fig. 10.[12] Extensive use has been made of the $Be^9(d,n\gamma)$ work (see reference 1) in constructing the decay scheme.

Table II gives the radiative widths predicted from the formulas of Blatt and Weisskopf[13] for various possible multipole transitions from the two prominent proton resonance levels to several of the states in B^{10}. The widths for the 993-kev resonance are somewhat lower, and the values for the 1085-kev resonance somewhat larger than the average values given in Table II.

The observed widths for the two $M1$ transitions indicated in Fig. 10, originating at the narrow proton resonance, compare favorably with the values predicted in Table II. The absence of other radiations is consistent with the spin and parity assignments given.

The three $E1$ transitions shown originating at the broad proton resonance are seen to be slower than predicted, particularly the transitions to the states at 0.72 and 2.15 Mev. It should be pointed out that these transitions are isotopic spin forbidden if the proton resonance level is taken as $T=0$. This last assignment is required by the observed deuteron and α-particle emission, assuming that only one resonance level is involved.[14]

The $M2$ transition to the state at 1.74 Mev is seen to be considerably faster than predicted, which may indicate a substantial feeding of this state by a mode not illustrated in Fig. 10 or may relate to the previous footnote.

The thick-target yield of γ radiations at $E_p=860$ kev (see Table I) shows large cascade probabilities, possibly indicating that the principal level involved has 1^+ character. The amount of 1.78-Mev γ radiation observed with a thick target at this energy, relative to the 1.02-Mev radiation, is not consistent with the former γ ray being the $M3$ transition from the 1.74-Mev state to the ground state, the intensity of the 1.78-Mev γ ray being much too large. A possible explanation is that the 1.78-Mev γ ray is a cascade transition between higher excited states in B^{10}. Intensity and energy considerations suggest that the 6.2- and 5.2-Mev γ rays are transitions from the proton capture state to the first and second excited states in B^{10} at 0.72 and 1.74 Mev, respectively.

We are indebted to Dr. A. Schardt for mounting the NaI crystals used in this experiment. We are particularly grateful to Dr. E. M. Hafner and Dr. J. Weneser for many helpful discussions.

[10] Note that if the 2.0–2.5 Mev radiation were between low-lying states in B^{10}, the known mode of decay of these states from the $Be^9(d,n\gamma)$ reaction would predict a substantial cascade through the state at 0.72 Mev.

[11] Thomas, Rubin, Fowler, and Lauritsen, Phys. Rev. **75**, 1612 (1949).

[12] It has been assumed for simplicity that resonant deuteron and α particle emission is from the 993-kev state which is evident in the resonant γ-ray yield.

[13] J. M. Blatt and V. F. Weisskopf, *Theoretical Nuclear Physics* (John Wiley and Sons, Inc., New York, 1952).

[14] The possibility of the existence of two separate levels cannot be ruled out, particularly since somewhat more yield of 0.72- and 1.02-Mev radiation is observed in the region $900<E_p<960$ kev than can be accounted for by an 88-kev wide resonance at 993 kev. The agreement of the yield of energetic γ radiation (see Fig. 7) with the single-level dispersion formula is not necessarily a contradiction to the two-level hypothesis if the relative probability of the direct ground state transition to cascade is markedly different for the two levels.

Drift Mobilities in Semiconductors. I. Germanium

M. B. PRINCE
Bell Telephone Laboratories, Murray Hill, New Jersey
(Received July 24, 1953)

The drift mobility of holes in *n*-type germanium and electrons in *p*-type germanium has been measured as functions of impurity concentration and temperature. In single crystals of resistivity greater than 10 ohm-centimeter, the mobility at 300°K of holes is $\mu_P = 1900 \pm 50$ cm²/volt-sec and of electrons is $\mu_N = 3900 \pm 100$ cm²/volt-sec. For this high resistivity material, the temperature dependence of mobility in the same units is $\mu_P = 3.5 \times 10^7 T^{-1.6}$ and $\mu_N = 9.1 \times 10^8 T^{-2.3}$, in agreement with conductivity-mobility measurements.

INTRODUCTION

THE drift mobility of holes and electrons has been measured in germanium and silicon single crystals grown from starting material of high purity. The drift mobility μ is defined as the drift velocity per electric field with which a charge carrier moves. Drift measurements were made on germanium samples that were cut from crystals whose resistivity values ranged from 0.05 to 30 ohm-centimeter at 300°K. From these measurements calculations give the effective mass and lattice scattering mobility of electrons and holes at 300°K. The variation of mobility with temperature was measured over a temperature range from 150°K to 350°K in some of these samples. Calculated from the experimental data are curves giving the relationship between the number of impurity centers and the resistivity, the ratio of electron mobility to hole mobility in *n*- and *p*-type germanium and the number of impurity centers, and the ratio of Hall mobility to drift mobility and the number of impurity centers. Similar results for silicon will be reported later.

THEORY

Before presenting any results, it is helpful to discuss briefly the individual scattering processes that affect the mobility of charge carriers in semiconductors. The most important scattering mechanism for high resistivity samples is that resulting from the thermal lattice vibrations. In addition there is coulomb scattering of the charge carriers by the ionized donors and acceptors, coulomb scattering by the other charge carriers both holes and electrons, scattering by neutral donor and acceptor centers, and scattering by lattice imperfections such as dislocations.

Calculations by Dexter and Seitz[1] have shown that, for at least one type of dislocation, lattice imperfection scattering at room temperature is negligible unless the crystal is extremely cold worked. Since the crystals from which the experimental samples have been cut were annealed slowly, it will be assumed that this scattering process can be disregarded in our calculations.

For scattering of the charge carriers by ionized donors and acceptors, calculations under the restriction of non-degenerate spherical constant energy surfaces in the band picture of semi-conductors lead to the Conwell-Weisskopf[2] fromula for impurity scattering. More recently, both Brooks[3] and Herring[4] have refined the Conwell-Weisskopf formula. However, the results of the calculations of Herman and Callaway[5] show that the above mentioned restriction does not hold for germanium and probably not for silicon. Therefore the Conwell-Weisskopf formula can only be a first approximation for the effect of impurity scattering on the mobility of the charge carriers and the Brooks-Herring refinement neglected. It will be assumed that, to the same approximation, the Conwell-Weisskopf formula also holds for electron-hole scattering. In this approximation no account is taken of the reduced mass of the scattering system. It can be shown from momentum conservation considerations that electron-electron and hole-hole scattering have no first-order effect on the mobilities. However, they do affect the mobilities indirectly by changing the energy distribution function[6] of the carriers but this will be neglected in our computations.

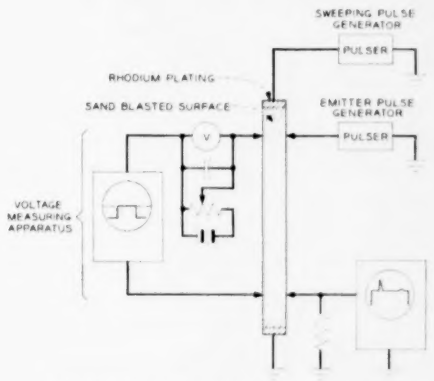

FIG. 1. Experimental drift mobility circuit.

[1] D. L. Dexter and F. Seitz, Phys. Rev. **86**, 964 (1952).

[2] E. Conwell and V. F. Weisskopf, Phy. Rev. **69**, 258 (1946); **77**, 388 (1950).

[3] H. Brooks, Phys. Rev. **83**, 879 (1951).

[4] C. Herring (unpublished).

[5] F. Herman and J. Callaway, Phys. Rev. **89**, 518 (1953).

[6] P. P. Debye and E. M. Conwell (to be published).

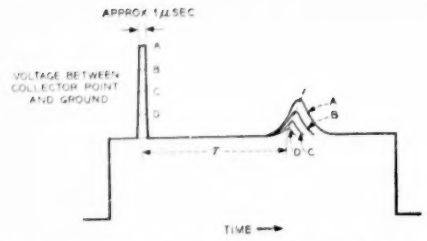

FIG. 2. Oscilloscope trace during measurement of drift time.

Relations giving the effect of neutral scattering centers on the mobilities of the charge carriers are given by Erginsoy.[7] It can be shown easily that the neutral scattering contributes a negligible effect in the temperature range of the work to be reported in this paper. Therefore neutral impurity scattering will not be considered further.

Thus, for the case of the drift-mobility experiment where minority carriers are injected into a semiconductor, these carriers are scattered by the lattice, by fixed charge impurities, and by the majority charge carriers. As far as charge scattering centers are concerned, a minority carrier sees N_D donors, N_A acceptors, and $|N_D-N_A|$ majority carriers, or a total of twice the number of donors or acceptors, whichever may be the larger. The majority carriers on the other hand see only N_D donors and N_A acceptors. When only one type of impurity is present in an appreciable quantity, the majority carrier sees only half as many charged scattering centers as the minority carrier. This means that the electrons will have a slightly higher mobility in n-type semiconductor than they will in p-type semiconductor. Likewise holes will have the higher mobility in p-type semiconductor. As a consequence of this, the ratio of electron mobility to hole mobility b will be larger in n-type material.

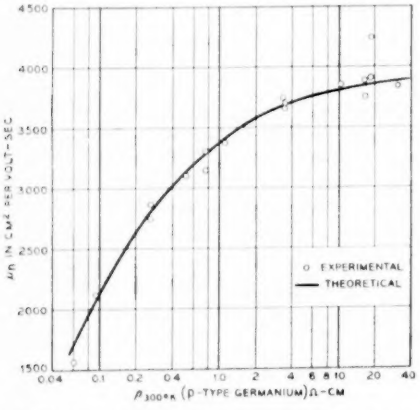

FIG. 3. Electron drift mobility *versus* resistivity of p-type germanium at 300°K.

[7] C. Erginsoy, Phys. Rev. **79**, 1013 (1950).

EXPERIMENTAL TECHNIQUES

The measurements were made using a circuit essentially the same as in the original drift mobility experiment of the Haynes and Shockley[8] (Fig. 1). An electric field is applied across the length of a rod specimen. At one point, the emitter, minority carriers are injected. They drift down the rod in the presence of the electric field and at a later time arrive at a second point, the collector, where some of them are collected. By measuring the drift time t of the minority carriers between the emitter and collector points, the distance L and the voltage drop V between these points, one can obtain the mobility $\mu=L^2/Vt$. The chief modification of the Haynes and Shockley circuit consists in self-biasing the collector point during the period that the sweeping field is applied. The difference in potential between the point and the germanium directly below it is usually sufficient (>0.2 volt) to give the point collector action.[9] In those few cases where the rectification properties of the collector point were poor and the necessary potential difference was not obtained, a resistance network was used to divide the sweeping-field pulse voltage into two parts and thus apply an appropriate potential to the collector point. Self bias is desirable because it reduces the heating of the specimen, an effect that becomes appreciable in all samples that have a resistivity of less than one ohm-centimeter.

A diagram of an oscilloscope trace under the conditions of the experiment is shown in Fig. 2. About one microsecond after the electric field is established in a specimen, a short pulse (about one microsecond) of minority carriers is injected into the rod at the emitter point. The condition of space-charge neutrality demands that an equal number of majority carriers flow into the rod, and the current flow gives the short pulse on the left portion of the oscilloscope trace. After a time t the injected minority carriers have drifted in the electric field to a position near the collector point where they reduce the impedance of the point causing the short pulse on the right portion of the oscilloscope trace. The shape and height of this latter pulse have been explained by minority carrier recombination and diffusion.

In practice, the drift or transit time from emitter to collector is measured as a function of the number of injected carriers and then extrapolated to zero-injected carrier density. In this way allowance is made for the local disturbance in the electric field caused by the finite injection pulses. This extrapolation is shown in Fig. 2.

PREPARATION OF SAMPLES

The samples were prepared like those described by Haynes and Shockley,[8] except that a different long-lifetime treatment and different sample dimensions

[8] J. R. Haynes and W. Shockley, Phys. Rev. **81**, 835 (1951).
[9] J. Bardeen and W. H. Brattain, Phys. Rev. **74**, 230 (1948); **75**, 1608 (1949).

were employed. The long-lifetime treatment consisted of immersing the rods for ten minutes in a 50 percent solution of HNO_3 in water. This treatment reduces the surface recombination velocity in germanium to the order of 100 cm/sec.[10] All the specimens were about 2.5 cm in length and the high resistivity specimens had cross-sectional dimensions of 0.05 cm. The lower resistivity specimens had smaller cross-sectional dimensions in order to keep the impedance above a minimum value. This enabled a sufficient electric field to be established such that a measurement of the mobility was possible. For the very low resistivity samples (0.1 ohm-cm and lower) a pulsing circuit using special low-impedance pulse transformers was used.

MOBILITY *VERSUS* IMPURITY CENTERS

The measurements of mobility reported in this section have been made on single crystal specimens in which only one type of impurity is present in concentrations greater than 10^{13} cm^{-3}. Therefore there is less compensation of impurities than this level and consideration of compensation can be neglected in this section. The experimental results showing the mobility of electrons in p-type germanium is given in Fig. 3 and of holes in n-type germanium in Fig. 4 as a function of the resistivity of the sample. All the data presented in this section have been corrected to 300°K values. Each experimental point represents the average of several or more individual measurements. These results agree for the case of electron mobility with those of Haynes and Shockley over the range of their resistivity values.

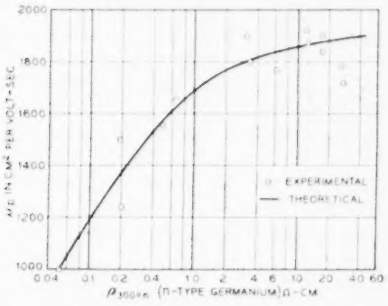

FIG. 4. Hole drift mobility *versus* resistivity of n-type germanium at 300°K.

The mobility falls to one-half its maximum value at a resistivity of about 0.06 ohm-cm. It is obvious that serious errors in design may be made by assuming standard values of mobility instead of the actual values, especially in the case of low resistivity material.

The scatter at the high-resistivity end of the plots can be explained in terms of the uncertainity in a correction that has to be applied to high-resistivity data. This correction has to do with the difference between the drift mobility of a particle and the drift mobility of a group of particles.[11]

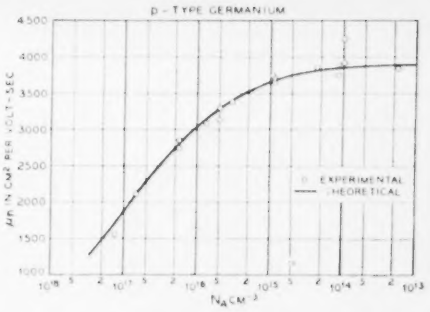

FIG. 5. Electron drift mobility *versus* acceptor density in p-type germanium at 300°K.

The lattice-scattering mobility may be obtained from these plots by extrapolating the high-resistivity data out to 40 ohm-cm. At this resistivity scattering resulting from charged impurities and majority carriers becomes negligible compared to the lattice scattering which then controls the mobility.

In order to use the Conwell-Weisskopf formula for calculating the effect of impurity scattering on the mobility, one has to know the density of impurities N_I in the crystal. These may be calculated from Eqs. (1) and (2) given below which are derived from the relations $np=n_i^2$, $1/\rho=nq\mu_N+pq\mu_P$ and $N_D-N_A=n-p$, where n_i is the density of electrons in intrinsic germanium; ρ_N, ρ_P are the resistivities of n-type and p-type germanium; μ_N, μ_P are the mobilities of electrons and holes; and q is the charge of an electron.

$$N_A=N_D+\frac{1+1/b}{2\rho_P q\mu_P}\left[1-4n_i^2\rho_P^2q^2\mu_N\mu_P\right]^{\frac{1}{2}}+\frac{1-1/b}{2\rho_P q\mu_P}$$

in p-type germanium, (1)

$$N_D=N_A+\frac{1+b}{2\rho_N q\mu_N}\left[1-4n_i^2\rho_N^2q^2\mu_N\mu_P\right]^{\frac{1}{2}}-\frac{b-1}{2\rho_N q\mu_N}$$

in n-type germanium. (2)

It will be assumed that $N_D\gg N_A$ or $N_A\gg N_D$, based on the fact that the starting material from which the

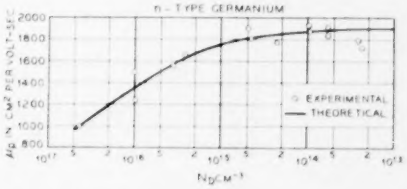

FIG. 6. Hole drift mobility *versus* donor density in n-type germanium at 300°K.

[10] J. R. Haynes (private communication).

[11] M. B. Prince, Phys. Rev. **91**, 271 (1953).

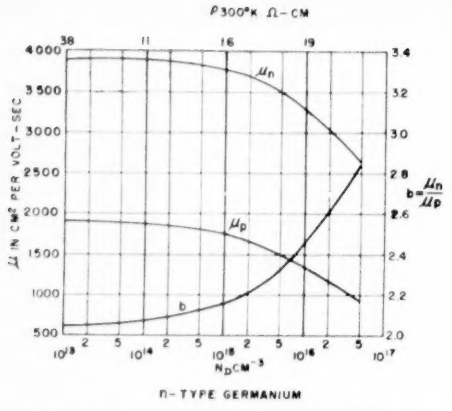

FIG. 7. Computed curves of mobility in n-type germanium at 300°K.

crystals were grown had less than 10^{13} minority impurities (N_A in n type, etc.) per cubic centimeter. Thus N_D may be dropped from Eq. (1) and N_A from Eq. (2). However, N_I is strongly dependent on b and, in order to find the relationship between N_I and μ, it is necessary to find how b varies with ρ. As a first approximation this relationship may be obtained by the following argument. For $N_I \gg n_i$,

$$N_I = N_A = 1/(\rho_P q \mu_P) \text{ in } p\text{-type germanium,}$$

and

$$N_I = N_D = 1/(\rho_N q \mu_N) \text{ in } n\text{-type germanium,}$$

or, for the same N_I, $\mu_N/\rho_N = \mu_P/\rho_N$. Therefore by plotting the μ_N *vs* ρ_P and μ_P *vs* ρ_N curves on logarithmic graph paper and drawing lines at 45° with respect to the axes, one obtains two intersections with each 45° line that correspond to two samples having the same N_I. Hence, b is determined by taking the ratio of the mobilities associated with the intersections. Using these values of b, one arrives at a first approximation to N_I. Refinements of these numbers may be obtained by successive approximations keeping in mind

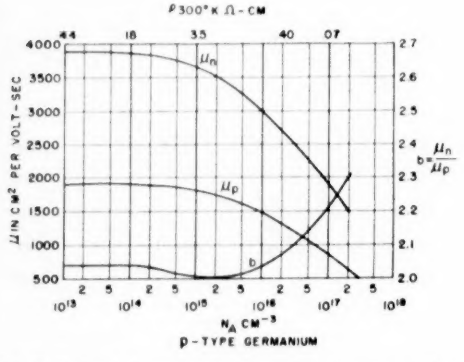

FIG. 8. Computed curves of mobility in p-type germanium at 300°K.

that the minority carriers are scattered by $2N_I$ scattering centers while the majority carriers are scattered by only N_I centers. The results of such a calculation are shown as experimental points in Figs. 5 and 6. Using the Conwell-Weisskopf formula one can fit the experimental data with theoretical curves. For electrons in p-type germanium, a good fit is obtained by using $\mu_L = 3900 \pm 100$ cm²/volt-sec and an effective mass for for the electron, m_N^*, equal to one-quarter of the free electron mass (m). An almost equally good fit can be made by assuming $m_N^* = \frac{1}{2}m$. For holes in n-type material, a good fit is obtained by using $\mu_L = 1900 \pm 50$ cm²/volt-sec and an effective mass for the hole, m_P^*, equal to three times the free electron mass. Using these theoretical curves, one can obtain curves of drift mobility of the majority carrier and b for n-type and p-type germanium. These are given as Figs. 7 and 8. Figure 9 shows the results of plotting the

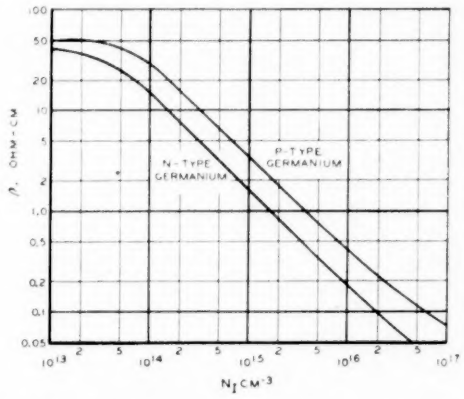

FIG. 9. Resistivity *versus* impurity density for n and p-type germanium at 300°K.

resistivity of n-type and p-type germanium *versus* the number of donors and acceptors respectively at 300°K.

MOBILITY IN IMPURITY COMPENSATED SAMPLES

The results presented in the last section were for uncompensated crystals of germanium. However in the art of making semiconductor devices, one constantly runs into compensated material as part of the device and one wishes to know what kind of mobilities to expect in such material.

As a check on the type of calculations that are made in obtaining the relations of the last section, a crystal was grown in which the number of donors was kept constant throughout the crystal ($N_D = 0.80 \times 10^{15}$ cm^{-3}) and various amounts of acceptors were added during the growth of the crystal. From resistivity measurements it is possible to calculate the number of acceptors in any particular rod sample. Thus, knowing the total number of scattering centers, one can predict a value of mobility for each rod cut from crystal. The

results of this experiment are shown in Fig. 10. The average deviation of the experimental points from the predicted curve is about 3 percent, which is within the expected error of such an experiment. For comparison, a curve showing the expected values of mobility for uncompensated samples is shown on the same figure.

Another crystal was grown in a similar manner in which $N_D = 2.0 \times 10^{16}$ cm^{-3} and with the compensated part of the crystal having $N_A = 7.0 \times 10^{16}$ cm^{-3} as determined from resistivity data. For an uncompensated sample having the same resistivity as the compensated sample (0.138 ohm-cm), one would expect to obtain a value of $\mu_N = 2360$ cm^2/volt-sec; whereas, for the compensated sample, one would expect a value of $\mu_N = 2075$ cm^2/volt sec. The experimental $\mu_N = 1960$ cm^2/volt-sec is thus a strong confirmation of the above calculations since the expected error in such a calculation should be less than 8 percent.

μ_H/μ *VERSUS* IMPURITY CENTERS

In order to help arrive at a better understanding of the band structures of germanium, one is interested in the relation of μ_H/μ at 300°K *versus* the concentration of impurity centers where μ_H is the Hall mobility. With the Hall mobility data obtained by Debye[6] on samples cut from the same crystals as the drift mobility samples and the drift mobility values taken as the majority carrier mobilities from Figs. 7 and 8, μ_H/μ values have been obtained and plotted as a function of N_I in Fig. 11. For electrons in n-type germanium μ_H/μ falls slightly below unity for samples with a large number of impurities. For holes in p-type germanium, the ratio maintains a value near 1.8 for high-resistivity samples. It has been pointed out that the variation with energy of the mean free time between collisions for a carrier lead to μ_H values greater than unity.[12] On the other hand, complex re-entrant surfaces in the band picutre will cause μ_H/μ to tend toward zero or even become negative.[13] More recently it has been noted that multiple energy surfaces of more or less spherical form can lead to arbitrarily high values of μ_H/μ.[14] From these factors it appears that the μ_H/μ values obtained are not unreasonable. On the other hand, few conclusions can be reached from them.

MOBILITY *VERSUS* TEMPERATURE

The results of measuring the temperature dependence of the drift mobility of electrons in p-type germanium are shown in Fig. 12. The high temperature data have been corrected for the difference between the pulse velocity and the charge carrier velocity.[11] Above 220°K, the results are consistent with the line $\mu_L = 3.5 \times 10^7 \times T^{-1.6}$ cm^2/volt-sec. Below this temperature, the curves

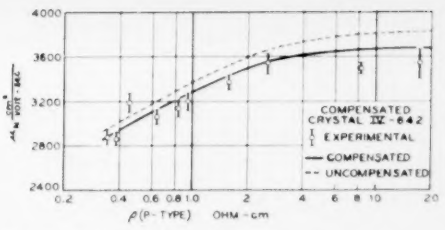

FIG. 10. Electron drift mobility in compensated p-type germanium at 300°K.

deviate from the line in agreement with the onset of appreciable impurity scattering with the μ_L given by the line and the m_N^* equal to one-quarter of the free electron mass.

The temperature variation of the drift mobility of holes in n-type germanium is given in Fig. 13. For this case the data are consistent with the line $\mu_L = 9.1 \times 10^8 T^{-2.3}$ cm^2/volt-sec. Impurity scattering causes the data to deviate from the line at temperature below 200°K.

The results of the lattice-scattering variation of both the electron mobility and the hole mobility with temperature are in agreement with measurements[15] of conductivity mobility made on extremely pure samples of germanium over a range of nearly 200 degrees in which the concentration of carriers remained constant.

According to theory,[16] the temperature exponent for lattice scattering mobility is -1.5. This dependence is derived by assuming that there is a single energy extremum in the Brillouin zone at the energy band edge and that the energy varies quadratically with momentum in any direction away from the extremum. If the energy band edge corresponds to several equivalent points in the Brillouin zone, then the mobility may decrease faster than $T^{-\frac{3}{2}}$. Alternatively if the thermal energies of the carriers are high enough, the quadratic relationship between energy and momentum may break down and the mobility may again decrease

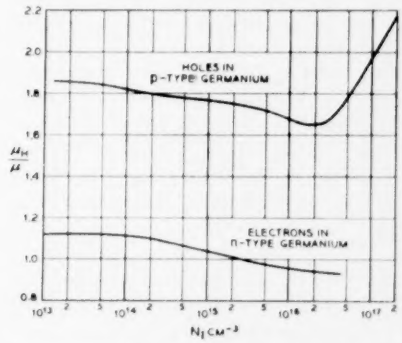

FIG. 11. μ_H/μ *versus* impurity density for n-type and p-type germanium at 300°K.

[12] W. Shockley, *Electrons and Holes in Semiconductors* (D. Van Nostrand Company, Inc., New York, 1950), p. 277.
[13] Reference 12, p. 338.
[14] W. Shockley (private communication).
[15] F. Morin (unpublished results).
[16] J. Bardeen and W. Shockley, Phys. Rev. **80**, 72 (1950).

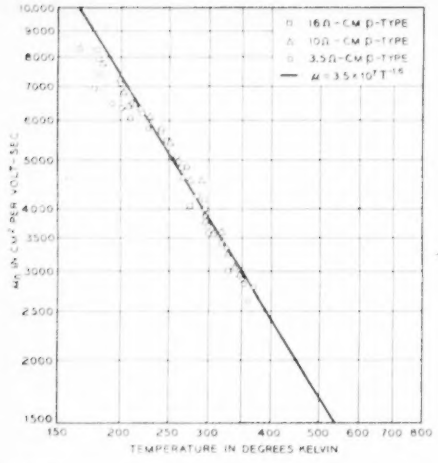

FIG. 12. Electron drift mobility *versus* temperature in *p*-type germanium.

rapidly. At the present time the theoretical analysis of the data does not appear adequate to come to a definite interpretation.[17]

DISCUSSION OF SOURCES OF ERROR

There are four sources of possible error in the determination of a drift mobility. These are the measurement of the drift time, the emitter collector spacing, the potential drop in the specimen between the emitter point and the collector point, and the temperature of the specimen.

The estimated percentage error in the measurement of the drift time by the method described earlier in the paper is about 2 percent. The distance L could easily be measured with an accuracy better than 0.5 percent while the accuracy of the voltage measurement V is about 1 percent. Therefore the expected error from these sources in a determination of the mobility is about 4 percent. This number agrees well with the spread of mobility values determined from a given specimen under various experimental conditions of L, t, and V.

Since the drift mobility is temperature dependent, the temperature at which the measurements are made should be given along with the value of the mobility.

The possible error in the determination of the temperature consists of three parts. First, the actual measurement of the ambient temperature was read from a laboratory thermometer placed as near to the sample as possible. The thermometer has been calibrated to within 1°C. Second, all the experimental data were taken under conditions of power dissipation such that the maximum temperature rise of the sample was less than 1°C. Third, the correction of the data to the standard 300°K introduces some error since the temperature dependence of the mobility is not known exactly. With the 1°C accuracy of the thermometer, the heating effect in the sample, and the 300°K correction, the value of the 300°K mobility may be off as much as 2 percent because of temperature corrections. At temperatures other than ambient, the temperatures were measured by a chromel-alumel thermocouple that was in thermal contact with the specimen. The accuracy of the thermocouple measurement is estimated to be 2 percent.

Thus, the over-all accuracy of any single measurement of mobility quoted at any temperature is expected to be about 6 percent.

CONCLUDING REMARKS

With the results presented in this paper, the author feels that the increasing value of drift mobility for holes and electrons in germanium as a function of the year of their measurement[13] has finally leveled off. The earliest measured drift mobilities[18] were made on single crystal samples of non-uniform resistivity. The next reported data[19] were measurements on single crystals that were grown from fairly pure starting material, i.e., about 10^{14} uncompensated impurities per cubic centimeter. The data as reported in this paper were obtained from crystals that were grown from starting material that had less than 10^{13} impurities per cubic centimeter. Even if the starting germanium is refined to a higher degree of purity, the effect on measurements of mobility will be within the errors reported in this paper. In the high-restivity range (>15 ohm-cm), any decrease of compensation of impurities will not affect the mobility measurement since even with the present impurity levels, the reduction of the mobility below the lattice-scattering value by impurity scattering is

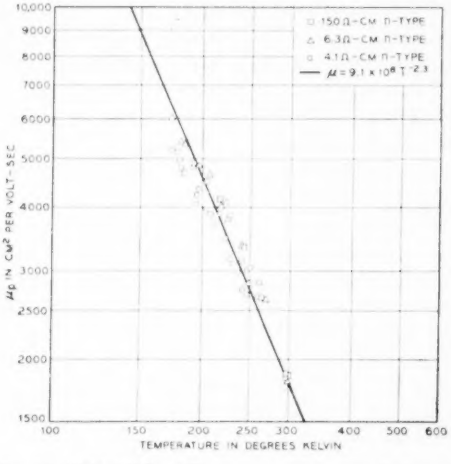

FIG. 13. Hole drift mobility *versus* temperature in *n*-type germanium.

[17] The writer is indebted to C. Herring for a discussion of the first possibility and to W. Shockley for the second.

[18] J. R. Haynes and W. Shockley, Phys. Rev. **75**, 691 (1949).
[19] Pearson, Haynes, and Shockley, Phys. Rev. **78**, 295 (1950).

less than one percent. In the lower-resistivity ranges where impurity scattering becomes effective, the accuracy of the determination of the number of impurities is no greater than the degree of purity obtained at present.

ACKNOWLEDGMENTS

The writer wishes to express his indebtedness to H. R. Moore who built the pulsing circuits, to A. A. Tartaglia who prepared the specimens, and to many of his colleagues in the Transistor Physics Group of the Bell Telephone Laboratories for their suggestions and stimulating discussions. He wishes especially to thank J. R. Haynes who advised generally on circuit problems, E. M. Conwell and W. Shockley for their theoretical help, and J. A. Hornbeck for help in preparing the manuscript.

PHYSICAL REVIEW VOLUME 92, NUMBER 3 NOVEMBER 1, 1953

K-Auger Electrons, Positrons, and Conversion Electrons of Zn^{65} Above 5 kev

J. F. PERKINS* AND S. K. HAYNES
Department of Physics, Vanderbilt University, Nashville, Tennessee

(Received July 20, 1953)

The momentum distributions of *K*-Auger electrons, positrons, and conversion electrons of Zn^{65} have been measured in a magnetic lens spectrometer, with very thin sources and counter windows. The positron Fermi plot was found to be linear from the end point of 325 ± 3 kev to about 50 kev. The positron decay is simple, contrary to some previously published results. From the observed intensities of *K*-Auger electrons, positrons, and conversion electrons, and values of capture branching ratio, fluorescence yield, and *L* to *K* capture ratios taken from the literature, the intensity ratios of the various spectral components have been obtained. The resulting conversion coefficient, $\alpha=(2.56\pm0.29)\times10^{-4}$, agrees with other experimental determinations and strongly suggests an *E2* transition. The observed ratio of *K* capture to the ground state to positrons, 28.0 ± 3.2, is in satisfactory agreement with the recently calculated theoretical value of 29.0 for an allowed transition. This agreement, in view of the high *ft* value, establishes the *l*-forbidden character of the transition.

I. INTRODUCTION

IN 1938 Perrier, Santangelo, and Segrè[1] reported a 245-day activity in zinc, separated from copper filings from a deflecting plate which had been subject to strong deuteron and neutron bombardment in the Berkeley cyclotron. A few months later Barnes and Valley[2] reported such an activity (7 months) in copper parts of a cyclotron in which only protons had been accelerated, and found both electrons and positrons to be emitted. Sagane[3] produced this activity by $Cu(d,n)$ and $Zn(n,\gamma)$ and assigned it to Zn^{65}. Livingood and Seaborg[4] also produced this activity by $Cu(d,n)$ and $Zn(n,\gamma)$ and in addition produced it by $Zn(d,p)$. On the basis of the latter reaction they confirmed the assignment to Zn^{65}, and they measured the half-life as 250 ± 5 days.

On the basis of cloud-chamber measurements Watase, Itoh, and Takeda[5] reported the presence of gamma rays of 0.45, 0.65, and 1.0 Mev. In magnetic spectrometers Deutsch, Roberts, and Elliott,[6] and Mandeville and Fulbright[7] found only one gamma ray, of energy 1.14 Mev. Jensen, Laslett, and Pratt[8] found the energy of this gamma ray to be 1.118 Mev and Mann, Rankin, and Daykin[9] reported it as 1.114 ± 0.005 Mev. The conversion coefficient of this 1.11-Mev gamma ray was measured in a magnetic spectrometer by Waggoner, Moon, and Roberts[10] and, more recently, by Strucken and Weber.[11] They reported values of $(2.28\pm0.26)\times10^{-4}$ and 2.5×10^{-4}, respectively.

The positron end-point energy has been measured with magnetic spectrometers by Peacock, Jones, and Overman,[12] by Mann, Rankin, and Daykin,[9] and by Yuasa.[13,14] They obtained 0.32 Mev, 0.325 ± 0.002 Mev, and 0.32 Mev, respectively. Shoupp[15] has measured the (p,n) threshold of Cu^{65} and assigned a positron end-point energy of 355 ± 20 kev, which becomes 327 ± 20 kev on the basis of the present value of the neutron-proton mass difference.[16]

Considerable disagreement exists on the shape of the

* U. S. Atomic Energy Commission Predoctoral Fellow during a part of this work.

[1] Perrier, Santangelo, and Segrè, Phys. Rev. **53**, 104 (1938).
[2] J. W. Barnes and G. W. Valley, Phys. Rev. **53**, 946 (1938).
[3] R. Sagane, Phys. Rev. **55**, 31 (1939).
[4] J. J. Livingood and G. T. Seaborg, Phys. Rev. **55**, 457 (1939).
[5] Watase, Itoh, and Takeda, Proc. Phys. Math. Soc. Japan **22**, 90 (1940).
[6] Deutsch, Roberts, and Elliott, Phys. Rev. **61**, 389 (1942).
[7] C. E. Mandeville and H. W. Fulbright, Phys. Rev. **64**, 265 (1943).
[8] Jensen, Laslett, and Pratt, Phys. Rev. **76**, 430 (1949).
[9] Mann, Rankin, and Daykin, Phys. Rev. **76**, 1719 (1949).
[10] Waggoner, Moon, and Roberts, Phys. Rev. **80**, 420 (1950).
[11] E. F. Strucken and A. H. Weber, Phys. Rev. **91**, 484 (1953).
[12] Peacock, Jones, and Overman, Plutonium Project Report Mon N-432, 56 (1947).
[13] T. Yuasa, Compt. rend. **235**, 366 (1952).
[14] T. Yuasa, Physica **18**, 1267 (1952).
[15] Shoupp, Jennings, and Jones, Phys. Rev. **73**, 421 (1948).
[16] R. Bouchez, Physica **18**, 1171 (1952).

TABLE I. Intensity ratios as measured by various observers.

γ/β^+	Total K capture/β^+	References	K_2/K_1	References
20.4[a]	41	Good, Peacock[b] 1946	54/46	Good, Peacock[b] 1946
16	32	Zumwalt[c] 1947	56/44	Furberg[d] 1951
19[a]	39	Major[e, f] 1951	55.2/44.8	Major[e, f] 1951
65±5[a]	132±10	Griffiths[g] 1951	50/50	Peacock (see Griffiths,[g] unpublished) 1951
64±12	130±25[a]	Townsend[h] 1951		
38±4[a]	77±8	Bouchez, Perrin[i] 1952		
20±3	41±5[a]	Yuasa[j, k] 1952		

[a] Indicates this value was measured. The value of the other ratio was calculated in each case from a value of 44.9 percent of the K captures going to the excited state and the assumption that L capture to the excited state is 0.10 times as probable as K capture to the excited state. [b] See reference 18. [c] See reference 19. [d] See reference 20. [e] See reference 21. [f] See reference 22. [g] See reference 23. [h] See reference 24. [i] See reference 16. [j] See reference 13. [k] See reference 14.

positron spectrum. Mann, Rankin, and Daykin,[9] using a 25-mg cm^{-2} source, obtained a linear Fermi plot down to 150 kev. Yuasa[13,14] used a 4-mg cm^{-2} source and reported two positron groups, of energies 320 kev and 150 kev, of roughly equal intensities. Cohn and Kurbatov[17] reported coincidences of positrons with 210-kev gamma rays and 200-kev electrons such as would be expected from a complex positron spectrum. The 210-kev gamma rays were also reported by Bouchez.[16]

The relative intensities of the 1.11-Mev gamma radiation, the positrons, and the decays by K capture have been studied experimentally in a number of ways. γ-K x-ray coincidences give the K-capture branching ratio K_2/K_1, where K_2 represents the rate of capture to the ground state of Cu^{65}, independent of fluorescence yield uncertainties. The three *published* values are shown in Table I and are in excellent agreement. Their average, 44.9±0.6 percent K captures to the excited state, will be used as the correct value in the remainder of this paper. The other ratios, γ/β^+ and (Total K capture)/β^+, have each been measured since 1945 by several observers, as shown in Table I.[13,14,16,18–24] The ratio, denoted by the superscript a, was directly measured in each case except Zumwalt's, and the value of the other ratio has been computed by use of the above branching ratio and by an allowance of 10 percent L capture to the excited state. The wide spread of values is apparent.

Thus, although strong K capture, 1.11-Mev gamma radiation, and weak 325-kev positrons are certainly present, many features of the decay scheme of Zn^{65} remain in doubt. The shape of the 325-kev positron spectrum has never been measured with a very thin source. There is still some question about additional low-energy gamma rays, and the relative intensity of the positrons as measured by different observers varies by more than a factor of four. It was therefore felt that an accurate measurement of the shape of the positron spectrum and of the relative intensities of the K-Auger electrons, the positrons, and the conversion electrons with high specific activity sources in a lens spectrometer would clarify many of these points. This paper will present the results of such a study.

II. EXPERIMENTAL METHODS

A. Introduction

The spectrometer has already been described elsewhere.[25] It is a lens type, with approximately 1.5 percent transmission, and has a resolution of approximately 2.5 percent to 3.5 percent, depending upon source size and baffle positions. This instrument was designed for accurate relative intensity measurements at low energies, for which purpose the earth's magnetic field is neutralized to within 0.1 percent by a special set of coils.[26] The instrument had previously been used for measurements down to 20 kev. The present measurement of the intensity of the 7-kev K-Auger electrons of Cu^{65} was the first use of the instrument in the 5-to 10-kev range so that it was necessary to investigate carefully its performance at these very low energies.

B. Sources

An accurate measurement of the momentum distribution of positrons, which are of very weak intensity, required material of rather high specific activity. An even stronger requirement of this type was imposed by the very low energies of the Auger electrons. Zn^{65} with a quoted specific activity of 10 000 mC g^{-1} was obtained from Oak Ridge, having been produced by deuteron bombardment of copper according to a technique developed by Maletskos, Backofen, and Irvine.[27] In order to insure uniform distribution of the source material over the desired area, the sources were prepared by vacuum evaporation of zinc chloride. A drop of this solution was placed on a tantalum filament and dried. The filament and a source backing were then placed in a small bell jar which was evacuated by an oil diffusion pump, and the filament was heated to a red heat for a second or two to evaporate the zinc chloride. Radioautographs of the sources showed a satisfactory uniformity of distribution of the source material. Source backings of 140 μg cm^{-2} Al were used for the positron and conversion electron measurements

[17] R. A. Cohn and J. D. Kurbatov, Phys. Rev. **78**, 318 (1950).
[18] W. M. Good and W. C. Peacock, Phys. Rev. **69**, 680 (1946).
[19] L. R. Zumwalt, Plutonium Project Report Mon N-432, 54 (1947).
[20] S. E. Furberg, Nature **168**, 1005 (1951).
[21] J. K. Major, Compt. rend. **233**, 947 (1951).
[22] J. K. Major, Phys. Rev. **86**, 631 (1952).
[23] G. M. Griffiths, Phys. Rev. **83**, 852 (1951).
[24] I. Townsend, Phys. Rev. **81**, 297 (1951).
[25] Broyles, Thomas, and Haynes, Phys. Rev. **89**, 715 (1953).
[26] S. K. Haynes and J. W. Wedding, Rev. Sci. Instr. **22**, 97 (1951).
[27] Maletskos, Backofen, and Irvine, J. Chem. Phys. **19**, 796 (1951).

and were tried for the K-Auger work. At the very low Auger energies there was appreciable backscattering from the foil, so that 10 μg cm^{-2} Zapon backings were used for the sources with which the K-Auger data were taken. Prior to being used as a source backing each Zapon film was given a very thin coating of aluminum by vacuum evaporation in order to avoid electrostatic charging of the source. The sources were 8 mm in diameter, except that a 4-mm diameter source was used for measurement of the intensity ratios of the three Auger lines, which gave an instrumental resolution of 2.5 percent. The sources used in the K-Auger measurements should have been considerably less than 1 μg cm^{-2} in thickness, but it is believed they were actually somewhat thicker, as the Auger lines showed a small low-energy tail. Plassman and Scott[28] have measured the K Augers of nickel on a 5 μg cm^{-2} source and find no low-energy tail, within intensity limits about equal to the size of the tail we observed in copper. The strong source used for positrons and conversion electrons had a calculated thickness of 5 μg cm^{-2} and broadened the Auger lines somewhat. Presumably it was also somewhat thicker since it was barely visible. It was not feasible to use this source to measure the Auger intensities, both because of the poor line shape and because of the very high counting rate of the Auger electrons.

C. Windows

A Zapon counter window of approximately 200 μg cm^{-2} was used for the measurement of the conversion electrons and all but the lowest energy portion of the positron spectrum; the intensity comparisons were made on the basis of these measurements, with the low-energy portion of the positron spectrum reconstructed on the basis of a linear Fermi plot fitted to the higher energy portion of the spectrum. This represented only a very small intensity correction. Because the 200-μg cm^{-2} window was expected to absorb some of the lower energy positrons, the positron spectrum was also measured with a 20-μg cm^{-2} counter window made from collodion. The K-Auger measurements were made with 6-μg cm^{-2} collodion counter windows. The thinner windows were mounted on Lektromesh which had an open area of the order of 30 percent and reduced the counting rate accordingly.

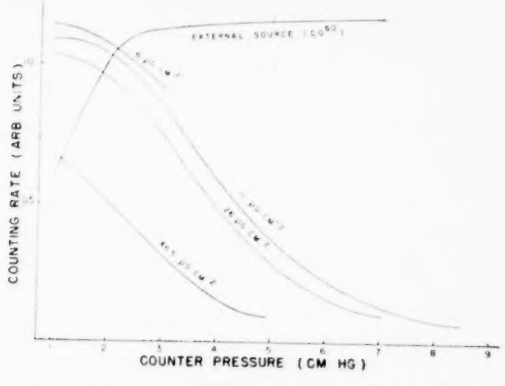

FIG. 1. Counting rate at 7 kev as a function of counter pressure at various counter window thicknesses.

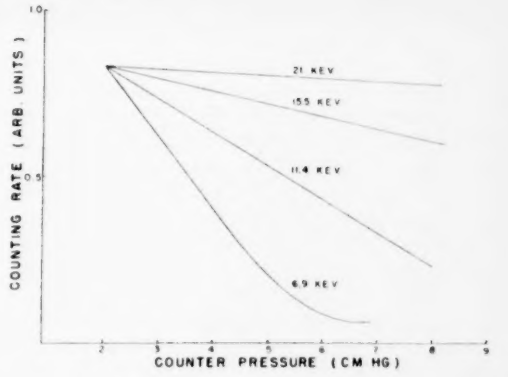

FIG. 2. Counting rate at various energies as a function of counter pressure, for a window thickness of 46 μg cm^{-2}. The curves were normalized to the same counting rate at 2 cm pressure.

D. Spectrometer Characteristics at Very Low Energy

The current control circuits and the coils for neutralizing the earth's field were found to function very satisfactorily down to at least 5 kev, and there was no appreciable scattering of electrons from residual gas in the spectrometer chamber when the vacuum was better than 10^{-5} mm Hg, a value which is fairly readily attained when 6-μg cm^{-2} windows are used. There was an almost negligible absorption of 7-kev electrons by a 6-μg cm^{-2} counter window. The counter, however, showed a counting rate at very low energies which decreased as the pressure of the argon-ethylene counter gas was increased. It was thus necessary to correct for the resultant loss in counting rate, most of which arose from absorption in the gaseous dead space of the counter. For this purpose the counting rate at 7 kev was measured as a function of counter pressure at different window thicknesses, as shown in Fig. 1. Figure 2 shows the variation of counting rate with counter pressure for a 46-μg cm^{-2} window at several energies. The dead-space absorption decreases as the electron energy increases, and is negligible above about 20 kev for the range of counter pressures which are normally used.

Measurements of the K-Auger spectrum with 3-cm Hg counter pressure revealed a statistical spread of the data greater than was to be expected from counting statistics alone, whereas the statistical spread of data obtained with 2-cm Hg counter pressure was normal. This difference presumably arose from the small variations in counter pressure resulting from leaking of the

[28] E. Plassman and F. R. Scott, Phys. Rev. **84**, 156 (1951).

counter windows and imperfect pressure regulation by the cartesian manostat. Small fluctuations about 3 cm Hg would be expected to produce larger variations in counting rate than fluctuations of pressure in the 2-cm Hg range, for the curves of Fig. 1 show a steeper slope at the higher pressure. The K-Auger intensity measurements which were compared with the positron and conversion electron intensities were made with 2-cm Hg counter pressure, and these data were corrected to 100 percent transmission on the basis of the curves of Fig. 1. This involved increasing the observed intensity by 15±4 percent. The relative intensities of the three Auger lines were later measured with 1-cm Hg counter pressure and with a different source and a different baffle arrangement.

A broad group of L-Auger electrons was observed at 700 ev, with a leaky 3-μg cm^{-2} window and 0.4-cm Hg counter pressure, which is a lower limit for satisfactory counting. Below this pressure pulses were followed by damped oscillations and the counter operation was erratic. No reliable intensity measurements could be made with the 3-μg cm^{-2} window because of poor vacuum in the spectrometer.

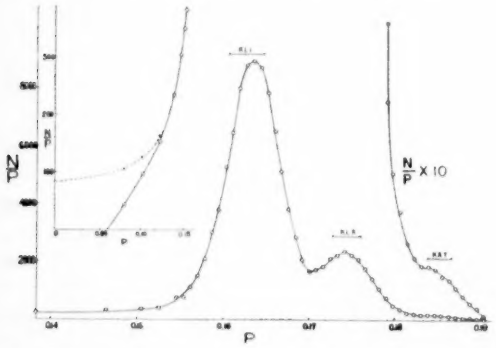

FIG. 3. K-Auger spectrum of copper with a 3.5 percent instrumental resolution. The circles show experimental points. The crosses on the low-energy tail show counting rate corrected for absorption of electrons between the spectrometer chamber and the sensitive volume of the counter.

E. Normalization

In order to compare the intensity of the K-Auger electrons with the positrons and conversion electrons it was necessary to correct for the difference in source strengths and window transmissions used in these measurements. The source strengths were compared within a probable error of 1 percent by a count of each source with a laboratory end-window counter at the same geometry. This comparison was checked by a count of the weaker source in the spectrometer at one point on the positron spectrum. Several hours of counting confirmed the counting comparison within a probable error of 7 percent.

The transmission of the Lektromesh support used with the thin windows was measured by a count of 189-kev electrons from a Cs^{137} source with both thin supported and thick unsupported windows, 6-cm Hg counter pressure being used in each case.

The data were of course corrected for decay of the sources, on the basis of the 250-day half-life measurement of Livingood and Seaborg.[4]

III. EXPERIMENTAL RESULTS

A. Auger Electrons

The observed K-Auger electron spectrum is shown in Fig. 3. The low-energy tail on the KLL-Auger line was unexpected in view of the high specific activity of the source material which was quoted by Oak Ridge. A series of experiments was performed to determine whether this low-energy tail might be the result of some effect other than self-absorption of the source. That the tail was not the result of backscattering was indicated by the fact that it remained unchanged when the backing was reduced from 30 μg cm^{-2} to 10 μg cm^{-2}. A 2-mg cm^{-2} cellophane absorber placed just in front of the source in the spectrometer eliminated the low-energy tail as well as the main part of the spectrum, showing that this low-energy distribution resulted from low-energy electrons from the source rather than from electrons knocked out of the spectrometer walls by gamma- or x-rays from the source. Use of paddle-wheel baffles established the negative charge of the low-energy particles, showing they did not result from the positron spectrum. Runs were made with various anti-scattering baffle arrangements and with different focusing baffle arrangements with the result that the low-energy electrons remained in the same proportion to the rest of the Auger spectrum. That these electrons were truly electrons, which had left the source with momenta proportional to the focusing currents at which they were observed, rather than scattered 7-kev electrons was further substantiated by examinations of the spectrum with thick windows. Windows which reduced the 7-kev electron intensity by 50 percent reduced by 85 percent the intensity of electrons observed at currents appropriate to 3.5-kev electrons. These experiments showed the low-energy tail to be the result of self-absorption; thus it was proper to consider the tail as part of the total Auger intensity.

The observed low-energy tail extended to about 1 kev, which represented the cut-off energy of the counter window. Thus it became necessary to make a rather large correction for absorption in the counter window and gaseous dead space. This correction has been made on the assumption that transmission of electrons into the sensitive volume of the counter is a function of the ratio of electron energy to window thickness, and the ratio of electron energy to counter pressure. That this assumption represents a valid first approximation was confirmed by a prediction, from

these assumptions and the results of Fig. 2, of the shape of the transmission curves for 7-kev electrons and various window thicknesses, and a comparison of these with visual interpolations of the curves of Fig. 1. In Fig. 3 the measured intensities are indicated by circles; the crosses represent points that have been corrected for absorption. The corrections become very large below about 2 kev, so that one is forced to extrapolate the distribution to zero energy. Because of the rather large uncertainty involved in this process, an uncertainty has been assigned to the total Auger intensity equal to ± 50 percent of the total area added to the tail by the absorption correction.

The intensity ratios of the KLL-, KLX-, and KXY-Auger groups have been measured both from the results presented in Fig. 3 and from measurements made with a smaller source and different baffle spacing which gave better resolution. The following values were obtained:

$$KLL:KLX:KXY=1.00:0.292\pm0.010:0.016\pm0.002.$$

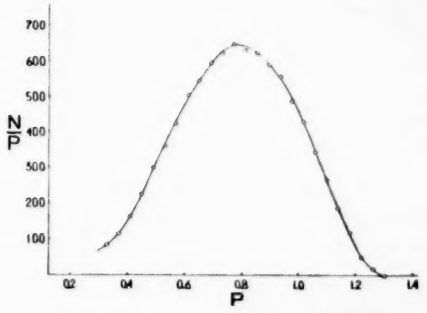

FIG. 4. Positron momentum distribution.

The indicated uncertainties were estimated on the basis of the necessary extrapolation of the low-energy sides of the KLX and KXY lines. The first of these ratios has been measured for a few other elements.[25] The present results are in satisfactory agreement with the trend established by the other results.

B. Positron Spectrum

Although the source was very thin, the high intensity of gamma rays relative to positrons resulted in a small contribution of Compton electrons over the range of the positron energies. In order to correct for this contribution to the counting rate from Compton electrons, these were measured with a set of paddle-wheel baffles introduced into the spectrometer so as to eliminate the positrons. This Compton distribution was then subtracted from the total distribution obtained without paddle-wheel baffles.

Correction for the distortion of the continuous positron spectrum which resulted from the finite instrumental resolution was made on the basis of formulas given by Owen and Primakoff.[29] The instrumental line shape was approximated by a Gaussian error function and the curvature of the spectrum was obtained from second-order finite difference equations applied to a reconstructed positron spectrum. The resulting distribution, which was taken from the 200-μg cm^{-2} data, is shown in Fig. 4.

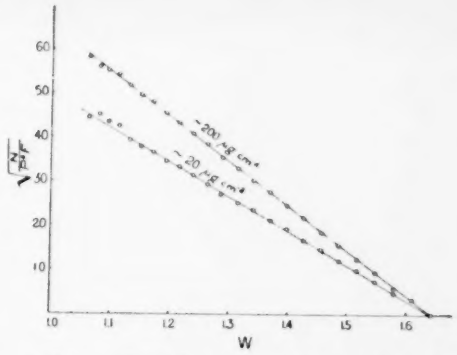

FIG. 5. Positron Fermi-Kurie plots, with screening corrections interpolated from Reitz's calculations by use of the approximate formula given in the NBS Tables for the Analysis of Beta Spectra (reference 30).

The Fermi plots of the 200-μg cm^{-2} and the 20-μg cm^{-2} positron data are shown in Fig. 5. The Fermi function was obtained by interpolation in the NBS tables,[30] using second and fourth order interpolation formulas. The positron screening correction was obtained from the approximate formulas given in these tables, with a screening potential of 2.5 kilovolts. The choice of this value was made after the results of these approximate formulas had been compared with the accurate screening corrections calculated by Reitz.[31] This comparison indicated that the approximate screening corrections used were accurate to within 6 percent over the entire range of energies shown in Fig. 5.

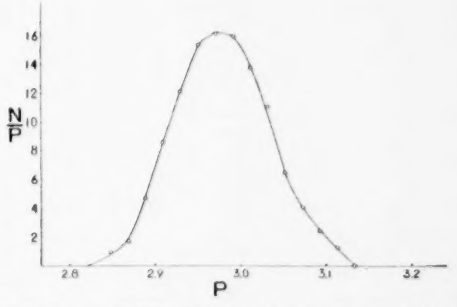

FIG. 6. Conversion line of the 1.11-Mev gamma ray. The line is somewhat wider than was expected on the basis of the instrumental resolution, suggesting $K/L<10$.

[29] G. E. Owen and H. Primakoff, Rev. Sci. Instr. **21**, 447 (1950).
[30] *Tables for the Analysis of Beta Spectra* (National Bureau of Standards, Washington, D. C., 1952).
[31] J. R. Reitz, Phys. Rev. **77**, 10 (1950).

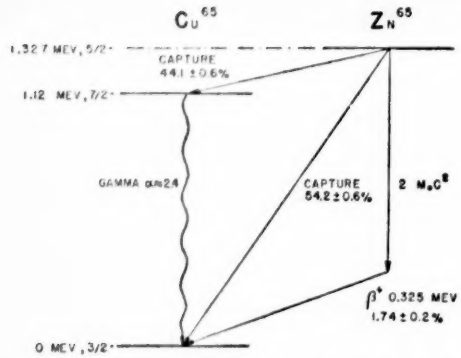

FIG. 7. Decay scheme of Zn^{65}. The spin of the Cu^{65} ground state has been measured. The spins of the other states and their like parities seem to be the only possibilities consistent with the experimental results given in this paper. The fact that the parities are odd depends only on shell theory. The values of log *ft* are 5.8 and 7.3 for the transitions to the excited and ground states, respectively, of Cu^{65}. The energy of the ground state of Zn^{65} should be 1.345, not 1.327 as shown in the figure.

C. Conversion Line

The only conversion line which was found was the well-known 1.11-Mev line, which is shown in Fig. 6. The observed width is somewhat greater than was expected on the basis of the instrumental resolution, and tends to favor a K/L conversion ratio of less than the theoretical value[32–34] of 10, in agreement with conclusions of Goldhaber and Sunyar.[35]

D. Intensity Ratios

The observed integrated intensity ratios of K-Auger electrons to positrons to conversion electrons were $10\,270\pm590:361\pm3:2.345\pm0.047$.

IV. INTERPRETATION

The linearity of the positron Fermi plot indicates the absence of an excited state at about 200 kev above the ground state of Cu^{65} and justifies the assumption of just two capture branches as shown in Fig. 7. From the value of the half-life (250 days), the K-capture branching ratio to the excited state (44.9±0.6 percent) which was previously discussed, and the known energies of the capture transitions 0.229 Mev and 1.345 Mev) approximate *ft* values were calculated from formulas given by Konopinski.[36] The value for capture to the excited state is clearly within the range of allowed transitions.[36,37] It is, therefore, clear that

(a) the parity of the excited state of Cu^{65} is the same as that of the ground state of Zn^{65}, and that

(b) Rose and Jackson's[38] value of 0.102 for L_I/K capture ratio for allowed transitions in Zn can be used for transitions to the excited state. In order to allow for M and higher orbital capture a value of 0.112 ± 0.01 was assumed for the ratio of outer orbit capture to K capture.

Using the measured ratio of conversion electrons to Auger electrons, the value of fluorescence yield for copper from Broyles *et al.*[25] of 0.44 ± 0.04, the K branching ratio discussed above, and the ratio of outer orbit capture to K capture to the excited state, one gets the following intensity ratios: K capture/conversion electrons $=7820\pm850$, K capture to excited state/conversion electrons $=3510\pm390$, Total capture to excited state/conversion electrons $=3903\pm430$, Conversion coefficient of the 1.11-Mev gamma ray $=(2.56\pm0.29)\times10^{-4}$.

The last value agrees within experimental error with previous measurements.[10,11] Table II shows the conversion coefficients expected for various transitions from $E1$ through $M3$. The values of K conversion coefficients are those of Rose *et al.*[39,40] The K/L conversion ratios are estimated from the empirical curves of Goldhaber and Sunyar.[35] Clearly the transition is predominantly $M1$ or $E2$ or a mixture of the two. Since all three experiments give values considerably higher than that predicted for $E2$ and much higher than that predicted for $M1$, the fraction of $M1$ present, if any, is probably small. When one considers that the radiative transition probability for $M1$ calculated according to Weisskopf[41] exceeds that for $E2$ by a factor of about 10^3, the high values of conversion coefficient offer strong evidence that $M1$ radiation must be excluded by spin change. One therefore concludes

(c) that the parity of the 1.11-Mev state of Cu^{65} is the same as that of the ground state,

(d) that the parity of the ground state of Zn^{65} is the same as that of the ground state of Cu^{65}

TABLE II. Experimental and theoretical conversion coefficients and radiative transition probabilities for various multipoles.

Experimental α	Multipole	α_K	α	Radiative transition probability
$(2.28\pm0.26)\times10^{-4}$	$E1$	1.2×10^{-4}		
	$M1$	1.69×10^{-4}	1.86×10^{-4}	4×10^{13} sec^{-1}
2.5×10^{-4}	$E2$	1.93×10^{-4}	2.12×10^{-4}	6×10^{10} sec^{-1}
$(2.56\pm0.29)\times10^{-4}$	$M2$	5.0×10^{-4}		
	$E3$	5.4×10^{-4}		
	$M3$	5.4×10^{-4}		1×10^{4} sec^{-1}

[32] I. S. Lowen and N. Tralli, Phys. Rev. **75**, 529 (1949).
[33] N. Tralli and I. S. Lowen, Phys. Rev. **76**, 154 (1949).
[34] M. H. Hebb and E. Nelson, Phys. Rev. **58**, 486 (1940).
[35] M. Goldhaber and A. W. Sunyar, Phys. Rev. **83**, 906 (1951).
[36] E. J. Konopinski, Revs. Modern Phys. **15**, 209 (1943).
[37] Mayer, Moszkowski, and Nordheim, Revs. Modern Phys. **23**, 315 (1951).
[38] M. E. Rose and J. L. Jackson, Phys. Rev. **76**, 1540 (1949).
[39] Rose, Goertzel, and Perry, *K-Shell Internal Conversion Coefficients, Revised Tables* (Oak Ridge National Laboratory, Oak Ridge, Tennessee, 1951), privately circulated.
[40] M. E. Rose *et al.*, Phys. Rev. **83**, 79 (1951).
[41] J. M. Blatt and V. F. Weisskopf, *Theoretical Nuclear Physics* (John Wiley and Sons, Inc., New York, 1952).

(e) that since Cu^{65} has a measured spin of 3/2,[42] the spin of the excited state is 7/2 and the gamma-ray transition is almost entirely *E2*.

There remains the possibility of a small admixture of *M3*, which is suggested by several lines of evidence. The conversion coefficient seems a little too high for pure *E2*. A little *M3* would reduce the discrepancy between theory and experiment both by having a higher *K* conversion coefficient and also by having a lower *K/L* conversion ratio. The need for a lower *K/L* ratio is suggested by the fact that the conversion line shown in Fig. 6 when compared to a monoenergetic line seems too wide to be accounted for by the expected *K/L* ratio for an *E2* transition. From a more general point of view, Goldhaber has shown that mixing sometimes occurs between *E1* and *M2*, and between *E3* and *M4*, so perhaps it might occur here in analogous fashion between *E2* and *M3* in spite of the apparent discrepancy in the calculated radiation transition probabilities.

From conclusion (d) above, it is evident that the transition to the ground state is either allowed or second forbidden. The approximate *ft* value, although considerably higher than allowed, is far too low for a second forbidden transition. The allowed character of the transition is also strongly supported by the linearity of the allowed Fermi-Kurie plot. One therefore concludes

(f) that the spin of the ground state of Zn^{65} must be 5/2 since only this spin could give allowed transitions to states of spins 3/2 and 7/2.

From the ratio of the area under the positron spectrum to that under the *K*-Auger lines, together with the other intensity ratios already computed, one obtains the intensity ratios: Total *K* capture/positrons $= 50.8 \pm 5.8$; *K* capture to ground state/positrons $= 28.0 \pm 3.2$.

The second of these ratios can be computed for an allowed transition independently of the nuclear matrix elements. Zweifel[43] has recently calculated a value of 29.0 for this ratio, which is in satisfactory agreement with our experimental value and substantiates the allowed character of the transition. This agreement is especially gratifying in view of the wide variation of previous experimental values shown in Table I.

Using for the ground state transition the ratio 0.112 ± 0.01 for (outer orbit capture)/(*K* capture), one finds for the fraction of disintegrations which go by positron emission 1.74 ± 0.2 percent. More precise *ft* values can now be computed and are given in Fig. 7, which shows the complete decay scheme.

The above conclusions have been obtained independently of any nuclear model. They are, however, in complete agreement with shell theory, which predicts odd parity for all three states. The ground state of Zn^{65}, the excited state of Cu^{65}, and the ground state of Cu^{65} are thus characterized in shell theory notation as $f_{5/2}$, $f_{7/2}$, and $p_{3/2}$, respectively. The larger than normally allowed *ft* value between ground states is explainable on a single particle shell model in terms of an *l*-forbidden transition. The orbital angular momentum changes by two units from 3 to 1 (*f* to *p*) while the total angular momentum changes by one unit (5/2 to 3/2). These assignments have already been suggested as the most probable by King[44] but other possibilities could not be excluded on the basis of the conflicting data available at the time.

These conclusions are also consistent with the experimental evidence concerning the beta decay of Ni^{65}. The ground state of this isotope is also $f_{5/2}$ according to shell theory, and the allowed and *l*-forbidden transitions which one would then expect to the 1.11-Mev excited state and ground state, respectively, of Cu^{65} are in agreement with the observed *ft* values. The spin and parity assignment of the 1.11-Mev state and the allowed *ft* values of the two softest beta groups in Ni^{65} [45] limit the 1.49-Mev state of Cu^{65} to either 7/2 odd or 5/2 odd. Either of these assignments corresponds to magnetic dipole 0.37-Mev radiation, whereas the 1.49-Mev radiation would be electric quadrupole (7/2) or magnetic dipole (5/2). On the basis of radiative transition probabilities calculated from the Weisskopf[41] formula and the observed comparable intensity of the 0.37-Mev and 1.49-Mev radiations,[45] it does not seem possible at present to distinguish between the two possible spins.

The authors wish to express their appreciation to Dr. I. Bloch, Dr. C. D. Broyles, and Mr. A. O. Burford for profitable discussions and to Mr. L. Velinsky for assistance in taking the data. The spectrometer was constructed largely from funds supplied by the Research Corporation and is operated under a contract with the U. S. Atomic Energy Commission.

[42] J. E. Mack, Revs. Modern Phys. **22**, 64 (1950).

[43] P. Zweifel (private communication). The details of these calculations will shortly be published in Mr. Zweifel's thesis, Duke University.

[44] R. W. King, *Beta-Decay Schemes and Nuclear Structure Assignments* (Washington University, St. Louis, 1952), privately circulated.

[45] K. Siegbahn and A. Ghosh, Phys. Rev. **76**, 307 (1949).

The Alpha Spectra of Cm^{242}, Cm^{243}, and Cm^{244}

FRANK ASARO, S. G. THOMPSON, AND I. PERLMAN
Radiation Laboratory and Department of Chemistry, University of California, Berkeley, California
(Received June 16, 1953)

The alpha and gamma spectra of Cm^{242}, Cm^{243}, and Cm^{244} have been studied with an alpha-particle spectrograph and gamma-ray scintillation counters. Cm^{242} has alpha groups of 6.116 (73.7 percent), 6.066 (26.3 percent), and 5.964 Mev (0.035 percent) and gamma rays of 44 (0.041 percent), 100 (0.006 percent), and 157 kev (0.0027 percent). Cm^{243} has alpha groups of 5.985 (6 percent), 5.777 (81 percent), and 5.732 Mev (13 percent) and gamma rays of 104, 226, and 278 kev in coincidence with the 5.777-Mev alpha group. Cm^{244} has alpha groups of 5.798 (75 percent) and 5.755 Mev (25 percent). The spectra are discussed relative to alpha-decay theory and corresponding excited states reached by β^- decay processes.

I. INTRODUCTION

THE examination of alpha spectra has been continued using the 75-cm radius of curvature, 60° sector electromagnetic analyzer described previously.[1,2] Certain improvements in the techniques of sample preparation and in the calibration and operation of the spectrograph have resulted in greater refinement of the measurements. As an example of the results, a new rare alpha group in the decay of Cm^{242} has been found, whereas previously[2] only two abundant groups were discernible. Two prominent alpha groups separated by a characteristic energy have been encountered repeatedly among the even-even nuclides,[3] and the implication of a "third alpha group" will be discussed later.

The major objective of the present study was to determine the spectra of curium isotopes of higher mass number than the familiar Cm^{242}. Since these isotopes are produced from Cm^{242} by successive neutron capture or through americium isotopes by a similar mechanism, they are not obtainable in isotopically pure state, and the spectra must be resolved from mixtures. It will be seen that the energy spread of alpha groups from Cm^{243} overlaps the Cm^{242} and Cm^{244} groups and an instrument of high resolution is necessary for their separation. This situation is similar to that encountered[4] with the alpha spectra of Pu^{239} and Pu^{240} in which it was found that two of the Pu^{239} alpha groups fell between the two groups of Pu^{240}. Assignment of the several groups to particular isotopes was made by measuring samples of altered isotopic composition.

The present study also gives further information for the developing systematics and theory of complex alpha spectra. It will be seen that Cm^{244} has a spectrum virtually identical with other even-even alpha emitters of the heaviest elements, and that Cm^{243} displays the pattern of alpha emitters with odd nucleons. The hindrance of decay directly to the ground state for odd nuclear cases is again in evidence; in fact, none of the alpha groups seen so far from Cm^{243} represents the ground-state transition.

[1] F. L. Reynolds, Rev. Sci. Instr. **22**, 749 (1951).
[2] Asaro, Reynolds, and Perlman, Phys. Rev. **87**, 277 (1952).
[3] F. Asaro and I. Perlman, Phys. Rev. **87**, 393 (1952).
[4] F. Asaro and I. Perlman, Phys. Rev. **88**, 828 (1952).

II. METHODS AND INSTRUMENT CALIBRATION

All samples which were used as sources in the spectrograph were prepared by vacuum sublimation. After chemical purification each sample of curium present in solution as the chloride was evaporated to dryness on a tungsten ribbon. Under vacuum, current was passed through the tungsten ribbon and the curium sublimed onto a 2-mil thick platinum plate masked to a band 1 in.×0.12 in. When placed in the spectrograph, the sample was made to approximate a line source by placing before it a stainless steel plate with a defining slit 1 in.×0.018 in. or 1 in.×0.005 in.

The alpha particles after magnetic analysis were intercepted on a photographic plate placed 30° to the direction of the beam and the tracks counted with a 450 power binocular microscope. The alpha spectrum was reproduced by plotting the numbers of tracks found in each $\frac{1}{4}$-mm scan of the plate.

One of the difficulties in the use of this spectrograph as a precision instrument is that the optics are not rigidly defined. The nominal radius of curvature of the magnet (75 cm) is only approximate, and the source and detector must be aligned for optimum focusing. It has been the practice to determine alpha energies by comparing with alpha emitters of known energy and by using these to correct the calculated dispersion of the instrument. The dispersion of the instrument should be given by the expression:

$$\text{dispersion}=\frac{E}{2r_0}=\frac{B^2r_0^2}{2(144)^2r_0}=\frac{B^2r_0}{2(144)^2},$$

where B is the magnetic field in gauss, r_0 is the normal radius of curvature of the magnet in centimeters, and E is the energy of the alpha particle in electron volts. It has been found upon use of the nominal radius, 75 cm, for r_0 that the calculated dispersion is some 6 percent lower than the measured dispersion.

Figures 1a and 1b illustrate data used to obtain the correction applied to the calculated dispersion and to show that the dispersion is essentially constant irrespective of the position on the 22-cm long plate upon which the alpha particles are focused. The circles of Fig. 1a, showing the energy difference between the two principal

alpha groups of Cm^{242}, were obtained on a single photographic plate by using six different magnetic field settings and employing the above expression for the dispersion with a +5.9 percent correction. The other symbols indicate other sets of data. It is seen that within the limits of determining the peak position (about one field of view in the microscope corresponding to 1-kev energy) the energy separation is constant over the part of the plate examined.

Figure 1b shows the method used for obtaining the correction term for calculating the dispersion. Sets of alpha emitters, each with two groups of known energy difference, were employed to make a series of exposures, and for each the empirical correction term for the dispersion formula was found. The alpha groups used were Rn-RaA, Rn-Po, and the two groups of Ra^{226} for which the respective energy differences 512 kev, 188 kev and 183 kev were assumed. The average value for the correction term was 5.9 percent. As indicated there was a rather large uncertainty in each measurement which is partly the result of an unsatisfactory method of locating peak position no longer employed.

For present purposes the correction term and its limits of error will be taken to be 5.9 (±2) percent. This allows liberal limits for the uncertainty in instrument calibration.

The method used to determine peak position alluded to above was to extrapolate the high-energy edge of the peak to the origin. It was later noted that peaks registering on different parts of the plate had different widths. A better comparison would result from the use of the position of maximum peak height, and this convention is now used.

The disparity in peak widths at different positions of the plate was partly due to misalignment of source and detector, but part is inherent in the focusing properties of the magnet. Some improvement resulted from partial disassembly and realignment of the source and receiver assemblies. In addition, a proton resonance fluxmeter has been installed in the magnet gap so that the magnetic field can be measured directly for each run. Previously a series of flux measurements had been made as a function of magnet coil current, and this relationship had been assumed to remain constant. Data shown in Figs. 3 and 4b were obtained before source realignment while the more constant peak width following the changes is reflected in Figs. 4a, c, and d. The data shown in Fig. 1a were taken after the instrument improvements were made.

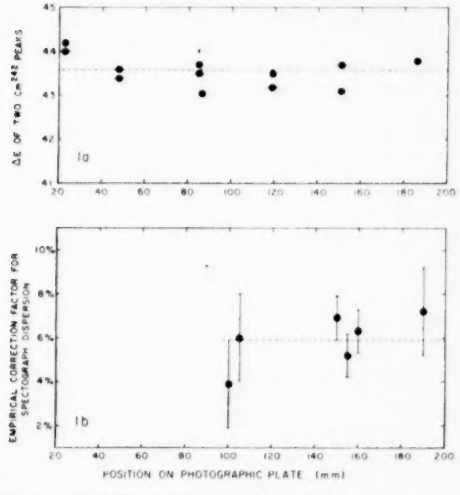

FIG. 1. a. Data illustrating uniformity of dispersion of spectrograph for focusing at different positions on photographic plate. b. Determination of the empirical correction for the dispersion formula.

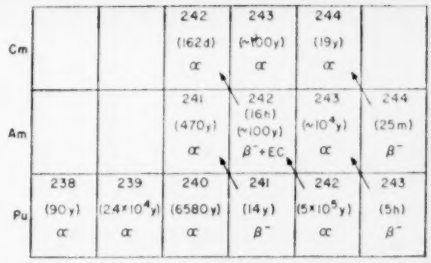

FIG. 2. Segment of isotope chart showing beta-decay relationships of plutonium, americium, and curium isotopes.

III. RESULTS

As already mentioned, the three curium isotopes under consideration could not be produced individually isotopically pure. The assignments of the alpha groups among the several curium isotopes were made principally by comparing samples with different isotopic ratios. Before discussing these, mention will first be made of the redetermination of the energy difference and relative abundances of the two principal alpha groups of Cm^{242} previously reported[2] as differing in energy by 45.7 kev and having abundances of 73 percent and 27 percent. The improvements made in such determinations, such as a better knowledge of the magnetic field strength, have resulted in some revisions.

Principal Alpha Groups of Cm^{242}

The difference in energy of the two groups taken as the average of the 13 values shown in Fig. 1a is 43.6 (±0.6) kev. The limits of error shown include the spread of all values. If we add to this the possible 2 percent error in instrument calibration a conservative limit of error would be ±1.4 kev. If we take the energy of the ground-state alpha group (α_0) to be 6.110 Mev,[2] that for the other prominent group (α_{44}) is 6.066 Mev.

The abundance of this low-energy group has been redetermined as 26.3 (±0.5) percent. Attention should be called to the fact that the difference in alpha-group energies is not quite the energy of the corresponding gamma-ray transition because of the difference in recoil energy given to the residual nuclei by the two

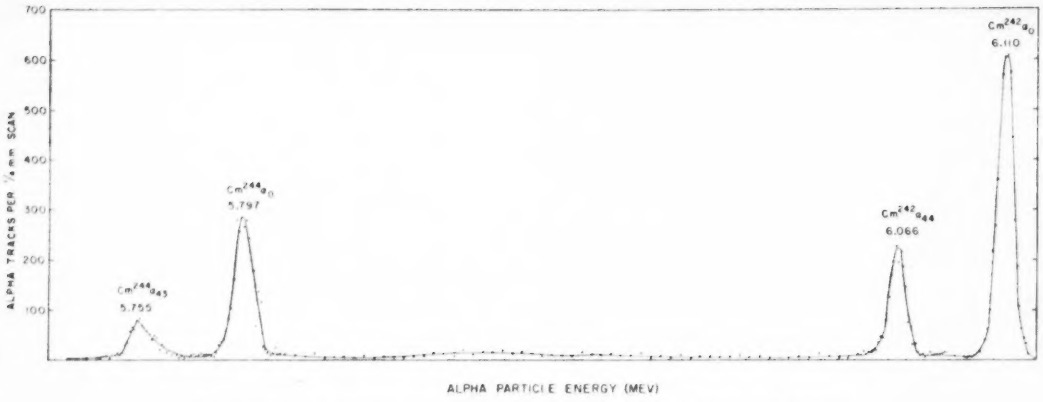

FIG. 3. Spectrum showing principal groups of Cm^{242} and Cm^{244} with Cm^{243} absent.

groups. The energy difference between the ground state and the first excited state of Pu^{238} is accordingly 44.3 kev.

Principal Alpha Groups of Cm^{244}

In order better to visualize the origin of the different isotopic compositions of curium to be discussed, reference is made to a segment of an isotope chart shown as Fig. 2. References to the data used here as well as other decay data to be mentioned will be found in a new edition of the "Table of Isotopes."[5] The first sample to be mentioned was composed principally of Cm^{242} and Cm^{244}. For its preparation, a sample of plutonium having a high concentration of Pu^{242} was available, and its preparation, which is similar to one already described,[6] will be mentioned first. A sample of Am^{241} was irradiated with neutrons to form 16-hour Am^{242} which by its electron capture branching gives Pu^{242} and through β^- decay forms Cm^{242}. The preponderance of β^- branching of 16-hour Am^{242} and the relatively short alpha-decay half-life of Cm^{242} conspire to produce more Pu^{238} than Pu^{242} if the duration of irradiation is the order of the half-life of Cm^{242}, or longer. With long irradiation Pu^{238} undergoes further transmutation to give small quantities of higher isotopes of plutonium. The pertinent information for present considerations is that the plutonium sample so prepared contained about 25 percent Pu^{242} and 0.1 percent Pu^{241} by weight.

The chemically purified plutonium fraction was further irradiated, and from this the curium fraction contained roughly equal quantities by radioactivity of Cm^{242} and Cm^{244}. The appearance of both curium isotopes is approximately second order with respect to irradiation time: Cm^{242} by the slow β^- decay of Pu^{241} followed by neutron capture by Am^{241}, and Cm^{244} from neutron capture by Pu^{242} and Am^{243}, successively. The pertinent neutron capture cross sections which explain these results will be found in a summary by Huizenga, Manning, and Seaborg.[7]

The alpha spectrum of this mixture of Cm^{242} and Cm^{244} is shown in Fig. 3. The limitation in sample size (10^6 alpha disintegrations per minute) prevented observation of possible rare alpha groups, but the identification of the two principal alpha groups of Cm^{244} relative to those of Cm^{242} was unambiguous by virtue of the method of making the curium isotopes. The energies of these alpha groups were found to be 5.798 and 5.755 Mev. There were small amounts of Am^{241} and Pu^{238} in the sample, but their alpha groups fall at energies well below those of the new Cm^{244}. The data shown in Fig. 3 were obtained from a 42-hour exposure; the sample was prepared by subliming the chloride from a tungsten filament onto a 1-in.$\times\frac{1}{8}$-in. band on platinum, and this band was collimated to approach a line source by a 1-in.$\times$0.018-in. slit in a stainless steel plate.

Low-Energy Alpha Groups of Cm^{242}

In an earlier study it was shown[2] that at energies lower than the two principal groups (6.110 and 6.066 Mev) there is no alpha group in abundance greater than about 0.1 percent. With the improvements made in the instrument, a weak group assigned to Cm^{242} has appeared at 5.964 Mev. This group appears in all of the spectra of Fig. 4 and in another taken but not shown. (The origins of the several samples having the spectra shown in Fig. 4 will be mentioned below.) The experimental proof that the 5.964-Mev group belongs to Cm^{242} lies in the invariance of its abundance relative to the principal groups of Cm^{242}. The data are summarized in Table I where the constancy of this ratio is apparent,

[5] Hollander, Perlman, and Seaborg, "Table of Isotopes," Revs. Modern Phys. **25**, 469 (1953). The values as shown in the "Table of Isotopes" are used here, although some have since been revised.

[6] Thompson, Street, Ghiorso, and Reynolds, Phys. Rev. **80**, 1108 (1950).

[7] Huizenga, Manning, and Seaborg, *The Actinide Elements* [McGraw-Hill Book Company, Inc., New York (to be published)], National Nuclear Energy Series, Plutonium Project Record, Vol. 14A, Chap. 20.

whereas the ratios of this group to those ascribed to Cm^{243} and Cm^{244} undergo considerable variation.

Two other possible groups have shown up (Figs. 4a and 4b) at 6.006 and 6.030 Mev, but these cannot be assigned definitely to either Cm^{242} or Cm^{243}. Further work will be necessary to establish these groups definitely and to make assignments. These groups will be mentioned further under the discussion of the decay schemes.

Alpha Spectrum of Cm^{243}

The curium preparations which gave rise to the spectra shown in Fig. 4 were made by neutron irradiation of mixtures of americium isotopes and of curium isotopes which in turn had been prepared from americium. The different isotopic compositions obtainable are a function of the starting materials, the neutron capture and fission cross sections, the intensity and duration of irradiation, and the time following irradiation. These factors as applied to the preparation of curium isotopes will be discussed by others.[8]

The objective of comparing the spectra of the different curium preparations is to assign the several groups by comparing abundances. We have already seen that the alpha group at 5.964 Mev follows the abundances of main Cm^{242} groups and is assigned accordingly as a component of the Cm^{242} spectrum. Also, groups at 5.755 and 5.797 Mev (Fig. 3) were attributed to Cm^{244} because the particular sample was prepared in such a way as to make Cm^{244} and not Cm^{243}.

It remains now to assign groups at 5.985, 5.777, and 5.732 Mev which appear in Fig. 4.

The pertinent numerical data of Figs. 3 and 4 as well as others not shown in graphical form are summarized in Table II in the form of ratios of abundances for the various groups. The group at 5.777 Mev is the most prominent and is used as the reference. Within

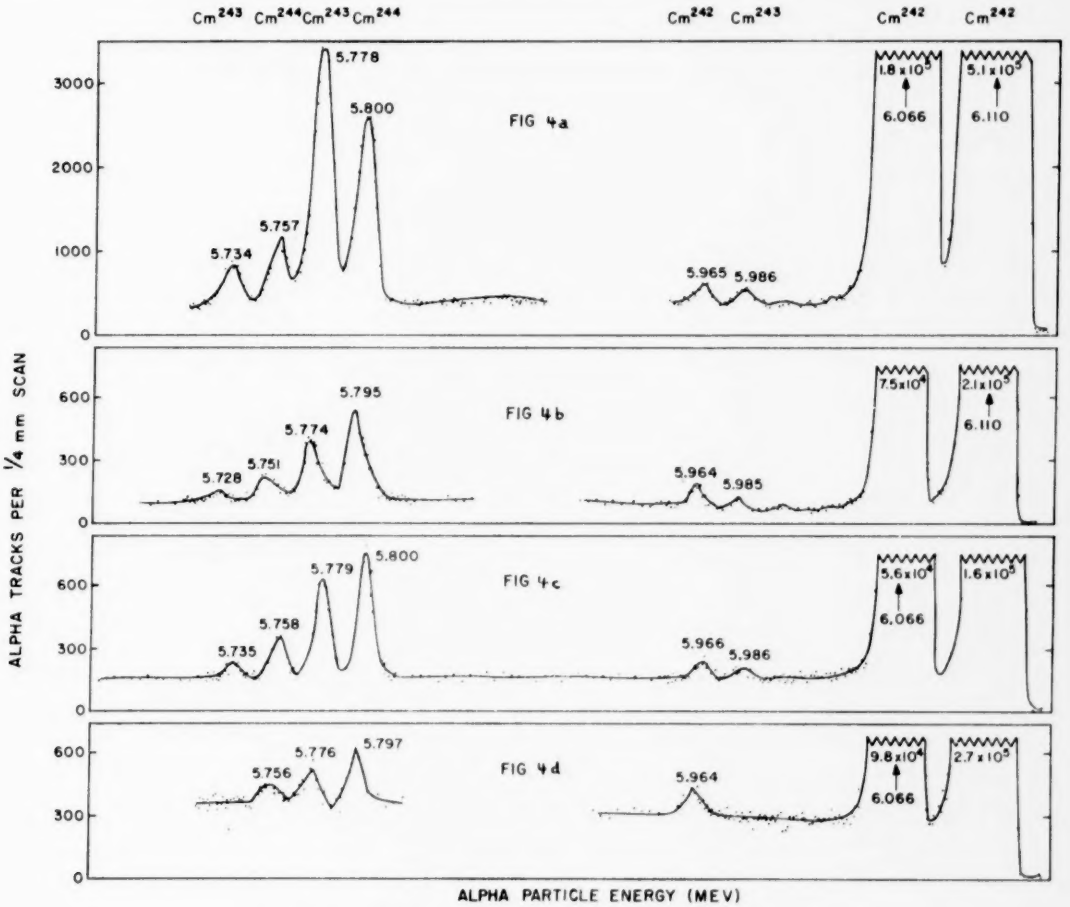

FIG. 4. Alpha-particle spectra of Cm^{242}, Cm^{243}, Cm^{244} isotopic mixtures.

[8] Thompson, Barrett, Reynolds, and Higgins (to be published).

TABLE I. Assignment of alpha group at 5.964 Mev to Cm^{242}.

Abundance relative to: \ Experiment number	Fig. 4a	Fig. 4b	not shown (No. 105)	Fig. 4c	Fig. 4d
Cm^{242} groups (at 6.110 and 6.066 Mev)	0.033%	0.035%	0.035%	0.036%	0.037%
Cm^{244} groups (at 5.798 and 5.755 Mev)	8%	16%	14%	11%	53%
Cm^{243} group at 5.777 Mev	8%	30%	32%	18%	107%
Energy of alpha group	5.965	5.964	5.963	5.966	5.964

the limits of error in the measurements the ratios of the three groups among themselves are constant.

On the contrary, the ratio in abundance of the 5.777-Mev group to the main group of Cm^{242} varies by almost a factor of 10 and varies by an even larger factor with respect to the main group of Cm^{244}. On this basis alone it is probable that all three groups belong to Cm^{243}. Other evidence will be discussed presently.

IV. GAMMA-RAY SPECTRA AND DECAY SCHEMES

Decay Scheme for Cm^{242}

Up to the present study only two alpha groups of Cm^{242} were known, the most abundant leading presumably to the ground state of Pu^{238} and the other to an excited state of about 44 kev, taken to be the first excited state.[2] The L- and M-shell conversion electrons corresponding to the 44-kev transitions were measured by O'Kelley,[9] and these were seen in the requisite quantity to account for all of the α_{44} transitions[10] of Cm^{242} by Dunlavey and Seaborg[11] using the photographic emulsion technique which indicates alpha particle-conversion electron coincidences. Coincidences between alpha particles and conversion electrons of the proper energy were also measured by electronic means by Prohaska.[12] Finally, conversion electrons which can be assigned to this transition have been observed in high abundances by Freedman, Jaffey, and Wagner[13] in the beta decay of Np^{238}.

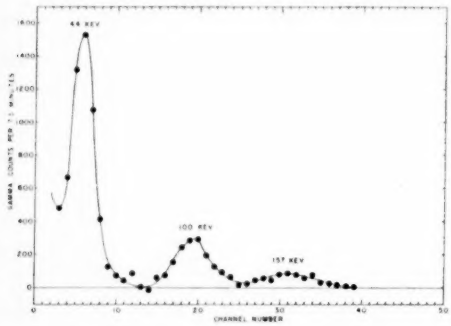

FIG. 5. Gamma-ray spectrum of Cm^{242}.

The absence of a gamma ray of comparable abundance to the conversion electrons has been known generally from the low gamma activity of Cm^{242} and this necessarily implies a high conversion coefficient. Goldhaber and Sunyar,[14] in their classification of excited states of nuclei, and Horie and coworkers,[15] independently have stated the generalization that the first excited states of even-even nuclei have spin 2 and even parity. This thesis has been analyzed further by Scharff-Goldhaber[16] who also discussed its implications on the shell model of nuclear structure. The gamma-ray transitions from these states $(2+\rightarrow 0+)$ are of the $E2$ type. Gellman, Griffith, and Stanley[17] have calculated L-shell conversion coefficients for $E1$, $M1$, and $E2$ transitions, and from their data we have estimated for the case in question coefficients of 1.5, 60, and 600 for $E1$, $M1$, and $E2$, respectively.

We have measured with a scintillation counter spectrometer the gamma-ray spectrum of Cm^{242} both in samples fairly pure isotopically and in mixtures of curium isotopes. Radiation corresponding to L x-rays was found in abundance, but the actual quantity was not calculated because of the large uncertain attenuation loss in the particular arrangement employed. In much lower intensity were found photons of 44 ± 3, 100 ± 2, and 157 ± 2 kev attributable to Cm^{242}. One such spectrum is shown in Fig. 5. The intensity of the 44-kev gamma ray was 1 per 2.4×10^5 total alpha particles of Cm^{242}. Since the first excited state is populated by only 26 percent of the alpha disintegrations, the corresponding yield of gamma rays from this state is 1 per 620 which should represent the *total* conversion coefficient. According to Dunlavey and Seaborg,[11] 83 percent of the electrons seen were L-conversion electrons and 17 percent from the M, $N\cdots$ shells. Applying this correction, the experimental L-shell conversion coefficient becomes 520 which is in good agreement with the theoretical expectations for an $E2$ transition. We can, therefore, have good confidence that the first excited state of Cm^{242} does indeed have spin 2 and even parity. This is indicated in the decay scheme (Fig. 6).

The photon of approximately 100 kev would not be distinguishable from a K x-ray of plutonium, but such an assignment is fairly well ruled out by intensity

[9] G. D. O'Kelley, Ph.D. thesis, University of California Radiation Laboratory Report UCRL-1243 (unpublished).

[10] The designation α_{44} refers to the alpha particles leading to the 44-kev excited state of Pu^{238}; α_0 refers accordingly to the alpha transition to the ground state.

[11] D. C. Dunlavey and G. T. Seaborg, Phys. Rev. **87**, 165 (1952).

[12] C. A. Prohaska, Ph.D. thesis, University of California Radiation Laboratory Report UCRL-1395 (unpublished).

[13] Freedman, Jaffey, and Wagner, Phys. Rev. **79**, 410 (1950).

[14] M. Goldhaber and A. W. Sunyar, Phys. Rev. **83**, 906 (1951).

[15] Horie, Umezawa, Yamaguchi, and Yoshida, Progr. Theoret. Phys. (Japan) **6**, 254 (1951).

[16] G. Scharff-Goldhaber, Phys. Rev. **90**, 587 (1953).

[17] Gellman, Griffith, and Stanley, Phys. Rev. **85**, 944 (1952).

TABLE II. Assignment of alpha groups at 5.985, 5.777, and 5.732 Mev to Cm^{242}.

Abundance ratios \ Experiment number	Fig. 3	Fig. 4a	Fig. 4b	not shown (No. 105)	Fig. 4c	Fig. 4d
Ratio 5.985/5.777/5.732		0.068/1/0.15	0.11/1/0.17	0.049/1/0.19	0.083/1/0.14	<0.16/1/<0.2
Ratio 5.777/6.110 (Cm^{242})	<0.03	5.8×10^{-3}	1.6×10^{-3}	1.5×10^{-3}	2.7×10^{-3}	4.9×10^{-4}
Ratio 5.777/5.798 (Cm^{244})	<0.05	1.4	0.70	0.62	0.78	0.69

considerations. Contrary to the decay scheme of Fig. 6, let us assume that the energy determination of the 157-kev gamma ray is in error and that this gamma ray represents the crossover transition from the state reached by α_{148} to the ground state. On this basis the 100-kev photon could be a K x-ray resulting from the K-shell conversion of this gamma ray. The measured abundance of the gamma ray is 2.7×10^{-5} relative to total Cm^{242} alpha particles, and the abundance of α_{148} is 3.5×10^{-4}. The K-shell conversion coefficient of this gamma ray would then be 12 and according to the calculations of Rose, Goertzel, and Perry[18] this conversion coefficient would correspond to an $E6$ transition.[19] Such a transition in this case can be ruled out on a number of grounds including the lifetime of the state. Furthermore, if the conversion coefficient is 12, the K x-rays should be several times more plentiful than observed. (The 100-kev photon is found in abundance 6×10^{-5}.) We therefore consider the ~100-kev photon to be a gamma ray in cascade with the 44-kev gamma ray giving a state 144 kev above the ground state which is in agreement with the existence of the alpha group α_{148}. This gamma ray is probably the same as the 103-kev gamma ray reported by Freedman, Jaffey, and Wagner[13] in the decay of Np^{238}.

In attempting to assign a multipolarity to the gamma-ray transition from the second excited state to the first and from this to deduce the spin and parity of the second excited state, we have recourse only to an estimation of the conversion coefficient for the ~100-kev gamma ray. Its abundance relative to the 44-kev gamma ray (Fig. 5) is 0.15 and as already indicated there is one 44-kev gamma ray per 2400 alpha particles; therefore, the abundance of the ~100-kev gamma ray is 6×10^{-5} relative to the total Cm^{242} alpha particles. The abundance of α_{148} is 3.5×10^{-4} from which it follows that the conversion coefficient is 5. The theoretical values of Gellman, Griffith, and Stanley[17] for L-shell conversion coefficients do not lend themselves for accurate comparison, since their closest gamma-ray energy was ~150 kev and the change of conversion coefficient with energy in this region is rapid. If we use measured conversion coefficients[20] for $E2$ transitions of Th^{228} (83 kev) and Th^{230} (68 kev) to fill out the curve of calculated values[17] the expected value for 100 kev is about 7. The calculated value for an $M1$ transition would be about 5 for this energy while for an $E1$ transition it would be about 0.1. Because of the uncertainties already mentioned in the present comparisons, values within a factor of 2 of each other should be considered in agreement so that we may assign this transition to the categories $E2$ or $M1$.

On this basis alone the second excited state of Pu^{238} would be 4+, 2+, 0+, 3+, 1+. We can rule out the odd states because of the rule mentioned that the odd states of an even-even alpha emitter must have odd parity. Of the other three possibilities we favor 4+ from the synthesis of a number of arguments based on: (1) the absence of a crossover transition to the ground state; (2) a detailed examination of the beta and gamma spectrum of Np^{238}; (3) analogies with the excited states of other even-even nuclei for which interpretations are more definite; and (4) the agreement of the energy of this state with the expectations for a 4+

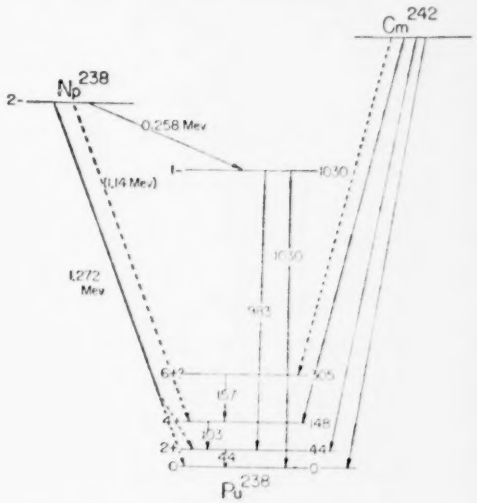

FIG. 6. Decay scheme for Cm^{242} and Np^{238}.

[18] Rose, Goertzel, and Perry, Oak Ridge National Laboratory Report ORNL-1023 (unpublished).

[19] Only electric transitions to the ground state are possible from states reached by an even-even alpha emitter. This follows because all even angular momentum quantum states must have even parity and all odd states have odd parity, and the transitions from such states to the 0+ ground state will involve change in parity from odd states and no change in parity from even states.

[20] For summary of data see reference 5.

state considered as the second rotational state[21,22] of the nucleus. These considerations will be applied generally to the excited states of even-even nuclei at a later date.

As shown in Fig. 5 there is also a gamma ray of 157 kev in low intensity. Its abundance is about one-third that of the ~100-kev gamma ray and consequently is found in abundance 2.7×10^{-5} of the total alpha disintegrations. As placed in Fig. 6, this gamma ray represents a transition from a state 305 kev above ground state to the excited state at 148 kev, and it is listed as an *E2* transition. The reasons for this assignment will appear shortly. For an *E2* transition of 157 kev, the total conversion coefficient should be about 2, and, therefore, the state from which it arises should be populated to the extent of about 8×10^{-5}. Such an alpha group (5.810 Mev) is just on the verge of detection

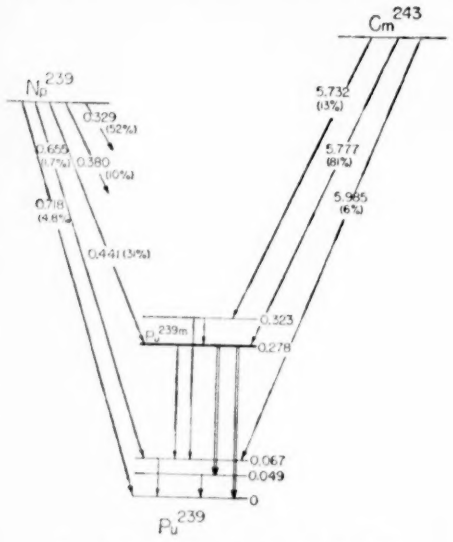

FIG. 7. Decay scheme for Cm^{243} and Np^{239}.

but could not have been seen in the present experiments in any case because the best samples contained Cm^{244} and the principal groups at 5.798 Mev would have obscured it.

Without conclusive justification at present, we shall hypothesize that the most prominent states reached by an even-even alpha emitter among the heaviest elements are states of even angular momentum and that these states represent some configuration of the nucleus as a whole, let us say rotational states. As pointed out by Bohr[21] and by Rasmussen,[22] such states for a nonspherical nucleus should lie at energies proportional to $I(I+1)$. The ratio of energies of the second rotational state to the first would therefore be 3.3 and the third to the first would be 7.0. Applying these factors to the value 44 kev, we arrive at 147 and 308 kev for the second and third rotational states in excellent agreement with energy levels already deduced from alpha- and gamma-ray spectra. In another publication[23] it will be shown that similar agreement is found for other nuclides in this region which have different energy level spacing.[24] However, despite this agreement with theory for the relative energy spacing of the "rotational" levels, the absolute values are not in agreement with reasonable moments of inertia considering the nucleus as a rigid rotator.

If we consider the first three excited states of Fig. 6 to be special in the sense that they represent some quantized behavior of the nucleus as a whole, the question arises as to the existence of other low-lying levels representative of some other mode of excitation. The only indication for such states is the tenuous evidence for two very rare alpha groups at 6.006 Mev and 6.030 Mev (see Figs. 4a and 4b). These would lie 106 kev and 81 kev above the ground state. More refined experiments will have to be performed before the existence of these groups in the decay of Cm^{242} can be considered seriously.

The partial decay scheme for Np^{238} and Cm^{242} shown in Fig. 6 makes use of data obtained by Freedman, Jaffey, and Wagner[13] on Np^{238}. The interpretation of these data is conditioned by the energy levels arrived at from the Cm^{242} alpha decay. The principal virtue of the scheme shown is that it is the simplest one which conforms with information now available.

It will be noted that a new β^- group is postulated leading to the 148-kev level. This group is needed because of the measurement[13] of coincidences between "hard beta radiation" and an ~100-kev photon. The beta group with end point at 1.272 Mev is taken to go either to the 44-kev state or the ground state, or it may consist of two groups going to both of these levels.

The spin and parity assignments were arrived at from the following arguments: From the alpha-decay data for Cm^{242} already discussed it is almost sure that there are low-lying states of Pu^{238} with designation 0+, 2+, and 4+. The high-energy β group (or groups) of Np^{238} has an *ft* value of 8.5,[13] therefore the ground state of Np^{238} most likely has odd parity as would be expected from the shell model. If this is established, then the high-lying excited state of Pu^{238} must also have odd parity since the *ft* value for the low-energy beta group could fall into the "allowed" category. The spin values were selected to conform with the selection rules and to account for the near equality in abundance of the two high-energy gamma rays. It is of interest to note that other odd-odd beta emitters (e.g., Ac^{228}) with sufficient decay energy also have pairs of hard gamma

[21] A. Bohr and B. R. Mottelson, Phys. Rev. **89**, 316 (1953).
[22] J. O. Rasmussen (private communication).
[23] F. Asaro and I. Perlman (to be published).
[24] Dr. Aage Bohr has kindly sent us the manuscript of a forthcoming publication (A. Bohr and B. R. Mottelson) in which is included a similar analysis of excited states of even-even nuclei.

rays differing by the energy of the first excited state known from alpha decay.

Decay Scheme for Cm^{243}

The alpha-particle spectrum of Cm^{243} thus far determined consists of the following three groups with indicated abundances: 5.985 (6 percent), 5.777 (81 percent), 5.732 (13 percent). If the 5.985-Mev group corresponds to the ground-state transition, the other two groups would lead to excited states of 212 and 258 kev. However, as will be shown, the 5.777-Mev group is in coincidence with a gamma ray of 278 kev so that the highest energy group seen (5.985 Mev) cannot lead to the ground state. In addition to the 278-kev gamma ray, one at 226 kev was found and a photon of 104 kev believed to be a plutonium K x-ray. All of these photons were attributed to Cm^{243} rather than to Cm^{242} from abundance arguments. Because it is highly likely that the spectrum for Cm^{244} is much like that for Cm^{242}, we do not believe that these gamma rays originate from the small amount of Cm^{244} present. Other evidence will be given presently.

The highly complex beta spectrum of Np^{239} [20] indicates strongly that there are a number of low-lying excited states of Pu^{239}. Limitations of sample intensity of our Cm^{243} preparations are such that alpha and gamma transitions even in moderate abundances could have been missed. The best that can be done at present is to attempt to define the decay energy of Cm^{243} and to reconcile the two abundant gamma rays with the alpha spectrum. The most likely arrangement of these data is shown in Fig. 7 along with a partial beta-decay scheme for Np^{239} involving common levels. Gamma rays observed both from the beta decay of Np^{239} and the alpha decay of Cm^{243} are indicated by double lines. Figure 8 shows, on the same plot, a portion of the gamma-ray spectrum measured with a scintillation spectrometer and the gamma-ray spectrum which is in coincidence with the most abundant alpha group of Cm^{243} (5.777 Mev). The latter measurement was made by setting the magnet field to focus the alpha group on a scintillation detector and using this pulse to trigger the gamma-ray spectrometer. It is seen that the 226-kev gamma ray and 278-kev gamma ray are both in coincidence with the alpha group. (The energies of the gamma rays as indicated are the averages from a number of measurements.) The data are in agreement with the work of Graham and Bell[25] who showed that these two gamma rays originate from the 10^{-9}-sec metastable state of Pu^{239}. As shown in Fig. 7, these gamma rays decay by parallel paths, one leading to the ground state and another to an excited state of 49 kev. Graham and Bell also found a 210-kev gamma ray from the 277-kev level which leads to a 67-kev excited state. We could not measure this gamma ray but did find a low-intensity alpha group which undoubtedly leads to the 67-kev state because its energy is almost exactly 210 kev higher than the group leading to the 278-kev state. The gamma rays shown from the 323-kev state could not be observed in the present study because of the relatively low population of this state by alpha decay, but gamma rays corresponding to transitions from this state have been observed by others[25–27] following the beta decay of Np^{239}.

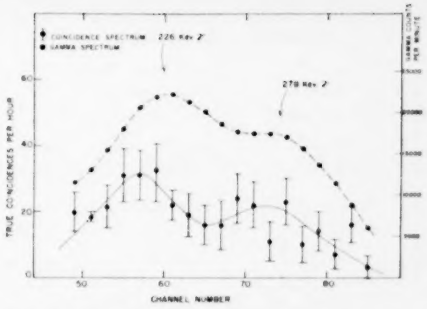

FIG. 8. Alpha-gamma coincidence spectrum of Cm^{243}.

It will be noted that the highest energy alpha group measured is in fairly low abundance and that no alpha groups have been observed leading to the two lowest-lying states. These facts are not in accord with unadorned alpha-decay theory which favors highest energy transitions. However, there is ample evidence that the type of spectrum noted for Cm^{243} is the rule rather than the exception for alpha emitters with odd nucleons.

It was mentioned above that the 104-kev photons are probably plutonium K x-rays arising from the internal conversion of the 278-kev and 226-kev gamma rays of Cm^{243}. Evidence for this assignment was obtained by setting the gamma-ray scintillation spectrometer for this energy and recording the alpha-gamma coincidences as the magnet current of the spectrograph was varied. Coincidences appeared when the main Cm^{243} group (5.777 Mev) was focused on the detector and not with either of the Cm^{244} groups. The 104-kev photon is therefore in coincidence with the same alpha group which gives rise to the 278-kev and 226-kev gamma rays and is most reasonably handled by assuming it to be a plutonium K x-ray arising from the internal conversion of these gamma rays.

Decay Scheme for Cm^{244}

The only information regarding the decay scheme of Cm^{244} is contained in the observation of two alpha groups differing by 42.5 kev and in abundance ratio of 3 to 1. The prevalence of this structure for even-even alpha emitters in this region makes it highly likely that the decay scheme is similar to that of Cm^{242}. On

[25] R. L. Graham and R. E. Bell, Phys. Rev. **83**, 222 (1951).

[26] Freedman, Wagner, Engelkemeir, Huizenga, and Magnusson (private communication).

[27] Tomlinson, Fulbright, and Howland, Phys. Rev. **83**, 223 (1951).

this basis the first excited state would be a 2+ state, and the conversion coefficient for the gamma transition would be about 500. Other excited states similar to those of Cm^{242} would be in too low intensity for observation with the preparations now available.

We wish to acknowledge the assistance of Miss Beverly Turner and Mrs. Marjorie Simmons in counting the alpha tracks. We would like to acknowledge the use of the pile facilities and the aid of the personnel of the Atomic Energy Project, National Research Council of Canada, Chalk River, Ontario, Canada, in the irradiations of plutonium, americium, and curium. This work was performed under the auspices of the U. S. Atomic Energy Commission.

PHYSICAL REVIEW VOLUME 92, NUMBER 3 NOVEMBER 1, 1953

Slow Neutron Velocity Spectrometer Studies. V. Re, Ta, Ru, Cr, Ga

E. MELKONIAN, W. W. HAVENS, JR., AND L. J. RAINWATER
Columbia University, New York, New York

(Received July 31, 1953)

New developments in the analysis of data near resonance levels are described. These allow more accurate values of the level constants to be determined from the measured areas above transmission curves and are more general in their applications. The effect of Doppler broadening is also taken into consideration. Transmission data on Re, Ta, Ru, Cr, and Ga are presented. The thermal region of Re is well matched by the relation $\sigma=5.0+15.8E^{-\frac{1}{2}}$. Resonances are found in Re at 2.18, 4.40, 5.92, 7.18, 11.3, 13.1, 17.7, and 21.1 ev. The strong level at 2.18 ev has been studied by the technique of using two samples of different thickness, giving $\sigma_0=5700$ barns and $\Gamma=0.090$ ev. The method of curve fitting was also applied to the transmission dip of the thick sample at 2.18 ev and confirms the values of σ_0 and Γ from the area method. Curve fitting was also used on the 4.40-ev level. New data for Ta in the region above 5 ev are presented. Some transmission dips thought previously to be due to one level have now been resolved into two levels. There are levels at 6.11, 10.2, 13.7, 20.0, 24.0, 35.1, and 38.2 ev. The thermal region of Ru is well matched by the relation $\sigma=6.4+0.39E^{-\frac{1}{2}}$. Resonance levels are observed at 9.8, 15.2, 24.1, and 40.9 ev. The thermal region of Cr is well matched by the relation $\sigma=3.8+0.7E^{-\frac{1}{2}}$. A resonance level is observed at 3800 ev. The nuclear cross section of Ga is given by $\sigma=7.3+0.35E^{-\frac{1}{2}}$ below 5 ev. In addition interference effects occur in the thermal region. Levels were found at 102 ev and 310 ev, with indications of levels at higher energies.

INTRODUCTION

THE results of previous investigations using the Columbia University slow neutron velocity spectrometer have been presented in a series of earlier papers.[1-3] The present paper is the fifth of a series[2] which presents the results of survey studies of nuclear resonance levels. The improvements and re-evaluation described in the fourth paper[2] apply here. In addition, some new developments in the analysis of data near resonance levels are presented and applied to the data of this report.

Analysis of Resonance Level Parameters

Techniques for obtaining information about the parameters σ_0 and Γ of a neutron resonance from the experimental transmission curve have been described in previous reports.[1-3] It has been repeatedly pointed out that in the vicinity of a resonance, it is not usually possible to obtain the cross section σ from the experimental transmission T by using the formula $T=e^{-n\sigma}$, where n is the number of atoms per cm^2 in the sample. The authors find, however, that there seems to be a strong tendency to give direct significance to the curve of σ *vs* E obtained in this manner,[4] in spite of the warning to the contrary given in the introduction to this compilation. It should be stressed that such a curve of σ *vs* E has little meaning in the region of a resonance level unless the instrumental resolution width is small compared to the level width. In most cases the maximum σ obtained in this manner is small compared to the true σ_0 and decreases with increasing thickness of sample. In certain favorable cases, where $n\sigma_0$ is not large and the level width is not small compared to the resolution width, trial values of level parameters may be chosen and the calculated expected transmission curve (including the effect of the instrumental resolution width) compared with the experimental transmission curve. In especially suitable cases, this may be done in the final stage of the analysis.

As has been pointed out previously, the determination of the level parameters is frequently possible only by an analysis of the area, defined below, of the trans-

[1] L. J. Rainwater and W. W. Havens, Jr., Phys. Rev. **70**, 136 (1946); W. W. Havens, Jr., and L. J. Rainwater, Phys. Rev. **70**, 154 (1946).

[2] (I) Rainwater, Havens, Wu, and Dunning, Phys. Rev. **71**, 65 (1947); (II) Havens, Wu, Rainwater, and Meaker, Phys. Rev. **71**, 165 (1947); (III) Wu, Rainwater, and Havens, Phys. Rev. **71**, 174 (1947); (IV) W. W. Havens, Jr., and L. J. Rainwater, Phys. Rev. **83**, 1123 (1951).

[3] Rainwater, Havens, Dunning, and Wu, Phys. Rev. **73**, 733 (1948); Havens, Rainwater, Wu, and Dunning, Phys. Rev. **73**, 963 (1948).

[4] *Neutron Cross Sections*, Atomic Energy Commission Report AECU-2040 (U. S. Government Printing Office, Washington (1952)).

mission dip in the vicinity of the resonance. This method is particularly valuable when the resolution function is not well-known.

In using the Breit-Wigner one-level formula, we adopt the usual simplifying conditions: (1) the interference term between potential and resonance scattering is neglected, and (2) $\Gamma/E_0 \ll 1$, so that $(E_0/E)^{\frac{1}{2}} \approx 1$ over the level.

Then

$$\sigma = \sigma_{\text{const}} + \sigma_r,$$
$$\sigma_r = \sigma_0\{1+[2(E-E_0)/\Gamma]^2\}^{-1},$$
$$T = (T_{\text{const}})(T_r) = (e^{-n\sigma_{\text{const}}})(e^{-n\sigma_r}).$$

If σ_{const} is evaluated in some way,[3] the experimental transmission curve may be divided by T_{const} to give T_r (experimental). For a strong resonance and a thin sample, $T_{\text{const}} \approx 1$ and the correction may be neglected. The "areas" A_E and A_t are defined as

$$A_E = \int_{-\infty}^{\infty} (1-T_r)dE,$$

if an energy abscissa is used, and

$$A_t = \int_{-\infty}^{\infty} (1-T_r)dt,$$

if a time-of-flight abscissa is used. If $\Gamma/E_0 \ll 1$, then $A_t = A_E(t_0/2E_0)$ is a good approximation and will be used in the following analysis. Subsequent developments will be in terms of A_E since simpler expressions

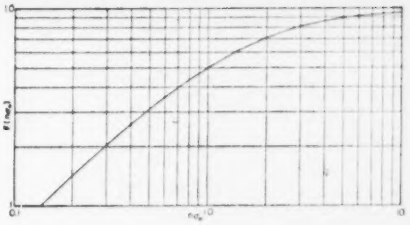

FIG. 1.

$$F(n\sigma_0) = \frac{1}{4\pi n\sigma_0}\left[\int_{-\infty}^{\infty}\{1-\exp[-n\sigma_0/(1+x^2)]\}dx\right]^2.$$

For $n\sigma_0 < 0.14$, $F(n\sigma_0) = \frac{1}{4}\pi n\sigma_0(1-\frac{1}{2}n\sigma_0)$ to 0.2 percent.
For $n\sigma_0 > 10$, $F(n\sigma_0) = 1-1/2n\sigma_0$ to 0.2 percent.

are obtained. However, A_t is generally measured when time-of-flight techniques are used, and the above formula must be used to obtain A_E. It should be noted that any analysis which makes use of the area above a resonance dip depends upon the fact that this area is independent of the resolution function of the measuring equipment, provided of course, that this function is reasonably well-confined.

For an extremely thick sample ($n\sigma_0 \gg 1$) or an extremely thin sample ($n\sigma_0 \ll 1$), the integral for A_E can be evaluated analytically, giving, respectively,

$$A_E^2 = \pi n\sigma_0\Gamma^2 \quad \text{for} \quad n\sigma_0 \gg 1,$$
$$A_E = \tfrac{1}{2}\pi n\sigma_0\Gamma \quad \text{for} \quad n\sigma_0 \ll 1.$$

For intermediate values of $n\sigma_0$, the integral for A_E has

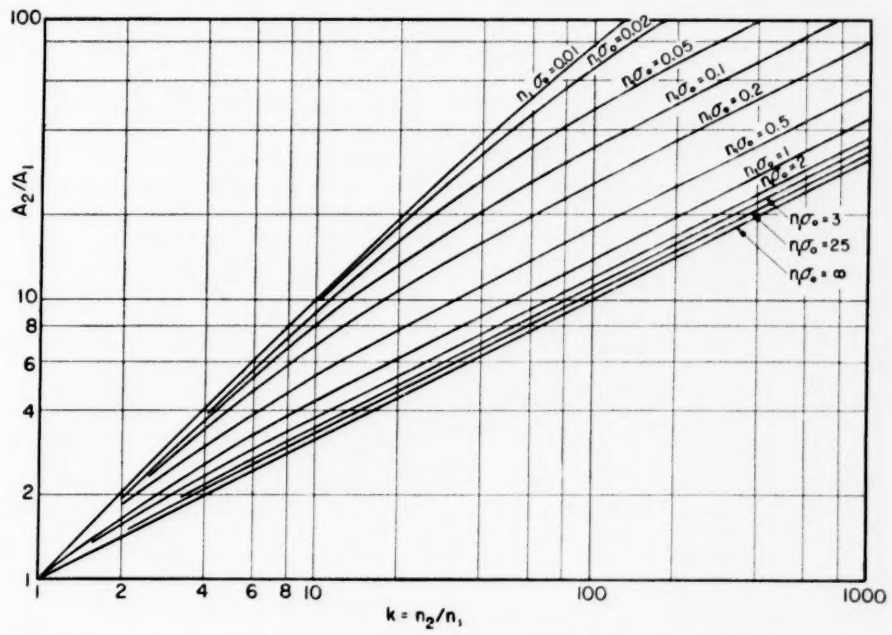

FIG. 2. A_2/A_1 as a function of n_2/n_1 where A = area above transmission dip, n = sample thickness, and the subscripts 1 and 2 refer to thin and thick samples, respectively. With the aid of this graph, σ_0 (and then Γ) for a level may be obtained when measurements on two samples have been made.

been evaluated numerically, and the functions,

$$F(n\sigma_0)=\frac{4E_0^2A_t^2}{\pi n\sigma_0\Gamma^2t_0^2}=\frac{A_E^2}{\pi n\sigma_0\Gamma^2}$$

and

$$G(n\sigma_0)=\frac{4E_0A_t}{\pi n\sigma_0\Gamma t_0}=\frac{2A_E}{\pi n\sigma_0\Gamma},$$

are plotted for the range $0.1\leq n\sigma_0\leq 10$ in Fig. 3 of Paper IV.[2] These functions may also be evaluated by the use of Bessel functions.[5] The function $F(n\sigma_0)$ is of particular significance in the present analysis and is shown in Fig. 1.

If now the expression for $F(n\sigma_0)$ be solved for Γ, we have

$$\Gamma=A_E/[\pi n\sigma_0F(n\sigma_0)]^{\frac{1}{2}},$$

which is an explicit relationship between Γ and σ_0 provided "A_E" and "n" are known. If measurements are available on a second sample of sufficiently different thickness, a second relationship between Γ and σ_0 is obtained. If these relationships are plotted, the intersection of the two curves gives the value of σ_0 and Γ directly.

The simultaneous solution of the two relationships between Γ and σ_0 may be obtained in a somewhat different fashion by eliminating Γ from the two relationships, giving

$$A_2/A_1=[kF(kn_1\sigma_0)/F(n_1\sigma_0)]^{\frac{1}{2}},$$

where $k=n_2/n_1$, and the subscripts 1 and 2 refer to the two samples. Figure 2 shows A_2/A_1 plotted against k for several values of $n_1\sigma_0$. The value of $n_1\sigma_0$ can thus be read off the graph directly when A_2/A_1 and k are known. Γ may then be evaluated in terms of σ_0. The only approximation used in this method of analysis is the assumption of the one level Breit-Wigner formula with the "$1/v$" term and the interference term neglected. These methods are similar to the one suggested in IV,[3] but eliminate the successive approximation feature inherent therein.

The usefulness of the above method of analysis is usually limited by the accuracy of the area determination. The least accurate part of this determination, in many cases, is the determination of the contribution to the area of the "wings" of the curve. The uncertainties arise in part from the presence of other unknown contributions to the cross section, e.g., uncer-

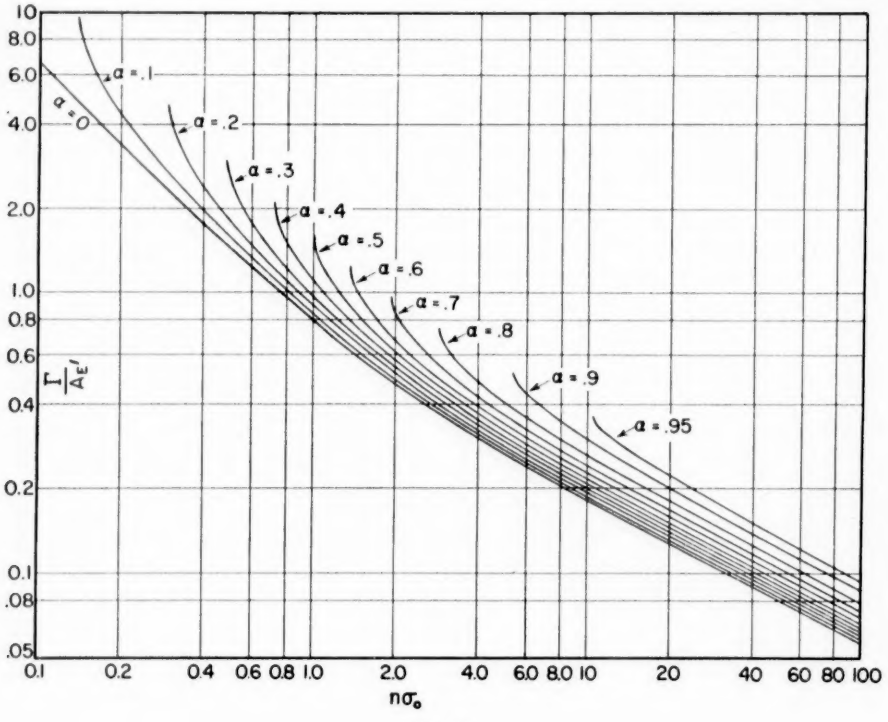

FIG. 3.

$$\frac{\Gamma}{A_E'}=\frac{1}{[\pi n\sigma_0F(n\sigma_0)]^{\frac{1}{2}}}\cdot\frac{2}{1+[1-\alpha/F(n\sigma_0)]^{\frac{1}{2}}}$$

as a function of $n\sigma_0$ and $\alpha=2A_E'/\pi\epsilon$, where $E\pm\epsilon$ are the cut-off points. (When measurements are made on a time-of-flight basis, $A_E'=2(E_0/l_0)A_t'$, and $\alpha=(2A_t'/\pi\tau)$, where $l_0\pm\tau$ are the cut-off points.)

[5] G. V. Dardel and R. Persson, Nature **170**, 1117 (1952).

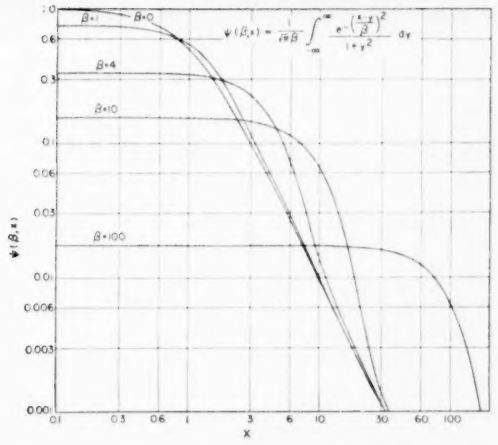

FIG. 4. $\psi(\beta, x)$ as a function of x for several values of β.

tainty in evaluating T_{const} and overlapping of nearby levels from other isotopes and spin states. These difficulties can be minimized by using the following procedure for the treatment of the wing area. First, only the portion of the wings which seems reliable is included in the area to give a partial area A_E' or A_t'. This is used to obtain the first approximate values of σ_0 and Γ. Using these values, the area under the portion of the wings not previously included is calculated and added to the original value to give the next approximation A_E'' or A_t'' and new values of σ_0 and Γ. This process may be repeated until succeeding values do not change.

The successive approximation feature of the method just described can be eliminated in the following manner. Let the wings of the experimental transmission curve be cut off symmetrically about the resonance energy (or time-of-flight) at a point such that T_r is 0.9 or greater. Under these conditions, if the instrumental resolution function does not itself have wings that partially smear the resonance over a wide region, the experimental curves and the actual T_r curves will nearly coincide in the wings. Then the Breit-Wigner relation may be used for T_r beyond the cut-off points. Using only the first term in the expansion of $(1-T)$ in the wing area, the calculated wing area which was omitted is $n\sigma_0\Gamma^2/2\epsilon$, where $E_0 \pm \epsilon$ are the energies at which the curve was cut off. Then,

$$(A_E) = (A_E') + n\sigma_0\Gamma^2/2\epsilon.$$

Using the previous expression for A_E, a solution for Γ may be obtained in the following form:

$$\Gamma = \frac{A_E'}{[\pi n\sigma_0 F(n\sigma_0)]^{\frac{1}{2}}} \cdot \frac{2}{1+[1-\alpha/F(n\sigma_0)]^{\frac{1}{2}}},$$

where $\alpha = 2A_E'/\pi\epsilon$.

The above expression gives Γ in terms of the measured (partial) area A_E' (i.e., excluding the wings) and the value of σ_0. Then, if two sample thicknesses are used, curves of Γ *vs* σ_0 may be plotted for both samples with the best selection determined from the intersection. To simplify these calculations, a plot of Γ/A_E' *vs* $n\sigma_0$ for various values of α is given in Fig. 3. The case $\alpha=0$ reduces to the earlier problem where the wings have not been cut off.

In many cases, only one sample thickness has been used for the measurement of A_E' with significant precision. If the sample has $n\sigma_0 \gg 1$ (or $n\sigma_0 \ll 1$), then $\sigma_0\Gamma^2$ (or $\sigma_0\Gamma$) is determined. For elements having mainly capture at resonance, Γ is usually found to be ~ 0.1 ev and σ_0 may be estimated assuming $\Gamma = 0.1$ ev. If the resulting $n\sigma_0$ is not $\gg 1$ (or $\ll 1$), a relation of the form $\sigma_0\Gamma^P = M$ gives a more accurate statement of the experimental result than either $\sigma_0\Gamma^2 = M'$ or $\sigma_0\Gamma = M''$. The proper choice of P, where $1 \leq P \leq 2$, is determined from the slope of a plot of $\log\Gamma$ *vs* $\log\sigma_0$ near $\Gamma = 0.1$ ev. Values of P and M are given in this report for many of the levels investigated. For $n\sigma_0 > 3$, it is a fair approximation to use

$$F(n\sigma_0) = 1 - 0.5/n\sigma_0.$$

With this expression for $F(n\sigma_0)$, p and M may be evaluated explicitly, giving

$$P = 2\left[1 + \frac{\pi}{8}\frac{[1+(1-\alpha)^{\frac{1}{2}}]^2}{(1-\alpha)^{\frac{1}{2}}}\frac{\Gamma^2}{A_E'^2}\right]^{-1},$$

$$M = \frac{1}{n}\{(4A_E'^2/\pi)[1+(1-\alpha)^{\frac{1}{2}}]^{-2} + \Gamma^2[2(1-\alpha)^{\frac{1}{2}}]^{-1}\} \times \exp[(2-p)\ln(1/\Gamma)].$$

The quantities are to be evaluated at a value of Γ,

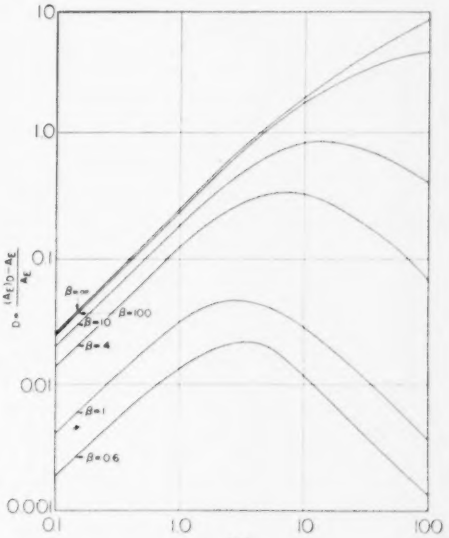

FIG. 5. Effect of Doppler broadening upon area above transmission dip. (D as a function of $n\sigma_0$ for various values of β.)

generally 0.1 ev, in the neighborhood of which these relationships are to hold.

Evaluation of the Doppler Effect

In the previous analysis, the thermal motion of the nucleus has been neglected. If the width of the level, Γ, is large compared to the Doppler width, the previous analysis can be applied directly. However, if this is not the case, then the cross section near resonance is no longer given by the one-level Breit-Wigner formula. Instead, this formula must be averaged over the thermal motion of the nucleus.[6] The area above the transmission dip will now be larger than that obtained when the Doppler width is neglected.

When the Doppler effect is included, the area above the transmission curve is given by the formula

$$[A_E]_D=\tfrac{1}{2}\Gamma\int_{-\infty}^{\infty}[1-\exp\{-n\sigma_0\psi(\beta, x)\}]dx,$$

where

$$x=2(E-E_0)/\Gamma, \quad \beta=2\Delta/\Gamma, \quad \Delta=(4mEkT/M)^{\frac{1}{2}},$$

and

$$\psi(\beta, x)=\frac{1}{\pi^{\frac{1}{2}}\beta}\int_{-\infty}^{\infty}\frac{1}{1+y^2}\exp\left\{-\frac{(x-y)^2}{\beta^2}\right\}dy,$$

where $y=2(E'-E_0)/\Gamma$ and E' is the energy of the neutron relative to the nucleus. These integrations probably cannot be carried out analytically and one must resort to the use of series expansions and numerical methods. $\psi(\beta, x)$ may always be calculated from the

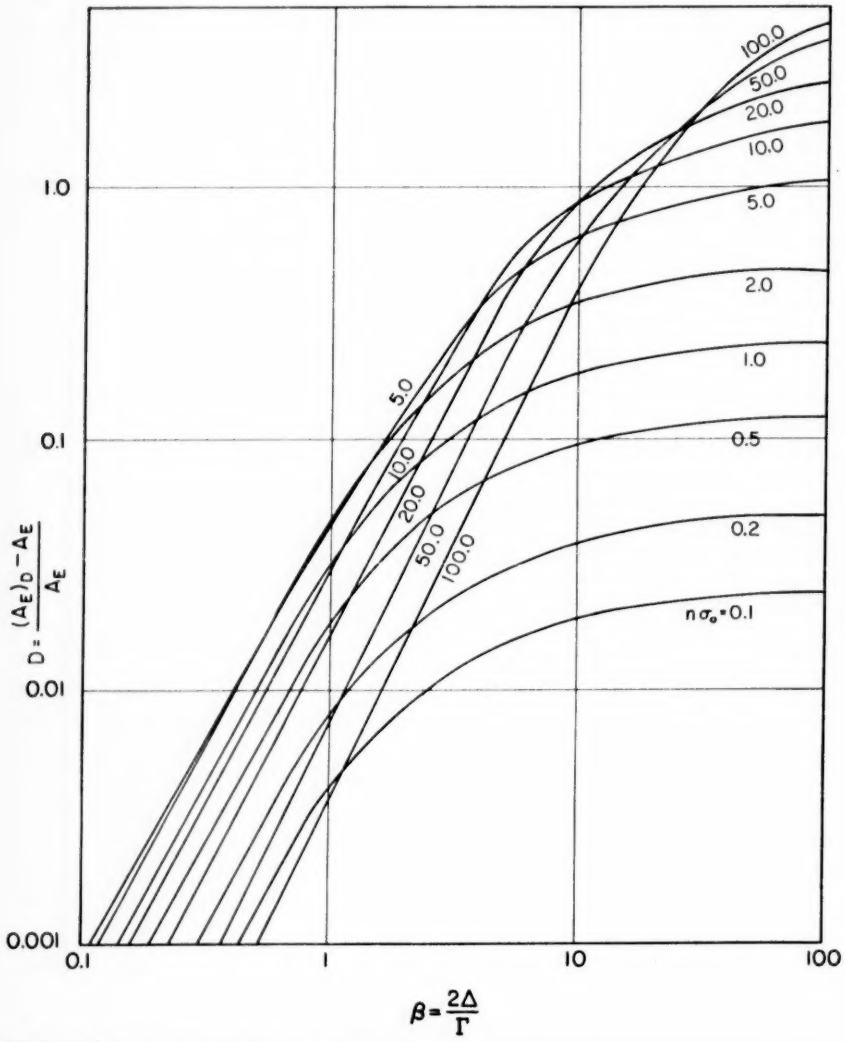

FIG. 6. Effect of Doppler broadening upon area above transmission dip. (D as a function of β for several values of $n\sigma_0$.)

[6] H. A. Bethe, Revs. Modern Phys. **9**, 67 (1937).

convergent series:

$$\psi(\beta, x)=\exp(-x^2/\beta^2)\left\{I_0+\frac{1}{2!}\left(\frac{2x}{\beta^2}\right)^2 I_1 + \frac{1}{4!}\left(\frac{2x}{\beta^2}\right)^4 I_2+\cdots+\frac{1}{(2n)!}\left(\frac{2x}{\beta^2}\right)^{2n} I_n+\cdots\right\},$$

where

$$I_0=(\pi^{\frac{1}{2}}/\beta)\exp(1/\beta^2)[1-\varphi(1/\beta)],$$

$$I_1=1-I_0,$$

$$I_{n+1}=\frac{1\cdot 3\cdot 5\cdots(2n-1)}{2^n}\beta^{2n}-I_n \text{ for } n\geq 1,$$

$$\varphi(1/\beta)=\frac{2}{\sqrt{\pi}}\int_0^{1/\beta}\exp(-t^2)dt.$$

However, this series converges too slowly unless $2x/\beta^2$ is small. For large values of x and/or small values of β, the semiconvergent series,

$$\psi(\beta, x)=\frac{1}{1+x^2}\left\{1+\frac{\beta^2}{2}\frac{3x^2-1}{(1+x^2)^2}+\frac{3\beta^4}{4}\frac{5x^4-10x^2+1}{(1+x^2)^4} + \frac{15\beta^6}{8}\frac{7x^6-35x^4+21x^2-1}{(1+x^2)^6} + \frac{105\beta^8}{16}\frac{9x^8-84x^6+126x^4-36x^2+1}{(1+x^2)^8}+\cdots\right\},$$

is convenient, but must be used with caution. The series for $[A_E]_D$,

$$[A_E]_D=\tfrac{1}{2}\Gamma\left\{\pi n\sigma_0-\tfrac{1}{2}(n\sigma_0)^2\int_{-\infty}^{\infty}\psi^2(\beta, x)dx + \tfrac{1}{6}(n\sigma_0)^3\int_{-\infty}^{\infty}\psi^3(\beta, x)dx-\cdots + (-1)^n\frac{1}{n!}(n\sigma_0)^n\int_{-\infty}^{\infty}\psi^n(\beta, x)dx+\cdots\right\},$$

is convergent, but the integrals

$$\int_{-\infty}^{\infty}\psi^n(\beta, x)dx$$

usually have to be evaluated numerically.

$\psi(\beta, x)$ for several values of β is shown in Fig. 4. The quantity

$$D=([A_E]_D-A_E)/A_E$$

gives the relative increase in area arising from the Doppler effect. This quantity is shown in Figs. (5) and (6) plotted in two different ways. For the limiting case of $\beta\to\infty$,

$$D\to\{(\pi n\sigma_0/2A_E)-1\}.$$

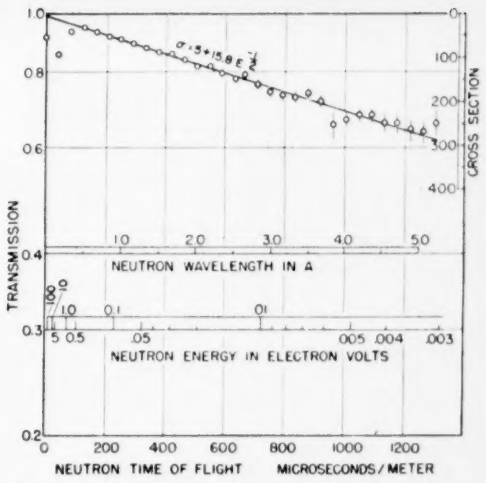

FIG. 7. Slow neutron transmission of 0.518 g/cm² of rhenium in the region below 1 ev showing the "1/v" absorption slope.

One can readily understand the qualitative behavior of the Doppler correction, $D=([A_E]_D-A_E)/A_E$, for the limiting cases of a very thin and a very thick sample for given β. If the sample is very thin ($n\sigma_0\ll 1$), the exponential can be expanded, and in the first approximation, we obtain

$$[A_E]_{D\text{ thin}}=\tfrac{1}{2}\Gamma\int_{-\infty}^{\infty}n\sigma_0\psi(\beta, x)dx,$$

which equals $\frac{1}{2}\pi n\sigma_0\Gamma$ and is exactly the same expression we would obtain if the Doppler effect were not present. Thus, D becomes zero for a very thin sample. If the sample is extremely thick ($n\sigma_0\gg 1$), the transmission of the sample will be effectively zero several level widths away from the center of the level, where the Doppler effect makes the greatest difference in cross section. Further out, when the transmission rises above zero, the Breit-Wigner formula is only slightly affected by the Doppler broadening, so that the area above the transmission curve is only slightly increased. For a given β, these effects become less and less as $n\sigma_0$ becomes greater, and the Doppler correction D approaches zero, in the limit.

Part of this numerical integration has been presented by Dandel and Pressen in a different manner.[5] In our notation, they have presented the region from $\beta=0$ to $\beta=1.2$ for $n\sigma_0$ from 0.2 to 10. However, for high values of $\beta\sim 1$ or greater, the semiconvergent series they used to evaluate their $[A_E]_D$ may not be a good approximation. Some useful expansions, and some values of $\psi(\beta, x)$ over a small range of values of β and x are given in Born's "Optik" (1943) 483 ff.

Summarizing, the application of the Doppler effect to the analysis is as follows. A_E' and α are determined and, for a selected value of $n\sigma_0$, Γ is calculated as usual. This is a first approximation result omitting the Doppler effect. The ratio $\beta=2\Delta/\Gamma$ is calculated and the quantity

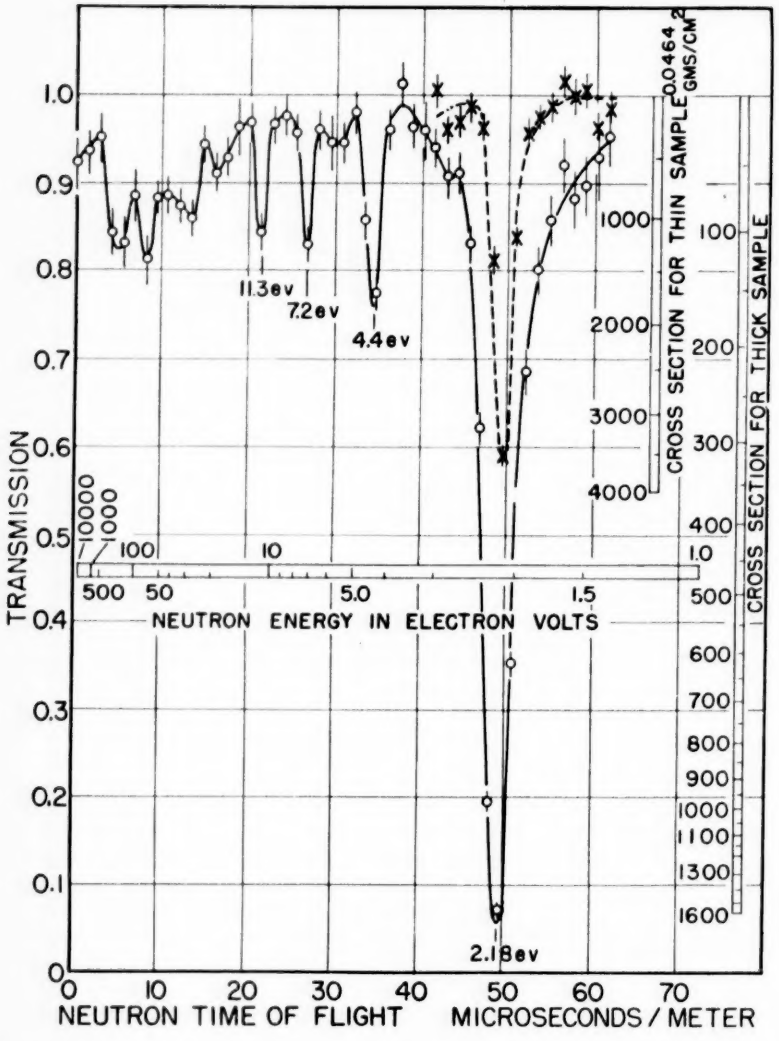

FIG. 8. Slow neutron transmission of 0.518-g/cm² and 0.0464-g/cm² Re with about 3.5-μsec/m resolution.

D read from Fig. (6), which is the more useful of the two plots for this purpose. New values for A_E' and α, are calculated by dividing the initial values by $(1+D)$. For the same $n\sigma_0$, a new Γ is calculated using the new values of A_E' and α. A new value for β is calculated, giving new values of A_E' and α. This successive approximation procedure is continued until the values for Γ do not change. As before, Γ is calculated for various values of $n\sigma_0$, giving the relationship between σ_0 and Γ, but now with the Doppler effect taken into account.

This treatment of the Doppler effect is valid only if the nucleus under consideration is in a gas or is weakly bound in a solid, so that its behavior is as in a gas of some temperature (not necessarily ambient temperature). Under strong binding, the Doppler effect may also shift the position of the level.[7]

[7] W. E. Lamb, Phys. Rev. **55**, 190 (1939).

RESULTS

Rhenium

The slow neutron transmission of rhenium has been investigated using samples of metallic rhenium. A 0.518-g/cm² sample was used throughout the entire energy interval covered. An additional sample of 0.0464 g/cm² was used in the neighborhood of the 2.18-ev level.

Figure 7 shows the measurements in the thermal region. The curve which best fits these data is

$$\sigma = 5.0 + 15.8E^{-\frac{1}{2}},$$

where σ is in barns and E in ev.

The resonance region, studied with better resolution, is shown in Fig. (8) and the higher energy portion, studied with still better resolution, is shown in Fig. (9).

The data in the neighborhood of the 2.18-ev level

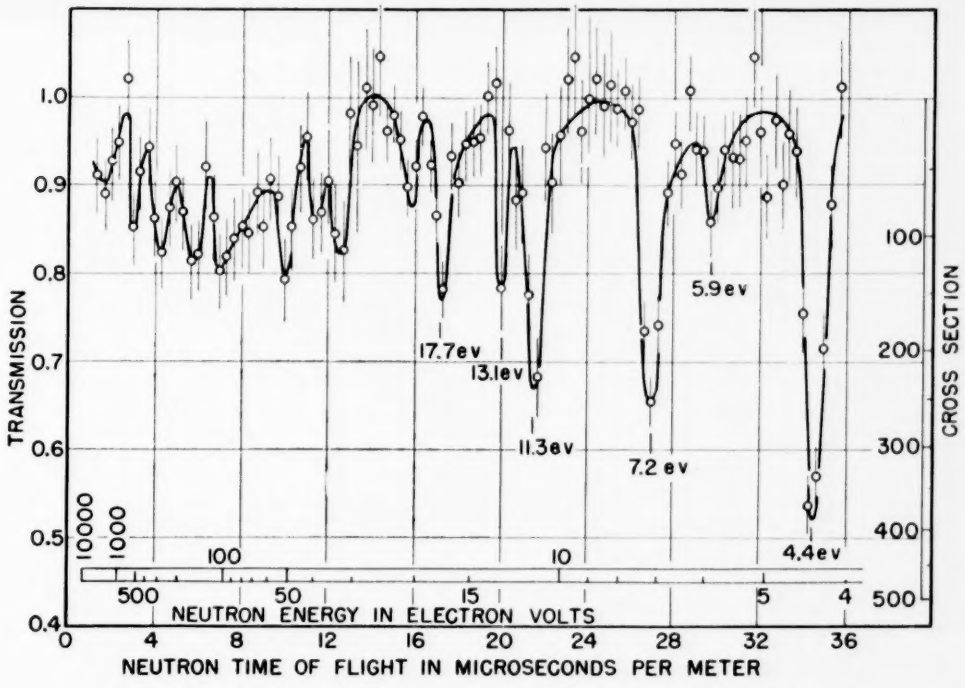

FIG. 9. The slow neutron transmission of 0.518-g/cm² Re with about 1.3-μsec/m resolution.

are suitable for two kinds of analysis: (1) measurement of area above the transmission curve of each of the two samples of different thickness, and determination of σ_0 and Γ from these measurements by the method described earlier in this report, and (2) curve fitting in which the resolution function is applied to successive theoretical curves until a best fit is obtained.

In applying the area method, the transmission was plotted against energy. The areas were determined to chosen values of the energy symmetrically placed on each side of the resonance energy. (For the "thin" sample, this cut-off energy was 0.40 ev from resonance, and for the "thick" sample 0.70 ev.) These values were chosen such that the transmission was greater than 0.90 so that there was very little resolution smearing beyond cutoff. The two curves of σ_0 *vs* Γ are shown in Fig. 10 and the intersection of the two curves gives the following values:

$$\sigma_0 = 5700 \text{ barns}, \quad \Gamma = 0.090 \text{ ev},$$

from which

$$\sigma_0\Gamma = 513 \text{ barn ev}, \quad \sigma_0\Gamma^2 = 46.2 \text{ barn ev}^2.$$

It is interesting to note that $n\sigma_0$ for the "thin" sample is 0.85, so that the thin sample approximation is in error by 17 percent (Fig. 3 of paper IV).[2]

The method of curve fitting has also been applied to this level. This method is particularly useful when data on only one sample thickness are available. In the case of the Re 2.18-ev level, application of both methods gives a check on the consistency of the data and the methods. Since an area measurement above the transmission dip gives a relationship between σ_0 and Γ, only one of these need be varied in seeking the best fit to the data. Figure 11 gives an enlarged plot of the thick sample data on the 2.18-ev level. The calculated transmission curves are based on a value of $\sigma_0\Gamma^2 = 46.2$ (which can be obtained by measurement on the thick sample alone), and three values of Γ: 0.070, 0.090, and 0.120 ev. The broadening arising from the Doppler effect was first applied to the calculated cross

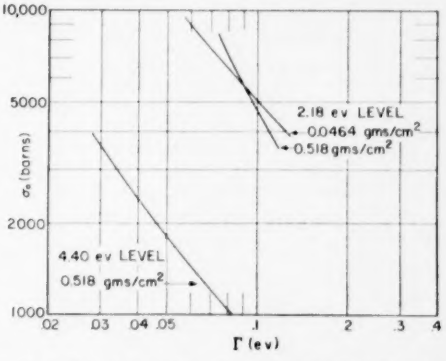

FIG. 10. A plot of σ_0 *vs* Γ for the 2.18-ev level of Re using two sample thicknesses and the 4.40-ev level of Re using one sample thickness.

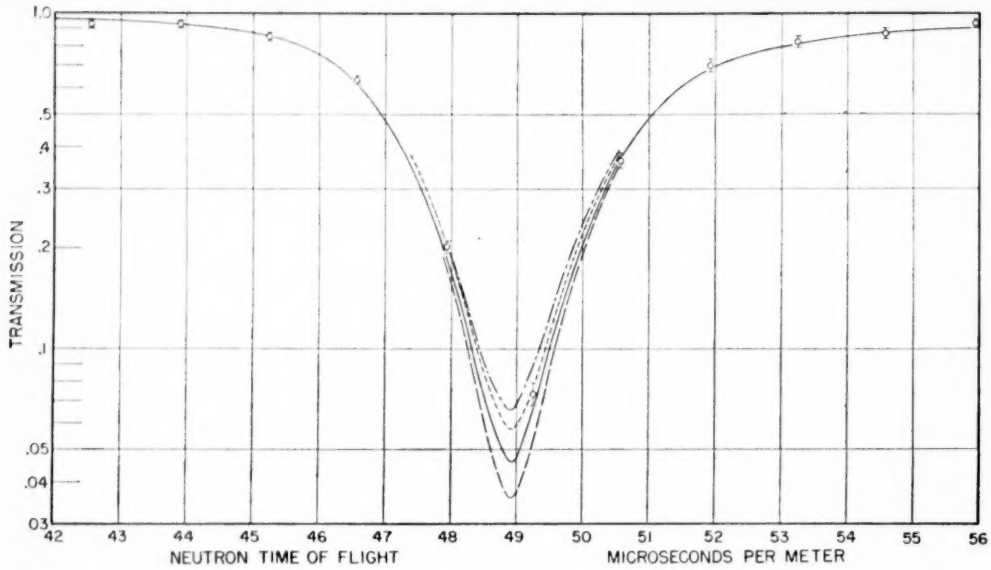

FIG. 11. Curve fits for the 2.18-ev level of Re with $\sigma_0\Gamma^2=46.2$. In the ——— curve, $\Gamma=0.09$, which is the best value from the area method; in the — — — curve, $\Gamma=0.07$; in the — · — · — curve, $\Gamma=0.012$; the - - - - curve is for $\Gamma=0.09$ without the Doppler correction.

section for each value of Γ, the same type of correction being assumed as for Re gas at room temperature. The transmission was then calculated and the resolution function applied to each curve. The resolution function was taken as a triangle of base 3.5 μsec/m which takes into account the arc pulse width (8 μsec), the detection width (8 μsec), and a broadening of 1.7 percent of the time of flight arising from the finite length (10 cm) of the BF_3 counter used. The resulting curves are shown in Fig. 11. The curve with $\Gamma=0.090$ ev gives a much better fit to the data, as expected from the results of the previous method of analysis. The transmission curve for $\Gamma=0.090$ ev, but without the Doppler broadening, is also included in Fig. 11, showing a difference equivalent to about 0.02 ev in Γ. This curve seems to fit the lowest transmission point better than the curve with the Doppler correction. However, for this level, the resolution width is almost twice the level width so that the curve fitting method is very sensitive to the choice of the shape and width of the resolution function.

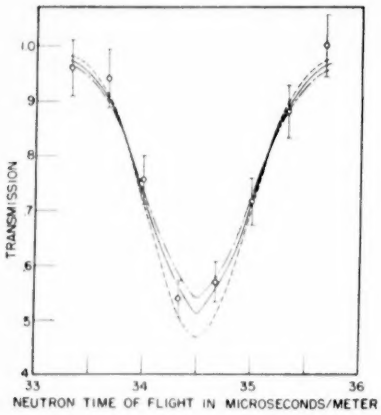

FIG. 12. The curve fit for the 4.40-ev level in Re. For each value of Γ, the value of σ_0 obtained from Fig. 10 is used. The — · — · — curve is for $\sigma_0=1300$ barns, $\Gamma=0.07$ ev; The ——— curve is for $\sigma_0=2000$ barns, $\Gamma=0.05$ ev; The - - - - curve is for $\sigma_0=4000$ barns, $\Gamma=0.03$ ev.

Since σ_0 and Γ are known, Γ_n can be calculated from the formula $\Gamma_n=\sigma_0\Gamma/4\pi\lambda^2 f$, provided f is known. Now $f=\frac{1}{2}a[1\pm(2i+1)^{-1}]$, where a is the isotopic abundance and i the nuclear spin of the responsible isotope. Re has two stable isotopes, 37.1 percent of the $A=185$ isotope, and 62.9 percent of the $A=187$ isotope. The spins of both isotopes are 5/2. Measurements in the separated Re isotopes show that the 2.18-ev level is in the $A=185$ isotope,[8] so that $f=0.159$ or 0.223. Since the responsible

TABLE I. Parameters for the first eight levels in Re.

l_0 (μsec/m)	E_0 (ev)	P	M	σ_0(barns) for $\Gamma=0.1$ ev	$\dfrac{\Gamma_n E_0^{-\frac{1}{2}}}{\sigma_0\Gamma E_0^{\frac{1}{2}}\,a}=\dfrac{\Gamma_n E_0^{-\frac{1}{2}}}{2.62\times10^6 f}$	$\dfrac{\sigma_0\Gamma^2}{4E_0^{\frac{1}{2}}}$	Isotopic assignment
49.0	2.18				15×10^{-4}	3.59	Re^{185}
34.5	4.40				3×10^{-4}	0.14	Re^{187}
29.7	5.92	1.00	26	260	1×10^{-4}	0.05	
27.0	7.18	1.41	43	1100	4×10^{-4}	0.14	
21.5	11.3	1.74	48	2600	13×10^{-4}	0.17	Re^{187}
20.0	13.1	1.60	48	1900	10×10^{-4}	0.10	
17.2	17.7	1.85	60	4200	27×10^{-4}	0.15	
15.8	21.1	1.73	35	1900	13×10^{-4}	0.05	
						4.4 (sum)	

[a] f taken as $\frac{1}{4}$ except when other values are given in the text.

[8] Argonne National Laboratory, Quarterly Report, March–May 1951, Physics Division (unpublished).

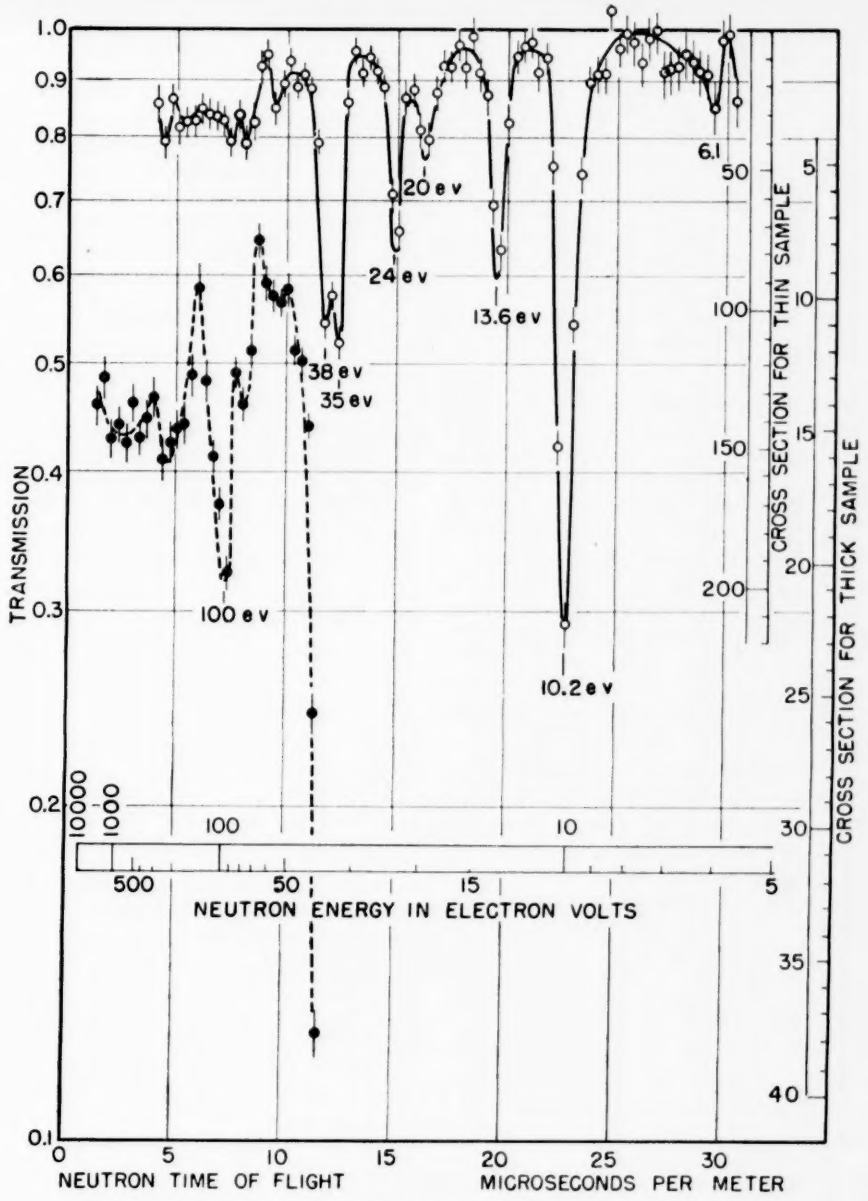

FIG. 13. The slow neutron transmission of 1.73 g/cm² (○) and 16.54 g/cm² (●) of Ta.

spin state is not known, an average value $f=0.19$, is used. This gives $\Gamma_n=0.0022$ ev.

Also,

$$\sigma_{0s}/\sigma_{0c}=\Gamma_n/\Gamma_\gamma=\Gamma_n/(\Gamma-\Gamma_n)=0.025,$$

so that this level has 97.5 percent capture and 2.5 percent scattering. The quantity $\Gamma_n E_0^{-\frac{1}{2}}=0.0015$.

The method of curve fitting has also been applied to the 4.40-ev level, for which data were taken on only one sample. An area measurement leads to the relationship between σ_0 and Γ which is shown in Fig. 10. Figure 12 shows an enlarged plot of this level with curves for three pairs of values of σ_0 and Γ from Fig. 10. The Doppler effect has been taken into account. The best values are seen to be $\sigma_0=2000$ barns, $\Gamma=0.05$ ev. However, uncertainties in the data and in the choice of resolution functions make for large possible errors in the values of σ_0 and Γ. This level is in $Re^{187,8}$ so that $\Gamma_n=0.00054$ ev (taking $f=0.31$).

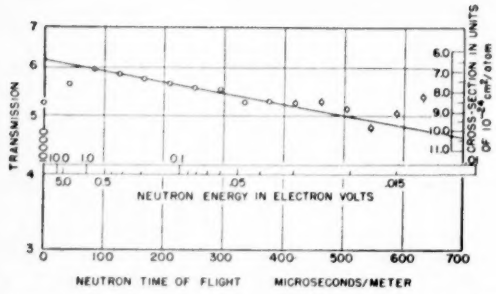
TRANSMISSION
CROSS-SECTION IN UNITS OF 10^{-24} cm²/atom
NEUTRON ENERGY IN ELECTRON VOLTS
NEUTRON TIME OF FLIGHT MICROSECONDS/METER

FIG. 14. The slow neutron transmission of 12.67 g/cm² of Ru with broad resolution. Below 1 ev the data are well fitted by $\sigma = 6.4 + 0.39E^{-\frac{1}{2}}$ until crystal interference effects begin.

For the levels at higher energies, measurements on only one sample are available. (A second, thinner sample would probably not be of much use unless the levels were much better resolved.) To get as much information as possible, area measurements were made on those levels which appeared reasonably well resolved as single levels. In measuring an area, a triangular approximation for the form of the transmission curve was assumed, since for resolution width large compared with Γ, as is the case here, the transmission curve outlines the shape of the resolution function rather than the shape of the level. Using the method described, which takes into account the "wing" area missed by the triangular approximation, the values of P and M in

$$\sigma_0 \Gamma^P = M$$

were calculated and are listed in Table I. Values of σ_0 for $\Gamma = 0.1$ ev are also given. Since the results on the higher energy levels are exceedingly rough, the Doppler effect has not been taken into account.

Each of these levels contributes to the thermal $E^{-\frac{1}{2}}$ slope the amount

$$\sigma_0 \Gamma^2 / 4E_0^{\frac{1}{2}}.$$

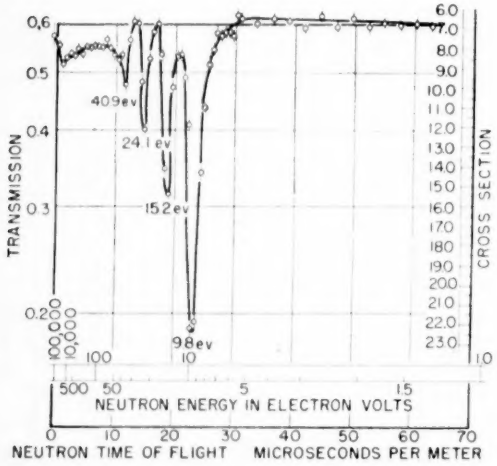

FIG. 15. The slow neutron transmission of 12.67 g/cm² of Ru with a resolution of 1.3 μsec/m (full width at base of triangle).

The sum of these contributions is seen to be 4.4 from Table I.

The measurement in the thermal region gives a value of 15.8 for the slope, indicating contributions from levels other than those considered. These may come from levels higher in energy and from negative levels close to zero. If the entire effect is due to a single negative level at -1 ev, it must have $\sigma_0\Gamma^2 = 44$ which is in line with $\sigma_0\Gamma^2$ for the other levels. Also, a separation of 3 ev from the 2.18-ev level is reasonable considering the close spacing of the higher levels.

Tantalum

Tantalum has been reinvestigated in the energy range from 40–5000 ev with a sample containing 16.54 g/cm², and in the energy range from 5–300 ev with a sample containing 1.73 g/cm². A spectrographic analysis of the sample showed lines of Fe, Ni, Cb, Si, Cu, Mg, Ca, and Mn. Concentration of all the impurities were estimated to be 0.01 percent or less. In both cases, the arc width was 4 μsec and the detection width was 2 μsec, with the base of resolution triangle being about

TABLE II. Parameters for some of the levels in Ta.

t_0 (μsec/m)	E_0 (ev)	$\sigma_0\Gamma^2$ (barn ev²)	P	M	$\Gamma_n E_0^{-\frac{1}{2}}$ (ev$^{\frac{1}{2}}$)	$\sigma_0\Gamma^2/4E_0^{\frac{1}{2}}$ (barn ev$^{\frac{1}{2}}$)
11.7	38.2	280	1.99	280	0.013	0.297
12.2	35.1	200	1.99	200	0.009	0.235
14.8	24.0	39	1.95	44	0.0015	0.083
16.2	20.0	10.3	1.80	16.0	0.0002	0.029
19.5	13.7	11	1.80	17.0	0.0002	0.054
22.6	10.2	48	1.96	54	0.0012	0.372
29.2	6.1	···	0.91	5.4	0.000008	0.009
					Sum:	1.08

1.4 μsec/m (including the broadening arising from the length of the counter). Results of these measurements are shown in Fig. 13. There is considerably more detail observed in this transmission curve than shown in a previously published one by Havens *et al.*[2] In particular, the level at 22 ev has been resolved into two levels at 20 and 24 ev and the level at 37 ev has been resolved into levels at 35 and 38 ev. There are other pronounced dips at higher energies. However, because of the closeness of level spacing, it is impossible to obtain any information about the level structure above 50 ev.

The levels between 5 and 50 ev are listed in Table II. For all but the 6.1-ev level, the thick sample approximation is fairly reliable and values of $\sigma_0\Gamma^2$ are included. More generally, the values of the parameter 'P' and 'M' are given for $\sigma_0\Gamma^P = M$. It is expected that P should be between 1 and 2 and at first glance, it seems surprising to find it 0.91 for the case of the 6.1-ev level. This can be accounted for in the following way: the level shape is approximated by a triangle plus an amount for the 'wings' of the Breit-Wigner curve. The amount added depends upon the value of Γ assumed, and since the contribution of the wings is quite large for this level (about 15 percent if $\Gamma = 0.1$ ev), the varia-

tion of the amount added is enough to affect the value of P appreciably and depresses it below what should be its lower limit. It is possible that this level is in an impurity, or even that it is spurious because of the large statistical uncertainty.

Table II also shows values for $\Gamma_n E_0^{-\frac{1}{2}}$, calculated taking $\Gamma=0.1$ ev when necessary and $\frac{1}{2}$ (average value) for the statistical weight factor. One might expect two distinct values, one for each spin state (Tantalum is monoisotopic.) However, no such grouping is observed.

Table II includes values of the quantity $(\sigma_0\Gamma^2)/(4E_0^{\frac{1}{2}})$. This is the contribution of each level to the $1/\sqrt{E}$ slope in the thermal region. The sum for these levels is 1.08. Recalculation for the case of the 4.1-ev level discussed in the previous report gives $\sigma_0\Gamma^2=55.4$, from which $(\sigma_0\Gamma^2)/(4E_0^{\frac{1}{2}})=1.67$, making a total of 2.75. The measured thermal $1/\sqrt{E}$ slope is 3.0. The difference is small and may be due to errors in calculating the quantities involved in the comparison, contributions from levels higher up in energy, and contributions from negative energy levels.

Ruthenium

Transmission curves are shown in Figs. 14 and 15 for a sample containing 12.67 g/cm². A spectrographic analysis of the sample showed no impurity lines. A trace mixture of other elements was then added to the sample. These trace elements were then observed to the degree expected. This analysis showed the Ruthenium to be extremely pure.

TABLE III. Parameters for the first four levels in Ru.

t_0 (μsec/m)	E_0 (ev)	$\sigma_0\Gamma^2$ (barn ev²)	$\sigma_0\Gamma^2/4E_0^{\frac{1}{2}}$ (barn ev$^{\frac{1}{2}}$)
11.3	40.9	32.0	0.031
14.7	24.1	18.0	0.038
18.6	15.2	14	0.061
23.1	9.8	15	0.125
		Sum:	0.255

Figure 14 shows the energy interval 0.01 ev to 10 ev taken with broad resolution. In the energy interval just above where crystal interference effects become important, the cross section is well matched by the curve $\sigma=6.4+0.39E^{-\frac{1}{2}}$.

Figure 15 shows the energy interval from 1 ev to 1000 ev with a resolution of about 1.3 μsec/m (full width at base). There are strong dips in transmission at 23.1, 18.6, 14.7, and 11.3 μsec/m. Each of these dips was assumed to be caused by a single resonance level. For all of these levels, the sample was found to be decidedly thick (i.e., $n\sigma_0\gg1$) so that Table III lists values of $\sigma_0\Gamma^2$.

Ruthenium has 7 isotopes ranging from $A=96$ to $A=104$, with concentrations ranging from 2.2 percent to 31.3 percent. No assignment of the levels to particular isotopes can be made with the normal sample used.

The four levels listed contribute $0.26E^{-\frac{1}{2}}$ to the thermal region, leaving $0.13E^{-\frac{1}{2}}$ to be made up by errors, higher energy levels, and negative levels. (With the observed spacing of levels, a nearby negative level is likely.)

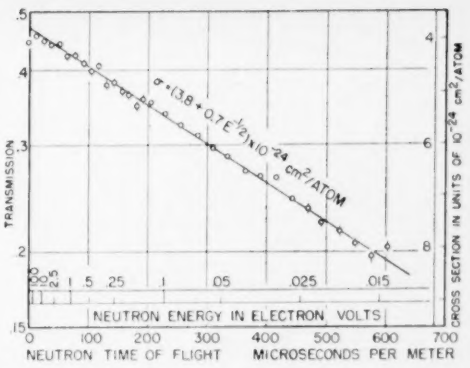
TRANSMISSION
CROSS SECTION IN UNITS OF 10⁻²⁴ cm²/ATOM
σ=(3.8+0.7E^½)×10⁻²⁴ cm²/ATOM
NEUTRON ENERGY IN ELECTRON VOLTS
NEUTRON TIME OF FLIGHT MICROSECONDS PER METER

FIG. 16. The slow neutron transmission of 17.2 g/cm² of Cr taken with broad resolution. The data are well-fitted by $\sigma=3.8+0.7E^{-\frac{1}{2}}$.

Chromium

A 17.2 g/cm² sample was used in all of these measurements. A spectrographic analysis of the sample showed ~0.1–1 percent Mn, ~0.1 percent Fe and Si, and 0.01 percent or less of Al, Ca, Cb, Cu, Mg, Mo, Ni, Ti, and V. Further analysis showed Mn and W to be present to 0.2 percent. The thermal region shown in Fig. 16 is well-matched by

$$\sigma=3.8+0.7E^{-\frac{1}{2}}.$$

Figure 17 shows the region above 3 ev taken with moderate resolution. Calculation of $\sigma_0\Gamma^2$ from the data of Fig. 17 for the known tungsten impurity of 0.2 percent, showed that the 18-ev level was due to tungsten. The dip at 12 ev did not repeat consistently in several runs and is probably spurious.

The level evident at higher energies, and shown with much better resolution in Fig. 18 to be at 3800 ev, has also been analyzed by the area method, giving $\sigma_0\Gamma^2=8.55\times10^7$ barn ev². If this is assumed to be a scattering level in the predominant isotope ($A=52$, 83.3 per-

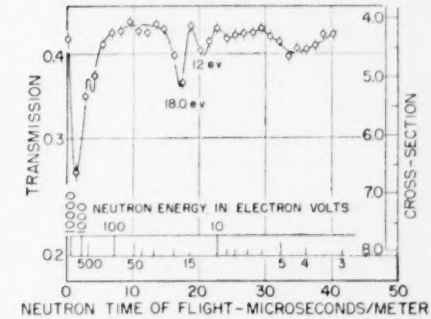

FIG. 17. The slow neutron transmission of 17.2 g/cm² of Cr taken with a resolution of 3.0 μsec/m (full width at base of triangle).

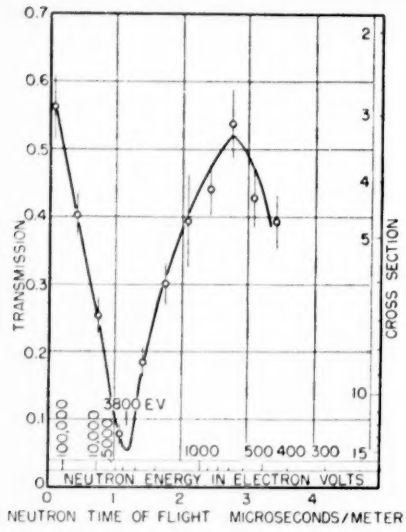

FIG. 18. The slow neutron transmission of 17.2 g/cm² of Cr taken with a resolution of 1.1 μsec/m (full width at base of triangle) showing the large level at 3800 ev.

cent) the maximum cross section is 690 barns for the isotope (taking spin=0), giving $\Gamma=385$ ev. If the thermal absorption is attributed to a small amount of capture in this level, calculation gives $\Gamma_\gamma/\Gamma=0.0076$, showing that only 0.76 percent of the neutrons forming the compound nucleus leads to a new isotope.

If the assignment of the 3800-ev level to the predominant isotope is correct, it is expected that the shape of the transmission curve at lower energies would be different from what it is. Calculations indicate that the interference minimum in cross section should be at about 1000 ev and very small (<1 percent) compared with $4\pi R^2=3.95$ barns. Recovery to this value at lower energies should also be very slow. There is no definite way to resolve this situation without further measurements. It is possible that the level is due to one of the other isotopes, say $A=53$, which is 9.43 percent abundant. Then, $\sigma_0\Gamma^2$ is increased to 1.81×10^9 for the isotope and spin state and Γ becomes 1620 ev. (The spin of the $A=53$ isotope is unknown, and only its average effect has been taken into account in this calculation.) If one of the rarer isotopes is actually responsible for this level, the low energy behavior of the cross section (<1000 ev) is reasonable since it is dominated by the constant cross section of the predominant isotope and hence approximately constant at about $4\pi R^2$. This explanation is also reasonable in the light of the data given in Table IV, taken from AECU-2040,[4] which shows that capture in the thermal region is due primarily to the two isotopes Cr^{50} and Cr^{53}.

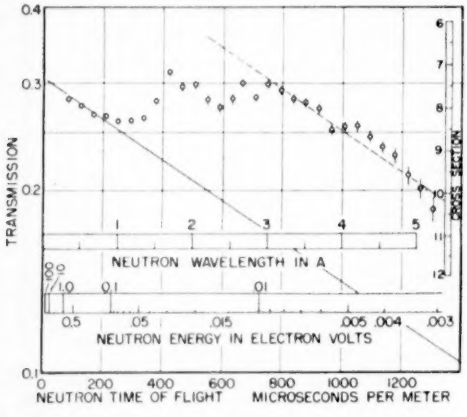

FIG. 19. The slow neutron transmission of 18.74 g/cm² of Ga in the thermal region showing interference effects. ——— represents $\sigma=7.3+0.35E^{-\frac{1}{2}}$; — — — represents $\sigma=3.6+0.35E^{-\frac{1}{2}}$.

TABLE IV. Abundance and absorption cross sections of the Cr isotopes.

Isotope	Percent abundance	σ_{abs} at 0.025 ev, in barns
Cr^{50}	4.4	16.3 ±1.3
Cr^{52}	83.7	0.73±0.06
Cr^{53}	9.5	17.5 ±1.4
Cr^{54}	2.4	<0.3

Figure 17 indicates, and other measurements show, that there is a transmission dip in this sample at 4 μsec/m. A portion of this dip is evident in Fig. 18. This dip is due to the 300-ev level in the 0.2 percent Mn impurity in the sample. The 3000-ev level in the Mn impurity is masked by the 3800-ev level in the Cr.

Gallium

An 18.74-g/cm² sample was used in all the investigations. The thermal region is shown in Fig. 19. Crystal interference effects are observed, although not as pronounced as in the case of some other crystals. Ga has a melting point of 29.8°C (=85.6°F), and since the thermal data were taken during summer, the sample was probably liquid part of the time. The interference effects may be due to the sample being solid part of the time. However, liquids are also known to exhibit interference effects as a result of short range order (e.g., liquid bismuth and vitreous quartz). This curve is not useful for determining the $E^{-\frac{1}{2}}$ slope.

Figure 20 shows the 0.05-ev to 5-ev region where a straight line matches the data well, giving $\sigma=7.3+0.35E^{-\frac{1}{2}}$. This equation is shown plotted on the graph of the thermal region. The situation is now clear. With decreasing energy, there are two competing effects: (1) a tendency towards transparency as the number of ways of removing neutrons from the beam (by Bragg reflection) decreases, and (2) an increase in cross section arising from a "1/v" capture term. At low energies, the experimental data indicate a straight line of approximately the same slope as the capture term. If the sample were a crystal, one would interpret the difference between the free cross section (7.3 barns) and the difference between the lowest energy data and the line

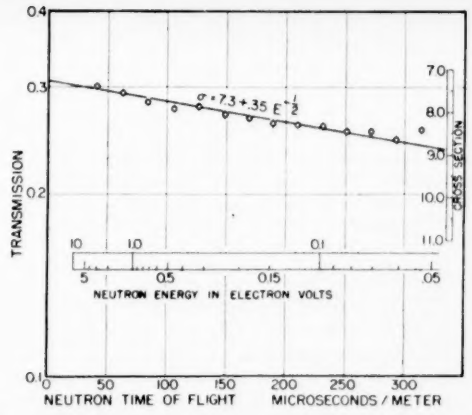
TRANSMISSION
CROSS SECTION
$\sigma = 7.3 + .35\ E^{-\frac{1}{2}}$
NEUTRON ENERGY IN ELECTRON VOLTS
NEUTRON TIME OF FLIGHT MICROSECONDS / METER

FIG. 20. The slow neutron transmission of 18.74 g/cm² of Ga between 0.05 and 5 ev. The data are well-fitted by $\sigma = 7.3 + 0.35E^{-\frac{1}{2}}$.

$\sigma = 7.3 + 0.35E^{-\frac{1}{2}}$ (3.6 barns) as the incoherent scattering cross section, giving about 3.7 barns. The validity of this in the case of a liquid sample is questionable. (Also, the energy may not yet be low enough to eliminate the last Bragg reflection if the sample is a solid.)

Using the slope of the formula for the σ as given above, the absorption cross section at 2200 m/sec (0.0253 ev) is 2.2 barns, which is somewhat lower than the value of 2.71±0.12 given in AECU-2040.[4]

Figure 21 shows that there are no levels until the large level at about 100 ev. Below this, the curve is essentially $\sigma = 7.3 + 0.35E^{-\frac{1}{2}}$, although as the level is approached, the transmission rises before dropping at the level.

Two clearly resolved levels at 102 ev and 310 ev are shown in Fig. 22. There are indications of levels at 500 ev and 1000 ev. It is difficult to make accurate calculations on the levels at 102 and 310 ev because the low

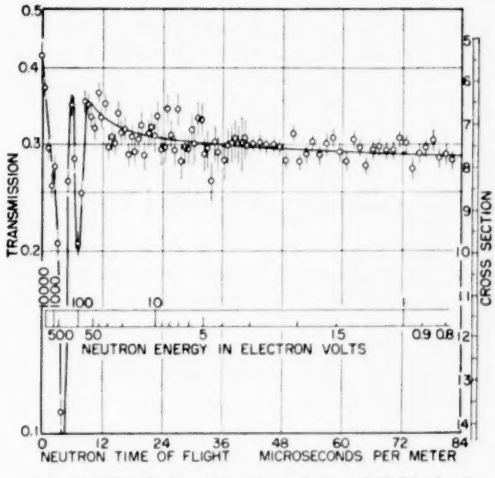

FIG. 21. The slow neutron transmission of 18.74 g/cm² of Ga with better resolution.

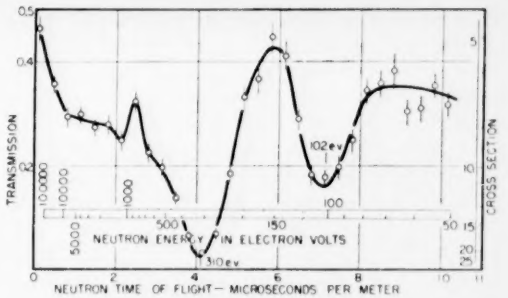

FIG. 22. The slow neutron transmission of 18.74g/cm² of Ga showing the two levels at 102 ev and 310 ev.

transmission (0.3–0.4) away from the levels makes it difficult to separate out the effect of the "background" portion of the cross section and also gives a large interference effect between the potential and resonant scattering terms. However, the area method was used to obtain approximate values of $\sigma_0\Gamma^2$. If $\Gamma_\gamma = 0.1$ ev is assumed, we can get values for Γ_n and Γ by using the relationship $\sigma_0 = 4\pi\lambda^2 f(\Gamma_n/\Gamma)$, where f is taken as $\frac{1}{4}$ on the average. (f has the following four possible values, with spin $= \frac{3}{2}$ for both isotopes,

$$A = 69: \quad f = 0.229,\ 0.382;$$
$$A = 71: \quad f = 0.145,\ 0.242.)$$

The results are given in Table V.

TABLE V

E_0 (ev)	$\sigma_0\Gamma^2$ (b·ev²)	Γ (ev)	Γ_n (ev)	σ_0 (b)	σ_{0c} (b)	$\Gamma_n E_0^{\frac{1}{2}}$ (ev$^{\frac{1}{2}}$)	$\sigma_{0c}\Gamma^2/4E_0^{\frac{1}{2}}$ (b·ev$^{\frac{1}{2}}$)
120	2200	0.71	0.61	6000	900	0.056	0.063
310	170 000	9.0	8.9	2100	23	0.50	0.086
						Sum:	0.149

The last column gives the predicted value for the thermal $E^{-\frac{1}{2}}$ slope on the bases of these two levels alone. The result is less than half of the measured value of 0.35. The difference may be due to the other levels and to negative levels. However, the calculations are sufficiently crude that anything better than order of magnitude agreement is not to be expected.

These data are essentially in agreement with the Harwell data (AECU-2040),[4] although there are some differences. In particular, the 102-ev level is found by the Harwell group to be at 95 ev and somewhat narrower.

The authors wish to express their appreciation to Miriam Levin for her extremely valuable assistance in taking, plotting, and analyzing the data. We also wish to acknowledge the assistance of Edward Stone and Murray Weinstein for computational help in the calculation of the Doppler effect. We wish to thank Jules Levin of the Brookhaven National Laboratory for his helpful criticism and valuable suggestions. Appreciation is also expressed to the U. S. Atomic Energy Commission for their financial support and interest in this research.

PHYSICAL REVIEW VOLUME 92, NUMBER 3 NOVEMBER 1, 1953

Thermal Neutron Absorption Cross Sections of Boron and Gold*

R. S. CARTER, H. PALEVSKY, V. W. MYERS, AND D. J. HUGHES
Brookhaven National Laboratory, Upton, New York
(Received July 16, 1953)

The cross sections of boron and gold, which are widely used as standards for slow neutron measurements, have been determined as functions of wavelength. Total cross sections were measured in the wavelength range 1.5–10A with the Brookhaven slow chopper, the long wavelengths being used to minimize the effects of scattering. The absorption cross section of boron of "normal" isotopic constitution is 749±4 barns at 2200 m/sec (1.80A); the variation of cross section with boron source is expected to be only about 1 percent. The measurement of the gold cross section is complicated by the deviation from $1/v$ resulting from a nearby resonance and by grain orientation effects in the scattering. The 2200-m/sec value, resulting from measurements at long wavelength together with a small correction for the 4.9-ev resonance, is 98.7±0.6 barns.

I. INTRODUCTION

FOR many applications of slow neutrons involving cross sections of various materials, the use of certain *standard* cross sections is of great value. The standard materials, of accurately known cross sections, can be used to determine other cross sections by relative measurements, which can be performed with much greater accuracy than absolute determinations. The cross-section standards are also applied to measurement of neutron flux and, by means of flux standardization, to calibration of neutron source strength. In these applications it is usually the absorption cross section σ_{abs} that is of interest, which is the cross section for all processes in which the neutron "disappears," consisting mainly, for slow neutrons, of the (n,p), (n,α), and (n,γ) reactions.

Whereas absorption cross sections are difficult to measure directly with precision, for example by the pile oscillator technique, they can for some materials be inferred from the total cross section with much greater accuracy. The latter approach is possible if the absorption is much larger than the scattering, which must be subtracted from the total to obtain the absorption cross section. Although the total cross section can be measured with great precision by transmission measurements, the subtraction of the calculated scattering, even when relatively small, introduces uncertainties of 1–3 barns because of neutron interference effects. It is possible, however, to obtain the absorption cross section from transmission experiments without subtraction of scattering because of the practical disappearance of the latter at long wavelength. This technique has been used only recently, and in the present paper its application to the important cases of boron and gold will be described.

The standard materials for slow neutron absorption are usually boron of normal isotopic constitution or gold; for both of these the absorption cross section at thermal energy (2200 m/sec) is much larger than the scattering. The values of the thermal absorption cross sections for these standards have been determined most accurately from transmission measurements of total cross sections and subtraction of scattering. As the direct absorption measurements, such as the pile oscillator, are used only to measure other materials relative to these standards, they are not applicable to the fundamental standards themselves. For some years the thermal absorption of boron in general use was about 705 barns, a value based on transmission measurements made by Fermi at Argonne Laboratory using neutrons whose velocity was selected by the slow chopper. The gold cross section measured with the same equipment[1] resulted in a value of 93 barns, which was used for several years. The scattering correction uncertainty is negligible in boron relative to the absorption but it amounts to 1–2 percent for gold.

In the last few years the boron cross section has risen by surprisingly large amounts, the most recent values lying in the range 750–760 barns.[2] During this period the gold cross section had risen slightly, to 95 barns, and several measurements[3] of its total cross section were in good agreement. In view of the importance of boron and gold as standards and the recent sharp rise in the boron value, it was thought advisable to make careful measurements of the absorption of these materials with the slow neutrons available with the Brookhaven slow chopper. The availability of long wavelengths makes it possible to avoid uncertainties involved in the subtraction of scattering by measuring the cross section at wavelength beyond the cutoff, where most of the scattering disappears.

II. EXPERIMENTAL METHOD

The method of obtaining absorption cross sections by subtraction of scattering from the total (measured by transmission at 2200 m/sec) involves some uncertainty in the scattering to be subtracted. This uncertainty arises because the scattering in the thermal energy region varies abruptly with wavelength in a manner typical of the Bragg scattering in the poly-

* Work carried out under contract with the U. S. Atomic Energy Commission.

[1] T. Brill and H. V. Lichtenberger, Phys. Rev. **72**, 585 (1947).
[2] Unpublished results of Argonne (R. Ringo *et al.*) and Columbia (W. Havens *et al.*) transmission measurements.
[3] Listed by H. Pomerance, Phys. Rev. **83**, 641 (1951).

crystalline samples usually used. The scattering is extremely difficult to measure in a separate experiment with monenergetic neutrons, and its calculation is uncertain because the coherent Bragg scattering is reduced by extinction effects in the microcrystals, and is modified by preferred orientation of the crystal grains. In the case of boron the scattering is so small that the uncertainty is negligible, but for gold it is sufficiently large as to affect the final accuracy seriously.

The effect of scattering can be avoided, however, by measuring the cross section at wavelengths longer than the crystal cutoff (twice the largest lattice spacing) because the coherent scattering is not observable beyond this wavelength. For most materials, the scattering is predominantly coherent, and the remaining incoherent scattering beyond the cutoff is usually negligible compared to absorption. The cutoff wavelength is of the order of 4–7A and sufficient neutron intensity is available with the slow chopper at longer wavelengths to make possible accurate transmission measurements.

At long wavelength the cross section is made up of capture and incoherent scattering only, the latter consisting of isotopic incoherence, spin-dependent incoherence, and thermal diffuse scattering.[4] The absorption, which is almost always $1/v$ in the long-wavelength region, can be separated from the various types of incoherent scattering because of its velocity dependence and independence of sample temperature. As the isotopic and spin-dependent incoherent cross sections are constant with wavelength, whereas the temperature-diffuse scattering varies rapidly with temperature, these components can be identified. The method of measuring absorption cross sections with long-wavelength neutrons has a great advantage when the scattering is not negligible relative to absorption because of the practical disappearance of the scattering (for the usual case of predominantly coherent scattering) beyond the cutoff. Some uncertainty exists, however, in the extrapolation of the absorption from the long-wavelength region, where it is measured, to the thermal value at 2200 m/sec. There is no uncertainty in the case of boron, but in gold the departure from $1/v$ is of the order of 1 percent. The smallness of this departure from $1/v$ in the case of gold, which has a prominent resonance near thermal energy, indicates that the effect is negligible for most other materials.

The source of velocity-selected neutrons for the present measurements is the Brookhaven slow chopper,[5] which has been used for "cold" neutron measurements, in the range 1–20A, extensively in the past two years. The chopper allows a burst of pile neutrons to pass periodically to a detector several meters distant and the velocity is selected by the time of flight to the detector (an enriched BF_3 proportional counter). The shutter action is obtained by means of cadmium slits in a rotating cylinder that passes one burst of neutrons per revolution. The distance between the detector and chopper is determined by the wavelength region being investigated and the resolution required for the measurement. The detector can be placed as far as 10 meters from the chopper without causing successive neutron bursts to overlap; at this distance and the normal chopper speeds the energy resolution is approximately 1 percent (full width at half-maximum) for the entire available energy range of 10^{-1} to 10^{-4} ev. For the present measurements, flight paths of about two meters were used hence 5 percent resolution.

The flight time of the neutrons is determined electronically, the timing sequence being initiated by light reflected from a mirror mounted on the shaft of the chopper. At the end of a pre-set time delay, the circuit allows the neutron pulses from the BF_3 counter to pass into twelve scaling and recording channels, spaced consecutively and of equal, variable, time duration. The electronic timing sequence is calibrated with a one-megacycle quartz crystal, with the frequency known to ± 0.1 percent. Although the electronic calibration allows the determination of elapsed time to one part in a thousand, the absolute wavelength scale would be affected by the possible time interval between the moment the neutrons pass the center of the chopper and the instant the zero-time pulse is generated. The proper adjustment of the zero-time pulse to make the two events simultaneous is determined by measuring the flight time corresponding to the Bragg cutoff in graphite. Graphite is used because of the large discontinuity in cross section (9 to 1.3 b) at the cutoff, and the long-cutoff wavelength, 6.70A, which gives a calibration point in the region of interest in the present work.

Because of finite resolution the discontinuity in cross section appears as a line of finite slope in the transmission curve. Figure 1 shows the transmission of neutrons through 1 in. of graphite, for which measurement the resolution function can be represented by a triangle with a full width at half-maximum of 0.15A. The solid line in Fig. 1 is the calculated transmission expected from the graphite crystal structure for infinite resolution, and the dotted line includes resolution. The position of the graphite cutoff is determined by graphical analysis to ± 0.02A, hence the wavelength scale is known to approximately the same accuracy.

The sample is placed between the chopper and the detector, usually about 18 in. from the latter to avoid the small-angle scattering[6] that takes place in fine grain materials, especially at long wavelength. The total cross section is determined by a transmission measurement, i.e., the neutron intensity is measured for the open beam and again for the sample in the beam. The effect of epi-cadmium neutrons that penetrate

[4] D. J. Hughes, *Pile Neutron Research* (Addison-Wesley Press, Cambridge, 1953), pp. 249–254, 270–272.

[5] Seidl, Palevsky, Randall, and Thorne, Phys. Rev. **82**, 345 (1951).

[6] R. J. Weiss, Phys. Rev. **83**, 379 (1951).

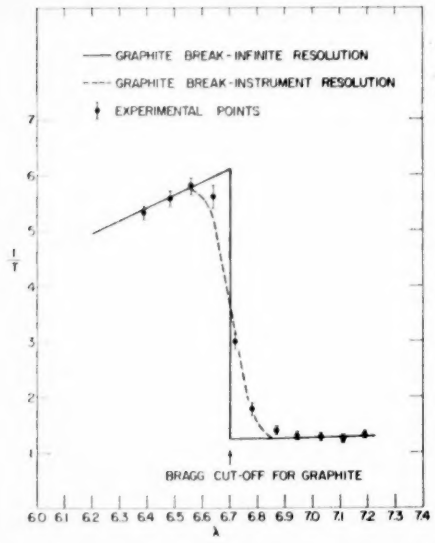
GRAPHITE BREAK-INFINITE RESOLUTION
GRAPHITE BREAK-INSTRUMENT RESOLUTION
EXPERIMENTAL POINTS
I/I
BRAGG CUT-OFF FOR GRAPHITE
6.0 6.1 6.2 6.3 6.4 6.5 6.6 6.7 6.8 6.9 7.0 7.1 7.2 7.3 7.4
λ

FIG. 1. The discontinuity in neutron transmission of a 1 in. graphite sample, which is used as a wavelength calibration of the slow chopper. The solid curve is calculated from the crystal structure of graphite and the dotted curve includes the instrumental resolution (0.15A).

the chopper as well as all other background neutrons can be accurately determined by placing a thin (0.010-in.) sheet of cadmium at the exit of the chopper. As this sheet removes more than 99 percent of the timed neutrons but does not affect the epi-cadmium background neutrons, the difference between a measurement without and with cadmium gives the correct intensity of the timed neutrons. The epi-cadmium neutron background is reduced as much as possible by adjusting the opening of the beam hole into the pile so that the cadmium ratio is a maximum. In addition, the ratio of timed to background neutrons (of wavelength greater than 3.9A) is improved by the use of a Be filter, which attenuates the epi-cadmium neutrons greatly with only a slight decrease in the intensity of timed neutrons. In the transmission measurements, a second BF_3 counter, mounted in a pile hole adjacent to the slow-chopper hole, serves as an incident intensity monitor. The open-beam counting rates for the present measurements were of the order of 1000 counts per minute per channel at 4A and 100 at 8A.

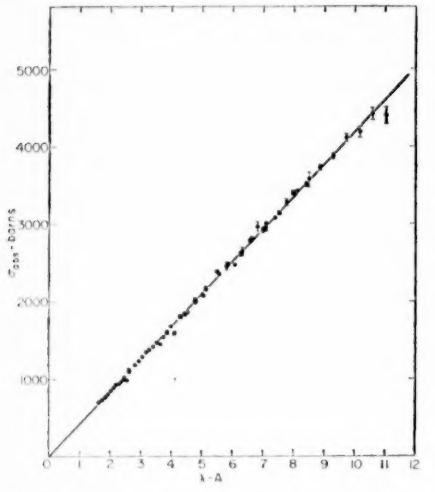

FIG. 2. The absorption cross section of boron as a function of neutron wavelength, obtained by subtraction of scattering from the measured total cross section of the boron solution.

III. BORON

The scattering correction is small for boron and cannot explain the much larger discrepancy among previous measured absorption cross sections (700–760 b) for normal boron. Neither can the discrepancy be ascribed to variations in B^{10} content (which isotope accounts for essentially the entire absorption), for this varies[7] by a *maximum* of ± 2 percent. The most likely explanation of the previous variation in results involves the boron content of the samples used, for instance, the presence of water in boric oxide.

The boron used in the present work was obtained in the form of boric acid powder from R. Ringo at Argonne National Laboratory. This particular born (mined in California) was used because its cross section had been measured at Argonne and its isotopic ratio determined at Oak Ridge. The question of the B^{10} content of this and other samples will be considered in more detail later.

The boric acid was converted into fused B_2O_3 by R. Stoenner of the Brookhaven chemistry department. The boric acid was heated to drive off the water and when the material had reached a point where its weight no longer changed it was checked by chemical analysis to see if it still contained any water. Several attempts were necessary before B_2O_3 was obtained that had less than 0.2 percent (by weight) water. The fused B_2O_3 was then weighed carefully and dissolved in a known amount of D_2O. The boron content was determined by chemical analysis before and after every slow chopper measurement made with each sample in order to detect any change in concentration. The chemical analysis was performed by saturating a given weight of solution with mannitol to increase its acidity, then titrating it with a standard alkali until it was neutralized. The amount of alkali used was thus an accurate measurement of the amount of B_2O_3 present. The boron content as determined by chemical analysis agreed to better than 0.2 percent with the weight determination in each case.

The B_2O_3 was dissolved in D_2O rather than H_2O in order to avoid the large scattering cross section of the

[7] Thode, Macnamara, Lossing, and Collins, J. Am. Chem. Soc. **70**, 3008 (1948).

latter. To increase further the contribution of the boron to the total cross section, the solution was heated to 40°C to increase the B_2O_3 concentration. For the concentrations used, about 30 mg/g of solution, the boron absorption constitutes about 60 percent of the total cross section at 4A. The solutions were used in thin-walled aluminum holders, which allowed the thickness of the sample to be accurately determined. The amount, in grams/cm², of B_2O_3 in the beam was obtained from the product of the concentration, density, and thickness of sample.

The boron transmission was measured by comparing the neutron intensity for the $B_2O_3+D_2O$ sample with a "blank" consisting of D_2O. Since the density of the D_2O is slightly decreased when the B_2O_3 is added, the D_2O blank was made slightly thicker to compensate for this small effect. The D_2O and the $B_2O_3+D_2O$ solution were run alternately in the slow-chopper beam, contained in a temperature-regulated furnace at 40°C.

Transmissions were measured in the range 1.7A to 9.5A, each cycle of measurements consisting of a D_2O blank run, a D_2O background (0.01-in. cadmium), a $B_2O_3+D_2O$ solution run, and a solution background run. Several cycles were completed for each wavelength range and the transmission determined from the ratio of the counting rates after subtraction of background. The total cross section of B_2O_3 per atom of boron determined from the transmission includes that of 1.5 atoms of oxygen as well as a slight contribution from the D_2O, because it was not practical to make the blank contain exactly the same number of D_2O molecules as the sample. The measured cross section was corrected for the D_2O contribution (an effect of approximately $\frac{1}{3}$ percent, determined from a separate cross section measurement of D_2O), as well as for the scattering of boron and oxygen (calculated) to obtain the absorption cross section. Because of the use of a liquid sample, the "cutoff" is not complete and some scattering from the boron and oxygen is present in the wavelength region used—(about $\frac{1}{2}$–1 percent of the total cross section).

In Fig. 2 is plotted the absorption cross section of boron as a function of wavelength, obtained by subtraction of the scattering and D_2O contribution from the measured cross section. A line drawn through zero cross section at zero wavelength fits the points very well, thus verifying the $1/v$ nature of the absorption cross section. The linearity of the curve and the statistical accuracy of the points is better demonstrated in Fig. 3 where σ/λ is plotted against λ. The points are well fitted by a horizontal line at $\sigma/\lambda=416.7$ b/A. Thus we obtain for the cross section of boron at 1.80A (2200 m/sec) the value;

$$\sigma_{abs}=749\pm4 \text{ b},$$

where the principal contributions to the standard error are statistics and uncertainty in wavelength calibration. This value is in good agreement with the unpublished result[8] of Ringo *et al.* at Argonne using the same boron source, but is much higher than older values in the 700–730 b range.

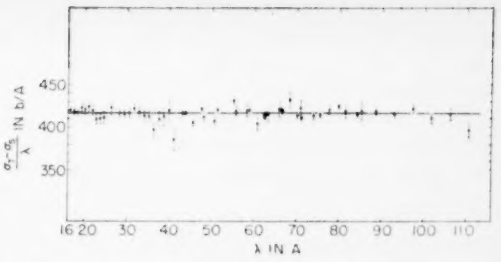

FIG. 3. The boron absorption cross section divided by wavelength as a function of the latter.

In addition to the above data a sample of boron glass was measured in the region 1.5 to 9A. Its transmission had previously been determined at Columbia University and it had been analyzed quantitatively by the Corning Glass Company. It consisted of 13.4 ±0.1 percent B_2O_3 by weight, 80.1 percent SiO_2, 4.5 percent Na_2O, and 2 percent Al_2O_3, these constituents giving rise to a scattering cross section of 46 b per atom of boron, assuming that the scattering adds algebraically. The observed cross section, after correction for this scattering, is plotted against wavelength in Fig. 4, where again a straight line through zero fits the points well. The value for the total cross section at 1.80A obtained from the "best" line through zero is 753 b. When this $1/v$ cross section is corrected for the 0.5 b contributed by the absorption cross section of the constituents other than boron, the value for the boron

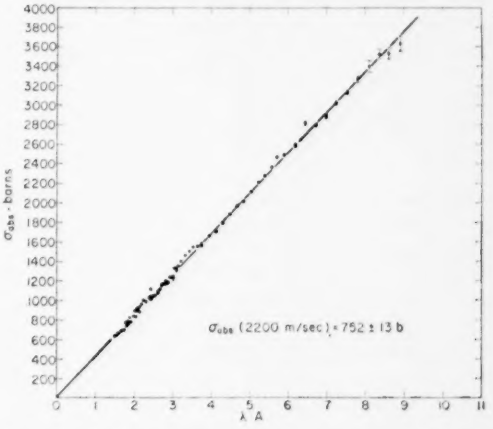

FIG. 4. The boron absorption cross section obtained by subtraction of scattering from the measured total cross section of the boron glass sample.

[8] Quoted by Kaplan, Ringo, and Wilzbach, Phys. Rev. **87**, 785 (1952), as 755±5 b; and by Hamermesh, Ringo, and Wexler, Phys. Rev. **90**, 603 (1953) as 755±3 b.

absorption cross section determined from the glass is 752±13 b. The 13-barn error is based entirely on statistical fluctuations, the error in the corrections being negligible compared to this amount. Although the boron glass was not measured as carefully as the fused B_2O_3, it furnishes a valuable check on the value given above as it was obtained from a different form of sample.

The isotopic content of the boron used in the Argonne and the present measurement has been analyzed by mass spectrograph at Oak Ridge. Although there exists some question concerning the absolute accuracy of isotopic ratios thus determined, the relative values from sample to sample are reliable. Thus the B^{10} content of our sample was measured as 0.185 (systematic error

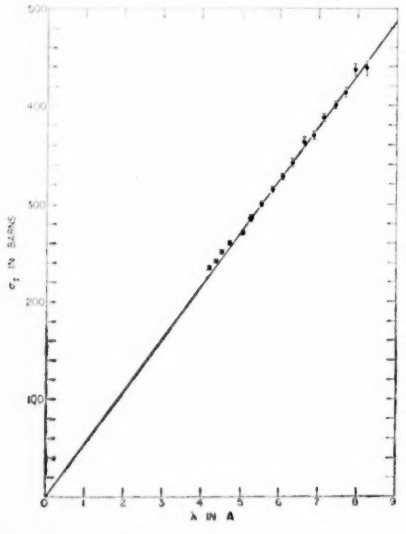

FIG. 5. Measured total cross section of rolled gold foil as a function of wavelength, showing the $1/v$ region beyond the crystal cutoff (4.71A) and the appearance of coherent scattering at shorter wavelengths. Measured points in the thermal region are not shown because the effects of grain orientation prevent calculation of the scattering corrections.

not estimated) but it was found to be the same within instrumental sensitivity ($\frac{1}{2}$ percent) as routine California boron measured at Oak Ridge. Thode *et al.*[7] have found 0.1871 for the B^{10} content of California boron in a careful absolute measurement, a range of $\pm\frac{1}{2}$ percent in California boron, and an extreme range of ±1.8 percent for world wide samples. The isotopic variation in "California" boron (any boron from western United States sources) thus seems to be so small that the cross section of different samples can be taken as equal.

IV. GOLD

The total cross section of gold was measured in the range 1.7 to 8.5A, using foils of purity greater than 99.9 percent, whose thickness varied from 0.010 in. to 0.040 in. Transmissions were obtained in the same manner as described for boron although no "blank" was needed in the open beam measurements.

The observed total cross section is plotted as a function of wavelength in Fig. 5, where the coherent scattering contribution to the cross section is evident at wavelengths less than the 4.7A cutoff. Beyond the cutoff wavelength, the cross section is almost entirely absorption, the calculated inelastic scattering amounting to only 0.3 b and the calculated incoherent (spin-dependent) scattering to 0.4 b,† both negligible compared to absorption.

The straight line drawn through zero cross section at zero wavelength in Fig. 5 fits the points very well, verifying the $1/v$ nature of the absorption cross section in the 5–9A range. The slope of the line is 54.4 ±0.25 b/A, giving the extrapolated $1/v$ absorption cross section at 1.80A (2200 m/sec) as:

$$\sigma_{abs}=97.8\pm0.5 \text{ b}.$$

As for boron, the principle sources of the error are statistics and wavelength calibration.

The 97.8-b result is based on an extrapolation of the $1/v$ cross section to thermal energy (1.80A), an extrapolation that requires some investigation, especially in view of the fact that the present value is higher than earlier results[3] (about 95 barns). The resonance at 4.9 volts should cause the absorption cross section to increase above the $1/v$ line by 1 percent at 1.80A (2200 m/sec) as this level is primarily responsible for the thermal cross section.[9,10] In order to study the variation of absorption for wavelengths less than 4.7A it is necessary to subtract the scattering from the observed total cross section. The scattering can be calculated[11] from the crystal structure of gold, but the result is uncertain because of the unknown effects of crystal orientation and extinction. The observed total cross section at thermal energy, if corrected for scattering by a calculation omitting crystal orientation and extinction effects, gives an absorption 3 percent *less* than the $1/v$ line. Actually a detailed examination of the total cross section reveals that the full value of the last coherent peak (at the crystal cutoff) is not observed. In addition, a total cross section measured with the sample at an angle to the beam revealed crystal orientation effects by changes in the observed peaks. Thus considerable doubt is thrown on the scattering correction in the thermal region for the rolled gold sample.

In order to investigate the cross section in the thermal region with less uncertainty in the scattering cross section, samples of powdered gold were measured,

† *Note added in proof:* Direct measurement of incoherent scattering by B. N. Brockhouse (private communication) gives 0.5±0.26.

[9] Unpublished Brookhaven fast chopper results.

[10] J. Tittman and C. Sheer, Phys. Rev. **83**, 746 (1951).

[11] See reference 4, pp. 270–272.

for which no effects of orientation and extinction should change the calculated scattering. The results of measurements in the wavelength region of interest are given in Fig. 6. Because the sample thickness is difficult to determine accurately for powdered gold, the total cross section is normalized at wavelengths just beyond the cutoff to the $1/v$ line of Fig. 5. The magnitude of the abrupt change in cross section at the cutoff, as well as the location of this change (4.7A), corresponds well with the theoretical scattering, given by the upper curved line.

The agreement of the observed behavior of the cross section at cutoff with the theoretical scattering justifies the use of the latter to the accuracy of the measurements, about one barn. Subtraction of the theoretical scattering for the entire energy range of Fig. 6 gives a result in agreement with the $1/v$ line, because the observed points agree well with the theoretical scattering. With the accuracy shown in Fig. 6, it is not possible to detect the 1 percent increase at thermal energy that should result from the resonance at 4.9 ev.

The value of the $1/v$ line at thermal energy, 97.8 $\pm$0.5 b, is known more accurately than the thermal cross section in Fig. 6 because no scattering cross section is involved. The most accurate value of the actual absorption cross section at thermal energy (2200 m/sec) is obtained by adding the effect of the resonance to the $1/v$ value, with the result:

$$\sigma_{abs}(2200\ \text{m/sec}) = 98.7 \pm 0.6\ \text{b}.$$

The slight increase in the error arises from uncertainty in the properties of the resonance level.[9,10] The fact that values of this cross section reported in the past have been somewhat lower is probably a result, at least partly, of the uncertainties in scattering. These uncertainties, together with the slight departure from $1/v$ in the thermal region and the prominent resonance absorption, tend to decrease the value of gold as a thermal neutron cross-section standard.

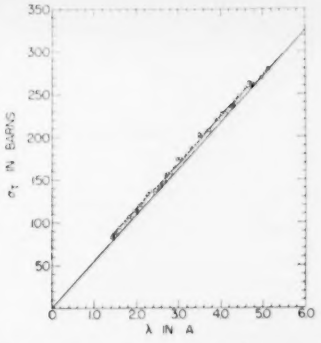

FIG. 6. Total cross section of powdered gold, normalized beyond the cutoff to the rolled gold results of Fig. 5 (straight line). The upper line represents the addition of the calculated scattering.

A Summary of *K*-Meson Data

L. LEPRINCE-RINGUET, *École Polytechnique, Paris, France*

AND

B. ROSSI, *Massachusetts Institute of Technology, Cambridge, Massachusetts*

(Received August 3, 1953)

The results of experiments on K mesons performed at the École Polytechnique of Paris and at the Massachusetts Institute of Technology are summarized and analyzed.

THE cosmic-ray groups at the École Polytechnique of Paris (E.P.) and at the Massachusetts Institute of Technology (M.I.T.) have recently reported new experimental data on charged heavy mesons (K mesons). These observations which refer to K mesons decaying at rest (S events) or in flight (V events) and giving rise to single charged secondary particles concur to establish the following results:

(1) The masses of K mesons observed to disintegrate at rest in photoemulsions or in cloud chambers are the same within the experimental errors. E.P. has made two different sets of measurements. The first set refers to K mesons emerging from stars and stopping in the emulsion;[1] the mean of six independent measurements obtained on three long tracks (three by scattering range and three by ionization range) gives a mass of $(940\pm 40)m_e$. The second set refers to S events observed at the Pic du Midi with an arrangement of two cloud chambers.[2] The magnetic curvature of the track was measured in the top chamber, and the range in a multiplate chamber placed below. Three S events gave the mass values 885, 915, 1030; the mean of these three measurements is very close to the one quoted above.

M.I.T. analyzed (by the range-scattering method) 16 S events; under the assumption that all particles were identical, the most probable value of the mass turned out to be $(1200^{+270}_{-200})m_e$. Moreover, the distribution of the scattering variable for those cases where the K particles stopped after traversing 4 or more plates was found to be consistent with a single mass of about $1000m_e$.[3]

(2) There is evidence for the direct production in nuclear interactions of K mesons (3 events observed in emulsion by E.P.,[1] similar to that observed first by Levi-Setti and Tomasini;[4] several S events observed in cloud chambers by M.I.T. and E.P.).

(3) K mesons which decay at rest in cloud chambers have a mean life greater than 10^{-9} sec. Those that decay at rest in emulsions have a mean life greater than 10^{-10} sec. There is no evidence that the two mean lives are different.

(4) E.P. and M.I.T. do not find any evidence for the presence of π mesons among the decay products of K mesons. The presence of such particles, however, is not ruled out. On the other hand, there is some evidence that the secondary charged products of K particles decaying at rest or in flight are, for the most part at least, μ mesons. In the S events observed at M.I.T., the charged products traversed a total thickness of about 950 g cm^{-2} of lead without clear evidence of nuclear interaction.[3] This result appears significant, even if one allows for an observational bias against the detection of nuclear interactions. M.I.T. found one case where the secondary charged product originating from a V event is a π meson;[5,6] this particular V event, however, could well represent the decay of a particle heavier than a proton. E.P. has observed in emulsions two K-meson secondaries which are probably μ mesons. Moreover, charged V-event secondaries were observed to traverse, in a multiplate chamber, a total thickness of material equal to 1.8 times the geometric collision mean free path;[2] no interaction was detected in the traversals of these fast particles.

(5) The charged decay products of K mesons found in S and charged V events do not form mono-energetic groups. M.I.T. found two S events in which the decay products traversed more than 73 and more than 85 g cm^{-2}, respectively.[3] The momentum corresponding to 85 g cm^{-2} Pb is 210 Mev/c, if the secondary particle is μ meson. In two other S events, however, the ranges were between 65.6 and 67.7 g cm^{-2} and between 64.4 and 74.3 g cm^{-2} of lead. In still another case, the range was between 19 and 29 g cm^{-2} (an alternate possible interpretation of this event would be a catastrophic stopping of a π meson).

E.P. has measured the transverse momenta of the secondaries of charged V events observed in a cloud chamber.[2] These momenta lie between 54 ± 5 and 270 ± 63 Mev/c. In one case one could obtain the value, p_t^* of the momentum of the secondary in the rest system of the primary particle; the value found was $p_t^* = 120\pm 30$ Mev/c assuming the secondary to be a

[1] Crussard, Leprince-Ringuet, Morellet, Orkin-Lecourtois, and Trembley, Compt. rend. **236**, 872 (1953); Phys. Rev. **90**, 1127 (1953).

[2] Fretter, Gregory, Johnston, Lagarrigue, Meyer, Muller, and Peyrou, Cosmic-Ray Conference, Bagneres, 1953 (unpublished).

[3] B. Rossi and H. S. Bridge, Cosmic-Ray Conference, Bagneres, 1953 (unpublished).

[4] R. Levi-Setti and G. Tomasini, Nuovo cimento **9**, 1244 (1952).

[5] H. S. Bridge and M. Annis, Phys. Rev. **82**, 445 (1951).

[6] Bridge, Peyrou, Rossi, and Safford, Phys. Rev. **90**, 921 (1953).

μ meson (or $p^*=116\pm30$ if the secondary is a π). This value, smaller than the largest measured values of transverse momenta, indicates clearly that secondaries of charged V events do not belong to a single mono-energetic group.

In the S events, the energy spectrum of the charged decay products appears to have a rather pronounced maximum at a momentum around 200 Mev/c.[3]

(6) M.I.T. found four S events in which the decay of a K meson gives rise to a photon of an apparent energy of the order of 100 to 200 Mev;[3,7] the direction of the photon is opposite to that of the charged decay product within the experimental uncertainty, which amounts to 5° in two cases and to 15° in the two other cases. However it is certain that photons with energies of the above magnitude are not associated with the decay of all K mesons.

The experimental results listed above are still sufficiently imprecise to allow several different interpretations. Here we only wish to point out that it appears possible to explain all K meson decays observed at E.P. and M.I.T. in terms of a single kind of particle with a single mode of decay. If one makes this assumption, one concludes from (1) that the mass of this particle must be between 900 and 1000m_e; from (4) and (6) that μ mesons and photons are among the decay products; and from (5) and (6) that the decay is at least a 3-body process. We are then led to assume the following decay scheme:

$$K\rightarrow\mu+\gamma+\nu. \tag{1}$$

Moreover, one will notice that the mass of the K mesons discussed above is identical to that of the τ mesons, within the limits of the experimental uncertainty, and that there is no evidence for a difference in the mean lives of the two kinds of particles. It is thus possible that the two particles are actually identical, i.e., that there is one kind of K particle with two alternate decay schemes; i.e., (1) and

$$K\rightarrow3\pi. \tag{2}$$

Notice that, if we take for the K meson mass the well established value of the τ-meson mass (970m_e), we find a value of 236 Mev/c for the maximum momentum of the μ meson in the decay process (1).

One has still to explain the pronounced peak of the momentum spectrum of the μ mesons in the neighborhood of the maximum value. One has also to justify theoretically the fact that in rare cases a photon of fairly high energy is emitted in a direction nearly opposite to that of the μ meson, while in most cases the photon has a sufficiently small energy to escape detection.

The data summarized above include only results obtained at M.I.T. and E.P. If we consider also results obtained in other laboratories we find that our tentative interpretation meets the following objections:

(a) The Bristol group observed 3 or 4 cases in which the K meson secondaries appear to be π's of a single energy.[8] It has been assumed that in these cases the primary, designed by the letter χ, was a particle decaying into a π, and a single neutral particle.

(b) A small number of K meson secondaries, observed in emulsions, seem to have a momentum larger than 236 Mev/c (from scattering and ionization).[9]

(c) Daniel and Perkins measured the masses of 20 fast K particles emerging from stars. The mean of the mass values obtained by scattering and ionization is around 1200m_e.[10]

(d) The studies on the nuclear absorption of negative K mesons made at Bombay (Peters)[11] and at Bristol (Friedlander)[12] seem to favor the assumption that the negative K mesons are of two different kinds and that only those representing the negative counterpart of τ mesons interact strongly with nuclei. If these preliminary observations should be confirmed, one could not maintain the assumption that τ mesons are identical to the K particles giving a single charged decay product. Moreover, there would be some difficulty in the assumption of the decay scheme (1) because, under this assumption, the K meson would have integer spin and should therefore interact strongly with nuclei if current views are correct.

Without minimizing the significance of the experimental results listed above, we feel that they need a further check before we can be sure that several different kinds of K mesons actually exist; and the main purpose of this note is to emphasize the importance of these checks. For the moment we only wish to point out that if all the available experimental data are taken at face value, even the assumption of three different kinds of K mesons (such as the τ, the χ, and the κ particle, according to the Bristol nomenclature) does not remove all difficulties of interpretation.

[7] Bridge, Courant, DeStaebler, and Rossi, Phys. Rev. **91**, 1024 (1953).

[8] M. G. K. Menon, thesis, Bristol, 1953 (unpublished). M. G. K. Menon and C. O'Ceallaigh, Cosmic-Ray Conference, Bagneres, 1953 (unpublished).

[9] C. F. Powell, Cosmic-Ray Conference, Bagneres, 1953 (unpublished).

[10] R. R. Daniels and D. H. Perkins, Cosmic-Ray Conference, Bagneres, 1953 (unpublished).

[11] Lal, Pal, and Peters, Cosmic-Ray Conference, Bagneres, 1953 (unpublished).

[12] G. G. Harris and M. Friedlander, Cosmic-Ray Conference, Bagneres, 1953 (unpublished).

Neutron-Proton Scattering near 180° at 93 Mev*

W. Selove, K. Strauch,† and F. Titus
Department of Physics, Harvard University, Cambridge, Massachusetts

(Received July 27, 1953)

A measurement has been made with neutrons of 93-Mev effective energy of the angular distribution of $n-p$ scattering near 180° in the center-of-mass system. The results show that the magnitude of the cross section approaches the 180° point smoothly, without any sudden increase.

THE angular distribution of $n-p$ scattering has been measured with neutrons of 93-Mev effective energy at six angles between 155° and 180° in the center-of-mass system. This angular region is of particular interest because of the relatively large uncertainties and disagreement shown by the previously published measurements in the high-energy region.[1–4] The method used in the work reported here is conventional; however, the equipment was specifically designed for operation in a region of high neutron background, and special care was taken to minimize the effect of energy changes in the cyclotron beam.

The neutron beam produced in a $\frac{1}{4}$-inch Be internal target was collimated to a $1\frac{3}{8}$-in.$\times 1\frac{7}{8}$-in. cross section by a pipe through a 6-foot water tank (Fig. 1). The

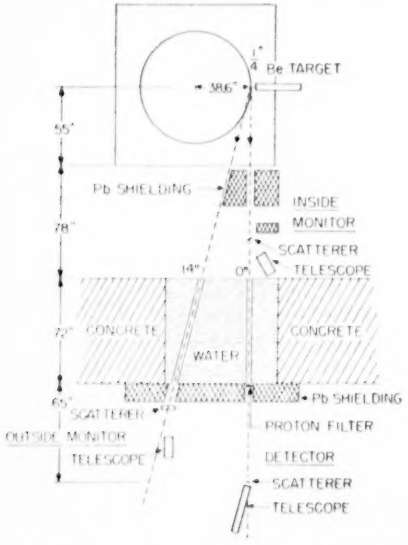

FIG. 1. Experimental arrangement showing the location of the detector and the two monitors.

scattering measurements were carried out with the *detector* telescope, while both an *inside* and *outside* monitor measured the neutron flux.

The detector telescope consisted of five stilbene-crystal 1P21 photomultiplier counters arranged in the geometry indicated in Fig. 2. This arrangement, in conjunction with the use of thin ($\sim$0.2 g/cm^2) crystals, gave a background low enough that the telescope could be operated satisfactorily when it was placed in the neutron beam. The solid angle within which protons from the scatterer were accepted was defined by the dimensions of the scatterer and crystal *E*, both of which had a rectangular shape of 1 in.$\times$1.5 in. in cross section. All other crystals were larger than crystal *E*.

The angular resolution of the detector telescope depends slightly on the angle of observation; the average value for the full width at half-maximum was 2.8°.

Scatterer and detector telescope were mounted on a rigid arm which could be rotated around an axis passing

FIG. 2. Geometry of detector telescope.

through the scatterer. By taking the CH_2-C difference, only those protons originating in $n-p$ collisions were detected. Measurements were carried out at angles of 0°, 2°, 4°, 6°, 9°, and 12° with respect to the neutron beam.

Since the neutron beam has a continuous energy distribution, absorbers were placed between counters *B* and *C* to set a lower limit of 84.0 Mev to the neutron energy for which recoil protons were detected. This threshold energy was chosen because there the rate of change of the number of neutrons (and recoil protons) with energy is slow enough so that differences in energy resolution at the various angular positions of the detector telescope could be neglected. In addition, this choice resulted in reasonable counting rates and energy definition. Figure 3 shows a plot of the energy spectrum of the 0° recoil protons (transformed from observations at 12°). The average effective neutron energy was 93$\pm$3 Mev, with a full width of 28 Mev at the base and of 17 Mev at the half-intensity point.

To keep the neutron threshold energy constant, ab-

* Supported by the joint program of the U. S. Atomic Energy Commission and the U. S. Office of Naval Research.
† Society of Fellows, Harvard University.
[1] Hadley, Kelly, Leith, Segrè, Wiegand, and York, Phys. Rev. **75**, 351 (1949).
[2] R. H. Fox, Atomic Energy Commission Report UCRL-867, 1950 (unpublished).
[3] Randle, Taylor, and Wood, Proc. Roy. Soc. (London) **213**, 392 (1952).
[4] Guernsey, Mott, and Nelson, Phys. Rev. **88**, 15 (1952).

TABLE I. Experimental data for neutron-proton scattering at 93 Mev. α is the angle between the neutron beam and the telescope, Φ is the average scattering angle in the laboratory system, θ is the corresponding angle in the center-of-mass system. Columns I and II give the relative differential cross section in the center-of-mass system obtained with outside and inside monitor, respectively. Column III gives the absolute differential cross section obtained by normalizing to the results of Hadley *et al.* (see reference 1).

α	Φ	θ	I	II	III (10^{-27} barn/sterad)
0°	1.2°	177.5°	100.0±2.5	100.0±2.5	12.90±.33
2°	2.3°	175.4°	99.2±2.4	98.7±2.4	12.73±.31
4°	4.2°	171.5°	96.5±2.2	96.9±2.3	12.50±.30
6°	6.1°	167.5°	93.9±2.2	92.7±2.2	11.96±.29
9°	9.1°	161.4°	83.5±2.0	83.3±2.1	10.75±.27
12°	12.0°	155.4°	74.9±2.0	73.9±2.0	9.53±.26

sorbers were added as the angle of observation was decreased from 12° to 0°. Graphite absorbers were used so that this addition would not appreciably affect the results. The increased nuclear absorption of the recoil protons is calculated to be small (<0.5 percent), and careful tests failed to show any effect of scattering.

The photomultipliers were connected in pairs (*AC*, *BD*, *BE*) to fast diode bridge coincidence circuits which have been described elsewhere.[5] Plateaus for all critical settings were obtained. When the detector telescope was placed directly into the neutron beam, the individual peak counting rate in each counter was of the order of 5×10^4 counts per second. This produced a 1 percent contribution from accidental coincidences to the observed *ABCDE* counting rate with the CH_2 scatterer. These accidentals resulted from the chance coincidence between random events in crystal *A* (or *E*) and particles passing through counters *BCDE* (or *ABCD*). The probability of accidental five-counter coincidence between other random events was negligible. Although small, the accidental rate was of the order of magnitude of the accuracy required, and it was measured and subtracted with the help of delay cables throughout the period in which data were taken.

The main experimental difficulty arose from the fact that a change in the energy distribution of the neutron beam resulted in a change in counting rate at a given angle since the telescope was sensitive to all neutrons above 84.0 Mev. The energy distribution of neutrons emitted by the Be target depends on the energy distribution of the internal cyclotron beam.[6] This in turn depends on the operating conditions of the cyclotron, which cannot always be kept constant or even reproduced over long periods of time. For instance, it was found at one time that when only the filament current was reduced in order to halve the beam intensity, a change in the energy distribution of the neutron beam occurred. The same procedure when carried out with another filament produced no apparent change, however. It was therefore decided to carry out the measurement at all angles with the same neutron beam intensity and to monitor the beam energy distribution. Of course, these precautions would not have been necessary if a beam monitor had been available which had the same energy sensitivity as the detector. In practice it is difficult to construct such a monitor without, at the same time, increasing the running time required to obtain a certain statistical accuracy.

Both the intensity and any change in energy distribution of the neutron beam were monitored with the help of two proton-recoil telescopes. The *inside monitor* was placed close to the cyclotron tank (Fig. 1) and had the same threshold and a similar energy sensitivity[7] as the detector telescope. The *outside monitor*, placed near the 14° exit hole (Fig. 1), consisted of a 1-inch thick polyethylene scatterer and a recoil-proton telescope combination which was sensitive to neutrons above 30 Mev. A change in neutron energy distribution had a different effect on the counting rates of the two monitors and could thus be detected.

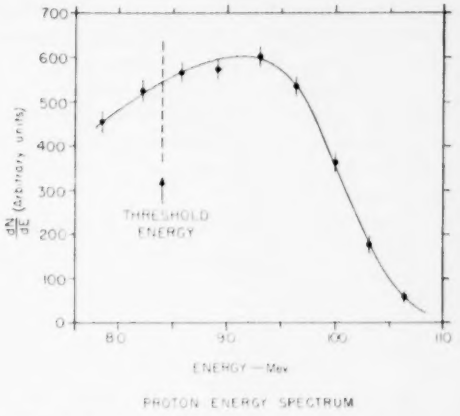

FIG. 3. Energy distribution of the 0° recoil protons produced by the neutron beam.

The data were taken in eleven cycles, each one lasting about $4\frac{1}{2}$ hours. In each cycle, one complete measurement was made at each of the six angles investigated and the order alternated. No cyclotron adjustments were made during a cycle. As seen below, this procedure is believed to have reduced the effect of changes in the neutron beam energy distribution to a fraction of the statistical accuracy obtained in this work. That such energy changes did occur was shown by small, but consistent, changes in the counting rate ratio of the two monitors.

The results of this experiment are reported in Table I. The angle α stands for the angle between the neutron beam and the detector telescope axis. The angle Φ represents the average neutron-proton angle in the

[5] K. Strauch, Rev. Sci. Instr. **24**, 283 (1953).
[6] J. A. Hofmann and K. Strauch, Phys. Rev. **90**, 449 (1953).
[7] The two energy sensitivities were not identical since the background of the inside monitor was more important and of a different energy distribution than that of the detector telescope.

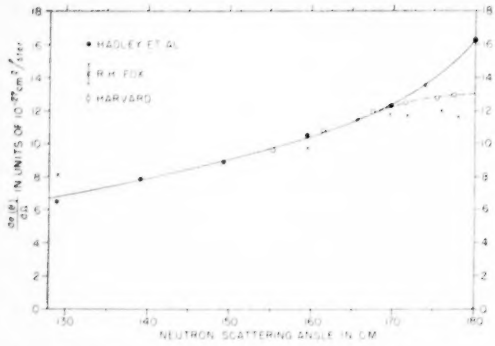

FIG. 4. Differential scattering cross section for $n-p$ scattering in the center-of-mass system in the 90-Mev region. The results of Hadley *et al.* and of Fox were taken from their papers in which no correction for the finite detector and scatterer sizes were made. This correction is appreciable only near 180° (see Table I).

laboratory system which corresponds to observations carried out at the angle α. The difference between the angles α and Φ is caused by the finite size of both scatterer and defining counter. The values of Φ were obtained by numerical integration. (The effect of multiple scattering is small and was neglected.) The angle θ is the corresponding neutron scattering angle in the center-of-mass system.

Columns 1 and 2 list the observed differential cross sections in the center-of-mass system obtained with the outside and inside monitor, respectively. The $\alpha=0°$ results have been arbitrarily set at 100. The indicated errors are of statistical origin only. Although the two monitors had quite different energy sensitivities, the results reported in columns 1 and 2 are consistent within the 0.7 percent statistical uncertainty in the monitor ratio. This indicates that within this accuracy, the small changes that did occur were averaged out over all angles and thus did not seriously affect our results.

Since the energy sensitivity of the inside monitor corresponded more closely to that of the detector telescope, the results presented in column 2 are the more reliable. By fitting our 6°, 9°, and 12° results to the cross section curve of Hadley *et al.*,[1] the absolute differential cross section values reported in column 3 are obtained.

Figure 4 can be used to compare the results of the three experiments carried out in the 90-Mev region. It must be emphasized that both the measurements of Fox and those reported here were relative measurements, and the absolute scale was obtained by fitting to the curve of Hadley *et al.* in the region in which the results overlapped. It appears that in the 90-Mev region the $n-p$ differential cross section curve approaches the 180° point smoothly, without any sudden increase or decrease.

The authors wish to thank the staff of the Harvard Cyclotron Laboratory for their valuable aid in making this work possible. Special thanks are due J. M. Teem for assistance in carrying out the work.

Search for V Particles Produced by 430-Mev Protons*

A. H. ROSENFELD† AND S. B. TREIMAN‡
Institute for Nuclear Studies, University of Chicago, Chicago, Illinois

(Received July 23, 1953)

Polyethylene was bombarded with 430-Mev protons from the Chicago synchrocyclotron and a search carried out in nearby nuclear emulsions for V_1^0 particles, as well as for possible charged analogs which decay by the process $V_1^+ \rightarrow n+\pi^++Q$. No events of either type were found. The upper limits of the cross sections are respectively 0.35 mb and 0.15 mb per carbon nucleus for the V_1^0 and V_1^+.

I. INTRODUCTION

UNTIL recently observed only in the cosmic radiation,[1-3] V_1^0 particles have now been produced in the neutron beam from the Brookhaven Cosmotron.[4] The V_1^0 is observed to decay into a proton and a negative pion, with a mean life of $\sim 3\times 10^{-10}$ sec. Assuming that there are no neutral particles among the decay products, the mass of the V_1^0 is about $2200m_e$.

Leighton[5] has recently reported examples of a heavy charged unstable particle which decays into a proton and one or more neutral particles. It is possible that this particle is the charged analog of the V_1^0. Without implying this identification, however, we shall refer to a possible positively-charged analog of the V_1^0 as a V_1^+ particle.

In addition to the affirmative Brookhaven results, there have been several negative or inconclusive attempts to detect V-particles produced at lower energies by protons[6,7] and photons[8,9] from accelerators. Experiments on V_1^0 production by 227-Mev pions are now in progress.[10]

We report here negative results of a search for V_1 particles produced by the bombardment of polyethylene (CH_2 gross composition) with protons in the energy range 420–440 Mev in the Chicago synchrocyclotron. Nuclear emulsions placed near the target were scanned for unusual decay events which might be attributed to unstable particles, neutral or charged, coming from the target. In the following discussion we have in mind particularly the V_1 particles, charged or neutral, although it will become apparent from the description of the experiment to what extent we could have detected other unstable particles (K mesons, V_2 particles, etc.).

Energy Considerations

If the decay of the V_1 particle is given by

$$V_1 \rightarrow \text{nucleon}+\text{pion}+Q, \qquad (1)$$

where $Q \approx 35$ Mev,[2] then it is energetically possible to produce V_1's with protons from the Chicago synchrocyclotron if one assumes the scheme:

$$\text{proton}+\text{nucleon} \rightarrow \text{nucleon}+\text{nucleon}+V_1. \qquad (2)$$

For a 440-Mev proton incident on a nucleon at rest, the reaction would be energetically possible even if Q were as large as 68 Mev. If the 440-Mev proton collides head-on with a nucleon of 20-Mev kinetic energy (within a nucleus), then Q could be as large as 200 Mev.

On the other hand, the V_2^0 particle, for example, is thought to have no nucleons among its decay products. Hence, if a V_2^0 could be produced according to Eq. (2), the sequence of production and decay would represent a net annihilation of nucleons. It is improbable that the V_2^0 can be produced in this way. Instead, the entire rest energy of the V_2^0 must be supplied in the center-of-mass system; for the 440-Mev protons this energy is only barely available, even when 20 Mev of internal kinetic energy is assigned to the target nucleon. It is for this reason that the experiment was designed chiefly for the detection of heavy unstable particles (V_1^0 and V_1^+). Note that conservation of charge rules out the possibility of V_1^- production by protons according to Eq. (2).

II. EXPERIMENTAL PROCEDURE

The experimental arrangement is shown in Fig. 1. A polyethylene target, 1.0 cm thick along the beam

* This work was in part supported by the joint program of the U. S. Office of Naval Research and the U. S. Atomic Energy Commission.

† National Science Foundation Fellow.

‡ Now at Palmer Physical Laboratory, Princeton University, Princeton, New Jersey.

[1] Armenteros, Barker, Butler, and Cachon, Phil. Mag. **42**, 1113 (1951).

[2] Leighton, Wanlass, and Anderson, Phys. Rev. **89**, 148 (1953).

[3] Fretter, May, and Nakada, Phys. Rev. **89**, 168 (1953).

[4] Fowler, Shutt, Thorndike, and Whittemore, Phys. Rev. **90**, 1126 (1953).

[5] York, Leighton, and Bjornerud, Phys. Rev. **90**, 167 (1953).

[6] R. H. Hildebrand and C. E. Leith, using 345-Mev protons, found a differential cross section $<1.4\times 10^{-28}$ cm^2 per carbon nucleus for the production of V_1^0's at 30° to the beam, assuming a mean life 3×10^{-10} sec.

[7] R. L. Garwin, Phys. Rev. **90**, 274 (1953), has looked for a V_1^0 which decays into a neutral pion and a neutron. The total cross section for production by 450-Mev protons on C nuclei is $<10^{-31}$ cm^2.

[8] C. Cocconi and A. Silverman, Phys. Rev. **84**, 1062 (1951). They used 310-Mev bremsstrahlung, and looked for V_1^0's at 90° to the beam. They find a differential cross section $<5\times 10^{-32}$ cm^2 sterad^{-1} Q^{-1} per carbon nucleus. This is <0.3 percent of the cross section for the production of charged pions.

[9] G. Bernardini and E. Segrè used 330-Mev bremsstrahlung on aluminum. They looked for V_1^0 decays in photographic plates and found two doubtful events. If the events are V_1^0's, the cross section is about 10^{-4} less than that for charged pion production.

[10] M. Schein, *Proceedings of the Third Annual Rochester Conference on High Energy Nuclear Physics* (Interscience Publishers, New York, 1953).

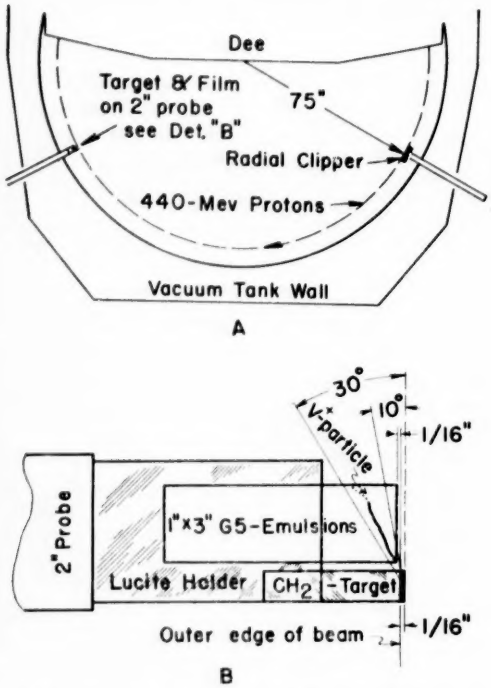

FIG. 1. Experimental arrangement: (A) Plan view inside vacuum chamber; (B) Plan view of target holder.

direction and 0.084 cm high, was exposed to the internal proton beam of the Chicago synchrocyclotron. The protons ranged in energy from 420 to 440 Mev, this spread originating from radial oscillations of the protons.

As shown in Fig. 1(B), only $\frac{1}{16}$ in. of the target stuck into the beam, which was cut off radially by a lead brick (clipper) machined to 75-in. radius of curvature and located 100° ahead of the target. This large separation of clipper and target is designed to cut down the flux of fast neutrons at the target and to reduce the number of multiple traversals of the target by the beam.

Pairs of 400μ and 600μ Ilford G5 plates, 1 in.×3 in., were placed with emulsion surfaces face to face in the plane of the target, as shown in the figure.

No shielding was used, since a small amount of shielding close to the beam does more harm than good. When the clipper was properly aligned the proton beam cut off so sharply with increasing radius that only about one beam proton was seen in the plate for every ten tracks from the target.

Monitoring

The number of nuclear collisions in the polyethylene target during one bombardment was monitored by determining the number of C^{11} nuclei produced in the polyethylene. The cross section for C^{11} production has been measured up to 340 Mev.[11] Extrapolation to 430 Mev is arbitrary, but the cross section is probably between 30 and 45 mb. We have assumed the value 45 mb, since it gives the more conservative upper limit to our cross sections for V_1 production.

The target was too thick to count in a 4π counter, so we irradiated a target consisting of a thick and thin piece of polyethylene glued together and cut to the same shape. The thick piece was counted under an end-window counter, the thin piece in an absolute 4π counter. The relative counting rates corrected by the ratio of the thicknesses provided the calibration for the end-window counter.

A suitable exposure produced ~50 000 C^{11} nuclei. This was achieved by adjusting the internal proton beam to 4×10^{-9} amp, with a repetition rate of 50 cps, and then exposing for 3 pulses.

III. SEARCH FOR THE NEUTRAL V PARTICLE

Detection

Any individual V_1^0 decay would be indistinguishable from the collision of a fast neutron with a nucleus of the emulsion where a pion and a single proton are emitted. However, if enough of the V-shaped pairs were detected one could analyze all of the events as V_1^0 decays and plot a histogram of apparent Q values, in order to test whether the Q value of the V_1^0 predominates.

In the present search no events resembling the type discussed above, whether due to neutrons or V particles were discovered.

The emulsions were scanned within the area between the 10° and 30° lines of Fig. 1. We used a 53× oil immersion objective and 12.5× oculars. Only 200μ of depth near the middle of the emulsion layer was scanned. This insured that most decay products would have a long path length in emulsion and could be readily identified.

Discussion

Since no V's were found, only an upper limit to the cross section can be stated. We define a "90 percent" upper limit as follows. If the cross section is equal to that specified by inequality (3), below, then in the volume scanned we should have found 2.303 (=ln10) V's, and the statistical probability that we should have discovered no events is less than $e^{-\ln 10}=0.1$.

Let $(d\sigma/d\Omega)_{Av}$ be the production cross section per steradian and per polyethylene unit (CH_2), averaged over angle between 10° and 30° (see Fig. 1), and integrated over V particle energy. Then our results lead to

$$(d\sigma/d\Omega)_{Av}\leq 1.4\times10^{-28}\ \text{cm}^2. \qquad (3)$$

[11] Aamodt, Peterson, and Phillips, Phys. Rev. **88**, 739 (1952).

Total Cross Section for Carbon

It is not possible to go beyond inequality (3) without further information on the angular distribution of V's, particularly those originating from proton-hydrogen collisions. This latter is very sensitive to Q. If Q is assumed to be 35 Mev,[2] all the V's from proton-hydrogen collisions come off within a forward cone of 23° half-angle, and many of them should pass through the region scanned. But if Q is 70 Mev the cone angle is only 10° and we would have seen none of the V's.

In the case of V production from carbon, the situation is improved. Internal nucleon motion leads to a range of possible V momenta corresponding to each angle of emission. The probability that a V falls into the scanned region therefore depends less sensitively on Q than in the hydrogen case. An order-of-magnitude calculation of the upper limit of the total carbon cross section was made in the following way. The assumption was made that V's are produced according to the reaction (2), where the internal motion of the carbon nucleons is now taken into account. The dependence of the cross section on nucleon energies was assumed to be governed by the phase-space volume of the final state. The energy distribution of the carbon nucleons was taken to correspond to that of a Fermi gas with maximum energy of 20 Mev. The choice of the upper limit does not affect the order of magnitude of the results. The angular distribution of the V particles was assumed to be isotropic in the center-of-mass-system.

From inequality (3) (neglecting any contribution from hydrogen), we then find for the total carbon cross section

$$\sigma^0 \leqslant 0.35 \text{ mb}.$$

IV. SEARCH FOR THE POSITIVE V PARTICLE

A positively-charged analog to the V_1^0 might decay according to either of the schemes $V_1^+ \rightarrow p + \pi^0$ or $V_1^+ \rightarrow n + \pi^+$. The unstable particles reported by Leighton[5] (if interpreted as V_1^+'s) decay according to the first scheme, but such a decay in emulsion would merely look like the interaction of a proton with a nucleus. We scanned for particles coming from the target and decaying into positive pions. This second decay scheme can be positively identified.

Unlike a V_1^0, a V_1^+ will be slowed down in emulsion and may come to rest before it decays. In order to reach the nearest part of the scanned area, a V_1^+ must have an energy of 25 Mev, in which case it will come to rest after 3×10^{-10} sec. If it has an energy of 100 Mev it will come to rest in the farthest part of the emulsion after 4×10^{-10} sec. Of the V_1^+ particles originating from carbon and passing through the emulsion, almost one-third should have energies between 25 and 100 Mev. These would be detected with very high probability, although some would decay before they reach the scanned area. This increased detection efficiency sets an upper limit on the production of the V_1^+ which is only about one-half that of the V_1^0.

If we assume that the V_1^+ has the same mean life as its neutral counterpart and define a "90 percent" upper limit as in Sec. III, then the cross section for V_1^+ production by a carbon nucleus is

$$\sigma^+ \leqslant 0.15 \text{ mb}.$$

V. SUMMARY AND ACKNOWLEDGMENTS

The cross sections for the production of neutral or charged V_1 particles by ~430-Mev protons on carbon nuclei are less than 0.35 and 0.15 mb, respectively. These upper limits may be compared with a geometrical cross section per carbon nucleus of 300 mb and with the cross section for the production of charged mesons, which is probably between 10 and 20 mb.

We wish to thank Professor E. Fermi for his help, C. del Rio and V. Telegdi for the use of their 4π counter, and the entire cyclotron staff for their cooperation.

Interaction of Negative Pions with Mercury*

NATHAN SUGARMAN AND AGNES HABER
Institute for Nuclear Studies, University of Chicago, Chicago, Illinois
(Received July 29, 1953)

Radiochemical separation of expected fission products from mercury irradiated with 122-Mev π^- mesons demonstrates that fission occurs. The fission products are distributed in yield similar to those from the fission of mercury by high-energy neutrons. The branching ratio for meson fission is about 0.5 percent. Thallium activities found in the meson-irradiated mercury are explained as produced by secondary fast protons.

I. INTRODUCTION

RADIOCHEMICAL studies of the interaction of negative pions with nuclei are in progress with the meson beams from the University of Chicago synchrocyclotron. Yields of the disintegration products of meson interaction on oxygen and nitrogen,[1] bromine,[2] arsenic,[3] zinc,[4] and iodine,[5] and preliminary studies of meson fission of mercury[6] have been reported. It had been shown earlier, in photographic plate experiments, that meson fission of uranium occurs.[7] Recently the probability for fission of uranium has been shown to be 37 percent[8] for negative pions and 15 percent for muons.

Results of the investigation of the interaction of 122-Mev negative pions with mercury are reported here. Isolation of expected radioactive products from the irradiated mercury demonstrates that fission occurs. It was found that the distribution of fission products is similar to that observed in bombardment of other heavy elements with high-energy particles,[9–11] and that the branching ratio of about 0.5 percent for the fission process is roughly that expected according to the models of meson interaction with nuclei.[12] Thallium activity was also isolated and it was demonstrated that secondary fast protons from pion interactions were responsible for its production.

TABLE I. Ratio of activity in wash solutions.

Element	Nuclide studied	Ratio of 1st to 2nd wash
As	91-min As^{78}	5
Br	4.4-hr Br^{80m}	2–7
Sr	9.7-hr Sr^{91}+2.7-hr Sr^{92}	>700
Y	3.5-hr Y^{92}+10-hr Y^{93}	>100
Ru	4.4-hr Ru^{105}	>20
Ba	38.8-hr Ba^{133m}	>100
Tl	1.8-hr Tl^{198}+7-hr Tl^{199}	200
Pb	~80-min Pb^{199}	8

II. EXPERIMENTAL PROCEDURE

Mercury was irradiated with 122-Mev π^- mesons. The mesons were produced by the bombardment of a beryllium target with 450-Mev protons, were deflected by the fringing field of the cyclotron magnet through a 6-in. channel in the iron-concrete cyclotron shield (6- to 12-ft thick), and were then deflected by an auxiliary magnet through an angle of about 45 deg. The mesons leaving the magnet were in a beam about 4 in. on edge. The intensity of the meson beam was measured by coincidence counting of the pulses of two 4-in. $\times$6-in.$\times\frac{1}{2}$-in. thick scintillation counters, placed about 4 ft from the magnet.[13] In the various experimental arrangements, the meson counting rates varied between 40 000 and 100 000 mesons/min for a proton beam dissipating 1 watt of power in the beryllium target.

The mercury irradiations were performed at meson intensities ranging from 4×10^5 to 3×10^6 mesons/min, and for irradiation times of 2 to 8 hr. The mercury was contained in a 5-in. square vessel about $2\frac{1}{2}$ in. deep. Generally, about 10 kg of mercury was used. After the irradiation, the mercury was transferred to a large sintered glass funnel. A wash solution consisting of 0.1M HNO_3 and carriers of the elements to be isolated was added above the mercury, and the mercury was agitated by passing air through it for about 20 minutes in order to extract the desired radioactive species. The wash solution was withdrawn and radiochemical analyses were performed.[14]

Experiments were done to test the efficiency of extraction of the radioactive species from the mercury to the wash solution and the retention of radioactivity on the walls of the vessel. Mercury was irradiated with

* This research was supported in part by a grant from the U. S. Atomic Energy Commission.

[1] A. Turkevich and J. B. Niday, Phys. Rev. **84**, 1253 (1951).
[2] T. T. Sugihara and W. F. Libby, Phys. Rev. **88**, 587 (1952).
[3] A. Turkevich and J. B. Niday, Phys. Rev. **90**, 342 (1953).
[4] S. C. Fung and A. Turkevich, Phys. Rev. **91**, 480 (1953).
[5] L. Winsberg, Phys. Rev. **90**, 343 (1953).
[6] N. Sugarman, Phys. Rev. **86**, 604 (1952); N. Sugarman and A. Haber, Phys. Rev. **90**, 342 (1953).
[7] S. G. Al-Salam, Phys. Rev. **84**, 254 (1951).
[8] W. John and W. F. Fry, Phys. Rev. **91**, 1234 (1953).
[9] R. H. Goeckermann and I. Perlman, Phys. Rev. **76**, 628 (1949).
[10] P. R. O'Connor and G. T. Seaborg, Phys. Rev. **74**, 1189 (1948).
[11] L. Jodra and P. Kruger, University of Chicago, unpublished work.
[12] S. Tamor, Phys. Rev. **77**, 412 (1950).
[13] The experimental arrangement does not differ significantly from that given in Fig. 1, reference 1.
[14] *Radiochemical Studies: The Fission Products* (McGraw-Hill Book Company, Inc., New York, 1951), Part VI, National Nuclear Energy Series, Plutonium Project Record, Vol. 9, Div. IV.

neutrons outside the cyclotron tank. The radioactivity in the sample was many times that obtained in the meson irradiations. The mercury was subjected to the washing process, the wash solution was withdrawn, and the mercury was washed again. The ratio of the activity of a given nuclide in the first wash solution to that in the second measures the efficiency of removal of that element from the mercury, if equilibrium is established. The data are given in Table I. There is a large range in washing ratios, varying from 5 for the less electropositive elements (arsenic and lead) to greater than 100 for the more electropositive elements (strontium, yttrium, barium, thallium). A low washing ratio indicates that a substantial fraction of the radioactivity remains in the mercury. It is assumed that interchange occurs between the carrier and tracer, such that the chemical yield correction for the carrier takes account of the low washing ratio. In a separate experiment it was found that the activity retained on the walls amounted to about 1 percent of the total activity.

The radioactivity measurements were made with end-window methane-flow proportional counters, operating at about 4000 volts. The counter window is made of rubber hydrochloride, ~ 0.7 mg/cm^2, Aquadaged on both sides. The backgrounds of the counters are about 9 counts/min, and are reproducible to about 0.3 count/min. The counting was usually reliable even for counting rates as low as 1 count/min above background. The isolated samples had counting rates ranging from 1 to 150 counts/min depending upon the half-life, meson intensity, and irradiation time. The samples were positioned about 1.5 mm from the counter window, and the geometry factor as determined with a RaDEF standard was found to be 34 percent for weightless samples with no backing, and 47 percent for samples of about 10 mg/cm^2, mounted on $\frac{1}{16}$-in. aluminum cards.

Experiments were also performed on the fission of mercury with high-energy neutrons. The fissionability of mercury by neutrons of energy up to 90 Mev had been reported earlier.[15] The neutrons are produced from protons on beryllium and have an energy distribution from 200 to 440 Mev, with a peak at about 350 Mev.[16,17] The neutron flux is about 2×10^9 neutrons/cm^2 sec over an area of about 50 cm^2. The activity from the neutron-irradiated samples was about one hundred times that from the meson-irradiated samples, which made it possible to identify some of the long-lived components, whereas this was not possible in the meson experiments.

[15] E. L. Kelly and C. Wiegand, Phys. Rev. **73**, 1135 (1948).
[16] J. Marshall and V. A. Nedzel, University of Chicago, unpublished work.
[17] Goodell, Loar, Durbin, and Havens, Phys. Rev. **89**, 724 (1953).

III. RESULTS

A. Fission

The elements isolated from the forty-meson and ten-neutron irradiations include some fission products as well as thallium and lead. Since the observed activity in a given sample was about 50 counts/min or less for the meson irradiations, it was assumed to be composed of known nuclides, and the decay curves were analyzed accordingly. The activity of an individual nuclide was corrected for chemcial yield and time of irradiation. The ratio of the saturation activity of the nuclide to that of the "7-hr" Sr (9.7-hr Sr^{91}, 2.7-hr Sr^{92} and 3.5-hr Y^{92} decaying with a half-life of 7 to 8 hr) was obtained as a measure of the yield of the nuclide. The data are given in Table II. It was found that the ratios thus obtained did not vary outside the experimental errors, estimated at about 20 percent for the meson data and about 10 percent for the neutron data, when the irradiation time was varied, despite the complexity of the species of which the "7-hr" Sr activity is composed. The ratio of Sr^{89} to "7-hr" Sr of ~ 1.5 for the meson experiments was the result of about twenty experiments in each of which the counting rate of Sr^{89} was about 0.5 count/min above background.

The fission yields of Table II were calculated on the assumption that Sr^{89} has a fission yield of 5.0 percent. This is the yield expected if the yield-mass distribution for the fission of mercury with mesons or high energy neutrons is single-humped with Sr^{89} near the maximum, similar to that of bismuth with high-energy deuterons or protons.[9,11] The general trend of the yield data, the relatively high yield of Br^{82}, and the absence of barium activity are all consistent with a high-energy fission process.

TABLE II. Activity data of fission products from meson- and neutron-irradiated mercury.

Nuclide	Ratio of activity to "7-hr" Sr: Meson	Neutron	Fission yield, percent: Meson	Neutron
17.5-day As^{74}		0.12		0.4
26-hr As^{76}		0.35		1.2
38-hr As^{77}		0.59		2.0
91-min As^{78}	~ 0.3	0.51	~ 1.0	1.7
4.4-hr Br^{80m}		1.0		3.3
36-hr Br^{82}	~ 0.3	0.41	~ 1.0	1.4
2.4-hr Br^{83}	0.81	0.45	2.7	1.5
19.5-day Rb^{86}	<3	1.3	<10	4.3
54-day Sr^{89}	~ 1.5	1.5	(5.0)	(5.0)
9.7-hr Sr^{91}		0.64		2.1
2.7-hr Sr^{92}		0.18		0.60
60-hr Y^{90}		1.4[a]		4.7[a]
3.5-hr Y^{92}	2.0[b]	1.4[b]	6.7[b]	4.7[b]
10-hr Y^{93}	1.7	1.2	5.7	4.0
4.4-hr Ru^{105}	0.47	0.47	1.6	1.6
2.0-hr Ba^{129}	<0.03	0.009	<0.1	0.03
38.8-hr Ba^{133m}	<0.2[c]	0.041[c]	<0.67[c]	0.14[c]
12.0-day Ba^{131} + 12.8-day Ba^{140}		0.01[c]		0.033[c]
85-min Ba^{139}	<0.03		<0.1	

[a] Independent yield of Y^{90}.
[b] Calculated as being produced directly in fission, independent of the Sr^{92} parent.
[c] Results uncorrected for counting efficiency of nuclide.

TABLE III. Activity data of thallium and lead nuclides from meson-, neutron-, and proton-irradiated mercury.

Nuclide	Half-life, reported	Half-life, observed	Ratio of activity to "7-hr" Sr, uncorrected	Counting corr. factor	Ratio to "7-hr" Sr, corr.	Branching ratio		
				Meson		Tl atoms/meson		
Tl^{198}	1.8 hr	1.8–2 hr	2.3	3.5	8.0	1.57×10^{-3}		
Tl^{199}	7 hr	7–8 hr	0.83	8.8	7.3	1.43×10^{-3}		
Pb^{199}	~80 min		<0.025					
Pb^{201}	8 hr		<0.03					
				Neutron				
Tl^{198}	1.8 hr	1.7–1.8 hr	5.6	3.5	19.6			
Tl^{199}	7 hr	6–7 hr	1.6	8.8	14.1			
Tl^{200}	27 hr	22–25 hr	0.48	~13	~6			
Tl^{201}	72 hr	64–67 hr	0.31	~19	~6			
Pb^{199}	~80 min	95 min	0.03					
Pb^{201}	8 hr	10 hr	0.01					
				Proton		Tl atoms/proton		
						37 Mev	55 Mev	72 Mev
Tl^{198}	1.8 hr	1.7–1.9 hr		3.5		3.7×10^{-3}	1.15×10^{-2}	1.4×10^{-2}
Tl^{199}	7 hr	6.7–7 hr		8.8		6.0×10^{-3}	1.05×10^{-2}	9.6×10^{-3}

In general, the yields of the fission products from meson fission agree with those high-energy neutron fission. The difference in the ratio of Br^{83} to Br^{82} in meson fission, as compared to neutron fission, is probably associated with the fact that meson fission is a lower energy process than neutron fission. The ratios of Br^{80m} to Br^{82} and Br^{83} to Br^{82} for the neutron fission of mercury are the same as those found in the fission of gold with 450 Mev protons,[11] whereas in the meson experiments, Br^{80m} was not evident and Br^{83} was correspondingly in much higher yield. Experiments on bismuth with varying proton energy[11] demonstrated that the ratios Br^{83} to Br^{82} and Br^{80m} to Br^{82} are energy dependent, the former increases and the latter decreases as the proton energy is lowered. Since these ratios do not change rapidly with the atomic number of the target nucleus, a comparison of the Br^{83} to Br^{82} ratio in meson fission of mercury with that in proton fission of bismuth leads to the conclusion that the meson fission process corresponds roughly to fission occurring with protons of about 150 Mev.

Experiments were performed to determine the fission-product activity induced in mercury by the stray radiation in the vicinity of the sample. The cyclotron was operated at the usual intensity of about 20 watts on the beryllium target, and the sample was irradiated at its usual position relative to the deflecting magnet. The current in the deflecting magnet was turned off. Under these circumstances, the counting rate in the scintillation counters used in measuring meson intensity was about 0.2 percent of that obtained when the magnet current was at the optimal value. Strontium analyses were performed on the mercury and it was found that the activity was low, about 5 percent of that produced in the meson irradiations.

The possibility that the observed fission of mercury was not the primary effect of meson interaction, but rather the effect of secondary interaction of fast neutrons and protons produced by meson interaction, was tested by irradiating a mercury sample directly behind another whose thickness was slightly greater than the range of the mesons in mercury. No activity of strontium was observed other than that expected from stray background radiation. This result is consistent with that calculated for secondary fission on the assumption that as many as one neutron or proton of about 60-Mev energy is produced for each meson interaction. The calculated fission contribution from the secondary particles is less than 1 percent of the observed fission under the usual irradiation conditions.

B. Thallium Production

Thallium was separated[18] from the meson-irradiated mercury and activity of about 100 counts/min was found which could be resolved into two components, 1.8-hr Tl^{198} and 7-hr Tl^{199}. There was also evidence for a longer-lived species, but the counting rate was less than 1 count/min, so no assignment of the activity could be made. About 5 percent of the thallium activity was produced by stray radiation, as determined in experiments in which the deflecting magnet was off. Thallium activity was also found in the neutron-irradiated mercury, and in this case the activity was high enough so that the decay curves could be analyzed into the periods reported[19] for masses 198 to 201. The yields of the thallium isotopes relative to the yield of "7-hr" Sr from fission, uncorrected for the counting efficiencies of these electron-capture species, are given in column 4 of Table III. A serach for lead activity in meson-irradiated mercury led only to the upper limits for the yields of Pb^{199} and Pb^{201} given in column 4 of Table III. Lead

[18] The chemical procedures for the separation of thallium and lead were those given by W. W. Meinke, University of California Radiation Laboratory Report UCRL-432, 1949 (unpublished), with some modifications.

[19] Hollander, Perlman, and Seaborg, *Table of Isotopes*, Revs. Modern Phys. **25**, 469 (1953).

activity was observed in the neutron-irradiated mercury, which could be attributed to Pb^{199} and Pb^{201}. The yields of these nuclides are given in Table III.

The thallium yield data of column 6 of Table III were obtained from those of column 4 by correcting for the counting efficiencies of thallium isotopes. Counting correction factors (column 5) were found by determining the counting rates of the K x-rays of the thallium isotopes in NaI crystal counters[20] and by comparing these counting rates, corrected for fluorescence yield and absorption, with those of the conversion electrons in the methane proportional counter. It was assumed in this work that all of the thallium isotopes decay by electron-capture processes.[21]

In order to determine the branching ratio of Tl^{198} absolutely, two experiments were performed in which the meson intensity was carefully measured and precautions were taken against loss of mesons from scattering out of the sample. The mesons were collimated by a 6-in. thick iron collimator with a 1-in. aperture. The sample, contained in the 5-in. square vessel, was placed at the position occupied by the counters, about 1 ft from the collimator. The collimator reduced the dimensions of the meson beam so that the scattered mesons would not leave the mercury sample. The meson intensity was reduced about sevenfold, and about 10 percent of the counting rate in the scintillation counters was attributed to energetic electrons and μ mesons. The initial counting rate of the thallium samples was about 20 counts/min. The ratio of the saturation activity of Tl^{198}, corrected for the geometry factor of counting but uncorrected for the counting efficiency of the radiations, to the meson intensity was found to be 4.5×10^{-4}. Using the value of the counting correction factor of 3.5, this ratio becomes 1.57×10^{-3} Tl^{198} atoms/meson. The meson branching ratio for Tl^{199} can be calculated from the data of column 6 and the branching ratio for Tl^{198} and is found to be 1.43×10^{-3} Tl^{199} atoms/meson. These results are presented in column 7, Table III.

C. Branching Ratio for Fission

The branching ratio for fission can, in principle, be determined by isolation of a suitable fission product of known fission yield from the meson-irradiated mercury used for the Tl^{198} branching ratio determination. Strontium was isolated in these two experiments but the activity was only about 5 counts/min. The data of Tables II and III on the yield of Tl^{198} relative to "7-hr" Sr and the branching ratio of Tl^{198} may be used to calculate the branching ratio for fission. If the fission yield of Sr^{89} is assumed to be 5 percent, the branching ratio for fission is calculated to be 5.9×10^{-3}. Since all of the pions interact with mercury, either during the slowing down process from 120 Mev to rest, or after capture into an atomic orbital, it is evident that the fraction of these interactions giving rise to fission is about 1 in 200.

IV. DISCUSSION

A. Fission Branching Ratio

The low branching ratio of about 0.5 percent for fission of mercury by pions can be understood on the basis of the current models for the interaction of pions with nuclei and the fission cross section of mercury with high energy particles. If it is assumed that the meson interacts with two nucleons and shares its energy between them,[12] then the excitation given the nucleus is essentially the same as that given it by a high-energy proton or neutron whose kinetic energy is equal to the sum of the kinetic and rest-mass energy of the meson. For mesons of low kinetic energy, where multiple particle interaction is more likely, comparison with fission by deuterons of the same total energy is perhaps more valid. The expected branching ratio for fission from these considerations would be the ratio of the fission cross section to the total cross section with high-energy protons and deuterons. For gold this ratio is about 1 percent.[22] It is expected, from the results of the fission experiments done with neutrons of up to 90 Mev energy,[15] that the cross section for fission of mercury would be only slightly higher than that of gold. It is thus evident that the fission branching ratio of mesons is in fair agreement with that expected from the model of the meson interaction with the nucleus.

B. Tl^{198} Branching Ratio

The production of thallium activity in the mercury may be explained by the interaction of the fast protons expected from the meson interactions with mercury. It is found in photographic plate studies that 0.3 fast proton of about 55 Mev is emitted for each fast meson interaction[23,24] (30 to 90 Mev), and 0.1 fast proton for each slow meson.[25] Since about 40 percent of the 122-Mev π^- mesons would interact in flight while being slowed down, assuming a cross section of 2 barns as observed for 85–137 Mev pions,[26] and 60 percent at rest, then the number of fast protons expected per meson is 0.18. On

[20] The scintillation counting of the thallium samples was done by Dr. J. R. Arnold of the Institute for Nuclear Studies of the University of Chicago and by Dr. D. W. Engelkemeir of the Argonne National Laboratory. The correction factors determined independently agreed to about 20 percent.

[21] Recent work of I. Bergström and R. D. Hill [Bull. Am. Phys. Soc. **28**, No. 4, 13 (1953)] shows that there is a 2-hr period among the thallium isotopes decaying by isomeric transition, and that the ground state of Tl^{198} has a half-life of ~4 hr. These results affects the yields reported here, but do not appreciably affect comparisons of production of a given thallium isotope by mesons, neutrons, or protons.

[22] J. Jungerman, Phys. Rev. **79**, 632 (1950).

[23] Bernardini, Booth, Lederman, and Tinlot, Phys. Rev. **82**, 105 (1951).

[24] G. Bernardini, Proc. Inter. Conf. Nuc. Phys. and Phys. Fundamental Particles, Univeristy of Chicago, September 17, 1951, p. 13 (unpublished).

[25] F. L. Adelman, Phys. Rev. **85**, 249 (1952).

[26] R. L. Martin, Phys. Rev. **87**, 1052 (1952).

the assumption that the number and energy of fast protons from meson interactions in mercury is the same as that found in photographic plates,[27] it is possible to calculate the expected production of Tl^{198} per meson. The reaction range of a 55 Mev proton in mercury[28] is 5.3 g/cm^2, after correction for the Coulomb barrier. If it is assumed that the only reactions which occur in appreciable yield are reactions in which neutrons are emitted, such as $(p,5n)$, $(p,4n)$, etc., and that each of these reactions occurs in succession, as the proton is being slowed down, with a geometric cross section of 2 barns and an average isotopic abundance of 0.19, then the expected yield of Tl^{198} per proton is 6.1×10^{-3}. The yield per meson is 1.1×10^{-3} for 0.18 fast protons per meson. This value compares favorably with that observed experimentally of 1.57×10^{-3}.

In view of the numerous assumptions needed to understand the production of thallium by secondary fast protons from mesons, some experiments were performed to measure directly the production of thallium activity from protons of 37 to 72 Mev. This information then permits a direct comparison with the thallium activity produced by mesons without assumptions on cross sections for (p,xn) reactions. The low-energy protons were produced by backward scattering from the meson target and deflection into the 122-Mev π channel of the 12-ft shield by the fringing field of the cyclotron magnet.[29] Further deflection by the deflecting magnet produced beams of protons of well-defined energy in good intensity, where the energy was controlled by the target position and the deflecting magnet current. Absorption measurements were made on three proton beams using two 2-in. diameter scintillation counters in coincidence. From the ranges, the proton energies[28] were found to be 40 ± 3 Mev, 57 ± 4 Mev, and 74 ± 4 Mev. The intensity in the three beams was about 40 000 protons/min for a cyclotron beam intensity of 1 watt. Proton irradiations were made with the three beams with the cyclotron operating at about 20 watts, using a mercury vessel 3 in. square in cross section and 1 cm deep. The proton energies were reduced somewhat by the $\frac{1}{32}$-in. aluminum wall of the irradiation vessel. Thallium was isolated from the proton-irradiated mercury and the decay curves were resolved into Tl^{198}, Tl^{199}, and a long-lived component, probably a mixture of Tl^{200} and Tl^{201}. Strontium samples isolated from the mercury were inactive, in keeping with the low cross section for fission at these energies.[22]

The yields of Tl^{198} and Tl^{199} for the proton-irradiated mercury are given in column 7 of Table III. It is seen that the yield of Tl^{198} per 55-Mev proton of 1.15×10^{-2} agrees well with that estimated earlier of 6.1×10^{-3}. The variation of the yields with energy can be used to estimate the average proton energy in the meson experiments. The ratio, Tl^{198}/Tl^{199}, in the meson experiments is about the same as that found for 55-Mev protons, the average energy of fast protons from mesons in emulsion. Assuming, then, that the average proton energy from meson interaction in mercury is about 55 Mev, we find that the number of such protons per meson is about 0.14, again in good agreement with that found in emulsion studies, 0.18. It is evident, then, that secondary proton bombardment satisfactorily explains the production of thallium in the meson-irradiated mercury. Similarly, the production of thallium and lead activities in the neutron-activitated mercury may be explained by secondary proton and alpha particle bombardment. The ratio Tl^{198}/Tl^{199} from the neutron-activated mercury is about that for protons of about 70 Mev.

It is a pleasure to acknowledge the advice of Professor E. Fermi and Professor A. Turkevich, and the cooperation of Professor H. L. Anderson, Mr. L. Kornblith, and members of the synchrocyclotron crew in these experiments.

[27] Preliminary observations of fast protons produced from meson interactions with mercury have been made by E. Silverstein and J. Orear of the Institute for Nuclear Studies, University of Chicago, using photographic plate techniques. Fast protons were observed although there are as yet no quantitative data on their yield.

[28] W. A. Aron, University of California Radiation Laboratory Report UCRL-1325, May 1951 (unpublished).

[29] The production of collimated, monoenergetic, low-energy proton beams by this technique was worked out by E. Fermi early in 1952. The experimental arrangement is essentially the same as that used in the meson irradiations.

Ionization Loss at Relativistic Velocities in Nuclear Emulsion

BERTRAM STILLER AND MAURICE M. SHAPIRO
Nucleonics Division, Naval Research Laboratory, Washington, D. C.
(Received July 8, 1953)

The variation of grain density in the tracks of singly-charged relativistic particles traversing a nuclear emulsion has been investigated as a function of velocity in Ilford G.5 plates exposed to the cosmic radiation at 100 000 feet. Multiple scattering measurements and "blob counts" were made on long tracks of electrons, mesons, and protons with energies γ up to 3400 rest mass units. The blob density G_{pl} at the Fermi plateau of ionization was found to be 1.14 ± 0.03 times G_{min}, in agreement with the result previously obtained by another method. Protons and electrons show the same value of G_{pl}. The data are compared with the theories of Halpern-Hall and of Sternheimer for AgBr, using the ionization potentials of Bakker and Segrè. Since only grains *along* the track were counted, the calculated energy loss is restricted to energy transfers less than an upper limit T_0. Calculations for two assumed values of T_0, 2 kev and 5 kev, fit the data equally well, yielding ratios G_{pl}/G_{min} of 1.15 and 1.14, respectively. The data are also consistent with the slow rate of rise from minimum ($\gamma\sim4$) to plateau ($\gamma>100$), which is predicted by the theory.

INTRODUCTION

IN our earlier work on the rate of ionization loss I of very fast charged particles ($\beta>0.95$) in nuclear emulsions,[1] we reported a relativistic rise of $\sim12_{-3}^{+4}$ percent above the ionization minimum to the Fermi "plateau." This result was obtained by comparing the Ag grain densities g of two groups of particle tracks, the thin shower tracks emerging from nuclear explosions and the "primary" tracks of high-energy stars with associated shower multiplicities $n_s\geq5$.

The former group originates primarily from pions and, from their known energy spectrum, their grain-density histogram was expected to have a peak at g_{min}. Similarly, the latter group is attributable mainly to protons so energetic that their histogram should display a peak at or near the plateau value g_{pl}. The theoretically expected peaks were observed, and an experimental value of the ratio I_{pl}/I_{min} for AgBr was deduced therefrom. Also, preliminary investigation of energetic electrons (total energy $\gamma>300$ rest masses, as determined from their multiple scattering) indicated that g_{pl} for electrons lies 16 ± 3 percent above g_{min} for mesons.

NEW MEASUREMENTS

We have improved and extended our previous work in the following ways:

(1) Measurements of multiple Coulomb scattering have been made on long tracks of many particles with velocities in the regions of minimum and plateau ionization. These measurements were especially desirable in view of the considerable uncertainty inherent in the estimates of the energies of the shower-producing primaries from their associated multiplicities.

(2) Measurements have also been made on tracks of particles with intermediate relativistic velocities in the region where the ionization increases appreciably with energy. It is important to provide experimental evidence on the variation of grain density in this region. Such evidence would show whether any ionization theory correctly describes this variation in nuclear emulsions. It is also essential for mass estimation (and hence identification) of particles in the energy interval $5<\gamma<100$.

(3) An experimental comparison between electrons and heavier particles in regards to their "restricted ionization loss" in AgBr grains at energies $\gamma>15$ rest masses, is possible from our new data. Contrary to the difference in *total* ionization between electrons on the one hand and mesons or protons on the other, there is no reason to expect a difference between the *grain densities* of these two groups of particles as a function of velocity.

(4) The tracks in our earlier study had been located on several plates of the same batch, exposed together and processed together in the same solutions. Nevertheless, even under these well-controlled conditions we found variations of a few percent in g_{min} among the several plates.[2] Therefore, we made the control more rigorous still by gathering most of the data presented here from a single plate 6×3 inches. The Ilford G.5 emulsion, 400 microns thick, had been exposed in the stratosphere for ~8 hours at an atmospheric depth of 11 g/cm^2. We took the precaution of looking for differences in g_{min} between various parts of this plate. Such differences, if any, were found to be well within experimental error. The plate selected was well suited for the work at hand; it had low background, high uniformity of grain density with depth, and a low level of distortion.

(5) Grain densities were replaced by "blob" densities. Even in very thin tracks, such as those with which we are dealing here, the grains of silver sometimes coalesce or overlap, so that two of them may be mistaken for one. This element of subjectivity can be removed by counting blobs instead of attempting to resolve grains. Thus we find that experienced observers agree within statistical errors in their blob

[1] M. Shapiro and B. Stiller, Phys. Rev. **87**, 682 (1952).

[2] It is, of course, possible to normalize the level of grain density in one plate to that in another. This was done for the data from another plate in the same batch; see Fig. 2.

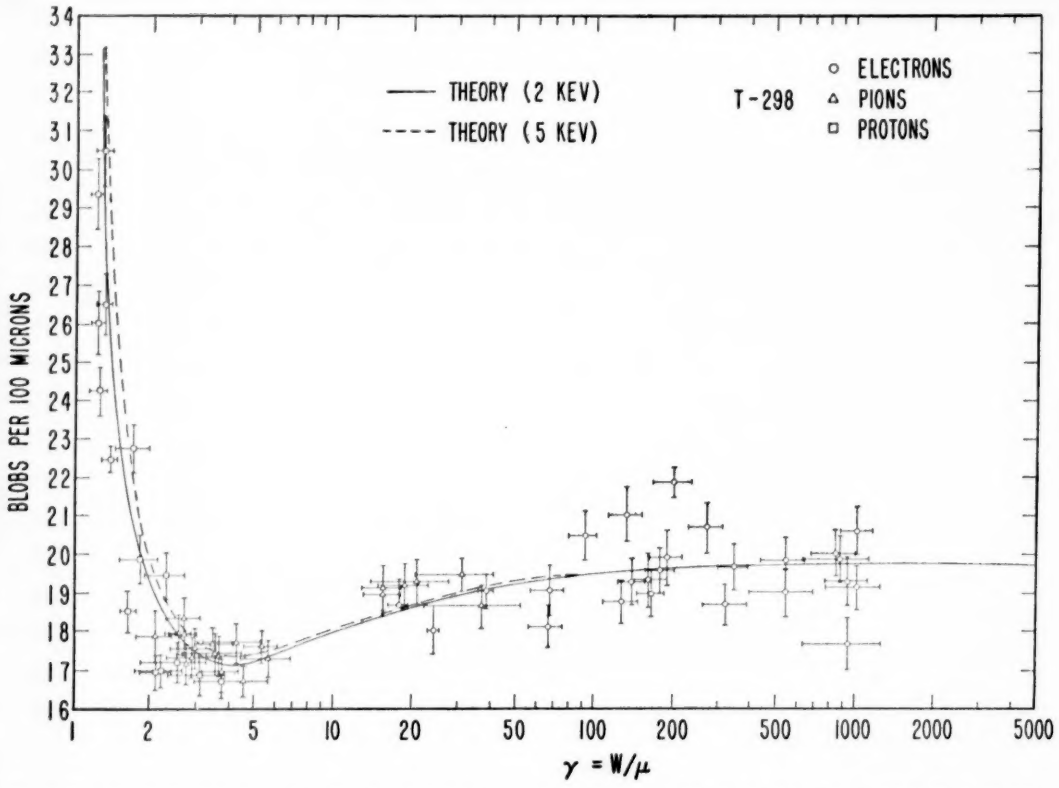

FIG. 1. Blob density is plotted as a function of γ, the total energy of the moving particle, deduced from its multiple Coulomb scattering. Measurements on 55 long tracks found in one 3 in.×6 in., Ilford G.5, 400-μ plate are shown.

counts, although not necessarily in their grain counts. For our thin tracks, a blob is simply a grain in most cases; in fact, the blob density G is only $\sim$7 percent below the grain density g, and we find no variation in the ratio G/g at these low levels ($G<1.25\,G_{\min}$).

RESULTS

Figure 1 shows the blob density as a function of γ for tracks gathered from a single plate, No. T-298. Since the abscissa is a function of velocity only, it is instructive to plot together the various particles of unit charge. It will be noticed that, at energies $\gamma>100$, only electron data appear. In the interval $10<\gamma<100$, both electron and meson tracks appear. Finally, at lower velocities, mesons and protons, but no electrons, are represented.

Ideally, one would prefer to measure the rate of ionization loss over the whole range of velocities for a single type of particle. In practice, such procedure proves to be extremely difficult because of the precision required in this experiment, where the variation with which we are dealing is so small. Electrons in the region of the theoretical minimum have energies <3 Mev and mean scattering angles $>7°/(100\mu)^{1/2}$. Their strong scattering imposes several obstacles to accurate determinations of grain or blob densities: (a) such electrons seldom stay in the emulsion over a sufficient path length; (b) when they do, the inclusion of spurious background grains in a highly bent track is more probable than in a straight track; (c) even the measurement of true length of track is subject to appreciable error; and (d) there is danger of shifting unwittingly to a neighboring electron track which crosses the one in question. For these reasons, measurements of G on electron tracks have been made with adequate precision only at energies $\gamma>10$. In the vicinity of the ionization minimum ($2<\gamma<6$), it has been found exceedingly difficult to use electrons.[3]

Conversely, if one wants energy determinations from scattering (as well as G) at energies $\gamma>70$, one must perforce use electrons. Protons of $\gamma>10$ have mean angles $\bar{\alpha}$ of multiple scattering which are much too

[3] Recent investigation of electron tracks in emulsions established the existence of an ionization plateau at high energies. See D. R. Corson and M. R. Keck, Phys. Rev. **79**, 209 (1950); I. B. McDiarmid, Phys. Rev. **84**, 851 (1951); A. H. Morrish, Phil. Mag. **43**, 533 (1952). However, because their investigations were confined to electrons, their measurements were not extended down to the minimum of ionization and hence could not yield the ratio $I_{\text{pl}}/I_{\min}$.

small and, hence, too close to the noise level to permit useful measurements. For pions the corresponding limit is $\gamma \sim 70$, whereas electron tracks lend themselves to reliable determinations of $\bar{\alpha}$ and G at energies up to several thousand rest masses. On the other hand, in the vicinity of $G_{\min}$, both $\bar{\alpha}$ and G can be measured for protons, and especially well for pions.

Fortunately, there also is an intermediate region $10<\gamma<40$ in which $\bar{\alpha}$ and G can be determined for both electrons and mesons. Thus, a direct comparison can be made between the two groups, and a useful link is provided between the regions of $G_{\min}$ and G_{pl} where, for our present purpose, only one or the other type of particle can be employed. Moreover, for both electrons and mesons, the rate of variation of I can be compared with theory in this intermediate region where experimental delineation of the ionization curve is particularly important.

The electron tracks were selected phenomenologically by their occurrence in electron pairs or in tridents. Long tracks (averaging $\sim$8000 microns) of mesons and protons occurring in the same 6×3 inch emulsion were obtained from shower stars. The multiple scattering of these tracks was measured by the coordinate method of Fowler[4] on a special Bausch and Lomb microscope stage which has a "noise" <0.15 micron. Grain and blob counts (>1000 blobs/track) were repeated by three observers for each track. The errors in both G and γ shown in Figs. 1 and 2 are standard errors. The curves shown in these figures are theoretical curves, which were calculated as described in the next section.

To arrive at a value of $G_{\text{pl}}/G_{\min}$ which might be compared with the theoretical $I_{\text{pl}}/I_{\min}$, we adopted the least-squares value $G_{\text{pl}}=19.70\pm0.40$ blobs/100μ for the electron tracks with $\gamma>100$. The least-squares slope is $0.15\pm5°$, i.e., the best-fitting line in this velocity region is a horizontal one. For $G_{\min}$ we averaged the G values of the meson tracks in the interval $3<\gamma<6$, which yielded the value 17.24 ± 0.35 blobs/100μ. (The theoretical minimum, in the theory described below, occurs at $\gamma=4.2$.) In this way we obtained the result

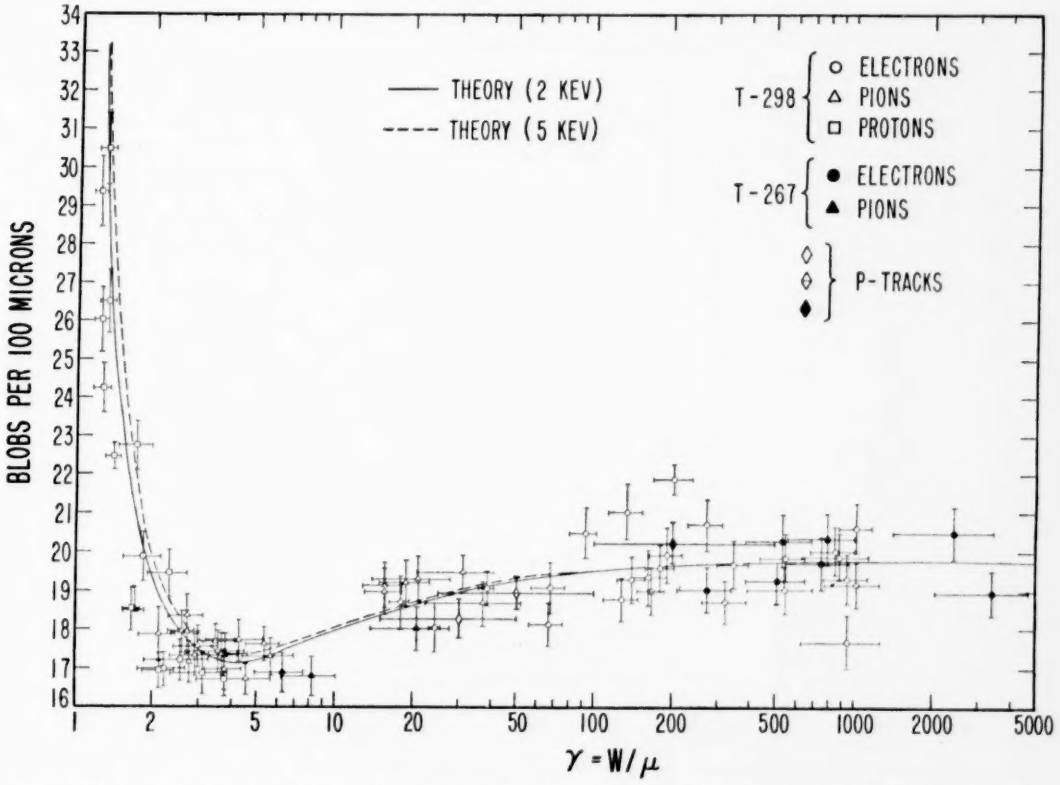

FIG. 2. Blob density is plotted as a function of γ, the total energy of the moving particle. Measurements on 85 tracks found in two 3 in.× 6 in., Ilford G.5, 400μ plates, of the same batch, exposure and processing are shown. The "ρ tracks" are tracks of shower-generating particles. The open diamond gives the average blob density of 4 tracks with $n_s=5$; the barred diamond shows the average of 6 tracks with $n_s=7$ or 8; and the black diamond, the average of 4 tracks with $n_s=9$ or 10.

[4] P. H. Fowler, Phil. Mag. **41**, 169 (1950).

$G_{pl}/G_{min}=1.143\pm0.03$. Since there is evidence that G is proportional to I at low-grain densities[4,5] this value applies also to the ratio I_{pl}/I_{min} in AgBr, where I is defined more precisely below.

Additional tracks were measured in T-267, a plate of the same batch and having the same history as T-298. G_{pl} was found to be 8 percent higher in the former than in the latter, but the ratio G_{pl}/G_{min} was unchanged. These data were normalized at plateau to those of Plate T-298 and the results for both plates are shown in Fig. 2.

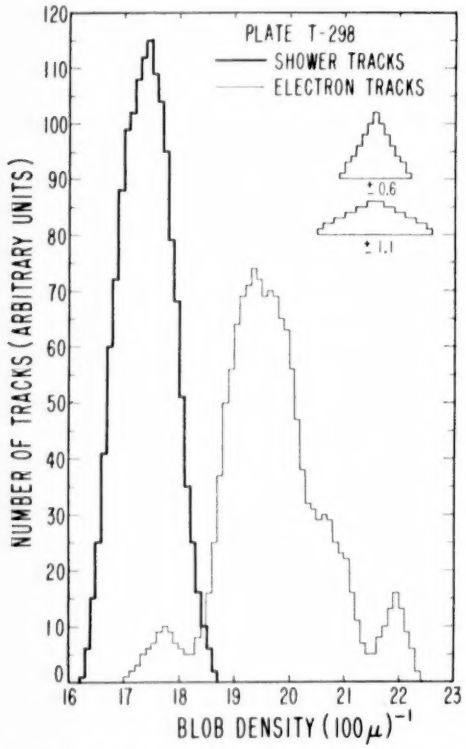

FIG. 3. Frequency of tracks as a function of blob density. Only data shown in Fig. 1 are plotted. Shower tracks with densities <18 blobs/100μ are included. The electron peak is 12.5 percent above the shower track peak. Tracks are plotted as triangles of equal area but with a base proportional to the standard error in the blob density.

The three diamond-shaped points in Fig. 2 represent the tracks of singly-charged shower-generating particles which gave rise to shower multiplicities $n_s\geq5$. We call these p tracks, where p denotes "primary," although it seems safe to assume that all or most of these are protons. These three points differ from the others in two respects: (a) each represents several (4 to 6) tracks rather than only one, and (b) no $\bar{\alpha}$ measurement could be made on these in view of their small $\bar{\alpha}$, as explained above. The lower limit $n_s=5$ was chosen so as to increase the likelihood that the shower primaries had very high energies (tens of Bev or higher).

In order to see how closely G for protons agrees with G for electrons at or near the plateau, we have estimated the energy of the p particles in each n_s group from their multiplicities. This can only lead to a very rough estimate of the energy, since for either plural or multiple theories of meson production one can expect a considerable spread in energy for a given n_s. Moreover, neither of these theories alone seems likely to account for the generation of meson showers in the variety of nuclei present in emulsions. It is reasonable to suppose that, especially in the heavier nuclei such as Ag or Br, meson production is in general a pluro-multiple process. Therefore, to arrive at energy estimates, we have taken into account both Fermi's theory of multiple production and the Heitler-Janossy theory of plural production. Our assignments of energy ($\gamma=30$ for $n_s=5$; $\gamma=50$ for $n_s=6, 7$; and $\gamma=200$ for $n_s=9, 10$) represent values considerably smaller than the mean-value predictions of multiple theory, and somewhat larger than those of plural theory. The crudeness of these energy estimates is indicated by the very wide limits of error for these three points shown in Fig. 2. Thus, for the point at $\gamma=200$, the limits are $100<\gamma<500$. Fortunately, the variation of I at these high velocities is so insensitive a function of the energy that it is useful to include these points despite the large uncertainty in energy. The G values, of course, must be determined rather precisely, and this was possible. It will be seen that the p track data agree satisfactorily with the electron and meson data.

If one wishes to evaluate the ratio G_{pl}/G_{min} alone, this can be done more quickly, without multiple scattering measurements, by the histogram method outlined in the Introduction, and described more fully in reference 1. In order to compare the present data directly with our earlier results, we have plotted in Fig. 3 the track frequency as a function of blob density for two groups of tracks from plate T-298, those around the minimum and those near the plateau. The former group consisted of star-shower tracks having less than 18 blobs per 100μ. The plateau group consisted exclusively of the fast electron tracks whose selection has been described above. From the locations of the peaks in this histogram, read at the centers of the respective half-maxima, we estimate that G_{pl} lies 12.5 percent above G_{min}.

A plate H-146, from another batch, having a completely different history, was scanned for similar shower-star and electron tracks and the data obtained were also plotted on a histogram, shown in Fig. 4. From this diagram, we estimate an increase of 13 percent between G_{min} and G_{pl}. Since G_{pl} in Fig. 4 is 8 percent higher than G_{pl} in Fig. 3, and since the height of G_{pl} above G_{min} is the same in the two plates, our data indi-

[5] Fowler's evidence (reference 4) is actually for g rather than G. However our results show that G is proportional to g for these thin tracks.

cate that the magnitude of the relativistic rise in ionization loss as measured by blob densities is not sensitive to the intensity of development, which largely determines the absolute value of G_{pl}.

It is noteworthy that, although the G_{pl} peak in Figs. 3 and 4 is obtained from electron tracks, the value of $G_{\text{pl}}/G_{\text{min}}$ is the same as that in our earlier determination, which employed "p tracks" (mainly protons) for G_{pl}. This shows that, within our experimental error, plateau protons and plateau electrons produce the same blob densities.

The values of the relativistic rise deduced from Figs. 1 to 4 as well as the histograms in reference 1 agree within experimental error. This suggests that the faster histogram method, which omits scattering measurements, is adequate for some purposes, though it gives no information about the *rate* of rise of G between minimum and plateau. As to the magnitude of the rise, we attach more weight to the value 14 ± 3 percent than to those deduced from the histograms, since the former is based on tracks for each of which the energy was measured. Thus the blob density, at minimum, is probably fixed more precisely.

COMPARISON WITH IONIZATION THEORY

The ionization theory of Bethe-Bloch-Williams, which predicted an indefinitely continued relativistic increase in I with velocity, was corrected by Fermi[6] to take account of the polarization of the medium.[7] He showed that the rate of ionization loss should saturate at sufficiently high velocities. Fermi's treatment, which employed a single dispersion frequency for the electrons in the medium, was modified by Wick,[8] Halpern and Hall,[9] Bohr,[10] and Sternheimer[11] who showed that it is necessary to construct a multifrequency theory.

We have calculated theoretical ionization curves for AgBr according to the Halpern-Hall and Sternheimer theories using the constants based on the recent experiments of Bakker and Segrè[12] on ionization potentials. For comparison with our experiment it is necessary to calculate not the *total* rate of ionization loss usually discussed in the theories but the limited rate of loss along a track, measured by its Ag grain density, which arises only from energy transfers to electrons up to a few kev.[13] Larger transfers give rise to delta rays consisting of 2 or more Ag grains and the grains lying off the track are ignored in ordinary grain counting. Accordingly, we computed the restricted rate of loss I as a function of γ, using 5 kev[14] for the "limiting effective energy transfer T_0" to the electrons of the medium.

The theoretical expression which we employed for the rate of energy loss is the one used by both Halpern-Hall and Sternheimer, *viz.*[15]

$$I\equiv-\frac{1}{\rho}\frac{dE}{dx}=\frac{2\pi ne^4}{\rho mv^2}\left[\ln\frac{mv^2T_0\gamma^2}{w^2}+\frac{1}{\gamma^2}-\delta\right].$$

Here I is the rate of loss per g cm^{-2}; E is the energy of the ionizing particle; ρ is the density of AgBr; n is the number of electrons per cm^3; m is the electron mass; $v=\beta c$ is the velocity of the particle; the upper limit T_0 (defined above) replaces T, the absolute maximum energy transfer; $\gamma=(1-\beta^2)^{-1/2}$; w is the average ionization potential of AgBr; and δ is the "density-effect correction," which is a function of the particle's velocity.

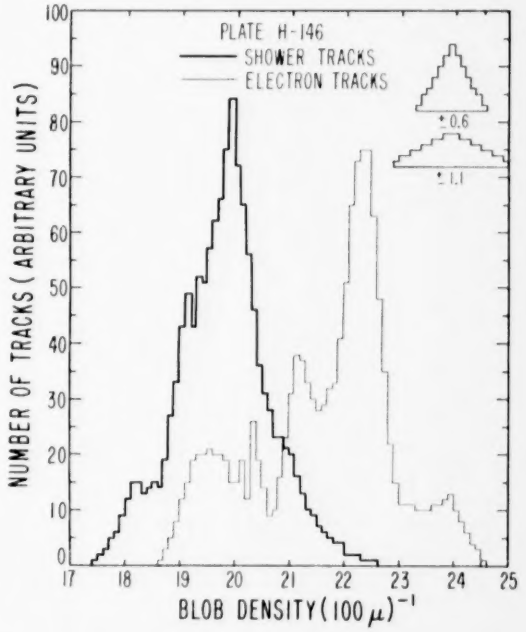

FIG. 4. Frequency of tracks as a function of blob density. This plate is of a different batch, exposure and processing than T-298 and T-267. The peak for electrons is 13 percent above the shower-track peak.

[6] E. Fermi, Phys. Rev. **56**, 1242 (1939); **57**, 485 (1940).

[7] The diminution of ionization loss by the shielding effect of electron displacement was suggested by W. F. G. Swann, J. Franklin Inst. **226**, 598 (1938).

[8] G. C. Wick, Ricerca sci. **11**, 274 (1940); **12**, 858 (1941); Nuovo cimento **1**, 302 (1943).

[9] O. Halpern and H. Hall, Phys. Rev. **57**, 459 (1940); **73**, 477 (1948).

[10] A. Bohr, Kgl. Danske Videnskab. Selskab, Mat.-fys. Medd. **24**, No. 19 (1948).

[11] R. M. Sternheimer, thesis, University of Chicago, 1946 (unpublished); Phys. Rev. **88**, 851 (1952). We used the constants for AgBr rather than those for emulsion, since we are concerned with the rate of ionization loss manifested in the AgBr grains which were rendered developable.

[12] C. J. Bakker and E. Segrè, Phys. Rev. **81**, 489 (1951).

[13] H. Messel and D. M. Ritson [Phil. Mag. **41**, 169 (1950)] first called attention to the importance of this distinction.

[14] The range of a 5-kev electron in AgBr is approximately the same as the radius of an average undeveloped grain of AgBr in a G.5 emulsion.

[15] See Eq. (11) of R. M. Sternheimer, Phys. Rev. **88**, 851 (1952).

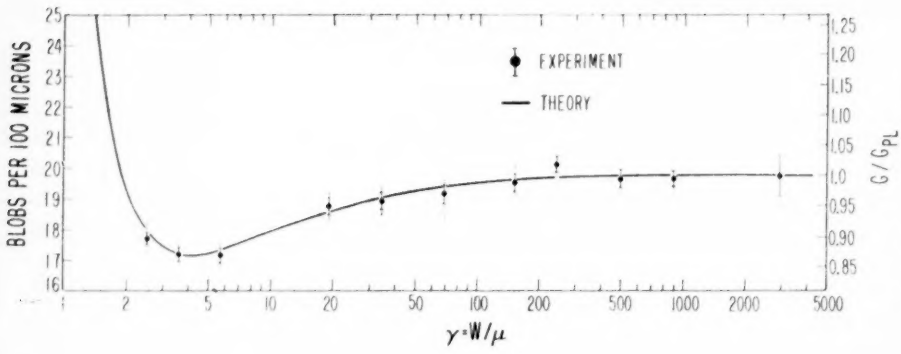

FIG. 5. Mean blob density $\bar{G}$, as given in Table I, plotted as a function of $\bar{\gamma}$. Tracks with $\gamma<2$ are omitted. The solid error line is based on the number of blobs contributing to the point; the dotted one represents the standard deviation of the group from their mean.

For computation we have used the convenient form[16]

$$I=\frac{A}{\beta^2}\left[B+\ln T_0+\frac{1}{\gamma^2}-\Delta\right],$$

where $A=2\pi ne^4/mc^2\rho$, $B=\ln[mc^2(10^6 ev)/w^2]$,

$$\Delta=\delta-2\ln\beta\gamma,$$

and T_0 is in Mev. For AgBr, Sternheimer[17] gives $A=0.0668$ Mev/g cm^{-2} and $B=15.1$. (This corresponds to an average ionization potential $w=376$ ev.) Δ was computed according to his Eq. (10) and Table II.

The dashed curve in Figs. 1 and 2 shows the results, normalized to the experimental least-squares plateau value at a single point, $\gamma=300$. We have also computed I for another value of T_0, 2 kev. The results of this calculation are shown in the solid curve which lies slightly below the dashed one. It is evident that I is not sensitive to the choice of T_0, and that either of these theoretical curves fits our data satisfactorily. The calculated ratio I_{pl}/I_{min} for the solid curve is 1.152, that for the dashed curve is 1.137. These may be compared with our experimental value, 1.143 ± 0.03. Our data as to the rate of rise toward the plateau support the theoretical prediction of a slow rise followed by saturation in the region $\gamma>100$.

The multiplicity of points and the overlapping of error lines in Figs. 1 and 2 make it difficult to use those diagrams in comparing theory with experiment. We have, therefore, constructed Fig. 5 in which the same data are grouped into energy intervals each containing about the same number of tracks. Table I gives the mean blob density, mean γ, and the total number of blobs counted for each group of tracks represented by a point in Fig. 5. Two types of standard error are shown for each point in this figure: the solid error line is based on the number of blobs contributing to the point; the dotted one represents the standard deviation of the group from their mean. The theoretical curve shown in the figure is the same as the solid curve in Figs. 1 and 2, i.e., it was calculated for $T_0=2$ kev. The tracks with $\gamma<2$ are omitted from this figure.

While our results show excellent agreement with the theories of Halpern-Hall and Sternheimer, they conflict with the theory of Huybrechts and Schönberg,[18] which departs more radically from Fermi's treatment. These authors predict an increase in I from minimum to plateau in AgBr of 3.8 percent, and they suggest a method whereby this theoretical value could be increased to 6 percent. Neither value seems capable of accounting for our results.[19]

As can be seen in Fig. 2, our G values show no significant differences between electrons and heavier particles. This is just what should be expected of the restricted ionization loss with which we are concerned. The predicted difference in total rate of ionization loss between the two groups of particles arises from the different upper limits to the possible energy transfers between the moving particle and the electrons of the surrounding medium. If one applies an upper limit of a few kilovolts in order to compute the restricted energy transfer to silver bromide grains *along* the track, then the difference vanishes. Our results bear this out in the plateau region, as well as in the interval $10<\gamma<100$.

The role of Čerenkov radiation in the energy-loss of relativistic particles was noted by Fermi[6] and further elucidated by A. Bohr.[10] The possibility that some of this radiation might escape from the AgBr crystals along the path of a particle in a nuclear emulsion and thus detract from the observable relativistic rise in grain density has been investigated by Messel and Ritson,[13] Schönberg,[19,20] Huybrechts,[18] Budini,[21] and Sternheimer.[22]

According to Sternheimer's analysis the escape of

[16] This is equivalent to Sternheimer's Eq. (13) [Phys. Rev. **88**, 851 (1952)], since Sternheimer's δ includes as its first term $2\ln(p/\mu c)=2\ln\beta\gamma$.

[17] Footnote 12 of reference 15.

[18] M. Huybrechts and M. Schönberg, Nuovo cimento **9**, 764 (1952).

[19] Schönberg's earlier theory disagrees even more sharply with our experimental results; see Nuovo cimento **8**, 159 (1951).

[20] M. Schönberg, Nuovo cimento **9**, 210 (1952); **9**, 372 (1952).

[21] P. Budini, Phys. Rev. **89**, 1147 (1953); Nuovo cimento **10**, 236 (1953).

[22] R. M. Sternheimer, Phys. Rev. **89**, 1148 (1953); a more detailed analysis is given in Phys. Rev. **91**, 256 (1953).

energy from the AgBr crystals in the form of Čerenkov radiation is so small, compared with the energy deposited in the grains, that the former may be neglected in comparing the theory with measurements on grain-density in emulsions. This conclusion is supported by the agreement between our experimental results and calculations based on Sternheimer's theory.

COMPARISON WITH OTHER EXPERIMENTS

In 1949 the Brussels group found no evidence in emulsions for the relativistic rise in g exceeding their experimental error.[23] In 1950 similar results appeared in publications from Bristol[4] and Rochester.[24] During the same year Pickup and Voyvodic[25] reported indications of a relativistic increase of about 10 percent to a plateau starting at $\gamma \sim 20$. These were, according to the authors, preliminary results based on a few tracks. Voyvodic subsequently extended this work and found a rise of 8 or 9 percent.[26] Similar results were obtained by Daniel *et al.*[27] Our present value is 14 ± 3 percent.

As to the rate of rise of g toward saturation, Voyvodic found indications that saturation is completed more quickly than for the ionization loss as calculated by him. Morrish's results[3] on electrons and those of Daniel *et al.*,[27] on heavier particles similarly suggest that saturation in g already sets in at $\gamma \sim 20$. Our data, on the other hand, are altogether consistent with the slow rate of rise calculated according to the Halpern-Hall-Sternheimer theory, and suggest that the polarization plateau is reached at values of $\gamma > 100$ as predicted by this theory.

In view of the appreciable magnitude of the total rise, we believe that it should now be possible to discriminate between pions and protons of 3 to 6 Bev and perhaps higher. The upper energy limit previously assigned to such discrimination was 1 Bev. The identification of these very fast particles requires, of course, tracks of sufficient length for good measurement of $\bar{\alpha}$.

In analyzing previously available data on the relativistic rise, Brown[28] is concerned with the explanation of a "trough in the experimental grain density *vs* energy curve $\frac{1}{3}$ to $\frac{2}{3}$ as deep and 3 to 10 times as narrow as the corresponding trough in the theoretical curve. . . ." As we have seen, however, our data are completely consistent with the theoretical trough both in "depth" and "width." The considerable area of agreement provides at least empirical justification for comparison with the theory upon which our calculations are based.

Brown shows that a detailed theoretical treatment of grain densities should take into account the phenomenon of fluctuations in the energy loss. His discussion makes it plausible that *large* differences in the intensity of development, with large resultant differences in the absolute values of G_{pl} may noticeably affect the value of the ratio $G_{\text{pl}}/G_{\text{min}}$. However, our measurements indicate that *moderate* changes ($\sim$10 percent) in the level of G_{pl} affect this ratio by less than 3 percent, if at all.

TABLE I. Data for the groups of tracks plotted in Fig. 5.

γ interval	No. of tracks	No. of blobs	Blobs per 100μ	$\bar{\gamma}$
$2 \leq \gamma < 3$	11	11,319	17.7	2.5
$3 \leq \gamma < 4$	7	7,593	17.2	3.6
$4 \leq \gamma < 10$	6	7,588	17.2	5.7
$10 \leq \gamma < 25$	7	6,591	18.8	19
$25 \leq \gamma < 50$	7	7,779	18.9	34
$50 \leq \gamma < 100$	9	8,143	19.2	69
$100 \leq \gamma < 190$	6	5,622	19.5	150
$190 \leq \gamma < 340$	9	9,397	20.1	240
$340 \leq \gamma < 700$	5	5,088	19.6	500
$700 \leq \gamma < 1500$	8	7,575	19.6	900
$1500 \leq \gamma < 3000$	2	2,058	19.7	2900

CONCLUSIONS

We draw the following conclusions about the restricted rate of ionization loss I in AgBr of singly charged particles moving at relativistic velocities:

1. As the velocity increases, I passes through a minimum at $\gamma \sim 4$ and then rises to a limiting value I_{pl} which lies 14 ± 3 percent above I_{min}.

2. At velocities corresponding to the interval $10 < \gamma < 100$, our data are consistent with the slow rate of rise predicted by theory.

3. I saturates at values of $\gamma > 100$, and maintains the plateau value at least as far as $\gamma = 3400$.

4. Electrons, mesons, and protons show a similar variation in I.

In all these respects our results are in agreement with the theoretical curves we computed according to Halpern and Hall and Sternheimer. We believe that these curves can be used, e.g., for velocity determinations based on G and for mass estimates based on both G and $\bar{\alpha}$. It should be emphasized, however, that in this region of extremely high velocities, such determinations are still subject to considerable errors because of the inherent insensitivity of G to the velocity.

ACKNOWLEDGMENT

We wish to thank Mr. F. W. O'Dell for substantial assistance with the balloon flight, emulsion processing, and figures. Mrs. H. F. Shapiro and Miss K. De Angelis have ably helped with microscopy. We are grateful to Professor R. F. Christy, Dr. R. M. Sternheimer, and Professor P. Budini for several stimulating discussions. Finally, we appreciate the interest which Dr. F. N. D. Kurie has shown in this work.

[23] G. P. S. Occhialini, Nuovo cimento **6**, 413 (1949).
[24] Bradt, Kaplon, and Peters, Helv. Phys. Acta **23**, 24 (1950), see footnote, p. 48.
[25] E. Pickup and L. Voyvodic, Phys. Rev. **80**, 89 (1950).
[26] According to unpublished reports by L. Voyvodic and C. F. Powell at the Bristol Conference, December, 1951. Recently in a private communication, Dr. Voyvodic informed us that his data are consistent with a rise of 10 ± 5 percent.
[27] Daniel, Davies, Mulvey, and Perkins, Phil. Mag. **43**, 753 (1952).
[28] L. M. Brown, Phys. Rev. **90**, 95 (1953).

The Stopping Cross Section of Gases for Protons, 30–600 kev*

H. K. Reynolds, D. N. F. Dunbar,† W. A. Wenzel, and W. Whaling
Kellogg Radiation Laboratory, California Institute of Technology, Pasadena, California

(Received July 27, 1953)

The stopping cross section of H_2, He, O_2, air, N_2, Ne, A, Kr, Xe, H_2O, NH_3, NO, N_2O, CH_4, C_2H_2, C_2H_4, and C_6H_6 for protons has been measured over the energy range $E_p = 30-600$ kev. An electrostatic analyzer measures the energy of protons incident on a gas cell, and the transmitted beam energy is measured with a magnetic spectrometer. The gas cell is closed off with thin aluminum windows. Comparison of the molecular stopping cross section of the compounds with the values obtained by summing the constituent atomic cross sections shows that Bragg's rule does not hold for any of these compounds below $E_p = 150$ kev; for NO the additive rule does not hold at any energy studied. Above 150 kev the stopping cross section of carbon is obtained by subtracting the hydrogen contribution from the values measured for the hydrocarbons. Average ionization potentials are calculated from these measurements. A range energy relation for protons in air is included. Sources of error are discussed; the probable error of the stopping cross section measurements varies between 2–4 percent.

I. INTRODUCTION

THE precision with which nuclear reaction cross sections can be measured often depends on the accuracy with which the stopping cross section of the target material is known. At proton energies below a few hundred kilovolts there are reliable measurements for only a few materials,[1] and the theoretical understanding of the energy loss process is not sufficient to make up for the lack of experimental results. The experiment described in this paper was undertaken primarily to supply reliable values for the stopping cross sections of hydrogen, helium, nitrogen, air, oxygen, neon, argon, krypton, and xenon for protons of energy from 30 to 600 kev. Measurements were also made on the compounds nitrous oxide, nitric oxide, water vapor, and ammonia, to test the validity of Bragg's rule for the addition of stopping cross sections. In the energy range in which Bragg's rule was found to hold it has been used to compute the stopping cross section of carbon from the measured values for carbon dioxide, methane, acetylene, ethylene, and benzene. It is hoped that the present results may provide some insight into the energy loss phenomenon in the region where the incident particle velocity is comparable with that of the atomic electrons. Here electron capture and loss and the effects of molecular and atomic binding introduce serious problems in the theoretical interpretation.

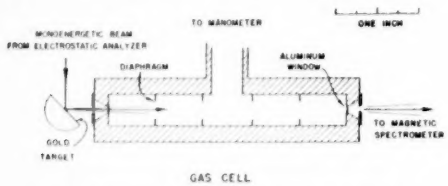

FIG. 1. Schematic diagram of target and gas cell.

In this experiment the molecular stopping cross section ϵ is determined from the measured energy loss of protons and deuterons passing through a cell of known length containing gas at a known temperature and pressure, since

$$\epsilon = -(1/N)(dE/dX),$$

where N = molecular gas density, and (dE/dX) = rate of energy loss by the moving charged particle along its path. Protons were used for the energy range from 150 to 600 kev, while deuterons of energy from 60 to 300 kev gave values for protons of energy from 30 to 150 kev.

II. EXPERIMENTAL

The monoenergetic proton or deuteron beam obtained with a 600-kev electrostatic generator and an electrostatic analyzer was scattered from a plane gold surface and entered the gas cell which was set at 90° to the incident beam. The target and gas cell are shown schematically in Fig. 1. The vacuum tight aluminum windows at either end of the gas cell were prepared after the method developed by Sawyer.[2] The total thickness of the two windows varied from 16 to 40 kev for protons of 100 kev. The diameter of the windows was 0.094 in. with stops of 0.047-in. diameter fixed immediately outside them so that only the central portion of the foils was struck by the beam. The diameter of the beam incident on the target, and hence of the apparent source of scattered particles, was 0.020 in. After emerging from the gas cell the particles entered the 16-in. double focusing magnetic spectrometer and were detected with a scintillation counter. The energy loss in the gas may be determined by measuring with the spectrometer the change in energy of the transmitted beam when gas is put into the cell, or equivalently, by measuring with the electrostatic analyzer the

* Supported in part by the joint program of the U. S. Office of Naval Research and the U. S. Atomic Energy Commission.

† On leave from the University of Melbourne, Melbourne, Australia.

[1] A recent review of the energy loss process will be found in the paper by H. A. Bethe and J. Ashkin in E. Segrè's *Experimental Nuclear Physics* (John Wiley and Sons, Inc., New York, 1953).

[2] G. A. Sawyer, Rev. Sci. Instr. **23**, 604 (1952).

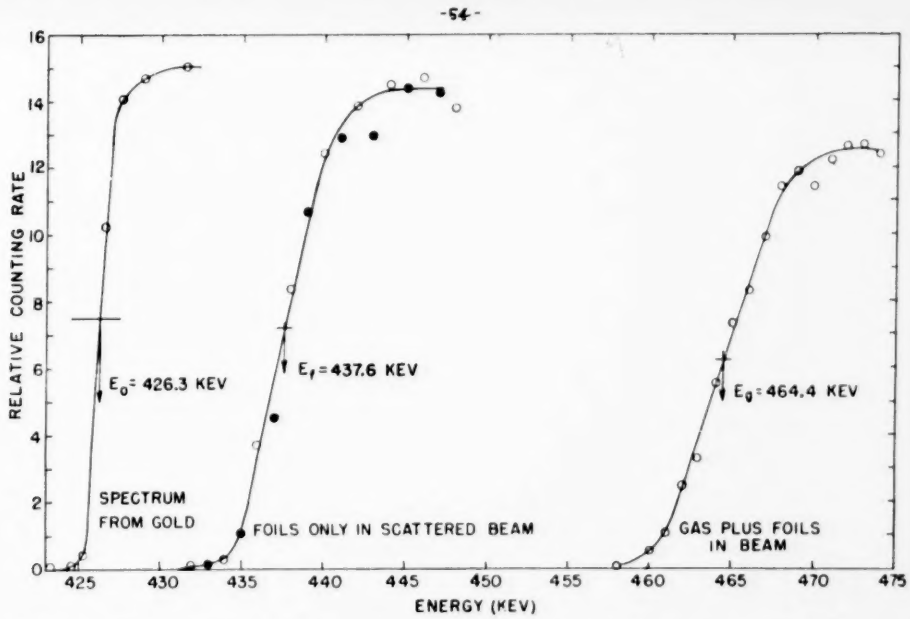

FIG. 2. Proton counting rate in magnetic spectrometer plotted as a function of incident proton energy. The curve at left was taken with gas cell removed. Middle curve was taken with empty cell in beam, and the displacement is a measure of the thickness of the cell windows. The right curve indicates displacement when A at 7.35-mm Hg pressure was admitted to cell.

change in the incident energy required to keep the transmitted particle energy constant when gas is admitted to the cell. The latter method was adopted in this experiment because the generator energy could be changed more rapidly than the magnetic field of the spectrometer.

The energy spectrum of the particles scattered from a thick gold target is an approximate step function. A similar step is observed if the magnetic spectrometer is set to detect particles of a constant energy and the energy of the beam incident on the target is varied. From Fig. 2 it is evident that the mid-point of the rise of such a step is easily located. The shift in this step energy when gas is put into the cell is a measure of the average energy loss in the gas. The experimental procedure was to measure successively the energy of this step (a) with the gas cell lifted out of the path of the scattered beam E_0; (b) with the empty gas cell lowered into the beam E_f; (c) with a known pressure of gas in the cell E_g; and (d) after the gas had been pumped out of the cell E_f again. A set of such steps is shown in Fig. 2 for argon. The points taken during part (d) of the cycle, which are represented in the figure by closed circles, show that the magnetic field of the spectrometer does not drift during the measurements and that a negligible amount of carbon was deposited on the target.

The energy lost by the beam in the gas volume itself can be found from E_0, E_f, and E_g as shown in Fig. 3. First a range energy curve for the aluminum was prepared by measuring (E_f-E_0) as a function of $(E_f+E_0)/2$. The exact normalization of the curve is unimportant. From E_f and E_0 the foil thickness in arbitrary units is found to be (R_f-R_0). If the two foils are of the same thickness, then E_2, obtained from $R_2=(R_f+R_0)/2$, is the energy of the beam leaving the gas. Similarly E_1 the energy of the beam entering the gas is obtained from $R_1=R_g-(R_f-R_0)/2$. The stopping cross section of the gas at energy $(E_1+E_2)/2$ may be calculated from the energy loss (E_1-E_2). Since the maximum difference between (E_g-E_f) and (E_1-E_2)

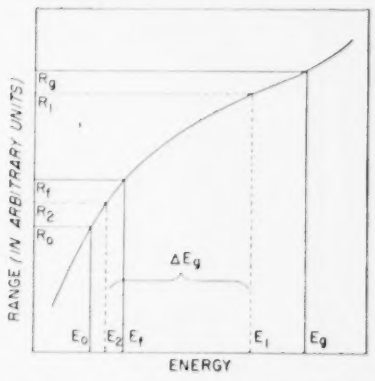

FIG. 3. Range energy curve for the aluminum foils. This curve is used in correcting for the change in window thickness with proton energy.

TABLE I. Gas suppliers and purity.

Gas	Manufacturer	Purity (%)	Principal impurity	Purification[a]
H	Linde Air Products	99.5		1
He	Air Reduction Company	99.7		2
Ne	Air Reduction Sales Company	99.996		
Ar	Linde Air Products	99.92	N_2	2
Kr	Air Reduction Sales Company	99.996		
Xe	Air Reduction Sales Company	99.996		
Air				2
N_2	Linde Air Products	99.92		2
O_2	Linde Air Products	99.5		2
NO	Mathieson Chemical Company	98.7	Higher oxides of N and N_2	4
N_2O	Ohio Chemical Company	98	N_2	2
NH_3	Dow Chemical Company	99.95		2
CO_2	Ohio Chemical Company	99.7		2
H_2O	Distilled Water	99.9		5
C_6H_6	Baker and Adamson	99.98	H_2O	5
CH_4	Texas Company	99.8 (not including H_2O)	H_2O	3
C_2H_4	Ohio Chemical Company	99.5		2
C_3H_7	Linde Air Products	99.62	Acetone	4

[a] Purification: 1. Palladium leak. 2. H_2O removed by "Drierite," W. A. Hammond Company, Xenia, Ohio. 3. Drierite, KOH, and charcoal. 4. Alcohol and dry ice trap. 5. Gases removed by repeated freezing and pumping.

is only about 4 percent, any small error in the foil correction will have a negligible effect on the stopping cross section. At the lowest energies the rapid variation of the stopping cross section with energy might necessitate a curvature correction when the energy lost in the gas is an appreciable fraction of the total energy. This correction has been calculated by approximating the stopping cross-section curve below the maximum with a curve of the form $\epsilon \propto E^n$. The resulting correction was never greater than $\frac{1}{2}$ percent and was not applied to any gas.

The number of gas atoms in the path of the particles is determined from the cell length L, the temperature T, and pressure P of the enclosed gas. The temperature of the walls of the gas cell was read on a thermometer after the pressure had remained constant long enough to show that thermal equilibrium had been reached in the cell. The pressure was measured with an oil manometer which registered the difference in pressure between the gas cell and the main vacuum system.

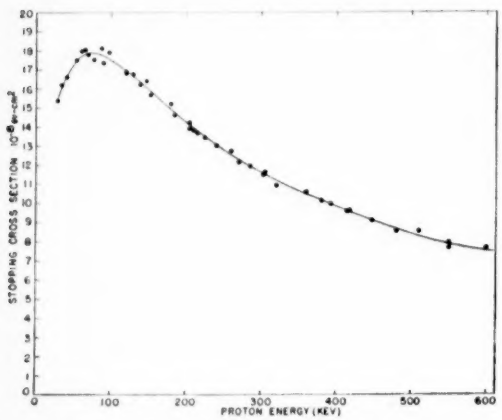

FIG. 4. Stopping cross section for protons in air.

From these measurements the stopping cross section is calculated from the relation

$$\epsilon=\left(\frac{T+273}{273}\right)\left(\frac{P}{760}\right)\frac{(E_1-E_2)}{AL},$$

where A is Loschmidt's number.

III. ACCURACY

The accuracy of the stopping cross sections determined in this experiment depends on the precision with which the following quantities have been measured.

1. Pressure

Litton vacuum pump oil was used in the manometer. The density of the oil after it had been outgassed was measured to be 0.886 ± 0.001 g cm^{-3}. The difference in height of the oil columns could be measured to ±0.3 mm which leads to a probable error in ϵ of about 0.3 percent since the total pressure usually amounted to about 10-cm oil.

2. Temperature

The wall temperature of the gas cell was measured to within 0.5°C with a mercury thermometer which had been previously compared with a thermometer calibrated by the National Bureau of Standards. This temperature uncertainty corresponds to an uncertainty in ϵ of 0.2 percent.

3. Length of Gas Cell

To the length of the cell, 2.876 in., has been added 0.010 in. to allow for the slight bulging of the foils under pressure. This correction, which was estimated visually, may be in error by as much as 50 percent; this uncertainty in the cell length introduces an error of 0.2 percent in the value of ϵ.

4. Gas Purity

For all of the gases except neon, krypton, and xenon, the gas lines, valves, drying bottle, etc., were always maintained at pressures greater than atmospheric. For the rare gases mentioned above, the manufacturer's flask was connected directly to the valve leading to the gas cell and particular care taken to insure that the connection was vacuum tight. For all gases the system was flushed many times with the gas before measurements were begun. On the assumption that no contamination was introduced in handling the gas, the purity is taken to be that claimed by the supplier and listed in Table I, and errors due to contamination are neglected.

5. Energy Scale Calibration

The procedure for the calibration of the electrostatic generator has been previously described.[3] The beam

[3] W. A. Wenzel and W. Whaling, Phys. Rev. **87**, 499 (1952).

energy is known to within 0.5 percent and is monoenergetic to a few hundred volts. Since, however, the measured step displacement may be only a small part of the generator voltage, it is important that the calibration remain steady to a few hundredths of one percent during a run. A drift in the generator voltage relative to the magnetic spectrometer energy will produce a shift in the step of the foil spectrum before and after the gas has been put in the gas cell. In most cases no shift was observed, but on the occasions when a small shift was observed—less than 5 percent of the displacement—the average of the two step-positions was used. Almost every shift of the step was in the direction which would result from the deposition of contamination on the gold target surface during the run. The target was moved frequently between observations to prevent the formation of such a surface layer.

6. Location of the Mid-Point of the Step in the Spectrum

This is the greatest source of error in the experiment since the uncertainty in locating the mid-point of the step due to the statistics of the counting alone may amount to as much as 5 percent of the measured displacement. Calculation of this uncertainty is difficult, but the net effect of all statistical fluctuations may be estimated from the spread of the series of measurements such as those for air shown in Fig. 4. It appears that 4 percent is a reasonable estimate of the statistical uncertainty in an individual measurement of ϵ.

Consideration of all the above errors shows that the systematic probable error due to the oil density, temperature, cell length, and absolute energy calibration amounts to 0.6 percent, while the statistical error in each individual measurement of ϵ is about 4 percent. The errors shown in Table II have been assessed by considering not only the error in each individual measurement but also the nu nber of measurements and their spread, since the values of ϵ listed in Table II are obtained from smooth curves drawn through the experimental points.

There are in addition to the above errors certain aspects of the measurements which require investigation to insure that the stopping cross section and not some

TABLE II.

Proton stopping cross section per atom (10^{-15} ev-cm^2).

Energy (kev)	H_2 (%)	He (%)	N_2 (%)	O_2 (%)	Air$_2$ (%)	C (%)	A (%)	Ne (%)	Kr (%)	Xe (%)
30	5.84±3.4		16.1 ±2.6		15.5 ±2.6					
40	6.25±3.4	6.67±3.4	17.1 ±2.6	15.2 ±2.6	16.48±2.6		31.4 ±2.6	10.6 ±2.6	35.6±2.7	50.0±2.7
50	6.43±3.4	6.97±3.4	17.8 ±2.6	16.4 ±2.6	17.16±2.6		33.4 ±2.6	11.9 ±2.6	38.3±2.7	52.6±2.7
60	6.45±3.4	7.22±3.4	18.2 ±2.6	16.9 ±2.6	17.7 ±2.6		34.3 ±2.6	12.8 ±2.6	39.8±2.7	53.5±2.7
70	6.36±3.4	7.33±3.4	18.5 ±2.6	17.15±2.6	17.9 ±2.6		34.4 ±2.6	13.45±2.6	40.5±2.7	53.5±2.7
80	6.23±3.4	7.37±3.4	18.5 ±2.6	17.25±2.6	17.87±2.6		34.1 ±2.6	13.95±2.6	40.5±2.7	53.2±2.7
90	6.04±3.4	7.37±3.4	18.25±2.6	17.25±2.6	17.72±2.6		33.5 ±2.6	14.3 ±2.6	40.3±2.7	52.0±2.7
100	5.83±3.4	7.30±3.4	17.9 ±2.6	17.17±2.6	17.5 ±2.6	16.25±2.1	32.6 ±2.6	14.6 ±2.6	39.8±2.7	50.6±2.7
150	4.70±2.7	6.37±2.7	16.1 ±1.7	16.13±1.7	15.98±1.7	14.6 ±2.1	28.2 ±1.7	14.6 ±1.7	35.0±1.8	45.2±1.8
200	3.90±2.7	5.55±2.7	14.2 ±1.7	14.70±1.7	14.21±1.7	12.70±2.1	24.5 ±1.7	14.10±1.7	30.7±1.8	41.8±1.8
250	3.33±2.7	4.91±2.7	12.5 ±1.7	13.26±1.7	12.74±1.7	11.28±2.1	21.6 ±1.7	13.20±1.7	27.4±1.8	38.6±1.8
300	2.91±2.7	4.41±2.7	11.2 ±1.7	11.99±1.7	11.56±1.7	10.20±2.1	19.5 ±1.7	12.34±1.7	25.1±1.8	35.8±1.8
350	2.60±2.7	4.01±2.7	10.13±1.7	11.01±1.7	10.60±1.7	9.30±2.1	17.9 ±1.7	11.50±1.7	23.3±1.8	33.4±1.8
400	2.35±2.7	3.69±2.7	9.34±1.7	10.23±1.7	9.79±1.7	8.54±2.1	16.6 ±1.7	10.75±1.7	22.0±1.8	31.4±1.8
450	2.14±2.7	3.42±2.7	8.62±1.7	9.45±1.7	9.05±1.7	7.94±2.1	15.55±1.7	10.15±1.7	20.9±1.8	29.8±1.8
500	1.97±2.7	3.18±2.7	8.08±1.7	8.84±1.7	8.39±1.7	7.38±2.1	14.7 ±1.7	9.58±1.7	19.9±1.8	28.6±1.8
550	1.82±2.7	2.99±2.7	7.61±1.7	8.38±1.7	7.9 ±1.7	6.95±2.1	13.9 ±1.7	9.09±1.7	19.1±1.8	27.4±1.8
600	1.70±2.7	2.81±2.7	7.21±1.7	7.91±1.7	7.51±1.7	6.55±2.1	13.3 ±1.7	8.65±1.7	18.4±1.8	26.4±1.8

Proton stopping cross section per molecule (10^{-15} ev-cm^2).

Energy (kev)	CH_4 (%)	C_2H_2 (%)	C_2H_4 (%)	C_3H_8 (%)	H_2O (%)	NH_3 (%)	NO (%)	CO_2 (%)	N_2O (%)
30	37.4 ±2.6	43.4±2.6		116.0±2.6		29.7±2.6			
40	39.7 ±2.6	47.4±2.6	54.4±2.6	126.0±2.6	25.0±2.6	32.0±2.6	32.6±2.8	44.2±2.6	47.0±2.8
50	40.9 ±2.6	49.5±2.6	57.4±2.6	133.0±2.6	26.1±2.6	33.6±2.6	34.5±2.8	46.8±2.6	48.6±2.8
60	41.3 ±2.6	49.8±2.6	58.7±2.6	135.7±2.6	26.9±2.6	34.6±2.6	35.7±2.8	48.4±2.6	49.9±2.8
70	41.2 ±2.6	49.2±2.6	58.8±2.6	135.5±2.6	27.5±2.6	34.7±2.6	36.4±2.8	49.6±2.6	50.5±2.8
80	40.8 ±2.6	48.0±2.6	58.0±2.6	134.4±2.6	27.6±2.6	34.4±2.6	36.6±2.8	50.2±2.6	50.9±2.8
90	40.0 ±2.6	46.7±2.6	56.7±2.6	133.5±2.6	27.5±2.6	33.9±2.6	36.6±2.8	50.5±2.6	51.0±2.8
100	38.9 ±2.6	45.0±2.6	55.5±2.6	131.7±2.6	27.3±2.6	33.5±2.6	36.4±2.8	50.5±2.6	50.7±2.8
150	33.6 ±1.7	38.5±1.7	48.8±1.7	116.5±1.5	24.7±1.7	30.1±1.7	33.2±1.9	47.1±1.7	47.0±1.9
200	28.6 ±1.7	32.9±1.7	41.4±1.7	102.0±1.5	22.0±1.7	25.6±1.7	29.7±1.9	42.5±1.7	42.0±1.9
250	24.8 ±1.7	29.0±1.7	36.1±1.7	89.2±1.5	19.7±1.7	22.3±1.7	26.7±1.9	38.1±1.7	37.6±1.9
300	22.0 ±1.7	25.9±1.7	32.0±1.7	79.8±1.5	17.9±1.7	19.9±1.7	24.1±1.9	34.6±1.7	34.0±1.9
350	19.8 ±1.7	23.5±1.7	28.8±1.7	72.2±1.5	16.2±1.7	17.9±1.7	22.0±1.9	31.6±1.7	31.0±1.9
400	18.1 ±1.7	21.4±1.7	26.2±1.7	66.3±1.5	15.0±1.7	16.4±1.7	20.3±1.9	29.2±1.7	28.6±1.9
450	16.65±1.7	19.7±1.7	24.1±1.7	61.4±1.5	13.9±1.7	15.1±1.7	18.9±1.9	27.0±1.7	26.6±1.9
500	15.5 ±1.7	18.4±1.7	22.4±1.7	57.3±1.5	13.0±1.7	14.0±1.7	17.6±1.9	25.2±1.7	25.0±1.9
550	14.5 ±1.7	17.2±1.7	20.9±1.7	53.9±1.5	12.2±1.7	13.1±1.7	16.6±1.9	23.7±1.7	23.5±1.9
600	13.6 ±1.7	16.2±1.7	19.6±1.7	51.0±1.5		12.3±1.7	15.7±1.9	22.4±1.7	22.2±1.9

related quantity is being determined. The following investigations have been carried out.

7. Geometry

It is assumed that the path of the particles as they traverse the gas cell is nearly a straight line, but because of multiple scattering this may not be true at low energies. The effect of this multiple scattering would be expected to depend on the diameter of the aluminum baffles which define the effective diameter of the gas cell. Varying the diameter of the baffles from $\frac{1}{8}$ in. to $\frac{1}{4}$ in. and removing them altogether introduced changes of less than 1 percent in the stopping cross section of argon measured at $E_p=53$ and 450 kev. From this we conclude that nearly all of the particles which reached the second window traveled in approximately straight paths.

Further, since the second window subtends a cone of half-angle only 1° at the front window, the measured energy loss may not be typical of the energy loss of the beam as a whole. This is particularly important at low energies where as much as 80 percent of the beam was scattered sufficiently by the gas to stop it from reaching the second window. The diameter of the second window was therefore increased by a factor of four and the measurements of the stopping cross section of air were repeated at $E_p=130$ kev. No change was observed.

8. End Effects

Bulging or stretching of the foils, or adsorption of gas on the foils may also introduce an error. To see if such effects were present, the energy loss was measured in a short cell whose length was only 1.4 percent of the length of the original cell. In the absence of end effects the energy loss in the cell should be proportional to the length of the cell. Measurements on ammonia, water vapor, oxygen, nitrogen, hydrogen, and benzene showed that for each of these gases the energy loss was proportional to the cell length within the experimental accuracy. It has been assumed that the end effects are negligible for all the gases studied.

9. Pressure Effect

Deviation from proportionality between energy loss and gas pressure might be expected from certain end effects or from the change in effective chamber geometry resulting from multiple scattering. Measurements at low energies using pressures which varied over a factor of four failed to show such a dependence even in the case of the heaviest gas, xenon.

10. Beam Density

Since it is possible that stopping cross section measurements made with a large beam passing through the gas cell are affected by local temperature variations or by the ionization conditions in the path of the beam, a measurement was made with the gas cell placed so that the primary beam passed through it before striking the target. The generator voltage was varied and the spectrometer used to detect the particles as before. In this way the stopping cross section of argon at 95 and 320 kev was measured to be within 1 percent of the previous value found with the scattered beam. The energy loss of protons in a 200-kev mica foil has been measured in the same way and was found to be the same for the direct and scattered beams. These results indicate that the stopping cross sections of argon and mica are independent of current densities from 10 to 10^{-3} amp cm^{-2}.

11. Spectrum Shape

The choice of the middle of the rise of the step as the energy of the step is based on the apparent symmetry of the curves in Fig. 2 about their midpoints. Because of the E^{-2} energy dependence of the nuclear scattering in the gas and foils, which attenuates the transmitted proton beam by as much as 80 percent at low energies, the steps may be distorted in shape as well as displaced and broadened by energy loss and straggling. This distortion should be most significant at low energies. If distortion were present, the median energy loss, determined by the displacement of the midpoint of the steps, would differ from the mean energy loss, the quantity which appears in the stopping cross section. Though no distortion is apparent in the experimental curves, statistics are not sufficient to preclude some asymmetry. Theoretical estimates of the difference $(\bar{E}-E_{\text{med}})$ due to nuclear scattering give a negligible difference, but it can be shown that the sign of this difference depends on the manner in which the experiment is done. With the procedure followed in this experiment of varying the incident energy and holding the detector energy constant, this distortion will yield an energy difference greater than the mean energy loss. But if the incident energy is held constant and the energy loss is measured by varying the magnetic spectrometer energy, the measured energy difference will be smaller than the mean energy loss. The stopping cross section of argon was remeasured at 56 kev by this latter technique. The result was within 0.5 ± 2 percent of the value previously determined and appears to justify our theoretical estimates that the error introduced by distortion of the spectrum is small.

IV. RESULTS

Values of ϵ for all gases measured are presented in Table II. The probable errors shown in this table are those calculated as described in the section above. These results may be compared with three other recent determination of the proton energy loss in this energy range. Weyl[4] has measured the energy loss in air and argon between 40 and 450 kev. His results are in excellent agreement with the present work. Chilton,

[4] P. K. Weyl, Phys. Rev. **91**, 289 (1953).

Cooper, and Harris[5] have measured the stopping cross section of protons in nitrogen, argon, neon, krypton, and xenon between 400 and 1000 kev. In the energy range common to the two experiments the results are in good agreement except for xenon where their value is lower by 13 percent than the present measurement. Phillips[6] has also measured the stopping cross section in hydrogen, helium, nitrogen, oxygen, argon, krypton, water vapor, and carbon dioxide of protons with energies between 10 and 80 kev. At 50 kev his results are lower than the present ones by as much as 10 percent for nitrogen and oxygen and about 6 percent low from argon, krypton and water vapor. While there is reasonable agreement for the remaining gases, in all cases there is a gradual increase in the discrepancy between the results as the proton energy is increased.

The stopping cross sections of the lighter gaseous elements follow more closely than might be expected the Bethe formula,

$$\epsilon=\frac{4\pi e^4 Z_1^2}{mv^2}\left(Z_2\ln\left(\frac{2mv^2}{I}\right)-C_K\right),$$

where eZ_1=charge of incident particle of velocity v; eZ_2=nuclear charge; m=electronic mass; I=average ionization potential of the atom; C_K=correction for strong K-shell binding.

From the experimental value of ϵ and values of C_K given by Walske,[7] I has been calculated for energies above 100 kev for each element measured. For elements $Z\leq 10$, the value 0.7 was used for Walske's parameter θ. This is probably not justified in the case of He. For heavier elements Walske's formulas were interpolated. For each gas I/Z has been plotted as a function of energy in Fig. 5. It is interesting to note that the value of I for carbon is in good agreement with the value of 74.4 ev determined from the energy loss of 340-Mev protons in carbon.[8]

A comparison of the measured stopping cross sections of several compounds with the values obtained by summing the stopping cross sections of their respective constituents is shown in Fig. 6. Above 200-kev H_2O, NH_3, and N_2O apparently follow this simple additive relation, but at energies below 100 kev the molecules have a lower stopping cross section than the sum of the atomic stopping cross sections. It should be noted that the "atomic" stopping cross section used in this comparison is really one half of the measured *molecular* stopping cross section, and binding in the homonuclear molecule would be expected to produce deviations from the true atomic stopping cross section.

Nitric oxide does not obey this Bragg rule at any energy in the range measured. The difference of 4 percent between the stopping cross section of NO and

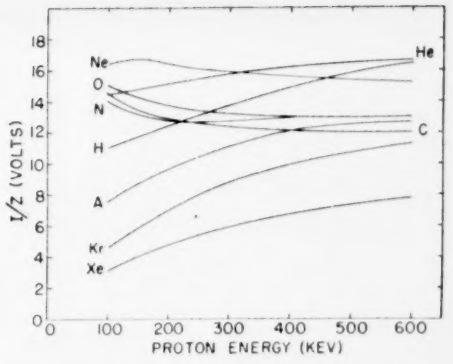

FIG. 5. Average ionization potential of gaseous elements; I/Z plotted as a function of E_p.

$\frac{1}{2}[\epsilon(N_2)+\epsilon(O_2)]$ at high energies is outside the experimental error. Although contamination of the nitric oxide with the higher oxides of nitrogen could account for this observed deviation, they could appear only by oxidation of the gas within the gas cell, since the gas from the supply bottle was passed through an alcohol-dry ice trap to remove any higher oxides initially present. No evidence was found for an increase of stopping cross section with time as might be expected if oxidation were proceeding in the gas cell. The only other likely contaminants, air or nitrogen, would have a negligible effect on the measured value of ϵ(NO). Schmieder[9] has measured the integral stopping power of NO and N_2O for 5.3-Mev alpha particles and finds that ϵ(NO) is 9 percent greater and $\epsilon(N_2O)$ is 8 percent less than the corresponding sums of ϵ(N) and ϵ(O). These deviations are in the same direction as in the

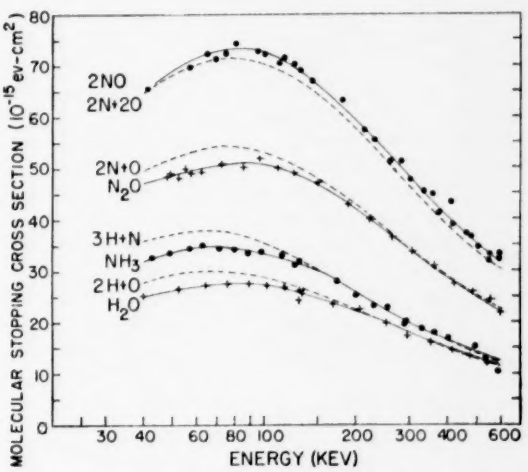

FIG. 6. Experimental stopping cross sections for several compounds (solid line) and values calculated from atomic stopping cross sections.

[5] Chilton, Cooper, and Harris, Phys. Rev. **91**, 495 (1953).
[6] J. A. Phillips, Phys. Rev. **90**, 532 (1953).
[7] M. C. Walske, Phys. Rev. **88**, 1283 (1952).
[8] R. Mather and E. Segrè, Phys. Rev. **84**, 191 (1951).
[9] K. Schmieder, Ann. Physik **35**, 445 (1939).

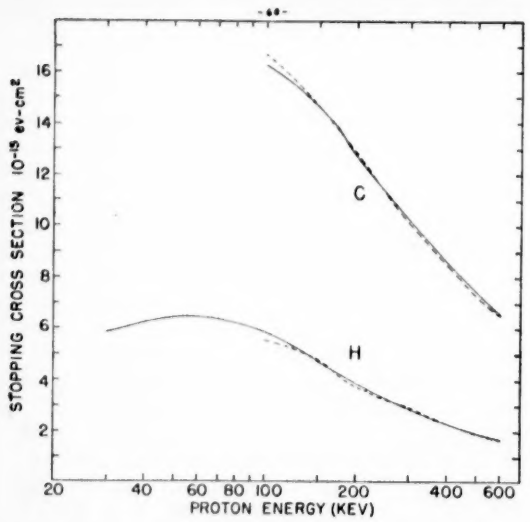

FIG. 7. Proton stopping cross section per atom. Solid curves: the experimental ϵ(H) from Table II and ϵ(C) obtained by subtracting hydrogen contribution from the stopping cross section of the hydrocarbons. Dashed curves: Average ϵ(C) and ϵ(H) obtained by combining values for pairs of hydrocarbons.

present work but are larger than might be expected from the present experiment.

From the stopping cross sections of any pair of hydrocarbons, values of ϵ(H) and ϵ(C) can be calculated. Below 150 kev the values obtained in this way show a wide spread, again indicating that the simple additive relation does not hold. Above 200 kev the various values obtained by this method agree within the experimental error. The average values of ϵ(H) and ϵ(C) obtained from the different pairs are plotted as dashed lines in Fig. 7. For comparison the experimental value of ϵ(H) from Table II is shown in the same figure by the solid line. The average of several values of ϵ(C) obtained by subtracting the experimental ϵ(H) from the hydrocarbons is also plotted in Fig. 7 as a solid line; the values of ϵ(C) listed in Table II were taken from this curve.

It appears that Bragg's rule is not applicable to any of the compounds studied below 150 kev. This result is not surprising since it is principally the outer and valence electrons that are effective in stopping at such low energy. Indeed, Platzman[10] has shown that deviations from Bragg's rule of as much as 5 percent are to be expected in compounds of C, N, O, and F because the valence bonding in molecules containing these atoms vary most markedly.

[10] In *Symposium on Radiobiology*, National Research Council, edited by J. J. Nickson (John Wiley and Sons, New York, 1952).

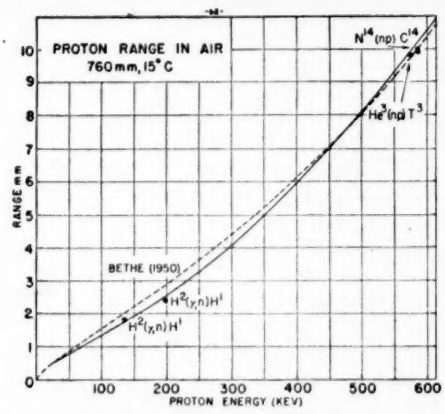

FIG. 8. Range energy curve for protons in air. The dashed curve is from reference 11. The experimental cloud chamber points are from J. K. Boggild [Kgl. Danske Videnskab. Selskab, Mat.-fys. Medd. **23**, No. 4 (1945)], D. J. Hughes and C. Eggler [Phys. Rev. **75**, 782 (1949)], and R. L. Clarke and G. A. Bartholomew [Phys. Rev. **76**, 146 (1949)]. The energy of the $H^2(\gamma,n)H^1$ points of Clarke and Bartholomew have been altered to conform to currently accepted values of the deuteron binding energy and the energies of the Ga^{72} and ThC″ gamma rays.

In Fig. 8 is plotted a range energy curve for protons in air obtained by integration of the experimental stopping cross section data. At 30 kev, the lower limit of the integration, the proton range has been taken from Bethe's 1950 range energy curve.[11] Negligible error is introduced in the numerical integration, and the percentage accuracy of the range differences obtained in this way is at least equal to the percentage accuracy of the stopping cross-section measurements, 3 percent for air. In the energy region 150–300 kev the present result gives a range 10–12 percent shorter than the Bethe curve. However, the cloud chamber range measurements at 0.58 Mev are only 1.5 percent below the range determined in this experiment. The good agreement is a demonstration of the consistency of these differential energy loss measurements with the integral range measurements and implies that ranges in other gases can be obtained by integrating these results.

We are indebted to Professor Christy for many interesting discussions of the energy loss problem.

[11] H. A. Bethe, Revs. Modern Phys. **22**, 213 (1950).

Characteristics of Neutral Meson Production in the Proton Bombardment of Carbon Nuclei

WALTER E. CRANDALL AND BURTON J. MOYER
Department of Physics and Radiation Laboratory, University of California, Berkeley, California

(Received May 25, 1953)

The photon spectra radiated from carbon targets bombarded by 340-Mev protons have been measured for various angles of view of the target. Assuming a unique origin of the photons from the decay of a neutral meson into two photons, the energy and rough angular distributions of neutral mesons are deduced from these spectra. The excitation function for producing neutral mesons is also inferred from the measured spectra for various energies of incident protons. The cross section for the production of neutral mesons per carbon nucleus for 340-Mev protons is $(3.4\pm0.8)\times10^{-27}$ cm^2.

I. INTRODUCTION

DURING the period since the first article[1] identifying the photon radiation ascribed to π^0-meson decay in the cyclotron target, the development of improved pair spectrometer equipment and techniques has allowed a better and more complete measurement of the photon spectrum than was there presented.

Out of these more detailed spectrum data information may be derived concerning the energy distribution of the emission of π^0 mesons from a target bombarded by high-energy protons and of the angular distribution with which they emerge from proton-nucleon collisions. Also an evaluation of the absolute yield has been made for the case of 340-Mev protons incident upon carbon nuclei and the variation of yield with proton energy determined. These allow comparison with the recent work of Marshall *et al.*[2] at the Chicago cyclotron.

The basic physical measurements consisted of determinations of the photon spectra radiated from the cyclotron target in various directions with respect to the incident proton beam. These were all monitored in relative intensity, and finally the spectrum in the 90° direction was placed upon an absolute scale by calculation of the pair spectrometer spectral efficiency and measurement of the proton beam current.

Deductions concerning angular and energy distributions are possible in view of the assumed unique origin of the photons: $\pi^0\rightarrow2\gamma$. The degree to which other processes may contribute to the high-energy photon yield is not definitely known, but certain symmetry tests upon the experimental spectra indicate that such contributions may be very small relative to the π^0-photon yield.[3,4]

[1] Bjorklund, Crandall, Moyer, and York, Phys. Rev. **77**, 213-18 (1950).
[2] Marshall, Marshall, Nedzel, and Warshaw, Phys. Rev. **88**, 632-41 (1952).
[3] Crandall, Crowe, Moyer, Panofsky, Phillips, and Walker, Phys. Rev. **85**, 771 (1952).
[4] Crandall, Panofsky, and Walker (private communication).

II. SPECTRAL PROPERTIES OF THE π^0-DECAY RADIATION

A. The Total Spectrum: Its Symmetry

Calculation of an expected gamma-ray spectrum for a given angular direction with respect to the incident proton beam would require prior knowledge of the angular and energy distributions with which the π^0 mesons are created. The properties of the *total* spectrum, however, are independent of angular distribution and may be put to experimental test. By "total spectrum" we mean the composite spectral emission obtained by integrating over all solid angular space surrounding the target.

It is this total spectrum with which the work of the Bristol group[5] deals in their photographic emulsion study of photons accompanying cosmic-ray star events. W. K. H. Panofsky recognized the possibility of constructing a total spectrum from measurements which could be made at the Berkeley cyclotron and of deducing from it the energy distribution of the π^0's together with a possible indication of non-π^0 high-energy photon emission. The pertinent features of the total spectrum are developed in reference 5 and will now be briefly presented here in a somewhat different manner more closely related to the experiment.

Consider a π^0 meson moving relative to the laboratory with velocity $c\beta$ indicated in Fig. 1. It decays into two photons which, in the π^0 rest frame, have equal energy k_0 and opposite directions. Due to aberration, the photon emitted at angle α in the π^0 rest frame is received in the laboratory at angle ϕ with respect to the π^0 motion and with energy k, where [with $\gamma=(1-\beta^2)^{-\frac{1}{2}}$]

$$k=k_0\gamma(1+\beta\cos\alpha) \tag{1}$$

and

$$\cos\phi=\frac{\cos\alpha+\beta}{1+\beta\cos\alpha}. \tag{2}$$

Thus, for a given β, energy increments in the observed laboratory spectrum depend simply upon increments in

[5] Carlson, Hooper, and King, Phil. Mag. **41**, 701-24 (1950).

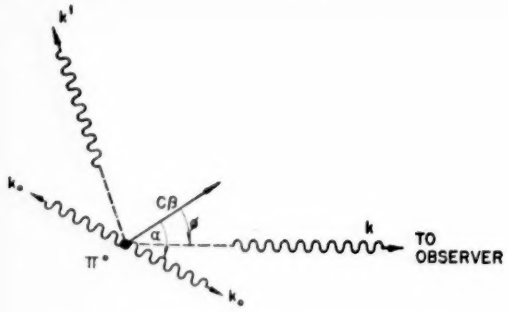

FIG. 1. Illustration of π^0-decay photon kinematics.

the emission angle α according to

$$dk = -k_0\gamma\beta \sin\alpha d\alpha. \tag{3}$$

Now in the total spectrum all values of α contribute with equal probability. So out of a large number of π^0-decay events, the number dn_β of photons, arising from mesons of velocity $c\beta$, within $d\alpha$ at angle α is (with two photons per π^0)

$$dn_\beta = N(\beta) \sin\alpha d\alpha, \tag{4}$$

where $N(\beta)$ is the number of π^0's per unit range in β at velocity $c\beta$.

Thus in the total spectrum arising from decay of π^0 mesons of this velocity the spectral intensity is, in view of Eqs. (3) and (4),

$$\left|\frac{dn}{dk}\right|_\beta = \frac{N(\beta)}{k_0\beta\gamma} = \text{const} \tag{5a}$$

between the limits [given by use of (1)] of

$$k_1(\beta) = k_0\left(\frac{1-\beta}{1+\beta}\right)^{\frac{1}{2}}, \quad \text{and} \quad k_2(\beta) = k_0\left(\frac{1+\beta}{1-\beta}\right)^{\frac{1}{2}}. \tag{5b}$$

It is clear then that the total spectrum contributed by π^0's with various values of β is compounded out of differential rectangular increments as qualitatively suggested in Fig. 2 and that the spectral intensity $I(k)$

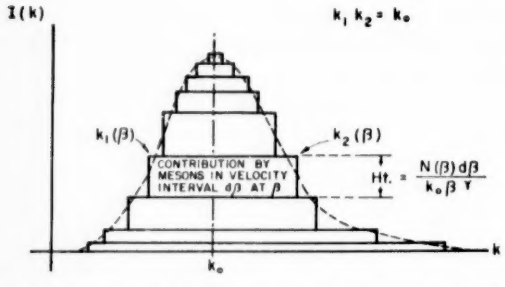

FIG. 2. Qualitative illustration of nature of total spectrum. (The equation at the top of the figure should read $k_1 k_2 = k_0^2$).

is given by integrating (5a) to obtain

$$I(k) = \int_{\beta'(k)}^{\beta_{\max}} \frac{N(\beta)}{k_0\beta\gamma} d\beta, \tag{6a}$$

where $\beta'(k)$ is the smallest relative velocity which can yield a laboratory photon energy of k, namely, by (5b)

$$\beta'(k) = \frac{k^2-k_0^2}{k^2+k_0^2}, \quad \text{for} \quad k>k_0;$$
$$\beta'(k) = \frac{k_0^2-k^2}{k_0^2+k^2}, \quad \text{for} \quad k<k_0. \tag{6b}$$

In view of Eqs. (5b) and from the construction of Fig. 2, the symmetry property of the total spectrum is evidently of the type $k_1k_2 = k_0^2$. If the abscissa scale is made logarithmic the spectrum curve should show simple symmetry with respect to a vertical line at $\log k_0$. This is to be applied as a test to the experimental data to indicate possible presence of non-π^0-photon radiation.

B. Deduction of Meson Energy Distribution

The velocity distribution function $N(\beta)$ may be evaluated at the lower limit β' by differentiation of Eq. (6a) and use of numerical data from the experimental total spectrum. Thus

$$N(\beta') = \beta'\gamma'^3 k_0 k(dI/dk),$$

where the associated values of β' and k are obtained from (6b).

This is readily transformed into a total-energy distribution function, since $E' = 2\gamma' k_0$. The result is

$$N(E') = \tfrac{1}{2}k|dI/dk|, \tag{7}$$

where

$$E' = (k^2+k_0^2)/k.$$

The best experimental spectrum data exist in the region $k \geq k_0$, so only the high-energy side of the spectrum peak will actually be used in obtaining values of $|dI/dk|$. E' is total energy, i.e., $M_\pi c^2$+K.E., or $2k_0$+K.E.

All the foregoing characteristics derived for the total spectrum would apply also to a π^0-photon spectrum observed within any reference frame in which the π^0 angular distribution were spherically symmetric, if such a reference frame existed.

C. Information on Angular Distribution of π^0-Meson Emission

In Fig. 3 is depicted the basis upon which some angular distribution information may be deduced. Let the spectrum observed in a direction θ be $I(\theta, k)$. All photons received of energy above an assigned lower limit k_1 will arise solely from π^0 mesons of energy greater

than $E_1=(k_1^2+k_0^2)/k_1$ emitted within a cone of solid angle opening about the direction of the observer; and the angular width $\psi_{\max}$ of the cone is determined by the maximum total energy, $E_{\max}$, with which the mesons may be created according to the relation

$$\cos\psi_{\max}=\frac{E_{\max}-2k_0^2/k_1}{(E_{\max}^2-4k_0^2)^{\frac{1}{2}}}. \tag{8}$$

By choosing k_1 sufficiently large, the size of the cone may be made arbitrarily small, and it becomes reasonable to treat the contribution of mesons emitted within the cone as if it were a small sample of a spherically symmetric emission. Use of relationship (7) then permits deduction of the energy distribution $N(E,\theta)$ for the high-energy tail of the mesons emitted in the direction θ. If the proper value of $E_{\max}$ to be associated with θ were everywhere known, it would now be possible to develop the angular distribution of mesons of various energies in the region of the high-energy tail.

The basic reference frame in which the π^0 production occurs is the center-of-mass system for an incident beam proton and the target nucleon which forms its collision partner. The angular distribution of π^0 emission in this system is desired, and the value of $E_{\max}$ within this system is presumably independent of angle. However, due to the motion of nucleons within nuclei there is no unique c.m. system, but rather a distribution of c.m. velocities about a mean value; but if the incident proton momentum is large compared to nucleon momenta in the target this spread of c.m. velocities is relatively small.

Determination of a mean c.m. velocity is possible by analyzing the Doppler shift of the photon spectra seen in observations at 0° and 180° with respect to the proton beam under the assumption of similar spectral emission at these angles in the c.m. system. The various spectra observed at different laboratory angles of view may then be transformed into related spectra in the mean c.m. system by the relations,

$$\begin{aligned} I_c(k_c,\theta_c)&=\gamma(1-\beta\cos\theta)I(k,\theta),\\ k_c&=k\gamma(1-\beta\cos\theta),\\ \cos\theta_c&=(\cos\theta-\beta)/(1-\beta\cos\theta), \end{aligned} \tag{9}$$

where the "c" subscripts denote quantities in this c.m. system, and the quantities β and γ refer to the motion of the center-of-mass with respect to the laboratory.

The analysis described in the foregoing paragraphs of this section then allows features of the angular distributions of the high-energy mesons in this mean c.m. system to be inferred.

III. THE EXPERIMENTAL SPECTRA

A. Cyclotron Facilities

Cyclotron tank windows, target-support probes, and holes through the concrete shielding limited the angles of view for the pair spectrometer to 0°, 47°, 90°, 133°, and 180°. These are angles of photon emission measured from the direction of the proton beam as it strikes the target placed at a radius of 80½ in. in the cyclotron tank.

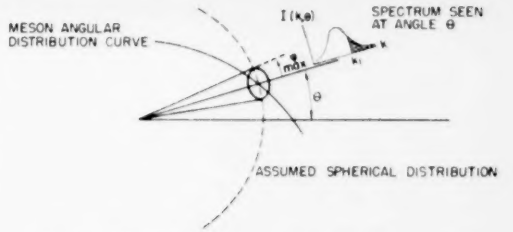

FIG. 3. Diagram to illustrate method for inferring angular distribution.

The pair spectrometer was in all cases outside the cyclotron shielding, at a typical distance of 60 ft from the target.

For the absolute yield determination described in Sec. VI, the external deflected proton beam was employed; but its intensity is too low for good spectrum data.

B. Pair Spectrometer

The pair magnet was originally designed by H. F. York and Paul Hernandez for this type of spectroscopy. The system of Geiger and proportional counters employed is that developed by Panofsky, Aamodt, and Hadley[6] for their work on the capture of π^- mesons in hydrogen and deuterium. In Fig. 4 are portrayed the magnet, converter, and counter system.

An electron pair triggers each of the two-chambered proportional counters. This quadrupole coincidence initiates a 1½-microsecond gate which is fed to the Geiger tube amplifiers, allowing them to register any events occurring during the gate duration. If the background counting rate is within limits, only the two Geiger tubes traversed by the pair particles will show signals within the gate period, and these define the two electron orbit radii and hence the photon energy.

Recording of the Geiger coincidence pairs in proper energy channels was accomplished by use of a 14-element square matrix array consisting of 196 coincidence units. The coincidence outputs were grouped into 27 energy channels which were registered. The development of this matrix system was promoted by Walker,[3,4] and is in principle an elaboration of the original system of this type used by MacDaniel *et al.*[7]

The various corrections which must be applied to the raw spectrometer data involve energy channel efficiencies, variation in pair production cross section, scattering loss calculations, electron energy loss in the converter, et cetera. These are discussed in the Appendix.

[6] Panofsky, Aamodt, and Hadley, Phys. Rev. **81**, 565 (1951).
[7] MacDaniel, von Dardel, and Walker, Phys. Rev. **72**, 985 (1947).

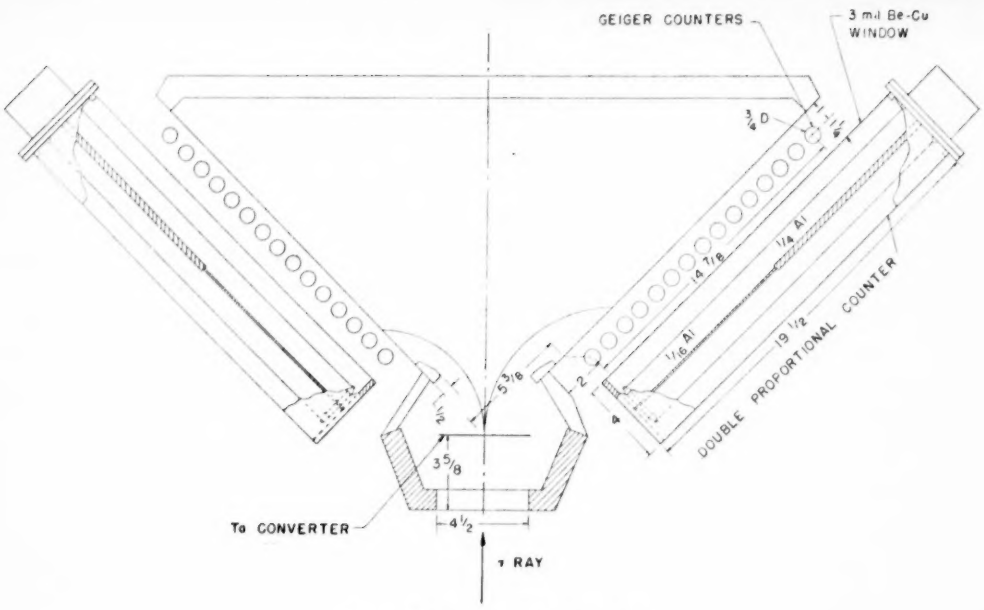

FIG. 4. Plan view of pair spectrometer.

The total energy span of the spectrometer does not include the complete spectrum for a given magnetic field setting, so that typically three separate settings were involved in a single spectrum determination. The agreement of extensive overlap regions gave confidence as to the validity of the data and its treatment.

C. Experimental Spectrum Results at 340 Mev

Displayed in Fig. 5 are the spectra obtained at various angles of view in the laboratory. The ordinate is plotted on an absolute scale as the cross section presented by a carbon nucleus for the production of a photon of energy k into unit solid angle in direction θ. The means of establishing an absolute scale will be discussed in Sec. VI.

Monitoring of the separate runs to provide proper relative intensity values was accomplished by use of thin aluminum foils mounted on the target. Generation of Na^{24} activity by the reaction: $Al^{27}(p;3p,n)Na^{24}$ gave relative integrated proton flux values. Excitation of C^{11} in polystyrene foils on the target has also been employed for monitoring in some cases; the bombardment time then being less than the C^{11} half-life.

IV. THE TOTAL SPECTRUM AND DEDUCTIONS FROM IT

A. Method of Construction

In order to compose the spectra observed into a total emission spectrum it is necessary to associate with each experimental spectrum a solid angle weighting factor. Thus it was assumed that the spectrum observed at 0° was representative of the photon emission in the forward cone out to 30°; the spectrum at 47° was taken as representative of the emission in the conical interval from 30° to 60°; the 90° spectrum served for the interval 60°–120°; the 133° spectrum for 120°–150°; and the 180° spectrum for the backward cone, 150°–180°. Each of the spectra of Fig. 5 were multiplied by the solid angle contained within the associated interval and these products added to obtain the total spectrum of Fig. 6. A logarithmic abscissa scale is used to facilitate the test for symmetry. Within reasonable limits, variation in the choice of angular intervals does not affect the form of the total spectrum enough to modify the conclusions drawn from it in the ensuing discussion.

B. Comments on Symmetry

In Sec. II-A, it was shown that a symmetry of the type $k_1k_2=k_0^2$ will obtain if all photons arise from π^0 decay, where k_1 and k_2 are minimum and maximum energies for a given intensity, respectively, and k_0 is the proper energy of a π^0-decay photon.

The present experimental data for photon energies below the peak are so poor as to make the symmetry test of questionable significance. The two dotted curves on the low-energy side of Fig. 6 correspond to reflections of the spectrum at vertical lines with the energies indicated. Clearly no definite conclusion may be drawn until better low-energy data from a modified spectrometer under preparation are available.

If, however, one demands a value of k_0 given by the experiments of Panofsky *et al.*,[6] namely 67.5 Mev, the symmetry criterion does not appear to be well satisfied.

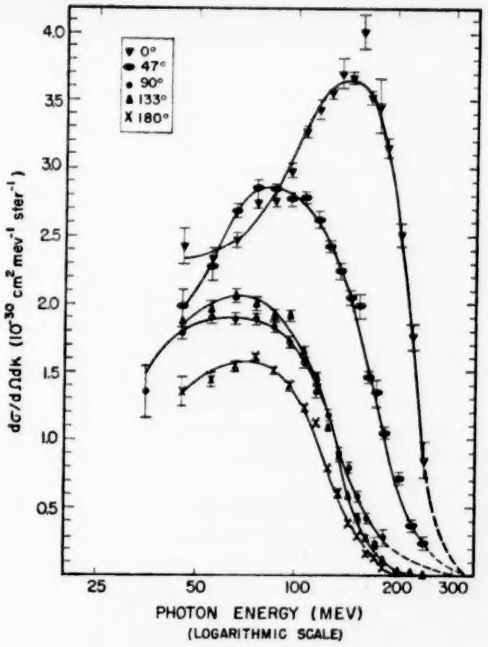

FIG. 5. Photon spectra at various angles of view from carbon target bombarded by 340-Mev protons.

It would be necessary to conclude that some radiation in addition to π^0 photons contributes particularly in the region above k_0. The total amount of photon emission to be subtracted away from the spectrum in order to produce symmetry need be only about 5 percent of the total emission,[4] though this might possibly represent of course only a minimum value.

Possible origins of non-π^0-photon emission are provided by such processes as:

(1) Radiative capture by neutrons of protons in flight (inverse photodisintegration of deuteron).

(2) Radiative capture of mesons in flight within the same nucleus in which they are produced.

(3) Bremsstrahlung from proton-nucleon collisions. These can give rise to photons in the required energy region, but the yield of photons from them is theoretically estimated to be not more than a few percent of the π^0 yield, and the spectrum from process (3) would be heavily weighted toward low photon energies and would not be expected to contribute selectively in the energy region involved here to account for nonsymmetry.

In view of the poor spectrum data below the k_0 energy, it is not possible to claim that the observation of non-π^0 photons has been certainly demonstrated; and since the yield from other processes is expected to be relatively very small, the total spectrum will tentatively be considered to arise solely from π^0 decay in the further topics of the present paper. Further justification for this is presented in Sec. VI-C.

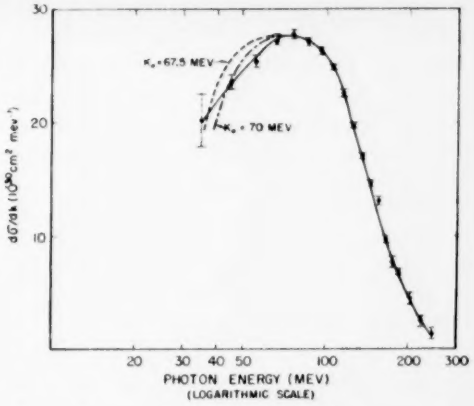

FIG. 6. Spectrum of total photon emission from carbon target bombarded by 340-Mev protons.

C. Energy Distribution of π^0 Mesons

By carrying out the operations indicated in Sec. II-B, using Eqs. (7), the distribution in total π^0 energy in the laboratory reference frame is deduced. Only the high-energy side of the total spectrum is used in obtaining the values of dI/dk. The result, when converted into a distribution in kinetic energy of emission is displayed in Fig. 7.

Cladis, Hess, and Moyer,[8] and Wolf[9] have experimentally obtained a momentum distribution for nucleons in a carbon nucleus. By use of their results, it is possible to calculate the distribution in energy available in the collisions of 340-Mev protons with nucleons

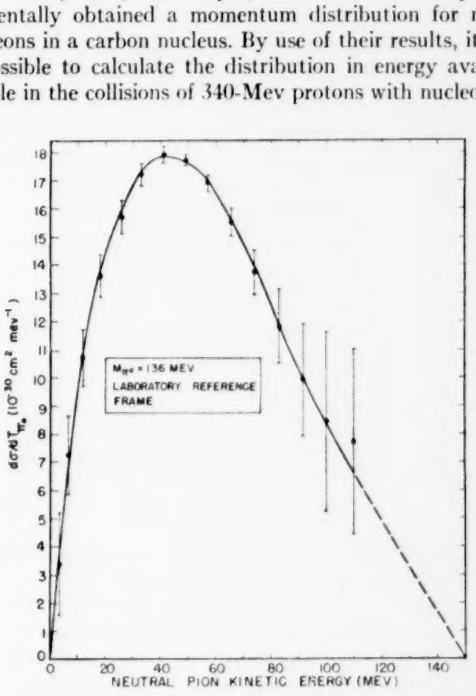

FIG. 7. Kinetic energy spectrum of neutral pion yield.

[8] Cladis, Hess, and Moyer, Phys. Rev. **87**, 425–33 (1952).
[9] P. Wolf, Phys. Rev. **87**, 434–8 (1952).

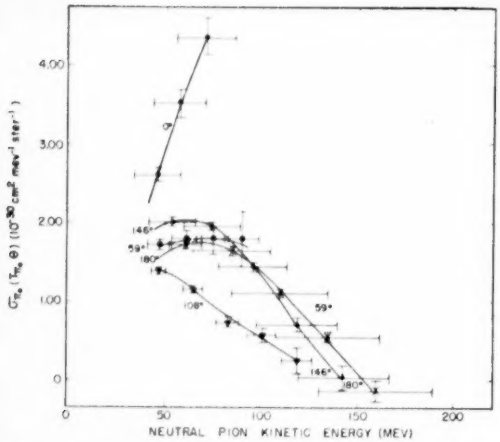

FIG. 8. Kinetic energy spectra for neutral pion emission at various angles in mean c.m. frame.

of the carbon nucleus. When this distribution in available energy is multiplied by an energy dependence for π^0 production in proton-nucleon collisions, the resulting energy distribution of the mesons when transformed into the laboratory frame is compatible with that observed in Fig. 7, when certain plausible assumptions are made about the excitation energy of the residual nuclear system.

The calculations of Henley and Huddlestone[10] on the production of π^- mesons in the proton bombardment of carbon employed a nucleon momentum distribution similar to that of reference 8. They obtained satisfactory agreement with available experimental data on π^--energy distributions, which were very much like Fig. 7.

V. ON THE ANGULAR DISTRIBUTION OF π^0 EMISSION

A. Mean Center-of-Mass Velocity

In Sec. II-C the means of inferring a mean velocity of the c.m. system for the nucleon collisions producing π^0 mesons was defined. Actually the simplest practical means of evaluating β, assuming forward-backward symmetry in the c.m. frame, is provided by observing that from relations (9) may be deduced the following relations between the 0° and 180° spectra, involving the relative velocity β of the center-of-mass.

$$I(k, 0^\circ)=\frac{1+\beta}{1-\beta}I(k', 180^\circ),$$
$$k=\frac{1+\beta}{1-\beta}k'. \tag{10}$$

Thus, intensity and energy both transform by the same multiplicative factor, so that on a log-log plot the 0° and 180° spectra should coincide upon sliding one spectrum in a forty-five degree direction until it best overlaps the other. The amount of translation along either axis will evaluate $(1+\beta)/(1-\beta)$, and hence β. The shapes of the 0° and 180° spectra are experimentally better determined than the relative ordinates; so in evaluating β we have paid more attention to obtaining proper transformation of spectrum shape and energy values than to agreement of intensities. The latter do not quite coincide using $\beta=0.3$, but seem to indicate somewhat greater emission at 0° than at 180° in the $\beta=0.3$ frame.

Clearly this β is less than that for the c.m. frame of a 340-Mev proton and a stationary nucleon. The strong energy dependence of the π^0 production accentuates the contribution from collisions with nucleons moving counter to the proton. In fact, the 0.3 value implies that the representative collision involves a nucleon in a carbon nucleus moving toward the proton with a velocity of $0.218c$ or a kinetic energy of 23 Mev.

B. Deduction of Angular Distributions in the Center-of-Mass System

By use of relations (9), the spectra in the five laboratory directions, 0°, 47°, 90°, 133°, and 180°, are now transformed into the related spectra in the mean c.m. system at the respective related angles, 0°, 59°, 108°, 146°, and 180°. As described in Sec. II-C, the high-energy tails of these c.m. spectra are now to be differentiated for use in Eqs. (7) to yield energy distributions for the neutral mesons emitted in the angular direction involved, within a cone whose generating angle is given by Eq. (8) for chosen values of $E_{\max}$ and k_1.

The collision of a 340-Mev proton with a nucleon in a carbon nucleus so moving as to provide a c.m. frame whose projected motion along the proton beam direction has a relative velocity $\beta=0.3$ provides, by calculation, a maximum available energy[11] of $E_{\max}=215$ Mev, or a maximum π^0 kinetic energy of about 80 Mev. Due to the distribution of nucleon momenta, however, meson kinetic energies in this reference frame will extend from essentially zero up to about 120 Mev in the forward direction, and up to values even higher in the backward direction. Yet the "representative collision" which gives rise to the mean value of $\beta=0.3$ will predominate sufficiently for reasonable momentum distributions and meson excitation functions to allow the following rough analysis of angular distributions in the c.m. frame.

If the photon spectra for various angles of view in the c.m. frame are limited to energies above $k_1=150$ Mev, the photons will arise from neutral meson emission within cones with generating angles $\psi_{\max}$ [by use of Eq. (8)] of about 25° opening about the respective angles of view, as shown in Fig. 3. The chosen lower

[10] E. M. Henley, Phys. Rev. **85**, 204–15 (1952).

[11] It is necessary to take account of the energy carried away by the residual nuclear system in making these calculations. If this is not done, unreasonably high values of available energy are calculated from the high-momentum components in the nucleon motion.

limit, $k_1=150$ Mev, requires that a π^0 meson possess at least 47-Mev kinetic energy to contribute to the spectrum region observed.

Now by application of Eq. (7), the kinetic energy distributions in the various directions are deduced, under the approximation that within the limited emission cone the angular distribution is treated as a portion of a spherically symmetric yield. These are displayed in Fig. 8. In Fig. 9 are sketched the angular distributions for mesons of certain energies, inferred from the data of Fig. 8. In view of the calculation mentioned in the second paragraph above, the mesons with kinetic energies near 80 Mev should most nearly display the angular distribution in the c.m. frame for a proton-nucleon collision.

While these results are admittedly very crude, they do infer a prominent $\cos^2\theta$ contribution. In view of the known small yield of π^0 mesons from p-p collisions,[12] it is possible that these results indicate the presence of the process $p+n\rightarrow\pi^0+d$ within the bombarded carbon nucleus, which is expected to yield the mesons with a prominent $\cos^2\theta$ distribution. Recent experiments by Hildebrand[13] at Chicago, on the production of π^0 mesons in free n-p collisions, show an angular distribution for the process $n(p,d)\pi^0$ described by $a+b\cos^2\theta$, where $b/a\simeq 5$.

VI. THE ABSOLUTE YIELD: DEPENDENCE UPON ENERGY

A. The Absolute Yield Experiment

Since absolute evaluation of the proton current at an internal cyclotron target at these energies is uncertain,

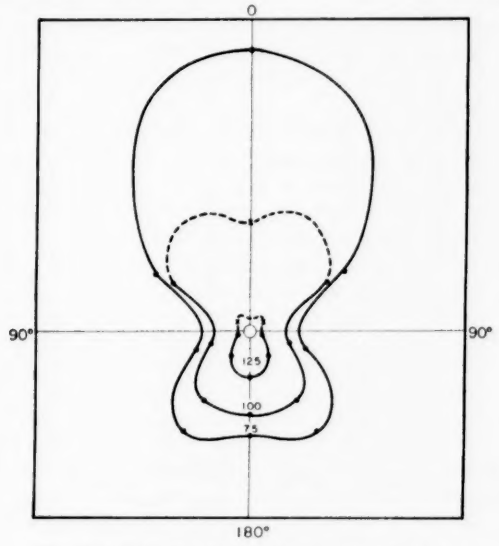

FIG. 9. Angular distributions in mean c.m. frame for neutral pions of various energies.

[12] R. W. Hales and B. J. Moyer, Phys. Rev. **89**, 1047–53 (1953).
[13] R. H. Hildebrand, Phys. Rev. **89**, 1090–92 (1953).

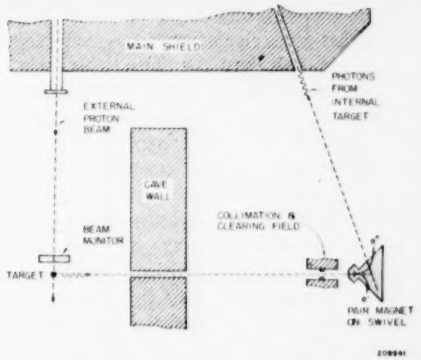

FIG. 10. Arrangement of absolute yield experiment.

the foregoing data were placed upon an absolute scale by observing the photon yield at one angle and one spectrum region from a target in the external proton beam. The fact that the external beam is 10^{-4} to 10^{-5} of the internal beam precluded the taking of more data in this manner.

In Fig. 10 the method of this absolute determination is shown. The pair spectrometer is mounted at a point where, by rotation, it can receive either the photons from an internal target or those from a target in the monitored external proton beam. Proper plateau conditions for the spectrometer counters are obtained with good counting rates by receiving photons from the internal target. The internal target is then removed and the spectrometer rotated so as to receive photons from the external target. Just preceding the pair spectrometer is a photon aperture definer and clearing field. The aperture permits only the converter foil of the spectrometer to "see" the target, and the clearing field removes electron pairs produced in air and at the aperture surfaces. The deflected beam passes through a calibrated ionization chamber just before striking the target.

B. Converter Efficiency Correction. Absolute Yield Result

Absolute calibration of the pair spectrometer involves a number of corrections to be applied to the basic data. These are discussed briefly in the Appendix. One of the most important of these is the converter efficiency correction which involves the following features.

For conversion of photons at depth x in a converter of thickness t, the yield of detectable electron pairs will depend upon attenuation of the photons as they progress through the thickness x of the converter material to the lamina dx in which conversion occurs, and then upon the survival of both pair particles against scattering and radiative collisions in the interval $t-x$, which would remove them from the trajectories which are received by the counters.

Use of well-known physical data relating to such processes allows the calculation of an "effective" converter thickness, less than the actual thickness, which in the absence of such attenuation and particle loss would yield the observed number of pairs. (Conversely, instead of considering the effective converter thickness, one could correct the pair yield for a given thickness by similar calculations.)

In the data of Fig. 11 the spectrometer counting rate is plotted as a function of effective thickness of Ta converter foil. Data of two different runs are presented; the different intercepts at zero thickness infer differences in efficacy of aperture and clearing field adjustments in removing undesired pairs. The initial sharp rise is probably due to conversion in the foil support device, but the extended linear portions are considered to represent by their slopes the correct conversion yield per unit thickness of Ta. From this, and the known pair production cross section, the absolute efficiency of the spectrometer may be established.

Since now an absolute yield of photons in the 90° direction, within a known spectrum interval of the total emission in this direction, is known, it becomes possible to place upon an absolute basis the relatively measured spectra in all the directions. Then by employment of solid angle weighting factors, as in the construction of the total spectrum in Sec. IV-A, the absolute total yield of photons is obtained.

Together with the measured value of proton beam current incident upon the target this results in a cross section for production of high-energy photons per

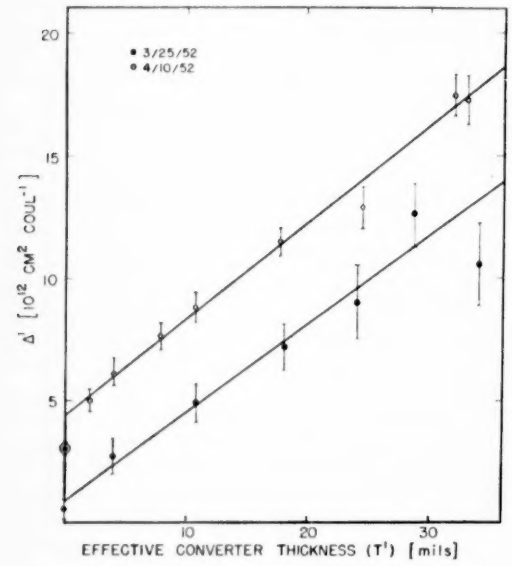

FIG. 11. Spectrometer counts *vs* effective converter thickness in the absolute yield experiment. (The unusual ordinate units are related to the beam monitoring system.)

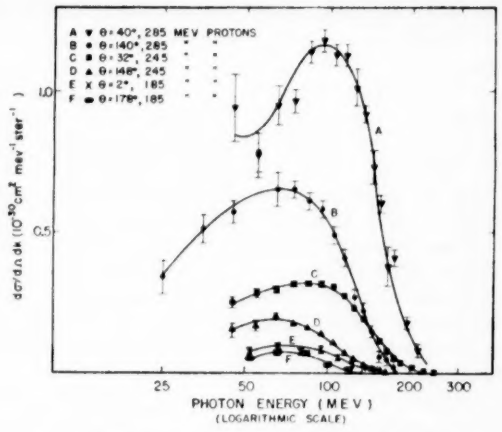

FIG. 12. Photon spectra at reduced proton energies for supplementary angles.

carbon nucleus of

$$\sigma_{\text{photon}} = (3.4 \pm 0.8) \times 10^{-27} \text{ cm}^2.$$

Under the assumption that these are all from π^0 decay, the π^0 production cross section is

$$\sigma_{\pi^0} = (1.7 \pm 0.4) \times 10^{-27} \text{ cm}^2$$

per carbon nucleus for 340-Mev protons.

These values are not directly comparable with those of Marshall *et al.*,[2] at Chicago because of lack of precise knowledge of the energy dependence of the cross section. However, if the Z dependence observed by Hales *et al.*[12] is combined with an extension of the energy dependence presented below in Sec. VI-C, the presented data predict a Be cross section at 430 Mev of $(5.8 \pm 1.5) \times 10^{-27}$ cm² which may be compared with $(8.7 \pm 2) \times 10^{-27}$ cm² observed by the Chicago group.

C. Variation of Yield with Proton Energy

Available shielding apertures permitted data to be obtained at reduced proton energies for certain supplementary pairs of angles of view. The spectra from these observations are displayed in Fig. 12.

These afford a further check on the smallness of radiation from sources other than π^0 decay. As the energy available for π^0 production approaches threshold, the incident protons must select nucleons moving with increasingly higher momenta opposite to their motion. Consequently the approach to a unique c.m. system is more evident in the smaller Doppler shift of the spectra involved in changing the angle of view. Likewise, the decreasing available kinetic energy for the π^0 results in somewhat narrower peaks, since the peak breadth is due to the Doppler shift of photons from the moving mesons. Finally, any photons originating in radiative meson capture would be expected to produce more pronounced asymmetry of these spectra than of those at higher energies. Such does not appear to be the case.

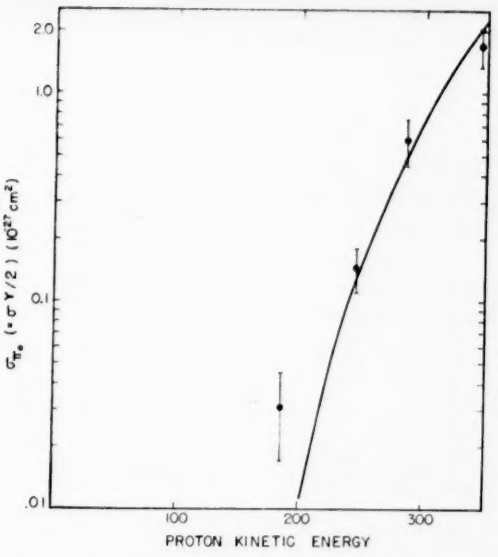

FIG. 13. Experimental points on neutral pion yield from carbon vs proton energy. The smooth curve is from theoretical calculation mentioned in text.

By estimated reconstruction of the total photon emission upon the basis of the spectra observed at supplementary angles, it is possible to present the variation in π^0 production cross section as a function of incident proton energy. The result is given in Fig. 13. It is displayed together with a curve calculated by Brueckner for a pseudoscalar pion with pseudovector coupling and a typical momentum distribution[8] which has appeared to best fit other data in meson production.[10]

The authors wish to recognize the considerable contribution of Professor W. K. H. Panofsky to this work, and also of Professor Herbert York in its early stages. Dr. Darcy Walker, of Birmingham, England, and Dr. Kenneth Crowe and Dr. Robert Phillips were largely involved in the development of the 14-square matrix coincidence circuit. The fine cooperation of the cyclotron crew under Mr. James Vale and Mr. Lloyd Hauser has been much appreciated.

APPENDIX

For a given photon energy the detection efficiency of the pair spectrometer is determined by the following items:

(1) Fraction of incident photons converted into pairs with a division of energy in the detectable interval.

(2) Fraction of pairs surviving against scattering and radiative collisions in the converter which would render them undetectable.

(3) Leakage of the particles between Geiger tubes.

The evaluation of Item (1) is accomplished by integration of the differential pair production expression $\phi(W, \mu)$, as given by Rossi and Greisen,[14] between the limits of the energy division parameter μ, for the pair energy W, which are allowed by the geometry. Figure 14 illustrates this process.

Due to a finite converter width, the average energy associated with a given pair of Geiger tubes in this 90° spectrometer is slightly greater than that defined by considering all pairs to originate at the converter center. This is a 4 percent correction at the lowest energies, and 0.5 percent at the highest.

In the case of Item (2) the losses are kept small by the use of thin converters of small height. At a given magnetic field setting the scattering caused negligible spectrum distortion due to the cancellation of the effects of particle energy and solid angle upon scattering loss. Also the energy degradation effects due to radiative collisions in the thin converters (<0.010-in. Ta) produce negligible distortion for spectra of this breadth. However, in the absolute yield experiment these effects must be accounted for, since larger converter thicknesses were used.

For a pair particle produced in dx at depth x in the converter, the probability of remaining within the vertical angle subtended by the detector is determined from the Gaussian projected scattering pattern calculated for the appropriate electron energy and converter depth. It is required that both pair particles thus survive, and the contributions from all depths are integrated to provide the survival factor for the converter. For a 0.020-in. Ta converter and 100-Mev photons the loss is 10 percent.

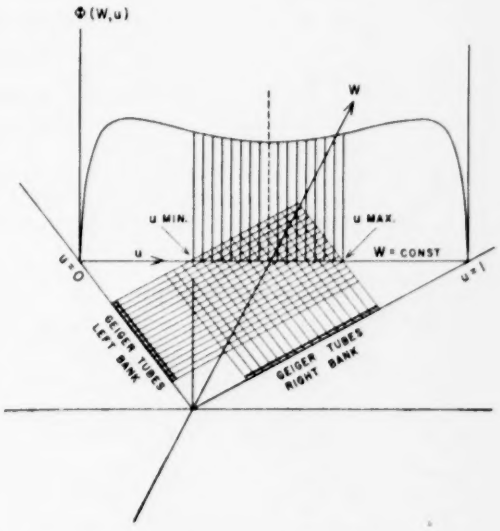

FIG. 14. Diagram illustrating calculation of energy channel efficiencies for pair spectrometer.

[14] B. Rossi and K. Greisen, Revs. Modern Phys. **13**, 240–309 (1941).

The considerations of radiative collision loss were the following. For a given photon energy the detectable pair contribution from dx at depth x in the converter is (for unit incident flux):

$$dn=e^{-N\sigma_1 x}(N\sigma_2 dx)[e^{-N\sigma_3(t-x)}][e^{-N\sigma_3'(t-x)}],$$

where σ_1 = total pair production cross section, σ_2 = cross section for producing pairs within the detectable energy division interval, σ_3 = cross section for radiative collision by positron with sufficient energy loss to remove it from detection, and σ_3' = same for electron. When the energy division is symmetric, $\sigma_3=\sigma_3'$.

By integrating over converter thickness (t), the total yield of detectable pairs is found to be

$$n=\frac{\sigma_2}{2\sigma_3-\sigma_1}e^{-N\sigma_1 t}[1-e^{-N(2\sigma_3-\sigma_1)t}].$$

Apart from such losses as discussed above, the "effective" converter thickness to produce a yield n is simply

$$t'=n/N\sigma_2.$$

This is the means of calculating the "effective" converter thickness used as abscissa in Fig. 12.

PHYSICAL REVIEW VOLUME 92, NUMBER 3 NOVEMBER 1, 1953

Decay of Gallium 67†*

W. E. MEYERHOF, L. G. MANN, AND H. I. WEST, JR.
Stanford University, Stanford, California

(Received July 20, 1953)

The decay of Ga^{67} has been investigated with scintillation spectrometers, single and in coincidence. No positrons have been found, in agreement with the total decay energy of 1.003 Mev measured by Trail and Johnson. Electron capture occurs to levels in Zn^{67} at 0.092, 0.182, 0.39, and 0.87 Mev. The 0.092-Mev level of Zn^{67} has a half-life of 9.5 ± 1.0 μsec and the total conversion coefficient of the 0.092-Mev gamma ray is 0.54 ± 0.05. Rough measurement of the angular correlation coefficient between the 0.21-Mev and 0.18-Mev gamma rays (cascading from the 0.039-Mev level of Zn^{67}) gives -0.22 ± 0.04. Spin and parity assignments of the Zn^{67} levels are discussed. The present work is in essential agreement with that of Ketelle, Brosi, and Porter.

INTRODUCTION

We were led to a study of Ga^{67} through our work[1] on Ga^{66} for which Ga^{67} provided long-lived background radiations. Approximately concurrently and independently Ketelle, Brosi, and Porter[2] studied Ga^{67}, and we refer to their paper for earlier references. We wish to report our results briefly since they are in essential agreement with those of Ketelle *et al.*, but in some ways they are complementary. Our present conclusions differ somewhat from those of Ketelle *et al.* and from our earlier report.[3]

SOURCE PREPARATION

The Ga^{67} was produced by the $Zn(p,n)$ reaction in 60-inch cyclotron at the University of California at Berkeley.[4] The Ga was extracted by an ether separation and sources of varying thickness were mounted on copper backings. The effect of these backings was taken into account in intensity measurements. The study of the Ga^{67} was started approximately ten days after the source was produced and consequently the 9.4-hour Ga^{66} had decayed to an undetectable level.

APPARATUS

We have used NaI(Tl) crystals of various shapes from $\frac{1}{2}$ in. to $1\frac{1}{2}$ in. thickness, rough ground,[5] and mounted under a magnesium-oxide smoked aluminum cover on RCA 5819 phototubes. The resolution of these crystals was 9 to 10 percent full width at half maximum for the 0.662-Mev gamma ray of Cs^{137}.

The electronic equipment consisted of linear amplifiers, discriminators, and a fast coincidence circuit (0.15-μsec resolving time) with pulse height discrimination on both sides. This equipment was part of a three-crystal pair spectrometer, described elsewhere.[6]

For some of the work we have used anthracene crystals mounted in the same way as the NaI(Tl) crystals. These had resolutions of 15 to 17 percent for the conversion electrons of the Cs^{137} gamma ray.

† A preliminary account of this work was given at the Pasadena meeting in 1952 of the American Physical Society, Bull. Am. Phys. Soc. **27**, No. 6, 18 (1952).

* Supported in part by the joint program of the U. S. Office of Naval Research and the U. S. Atomic Energy Commission.

[1] Mann, Meyerhof, and West (to be published).

[2] Ketelle, Brosi, and Porter, Phys. Rev. **90**, 567 (1953). We are indebted to Dr. Brosi for communication of these results prior to publication.

[3] Meyerhof, Mann, and West, Bull. Am. Phys. Soc. **27**, No. 6, 18 (1952).

[4] We are very much indebted to the staff of the Crocker Radiation Laboratory for producing a number of these sources for us.

[5] W. H. Jordan, Ann. Revs. Nuc. Sci. **1**, 207 (1952).

[6] H. I. West, Jr., and L. G. Mann, Rev. Sci. Instr. (to be published).

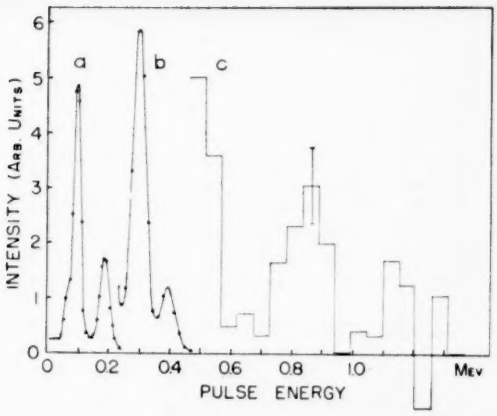

FIG. 1. Pulse-height distribution of Ga^{67} gamma rays in NaI(Tl) crystal. Curve *b* is enlarged 10 times and curve *c* 2000 times with respect to curve *a*. For measured energies see Table I.

SEARCH FOR POSITRONS

At the start of our investigation it was known from a $Zn^{67}(p,n)$ threshold measurement[7] that the decay energy of Ga^{67} was less than 1.2 Mev. We searched for positrons by replacing the center crystal in the three-crystal pair spectrometer[6] by an anthracene crystal and determining the pulse-height distribution in this crystal in coincidence with 0.5-Mev pulses in both the side crystals. The source was placed out of line of the two side crystals so that no possible positron-gamma coincidences could give rise to counts in the center crystal. No coincident pulses in the center crystal above background were found. As a result, an upper limit of 0.01 percent positron decay of Ga^{67} could be set, this number being determined from the statistics. The positron energy range covered was 0.02 to 0.7 Mev. This result is consistent with the decay energy of 1.003 ± 0.005 Mev inferred from a recent $Zn^{67}(p,n)$ threshold determination.[8]

GAMMA-RAY MEASUREMENTS

A. NaI(Tl) Spectrometer

Figure 1 shows the pulse-height distribution (background subtracted) obtained with a cylindrical NaI(Tl) crystal, $1\frac{1}{2}$ in. thick and $1\frac{1}{2}$ in. high, mounted as described above. Gamma rays at 0.092, 0.182, 0.30, 0.39, 0.5, and 0.9 Mev are indicated, with the possibility of more than one gamma ray contributing to the peak at 0.9 Mev. A small escape peak is associated with the 0.092-Mev gamma ray. Pulses above 1.0 Mev made us believe originally[3] that a higher-energy gamma ray might be present, but they are probably due to poor statistics, as shown by the Compton spectrometer results (see below). The now known decay energy of course does not allow these gamma rays.

Pulse-height distributions similar to Fig. 1 taken with different crystals varying in size and shape have

TABLE I. Summary of gamma-ray data. (-1), (-2) and (-3) in this table mean $\times10^{-1}$, $\times10^{-2}$, and $\times10^{-3}$, respectively.

Gamma ray (Mev):	0.090	0.092	0.182	0.21	0.30	0.39	rest[a]	Reference
A. Relative gamma-ray intensities	7.0±0.5 6.8	93±0.5 93.2 100	44.1±3 75.6 34	3.0±0.8 1.9 3.2	27.5±1 50.4 19.4	9.7±1 12.1 4.8	~1 2.5	Meyerhof *et al.* Ketelle *et al.*[b] Mukerji *et al.*[c]
B. Relative K-electron intensities		100 100 100	1.4 1.1 1.3	9.8 (−2) 6.3 (−2)	2.5 (−1) 1.7 (−1) 2 (−1)	3.9 (−2) 2.9 (−2) 4 (−2)		Ketelle *et al.*[b] Mukerji *et al.*[c] Siegbahn[d]
C. Experimental α_K	(5.7±1.3)(−2)[e] 7.4 (−2)	(4.7±0.5)(−1) 6.3 (−1) 3.0 (−1)[f] (5.5±2.5)(−1)[f,g]	(1.4±0.3)(−2)[e] 1.1 (−2) 0.9 (−2) (1.1±0.2)(−2)[g]	(1.5±0.6)(−2)[e] 2.9 (−2) 0.5 (−2)	(4.0±0.7)(−3)[e] 2.9 (−3) 2.5 (−3) (3.4±0.6)(−3)[g]	(1.8±0.4)(−3)[e] 1.9 (−3) 1.7 (−3) (1.0±0.9)(−3)		Meyerhof *et al.* Ketelle *et al.*[b] Mukerji *et al.*[c] Easterday[h]
D. Theoretical $\alpha_K(M1)$ $\alpha_K(E2)$	7.8 (−2) 9.6 (−1)	7.2 (−2) 8.7 (−1)	1.2 (−2) 6.4 (−2)	0.9 (−2) 4.0 (−2)	3.5 (−3) 1.0 (−2)	1.9 (−3) 4.4 (−3)		Reitz[i] Rose *et al.*[j]
E. Assignment from α_K	$M1$	$M1$ and $E2$	$M1$	$M1$	$M1$	$M1$		
F. Experimental K/L ratio		7.0 6.5±0.5 7.4 8	12.6 9±1 ~8	~14	7.6			Ketelle *et al.*[b] Mukerji *et al.*[c] Stevenson *et al.*[k] Helmholz[k]
G. Assignment from K/L ratio		$M1$, $E2$	$M1$	$M1$	$M1$			
H. Total transition intensities in Ga^{67} decay (percent)[l]	3.5±0.25	72.2±2.8	22.6±1.5	1.5±0.4	13.9±0.5	4.9±0.5	~0.5	Meyerhof *et al.*

[a] Rest of gamma rays have measured energies 0.48, 0.69, ~0.8, ~0.9 Mev, and have absolute transition intensities in Ga^{67} decay of ~0.1, ~0.05, ~0.1, and ~0.3 percent, respectively. For intensities ~ means within a factor of 2.
[b] See reference 2.
[c] See reference 12.
[d] K. Siegbahn, Arkiv Fysik **4**, 223 (1952).
[e] Calculated using K-electron intensities of Ketelle *et al.* (reference 13).
[f] Corrected for the presence of the 0.090 Mev gamma ray.
[g] Corrected for K/L ratio.
[h] See reference 17.
[i] See reference 19.
[j] P. C. Stevenson and H. G. Hicks (unpublished), quoted in reference 24.
[k] A. C. Helmholz, Phys. Rev. **60**, 415 (1941).
[l] Calculated assuming no electron capture to the ground state of Zn^{67}.

[7] Blaser, Boehm, Marmier, and Peaslee, Helv. Phys. Acta **24**, 3 (1951).
[8] C. C. Trail and C. H. Johnson, Phys. Rev. **91**, 474 (1953).

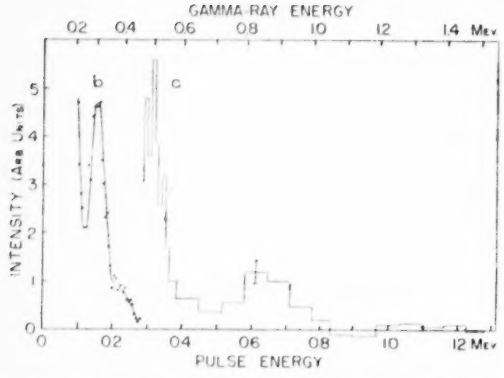

FIG. 2. Pulse-height distribution of Ga^{67} gamma rays in the Compton spectrometer. Curve *c* is enlarged 200 times with respect to curve *b*. These curves correspond to similar ones in Fig. 1.

been used to calculate the relative intensities of the gamma rays. This was done by taking into account (1) the amount of Compton effect associated with each photopeak (measured in separate experiments with different sources of gamma rays), (2) the absorption in the crystal, and (3) the absorption in material between source and crystal. In making this analysis we found that all pulses below the 0.092-Mev escape peak were accounted for by Compton electrons of higher-energy gamma rays. Averaging all our results we find for the relative intensity ratios of the above gamma rays $100:47\pm2:27.5\pm1:9.7\pm1:\sim0.2:\sim0.8$. These results are incorporated in Table IA. Coincidence experiments described below have shown the 0.092-, 0.182-, and 0.9-Mev gamma-ray peaks to be double.

B. Compton Spectrometer

Figure 2 shows a Compton electron pulse-height distribution obtained with a two-crystal Compton spectrometer.[9] The scattering crystal was a 1-in. diameter anthracene cylinder, $\frac{1}{2}$-in. high, and the crystal receiving the scattered Compton gamma ray (at an angle of 135°) was a $1\frac{1}{2}$-in. diameter NaI(Tl) cylinder, $1\frac{1}{2}$ in. high. The pulse-height distribution in the anthracene crystal in coincidence with pulses below 0.3 Mev in the NaI(Tl) crystal was measured. Figure 2 indicates the presence of 0.30-, 0.4-, 0.5-, and 0.9-Mev gamma rays, but no higher-energy gamma rays seem to be present. By using the differential Compton scattering cross section at 135° [10] and taking into account absorption and electron escape effects in the anthracene crystal, one can use Fig. 2 to calculate the relative intensities of the various gamma rays. These agree with the NaI(Tl) spectrometer results within the accuracy stated in Table IA.

[9] R. Hofstadter and J. A. McIntyre, Phys. Rev. **78**, 619 (1950).
[10] C. M. Davisson and R. D. Evans, Revs. Modern Phys. **24**, 79 (1952).

COINCIDENCE EXPERIMENTS

Since the decay scheme of Ga^{67} is now well established,[2] it does not seem worthwhile to present the reasoning by means of which we arrived at the same scheme. Therefore we present our coincidence experiments in Figs. 3 and 4, and will show briefly that they are consistent with the decay scheme (see Fig. 8). As discriminating and analyzing detectors, we used in most of the experiments two $1\frac{1}{2}$-inch diameter NaI(Tl) cylinders, $1\frac{1}{2}$-in. high, which were shielded from each other by $\frac{1}{4}$-in. thick lead in all experiments except those

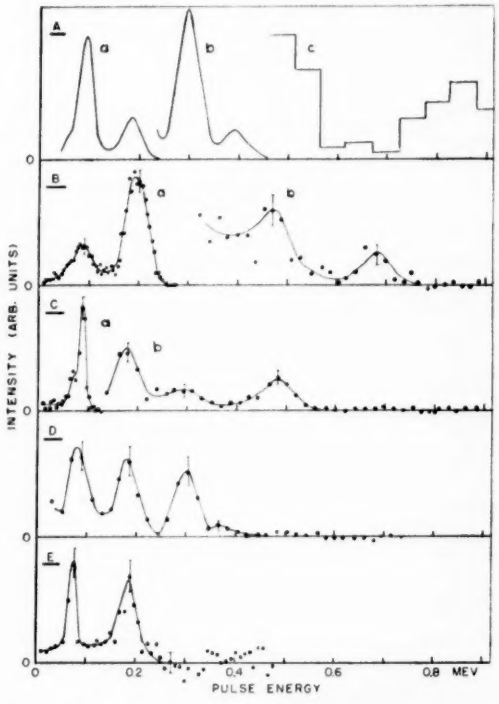

FIG. 3. Pulse-height distributions of coincident Ga^{67} gamma rays. Curve *A* gives the single distribution (Fig. 1) for comparison. Curves *B*, *C*, *D*, and *E* show the pulse-height distributions coincident with pulses around 0.18, 0.30, 0.50 and above 0.66 Mev, respectively. (For exact energy channels see text.) In *A*, curves *b* and *c* are enlarged 10 and 2000 times respectively with respect to *a*. In *B*, curve *b* is enlarged 450 times with respect to *a*. In *C*, curve *b* is enlarged 7 times with respect to *a*.

shown in Figs. 3D and 3E. The source was placed out of line with the detectors, so that no radiation could scatter from one detector into the other. Nevertheless, spurious coincidence peaks are found in the analyzing crystal (1) because of accidental coincidences (these were mostly negligible), and (2) because, when the discriminating crystal channel is set on the photopeak of one gamma ray, it also receives some Compton electron pulses from higher-energy gamma rays.

Figure 3A gives the single pulse-height distribution (see Fig. 1) for comparison. Figure 3B shows pulses in

the analyzing crystal in coincidence with pulses between 0.16 and 0.23 Mev in the discriminating crystal. The peak at 0.09 Mev is the result of coincidences with the 0.21-Mev gamma ray and with some Compton electrons from the 0.30-Mev gamma ray. The peak at 0.20 Mev is the result of 0.21-Mev–0.18-Mev gamma-ray coincidences. The peak at 0.48 Mev is the result of coincidences with the 0.18- and 0.21-Mev gamma rays and some Compton electron pulses from the 0.30- and 0.39-Mev gamma rays. The peak at 0.69 Mev shows that the 0.87-Mev level of Zn^{67} also decays to the 0.18-Mev level.[2]

Figure 3C shows the pulse-height distribution in the analyzing crystal coincident with 0.28- to 0.35-Mev pulses in the discriminating crystals. The peak at 0.09 Mev is many times smaller than would be expected from prompt 0.30-Mev–0.092-Mev gamma-ray coincidences and shows that the 0.092-Mev gamma ray is delayed.[11] Compton electrons from the 0.48 and the 0.69-Mev gamma rays contribute slightly to this peak and cause the peaks at 0.30 and 0.39 Mev. The peak at 0.48 Mev shows that the 0.87-Mev level of Zn^{67} cascades to the 0.39-Mev level.

Figure 3D shows the pulse-height distribution coincident with 0.45 to 0.57-Mev pulses. Peaks at 0.30 and 0.39 Mev are due to the cascading from the 0.87-Mev level of Zn^{67} to the 0.39-Mev level. The peak at 0.18 Mev is mainly due to Compton electrons from the 0.69-Mev gamma ray, and the peak at 0.08 Mev is caused mostly by backscattered radiation from the 0.18-Mev gamma ray. (The source was placed between the counters in this experiment and in the next one.)

Figure 3E gives the pulse-height distribution coincident with pulses above 0.66 Mev and shows again that the 0.87 level of Zn^{67} decays to the 0.18 level. The peak at 0.08 Mev is the result of back-scattered radiation from the 0.18-Mev gamma ray.

We have already indicated some evidence for the existence of a metastable state in Zn^{67} at 0.092 Mev. In order to show which radiation precedes this state, we delayed the analyzing crystal pulses by 1 μsec before letting them enter the coincidence circuit. Figure 4B shows the corresponding pulse-height distribution and confirms that 0.09-, 0.21-, and 0.30-Mev gamma rays feed the metastable level. The presence of a gamma ray of about 0.75±0.05-Mev energy is also indicated. Figure 4C gives the pulse-height distribution obtained when the discriminating crystal pulses were delayed by 1 μsec and shows that only the gamma ray of 0.092-Mev energy leaves the metastable level. In both these experiments the discriminating crystal accepted pulses of all energies.

The preceding experiments were analyzed in order to determine the intensity ratios of the various gamma rays and the results are incorporated in Table IA. Several cross checks were possible and these are consistent within the accuracy stated in the table. Table IA shows also the results of other experimenters[2,12] and these are in fair agreement with ours.

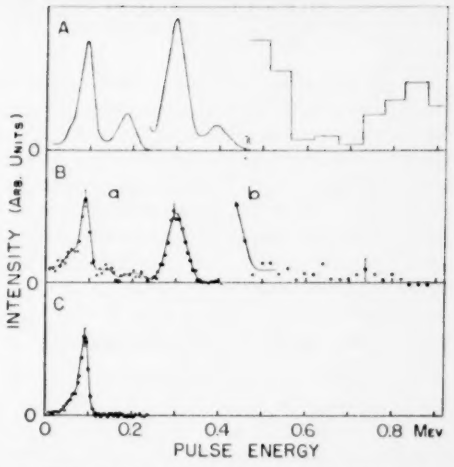

FIG. 4. Delayed coincidence pulse-height distributions in Ga^{67}. Curve *A* gives the single distribution (Fig. 1) for comparison. Curves *B* and *C* show the radiation preceding and following the metastable state in Zn^{67}, respectively. In *A*, curves *b* and *c* are enlarged 10 and 2000 times, respectively, with respect to *a*. In *B*, curve *b* is enlarged 150 times with respect to *a*.

Comparison with the values of Ketelle *et al.* (reference 2) indicates that their relative 0.09-Mev intensities are approximately 1½ times lower than ours. This discrepancy is mainly one of interpretation of our Fig. 1 and their Fig. 1 which are in excellent agreement except for the number of pulses below the 0.09-Mev peak, where Ketelle *et al.* find approximately twice as many pulses as we do. Apparently this increases their Compton electron-photo-peak ratio for the gamma rays above 0.09 Mev sufficiently to cause the above discrepancy.

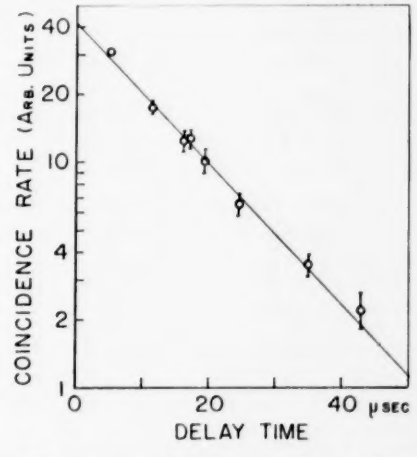

FIG. 5. Decay curve of the Zn^{67} metastable state. The curve indicates a half-life of 9.5±1.0 μsec.

[11] Fultz, Nash, Woodward, and Pool, Phys. Rev. **88**, 170 (1952); M. L. Pool, Physica **18**, 1304 (1952).

[12] A. Mukerji and P. Preiswerk, Helv. Phys. Acta **25**, 376 (1952).

METASTABLE STATE OF Zn^{67}

A. Half-Life

The experiments of Figs. 3C, 4B, and 4C indicated a half-life of the metastable state of the order of 10^{-5} sec. In order to measure the half-life more accurately we used a univibrator delay circuit[13] of 50-μsec range to delay the appropriately biased crystals by various times. Figure 5 gives the resulting coincidence rate *versus* delay time and indicates a half-life of 9.5 ± 1.0 μsec, in agreement with Ketelle *et al.*,[2] but in disagreement with some other workers.[11]

B. Conversion Coefficient

The absence of positrons in the decay of Ga^{67} and also the half-life of the metastable state, which is long compared to decay time of NaI(Tl) light pulses and the resolution of our amplifiers, permit an interesting way to measure the conversion coefficient of the metastable 0.092-Mev gamma ray. Since the conversion coefficient of all other gamma rays is small[2,12] the conversion coefficient of the 0.092 may be calculated from the following two ratios, R_1 and R_2, obtained by measuring two simple pulse-height distributions with the same NaI(Tl) crystal:

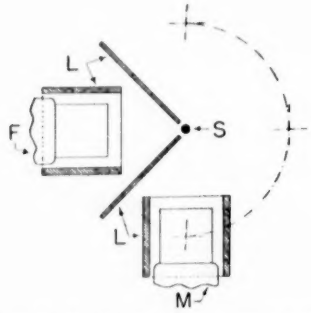

FIG. 6. Schematic diagram of the angular correlation apparatus. F is the fixed crystal and M the movable crystal, shown at the 270° position. S is the source and L the lead shielding. The actual distance between the source and the front face of each crystal was approximately 3 inches.

R_1 = No. of pulses due to gamma rays and electrons of the 0.09-Mev transitions/No. of pulses due to other gamma rays.

R_2 = No. of pulses due to gamma rays of 0.09 Mev/No. of pulses due to other gamma rays.

The total conversion coefficient α of the 0.092-Mev gamma ray is then $\alpha=\theta(R_1-R_2)/R_2$, where $\theta=100/93$ (see Table IA) corrects for the presence of the 0.090-Mev gamma ray.

The above ratios were measured by first placing a source of Ga^{67} wrapped in 0.003-inch copper foil between the two halves of a small cleaved crystal, with the cleavage face perpendicular to the phototube surface and mounted as described above. After taking into account absorption in the copper foil and the Compton electrons from the gamma rays above 0.09 Mev, the pulse-height distribution obtained yielded R_2. The crystal was then dismounted and a very thin source of Ga^{67} was deposited on a small part of the cleavage face of the crystal. Any loose material was rubbed off with soft tissue to assure that no electron energy loss would occur in inert crystal material. The crystal was assembled once more and the pulse-height distribution obtained gave R_1, after taking into account the Compton electrons of gamma rays above 0.09 Mev.

Two experiments of this kind gave a total conversion coefficient of 0.51 and 0.57, respectively, which we quote as 0.54 ± 0.05 in order to allow for the consistency of the results and the uncertainty in making the Compton electron subtraction under the 0.09-Mev peak. Using a $K/(L+M\cdots)$ ratio of 7,[2] we obtain a K-conversion coefficient of 0.47 ± 0.05 for the 0.092-Mev gamma ray. This result is compared in Table IC with the results of other investigators.

ANGULAR CORRELATION OF GAMMA RAYS

In order to help in the assignment of spins of the excited states of Zn^{67} we performed a rough angular correlation experiment between the 0.21- and 0.18-Mev gamma rays. For this purpose the analyzing crystal and the discriminating crystal were placed at a distance of about 3 inches from a cylindrical source of Ga^{67} in HCl. The discriminating crystal was set to accept pulses from 0.14 to 0.26 Mev. The crystals were surrounded with $\frac{1}{4}$-in. thick lead on the side and additional $\frac{1}{8}$-in. thick lead was placed as shown in Fig. 6 in order to avoid as much as possible the back-scattered Compton gamma ray from the 0.30-Mev gamma ray, which would give rise to spurious coincidences at the 180° position.

Pulse-height distributions were alternately measured at the 90°, 180°, 270°, and 180° positions (see Fig. 6). Figure 7 shows the results of one set of experiments, after correction for accidental coincidences, background coincidences, source anisotropy, and source decay. It can be seen that in the region above 0.18 Mev there are more pulses at 90° and 270° than at 180° indicating a negative angular correlation coefficient[14] ϵ between the 0.21 and 0.18 gamma rays. In the region of 0.12 to 0.18 Mev the 180° curve lies above the 90° and 270° curve because of the Compton coincidences of the 0.30-Mev gamma ray, mentioned above, which occurred despite the shielding by penetration of the source at the 180° position. Pulses resulting from these spurious coincidences would fall into the shaded energy

[13] We are indebted to Dr. W. C. Barber for the loan of this circuit. See W. C. Barber, Phys. Rev. **80**, 332 (1950).

[14] $\epsilon=[C(180°)-C(90°)]/C(90°)$, where $C(\theta)$ is the corrected coincidence rate at angle θ between analyzing and discriminating crystal.

region in Fig. 7 and this region was not counted in the angular correlation measurement.[15]

Three different sources of Ga^{67} under slightly different conditions of amplifier gain and shielding yielded the following results: $\epsilon=-0.168\pm0.045$, -0.243 ± 0.066, -0.192 ± 0.053, which give as weighted mean $\epsilon=-0.19\pm0.03$. All the errors quoted are statistical. In order to compare this coefficient with theoretical values it has to be corrected for the finite solid angle of the detectors and the finite extension of the source.[16] Assuming that one of the radiations in the measured correlation is dipole (see below), our measured ϵ has to be divided by 0.88 to give the true $\epsilon=-0.22\pm0.04$.

CONCLUSIONS

Tables I to III and Fig. 8 present the results and conclusions from our and other experiments on Ga^{67}. As a result of the coincidence experiments the decay scheme is uniquely determined as presented in Fig. 8; it is in very good agreement with the scheme of Ketelle *et al.*[2] and in good agreement with that of Mukerji and Preiswerk.[13] Since we have not measured the branching ratio of electron capture leading to the ground state of Zn^{67}, we have relied on the statement of Ketelle *et al.*[2] that it is less than a few percent and on a similar statement by Mukerji and Preiswerk.[12] Figure 8 and Table II also include information on the decay of Cu^{67}, which was investigated recently by Easterday.[17]

In an attempt to assign spins and parities to the levels of Zn^{67} we have compared the experimental data with theoretical and semi-empirical considerations of (a) beta decay,[18] (b) conversion coefficients,[19] (c) K/L ratios,[20] (d) lifetime energy relationships of excited states,[21] (e) angular correlation coefficients,[22] and (f) the

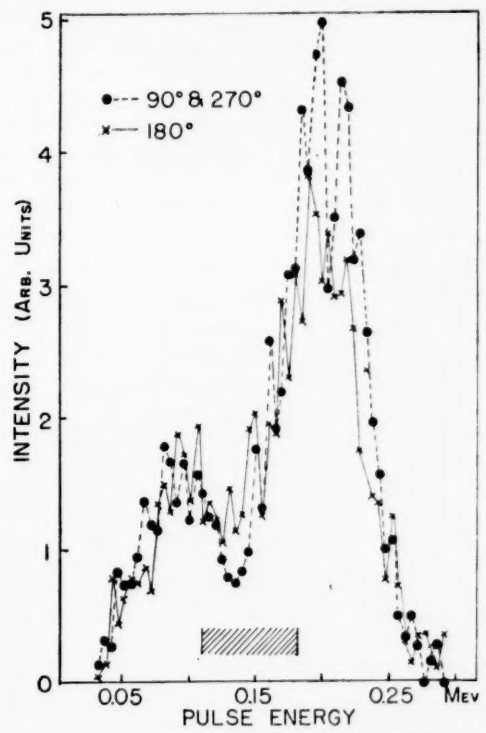

FIG. 7. Coincident pulse-height distribution at 90° and 270° (●– – –) compared with that at 180° (×——) in the angular correlation experiment. The distributions were coincident with pulses around 0.20 Mev. The shaded energy region indicates the region in which scattered Compton coincidences from the 0.30-Mev gamma ray should fall at the 180° position (see text).

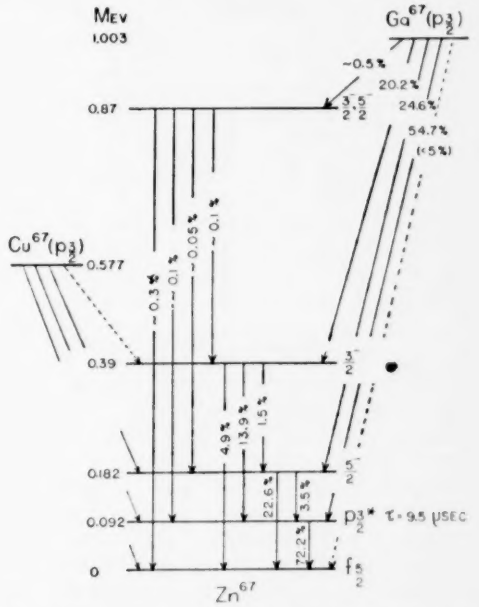

FIG. 8. The decay scheme of Ga^{67}. For a summary of data not indicated here see Tables I to III. The branching from Ga^{67} to the ground state of Zn^{67} (≤ 5 percent) was estimated from Ketelle *et al.* (reference 2) but is not included in the sum total of the transitions. The Cu^{67} decay energy was taken from Easterday (reference 17).

[15] Theoretically, Fig. 7 could also be used to measure the 0.21-Mev–0.090-Mev gamma-ray angular correlation coefficient, but the poor statistics and the sensitive dependence on the amount of Compton effect of the higher-energy gamma rays to be subtracted under the 0.09-Mev peak make this measurement meaningless in the present experiment. It might be noted that the lack of pulses below 0.04 Mev in Fig. 7 is instrumental.

[16] Walter, Huber, and Zünti, Helv. Phys. Acta **23**, 697 (1950); H. Frauenfelder, Ann. Revs. Nuc. Sci. **2**, 129 (1953).

[17] H. T. Easterday, Bull. Am. Phys. Soc. **27**, No. 6, 15 (1952); Phys. Rev. **91**, 653 (1953); University of California Radiation Laboratory Report 2162 (March, 1952). We are indebted to Dr. Easterday for providing us with information on the decay of Cu^{67} prior to publication and for sending us his original data.

[18] Mayer, Moszkowski, and Nordheim, Revs. Modern Phys. **23**, 315 (1951).

[19] J. R. Reitz, Phys. Rev. **77**, 10 (1950); Rose, Goertzel, Spinrad, Harr, and Strong, Phys. Rev. **83**, 79 (1951).

[20] M. Goldhaber and A. W. Sunyar, Phys. Rev. **83**, 906 (1951).

[21] V. F. Weisskopf, Phys. Rev. **83**, 1073 (1951). We have used the nomogram from R. Montalbetti, Can. J. Phys. **30**, 660 (1952).

[22] S. P. Lloyd, Phys. Rev. **83**, 717 (1951).

TABLE II. Branching ratios in Ga^{67} decay.

Level in Zn^{67}, Mev	Percent electron capture from Ga^{67}	Log ft from Ga^{67} [a]	Log ft from Cu^{67} β^- decay[b]	Type of decay
0	≤ 5[c]	≥ 6.2	6.3	Δl—forbidden[d]
0.092	54.7 ± 3.5	5.1	5.7	allowed
0.182	24.6 ± 2.2	5.4	5.3	allowed
0.39	20.2 ± 1.4	5.2	≥ 5.2	allowed
0.87	~ 0.5	~ 5.5	—	allowed

[a] Calculated using nomograph from S. A. Moszkowski, Phys. Rev. **82**, 35 (1951).
[b] Taken from H. T. Easterday, reference 17.
[c] Estimated from Ketelle *et al.* (reference 2). This percentage is not included in the sum total.
[d] See reference 18.

shell model.[23] It will be seen that despite all this information, which is summarized in Table III, the spins of the excited states of Zn^{67} cannot all be assigned with certainty.

A. Beta Decay

Table II summarizes the decay data from Ga^{67} (and Cu^{67})[17] to Zn^{67}. Since the stable isotopes Cu^{63}, Cu^{65}, Ga^{69}, and Ga^{71} all have spin 3/2 and the shell model predicts odd parity ($p_{\frac{3}{2}}$), the information of Table II leads to the assignment of spins 1/2, 3/2, or 5/2 and odd parity for all the states of Zn^{67} mentioned in the table. The ground state of Zn^{67} is known to have a spin 5/2 and the shell model predicts odd parity ($f_{5/2}$), leading to Δl-forbidden decay from Cu^{67} and Ga^{67}.

B. Conversion Coefficients

The relative K-electron intensities of the main gamma rays occurring in the decay of Ga^{67} are given in Table IB. (None of these were measured by us.) In order to obtain K-conversion coefficients from these data, the conversion coefficient of at least one of the gamma rays has to be measured directly. We have done this, as described above, for the 0.092-Mev gamma ray. Using the relative K-electron intensities of Ketelle *et al.*[2] and our relative gamma-ray intensities we have calculated the conversion coefficients shown in Table IC. Results of other investigators are quoted directly with some slight corrections.

Since the parities of all the Zn^{67} levels occurring in the decay of Ga^{67} are the same and the maximum spin difference occurring is 2 (see Beta Decay), we compare the experimental conversion coefficients with the theoretical ones for $M1$ (magnetic dipole) and $E2$ (electric quadrupole) only (see Table ID). We have used Reitz's values[19] for $Z=29$ and extrapolated them in energy and nuclear charge by means of the tables of Rose *et al.*[19] The assignments of the type of radiation given in Table IE seem to be rather unambiguous, except in the case of the 0.092-Mev gamma ray where it appears necessary to invoke a mixture of $M1$ and $E2$ (in approximately equal proportions) despite the contrary prediction of the lifetime energy relationships (see below). As a result of these assignments, the 0.092-, 0.182-, and 0.30-Mev levels of Zn^{67} may have spins 3/2 or 5/2 only.

C. K/L Ratios

Table IF summarizes the measured K/L ratios of some of the gamma rays. (None of this work was done by us.) One can compare these ratios with the semi-empirical curves of Goldhaber and Sunyar[20] for $M1$ and $E2$ transitions. A cursory examination of the literature[24] shows that additional K/L ratios are now available. It seems that for $M1$ transitions K/L is expected to be in the neighborhood of 7, although ratios as low as 5.5 (Sr^{85m}) and as high as 11 (As^{75}) have been reported. For $E2$ transitions in our energy range one expects K/L to be less than 5.5,‡ especially if one extrapolates the semi-empirical curves[20] (with Pd^{106}, Cd^{110}, and Ba^{134}, $K/L=8$, 4.3, 6.0, respectively, all of which are expected to have a first excited state with spin 2, even parity).[25] The measured K/L ratios for Zn^{67} all seem consistent with $M1$ transitions. One would not like to base too much emphasis on this statement for the 0.092-Mev gamma ray for which $E2$ gives nearly the same K/L ratio as $M1$ (so that this gamma ray could also be pure $E2$ as far as the K/L ratio is concerned).

D. Lifetime Energy Relationships

The measured half-life of 9.5×10^{-6} sec of the 0.092-Mev state of Zn^{67} is to be compared with 2×10^{-11} sec predicted for $M1$ and 5×10^{-6} sec predicted for $E2$ by the Weisskopf formula[21] corrected for internal conversions. If one trusts the measured and calculated conversion coefficients for the 0.092-Mev gamma ray (indicating an $M1$ and $E2$ mixture in equal proportions), one is at a loss to know how to combine the available evidence consistently, since any (even small) admixture of $M1$ in $E2$ radiation would give a predicted half-life many times smaller than the measured one. The present authors are unable, with the Weisskopf formula, to resolve this discrepancy which appears to be larger than usual.[26]

If one does not trust the conversion coefficient evi-

[23] M. G. Mayer, Phys. Rev. **78**, 16 (1950); P. F. A. Klinkenberg, Revs. Modern Phys. **24**, 63 (1952).

[24] Hollander, Perlman, and Seaborg, Revs. Modern Phys. **25**, 469 (1953).

‡ *Note added in proof:*—This statement probably has to be modified in view of recent work on K/L ratios by J. B. Swan and R. D. Hill, Australian J. Research (to be published). We are indebted to Dr. Hill for communicating these results to us prior to publication.

[25] G. Scharff-Goldhaber, Phys. Rev. **90**, 587 (1953).

[26] A similar occurrence of a "slow $M1$ transition" has been noted by J. R. Haskins and J. D. Kurbatov, [Phys. Rev. **88**, 884 (1952)], for the 0.364-Mev and other levels of Xe^{131}. Their postulated selection rule apparently cannot be invoked here. Professor E. Feenberg has kindly called our attention to the fact that if the 0.092-Mev state is a pure $p_{3/2}$ and the ground state a pure $f_{5/2}$ state (see Shell Model), then $M1$ radiation should be forbidden. The experimental reduction in the $M1$ matrix element is by a factor of 10^3 over that predicted by the Weisskopf formula (reference 21), indicating that these states may be quite pure.

TABLE III. Spin predictions for Zn^{67} states. (All parities are odd.)

Level energy Mev	Beta decay	Conversion coefficient	K/L ratio	Lifetime energy	Angular correlation	Authors' preferred choice and shell model
0	measured 5/2[a]	5/2	5/2	5/2	5/2	5/2 ($f_{5/2}$)
0.092	1/2, 3/2, 5/2	3/2, 5/2	1/2, 3/2, 5/2	1/2		3/2 ($p_{3/2}$)
0.182	1/2, 3/2, 5/2	3/2, 5/2	3/2, 5/2	3/2	5/2	5/2
0.39	1/2, 3/2, 5/2	3/2, 5/2	3/2, 5/2	3/2	3/2	3/2
0.87	1/2, 3/2, 5/2			3/2		3/2, 5/2

[a] For references see K. Way *et al.*, *Nuclear Data*, National Bureau of Standards Circular 499 (U. S. Government Printing Office, Washington, D. C., 1950).

dence, one is led to the assignments of Ketelle *et al.*[2] and our earlier ones,[3] giving the 0.092-Mev state spin 1/2; all the other states would then necessarily have spin 3/2, because these states decay to states of spin 1/2, 5/2 (and 3/2) with comparable probabilities (all $M1$ radiations; any radiation of $E2$ character would have a predicted intensity[21] differing by a factor of at least 10^3).

E. Angular Correlation

The corrected angular correlation coefficient of -0.22 ± 0.04 for the 0.21−0.18-Mev gamma-ray correlation has to be compared with the theoretical predictions[22] $+0.376$ (1/2−5/2−5/2), $+0.302$ (5/2−5/2−5/2), $+0.077$ (1/2−3/2−5/2), $+0.015$ (5/2−3/2−5/2), 0.000 (I−1/2−5/2), -0.059 (3/2−3/2−5/2), -0.222 (3/2−5/2−5/2). No other possibilities exist with the known spin of 5/2 for the ground state of Zn^{67}. Only the 3/2−5/2−5/2 prediction seems to fit the experimental data if the radiations are assumed to be pure. If the first (0.21-Mev) transition is assumed to be a mixture of $M1$ and $E2$ in approximately equal amounts ($\beta/\alpha = -1$ in Ling and Falkoff's notation[27]) the theoretical angular correlation coefficient for the 3/2−3/2−5/2 cascade can be brought to -0.14, which perhaps also could be called consistent with the experimental result.

It is known that liquid sources can reduce the angular correlation[28] by quadrupole interaction,[29] but since we find the maximum theoretically predicted anisotropy (for pure radiations), these effects do not appear to enter in our case, probably because the lifetime of the 0.182-Mev state of Zn^{67} is expected[21] to be between 10^{-11} and 10^{-12} sec. Impurities and scattering could also affect the experimental distribution,[16] but since we have a complete pulse-height analysis of the radiation and have eliminated the pulses affected by scattering, we believe that our result can be trusted.[30]

F. Shell Model

Both the neutrons and the protons occurring in Cu^{67}, Zn^{67}, and Ga^{67} fall into the 29 to 50 nucleon shell which on the whole seems to fill in the following order:[23] $(28)(p_{3/2})(f_{5/2})(p_{1/2})(g_{9/2})$, although there seems to be strong competition between the $p_{3/2}$ and $f_{5/2}$ shells, showing that they must be close in energy. It may therefore not be out of order to postulate that the ground state of $_{30}Zn^{67}$ is[22] p: $(28)(p_{3/2})^2$ n: $(28)(p_{3/2})^4$ $-(f_{5/2})^5$ and its first excited state n: $(28)(p_{3/2})^3(f_{5/2})^6$ (p: means proton configuration, n: neutron configuration). Similar 37-nucleon configurations appear to occur for $_{37}Rb^{85}$.[31] Most higher excited states of Zn^{67} must be many-particle states.[12] Since the first excited state of Zn^{66} occurs at 1.04 Mev,[32] core excitation[25] is not expected to play a predominant role here.

The ground state configurations of $_{29}Cu^{67}$ and $_{31}Ga^{67}$ can be assigned in a manner analogous to Cu^{63}, Cu^{65}, Ga^{69}, and Ga^{71} as[23] p: $(28)(p_{3/2})$ n: $(28)(p_{3/2})^4(f_{5/2})^6$ and p: $(28)(p_{3/2})^3$ n: $(28)(p_{3/2})^2(f_{5/2})^6$, respectively. All the foregoing assignments are in agreement with those of Mukerji and Preiswerk[12] and, except for the 0.092-Mev state of Zn^{66}, with Easterday.[17]

The above considerations are summarized in Table III.

The authors wish to thank Mr. L. Chase for generous help in taking some of the experimental data.

[27] D. S. Ling and D. L. Falkoff, Phys. Rev. **76**, 1639 (1949). This amount of mixing would not be out of line with the measured conversion coefficients for the 0.21-Mev gamma ray, but would be inconsistent with the K/L ratio.

[28] J. J. Kraushaar and M. Goldhaber, Phys. Rev. **89**, 1081 (1953).

[29] R. V. Pound and A. Abragam, Phys. Rev. **90**, 993 (1953).

[30] We are grateful to Dr. R. M. Steffen for a discussion of this point.

[31] M. Goldhaber and R. D. Hill, Revs. Modern Phys. **24**, 179 (1952); compare the quite different assignment given to Rb^{87} by S. Thulin, Phys. Rev. **87**, 684 (1952).

[32] G. Friedlander and D. E. Alburger, Phys. Rev. **84**, 484 (1951); Roderick, Meyerhof, and Mann, Phys. Rev. **84**, 887 (1951).

PHYSICAL REVIEW VOLUME 92, NUMBER 3 NOVEMBER 1, 1953

Lattice-Space Quantization of a Nonlinear Field Theory*

L. I. SCHIFF
Stanford University, Stanford, California
(Received July 30, 1953)

A method for the approximate diagonalization of certain types of quantum field Hamiltonians is developed which is not limited to weakly nonlinear systems. It consists in omitting the gradient terms in zero order, and diagonalizing the resulting Hamiltonian by replacing the field defined in a continuum space by a field defined in a lattice space. This unperturbed system is equivalent to a countably infinite number of uncoupled nonlinear oscillators, which are then coupled together when the gradient terms are included as a perturbation. The method is applied to the quantization of the classical nonlinear meson theory that was introduced in an earlier paper to provide a qualitative explanation of the saturation of nuclear forces, according to which a positive ϕ^4 term is added to the field Hamiltonian. Although the quantized theory is manifestly noncovariant, it is found that a single-particle solution exists that has an approximately relativistic relation between energy, momentum, and rest mass. It turns out to be essential that the lattice constant be kept finite, as all computed physical quantities become meaningless in the continuum limit (in which the lattice constant approaches zero). It is shown that these particles obey Einstein-Bose statistics, and that they scatter from each other. Nucleons are introduced as classical sources for the meson field, and calculations are made on the nucleon isobaric state, interaction of mesons with nucleons and heavy nuclei, and nucleon-nucleon interaction. Most of the results of the earlier classical theory have close counterparts in the present quantized theory. The possibility of extending the method to the quantization of both meson and nucleon fields when they are strongly coupled together is discussed briefly.

I. INTRODUCTION

THE quantization of non-interacting wave fields that satisfy linear equations can be carried through without difficulty, and energy eigenvalues can be obtained that correspond to particles of well-defined energy and momentum. No such simple and satisfactory treatment exists for wave fields that satisfy nonlinear equations, regardless of whether the nonlinearity arises from the interaction of otherwise linear fields or from an inherent property of the field itself. In most cases of physical interest, the difficulty does not appear in the formal process of quantization, which can be accomplished in the usual way, but rather in the diagonalization of the field Hamiltonian. Where the nonlinear term arises from an interaction and has a small coefficient, perturbation techniques can be used. The application of covariant mass and charge renormalization to quantum electrodynamics illustrates the high degree of success that can be achieved in this way. But where the nonlinear term is large, as in the meson-nucleon system, there is real doubt as to whether perturbation calculations provide even a qualitative guide to the actual situation. In such cases, calculations have sometimes been based on the Tamm-Dancoff method, the reliability of which is difficult to evaluate.

The present paper describes a different method, not limited to weakly nonlinear systems, for the approximate diagonalization of certain types of quantum field Hamiltonians. The method is based on the observation that for many field Hamiltonians, omission of the gradient terms leaves a system that can be regarded as a set of a continuously infinite number of uncoupled nonlinear oscillators, one at each point in space. A solution can be obtained if (1) the modified Hamiltonian can be exactly diagonalized, (2) the gradient terms can justifiably be treated as a perturbation, and (3) a perturbation calculation can be carried through to sufficiently high order to yield physically interesting results. Step (1) requires that the field defined in a continuum space be replaced by a field defined in a lattice space, so that the continuously infinite number of oscillators is replaced by a countably infinite number, one at each lattice point. Step (2) imposes restrictions on the general structure of the Hamiltonian and on the lattice constant. Step (3) depends to a large extent on the quantity being calculated; we shall see that various orders of perturbation calculation are of interest in different situations.

The theory outlined above is manifestly noncovariant, because of the different treatment of space and time derivatives. It is not even Galilean-invariant, because of the introduction of the lattice. The second difficulty is not serious if we deal with solutions that do not vary appreciably from one lattice point to the next. The situation here is roughly analogous to the propagation of sound waves in a crystal; the lattice structure is not significant if the wavelength is large in comparison with the lattice constant. The first difficulty is of course a major defect of the present work. Nevertheless, it is possible to find solutions that have a kind of relativistic behavior.

The nonlinear meson theory introduced earlier[1] provides a convenient example to which the present method can be applied. In this theory, a neutral scalar field ϕ interacts with itself through a positive term in the Hamiltonian proportional to $|\phi|^n$, where n is generally equal to 4, and may also interact with a classical source function which is related to the density of nucleons. Thus the present paper contains mainly a

* Supported in part by the joint program of the U. S. Office of Naval Research and the U. S. Atomic Energy Commission, and in part by the Office of Scientific Research, Air Research and Development Command.

[1] L. I. Schiff, Phys. Rev. **84**, 1 (1951), referred to here as I; W. E. Thirring, Z. Naturforsch. **7a**, 63, 379 (1952); B. J. Malenka, Phys. Rev. **86**, 68 (1952); E. M. Henley, Phys. Rev. **87**, 42 (1952).

particular kind of quantization of the classical theory developed previously.[2] The method can, however, also be applied to the quantization of certain coupled meson-nucleon fields, provided that a ϕ^4 term is introduced either *ad hoc* or because of renormalization.[3] There need then be no limitation on the strength of the meson-coupling. This extension of the theory is discussed briefly in Sec. VI.

The lattice space and the quantization procedure are set up in Sec. II. The fact that solutions exist that correspond to particles is far from obvious in a theory in which the nonlinear term is large; it is established in Sec. III. The interaction of two such particles in the absence of sources (meson-meson scattering) is discussed in Sec. IV. Classical sources that correspond to nucleons are introduced in Sec. V, and calculations are made of the nucleon isobaric state, meson-nucleon scattering, nucleon-nucleon interaction, saturation of nuclear forces, and the interaction of mesons with nuclear matter.

II. LATTICE SPACE

The continuum field Hamiltonian with which we shall work is[1]

$$H=\int[\tfrac{1}{2}\pi^2+\tfrac{1}{2}(\nabla\phi)^2+\tfrac{1}{2}\mu^2\phi^2+\tfrac{1}{4}\alpha^2\phi^4]d\tau, \tag{1}$$

where ϕ is a real scalar field and π is its canonical momentum. μ is the field rest mass, α is the nonlinear parameter ($\alpha^2>0$), and we choose units such that $\hbar=c=1$. The canonical commutation relation is

$$[\phi(\mathbf{r},t),\pi(\mathbf{r}',t)]=i\delta(\mathbf{r}-\mathbf{r}'). \tag{2}$$

As is well known, limitation of the volume within which the field is defined has no essential effect on the quantization; if this volume is assumed to be a cube of edge length L, the limit $L\to\infty$ can later be taken without difficulty.

For simplicity, the lattice space is introduced in simple cubic form, with lattice constant l. The large cube of volume L^3 is still assumed, so that the space consists of $N=(L/l)^3$ points. As in the continuum case, the limit in which N and L become infinite while l is fixed can readily be taken later.

We now assert that the field is defined only at the lattice points, where it is characterized by quantum mechanical operators ϕ_s and π_s. Our first object is to find a lattice field Hamiltonian and commutation relations that become Eqs. (1) and (2), respectively, in the limit $l\to0$. It is apparent that this cannot be done uniquely, since terms can always be included in the lattice Hamiltonian that vanish in this limit. We shall adopt a form that is convenient and plausible, which was first introduced by Wentzel.[4]

We introduce an averaging function

$$f(\mathbf{r}-\mathbf{r}_s)=L^{-3}\sum_{\mathbf{k}}e^{i\mathbf{k}\cdot(\mathbf{r}_s-\mathbf{r})}, \tag{3}$$

where $\mathbf{r}_s$ is a lattice point, and write

$$\phi_s\equiv a\int f(\mathbf{r}-\mathbf{r}_s)\phi(\mathbf{r})d\tau,$$
$$\pi_s\equiv b\int f(\mathbf{r}-\mathbf{r}_s)\pi(\mathbf{r})d\tau, \tag{4}$$

where the coefficients a and b are as yet undetermined. The summation variable $\mathbf{k}$ in Eq. (3) is restricted to the points of a reciprocal lattice space which is also simple cubic; each component of $\mathbf{k}$ ranges from $-\pi/l$ to π/l in steps of $2\pi/L$, so that there are N terms in the $\mathbf{k}$-sum. The averaging function f has unit integral over the large cube of volume L^3, has its maximum value $1/l^3$ when its argument is zero, has linear dimensions of order l, and approaches a δ function when $l\to0$. Equation (3) therefore states that the lattice field is an average of the continuum field over a distance of order l about the lattice point, multiplied by a coefficient a or b. In the following, we shall frequently use the relations:

$$\textstyle\sum_{\mathbf{k}}e^{i\mathbf{k}\cdot(\mathbf{r}_s-\mathbf{r}_t)}=N\delta_{st},\quad \sum_s e^{i(\mathbf{k}-\mathbf{k}')\cdot\mathbf{r}_s}=N\delta_{\mathbf{k}\mathbf{k}'}. \tag{5}$$

The commutation relations associated with the lattice fields (4) are easily shown to be

$$[\phi_s,\pi_t]=iabl^{-3}\delta_{st}, \tag{6}$$

when use is made of Eqs. (2), (3), and (5). Thus for a canonical theory, we require that $ab=l^3$. The value chosen for a or for b is of no physical significance, since it appears only as an arbitrary scale factor in ϕ_s or π_s. It is convenient to choose $a=b=l^{\frac{3}{2}}$. When this is done, it is easily verified that

$$\sum_s\pi_s^2\underset{l\to0}{\longrightarrow}\int\pi^2d\tau,\quad \sum_s\phi_s^2\underset{l\to0}{\longrightarrow}\int\phi^2d\tau,$$
$$l^3\sum_s\phi_s^4\underset{l\to0}{\longrightarrow}\int\phi^4d\tau. \tag{7}$$

There are several ways in which the gradient term in Eq. (1) can be represented in the lattice space. With the form (3) for the smoothing function, the most convenient choice consists in replacing

$$\int(\nabla\phi)^2d\tau$$

by[4]

$$\textstyle\sum_s\sum_t A_{st}\phi_s\phi_t,\quad A_{st}\equiv N^{-1}\sum_{\mathbf{k}}k^2e^{i\mathbf{k}\cdot(\mathbf{r}_s-\mathbf{r}_t)}, \tag{8}$$

[2] Quantum aspects have been treated from other points of view by D. R. Yennie, Phys. Rev. **88**, 527 (1952); H. B. Rosenstock, Ph.D. thesis, University of North Carolina, 1951 (unpublished); D. Finkelstein, Ph.D. thesis, Massachusetts Institute of Technology, 1953 (unpublished).

[3] P. T. Matthews, Phil. Mag. **42**, 221 (1951).

[4] G. Wentzel, Helv. Phys. Acta **13**, 269 (1940).

which has the proper limit as $l\to 0$. The quantity A_{st} could also be represented as a second difference, for example, but this is less convenient for the following development, and makes little difference so long as we deal with solutions that do not vary appreciably from one lattice point to the next.

The lattice Hamiltonian can now be written:

$$\mathcal{H}=\mathcal{H}_0+\mathcal{H}',$$

$$\mathcal{H}_0=\sum_s\left[\tfrac{1}{2}\pi_s^2+\tfrac{1}{2}(P+\mu^2)\phi_s^2+\frac{\alpha^2}{4l^3}\phi_s^4\right], \tag{9}$$

$$\mathcal{H}'=\tfrac{1}{2}\sum_s{\sum_t}'A_{st}\phi_s\phi_t, \quad P\equiv A_{ss}=N^{-1}\sum_k k^2\xrightarrow[N\to\infty]{}\frac{\pi^2}{l^2},$$

where the dash on the summation over t means that the term $t=s$ is omitted. Because of (7) and (8), $\mathcal{H}$ approaches the H given by Eq. (1) as $l\to 0$. The unperturbed lattice Hamiltonian $\mathcal{H}_0$ is separable and describes a set of uncoupled nonlinear oscillators. The perturbation $\mathcal{H}'$ then couples these oscillators together.

It is convenient to adopt a representation in which $\pi_s=-i(\partial/\partial\phi_s)$, which is consistent with the commutation relations (6). Then the unperturbed Schrödinger equation may be separated as follows:

$$\mathcal{H}_0\Psi=E\Psi, \quad \Psi=\prod_s u_{n_s}(\phi_s), \quad E=\sum_s \epsilon_{n_s},$$

$$\left[-\tfrac{1}{2}\frac{d^2}{d\phi^2}+\tfrac{1}{2}(P+\mu^2)\phi^2+\frac{\alpha^2}{4l^3}\phi^4\right]u_n(\phi)=\epsilon_n u_n(\phi). \tag{10}$$

The energies ϵ_n are the eigenvalues for the one-dimensional motion of a particle in a potential that becomes positively infinite for large displacements from the equilibrium point ($\phi=0$); they therefore form a discrete set extending from a smallest positive value to $+\infty$. The eigenfunctions u_n form a complete *ortho*normal set with parities $(-1)^n$.

We can put this equation in dimensionless form by substituting

$$x=(\alpha^{\frac{1}{3}}/2^{1/6}l^{\frac{1}{2}})\phi, \quad \lambda_n=(2^{1/3}l/\alpha^{\frac{1}{3}})\epsilon_n,$$

whence

$$\frac{d^2u_n}{dx^2}+\left[\lambda_n-\frac{2^{\frac{1}{3}}}{\alpha^{4/3}}(\pi^2+\mu^2l^2)x^2-x^4\right]u_n=0. \tag{11}$$

This form is well-adapted to a study of the situation in which $\alpha\gg 1$, since then the dominant character of the x^4 term is evident (this assumes that μl is not large in comparison with unity). For very large α, the x^2 term may be neglected, and the λ's are a well-defined set of dimensionless numbers. Then the ϵ's are of order $\alpha^{\frac{1}{3}}/l$, and all matrix elements of ϕ are of order $l^{\frac{1}{2}}/\alpha^{\frac{1}{3}}$. Thus if we treat $\mathcal{H}'$ as a perturbation on $\mathcal{H}_0$, a suitable parameter for gauging the validity of the perturbation calculation is the ratio of a typical matrix element of $\mathcal{H}'$ to the spacing of the eigenvalues of $\mathcal{H}_0$; this ratio is a rough measure of the extent to which other states mix in with a particular unperturbed state. In cases of physical interest, only a small number of terms of the series in $\mathcal{H}'$ will contribute, so a typical matrix element is of order $(1/l^2)(l^{\frac{1}{2}}/\alpha^{\frac{1}{3}})^2=(1/l\alpha^{\frac{1}{3}})$, and the above ratio is of order $1/\alpha^{4/3}$. Thus the perturbation treatment envisaged here is useful if α is large, regardless of the magnitude of l.

It is of interest to see how this perturbation treatment of $\mathcal{H}'$ is modified if the nonlinearity is chosen to have the form $\alpha^2|\phi|^n$, where n is not necessarily equal to 4. The ratio of perturbation to eigenvalue spacing is then of order $l^{4(n-4)/(n+2)}/\alpha^{8/(n+2)}$. Thus if $n>4$ the validity of the perturbation approach is improved if l is made small, and if $n<4$ it is improved if l is made large; only for $n=4$ is it independent of l. This explains why Wentzel[4] was forced to assume large l for the linear field theory (which is equivalent to $n=2$).

It is also interesting to note that the unperturbed energy eigenvalues are of order $\alpha^{4/(n+2)}/l^{3(n-2)/(n+2)}$ in the general case. Thus only in the case $n=2$ (linear field theory) do they remain finite as $l\to 0$. In this case, the continuum field Hamiltonian has positively infinite energy eigenvalues, but only for the trivial reason that there is an infinite number of degrees of freedom ($N\to\infty$) each of which has a finite zero-point energy. In the case $n=4$, all the eigenvalues for each of the N degrees of freedom become positively infinite as $l\to 0$. Thus so long as the perturbation theory is valid (large α), we can use this result as a demonstration that the continuum field Hamiltonian (1) has energy eigenvalues that are positively infinite in a nontrivial way.[5] This means that sensible results can be obtained only by some sort of renormalization or cut-off procedure. We have attempted various types of renormalization, without success; an obvious difficulty is that covariance cannot be used as a guide. A cutoff is provided automatically by the lattice constant l; so long as l is finite, all results of the theory are finite and, as we shall see in the next section, there exists a maximum momentum of order $1/l$. We therefore reconcile ourselves to the idea that the limit $l\to 0$ cannot actually be taken, and regard l as a parameter of the theory.

III. ENERGY AND MOMENTUM OF A FREE PARTICLE

Lattice Energy

The lowest state of the unperturbed system is that in which each lattice-point oscillator has its smallest energy eigenvalue. This state is nondegenerate, and has energy $N\epsilon_0$. The first excited state of the unperturbed system is that in which all but one lattice-point oscillator has its smallest energy eigenvalue, and that one has its second eigenvalue. This state is N-fold degenerate, and has energy $(N-1)\epsilon_0+\epsilon_1$, or an excitation energy of $(\epsilon_1-\epsilon_0)$ above the lowest state. If we apply

[5] This supplements the similar result obtained by D. R. Yennie (reference 2) for the case in which the nonlinear term can be treated as a perturbation (small α).

first-order perturbation theory, and remember that the oscillator eigenfunctions $u_n(\phi)$ of Eq. (10) have parities $(-1)^n$, it is apparent that the lowest state is unaffected. This state is

$$\Psi_0=\prod_t u_0(\phi_t). \tag{12}$$

The N-degenerate first-excited states of the unperturbed system are

$$U_1(s)=u_1(\phi_s)\prod_t{}' u_0(\phi_t), \quad s=1, \cdots N, \tag{13}$$

where the dash on the product means that the term $t=s$ is omitted. Diagonalization of the matrix for $\mathfrak{H}'$ computed from the functions (13) leads to the following first-order normalized eigenfunctions and perturbation matrix:

$$\begin{aligned}\Psi_1(\mathbf{K})&=N^{-\frac{1}{2}}\sum_s e^{i\mathbf{K}\cdot\mathbf{r}_s}U_1(s),\\ \mathfrak{H}'(\mathbf{K},\mathbf{K}')&=(K^2-P)\phi_{01}{}^2\delta(\mathbf{K},\mathbf{K}').\end{aligned} \tag{14}$$

Here $\mathbf{K}$ is any one of the set of vectors $\mathbf{k}$ of the reciprocal lattice space, and

$$\phi_{01}\equiv\int_{-\infty}^{\infty}\bar{u}_0(\phi)\phi u_1(\phi)d\phi$$

is a real matrix element since the u's are taken to be real. Thus the excitation energy through first order is

$$\epsilon_1-\epsilon_0=P\phi_{01}{}^2+K^2\phi_{01}{}^2. \tag{15}$$

The wave function $\Psi_1(\mathbf{K})$ given by Eq. (14) is a kind of wave of excitation running through the lattice; it is analogous to the excitation waves in the theory of solids or to the spin waves in the theory of ferromagnetism.

Lattice Momentum

We now consider the momentum contained in the lattice. The continuum field momentum is

$$\mathbf{G}=-\tfrac{1}{2}\int[\pi(\nabla\phi)+(\nabla\phi)\pi]d\tau, \tag{16}$$

and it is natural to write for the lattice momentum

$$\mathfrak{G}=-\sum_s\sum_t\mathbf{B}_{st}\pi_s\phi_t, \quad \mathbf{B}_{st}\equiv N^{-1}\sum_{\mathbf{k}}i\mathbf{k}e^{i\mathbf{k}\cdot(\mathbf{r}_s-\mathbf{r}_t)}, \tag{17}$$

where $\mathbf{B}_{st}=-\mathbf{B}_{ts}$ and $\mathbf{B}_{ss}=0$; moreover, $\mathfrak{G}$ is Hermitian and approaches $\mathbf{G}$ as $l\to 0$. It turns out, however, that $\mathfrak{G}$ defined by Eq. (17) does not commute with $\mathfrak{H}$, so that it is not a constant of the motion. In the absence of external forces, we expect the momentum to be a constant, so that we cannot reasonably regard $\mathfrak{G}$ as the momentum of the lattice.

There is nevertheless a close correspondence between the translational properties of $\mathbf{G}$ and $\mathfrak{G}$.[6] As is well known, $\mathbf{G}$ is the generator of displacements of the continuum field variables in that the unitary transformation $S_{\mathbf{a}}\equiv\exp(-i\mathbf{a}\cdot\mathbf{G})$ displaces $\phi(\mathbf{r})$ and $\pi(\mathbf{r})$ by an arbitrary vector $\mathbf{a}$. In the same way, the unitary transformation $\mathcal{S}_{\mathbf{a}}\equiv\exp(-i\mathbf{a}\cdot\mathfrak{G})$ displaces ϕ_s and π_s by the vector $\mathbf{a}$, where, however, $\mathbf{a}$ must now be one of the lattice vectors. In both the continuum and the lattice cases, the fact that the field Hamiltonian is invariant with respect to displacements means that it commutes with the displacement operator; for a space of finite extent, it is of course always necessary to assume that there are periodic boundary conditions at the edges. This commutativity can be used, in the continuum case, to show that $\mathbf{G}$ itself commutes with H, by allowing the displacement vector $\mathbf{a}$ to become infinitesimal. In the lattice case, however, there is no infinitesimal lattice vector, so that we cannot prove in this way that $\mathfrak{G}$ and $\mathfrak{H}$ commute, and in fact they do not.

We wish to find a momentum operator that is Hermitian, reduces to $\mathbf{G}$ in the limit $l\to 0$, and is a constant of the motion. A simple choice for the x component that meets all these requirements is

$$\mathfrak{p}_x=[\exp(il\mathfrak{G}_x)-\exp(-il\mathfrak{G}_x)]/2il=(\sin l\mathfrak{G}_x)/l, \tag{18}$$

with corresponding expressions for the other two components. Any energy eigenfunction, if nondegenerate, must also be an eigenfunction of Eq. (18), and of $\mathcal{S}_{lx}\equiv\exp(-il\mathfrak{G}_x)$, since both of these operators commute with $\mathfrak{H}$. If an energy eigenfunction is not an eigenfunction of $\mathfrak{p}_x$, it must be degenerate, and linear combinations of these degenerate energy eigenfunctions can then be chosen that diagonalize $\mathfrak{p}_x$, i.e., that are also eigenfunctions of $\mathfrak{p}_x$. The corresponding eigenvalues can be found as follows.

Consider a wave function that is an eigenfunction of both $\mathfrak{H}$ and $\mathfrak{p}$. It is then also an eigenfunction of $\mathcal{S}_{lx}$, $\mathcal{S}_{ly}$, and $\mathcal{S}_{lz}$. If we operate on it L/l times with $\mathcal{S}_{lx}$, we displace it by the distance L along the positive x direction, and hence bring it back into itself (periodic boundary conditions). Thus the eigenvalue of $\mathcal{S}_{lx}$ is one of the (L/l)th roots of unity: $\exp(-2\pi i\nu_x l/L)$, where ν_x is an integer; the eigenvalues for $\mathcal{S}_{ly}$ and $\mathcal{S}_{lz}$ have the same set of possible values. Then if we define a vector $\boldsymbol{\kappa}$ by putting $\kappa_x=2\pi\nu_x/L$, etc., it is one of the vectors $\mathbf{k}$ of the reciprocal lattice; the eigenvalue of $\mathcal{S}_{lx}$ is $\exp(-il\kappa_x)$, and similarly for $\mathcal{S}_{ly}$ and $\mathcal{S}_{lz}$. The possible eigenvalues of Eq. (18) are then $(\sin l\kappa_x)/l$, with analogous eigenvalues for $\mathfrak{p}_y$ and $\mathfrak{p}_z$. So long as $\boldsymbol{\kappa}$ is small in comparison with $1/l$, the eigenvalue of $\mathfrak{p}$ is very nearly equal to $\boldsymbol{\kappa}$, and we shall usually assume that $\boldsymbol{\kappa}$ is small. It should be noted, however, that the eigenvalue of any component of $\mathfrak{p}$ cannot exceed $1/l$, and that the maximum value occurs when the corresponding component of $\boldsymbol{\kappa}$ is equal to $\pi/2l$.

The wave function (14) provides an instructive example of the effect of operating with $\mathcal{S}_{lx}$. We denote by s' the lattice point whose x coordinate is larger by

[6] The writer is indebted to F. Bloch for pointing out the properties of the displacement operator.

l than the x coordinate of s. We then have

$$\begin{aligned}\mathcal{S}_{lx}\Psi_1(\mathbf{K}) &= N^{-\frac{1}{2}}\sum_s e^{i\mathbf{K}\cdot\mathbf{r}_s}U_1(s') \\ &= N^{-\frac{1}{2}}e^{-ilK_x}\sum_s e^{i(\mathbf{K}\cdot\mathbf{r}+lK_x)}U_1(s') \\ &= N^{-\frac{1}{2}}e^{-ilK_x}\sum_{s'} e^{i\mathbf{K}\cdot\mathbf{r}_{s'}}U_1(s') \\ &= e^{-ilK_x}\Psi_1(\mathbf{K}),\end{aligned}$$

so that $\Psi_1(\mathbf{K})$ is in fact an eigenfunction of $\mathcal{S}_{lx}$, and hence also of $\mathfrak{p}$. This shows also that the momentum associated with the state (14) is very nearly equal to the vector $\mathbf{K}$ that appears in $\Psi_1(\mathbf{K})$, so long as $\mathbf{K}$ is not comparable with $1/l$.

Interpretation as a Particle

We are now in a position to relate the expression (15) for the first-order energy of the first excited state of the lattice, to the lattice momentum $\mathbf{K}$ in the same state. We first assume that the nonlinear parameter α is large compared to unity. The term $(\epsilon_1-\epsilon_0)$ in Eq. (15) is of order $\alpha^{\frac{1}{2}}/l$, and the term $P\phi_{01}^2$ is of order $1/(l\alpha^{\frac{1}{2}})$, so that the latter can be neglected for the present. We interpret $(\epsilon_1-\epsilon_0)$ as the rest mass of a particle, $K^2\phi_{01}^2$ as the kinetic energy of that particle, and $\mathbf{K}$ as its momentum. In other words, we say that the first excited state of the lattice, which possesses the above energy and momentum with respect to the lowest state of the lattice, is to be interpreted as a particle which has made its appearance in a vacuum. This interpretation is limited by the nonrelativistic form of Eq. (15), but this is not surprising since the kinetic energy term in (15) is the result of a first-order calculation, and it might be expected that higher-order terms in $\mathfrak{IC}'$ would yield higher-order relativistic corrections to the simple formula (15). Equation (15) is at least consistent with the present view insofar as the kinetic energy term is small (of order $\alpha^{-4/3}$) in comparison with the rest mass term.

The crucial test of Eq. (15) as a description of a particle is the requirement that the kinetic mass $1/(2\phi_{01}^2)$, which is the ratio of the square of the momentum to twice the kinetic energy, be equal to the rest mass $(\epsilon_1-\epsilon_0)$. This means that the quantity $2\phi_{01}^2(\epsilon_1-\epsilon_0)$ should be equal to unity. If we use the substitutions associated with Eq. (11) to put this in dimensionless form, it becomes $x_{01}^2(\lambda_1-\lambda_0)$, where $x_{01}\equiv\int_{-\infty}^{\infty}\bar{u}_0(x)xu_1(x)dx$ is a real matrix element since the u's which satisfy Eq. (11) are taken to be real. The following sum rule is easily established:

$$\sum_n x_{mn}^2(\lambda_n-\lambda_m)=1. \tag{19}$$

If we take $m=0$, each term in Eq. (19) is positive, and we can conclude that $x_{01}^2(\lambda_1-\lambda_0)\leqq 1$. The equality holds only if all higher matrix elements x_{03}, x_{05}, etc. are zero. This is true in the linear case, in which the x^4 term does not appear in Eq. (11), since then the u's are harmonic oscillator wave functions; thus the present methods can deal with the linear field (although they are of course unnecessarily complicated in this case).

The actual value of $x_{01}^2(\lambda_1-\lambda_0)$ in the nonlinear case must be found by numerical integration of Eq. (11). For large α, where the x^2 term in Eq. (11) can be neglected, several numerical values are collected in the next subsection. The above quantity is equal to 0.9884, so that the kinetic and rest masses of our particle differ by only about one percent.[7] This agreement is not only gratifying in itself, but implies, as shown below, that the matrix elements x_{03}, x_{05}, etc., are small in comparison with x_{01}; as we shall see, this makes it feasible to carry the energy calculation to higher order in $\mathfrak{IC}'$.

Numerical Values[8]

The first four eigenvalues of Eq. (11) with $\alpha=\infty$ are $\lambda_0=1.0605$, $\lambda_1=3.7998$, $\lambda_2=7.465$, and $\lambda_3=11.650$. The matrix elements of x and x^2 computed from the corresponding eigenfunctions are $x_{01}=0.6007$, $x_{12}=-0.7336$, $x_{23}=0.8384$, $x_{03}=-0.0320$, $(x^2)_{00}=0.3618$, $(x^2)_{11}=0.9016$, $(x^2)_{22}=1.2426$, $(x^2)_{33}=1.5522$, $(x^2)_{02}=-0.4674$, and $(x^2)_{13}=-0.6943$.

It would provide an enormous simplification for the higher-order calculations if we could assume, as is true in the harmonic oscillator case, that all matrix elements x_{nm} can be neglected unless $m=n\pm1$. If this were a valid assumption, the sum rule (19) and the matrix product rule could be used to find several quantities that would be equal to unity. These quantities, and their numerically computed values, are

$$\begin{gathered}x_{01}^2/(x^2)_{00}=0.9973,\quad (x_{01}^2+x_{12}^2)/(x^2)_{11}=0.9971, \\ (x_{12}^2+x_{23}^2)/(x^2)_{22}=0.9988;\end{gathered} \tag{A}$$

$$\begin{gathered}(\lambda_1-\lambda_0)x_{01}^2=0.9884, \\ (\lambda_2-\lambda_1)x_{12}^2-(\lambda_1-\lambda_0)x_{01}^2=0.9841, \\ (\lambda_3-\lambda_2)x_{23}^2-(\lambda_2-\lambda_1)x_{12}^2=0.9692;\end{gathered} \tag{B}$$

$$x_{01}x_{12}/(x^2)_{02}=0.9428,\quad x_{12}x_{23}/(x^2)_{13}=0.8859. \tag{C}$$

It is interesting to note that the neglected terms in group (A) are of second order in the small matrix elements, and hence very small. The neglected terms in group (B) are also of second order, but are multiplied by the difference of two λ's, and are therefore somewhat larger. In group (C), the neglected terms are of first order, so that the errors are largest in this case.

For finite α in Eq. (11), the eigenvalues and matrix elements approach more closely those of the harmonic oscillator, for which all x_{nm} with $m\neq n\pm1$ are zero. We

[7] The writer is indebted to D. Saxon of the National Bureau of Standards, Institute for Numerical Analysis, for arranging for these precise numerical computations, which provided a very important stimulus to the present work, and also to E. Osborne and P. Kaus who carried them out.

[8] Values of λ_0 and λ_1 were first computed by W. E. Milne, Phys. Rev. **35**, 863 (1930). The other λ's and all the u's were computed at the Institute for Numerical Analysis (reference 7). The matrix elements were computed from the u's by connecting on the asymptotic form beyond the range of the numerical computations.

expect, therefore, that the neglect of such matrix elements in the nonlinear case is an even better approximation for finite α than is indicated by the above numerical results for infinite α.

Higher-Order Terms in the Energy of a Particle

In everything that follows, we assume that all matrix elements x_{nm} or ϕ_{nm} with $m \neq n \pm 1$ can be neglected. This is expected to introduce errors of the general order of magnitude of one to ten percent. The perturbation treatment of $\mathcal{H}'$ has been carried to third order; this is feasible because the sums over intermediate states are severely limited in scope by the assumed structure of the matrix elements.

For the lowest (vacuum) state of the lattice, the zero-order energy is $N\epsilon_0$, and the first-order energy is zero, as stated earlier. The second-order energy is

$$-\frac{{\phi_{01}}^4}{4(\epsilon_1-\epsilon_0)}\sum_s\sum_t{}' A_{st}{}^2 = -\frac{{\phi_{01}}^4}{4(\epsilon_1-\epsilon_0)}N(Q-P^2), \tag{20}$$

$$Q \equiv N^{-1}\sum_{\mathbf{k}} k^4 \xrightarrow[N\to\infty]{} \frac{19}{15}\frac{\pi^4}{l^4} = \frac{19}{15}P^2.$$

The third-order vacuum energy is

$$\frac{{\phi_{01}}^6}{4(\epsilon_1-\epsilon_0)^2}\sum_s\sum_t{}'\sum_q{}'' A_{st}A_{tq}A_{qs} = \frac{{\phi_{01}}^6}{4(\epsilon_1-\epsilon_0)^2}N(R-3QP+2P^3), \tag{21}$$

$$R \equiv N^{-1}\sum_{\mathbf{k}} k^6 \xrightarrow[N\to\infty]{} \frac{583}{315}P^3.$$

The dashes on the summations over t in Eqs. (20) and (21) mean that the terms $t=s$ are omitted, and the double dash on the summation over q in (21) means that the terms $q=t$ and $q=s$ are omitted.

The zero- and first-order energy of the first excited state of the lattice was obtained earlier: $(N-1)\epsilon_0+\epsilon_1+(K^2-P)\phi_{01}{}^2$, and corresponds to the first-order perturbed eigenfunction (14). The second-order energy of this state is

$$-\frac{{\phi_{01}}^4}{2(\epsilon_1-\epsilon_0)}(K^4-2K^2P-2Q+3P^2) - \frac{{\phi_{01}}^2{\phi_{12}}^2}{\epsilon_2-\epsilon_0}(Q-P^2) - \frac{{\phi_{01}}^4}{4(\epsilon_1-\epsilon_0)}N(Q-P^2). \tag{22}$$

Up to this point, all of the summations over s, t, etc. have been reducible to the form (5); that is, there have never been more than two $\mathbf{k}$ vectors in a single exponent. In the calculation of the third-order energy of the excited state, however, there appear summations of the form

$$\sum_s e^{i(\mathbf{k}+\mathbf{k}'+\mathbf{k}''+\mathbf{K})\cdot\mathbf{r}_s}. \tag{23}$$

The summation (23) is zero unless the sum of the four $\mathbf{k}$ vectors in the exponent is equal to zero or to one of the 26 other vectors with Cartesian coordinates 0, $\pm 2\pi/l$, in which case it is equal to N. These 26 other vectors, which can be reached by the sum of four $\mathbf{k}$ vectors, cannot be reached by the sum of two $\mathbf{k}$ vectors as in (5), since each $\mathbf{k}$ vector is confined to the interior of a cube whose edges are at $\pm\pi/l$; that the edges and surfaces of the reciprocal lattice cube are not accessible to the individual $\mathbf{k}$ vectors is most easily seen by considering the case in which L/l is an odd number, when each component of a $\mathbf{k}$ vector can have values $0, \pm 2\pi/L, \pm 4\pi/L, \cdots \pm[(\pi/l)-(\pi/L)]$. In similar fashion, there are no contributions to (23) from $\mathbf{k}$-sum vectors with components $\pm 4\pi/l$, since these cannot be reached by the sum of four $\mathbf{k}$ vectors.

All terms that contain summations of the form (23), with four $\mathbf{k}$ vectors in a single exponent, can be reduced to

$$Z \equiv N^{-4}\sum_s\sum_t{}'\sum_{\mathbf{k}}\sum_{\mathbf{k}'}\sum_{\mathbf{k}''} k^2k'^2k''^2 e^{i(\mathbf{k}+\mathbf{k}'+\mathbf{k}''+\mathbf{K})\cdot(\mathbf{r}_s-\mathbf{r}_t)}.$$

To evaluate Z, we first perform the summations over s and t, to give

$$Z = N^{-2}\sum_{\mathbf{k}}\sum_{\mathbf{k}'}\sum_{\mathbf{k}''}\sum_i k^2k'^2k''^2\delta(\mathbf{k}+\mathbf{k}'+\mathbf{k}''+\mathbf{K}-\boldsymbol{\kappa}_i) - P^3,$$

where the vectors $\boldsymbol{\kappa}_i$ are the 26 referred to above, and the δ symbol is unity if its argument is zero and is zero otherwise. Next we sum over $\mathbf{k}''$ for fixed values of $\mathbf{k}$, $\mathbf{k}'$, and $\mathbf{K}$, and note that any $\boldsymbol{\kappa}_i$ can only be reached with $\mathbf{k}''$ by starting from a value of $\boldsymbol{\gamma} \equiv \mathbf{k}+\mathbf{k}'+\mathbf{K}$ that lies within the cube of edge length $2\pi/l$ whose center is at that $\boldsymbol{\kappa}_i$. Thus all possible combinations of $\mathbf{k}$, $\mathbf{k}'$ and $\mathbf{K}$ contribute, each just once, and to various $\boldsymbol{\kappa}$'s. We thus get

$$Z + P^3 = N^{-2}\sum_{\mathbf{k}}\sum_{\mathbf{k}'} k^2k'^2(\boldsymbol{\kappa}_i-\mathbf{k}-\mathbf{k}'-\mathbf{K})^2,$$

where now $\boldsymbol{\kappa}_i$ is a discontinuous function of $\boldsymbol{\gamma}$.

We now take the limit $N\to\infty$ by replacing the $\mathbf{k}$ summations by integrations: $N^{-1}\sum_{\mathbf{k}}[\ ] \to (l/2\pi)^3 \times \int[\ ]d\tau_k$, where the integral is over a cube of edge positions $\pm\pi/l$. When the integrand is squared out, we obtain

$$Z + P^3 = K^2P^2 + 2QP + W, \tag{24}$$

$$W \equiv (l/2\pi)^6 \int\int k^2k'^2[\boldsymbol{\kappa}^2 - 2\boldsymbol{\kappa}\cdot(\mathbf{k}+\mathbf{k}'+\mathbf{K})]d\tau_k d\tau_{k'},$$

where the subscript has been dropped from $\boldsymbol{\kappa}_i$. The vector $\boldsymbol{\kappa}$ is a discontinuous function of $\boldsymbol{\gamma}(=\mathbf{k}+\mathbf{k}'+\mathbf{K})$; the relation between x components of $\boldsymbol{\kappa}$ and $\boldsymbol{\gamma}$ is $\kappa_x = 2\pi/l$ for $\gamma_x > \pi/l$, $\kappa_x = 0$ for $-\pi/l < \gamma_x < \pi/l$, $\kappa_x = -2\pi/l$ for $\gamma_x < -\pi/l$, with corresponding relations for the other components. The evaluation of W is rather

tedious; it can be done either by breaking up the domain of integration according to the value of $\varkappa$, or by representing the components of $\varkappa$ as discontinuous integrals. Both methods were used in order to have a check available; the result is

$$W=-\frac{1}{30}K^6-\frac{1}{6}K^4P-\frac{83}{30}K^2P^2-\frac{997}{630}P^3. \tag{25}$$

The third-order energy of the excited state may now be calculated; it exceeds the third-order vacuum energy (21) by the amount

$$\frac{\phi_{01}^6}{2(\epsilon_1-\epsilon_0)^2}(K^6-3K^4P+6K^2P^2-3K^2Q-3R+12QP-10P^3+2Z)$$
$$+\frac{\phi_{01}^4\phi_{12}^2}{(\epsilon_1-\epsilon_0)(\epsilon_2-\epsilon_0)}[2(K^2-P)(Q-P^2)-2Z+R-3QP+2P^3]$$
$$+\frac{\phi_{01}^4\phi_{12}^2}{(\epsilon_2-\epsilon_0)^2}[-(K^2-P)(Q-P^2)+R-3QP+2P^3]+\frac{\phi_{01}^2\phi_{12}^4}{(\epsilon_2-\epsilon_0)^2}Z, \tag{26}$$

where Z may be obtained from Eqs. (24) and (25). In order to obtain the particle energy through third order, we must add to this the energy through second order, which is the sum of (15) and (22) minus (20):

$$(\epsilon_1-\epsilon_0)+\phi_{01}^2(K^2-P)-\frac{\phi_{01}^4}{2(\epsilon_1-\epsilon_0)}$$
$$\times(K^4-2K^2P-2Q+3P^2)-\frac{\phi_{01}^2\phi_{12}^2}{\epsilon_2-\epsilon_0}(Q-P^2). \tag{27}$$

Approximate Relativistic Relation Between Particle Energy and Momentum

The energy of the particle, through third order in $\mathfrak{IC}'$, is given by the sum of Eqs. (26) and (27), within the limits of the approximation that matrix elements ϕ_{nm} with $m\neq n\pm1$ are neglected. The momentum of this particle is $\mathbf{K}$, provided $\mathbf{K}$ is small in comparison with $1/l$. The relation between $\mathbf{K}$ and the momentum is not affected by the higher-order corrections to Eq. (14); this is because $\mathfrak{p}$ commutes with $\mathfrak{IC}_0$ and $\mathfrak{IC}'$ separately, so that only unperturbed energy eigenfunctions that are eigenfunctions of $\mathfrak{p}$ with the same value of $\mathbf{K}$ as Eq. (14) can mix in with it.

Before considering the relation between the energy and momentum of this particle, it is instructive to see what this relation is in the linear case ($\alpha=0$). The solutions of Eq. (10) are the harmonic oscillator wave functions; the eigenvalues and matrix elements are

$$\epsilon_n=(n+\tfrac{1}{2})(P+\mu^2)^{\frac{1}{2}},$$
$$\phi_{n,\,n+1}=(P+\mu^2)^{-\frac{1}{4}}[\tfrac{1}{2}(n+1)]^{\frac{1}{2}},$$

with other matrix elements equal to zero. With these substitutions, the sum of Eqs. (26) and (27) becomes

$$(\epsilon_1-\epsilon_0)+\phi_{01}^2(K^2-P)-\frac{\phi_{01}^4}{2(\epsilon_1-\epsilon_0)}(K^2-P)^2$$
$$+\frac{\phi_{01}^6}{2(\epsilon_1-\epsilon_0)^2}(K^2-P)^3=(P+\mu^2)^{\frac{1}{2}}+\frac{(K^2-P)}{2(P+\mu^2)^{\frac{1}{2}}}$$
$$-\frac{(K^2-P)^2}{8(P+\mu^2)^{\frac{3}{2}}}+\frac{(K^2-P)^3}{16(P+\mu^2)^{5/2}}. \tag{28}$$

The right side of Eq. (28) will immediately be recognized as the first four terms in the power series expansion of

$$[(P+\mu^2)+(K^2-P)]^{\frac{1}{2}}=(\mu^2+K^2)^{\frac{1}{2}}, \tag{29}$$

which is the relativistic expression for the energy of a particle of rest mass μ and momentum $\mathbf{K}$. This is hardly a surprising result, since the quantization of Eq. (1) with $\alpha=0$ is easily carried through exactly by using expansions of the field variables in plane waves, both in the continuum and lattice cases. The energy of a single particle is known to be given by Eq. (29), and the foregoing derivation of Eq. (28) might well be regarded as unnecessarily complicated.

It is nevertheless important to observe that Eq. (28) was derived by using a perturbation method that in the linear case can only be justified for large l (see the next to the last paragraph of Sec. II). In spite of this restriction, we presumably could, by continuing the development in powers of $\mathfrak{IC}'$, sum the series to obtain Eq. (29), which we would then be willing to accept regardless of whether or not l is large. We therefore argue that it is possible in this way to obtain a result that is valid even when the perturbation expansion from which it was derived cannot justifiably be used. We further argue that results like Eq. (29) that have a kind of relativistic character can be obtained in this way from a manifestly non-covariant theory.

We now proceed with the nonlinear case, and see how closely the sum of Eqs. (26) and (27) agrees with the left side of Eq. (28), when allowance is made in the latter for altered values of $(\epsilon_1-\epsilon_0)$ and ϕ_{01}. It is apparent that the zero- and first-order parts of both are the same. The second-order part of Eq. (27) exceeds the second-order part of Eq. (28) by

$$\left[\frac{\phi_{01}^4}{\epsilon_1-\epsilon_0}-\frac{\phi_{01}^2\phi_{12}^2}{\epsilon_2-\epsilon_0}\right](Q-P^2). \tag{30}$$

The third-order energy (26) exceeds the third-order

part of (28) by

$$\left[-\frac{3\phi_{01}^6}{2(\epsilon_1-\epsilon_0)^2}+\frac{2\phi_{01}^4\phi_{12}^2}{(\epsilon_1-\epsilon_0)(\epsilon_2-\epsilon_0)}-\frac{\phi_{01}^4\phi_{12}^2}{(\epsilon_2-\epsilon_0)^2}\right]\times(K^2-P)(Q-P^2)+\left[-\frac{3\phi_{01}^6}{2(\epsilon_1-\epsilon_0)^2}+\frac{\phi_{01}^4\phi_{12}^2}{(\epsilon_1-\epsilon_0)(\epsilon_2-\epsilon_0)}+\frac{\phi_{01}^4\phi_{12}^2}{(\epsilon_2-\epsilon_0)^2}\right](R-3QP+2P^3)+\left[\frac{\phi_{01}^6}{(\epsilon_1-\epsilon_0)^2}-\frac{2\phi_{01}^4\phi_{12}^2}{(\epsilon_1-\epsilon_0)(\epsilon_2-\epsilon_0)}+\frac{\phi_{01}^2\phi_{12}^4}{(\epsilon_2-\epsilon_0)^2}\right]Z. \quad (31)$$

In estimating the errors implied by Eqs. (30) and (31), we shall use for the ϵ's and matrix elements the numerical values given previously for the case $\alpha=\infty$. Since the individual square brackets in Eqs. (30) and (31) all vanish in the linear case ($\alpha=0$), this procedure is likely to overestimate the errors. We then find for the errors in the coefficients of K^4, K^2, and K^0 in the second-order part, 0, 0, and 19.4 percent, respectively. In similar fashion, we find for the errors in the coefficients of K^6, K^4, K^2, and K^0 in the third-order part, 0.9, 1.5, 24.5, and 19.3 percent, respectively. Thus of the ten coefficients that can be compared with the left side of Eq. (28), five are in agreement, two show about one percent errors, and three show about twenty percent errors; these are believed to overestimate the errors that would be obtained with finite α.[9]

This encourages us to regard the series on the left side of Eq. (28) as a sufficiently accurate representation of the energy of the particle. If we also equate $2\phi_{01}^2(\epsilon_1-\epsilon_0)$ to unity (the error here is 1.2 percent when $\alpha=\infty$), then these are the first four terms in the power series expansion of

$$[(\epsilon_1-\epsilon_0)^2+(K^2-P)]^{\frac{1}{2}}=(M^2+K^2)^{\frac{1}{2}},$$
$$M\equiv[(\epsilon_1-\epsilon_0)^2-P]^{\frac{1}{2}}. \quad (32)$$

We therefore interpret the quantity M in Eq. (32) as the rest mass of the particle. Moreover, following the lead provided by the discussion of the linear case above, we assume that Eq. (32) is valid for all α, and not only for large α where the perturbation calculation is justified.

Comparison of Eqs. (32) and (10) shows that M is a well-defined function of the three parameters of the theory: μ, α, and l. We have already observed that if $\alpha=0$, $M=\mu$ regardless of the value of l [see Eq. (29)]. We can now see from the structure of Eq. (10) that the addition of any positive fourth-power potential to the harmonic potential increases the spacing of the energy levels, so that $(\epsilon_1-\epsilon_0)$ is larger for finite α than it is for $\alpha=0$. It is also apparent that for any fixed finite α, the importance of the fourth-power potential increases as l decreases, and we have already seen (Sec. II) that the energy levels become infinite like $1/l$ as $l\to 0$. We therefore conclude that so long as $\alpha\neq 0$, M is larger than μ, and by an amount that becomes infinite as $l\to 0$. This is a physically satisfactory conclusion, since we expect the nonlinearity, which corresponds to an internal self-repulsion of the field, to increase the self-energy of any particle that is described by the field. It is also not surprising that this self-energy should become infinite as $l\to 0$, since this makes the particles more nearly like points.

Quantitative results can be expressed in terms of Eq. (11). We put $\beta\equiv 2^{\frac{1}{2}}(\pi^2+\mu^2l^2)/\alpha^{4/3}$ and $z(\beta)\equiv\lambda_1(\beta)-\lambda_0(\beta)$. For small values of β, $z(\beta)$ may be found by perturbing the solutions already obtained with $\beta=0$:

$$z(\beta)\cong\lambda_1(0)-\lambda_0(0)+\beta[(x^2)_{11}-(x^2)_{00}]$$
$$=2.7393+0.5398\beta.$$

For large values of β, $z(\beta)$ may be found by perturbing the harmonic oscillator solutions which are valid for $\beta=\infty$:

$$z(\beta)\cong 2\beta^{\frac{1}{2}}+3\beta^{-1}-9\beta^{-5/2}.$$

For three intermediate values of $\beta(=3, 6, 9)$, numerical integrations of Eq. (11) were performed.[10] It is then convenient to define two new variables:

$$y\equiv\frac{z^2-4\beta}{2^{8/3}}=\frac{l^2}{\alpha^{4/3}}(M^2-\mu^2),$$
$$x\equiv\frac{2^{\frac{1}{2}}\pi^{\frac{1}{2}}}{\beta^{\frac{1}{2}}}=\frac{\alpha}{(1+\mu^2l^2/\pi^2)^{\frac{1}{2}}}. \quad (33)$$

A curve of y against x is plotted in Fig. 1; from this, the value of M that corresponds to any combination of values of μ, α, and l is readily found.

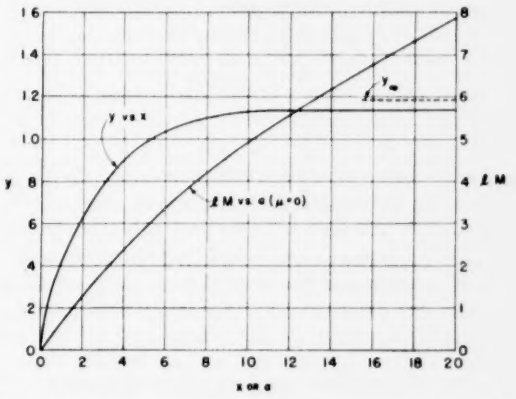

FIG. 1. Plots of quantities related to the rest mass of a free particle; see Eq. (33) *et seq.*

[9] This agreement could be improved upon by altering the definition of M in Eq. (32) to compensate for the errors in the higher-order terms. This added complicated hardly seems worthwhile at the present time.

[10] The writer is indebted to D. L. Judd of the Radiation Laboratory, University of California, for arranging for these numerical computations, and also to J. Killeen and the differential analyzer group who carried them out.

Since for finite α the field rest mass μ must always be less then the particle rest mass M, it might be argued that μ does not fulfill any useful purpose in the present theory. Then one free parameter can be eliminated by setting $\mu=0$, which means that the entire rest mass of the particle arises from the nonlinearity. From Eqs. (33), we see that for $\mu=0$, $x=\alpha$, and $lM=\alpha^{\frac{1}{2}}y^{\frac{1}{2}}$, so that it is possible to plot lM against α directly; this is also done in Fig. 1. If, for example, we choose $l=1/M$, so that l is equal to the reduced Compton wavelength of the particle, Fig. 1 shows that $\alpha\cong 1.6$.

Higher Energy Eigenvalues

We have interpreted the first two eigenvalues of Eq. (10) in terms of the particle rest mass, through Eq. (32). A question then arises as to the role played by the higher energy eigenvalues. It might at first be thought that they correspond to particles of higher rest mass. To investigate this idea, consider the analog of Eq. (15) for the excitation energy through first order of the N-fold degenerate state in which a single lattice-point oscillator has the eigenvalue ϵ_n: $\epsilon_n-\epsilon_0=P\phi_{0n}^2+K^2\phi_{0n}^2$. We have already seen that all matrix elements ϕ_{0n} are very small unless $n=1$, so that there is a wide discrepancy between the approximate rest mass $\epsilon_n-\epsilon_0$ and the approximate kinetic mass $1/(2\phi_{0n}^2)$; the momentum is of course still given by $\mathbf{K}$. It is not reasonable, therefore, to interpret the higher energy eigenvalues in terms of particles of higher rest mass.

A clue as to the part they play in the theory can be obtained by comparison with the linear case. Here the energy levels are equally spaced, so that there is degeneracy between any higher eigenvalue and multiply excited lower eigenvalues; for example, the eigenvalue ϵ_n is degenerate with excitation of n lattice points to the eigenvalue ϵ_1. Now n-fold excitation to ϵ_1 corresponds physically to the presence of n particles, so that all the other modes of excitation that are degenerate with this must be thought of as part of the description of the n-particle system, at least in the case of large l, where the perturbation theory may be used in the linear case.

We believe that a similar interpretation of the higher eigenvalues is required in the nonlinear case as well, even though the system is no longer degenerate. We shall see in the next section that such states form part of the description of the scattering of one particle by another, and are essential if the result is to have the proper behavior when $\alpha=0$ (linear case).

IV. SCATTERING OF ONE FREE PARTICLE BY ANOTHER

We have seen that a single free particle of momentum $\mathbf{K}$ can be described to first order by the wave function (14). We therefore expect that two particles with momenta $\mathbf{K}_1$ and $\mathbf{K}_2$ can be described, at least approximately, by the wave function

$$\Psi_{11}(\mathbf{K}_1,\mathbf{K}_2)=N^{-1}\sum_s{\sum_t}' e^{i(\mathbf{K}_1\cdot\mathbf{r}_s+\mathbf{K}_2\cdot\mathbf{r}_t)}U_{11}(s,t),$$
$$U_{11}(s,t)\equiv u_1(\phi_s)u_1(\phi_t)\prod_q{}'' u_0(\phi_q); \tag{34}$$

the dash on the second summation means that the terms $t=s$ is omitted, and the double dash on the product means that the terms $q=t$ and $q=s$ are omitted. Note that since the states $\Psi_{11}(\mathbf{K}_1,\mathbf{K}_2)$ and $\Psi_{11}(\mathbf{K}_2,\mathbf{K}_1)$ are identical and the state $\mathbf{K}_1=\mathbf{K}_2$ is permitted, the particles obey Einstein-Bose statistics.

An important difference between Eqs. (14) and (34) is that (14) diagonalizes the perturbation $\mathcal{H}'$ to first order while (34) does not. This is because there is first-order interaction with all the states $\Psi_{11}(\mathbf{K}_1',\mathbf{K}_2')$ for which $\mathbf{K}_1'+\mathbf{K}_2'=\mathbf{K}_1+\mathbf{K}_2$, and also with the state

$$\Psi_2(\mathbf{K}_1+\mathbf{K}_2)=N^{-\frac{1}{2}}\sum_s e^{i(\mathbf{K}_1+\mathbf{K}_2)\cdot\mathbf{r}_s}U_2(s),$$
$$U_2(s)\equiv u_2(\phi_s)\prod_t{}' u_0(\phi_t). \tag{35}$$

Because of the commutativity of $\mathfrak{p}$ and $\mathcal{H}'$, the total $\mathbf{K}$ vector must be the same for all combining states.[11] We now proceed to make a first-order diagonalization of $\mathcal{H}$, using an arbitrary linear combination of the above states:

$$\Psi=\sum_{\boldsymbol{\kappa}} B(\boldsymbol{\kappa})\Psi_{11}(\boldsymbol{\kappa},\mathbf{K}-\boldsymbol{\kappa})+A\Psi_2(\mathbf{K}). \tag{36}$$

If the wave function (36) were an exact eigenfunction of $\mathcal{H}$, we would have $(\mathcal{H}-E)\Psi=0$, where E is the total first-order energy of the initial collision state with momenta $\boldsymbol{\kappa}_0$ and $\mathbf{K}-\boldsymbol{\kappa}_0$:

$$E=(N-2)\epsilon_0+2\epsilon_1+[\kappa_0^2+(\mathbf{K}-\boldsymbol{\kappa}_0)^2-2P]\phi_{01}^2.$$

Since it is not a solution, the best we can do is require that when $(\mathcal{H}-E)\Psi$ is analyzed into states that correspond to the excitation of 1, 2, $\cdots$ lattice points by various amounts, the coefficients of Ψ_{11} and Ψ_2 are zero. This means that

$$\int\cdots\int\Psi_{11}^*(\boldsymbol{\kappa}',\mathbf{K}-\boldsymbol{\kappa}')(\mathcal{H}-E)\Psi d\phi_1\cdots d\phi_N=0,$$
$$\int\cdots\int\Psi_2^*(\mathbf{K})(\mathcal{H}-E)\Psi d\phi_1\cdots d\phi_N=0, \tag{37}$$

where $\boldsymbol{\kappa}'$ is arbitrary. The first of Eqs. (37) gives

$$[B(\boldsymbol{\kappa}')+B(\mathbf{K}-\boldsymbol{\kappa}')][\kappa'^2+(\mathbf{K}-\boldsymbol{\kappa}')^2-\kappa_0^2$$
$$-(\mathbf{K}-\boldsymbol{\kappa}_0)^2]\phi_{01}^2-2\phi_{01}^2N^{-1}\sum_{\boldsymbol{\kappa}}B(\boldsymbol{\kappa})$$
$$\times[\kappa'^2+(\mathbf{K}-\boldsymbol{\kappa}')^2+\kappa^2+(\mathbf{K}-\boldsymbol{\kappa})^2-\kappa_0^2$$
$$-(\mathbf{K}-\boldsymbol{\kappa}_0)^2-2P]+A\phi_{01}\phi_{12}N^{-\frac{1}{2}}$$
$$\times[\kappa'^2+(\mathbf{K}-\boldsymbol{\kappa}')^2-2P]=0, \tag{38}$$

[11] There would also be interaction with the vacuum state (12) if $\mathbf{K}_1+\mathbf{K}_2$ were exactly zero, that is, if the lattice were at rest in the center-of-mass coordinate system. The extra term introduced does not seem physically plausible, so we avoid it by assuming that $\mathbf{K}_1+\mathbf{K}_2\neq 0$.

and the second gives

$$A\{\epsilon_2+\epsilon_0-2\epsilon_1-[\kappa_0^2+(\mathbf{K}-\kappa_0)^2-2P]\phi_{01}^2\}$$
$$+\phi_{01}\phi_{12}N^{-1}\sum_{\kappa}B(\kappa)[\kappa^2+(\mathbf{K}-\kappa)^2-2P]=0. \quad (39)$$

Elimination of A between Eqs. (38) and (39) yields a set of simultaneous algebraic equations for the quantities $B(\kappa')$ with all possible values for κ':

$$[B(\kappa')+B(\mathbf{K}-\kappa')][\kappa'^2+(\mathbf{K}-\kappa')^2-\kappa_0^2-(\mathbf{K}-\kappa_0)^2]$$
$$=2N^{-1}\sum_{\kappa}B(\kappa)\{[\kappa'^2+(\mathbf{K}-\kappa')^2+\kappa^2+(\mathbf{K}-\kappa)^2$$
$$-\kappa_0^2-(\mathbf{K}-\kappa_0)^2-2P]-(2\Delta E)^{-1}$$
$$\times\phi_{12}^2[\kappa'^2+(\mathbf{K}-\kappa')^2-2P][\kappa^2+(\mathbf{K}-\kappa)^2-2P]\}, \quad (40)$$
$$\Delta E\equiv[\kappa_0^2+(\mathbf{K}-\kappa_0)^2-2P]\phi_{01}^2+2\epsilon_1-(\epsilon_2+\epsilon_0).$$

Equation (40) is a Tamm-Dancoff-type approximation to the field equation, in which only the states corresponding to two singly excited lattice points and to one doubly excited lattice point are included. We do not solve Eq. (40) exactly, but rather find the first Born approximation to the solution, by putting

$$B(\kappa)=\delta_{\kappa,\kappa_0}+b(\kappa), \quad b(\kappa)\ll 1, \quad (41)$$

and neglecting $b(\kappa)$ in comparison with unity. Substitution of Eq. (41) into Eq. (40) gives, for κ' different from κ_0 and $\mathbf{K}-\kappa_0$:

$$b(\kappa')+b(\mathbf{K}-\kappa')=\frac{2[\kappa'^2+(\mathbf{K}-\kappa')^2-2P]}{N[\kappa'^2+(\mathbf{K}-\kappa')^2-\kappa_0^2-(K-\kappa_0)^2]}$$
$$\times\left\{1-\frac{[\kappa_0^2+(\mathbf{K}-\kappa_0)^2-2P]\phi_{01}^2}{2\Delta E}\right\}. \quad (42)$$

The two-particle part of Ψ may now be found by rewriting the first term on the right side of Eq. (36) as

$$\tfrac{1}{2}\sum_{\kappa}[B(\kappa)+B(\mathbf{K}-\kappa)]\Psi_{11}(\kappa,\mathbf{K}-\kappa)$$

and substituting from Eqs. (41) and (42):

$$\Psi_{11}(\kappa_0,\mathbf{K}-\kappa_0)+N^{-1}\sum_{\kappa}\frac{[\kappa^2+(\mathbf{K}-\kappa)^2-2P]}{[\kappa^2+(\mathbf{K}-\kappa)^2-\kappa_0^2-(\mathbf{K}-\kappa_0)^2]}$$
$$\times\left\{1-\frac{[\kappa_0^2+(\mathbf{K}-\kappa_0)^2-2P]\phi_{01}^2}{2\Delta E}\right\}\cdot\Psi_{11}(\kappa,\mathbf{K}-\kappa). \quad (43)$$

The physical significance of Eq. (43) can be seen by substituting for Ψ_{11} from Eq. (34), and interpreting the coefficient of $U_{11}(s,t)$ as the probability amplitude for finding the two particles at $\mathbf{r}_s$ and $\mathbf{r}_t$. We take the limit $N\to\infty$ by replacing the summation over κ by an integral, as in Sec. III:

$$N^{-1}\sum_{\kappa}[\quad]\to(l/2\pi)^3\int[\quad]d\tau.$$

As with the usual Born approximation, the requirement that the scattered wave be outgoing means that the path of integration must pass below the singularity in the integrand when the integral over the magnitude κ of the momentum is carried out. The square of the amplitude of the outgoing wave gives the differential scattering cross section. Since the summand in Eq. (43) is independent of the directions of the momenta in the center-of-mass coordinate system, the scattering is spherically symmetric in this coordinate system. The total cross section, when allowance is made for the identity of the two particles in the normalization of the incident plane wave, is

$$\sigma=\frac{l^6}{\pi}(K_0^2+\tfrac{1}{4}K^2-P)^2\left\{1-\frac{(K_0^2+\tfrac{1}{4}K^2-P)\phi_{12}^2}{\Delta E}\right\}^2,$$
$$\Delta E=2(K_0^2+\tfrac{1}{4}K^2-P)\phi_{01}^2+2\epsilon_1-(\epsilon_2+\epsilon_0), \quad (44)$$

where $\mathbf{K}_0\equiv\frac{1}{2}\mathbf{K}-\kappa_0$ is the momentum of one of the particles with respect to the center of mass.[12]

We note first that for the linear case, which is included in the present calculation because all of the degenerate states are retained, $2\epsilon_1=\epsilon_2+\epsilon_0$ and $\phi_{12}^2=2\phi_{01}^2$, so that the scattering cross section is zero. This is as it should be in a theory that admits of a superposition principle.

In the nonlinear case, the two terms in the curly bracket of Eq. (44) do not cancel. The first term can be shown to arise from the fact that there is no term $U(s,s)$ is the summation of Eq. (34); the product of plane waves is not quite complete, and the "hole" when s and t are equal results in scattering. The second term arises from the second-order transition through the state $\Psi_2(\mathbf{K})$, as is evident from the fact that it contains ϕ_{12} and ϵ_2. Since this calculation makes use of the perturbation theory, it is only valid when $\alpha\gg 1$. Then the second term is smaller than the first term by a factor of order $1/\alpha^{4/3}$. A further analysis shows that the first term corresponds to a repulsive and the second to an attractive interaction. The second term can in principle give rise to a resonance when $\Delta E\cong 0$, that is, when the total energy of the colliding particles equals that of the state $\Psi_2(\mathbf{K})$. This resonance is masked by the P term in the kinetic energy of the colliding particles, which cannot be treated correctly by a calculation of this order (see Sec. III).

Since the total momentum $\mathbf{K}$ of the two colliding particles appears in the cross section, the result is not Galilean-invariant.[13] However, as might be expected, the lack of Galilean invariance appears only when the wavelengths of the particles are comparable with the lattice constant, and then the interpretation in terms of momentum breaks down. For long wave lengths, K_0^2 and K^2 can be neglected in comparison with P, and

[12] Equation (44) in the case $\mathbf{K}\cong 0$ was first derived by D. R. Yennie, who kindly informed the writer of this calculation.

[13] A further lack of Galilean invariance is present in that the case $\mathbf{K}=0$ is exceptional (see reference 11).

the total cross section for large α is

$$\sigma \cong l^6 P^2/\pi = \pi^3 l^2. \tag{45}$$

The spherical symmetry of the scattering implies that the interaction is of very short range, and the proportionality of Eq. (45) with l^2 is consistent with this since the smallest length that can occur in the theory is l. This appearance of an essentially point repulsion between particles is in agreement with the interpretation of the ϕ^4 term in the continuum field Hamiltonian as a point-contact repulsion.[14]

V. INTERACTION WITH NUCLEONS

Nucleons as Classical Sources

Nucleons may be introduced into the theory as classical sources for the quantized field.[1] We assume that the source-field (nucleon-meson) coupling is linear,[15] and add to the continuum Hamiltonian (1) the interaction

$$H_i = -\int g(\mathbf{r})\phi d\tau, \tag{46}$$

where $g(\mathbf{r})$ is proportional to the density of nucleons. Neutrons and protons are coupled to mesons in the same way in the present treatment, and their distribution is assumed to be constant in time. In analogy with Eq. (4), we define the lattice source density

$$g_s \equiv l^3 \int f(\mathbf{r}-\mathbf{r}_s) g(\mathbf{r}) d\tau,$$

where the coefficient has been chosen so that

$$\sum_s g_s = \int g(\mathbf{r}) d\tau.$$

We then write for the lattice interaction Hamiltonian

$$\mathcal{H}_i = -l^{-\frac{1}{2}} \sum_s g_s \phi_s, \tag{47}$$

which approaches H_i as $l \to 0$.

Since $\mathcal{H}_i$ is a sum of terms each of which involves a single lattice point, it can be included with $\mathcal{H}_0$ as part of the unperturbed Hamiltonian. This means that arbitrarily strong couplings can be included within the framework of the present theory. Equation (10) then becomes

$$\left[-\frac{1}{2}\frac{d^2}{d\phi_s^2} + \tfrac{1}{2}(P+\mu^2)\phi_s^2 + \frac{\alpha^2}{4l^3}\phi_s^4 - \frac{g_s}{l^{\frac{1}{2}}}\phi_s\right] u_{sn}(\phi_s) = \epsilon_{sn} u_{sn}(\phi_s), \tag{48}$$

where the subscript s must be retained in case g_s in Eq. (47) is not the same for all lattice points. It is apparent that the energy eigenvalues of Eq. (48) form a discrete set extending from a smallest value (which is negative if $|g_s|$ is sufficiently large) to $+\infty$. The eigenfunctions u_{sn} with given s form a complete *orthonormal* set, but do not have definite parities if $g_s \neq 0$.

Nucleon Isobaric State

Suppose that a single nucleon is present at the point $\mathbf{r}_0$, so that $g_0 = g$, and $g_s = 0$ for $s \neq 0$. We assume that α is large so that $\mathcal{H}'$ can be treated as a perturbation. Then the vacuum state is that in which all lattice points are in their lowest states, and has the zero-order energy $(N-1)\epsilon_0(0) + \epsilon_0(g)$, where $\epsilon_n(g)$ is the $(n+1)$th energy level of Eq. (48) when $g_s = g$. The first excited state has a zero-order energy that exceeds the vacuum energy by $\epsilon_1(g) - \epsilon_0(g)$ or $\epsilon_1(0) - \epsilon_0(0)$, according as the nucleon lattice point is or is not the one that is excited. As discussed in Sec. III, the latter excitation energy is related to the rest mass of a free particle; it is then natural to interpret the former excitation energy in terms of an isobaric state of the nucleon. If $\epsilon_1(g) - \epsilon_0(g)$ is larger than $\epsilon_1(0) - \epsilon_0(0)$, as is actually the case, the isobaric state will be degenerate with the state of a nucleon plus a free meson with an appropriate amount of kinetic energy. Then since these two states are coupled together by $\mathcal{H}'$, the isobaric state will be short-lived and manifest itself mainly as a resonance in the meson-nucleon scattering, as is discussed in the next subsection.

If we apply to Eq. (48) the change of variables that takes Eq. (10) into Eq. (11), we get

$$\frac{d^2 u_n}{dx^2} + (\lambda_n - \beta x^2 - x^4 + \gamma x) u_n = 0, \qquad \beta \equiv 2^{\frac{1}{3}}(\pi^2 + \mu^2 l^2)/\alpha^{4/3}, \quad \gamma \equiv 2^{\frac{1}{3}} g/\alpha. \tag{49}$$

For α large compared to unity but not necessarily large compared to g, the βx^2 term can be neglected, and the effect of the γx term by itself can be investigated. A combination of perturbation and variational methods can be used to show that, for small γ,

$$\lambda_0 \cong 1.0605 - 0.1318\gamma^2, \qquad \lambda_1 \cong 3.7998 - 0.0152\gamma^2. \tag{50}$$

For large γ, the "potential" $x^4 - \gamma x$ can be approximated by a parabola, and a WKB calculation shows that

$$\lambda_0 \cong -3(\gamma/4)^{4/3} + 6^{\frac{1}{3}}(\gamma/4)^{\frac{1}{3}}, \qquad \lambda_1 \cong -3(\gamma/4)^{4/3} + (54)^{\frac{1}{3}}(\gamma/4)^{\frac{1}{3}}. \tag{51}$$

For three intermediate values of $\gamma (= 1, 2, 3)$, numerical calculations were carried out at Berkeley.[10] Figure 2 is a plot of $[\lambda_1(\gamma) - \lambda_0(\gamma)] - [\lambda_1(0) - \lambda_0(0)]$ against γ for $\beta = 0$, which shows that the isobaric state is in fact unstable in this case.

[14] See I; the scattering predicted by the usual quantization of Eq. (1), treating the ϕ^4 term as a perturbation ($\alpha \ll 1$), is also spherically symmetric and the total cross section is $9\alpha^4/16\pi\mu^2$ for low-energy particles.

[15] Other possibilities are discussed by L. I. Schiff, Phys. Rev. **84**, 10 (1951); **86**, 856 (1952); Berger, Foldy, and Osborn, Phys. Rev. **87**, 1061 (1952).

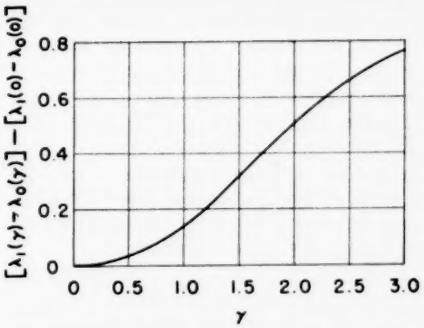

FIG. 2. The ordinate is proportional to the isobaric state energy, and the abscissa to the nucleon source strength.

Meson-Nucleon Scattering

The cross section for meson-nucleon scattering can be calculated in exact analogy with the meson-meson scattering calculation of Sec. IV. In place of Eq. (36) we adopt the following Tamm-Dancoff-type wave function:

$$\Psi=\sum_{\mathbf{k}} B(\mathbf{K})\Psi_1'(\mathbf{K})+AU_1(0),$$

where $\Psi_1'(\mathbf{K})$ is given by Eq (14) except that the nucleon lattice point ($s=0$) is excluded from the summation. Note that because of the presence of the nucleon, K is no longer a strict constant of the motion, so that states with different total $\mathbf{K}$ vectors can mix together. In solving the resulting equations by the Born approximation, we put $B(\mathbf{K})=\delta_{\mathbf{K},\mathbf{K}_0}+b(\mathbf{K})$, where $b(\mathbf{K})\ll 1$ and $\mathbf{K}_0$ is the incident meson momentum.

The scattering is spherically symmetric, and the total cross section is

$$\sigma=\frac{l^6}{4\pi}(K_0^2-P)^2\left\{1-\frac{(K_0^2-P)\phi_{01}'^2}{\Delta E}\right\}^2,$$
$$\Delta E=(K_0^2-P)\phi_{01}^2+(\epsilon_1-\epsilon_0)-(\epsilon_1'-\epsilon_0'). \tag{52}$$

The primes in Eq. (52) refer to quantities calculated at the nucleon lattice point. We note first that for the linear case, the energy levels and matrix elements are not affected by the presence of the nucleon, so that the two terms in the curly bracket cancel. Such a vanishing cross section is to be expected since, as is well known, the presence of a fixed source does not affect the quantization of a real linear field.[16] The same cancellation occurs, as it must, in the nonlinear case when g is set equal to zero.

In the nonlinear case with $g\neq 0$, the two terms in the curly bracket of Eq. (52) do not cancel. In analogy with the meson-meson scattering calculation (Sec. IV), the first term arises from the "hole" in the normal structure of the lattice at the point $\mathbf{r}_0$, while the second term comes from the second-order transition through the state $U_1(0)$. Again the first term corresponds to a repulsive and the second to an attractive interaction. The second term should give rise to a resonance when $\Delta E\cong 0$, that is, when the total energy of the incident meson equals that of the isobaric state $U_1(0)$; however, the resonance is masked by the P term in the kinetic energy of the incident meson, which requires a higher-order calculation for its correct treatment. When the perturbation theory is taken seriously ($\alpha\gg 1$), the second term is small in comparison with the first term, and the total cross section for scattering of a slow meson by a nucleon is

$$\sigma\cong l^6P^2/4\pi=\pi^3l^2/4. \tag{53}$$

The spherical symmetry of the scattering and the proportionality of Eq. (53) with l^2 imply an essentially point interaction.

Interaction Between Two Nucleons

The zero-order vacuum energy of the lattice with two nucleons present is $(N-2)\epsilon_0(0)+2\epsilon_0(g)$, regardless of where the nucleons are located provided that they do not occupy the same lattice point. There is a first-order change in the energy since the parity is not a good quantum number for the nucleon lattice points, and also a second-order change in the energy which arises from states in which one or another lattice point is excited. Both of these are position-dependent, but are small if the perturbation treatment of $\mathcal{H}'$ is justified.

There still remains a zero-order point interaction between the two nucleons, since the vacuum energy is altered when the two nucleons occupy the same lattice point. This interaction may be thought of as having a range of order l and a value

$$[\epsilon_0(2g)+\epsilon_0(0)]-2\epsilon_0(g),$$

which is negative. With the notation of Eq. (49), the quantity $2\lambda_0(\gamma)-[\lambda_0(0)+\lambda_0(2\gamma)]$ is proportional to the negative of the interaction energy. It is plotted against γ for $\beta=0$ in Fig. 3, which shows that the interaction is attractive in this case.

Saturation of Nuclear Forces

Thus far in this section we have considered situations in which one or two nucleons are introduced as classical

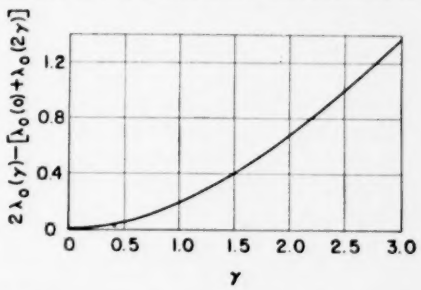

FIG. 3. The ordinate is proportional to the strength of the nucleon-nucleon interaction, and the abscissa to the nucleon source strength.

[16] See for example G. Wentzel, *Quantum Theory of Fields* (Interscience Publishers, Inc., New York, 1949), p. 47.

sources localized at as many lattice points. In considering many nucleons assembled to form a nucleus, we could continue in this way, or we could spread the sources out over more lattice points than there are nucleons. It seems more reasonable to follow the former course, according to which an assembly of n_N nucleons has a zero-order energy which is proportional to $(N-n_N)\lambda_0(0)+n_N\lambda_0(\gamma)$, regardless of how they are located so long as they are not crowded together onto fewer lattice points than there are nucleons.

If now the nucleon density is increased, so that the n_N nucleons are crowded into n_l lattice points ($n_l \leqq n_N$), the energy will be proportional to

$$(N-n_l)\lambda_0(0)+n_l\lambda_0(\zeta\gamma), \quad \zeta \equiv n_N/n_l. \tag{54}$$

The potential energy per nucleon is proportional to the difference between Eq. (54) and the value of Eq. (54) with $\zeta=1$, divided by n_N:

$$\frac{1}{\zeta}[\lambda_0(\zeta\gamma)-\lambda_0(0)]-[\lambda_0(\gamma)-\lambda_0(0)]. \tag{55}$$

For small values of $\zeta\gamma$, Eq. (50) shows that this potential energy per nucleon is negative (attractive) and a linear function of the nucleon density ζ. For large values of $\zeta\gamma$, Eq. (51) shows that Eq. (55) is a linear function of $-\zeta^{\frac{1}{3}}$. Figure 4 is a plot of $-[\lambda_0(\gamma)-\lambda_0(0)]$ against γ, that can be used to evaluate Eq. (55) in the general case.

The stability of nuclear matter and the saturation of nuclear forces can now be discussed qualitatively, as was done earlier with the help of classical field theory.[17] For lack of a more consistent mode of description, we say that the kinetic energy per nucleon is proportional to the $\frac{2}{3}$ power of the density or of ζ; this regards the nucleons as described by wave functions in a continuum, not a lattice space. Then stability is attained only when the density becomes so great that the $\frac{1}{3}$-power law for the potential energy dominates. This evidently occurs only for nucleon densities somewhat greater than $1/l^3$. In this domain, the lattice-space quantization and the classical theory[17] give similar results for any power of nonlinearity (not only for the fourth power considered above), since the derivation of the leading terms in Eq. (51) is based on the WKB method and hence is essentially classical.

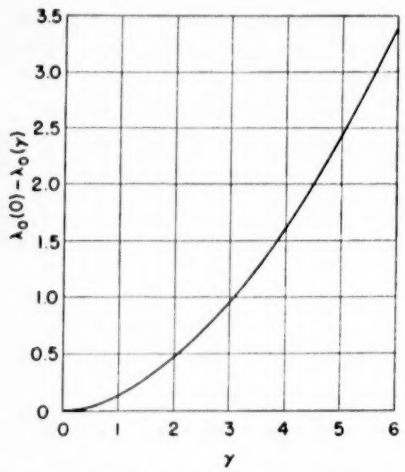

FIG. 4. Curve from which Eq. (55), which is related to the saturation of nuclear forces, can be computed.

[17] See I, Sec. II.

It is also worth noting that a qualitatively similar result would have been obtained if we had permitted each nucleon to be spread out initially over several lattice points. Collapse would again occur down to a density somewhat greater than $1/l^3$.

In the classical theory, the interaction between two nucleons embedded in nuclear matter was found to be weaker than that in empty space.[18] The quantity plotted in Fig. 3, which is proportional to the negative of the interaction energy in empty space, must be replaced in nuclear matter by $2\lambda_0(\zeta\gamma+\gamma)-[\lambda_0(\zeta\gamma)+\lambda_0(\zeta\gamma+2\gamma)]$. This quantity decreases as the curvature of a plot of $-\lambda_0(\zeta\gamma)$ against $\zeta\gamma$ decreases, that is, as ζ increases, since the curve in Fig. 4 straightens out as the abscissa increases. Thus, as in the classical theory, the two-nucleon interaction decreases as the density of nucleons increases.

Interaction of Mesons with Nuclear Matter

In the last subsection, the ground-state energy of a distribution of classical sources was considered. A study of the first excited state of this system yields information on the interaction of mesons with nuclear matter, and provides an extension of the meson-nucleon scattering calculation that was given earlier in this section.

It is apparent that for an arbitrary distribution of sources, **K** is not even approximately a constant of the motion, so that it is disadvantageous to use wave functions of the type (14). Instead, we take for our Tamm-Dancoff-type wave function

$$\Psi=\sum_s b(s)U_1(s),$$

and require that

$$\int\cdots\int U_1^*(t)(\mathcal{H}-E)\Psi d\phi_1\cdots d\phi_N=0$$

for all t. This leads to the following equation:

$$\{(\epsilon_{t1}-\epsilon_{t0})-P(\phi_t)_{01}{}^2+[(\phi_t)_{11}-(\phi_t)_{00}]\times\sum_s{}' A_{st}(\phi_s)_{00}-E_0\}b(t)+(\phi_t)_{01}\sum_s{}' A_{st}(\phi_s)_{01}b(s)=0, \tag{56}$$

$$E_0\equiv E-\sum_s \epsilon_{s0}-\tfrac{1}{2}\sum_s\sum_q{}' A_{sq}(\phi_s)_{00}(\phi_q)_{00}.$$

[18] See I, Sec. IX.

E_0 is the amount by which the energy E of the first excited state under consideration exceeds the first-order ground-state energy.

If the source strength g_s is different from zero at several lattice points, Eq. (56) will be very difficult to solve. However, if g_s changes little between neighboring lattice points, we can assume that there exist solutions for which $b(s)$ is also slowly varying. It is then convenient to define a function $\chi(\mathbf{r}_s)\equiv(\phi_s)_{01}b(s)$, and make use of the easily established relation

$$\sum_s A_{st}\chi(\mathbf{r}_t)\underset{l\to 0}{\longrightarrow}-[\nabla^2\chi(\mathbf{r})]_{\mathbf{r}=\mathbf{r}_t}. \tag{57}$$

This does not mean that we actually take the limit $l\to 0$, but rather that we assume that $\chi(\mathbf{r}_t)$ varies sufficiently slowly from one lattice point to the next so that we can regard it as a continuous function of the lattice-point coordinates. We are thus led to the approximate wave equation

$$\begin{aligned}&-(\phi_t)_{01}{}^2\nabla^2\chi(\mathbf{r}_t)+V(\mathbf{r}_t)\chi(\mathbf{r}_t)=E_0\chi(\mathbf{r}_t),\\ &V(\mathbf{r}_t)\equiv(\epsilon_{t1}-\epsilon_{t0})-P(\phi_t)_{01}{}^2\\ &\qquad+[(\phi_t)_{11}-(\phi_t)_{00}]\sum_s{}' A_{st}(\phi_s)_{00}.\end{aligned} \tag{58}$$

A simple example of Eq. (58) is that in which all g_s are zero (single free meson). Then $(\phi_t)_{11}=(\phi_t)_{00}=0$, and $V(\mathbf{r}_t)=\epsilon_1-\epsilon_0-P\phi_{01}{}^2=$constant. There are plane wave solutions $\chi(\mathbf{r}_t)=C\exp i(\mathbf{K}\cdot\mathbf{r}_t)$, where

$$E_0=\epsilon_1-\epsilon_0+(K^2-P)\phi_{01}{}^2,$$

in agreement with Eqs. (14) and (15). The point at which the limiting procedure (57) shows up as an approximation is that in the present analysis $\mathbf{K}$ can be any vector, whereas for a correct solution $\mathbf{K}$ must be one of the reciprocal lattice vectors. So long as $\mathbf{K}$ is small in comparison with $1/l$, χ is actually slowly varying as assumed in Eq. (57), and it makes little difference whether or not $\mathbf{K}$ is precisely a reciprocal lattice vector.

Suppose now that g_s is different from zero only within a restricted region of space, which corresponds to a nucleus. Then outside the nucleus, χ may be built up out of solutions of the free-particle wave equation with definite values for the energy and the magnitude $\mathbf{K}$ of the propagation vector. Inside the nucleus, Eq. (58) is the nonrelativistic Schrödinger equation for the motion of a particle with potential energy $V(\mathbf{r}_t)$, position-dependent rest mass $\frac{1}{2}(\phi_t)_{01}{}^2\cong\epsilon_{t1}-\epsilon_{t0}$, and total energy E_0. For large α, the dominant part of $V(\mathbf{r}_t)$ is $\epsilon_{t1}-\epsilon_{t0}$, which is larger inside the nucleus than it is outside (see Fig. 2). Thus the nucleus acts as a repulsive potential for mesons incident from without. This confirms the result obtained earlier from classical field theory.[19] As pointed out there, a consequence of this result is that production of mesons in heavy nuclei should be primarily a surface effect, since the wave function of the created meson does not penetrate far into the nucleus.

[19] See I, Sec. XI.

VI. CONCLUDING REMARKS

The method of quantization employed in this paper is a natural one to use whenever the gradient terms in the field Hamiltonian can be treated as a perturbation and there is no immediate requirement of covariance. Then the continuum solutions are expected to be limiting cases of the lattice solutions as $l\to 0$, and the fact that solutions cease to exist in this limit must be regarded as a strong indication that they do not exist at all for the continuum field Hamiltonian This has indeed been the presumption that underlies most of the recent work in quantum field theory; meaningful results can be obtained only by a renormalization procedure, using covariance as a guide. In the present case, covariance cannot be used in this way; nevertheless, a quasi-relativistic solution for the motion of a single free particle has been obtained.

It is tempting to regard the introduction of the lattice constant l as analogous to the renormalization procedure, in that it enables one to extract finite results from an otherwise divergent theory. It would then follow that l is a physically real quantity, and not just a mathematical artifice that is to be eliminated at as early a stage as possible. Unfortunately for this point of view, Fig. 1 shows that for $\mu=0$ and M equal to the rest mass of a meson, either l must be larger than is physically reasonable or α must be so small that the perturbation theory cannot be employed. This last may not be an obstacle if the results of Secs. IV and V can be given the quasi-relativistic form of the results of Sec III.

It is possible in principle to apply lattice-space quantization to coupled meson-nucleon fields. The gradient term in the Dirac Hamiltonian for the nucleon field is then included as part of the perturbation, and the nucleon rest mass and coupling term (when the latter is of point type) are included in the unperturbed Hamiltonian. The neutral scalar nonlinear meson theory with scalar coupling differs in only minor respects from the classical source theory considered in Sec. V. The principal difference is that g_s is limited to an integer multiple m of some basic value, where m ranges from -4 to $+4$; the number 4 appears because there are two kinds of Dirac particles (neutrons and protons) each with two spin states. For pseudoscalar particles with pseudoscalar coupling, the calculation is far more complicated because the different components of the Dirac fields are coupled together. It is then necessary to solve a set of simultaneous differential equations at each lattice point. Some aspects of this situation are being explored.

The writer takes pleasure in expressing his appreciation to Dr. D. R. Yennie for several helpful and illuminating conversations.

Production of Neutral Mesons by 340-Mev Protons on Hydrogen

J. W. MATHER AND E. A. MARTINELLI
Radiation Laboratory, Department of Physics, University of California, Berkeley, California
(Received April 15, 1953)

The production of neutral mesons by 340-Mev protons on hydrogen has been measured directly by detecting a single gamma ray from the two gamma-ray decay of a neutral meson, at 90° to the proton beam. A liquid hydrogen target and a focusing Čerenkov counter are described. The ratio of the cross section for neutral meson production from hydrogen relative to carbon is

$$\sigma_H/\sigma_C=0.0059\pm0.0009,$$

where the error is standard deviation. Using the absolute cross section of neutral meson production from carbon as 1.5×10^{-27} cm², one obtains the neutral meson production cross section for hydrogen to be 8.8×10^{-30} cm².

The transition ${}^3P\rightarrow{}^1S$ (allowed by the conservation of angular momentum and parity) for the protons can be interpreted as a triplet p-state interaction with emission of an s-state neutral meson. The agreement with the existing data at proton energies of 440 Mev is fair. The 340- and 440-Mev data give two points on the neutral meson excitation function curve, showing a steep rise. The experimental results give some evidence for the breakdown of the approximate selection rule which forbids the emission of s-state neutral mesons with final s-state nucleons. The relative cross section for carbon and nitrogen indicates that the yield of neutral mesons is due to the interaction of the incident protons with the neutrons in the nuclei.

INTRODUCTION

IT has been established by Hales, Hildebrand, Knable, and Moyer[1] using a CH_2-C subtraction method, that the production cross section of neutral mesons by 340-Mev protons on hydrogen is either zero or less than two percent of the carbon yield. An attempt was made to measure the direct production of neutral mesons from a liquid hydrogen target at 90° to the 340-Mev proton beam, using a Čerenkov radiation counter[2,3] that employs a triple coincidence technique to view the Čerenkov radiation. At the beginning of the experiment, it was thought that the experimental result would yield at least an upper limit for neutral meson production from hydrogen because only one gamma ray from a two gamma-ray neutral meson decay[4,5] was detected. No attempt was made to detect the coincident gamma rays from neutral meson decay, because of the expected low yield.

TABLE I. Transitions allowed by Pauli principle, conservation of angular momentum and parity for production of pseudoscalar neutral mesons in nucleon-nucleon collisions $(p, p\pi^0)$.

Initial state p, p	Final state π^0 meson	p, p	Transition
${}^1S_0$	s	${}^3P_0$	${}^1S_0\rightarrow{}^3P_0$
	p	forbidden	none
${}^3P_0$	s	${}^1S_0$	${}^3P_0\rightarrow{}^1S_0$
↓	p	${}^3P_1$	${}^3P_0\rightarrow{}^3P_1$
etc.			

Recent evidence of the hydrogen cross section at bombarding proton energies of 440 Mev has been obtained by Marshall, Marshall, Nedzel, and Warshaw,[6] showing that the production cross section of neutral mesons from hydrogen is $0.45\pm0.15\times10^{-27}$ cm² at that energy.

For the reaction $(p, p\pi^0)$, assuming a pseudoscalar neutral meson emitted in a p state, and if only s states for the product nucleons are considered, it can be shown from the conservation laws of total angular momentum and parity that the above reaction is forbidden. If the production of mesons in p states represents a universal type of coupling for nucleon-nucleon collisons, then there exists a general selection rule prohibiting the $(p, p\pi^0)$ process for final s-state nucleons.

From an examination of Table I, transitions yielding higher angular momentum states for the two final protons are possible, but since the energy available to the two final protons in the center-of-mass system is approximately 8 Mev, higher angular momentum states than s states will be suppressed. However, the transition ${}^3P\rightarrow{}^1S$ yielding an s-state meson is possible and is thought to be responsible for the neutral mesons observed near the threshold.

There is evidence from the $(p, p\pi^+)$ experiment by Cartwright, Richman, Wilcox, and Whitehead[7] and more recently by Schulz[8] that the positive pi meson is emitted predominately in a p state in the center-of-mass system. However, the s-state yield of positive mesons is not zero[8] and is thought to be approximately one-eight to one-tenth of the p-state yield.

[1] Hales, Hildebrand, Knable, and Moyer, Phys. Rev. **85**, 373 (1952).
[2] J. Marshall, Phys. Rev. **81**, 275 (1951).
[3] J. W. Mather and E. A. Martinelli, University of California Radiation Laboratory Report UCRL-1646, 1952 (unpublished).
[4] Steinberger, Panofsky, and Steller, Phys. Rev. **78**, 802 (1950).
[5] C. N. Yang, Phys. Rev. **77**, 242 (1950).
[6] Marshall, Marshall, Nedzel, and Warshaw, Phys. Rev. **88**, 632 (1952).
[7] Cartwright, Richman, Wilcox, and Whitehead, Phys. Rev. **78**, 823 (1950) and **81**, 652 (1951).
[8] A. G. Schulz, Jr., Ph.D. Thesis, University of California Radiation Laboratory Report UCRL-1756, 1952 (unpublished).

Even though the pi meson is emitted primarily in a p state with respect to the nucleon, it can nevertheless be shown qualitatively that there exists some s-state meson emission with respect to the center of mass of the two proton system. For example, if for distances close to the nucleon the meson wave function for p-state emission is given as $\psi \sim kr$, where k is the meson momentum in the center of mass, and r the relative distance from the nucleon, then ψ can be transformed to $\psi' \sim k(r_0 \cos\theta + R)$, where r_0 can be taken as half the range of nuclear forces in p-p collisions, and R is the distance relative to the center of mass of the two nucleon system. In evaluating the matrix element, however, the p-state term vanishes because of the selection rule; the cross term vanishes due to the orthogonality of the s and p waves, leaving only the s-state term.

Hence the quantity $(r_0/\lambda\!\!\!^{-})^2$ can be interpreted as the fraction of mesons that are emitted in p states with respect to the nucleon, but in s states with respect to the center of mass of the two nucleon system. The above discussion holds only for the case where $r_0 < \lambda\!\!\!^{-}$. As the energy increases, r_0 may become large compared to $\lambda\!\!\!^{-}$, and the estimate breaks down because the wave functions are no longer valid for large R. Thus it may be said that in the $^3P \rightarrow {}^1S$ transition, the meson is emitted from a p state with respect to either nucleon, but comes out in an s state with respect to the center of mass of the two nucleon system, leaving the product nucleons in s states.

EXPERIMENTAL ARRANGEMENT

The general plan view of the 184-inch synchrocyclotron is shown in Fig. 1(a). The 340-Mev proton beam was initially collimated by a premagnet collinating slit system before it was bent by the steering magnet so as to enter a two-inch diameter, 48-inch long brass collimator extending through the concrete shielding surrounding the cyclotron. Most of the beam shaping is achieved at the premagnet slits to prevent the spray of neutrons and general radiation from entering the detection area.

The scattered beam has approximately a 20-microsecond duration with a repetition rate of 50 cycles per second. This yields a duty cycle of 10^{-3} defined as the fraction of time the beam is on. The flux of protons in the scattered beam for this experiment was maintained at approximately 5×10^8 protons per second, and was continuously monitored by a CO_2-argon filled ionization chamber which was connected to an electrometer in the counting area. The electrometer actuated a Speedomax recorder which gave a visual indication of the proton beam level at all times.

The general arrangement of the liquid hydrogen flask, magnet and Čerenkov counter is shown in Fig. 1(b). The physical size of the water-cooled magnet determined both the position of the hydrogen target relative to the proton beam snout and also the location of the Čerenkov counter with respect to the hydrogen target. With this geometry, the counting rate will vary inversely as the distance from the target, because the effective target thickness varies as the distance from the target to the detector, while the solid angle subtended by the detecfor at the target varies inversely as the distance squared. The water cooled magnet served to sweep the $\frac{3}{4}$-inch diameter channel free of charged particles which would have given an erroneous hydrogen counting rate. Sources of background are discussed in a later section.

Since the neutral meson counting rate was expected to be not more than 1 percent of the carbon yield, it

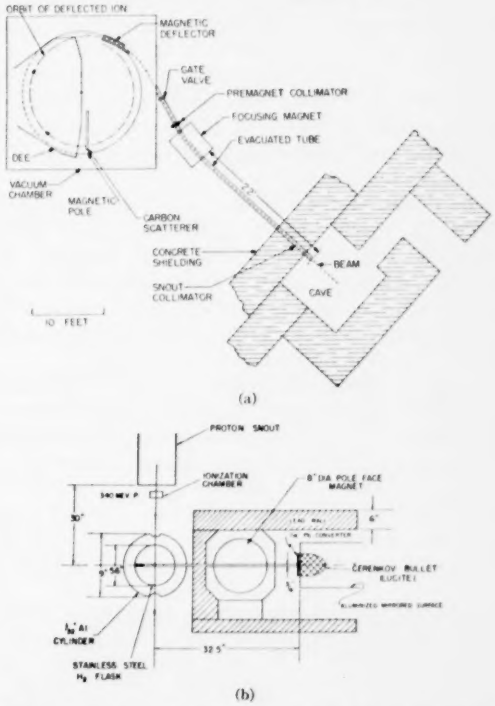

FIG. 1(a) Cyclotron layout. (b) Experimental arrangement in the cave, showing relative positions of hydrogen target, magnet, and Čerenkov counter.

was desirable that the background rate be at least an order of magnitude lower. Even though we employed a focusing type Čerenkov radiation counter, it was to our advantage to set up at 90° to the proton beam to obtain adequate shielding of the photomultipliers. The amount of shielding required was determined during previous cyclotron runs, and also the possibility of setting up at angles other than 90° were investigated.

ČERENKOV COUNTER

The theory of Čerenkov radiation as developed by Frank and Tamm,[9] leads to the equation $\cos\theta = c/\eta v$,

[9] I. Frank and I. Tamm, J. Phys. (U.S.S.R.) 1, 439 (1939).

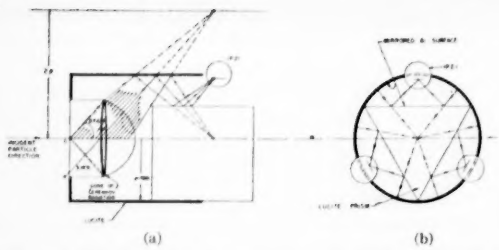

(a) (b)

FIG. 2. Detail of Čerenkov counter. (a) Side view of triples detection scheme showing only 1 tube. (b) End view showing placement of three 1P21 photomultipliers.

where θ is the half-angle of the Čerenkov radiation cone, η is the index of refraction of the medium, v is the velocity of the charged particle in the medium, and c the velocity of light in vacuum. For a very fast electron ($v \approx c$) passing through Lucite ($\eta = 1.5$), the number of quanta emitted in the 1P21 photomultiplier spectral region per centimeter of path is approximately 425 quanta per centimeter.

The design of the Čerenkov counter is similar to Marshall's, except that a triple coincidence photomultiplier arrangement is employed to view the Čerenkov radiation. Figure 2 shows the general view of the counter. Gamma rays from the neutral meson decay are converted to fast electrons in a thin lead plate placed before the Lucite radiator [Fig. 1(b)].

Before we discuss the performance of the Čerenkov counter, a brief account of the general problem of focusing of Čerenkov radiation should be mentioned. The Lucite radiator is a partial spherical surface of radius 3.14 inches and neglecting any dispersion in angle, the cone of radiation will be focused into a ring twice the radius of curvature as measured from the vertex of the spherical surface. A cylindrical aluminized mirror of half the ring diameter intercepts the Čerenkov rays and reflects them to a focal spot on the central axis, assuming that the initial particles enter the Lucite radiator along the central axis. An aluminized prism is so placed to intercept these rays and focus them onto the cathodes of the photomultipliers (Fig. 3). Each particular particle direction in the Lucite generates its own cone of radiation, and if the Čerenkov rays are geometrically followed through the optical system it is then clear that each cone of radiation will be focused at a place determined by the original particle direction. In particular, neglecting spreading of the Čerenkov cone, the radiation from an on-axis particle will be focused at a point on the central axis because the cone originated on the axis. However, for off-axis origin of the Čerenkov cone, a large fraction of the Čerenkov rays will never intersect the axis and, consequently, will come to a focus off the central axis. Thus, one can expect a general region of focal points at the detector from all the photons that make up the initial cone of radiation.

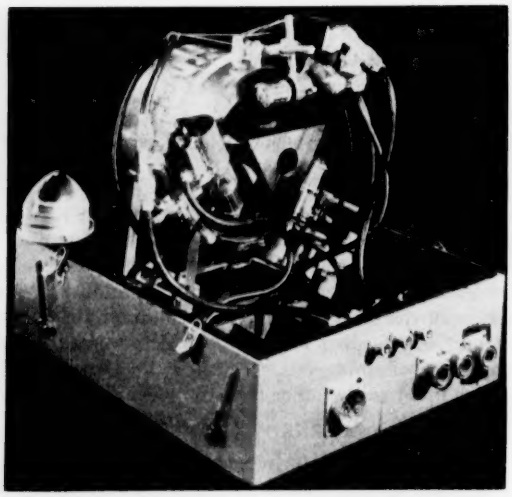

FIG. 3. Photograph of Čerenkov counter.

Initially a double coincidence arrangement[3] was constructed, using only two photomultipliers as detectors. This design was subjected to experiment to determine the effective aperture, directional properties, and, if possible, an efficiency for detecting gamma rays. It was determined, prior to experiment, that off-axis particles would not be counted as effectively as on-axis particles, and furthermore, particles entering the Lucite radiator making a large angle with the central axis would not be effectively counted. These effects can be approximated, but the analysis is complicated by the small multiple angle Coulomb scattering occurring in the radiator, and since Čerenkov radiation contains a mixture of wavelengths extending over the entire visible spectrum, one can expect a small amount of dispersion in Lucite. Dispersion, therefore, will will spread the Čerenkov cone of radiation in angle. The foregoing effects, combined with the problem of focusing the Čerenkov radiation cone, make it necessary to use positioning devices for the photomultipliers. Other designs of Čerenkov counters (Marshall[10] gives a complete account of various designs) have been used successfully. Lucite material was chosen for the Čerenkov radiator because of (1) the ease of machining and polishing to the desired form, (2) the low atomic number, approximately 7, leading to small multiple angle Coulomb scattering, and (3) the low density and atomic number resulting in a small rate of energy loss through ionization for a charged particle traversing the Lucite.

The performance of a two-photomultiplier Čerenkov counter[3] was determined, using the 320-Mev Berkeley synchrotron. The x-ray beam was collimated to $\frac{1}{8}$-inch diameter and allowed to impinge on a thin lead converter placed before the Lucite radiator. By careful

[10] J. Marshall, Phys. Rev. **86**, 685 (1952).

alignment of the axis of the Čerenkov radiator with the direction of the x-ray beam, it was possible to obtain the curves shown in Figs. 4 and 5 giving the aperture width at half maximum of 0.6-inch and the angular acceptance at half maximum of approximately 2.5°, respectively. Prior to this, data were obtained giving the response of the Čerenkov counter as a function of the photomultiplier position on the metal ring. The positioning devices were adjustable in all directions, and maximum counting rate was obtained approximately at the predicted angle for fast electrons, with the Čerenkov rays coming to a focus at the sensitive cathode surface. The velocity selection was checked by moving one photomultiplier one cathode-width off the determined position; the counting rate dropped a factor of 7. A further check to test the Čerenkov effect was made by reversing the counter 180°, allowing the electrons to impinge on the back of the Lucite radiator. No counts were obtained that were statistically significant from pure accidentals as determined from a known length of delay cable placed in one leg of the coincidence circuit.

At the 184-inch cyclotron, it was possible to obtain a figure for the efficiency of detecting gamma rays with energies in the range of 40–120 Mev by using the gamma-ray decay of the neutral meson. The neutral mesons were produced by the 340-Mev circulating proton beam incident on a ¼-inch carbon target at point "*a*" shown in Fig. 1(a). The decay gamma rays were observed through the neutron hole in the concrete shielding in the zero degree direction approximately 50 feet from the internal carbon target. Since previous experiments on neutral mesons from carbon were performed by Crandall[11] using the pair spectrometer, it was felt that the efficiency of the Čerenkov counter, based on the gamma-ray yield as recorded by the spectrometer, would be a reliable figure. The ratio of observed coincidences to the total number of gamma rays incident on the Lucite radiator (effective aperture approximately 0.6 inch in diameter was as high as 21 percent). This efficiency is not to be construed to mean that a coincidence plateau was obtained, but rather indicates a result for a given voltage and discriminator setting.

If the effect of spreading in angle of the Čerenkov cone is considered along with the foregoing discussion of off- and on-axis particles, then it is clear that the curves shown in Figs. 4 and 5 are indicative that Čerenkov radiation was being detected and not general fluorescence. One would not expect fluorescence in Lucite, if present, to exhibit the directional property as shown.

In conclusion, the curves shown in Figs. 4 and 5 indicate (1) this particular design of counter has the advantage of being directional; (2) the Lucite radiator has no definite sensitive detection area; (3) even though the half-maximum width be taken as the effective area, the resulting solid angle is extremely small; (4) the efficiency of detection of off-axis particle is falling extremely rapidly; and (5) the effective aperture of the Lucite radiator at half-maximum is reasonably close to the combined widths of the photocathode surfaces (approximately 2 centimeters) as expected.

Whenever high-energy gamma rays are detected, it is important to determine whether a converter effect is

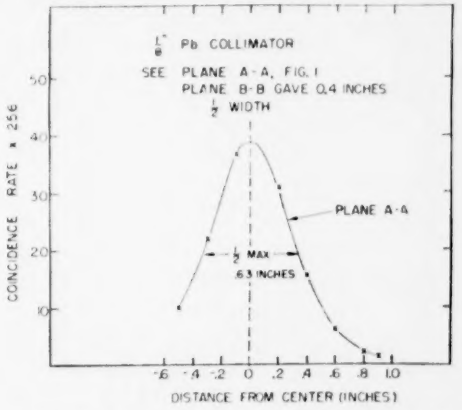

FIG. 4. Variation of response across diameter of Lucite radiator.

obtained. For the Čerenkov counter, this was carried out by placing thin sheets of lead before the Lucite radiator and observing the coincidence rate as a function of the thickness of the converter. This procedure was

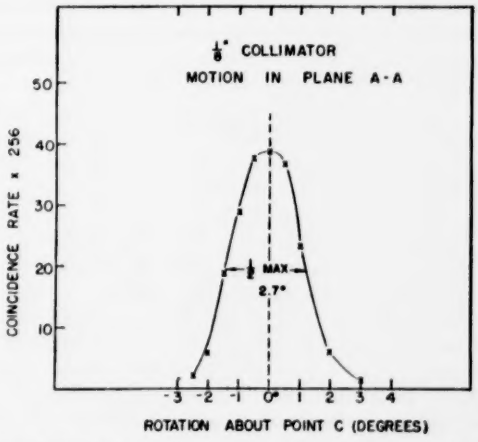

FIG. 5. Variation of response under rotation of counter about point *C*.

also used for the double scheme, yielding similar results. Considering only the lead converter, although copper curves (Fig. 6) were also obtained. characteristic curves were obtained for the attenuation part of the curve, but the transition from no lead to the peak of the transition curve was, at most, a factor of 2–3 at a

[11] W. Crandall, Ph.D. thesis, University of California Radiation Laboratory Report UCRL-1637, 1952 (unpublished).

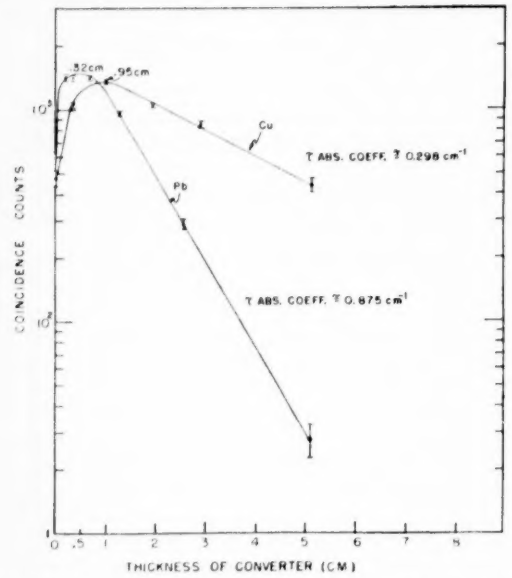

FIG. 6. Attenuation curves for the neutral meson decay gamma rays in lead and copper. The data were taken with a Čerenkov counter directed at a $\frac{1}{4}$-inch internal carbon target in the 340-Mev circulating proton beam.

converter depth of $\frac{1}{16}$- to $\frac{1}{8}$-inch lead. The directional properties of the counter have already been discussed; hence, it is not unreasonable to expect the small multiple angle scattering in lead and Lucite to cancel the effects of the increased pair production in lead. Some evidence for this is given by the lead and copper transition curves in Fig. 6, showing that the same maximum counting rate is obtained for each converter materials.

ELECTRONICS

A block diagram of the electrical arrangement is shown in Fig. 7. The general sequence is clear; each photomultiplier pulse is limited, clipped, and amplified before a coincidence is made. However, two separate coincidence circuits were employed. Pulses 1 and 2 (Fig. 7) are placed in coincidence, using one 6BN6 (minature beam tube). The output of this coincidence is further placed in coincidence with a properly delayed third photomultiplier signal. The resolving time obtained with this arrangement is approximately 10^{-8} second. The triple coincidence output is then amplified and scaled in the conventional manner.

A few remarks should be made concerning the components of the electrical system, for it may seem that more effective circuitry should have been used. The limiter circuit (not shown) employs a sharp cutoff pentode 6AH6, mounted at the base of a 1P21 photomultiplier (Fig. 3) to avoid long signal leads which would increase the capacitance to ground and thereby decrease the high frequency response of the circuit. To avoid using more than one distributed amplifier per photomultiplier, a large grid resistance of approximately 9K is placed in the grid circuit of the 6AH6. The voltage developed across the grid resistance is ample for limiting action. However, it is to be remarked that the dead time of the circuit seriously limits fast counting. Fast counting in this particular experiment is of no importance; however, we were concerned with the thermal noise rate of the photomultiplier jamming the limiter circuit. By selecting good photomultipliers with a low noise component, we operated well below the allowed repetition rate. The use of this circuit required only one amplifier per photomultiplier and thus avoided complex electronic setup and maintenance.

The triple coincidence circuit (Fig 8), employing the miniature beam tube 6BN6, has the advantage of simplicity of design. Resolving times of approximately 10^{-10} second have been reported using square pulses, while resolving times of approximately 5×10^{-9} second have been obtained using photomultiplier pulses. The tube normally operates completely cut off, requiring positive pulses on both grids for coincidence. However, the control grid nearest the plate, being unshielded from the plate circuit, allows grid pulses to capacity feed-through to the plate. The feed-through problem is particularly important when a slight negative overshoot is present on the signal pulse, as is the usual case with amplified pulses. It is seen that the negative part of the impressed signal will capacity-couple to the plate, giving rise to a pulse of the same polarity as the real coincidence pulse. By increasing the plate load resistance, the feed-through pulse height can be made negligible compared to the coincidence pulse. However, one does not gain pulse height selection without losing in another respect. If the coincidence pulse is to be used in coincidence with a third signal as is done in this experiment, one must be concerned with the RC time constant of the grid plate circuit. Attempts were made to keep the time constant to approximately 10^{-8} second. However, if the coincidence pulse is to be scaled directly, then the broadening of the coincidence pulse matters little. In any event, this broadening is not a serious objection, but one must be cognizant of its presence in this particular tube. Another remark should be made concerning the time delay between the signals applied to both grids.

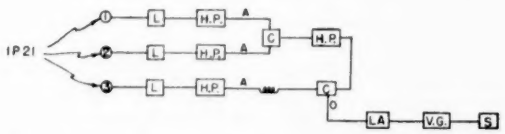

FIG. 7. Block diagram of electronics. L=limiter (6AH6); $H.P.$=distributed amplifier (100 Mc/sec); LA=linear amplifier (10 Mc/sec); C=6BN6, coincidence $\tau\sim10^{-8}$ sec; $V.G.$=variable gate; S=scaler.

The grid nearest the plate should be delayed approximately 2×10^{-9} second for resolving times of this order. However, this is a small correction for resolving times of 10^{-8} second.

The grid bias for the 6BN6 can be controlled separately by negative bias, or both grids can be controlled simultaneously by the cathode bias. The authors have tried both methods of control, with the result that separate control is more flexible for Čerenkov signals. It is further known that all the light pulses from Čerenkov radiation are not limited, and further, that the gain of the wide band amplifiers were not the same. It was for this reason that we found separate grid control advantageous.

The coincidence circuit (Fig. 9) was used in the double photomultiplier scheme referred to in the previous section. This circuit follows closely that outlined by Bay[12] but was further developed by Neher.[13] The balanced bridge circuit is well understood; however,

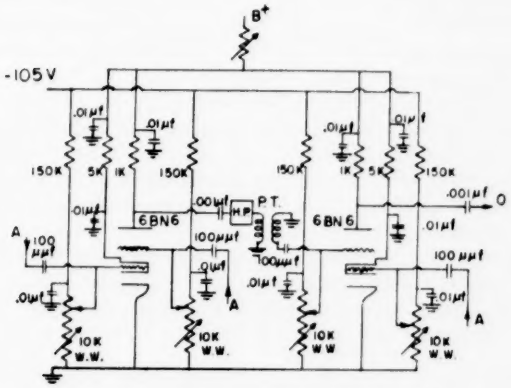

FIG. 8. Triple coincidence network. *A*—positive signal in; *O*—positive signal out (see Fig. 9). *P.T.*—pulse transformer. $\tau\sim10^{-8}$ sec.

for successful operation the crystal diodes should have a high-backward to low-forward resistance. The unbalance at the midpoint of the bridge by two positive signals is then detected by a difference amplifier. It is known that this coincidence circuit is strongly pulse-height dependent, and for this reason, and also to avoid the complexity of a triple coincidence bridge network, the circuit in Fig. 8 was developed.

LIQUID HYDROGEN TARGET

The problem of converting an in-line liquid target[14] to an approximate point source was carried out by Garrison.[15] The in-line target superstructure, however, was carried over to the new design without change. A cross-sectional view of the target is shown in Fig. 10.

[12] Z. Bay, Rev. Sci. Instr. **21**, 297 (1951).
[13] L. Neher (private communication).
[14] L. Cook, Rev. Sci. Instr. **22**, 1006 (1951).
[15] J. Garrison (private communication).

Since the Čerenkov counter detects only gamma rays from the hydrogen target, local sources of gamma rays had to be considered, and these are discussed in the next section. Fortunately, the important source of background gammas originated in a second-order process, and were effectively reduced by requiring that the wall thickness of the liquid hydrogen container be as thin as possible. It was felt that a 2-mil stainless steel foil would be sufficient for mechanical strength, but the quality of the available stainless steel foil was poor As a result, the liquid flask was fabricated from a 4-mil stainless steel foil in the form of a cylinder 5.6 inches in diameter and 8 inches in length. The foil was soft-soldered to a stainless steel base and to a collar arrangement on the vertical hydrogen tube. To prevent appreciable loss of liquid hydrogen by conduction up the vertical hydrogen tube, a liquid nitrogen jacket was used. The outside aluminum jacket surrounding the hydrogen flask was 9 inches in diameter with $\frac{1}{16}$-inch wall thickness, except where the proton beam penetrated. At this point there was a 3-inch diameter hole, covered with a 5-mil aluminum foil to reduce negative meson production. Since the proton beam emerges from a 2-inch diameter collimator [Fig. 1(a)], there is sufficient tolerance in the 3-inch diameter hole so that no protons impinge on the thick-walled aluminum jacket. Frequent photographs of the beam alignment were made throughout the experiment.

A test (using liquid nitrogen in place of liquid hydrogen) was performed to determine whether any gas bubbles were present in the liquid nitrogen. When the liquid nitrogen reached a quiescent state, it was possible to look down the hydrogen tube and observe the liquid surface. This was checked several times and no bubbles were observed. Therefore it was assumed that liquid hydrogen would not bubble to any great extent because the temperature difference between liquid nitrogen and hydrogen is only 50°. A further

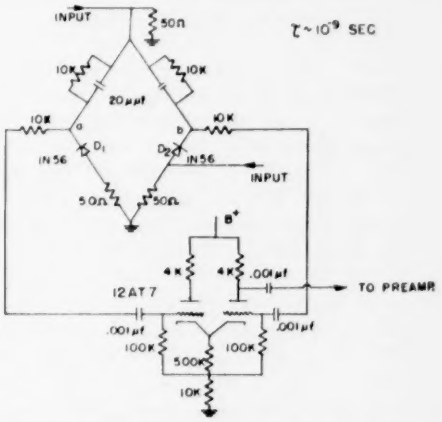

FIG. 9. Crystal diode coincidence circuit and difference amplifier.

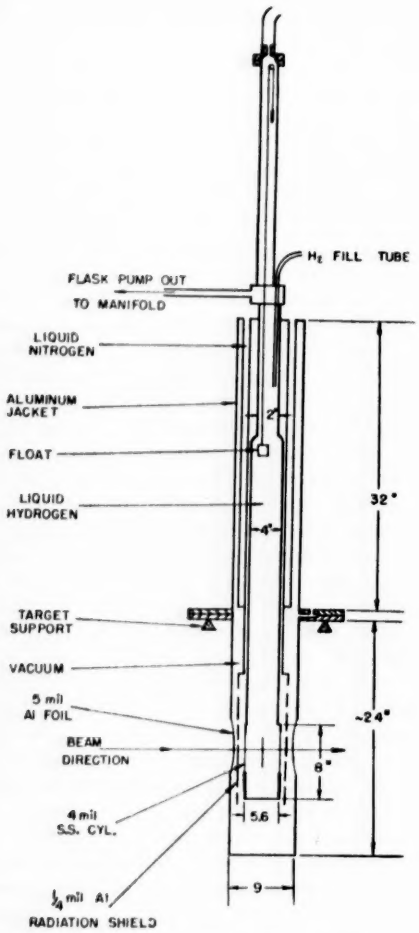

FIG. 10. Detail of liquid hydrogen target.

check of all heat losses was obtained during the hydrogen experiment over a period of twenty-four hours; it was found that the disappearance of liquid hydrogen corresponded to a heat flow of approximately 0.2 calories sec^{-1}. Since the hydrogen was continually vented to the atmosphere through a 2-inch diameter rubber hose, it is not difficult to account for most of the heat loss in this way. Thus, it was concluded that no boiling of the liquid hydrogen in the sensitive volume of the proton beam was present.

No provision was made for filling and emptying the hydrogen target during the experiment. However, the hydrogen target assembly provided a blank target, identical to the hydrogen target, except that it was not evacuated. The blank target and the liquid hydrogen target were fixed in place on a movable carriage, facilitating a change in target in a matter of minutes. Because of the orientation of the target frame relative to the proton beam, it was necessary to remove the dummy target each time the liquid hydrogen target was used.

SOURCES OF BACKGROUND

Before considering the kind of background that could conceivably lead to an erroneous interpretation of the hydrogen result, it might be well to indicate the magnitude of the expected yield of neutral mesons from protons bombarding hydrogen. Taking the hydrogen yield of neutral mesons to be approximately one percent of the carbon yield[16] as indicated by Hales *et al.*, then the gamma-ray intensity[17] at the target can be expressed as

$$N(\gamma)=0.52\times10^{-29}N_0F_P,$$

where N_0 and F_P are Avogadro's number and proton flux, respectively. However when the efficiency and solid angle factors are included, the expected rate is of the order of one count per 15 minutes. It was therefore obvious at the beginning that the background counting rate must be made at least an order of magnitude lower; otherwise cyclotron running time would be prohibitively long to obtain reasonable counting statistics. The experiment was undertaken, using a Čerenkov focusing detector previously described which had demonstrated its ability to select only those particles which enter the Lucite radiator making a small angle with the normal to the radiator of approximately 1.5°.

Besides maintaining the accidental rate due to photomultiplier tube noise to a negligible value, the following possible sources of background were considered:

(1) π^+ production in hydrogen and its associated μ-e electron decay;
(2) fast electrons from targets;
(3) π^-, π^+ ordinary scattering in hydrogen at 90°;
(4) π^- charge exchange in hydrogen;
(5) π^0 production in the walls of the hydrogen container;
(6) π^- production in the window of the container, leading to capture in hydrogen.

All reactions involving the production or scattering of charged particles in hydrogen were mitigated by the use of a small magnet [Fig. 1(b)] capable of producing a magnetic field of approximately 20 000 gauss across a one-inch gap. The positive pi mesons produced in the reaction $(p, p\pi^+)$, fast electrons from nuclei bombarded by 340-Mev protons as found by Neher, Alvarez, and Moyer,[18] and the ordinary scattering of negative and positive mesons in hydrogen as

[16] The absolute cross section for neutral meson production from carbon is 1.5×10^{-27} cm^2 as measured by Crandall.
[17] The neutral meson decays into two gamma rays.
[18] Neher, Alvarez, and Moyer (private communication).

considered by Anderson,[19] and Fermi,[20] were bent out of the field of view of the Čerenkov detector.

Using the Fermi *et al.* data on the charge exchange of negative pi mesons[21] in hydrogen at 90°, and considering only the upper end of the negative pi spectrum for 340-Mev protons on carbon and lead, one obtains for the number of π^- mesons that will charge exchange in hydrogen at 90°:

$$N(\pi^-)=0.000065N_0F_P\times10^{-29}.$$

Clearly, this will give a negligible contribution of neutral mesons.

The directional properties of the Čerenkov counter made it possible to avoid π^0 contamination from the walls of the hydrogen container. The probability of a proton scattering to the far wall, as seen by the counter, and producing a π^0 meson is extremely small.

Reaction (6) was thought to be the only local source of significant background. Negative mesons produced by protons[22] on aluminum and the stainless steel foil surrounding the hydrogen can lead to capture in hydrogen giving rise to neutral mesons. With reference to Richman, Weissbluth, and Wilcox's[23] data, the low-energy π^- yield from aluminum and stainless steel windows was estimated, assuming that the negative meson production depends on the number of neutrons in the nucleus. The negative meson was chosen to stop in the sensitive portion of the target and thus be captured. Both the forward and backward production of negative mesons were considered, with the appropriate solid angle factor. If one combines the yield of negative mesons from 10-mils of aluminum and 8-mils of stainless steel, one obtains the number of gamma rays as a result of negative meson capture in hydrogen to be:

$$N(\gamma)=0.0124\times10^{-29}N_0F_P.$$

This estimation is based on a conservative analysis and therefore represents the bulk of the background. By inserting additional thicknesses of aluminum in front of the hydrogen container it is possible to test whether or not negative pi meson capture is important. A linear effect in counting rate should be observed if capture is taking place.

RESULTS

Since the experiment was expected to yield a low counting rate, the authors were constantly on guard to assure that all electronics equipment continued to perform in good order. To dispel any uncertainty, a carbon target approximately 1½ inches thick was placed in the proton beam periodically in place of the liquid target. Repeating this procedure after a blank- or liquid-target exposure gave full assurance of the operation of the coincidence circuit and Čerenkov counter throughout the 32-hour run. In addition, the carbon target offered a convenient source of neutral mesons, thus providing means of obtaining the proper coincidence pulse levels. The alignment of the Čerenkov counter and lead channel with the proton beam was rather critical because 90 percent of the protons emerging from the proton snout were concentrated in a line pattern approximately one-eighth inch wide, characteristic of the proton beam from the Berkeley synchrocyclotron.

After adjusting the electronic gear to count neutral mesons from carbon, the empty hydrogen target was bombarded for a period of two hours, with no measurable yield. The empty target was then filled with liquid hydrogen, and it remained filled through the entire experiment.

A further check on the possibility of observing neutral mesons from the far target wall [Fig. 1(b)] was made by comparing the coincidence rate of the blank target to that when no target was present. The yield in both cases was the same within statistics and was compatible with the neutral meson yield expected from air, based on the nitrogen and oxygen content of the air column in front of the Čerenkov counter. However, the statistics are poor but nevertheless significant. It is on this basis that no subtraction of the counts due to the air was made to the hydrogen result. At the end of the experiment, the liquid hydrogen was removed from the target and replaced by liquid nitrogen for the purpose of comparing the nitrogen results with carbon. The yield of neutral mesons from nitrogen was in good agreement with the carbon data and gave a further check on the consistency of operation of the electronic gear.

During one or two carbon target exposures, the accidental coincidence rate was checked by delaying[24] one leg of the coincidence circuit; no accidentals were measured, and on this basis none were expected from the liquid hydrogen target.

Because of the small sensitive volume of the target, compared to its dimensions [Fig. 1(b)], it was necessary to correct the experimental data for the attenuation of the proton beam through ionization and also for the decrease in intensity of the neutral meson decay gamma rays due to pair production in the target material.

Since the sensitive volume of each target as defined by the collimating system was at the center of the target in each case, it was necessary to consider the energy loss of a 340-Mev proton in passing through the insensitive part of the target. The insensitive portion

[19] Anderson, Fermi, Long, Martin, and Nagle, Phys. Rev. **85**, 934 (1952).
[20] Fermi, Anderson, Lundy, Nagle, and Yodh, Phys. Rev. **85**, 935 (1952).
[21] Positive mesons do not charge-exchange in hydrogen because of charge conservation.
[22] Negative mesons are not produced in hydrogen by protons because of charge conservation.
[23] Richman, Weissbluth, and Wilcox, Phys. Rev. **85**, 161 (1952).
[24] Delay of approximately 6×10^{-8} second was used corresponding to the interval of time between two radio frequency pulses of the cyclotron.

of each target, i.e., 2.5 centimeters of carbon, 7 centimeters of liquid nitrogen, and 7 centimeters of liquid hydrogen, resulted in an energy loss in the proton beam of 11, 16, and 3 Mev, respectively, as obtained from the range energy curves. Since the neutral meson yield from carbon as a function of the proton energy is given by Crandall, the percentage decrease in meson yield from that at 340 Mev could be obtained. The values chosen were 26 percent for carbon and 41 percent for liquid nitrogen. The correction for hydrogen is uncertain. By referring to the excitation function obtained by Schulz for the $(\rho, \rho\pi^+)$ process, a 5 percent reduction in meson yield would be expected.

When gamma rays pass through matter, their intensity decreases owing to absorption or scattering. Since the energy of the neutral meson decay gamma rays is approximately 70 Mev, the disappearance of the gamma rays will be due to pair production. Knowing the mean free path for pair production for a given material, it is then possible to estimate the percentage decrease in the gamma ray intensity. For the thicknesses of carbon and liquid nitrogen as previously given, the gamma-ray intensity will decrease 4.5 and 8 percent respectively. The liquid hydrogen gives a very small contribution (less than 0.5 percent).

The foregoing corrections were applied to the experimental data and Table II lists the corrected experimental values for proton energies of 340 Mev.

The values obtained for the neutral meson yield from carbon and liquid hydrogen at 90° to the proton beam are listed in Table II. The neutral meson cross section for hydrogen relative to carbon is

$$\sigma_H/\sigma_C = 0.0059 \pm 0.0009.$$

The experimental corrected ratio of the counting rate from liquid nitrogen relative to carbon offers a further check of the consistency of the results as

$$N(\gamma)_N/N(\gamma)_C = 0.546 \pm 0.037.$$

Taking into account of the difference in density of carbon and liquid nitrogen, and further assuming the neutral meson production from liquid nitrogen to be 7/6 of the carbon yield, the expected ratio of the counting rate from liquid nitrogen relative to carbon is

$$N(\gamma)_N/N(\gamma)_C = 0.537.$$

The agreement between the experimental and estimated values listed in Table II give additional evidence that neutral meson production in light nuclei depends primarily on the number of neutrons in the nucleus.

DISCUSSION

On the basis of the discussion given in the introduction, the cross section at higher proton energies may be estimated by using the present experimental results. Since the charged mesons in the $(\rho, \rho\pi^+)$ process are emitted predominately in p states, the quantity $(r_0/\lambda)^2$ can be estimated giving the fraction of mesons that are emitted in p states with respect to the nucleon, but in s states with respect to the center of mass. By forming

$$(r_0/\lambda_{22})^2 \sigma_{340}(\rho, \rho\pi^+) = \sigma_{340}(\rho, \rho\pi^0),$$

and a similar expression for the 440-Mev reaction one can solve for $\sigma_{440}(\rho, \rho\pi^0)$ at 440 Mev as

$$\sigma_{440}(\rho, \rho\pi^0) = \left(\frac{\lambda_{22}}{\lambda_{75}}\right)^2 \frac{\sigma_{440}(\rho, \rho\pi^+)}{\sigma_{340}(\rho, \rho\pi^+)} \sigma_{340}(\rho, \rho\pi^0),$$

where λ is the wavelength of the meson in the center-of-mass system. To evaluate the above expression, it is necessary to estimate the ratio of the $(\rho, \rho\pi^+)$ cross section at 440 Mev to that at 340 Mev.

The $(\rho, \rho\pi^+)$ data at energies of 380 Mev obtained by Passman and Block[25] indicate a T^2 meson energy dependence, where T is the maximum meson kinetic energy in the center-of-mass system. From the data of Schulz at 340 Mev, partial agreement is obtained with a $T^{3/2}$ dependence. A straight T^2 meson energy dependence yields a value for $\sigma_{440}(\rho, \rho\pi^+)/\sigma_{340}(\rho, \rho\pi^+)$ of 11.5. However, if the data of Passman and Block are extrapolated to proton energies of 440 Mev, then the ratio would be approximately 7.

If the extrapolated value is used, the cross section for the $(\rho, \rho\pi^0)$ process at 440 Mev is estimated to be approximately 0.24×10^{-27} cm^2 using the value for the 340-Mev $(\rho, \rho\pi^0)$ process from the experiment. Only fair agreement is obtained with the Chicago result of $0.45 \pm 0.15 \times 10^{-27}$ cm^2; it is uncertain whether the extrapolation is valid.

TABLE II. Neutral meson yields[a] for various targets at 90° to the 340-Mev proton beam. (All errors are standard deviations.)

Target	Total integrator sweeps	Total counts	Time (min)	Experimental value[b] σ/σ_C	Experimental value[b] $N(\gamma)/N(\gamma)_C$	Estimated value[c] σ/σ_C	Estimated value[c] $N(\gamma)/N(\gamma)$
Carbon	60	382±19	27.5	1.0	1.0	1.0	1.0
Liquid nitrogen	145	392±20	66	1.19±0.08	0.546±0.037	1.17	0.536
No target	625	4±2	265	1.0±0.5	0.0009±0.0003	1.2	0.00086
Liquid hydrogen	1659	47±6.8	570	0.0059±0.0009	0.0033±0.0005	...	...

[a] Yields are given per nuclus. The absolute cross section for neutral meson production by 340-Mev protons on carbon was measured by Crandall (reference 11) to be 1.5×10^{-27} cm^2.
[b] Corrected for energy degradation in target and for gamma-ray conversion in the target material.
[c] Values obtained assuming production of neutral mesons to depend only on the number of neutrons.

[25] S. Passman and M. M. Block, Ph.D. dissertation submitted by S. Passman, Columbia University, 1952 (unpublished).

In conclusion, it is shown (1) that the yield of neutral mesons by protons on protons at 440 Mev can be approximately obtained from the result at 340 Mev by a consideration of the energy dependence of meson production, and (2) that there is some evidence for the breakdown of the approximate selection rule which forbids the emission of s state mesons with final s state nucleons.

It is a pleasure to thank Professor E. M. McMillan for his continued interest in this experiment. I am grateful to Drs. J. Lepore, M. Ruderman, and P. Wolff for discussions of the theoretical aspects of the work. I also wish to express appreciation to Mr. J. Garrison for the loan of his liquid hydrogen target, and to the accelerator technical group under the direction of Mr. W. Stockton and Mr. D. O'Connell for their assistance in the construction of the Čerenkov counter. Thanks are also due to the cyclotron operating crew under Mr. J. Vale for their cooperation in making the bombardments.

PHYSICAL REVIEW VOLUME 92, NUMBER 3 NOVEMBER 1, 1953

Studies of X-Rays from Mu-Mesonic Atoms*

VAL L. FITCH AND JAMES RAINWATER
Department of Physics, Columbia University, New York, New York
(Received July 23, 1953)

A new technique of x-ray spectroscopy of μ-mesonic atoms has been developed. The x-rays are produced when a μ^-meson undergoes transitions between Bohr orbits about nuclei of various Z. The mesons are produced by the Columbia University 164-in. Nevis cyclotron. The x-rays are detected, and their energies are measured to better than 1 percent accuracy (for $Z \geq 22$) using a NaI crystal scintillation spectrometer. The $2p \rightarrow 1s$ transition energies were measured to be 0.35, 0.41, 0.955, 1.55, 1.60, 3.50, 5.80, 6.02, and 6.02 Mev for $Z=13$, 14, 22, 29, 30, 51, 80, 82, and 83. Special attention was paid to the Pb spectrum, and it is believed that an 0.2-Mev fine structure splitting has been observed. This is the expected splitting if the μ^- meson is a spin $\frac{1}{2}$ Dirac "heavy electron" of 210 electron masses, having the expected Dirac magnetic moment and having no strong nonelectromagnetic interaction with nuclear matter.

Since the μ^-meson Bohr orbits are 210 times closer to the nucleus than the equivalent electron orbits, the x-ray energies are quite sensitive to nuclear size for medium and large Z. In the case of Pb, a 1 percent change in nuclear radius gives a 1 percent change in the calculated x-ray energy. Assuming constant proton density inside a spherical nucleus of radius $R_0=r_0A^{\frac{1}{3}}$ and the above properties for the μ meson, we obtain $r_0=1.17$, 1.21, 1.22, and 1.17×10^{-13} cm for $Z=22$, 29, 51, and 82. The significance of these results in relation to other nuclear size measurements is discussed.

INTRODUCTION

WHEN a μ^- meson is slowed to rest in condensed matter through loss of its kinetic energy to electrons, it is captured in Bohr type orbits about a nucleus. Then, by a series of radiative and nonradiative (Auger) transitions, the meson proceeds to its K shell in an elapsed time of roughly 10^{-13} to 10^{-14} sec.[1] Thereafter, two competing mechanisms, natural beta decay and nuclear capture, account for the disappearance of the meson from the K shell. The characteristic decay time has been measured to be 2.1 μ sec. The mean time for nuclear capture has been investigated over a wide range of atomic numbers and has been found[2] to vary as Z^{-4} for low Z materials and saturate near 7×10^{-8} sec for $Z=82$. This is a manifestation of the extremely weak interaction (nonelectromagnetic) of μ mesons with nuclear matter. In comparison, the π^- meson will seldom reach the K shell except in the case of nuclei with low atomic number. Experimental studies of π-mesonic x-rays in light elements have been made[3] for low Z elements to investigate this strong absorption. Previously reported results[4] for μ^- mesons have been of a more qualitative nature than the present work and will not be discussed in detail since they are in rough agreement with the present more definite determinations of the transition energies.

When a μ^- meson is "stopped" in a target material and is captured in a Bohr orbit about a particular nucleus, the initial states are characterized by large quantum numbers n and l in view of the large statistical weight associated with these states. The decrease in n soon reaches the point where $n=l+1$, and subsequent transitions have $\Delta n=\Delta l=-1$. Thus the lower states in the cascade usually possess the largest l value consistent with the given total quantum number n (circular orbits).

* This research was supported by the joint program of the U. S. Office of Naval Research and the U. S. Atomic Energy Commission.

[1] E. Fermi and E. Teller, Phys. Rev. **72**, 399 (1947); see also R. E. Marshak, *Meson Physics* (McGraw-Hill Book Company, Inc., New York, 1952), Chaps. 5 and 6 for a general discussion of matters related to the present papers, and for further references.

[2] Keuffel, Harrison, Godfrey, and Reynolds, Phys. Rev. **87**, 942 (1952); see also J. M. Kennedy, Phys. Rev. **87**, 953 (1952).

[3] Camac, McGuire, Platt, and Schulte, Phys. Rev. **88**, 134 (1952).

[4] W. Y. Chang, Revs. Modern Phys. **21**, 166 (1949); E. P. Hinks, Phys. Rev. **81**, 313 (1951); G. G. Harris and T. J. B. Shanley, Phys. Rev. **89**, 983 (1953); F. D. S. Butement, Phil. Mag. **44**, 208 (1953); see G. R. Burbidge and A. H. de Borde, Phys. Rev. **89**, 189 (1953) for other references.

It has been shown[5] that the transitions involving states of high quantum number will be primarily nonradiative (Auger processes), while these in the region of low quantum number will be radiative. These x-rays have a small natural line width compared to the transitional energies between the lowest states. For example, in the case of lead the transition rate $2p \rightarrow 1s$ is approximately 10^{18} sec^{-1}, while the capture rate is approximately 10^{7} sec^{-1}. The resulting natural line width is approximately 1 kev for a total x-ray energy of 6 Mev.

Considering the nucleus as a point charge, the radius of a Bohr orbit is $2.82\times10^{-13}\ (m_e 137^2/\mu Z)n^2$ cm, where m_e and μ represent the electron and μ^--meson masses. Thus the μ-mesonic orbit will be smaller than the corresponding electron orbit by the mass factor 210. In the case of lead this gives $r=3.07\times10^{-13}$ cm for $n=1$, which is well inside the nucleus, and $r=1.23\times10^{-12}$ cm for $n=2$, which is just outside the nuclear surface. Again in the case of Pb, the predicted $2p_{\frac{1}{2}} \rightarrow 1s$ transition energy for a point nucleus is 16.41 Mev, whereas we have measured the energy of this transition as 6.02 Mev. Thus the finite nuclear size results in almost a factor of three decrease in the transition energy. Assuming a nuclear model of constant density inside a sphere of radius R_0, with a sharp edge and zero density outside, we find that a 1 percent change in R_0 gives a 1 percent calculated change in the transition energy. Since the x-ray energy is measured to better than 1 percent accuracy, a corresponding accuracy is obtained for the best fitting value of R_0. This great sensitivity of the μ^- meson as a "probe" of the nucleus was first pointed out by Wheeler[5] and served as a stimulus for the research reported in this paper. This sensitivity to nuclear size decreases rapidly with decreasing Z and amounts to only a 2 percent total effect for aluminum. The transition energy is mainly sensitive to the meson mass rather than nuclear size for low Z, and mainly sensitive to nuclear size for high Z materials. By exploiting this fact we have obtained an independent evaluation of the μ-meson mass in agreement with the results of other techniques.

The fine structure splitting of the $2p$ level depends on the spin and magnetic moment of the μ meson which is usually assumed to be a Dirac particle of spin $\frac{1}{2}$. Thus the anomalous g factor of 2 is expected. Other spin $\frac{1}{2}$ particles believed to obey the Dirac theory include the electron, proton, neutron, and neutrino. The electron moment in the hydrogen atom is now known to be slightly different from one electron magneton, and this has recently been explained in terms of higher-order effects in quantum electrodynamics. The neutron and proton moments deviate considerably from the expected Dirac values of 0 and 1 nuclear magnetons, presumably because of their strong coupling to meson fields. The μ meson, unlike the nucleons, has no known strong (non-electromagnetic) coupling to other particles, and it is reasonable to expect, therefore, that its magnetic moment would be close to one μ-mesonic magneton if it is a spin $\frac{1}{2}$ Dirac type particle. (The $\pi^- \rightarrow \mu^- + \nu$ and $\mu^- \rightarrow e^- + 2\nu$ processes and the nature of the stars produced following nuclear capture seem to require that the μ meson have Fermi-Dirac statistics, and thus odd half-integral spin.) Results of the investigation of cosmic-ray bursts seem to rule out spin $\frac{3}{2}$ or higher.

For spin $\frac{1}{2}$, the $2p$ level will split into $2p_{\frac{1}{2}}$ and $2p_{\frac{3}{2}}$ with relative statistical weighting factors of 2 and 1. (This weighting is found theoretically to apply even for the situation where the $2p$ level is reached by successive transitions having $\Delta n=\Delta l=-1$.) In the case of a point Pb nucleus, the expected fine structure splitting is 0.55 Mev. This is reduced to about 0.2 Mev for the actual size, and we believe that we have probably observed this fine structure splitting in the Pb spectrum. If the μ meson has spin 0, there would be no fine structure splitting. If its spin is 1 or more, there will be three lines in the fine structure. Thus a study of the fine structure can determine both the spin and magnetic moment of the μ meson.

This paper reports experimental studies of the x-rays from the $2p \rightarrow 1s$ transition in μ-mesonic atoms for $Z=13$, 14, 22, 29, 30, 51, 80, 82, and 83. The Columbia University Nevis Cyclotron produces an external meson flux which is collimated in the main shielding wall to produce meson beams of relatively well-defined momenta. The beams consist of both π and μ mesons, the mu's originating from decay of pi's close to the cyclotron target. The μ mesons with the same momenta as the π mesons have a greater range, thus the π mesons can be removed from the beam by using absorbers. The x-rays associated with the μ mesons stopping in various materials were studied using a NaI crystal spectrometer with an accuracy of about 1 percent or better in the energy determination, depending on the Z of the target material.

THEORY

Wheeler[5] has calculated the $1s$, $2p_{\frac{1}{2}}$, $2p_{\frac{3}{2}}$, and $2s_{\frac{1}{2}}$ levels for a μ^- meson of $200m_e$ in atoms of various Z. Since the results quoted were not found to be sufficiently accurate for a precise comparison with our experiments, we have recalculated these levels using more exact methods using $\mu=210m_e$ and a model of the nucleus having constant charge density to $R_0=1.30A^{\frac{1}{3}}\times10^{-13}$ cm, with zero density for $r>R_0$. The μ meson was assumed to obey the Dirac equation and only the electrostatic potential was considered. In this case the Dirac equation becomes[6]

$$[E-V+c\boldsymbol{\alpha}\cdot\mathbf{p}+\beta\mu c^2]\psi=0, \qquad (1)$$

[5] J. A. Wheeler, Revs. Modern Phys. **21**, 133 (1949); R. E. Marshak, reference 1, Chap. 5. See also G. R. Burbidge and A. H. de Borde, Phys. Rev. **89**, 189 (1953).

[6] See L. I. Schiff, *Quantum Mechanics* (McGraw-Hill Book Company, Inc., New York, 1949), Chap. 12 for derivations of the following equations, or of approximations to them. The notation follows that of Schiff for the most part.

where $E=\mu c^2+E'=$ total meson energy, and $E'=$ binding energy, V is the potential energy, and $\mathbf{p}$ is the meson momentum. $\boldsymbol{\alpha}$ and β are 4×4 Dirac operators. $\psi=\begin{pmatrix}\varphi_a\\ \varphi_b\end{pmatrix}$ is the 4-component wave function, where φ_a and φ_b, representing the (1, 2) and the (3, 4) terms of ψ respectively, are two-component functions. This is easily transformed to the form

$$\{(E-V)^2-c^2p^2-\mu^2c^4\}\psi-\left\{i\hbar c\left(\frac{1}{r}\frac{\partial V}{\partial r}\right)(\boldsymbol{\alpha}\cdot\mathbf{r})\right\}\psi=0, \quad (2)$$

where the first bracket corresponds to the Klein-Gordon equation appropriate for a spin zero particle, and the last term is the characteristic Dirac term. Expressed in terms of φ_a and φ_b, Eq. (2) becomes

$$\{(E-V)^2-c^2p^2-\mu^2c^4\}\varphi_a-\left\{i\hbar c\left(\frac{1}{r}\frac{\partial V}{\partial r}\right)(\boldsymbol{\sigma}\cdot\mathbf{r})\right\}\varphi_b=0, \quad (3a)$$

$$\{(E-V)^2-c^2p^2-\mu^2c^4\}\varphi_b-\left\{i\hbar c\left(\frac{1}{r}\frac{\partial V}{\partial r}\right)(\boldsymbol{\sigma}\cdot\mathbf{r})\right\}\varphi_a=0, \quad (3b)$$

where $\boldsymbol{\sigma}$ is the usual 2×2 Pauli spin operator ($\mathbf{S}=\hbar\boldsymbol{\sigma}/2$ = meson spin operator). Similar expansion of Eq. (1) gives two coupled equations for φ_a and φ_b in a form that shows that φ_b is the "larger" component for $E>0$ and yields the relation

$$\varphi_a=-c[E'+2\mu c^2-V]^{-1}(\boldsymbol{\sigma}\cdot\mathbf{p})\varphi_b. \quad (4)$$

On insertion of Eq. (4) in (3b), using $(\boldsymbol{\sigma}\cdot\mathbf{r})(\boldsymbol{\sigma}\cdot\mathbf{p})=\mathbf{r}\cdot\mathbf{p}+i\boldsymbol{\sigma}\cdot\mathbf{L}$, where $\mathbf{L}=\mathbf{r}\times\mathbf{p}=$orbital angular momentum, this gives the exact relation

$$\{(E-V)^2-c^2p^2-\mu^2c^4\}\varphi_b+\frac{\hbar}{2}\left[1+\frac{(E'-V)}{2\mu c^2}\right]^{-1}\frac{\partial V}{\partial r}\left[\hbar\frac{\partial}{\partial r}-(\boldsymbol{\sigma}\cdot\mathbf{L})\right]\varphi_b=0. \quad (5)$$

The first bracket again contains the Klein-Gordon term and the last contains the characteristic Dirac terms. In the last bracket, the second term gives the usual spin-orbit interaction. Since $\boldsymbol{\sigma}\cdot\mathbf{L}$ and L^2 are not constants of the motion, it is perferable to use the variable $\hbar k=\beta(\boldsymbol{\sigma}'\cdot\mathbf{L}+\hbar)$ which is a constant of the motion. Here $|k|=(j+\frac{1}{2})$, and $k=-1$, $+1$, and -2 for the $1s_{\frac{1}{2}}$, $2p_{\frac{1}{2}}$, and $2p_{\frac{3}{2}}$ states, respectively. The Dirac equation reduces to a purely radial equation for a two component wave function with components $[F(r)/r]$ and $[G(r)/r]$ respectively, where G is the "large" component function in the coupled equations:

$$(E'+2\mu c^2-V)F-\hbar c\left(\frac{d}{dr}+\frac{k}{r}\right)G=0, \quad (6a)$$

$$(E'-V)G+\hbar c\left(\frac{d}{dr}-\frac{k}{r}\right)F=0. \quad (6b)$$

Solving Eq. (6a) for F and substituting in (6b) gives

$$\left\{(2\mu c^2+E'-V)^2-\mu^2c^4+\hbar^2c^2\left[\frac{d^2}{dr^2}-\frac{k(k+1)}{r^2}\right]\right\}G+\left\{\frac{\hbar^2}{2}\left[1+\frac{(E'-V)}{2\mu c^2}\right]^{-1}\frac{dV}{dr}\left[\frac{d}{dr}+\frac{k}{r}\right]\right\}G=0, \quad (7)$$

which is similar to Eq. (5). Since the second bracket Dirac terms are small compared to the first bracket main Klein-Gordon term, there is very little error made by replacing $[1+(E'-V)/2\mu c^2]^{-1}$ in the second bracket by unity. This is usually done.

In the case of a point nucleus Eqs. (6a, b) may be solved exactly to give

$$E'=\mu c^2\left\{\left[1+\frac{(Z/137)^2}{\{n-|k|+[k^2-(Z/137)^2]^{\frac{1}{2}}\}^2}\right]^{-\frac{1}{2}}-1\right\}, \quad (8)$$

where the fine structure constant is taken approximately as 1/137.

The energies given by Eq. (8) are listed in Table I for selected values of Z along with the modified values using $R_0=1.3A^{\frac{1}{3}}\times10^{-13}$ cm and a nucleus of uniform charge distribution. Several methods of varying precision were used to obtain the values listed for finite nuclear radius. Particular attention was paid to the case of Pb($Z=82$) since the various corrections to approximate calculations are most serious for high Z, and since Pb is a particularly interesting material to

TABLE I. Calculated energies of μ-meson orbits for $\mu=210m_e$. All energies are in Mev.

	Dirac energies $R_0=0$			Dirac energies $R_0=1.3A^{\frac{1}{3}}\times10^{-13}$ cm			Klein-Gordon energies $R_0=1.3A^{\frac{1}{3}}\times10^{-13}$ cm	
Z	$E(1s)$	$2p_{\frac{1}{2}}\to1s$	$2p_{\frac{3}{2}}\to1s$	$E(1s)$	$2p_{\frac{1}{2}}\to1s$	$2p_{\frac{3}{2}}\to1s$	$E(1s)$	$2p\to1s$
13	0.4849	0.3631	0.3628					
14	0.5614	0.4213	0.4209					
22	1.3917	1.0455	1.0432	1.282	0.935	0.933		
29	2.4300	1.8277	1.8208	2.12	1.52	1.51		
30	2.6026	1.9579	1.9500					
51	7.7071	5.8332	5.7627	5.22	3.41	3.37		
80	20.181	15.508	15.011					
82	21.328	16.414	15.857	10.11	5.48	5.30	10.24	5.52
83	21.919	16.880	16.291					

TABLE II. Comparison of the calculated μ-meson orbit energies for Pb using the various computational methods discussed in the text.

	Dirac energies	Klein-Gordon energies	Klein-Gordon correction terms $\frac{1}{r}\left(\frac{dV}{dr}\right)\mathbf{L}\cdot\mathbf{S}$	Klein-Gordon correction terms $\frac{d\varphi}{dr}\frac{d\psi}{dr}$	Klein-Gordon energies plus correction terms
$E(1s)$	-10.11	-10.24		$+0.157$	-10.08
$E(2p_{\frac{1}{2}})$	-4.807	-4.72	-0.125	$+0.032$	-4.81
$E(2p_{\frac{3}{2}})$	-4.63	-4.72	$+0.062$	$+0.032$	-4.63

use to investigate the fine structure splitting. We include a discussion of the more approximate methods to illustrate the order of magnitude of the different terms and the errors introduced by various approximate methods. The first method used the Klein-Gordon

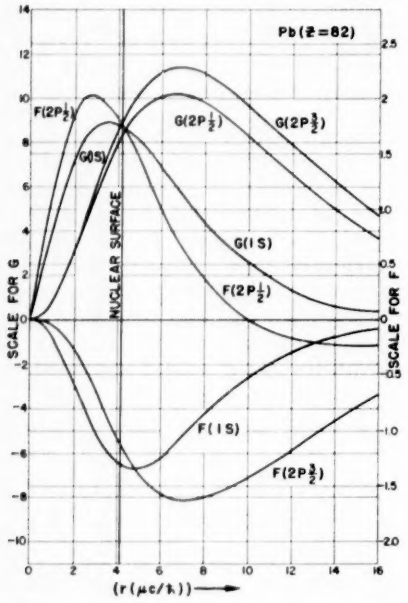

FIG. 1. The $1s$, $2p_{\frac{1}{2}}$, and $2p_{\frac{3}{2}}$ unnormalized meson radial wave functions G and F [of Eq. (6a, b)] in the field of a Pb nucleus. A uniform nuclear model is used with $r_0=1.3\times10^{-13}$ cm. Radii are expressed in units of $\hbar/\mu c=1.84\times10^{-13}$ cm, with the position of the nuclear surface (4.18 units) indicated.

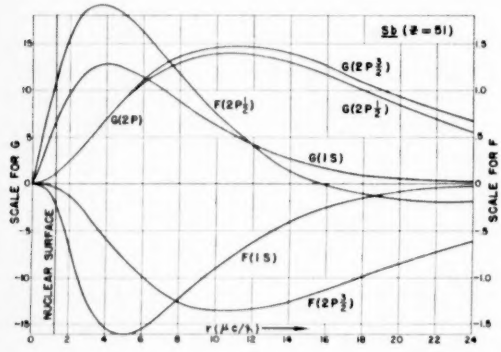

FIG. 2. Curves similar to those of Fig. 1, but for Sb($Z=51$). The nuclear surface is at 2.62 units of radius. *Note added in proof:* The position of the nuclear surface is shown incorrectly in the figure.

equation and the $V(r)$ for finite nuclear size. A point by point method of numerical integration was employed, trying various grid lengths, starting at $r=0$ and continuing until it was clear that E' had been chosen too large or too small. This method was poor for the L shell due to the $2/r^2$ angular momentum term, and a (semiconvergent) series method was tried and found to be much easier to use. In the case of $r<R_0$ a series in positive powers of r was used. For $r>R_0$ a solution of the form $e^{-br}r^m\sum a_n r^{-n}$ was used. The values of (G'/G) for the two functions at $r=R_0$ were compared as a function of E', with the correct value usually determined by interpolation after the first two trials. The (dV/dr) (dG/dr) and the $(k/r)(dV/dr)G$ terms in Eq. (7) were then treated as perturbations and evaluated by first-order perturbation theory with the results shown in Table II. Similarly, the effect of changing the value of the nuclear radius R_0 was evaluated in the Klein-Gordon term by treating the *difference* in V for the two choices of R_0 as a perturbation. It was found that an attempt to calculate the effect of finite nuclear radius by using $R_0=0$ functions to calculate the entire effect as a first-order perturbation gave quite poor results. However, the result of a change of ±10 percent in R_0 about the chosen radius is given with good accuracy.

It was later found to be feasible to carry out the (semiconvergent) series expansions of the inside and outside functions, using the complete coupled equations (6a, b) directly, and this has been carried through for a number of cases with results in close agreement with the previous method. For a given l and j, the G function starts as r^{l+1} and the F function as r^l when $j=l-\frac{1}{2}$, and as r^{l+2} when $j=l+\frac{1}{2}$. A plot of these unnormalized functions for Pb and Sb ($Z=82$ and 51) are shown in Figs. 1 and 2, where the F and G functions are shown with the proper relative amplitudes indicated by the two ordinate scales.

Additional effects of interest include (a) the effect of the polarization of the nucleus by the μ meson, (b) the hyperfine splitting due to the nuclear magnetic moment for odd-A nuclei (Pb has mainly spin-zero isotopes), (c) the effect of a nuclear electrical quadrupole moment, (d) the effect of nonuniform charge distribution as a function of r within the nucleus, including the effect of an expected gradual dropping off of the nuclear charge density beyond the nuclear "surface," (e) the effect of other forces not considered, or of a different spin for the μ meson.

Cooper and Henley[7] have studied some of these effects. They estimate that nuclear polarizability may effect the Pb transition energies by about 0.06 Mev or less (a 1 percent effect or less) and set 0.15 Mev as an upper limit for this effect. Wheeler[4] has calculated the hyperfine splitting for Al($Z=13$) as 9.7 ev. For higher Z the splitting should vary more slowly than Z^3, so the splitting would probably be less than 1 kev in all cases.

The effect of the quadrupole splitting has been investigated by Wheeler.[8] It should be negligible for the materials reported in this paper. The possibility of spin $\frac{1}{2}$ will affect the number of fine structure lines and

[7] L. Cooper and E. Henley (following article), Phys. Rev. **92**, 801 (1953).

[8] J. A. Wheeler (Paper III of this series), Phys. Rev. **92**, 812 (1953).

would be observed experimentally. The existence of any other important attractive interaction between the μ meson and nuclei seems very unlikely but cannot be completely excluded. It would shift the energies in a manner similar to that of a decrease in nuclear radius.

EXPERIMENTAL METHOD

The two main facilities required for this experiment are (1) a source of reasonably monoenergetic μ^- mesons which can be made to stop in a relatively thin target material of selected atomic number under conditions such that the background radiation effects are not too severe, and (2) a photon detector of high sensitivity and good energy selection for the region of 50 kev to 10 Mev.

The μ^- mesons were obtained as follows. Referring to the floor plan, Fig. 3, the 385-Mev protons rotating clockwise inside the cyclotron chamber strike a thin Be target and produce various reaction products including fast neutrons, π^+, π^-, and π^0 mesons, which are emitted in all directions. Near the target the π^0 mesons decay to photons and eventually some electron-positron pairs are formed. These contribute some

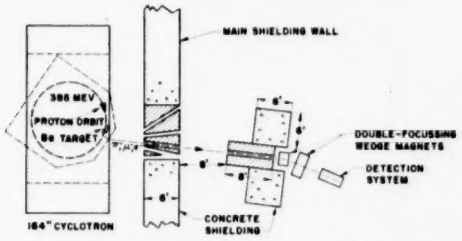

FIG. 3. Floor plan showing location of cyclotron shielding, focusing magnets, and detection system. A typical meson path is shown.

electrons to the final beam. The π^- mesons of approximately 100-Mev kinetic energy have a mean path of approximately 10 meters for $\pi^- \rightarrow \mu^- + \nu$ decay and a certain fraction decay near the target, where the π^- density is highest. The fringing magnetic field of the cyclotron provides a horizontal focusing action for negative particles of any definite energy group emitted in the horizontal plane at angles inward from the forward proton direction. Ports through the shielding wall then serve to select definite momentum beams of negative particles. A beam analysis indicates that approximately 10 percent of the beam particles are μ^- mesons of the same momentum as the π^- mesons. Most of the μ^- mesons originating from decay of the pi's in the beam are projected out of the beam and lost. A typical useful path is indicated in Fig. 3.

The general level of background radiation in the region just outside the shielding was found to be too large for successful performance of this experiment, mainly as a result of the secondary effects of fast neutrons. The method finally employed to reduce background in the photon detector to a reasonable level

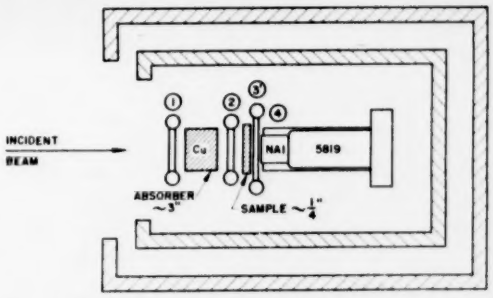

FIG. 4. Diagram of detection system. Stilbene scintillation counters 1, 2, and 3′ select particles stopping in the sample material. NaI scintillation counter 4 serves as the photon detector. The copper absorber between counters 1 and 2 removes the π mesons from the beam. Magnetic shielding is provided by a double walled box of $\frac{1}{2}$-in. iron plate.

is shown in Fig. 3. A secondary barricade of concrete blocks was used starting 8 feet from the main shielding wall. The beam traversed a 6-in. diameter hole in an 8-ft long shielding block and was then double-focused using two magnets having triangular "wedge" pole faces. The magnets served to deflect the beam from the direct line of the collimator and to concentrate it at the detection system.

The detection system is illustrated in Fig. 4. Counters 1, 2, and 3 consist of stilbene scintillation crystals viewed by 1P21 phototubes. Counter 4 functions as the photon detector. It consists of a NaI(Tl) crystal viewed by a 5819 phototube. All pertinent counter dimensions are listed in Table III. For the purpose of shielding the phototubes from stray magnetic fields the whole detection system is surrounded by a double-walled steel box made of $\frac{1}{2}$-in. material except in the region where the meson beam enters. This assembly was then mounted on an adjustable rolling cart.

The beam was analyzed as follows. One inch of carbon

TABLE III. Approximate values of counting parameters.

1. (1, 2) rate, no absorber: 450/sec.

2. (1, 2) rate, full absorber: 50/sec.

3. Approximate beam composition:
   115-Mev $\pi^- \approx 90\%$
   130-Mev $\mu^- \approx 10\%$
   214-Mev $e^- < 3\%$

4. Detector dimensions:

Counter	Diameter, in.	Thickness, in.
1	2	$\frac{1}{4}$
2	2	$\frac{1}{4}$
3	3	$\frac{1}{4}$
4	$1\frac{1}{2}$	1

5. Approximate interval counting rate of the x-ray. Analyzer near the peak of the spectrum.

Element	Interval width	Interval counts/min
Pb (5 Mev)	100 kv	1
Cu (1.53 Mev)	50 kv	2
Al (0.35 Mev)	20 kv	6

was placed in the sample position directly in front of counter 3, and a count of 123′ (123′ denotes coincidence between counters 1 and 2 and anticoincidence with counter 3) was taken as a function of copper thickness yielding a differential range curve of the meson beam. The beam was monitored by a second counter telescope positioned in one of the other beams. A sample curve is shown in Fig. 5. Two groups of particles with the same momentum are present. If the short range group is identified as π mesons then from range consideration the particles in the second group must have a mass of approximately 210 electron masses, and these are identified as μ mesons. For a further check on this identification, the decay of the μ meson to an energetic electron was utilized. An organic crystal of 1 square inch replaced the NaI crystal as counter 4. A delayed coincidence between counters 3 and 4 was tabulated in 8

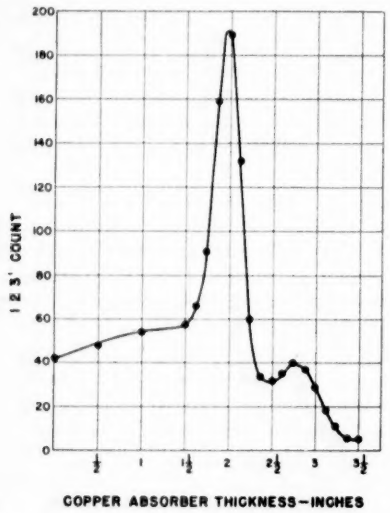

FIG. 5. Differential range curve of the meson beam. The peaks at 2 in. and 2¾ in. correspond to π and μ mesons respectively.

consecutive time intervals each approximately one microsecond in duration. The timing chain was triggered by 123′. Subtraction of the sum of the counts received in the final four channels from the sum of those in the initial four channels gives a measure of the short-lived activity associated with particles stopping in the carbon sample. This measurement was made as a function of copper absorber thickness between counters 1 and 2. The results are plotted in Fig. 6. It is observed that the delayed activity is a maximum for that thickness of copper which corresponds to the range of the second group of particles in Fig. 5. This delayed activity we associate with the decay of the μ^- mesons in the carbon. That the thickness of copper determined in this way was the optimum value was confirmed later by examining the μ-mesonic x-ray spectra as a function of copper thickness.

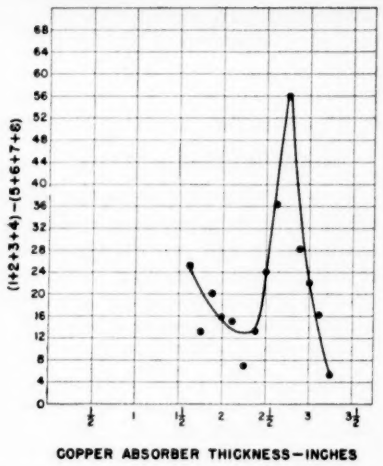

FIG. 6. Delayed activity [channels (1+2+3+4)−(5+6+7+8)] associated with particles stopping in carbon sample as a function of copper thickness between counters 1 and 2.

When the NaI detector pulses were also analyzed for pulse height to measure the photon energy, a fast 1, 2, 3′, 4 coincidence, using the collector anode of the 5819 tube, was used to trigger the pulse height analyzer which then measured the slower pulse from the 8th dynode of the 5819 tube. Provisions were also made to render the circuit insensitive for approximately 8 microseconds after each NaI pulse to assure complete recovery of the pulse level to the reference value. A thermostatic temperature control for the detector box was found to improve stability.

In addition to the NaI photon detector, the scintillation spectrometer consisted of a 10-channel differential pulse-hieght analyzer and associated amplifiers, scaling circuits, and registers. For the measurements reported here, the pulse-height analyzer was adjusted to separate the pulse spectrum into sixty intervals, which could be explored ten at a time. Thus, over a 6-Mev energy spectrum, the minimum channel width was 100 kev. All amplifier circuits were designed for optimum stability consistent with reasonable speed and insensitivity to extreme overload both in pulse rate and amplitude. The over-all spectrometer system was stable to better than ½ percent over operating periods of three days.

Interpretation of the NaI pulse-height distribution is somewhat complicated by the fact that the primary processes by which the photon loses energy to the NaI crystal above 1 Mev are the Compton scattering and pair production. Figure 7 shows the probability per cm *vs* photon energy, of a primary interaction corresponding to photoelectric absorption, Compton scattering, or pair production. The photoelectric effect becomes negligible above approximately 1 Mev but is important at lower energies, particularly for the absorption of lower-energy Compton scattered photons.

The energy transfer in the Compton scattering of a photon of energy E_0 shows a continuous distribution from zero to about $(E_0-0.25)$ Mev (the energy transfer for backscattering). The distribution rises to a sharp peak at the high-energy end,[9] and this peak is evident when a thinner NaI crystal is used. However, the scattered photons here have approximately 0.25 Mev and are strongly absorbed in a thick detector. Thus the upper end of the Compton distribution is depleted and contributes somewhat to a full energy peak. This is again complicated, in principle, by the fact that the range of the knock-on electrons, for approximately 5-Mev photons, is not small compared to a radiation length in NaI and brehmsstrahlung processes should occur frequently. Fortunately this mainly involves the emission of low-energy x-rays which are readily absorbed.

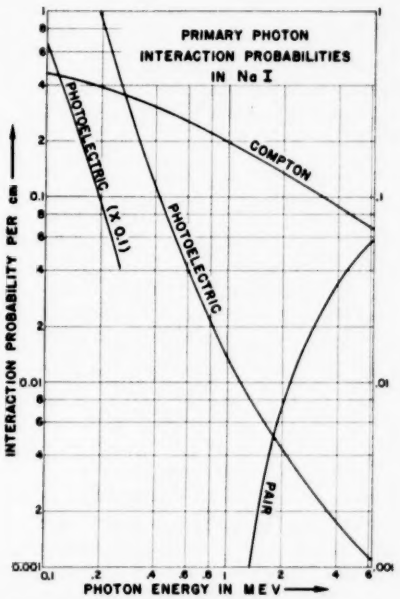

FIG. 7. The probabilities per cm of path in NaI of photoelectric absorption, Compton scattering, or pair production primary interactions as a function of photon energy.

The pair production process becomes increasingly important as the energy is increased above approximately 2 Mev. However, the direct pair process gives a pulse 1.02 Mev lower than the full energy with two 0.511-Mev annihilation gamma rays emitted when the positron stops. Again, one or both of these secondary photons may be wholly or partially absorbed to contribute to a peak at $(E_0-0.51$ Mev), or at E_0.

The curves of Fig. 7 thus are useful in showing the efficiency of various primary processes as a function of primary photon energy, but they do not tell the full story because of the complications of secondary processes. The spectrum shape $f(E_0, E)$ obtained from a photon of energy E_0 is thus a complicated function of E_0 and E which, we believe, cannot readily (or reliably) be computed by multiple application of the laws for primary interactions. It is thus necessary to obtain $f(E_0, E)$ experimentally by using known energy calibration sources. This problem is separate from the calibration of the pulse height scale in energy units. We have detected no observable deviation from linearity in the calibration of pulse height *vs* energy based on the comparison of pulse-height distribution curves using photons of the following energies: annihilation photons (0.511 Mev); Cs^{137} photons (0.662 Mev), Na^{24} photons (1.38, 2.76 Mev), C^{12*} photons (4.43 Mev), and Co^{60} (1.17, 1.33 Mev) photons, for the full energy and the different reduced energy peaks.

The spectrometer energy calibration was performed occasionally during cyclotron runs by measuring the pulse spectrum of the gamma rays from Na^{24}. The extrapolation to higher energies was accomplished by the use of carefully calibrated attenuators in the amplifier circuits. Confidence in the method was established by comparing the measured energies of known gamma rays using the same attenuation settings. Possible rate dependence of the measured pulse amplitude was explored by subjecting the spectrometer to background radiation from natural sources which

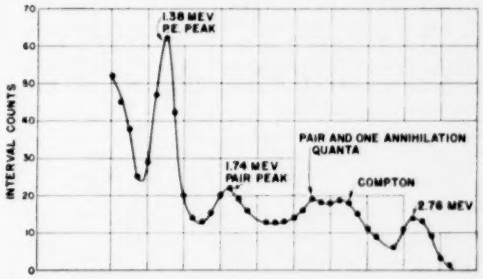

FIG. 8. Typical energy calibration curve using Na^{24}. The two γ rays at 2.76 and 1.38 Mev occur in equal number. The relative heights of the various peaks gives information about the relative efficiencies of the several interaction processes in NaI.

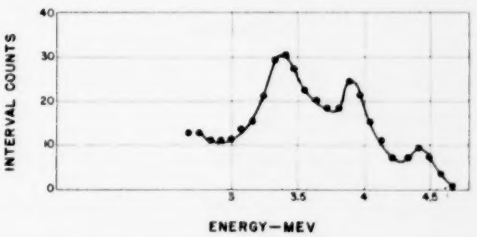

FIG. 9. Pulse-height distribution for the 4.43-Mev γ rays from C^* produced in the reaction $\alpha+Be^9\rightarrow C^{12*}+n$, using Po as a source of α particles. The peaks show a Doppler broadening of $\sim$2 percent due to the motion of the C^{12*} nuclei.

[9] C. M. Davisson and R. D. Evans, Revs. Modern Phys. **24**, 79, (1952). See Fig. 49 for several such plots. (The curves in Fig. 8 were calculated from Table XIV of this reference.)

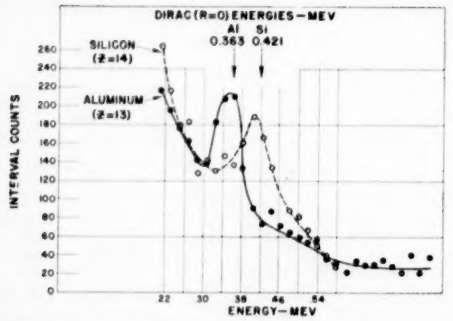

FIG. 10. Pulse-height distribution using Al and Si as the target materials ($Z=13$, 14). The peaks represent the full energies of the x-rays emitted in the $2p \rightarrow 1s$ transition. The expected energies for a point nucleus using $\mu = 210 m_e$ are included for reference. The shift in energy due to the finite extension of the nucleus is ~ 2 percent. In the case of Al in the region below 0.39 Mev the points are based on double the indicated number of counts. The interval width is approximately 50 kev.

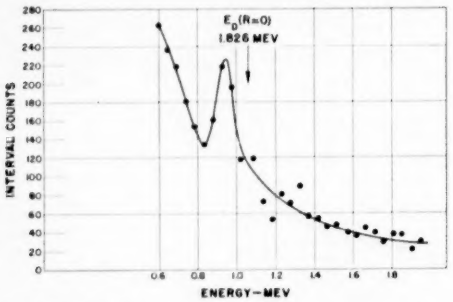

FIG. 11. Pulse-height distribution for Ti($Z=22$). The energy shift of 5 percent of the measured value due to finite nuclear extension is apparent. (In the figure 1.826 mev should read 1.045 mev.)

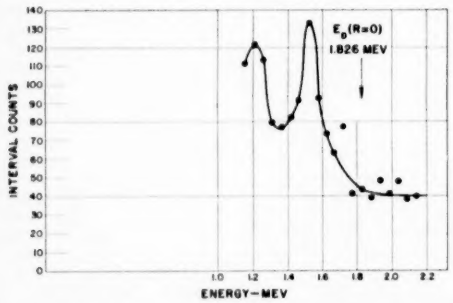

FIG. 12 Pulse-height distribution for Cu($Z=29$). Above 1.7 Mev the points are based on 0.6 the indicated number of counts. The energy shift due to finite nuclear extension is 18 percent of the measured value.

contributed a pulse rate that was considerably higher than the instantaneous rates encountered when using the cyclotron. No shift in pulse amplitude was observed until the rate was about four times the instantaneous rate experienced with the cyclotron. Also large variations in the cyclotron intensity did not cause noticeable shifts in the positions of the peaks.

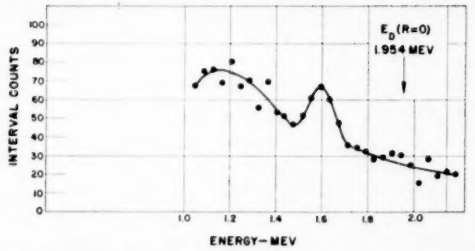

FIG. 13. Pulse-height distribution of Zn($Z=30$). In the region of the peak the points are based on 3 times the indicated number of counts. The energy shift due to finite nuclear extension is 22 percent of the measured value.

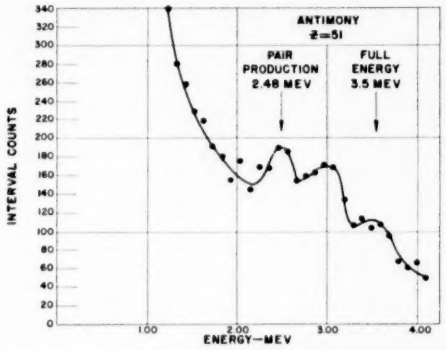

FIG. 14. Pulse-height distribution for Sb($Z=51$). The three peaks expected for a single photon of this energy are observed. The energy shift due to finite nuclear extension is 66 percent of the measured value.

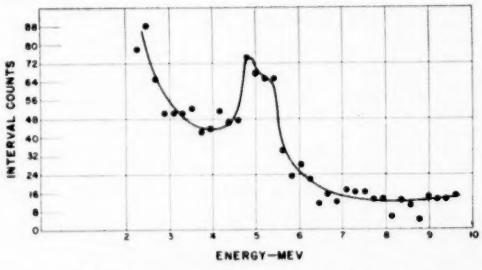

FIG. 15. Pulse-height distribution for Pb($Z=82$) taken with relatively coarse resolution (212 kev) and poor statistics over a wide energy range. The distinctive peak around 5 Mev defines the region of interest which was then investigated with higher resolution as is shown in the next figure.

Interpretation of the observed pulse height distribution curves is facilitated by examination of the Na^{24} and C^{12*} calibration curves of Figs. 8 and 9. In Fig. 9 the full energy peak of the 2.76-Mev photon is due mainly to the backward Compton scattering followed by the absorption of the secondary photon. The full energy peak for the 1.38-Mev photon is much larger. The 2.76-Mev photon also contributes peaks corresponding to pair production, and pair plus one annihilation photon. The effect of the Compton scattering, modified by some secondary absorption is also evident for the

2.76-Mev photon. It is important to remember that the 2.76- and 1.38-Mev photons are in cascade and are thus emitted in equal number. The relative peak heights thus give direct evidence concerning the relative efficiencies of various processes for these two energy photons.

Figure 9 shows the pulse spectrum resulting from the radiation from the Po-Be neutron source. The 4.43-Mev gamma rays result from a transition from the first excited level[10] of O^{12} to the ground state following the neutron-producing reaction. The source is uot monochromatic but shows a 2 percent Doppler broadening due to the momentum of the C^{12*} nucleus in the reaction. This Doppler broadening affects the shape of the pulse-height curve since the peaks would be expected to be significantly higher and narrower for a monochromatic source.

The coincidence resolution was somewhat better than 10^{-7} sec. This is sufficient to remove from the spectrum approximately half of the gamma rays originating from nuclear capture of the μ^- meson in the high-Z materials, and essentially all of them for lower-Z materials where nuclear absorption is slower.

EXPERIMENTAL RESULTS

The pulse-height distribution curves of Figs. 10 to 18 show the experimental results for studies of the x-rays resulting when μ^- mesons are stopped in Al, Si, Ti, Cu, Zn, Sb, Pb, Hg, and Bi ($Z=13$, 14, 22, 29, 30, 51, 82, 80, and 83). In the first few curves the predicted full energy position of the $2p\rightarrow 1s$ transition for a point nucleus is shown for reference (using $\mu=210m_e$). The x-ray energies vary from about 0.35 Mev for Al to 6.0 Mev for Pb and Bi. In the cases of Al, Si, Ti, Cu, and Zn, the main x-ray peak occurs at the full energy and general background and Compton scattering pulses contribute other pulse heights to the spectrum. For Sb the full energy occurs at about 3.5 Mev and three peaks, like those of Fig. 9, are obtained for E_0, $E_0-0.51$ Mev and $E_0-1.02$ Mev superimposed on a general background level.

Figure 15 shows the results for Pb over a region from about 2 Mev to 10 Mev using an interval width of about 210 kev. The x-ray peak stands out strongly near 5 Mev. The region from 4.2 to 6.0 Mev was then investigated using approximately 100-kv resolution width, with the typical results given in Fig. 16. This curve should be compared with Fig. 9 for interpretation. We have adopted, as most likely, the interpretation that the 5.0-Mev peak is the $2p_{\frac{3}{2}}\rightarrow 1s$ pair peak corresponding to 6.0 Mev for the x-ray energy. The $2p_{\frac{1}{2}}\rightarrow 1s$ peak should be 0.2 Mev lower in energy with half the intensity of the other. The peak near 5.3 Mev and the effects near 4.8 Mev and 5.6 Mev are not consistent with the pattern of Fig. 9 of three nearly symmetric peaks 0.5 Mev apart. In using Fig. 9 for reference, it should be noted that theoretical considerations, and the experimental results of other investigators (using similar sized NaI crystals), show that the pair peak should be relatively much larger compared to the intermediate and full energy peaks at 6 Mev than for 4.5-Mev photons.

Our tentative interpretation of Fig. 16 is thus that there are present $2p_{\frac{3}{2}}\rightarrow 1s$ and $2p_{\frac{1}{2}}\rightarrow 1s$ x-rays of 6.0 and 5.8 Mev respectively. The main peak at 5.0 Mev and the shoulder at 5.5 Mev followed by a sharp drop at

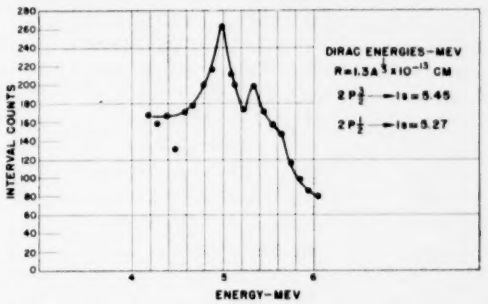

FIG. 16. Pulse-height distribution for Pb with ~100-kev interval width. The main peak at 5.00 Mev is interpreted as the pair production peak due to the x-rays from the $2p_{\frac{3}{2}}\rightarrow 1s$ transition. Further discussion of this curve is in the text. The energy shift due to finite extension is 172 percent of the measured value.

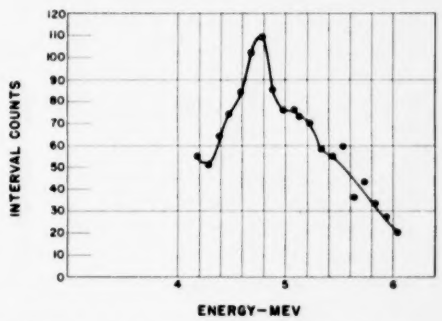

FIG. 17. Pulse-height distribution for Hg($Z=80$). The peak at 4.8 Mev obviously corresponds to the one at 5.0 Mev for Pb.

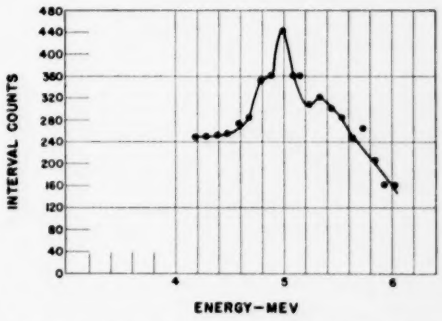

FIG. 18. Pulse-height distribution for Bi($Z=83$). The peak at 5.0 Mev obviously corresponds to the similar peak at the same energy for Pb.

[10] F. Ajzenberg and T. Lauritsen, Revs. Modern Phys. **24**, 354–359 (1952).

higher energies are thus the pair and pair plus one annihilation photon peaks for the 6.0-Mev photon. The effects at 4.8 and 5.3 Mev then correspond to the similar peaks for the 5.8-Mev photon. The assymetry and other features would seem to preclude a single photon. The peaks at 5.0 and 5.3 Mev would be hard to reconcile with the expected 0.51-Mev spacing expected for a single photon. Thus we believe that we see the expected fine structure splitting for Pb. The total counts for each point are indicated on the ordinate. The statistics suggest considerable uncertainty in the proper drawing of a curve. However, many separate runs of this type were taken and the essential features of this curve repeated in most of the runs. Thus we believe that the effects are much more likely to be real than the statistics of Fig. 16 alone would suggest. The absence of a large pair peak at 4.0 to 4.7 Mev in Figs. 15 and 16 seems to exclude an interpretation having the x-ray energy near 5.0 or 5.5 Mev. We intend to continue these measurements using a smaller interval width and faster resolving time to eliminate most of the nuclear gamma rays following the absorption of the μ meson.

The similar curves for Hg and Bi are shown in Figs. 17 and 18 and show similar structure. The main peak which came at 5.0 Mev for Pb is at 4.8 Mev for Hg and at 5.0 Mev also for Bi. Rembembering that the x-ray energy increases as the nuclear size decreases, the relatively high energy of the Pb peak compared with that for Bi (i.e., the same x-ray energy for $Z=82$ as for $Z=83$) may be associated with the closed proton shell at $Z=82$, giving a particularly "tight" configuration.

In the analysis of the experimental curves various assumptions are possible about what is assumed "known" or "unknown." Such parameters include (a) the meson mass, (b) the nuclear radius (for a uniform model of the nucleus), (c) the meson spin and magnetic moment. Since the meson mass is known[11] to be close to $210m_e$, we can first consider (b) and (c) using this mass value. As mentioned above, we believe that our results for Pb can best be explained in terms of the expected fine structure splitting for spin $\frac{1}{2}$ and the expected Dirac magnetic moment. Wheeler[5] discusses the expected effect of an anomolous moment.

TABLE IV. Assuming $\mu=210m_e$ and using a uniform nuclear model with $R_0=r_0A^{\frac{1}{3}}$, values of r_0 shown in column 3 gave the best fit to the experimental measured $2p_{\frac{1}{2}}\rightarrow 1s$ transition energies given in column 2 as a function of Z.

Z	$E(2p_{\frac{1}{2}}\rightarrow 1S)$ (experimental, Mev)	r_0 (10^{-13} cm)
22	0.955	1.17
29	1.55	1.21
51	3.50	1.22
82	6.02	1.17

[11] See R. E. Marshak, reference 1, Chap. 6, for a discussion and listing of further reference.

Using $\mu=210m_e$, the nuclear radii which provide the best fit to the data for various elements are given in Table IV. The values all lie near $R_0=1.2\times10^{-13}A^{\frac{1}{3}}$ cm which is much smaller than the radius indicated by other nuclear "size sensitive" experiments. This matter is discussed in more detail below.

For a low-Z element the probability density of the K shell meson near $r=0$ varies as Z^3 and the probability of finding it in the nucleus as $Z^3R_0^3$. The mean change, ΔV, in the potential energy inside the nucleus, because of its nonzero size, is proportional to Z/R_0. Thus the energy shift ΔE due to finite nuclear size should be proportional to $Z^4R_0^2$ for light nuclei. Since the binding energy is proportional to Z^2, the *fractional* energy shift should be proportional to $Z^2R_0^2$. The x-ray energy is relatively insensitive to R_0 for elements of low Z. In the case of Al the total nuclear size effect is only approximately 2 percent. Thus, in principle, the most precise determination of the meson mass could be made using a material of very low Z. However, the limited number of photons producing photoelectrons at the 5819 cathode causes the fractional resolving power of the NaI-5819 detection system to be proportional to $E^{\frac{1}{2}}$ for small E (photon energy). The greatest accuracy in the determination of μ with the present detection system was obtained using $Z=22$, where the energy resolution is not too poor and the nuclear size effect is still small.

The curve for Ti is shown in Fig. 11. Because of the prominent nature of x-ray peak for this element, it was often measured when an over-all check of the operation of the complete system was desired. Since independent calibration runs were made at regular intervals during all runs, a large number of independent evaluations of the x-ray energy for Ti were obtained, all values falling within 1 percent of the mean energy 0.955 Mev. Figure 19 gives a plot of the predicted x-ray energy as abscissa *vs* the μ-meson mass as ordinate. The four lines are for four possible choices of nuclear radius parameter $r_0=R_0A^{-\frac{1}{3}}$ in units of 10^{-13} cm. The experimental results all came within the cross-hatched region about 0.955 Mev. For $\mu=210m_e$, this gives $r_0=1.17\times10^{-13}$ cm in essential agreement with the results for higher Z. The choice $r_0=1.4\times10^{-13}$ cm gives $\mu=217m_e$ which is outside the range allowed by other experimental determinations.

The calculated nuclear radii of a number of elements for $Z=22$ to $Z=83$ (Table IV) are in close agreement and require $r_0\approx1.2\times10^{-13}$ cm, with $r_0=1.17\times10^{-13}$ cm for Pb (in terms of the uniform model). Since many other nuclear-size-sensitive experiments seemed to agree on a choice $r_0=1.4$ to 1.5×10^{-13} cm, and since the precision of the present results for high-Z materials is better than 1 percent for r_0, it is important to examine the present results in more detail. This is done by Cooper and Henley in a following paper.[7] The alternative choices seem to be (a) the present results need large corrections due to effects not considered in the present analysis, or (b) a modification of the "uniform

model" of the nucleus is necessary to account simultaneously for the results of the present experiment and also those of other methods.

Under possibility (a) above we consider the nuclear polarizability in the field of the meson. This would increase the interaction energy and thus the x-ray energy. As mentioned above, estimates[7] of this effect indicate that it is probably less than 0.06 Mev for Pb. The similar results for $Z=80$, 82, and 83 seem to rule out the possibility of any strong "resonance" effect in the polarizability of Pb due to accidental features of the position of its low-lying nuclear energy levels. The second possibility is that there is some additional, at present unknown, specific interaction of μ mesons with nuclear matter. This would have to be an attractive interaction of 3-Mev depth to shift r_0 for Pb from 1.17 to 1.4×10^{-13} cm. Although this possibility cannot be completely dismissed, it seems the least likely of the alternative choices. Thus we believe that neither of these effects are present in significant amount in our measurements.

The alternate choice is to accept the results of the present experiment as stated and also accept the 15 to 20 percent larger results for r_0 of other methods and try to arrive at a nuclear model which will "explain" all of the results simultaneously. To do this we note that total cross sections from scattering experiments, and α-decay lifetimes, are mainly sensitive to conditions at the "edge" of the nucleus. The present experiment is mainly sensitive to the proton density in the inner region of the nucleus and requires an interior charge density $(1.4/1.17)^3=1.7$ times larger (on the uniform model) than do other experiments. This would suggest a nuclear model with a central density two or more times the usually accepted value. The density should then fall off relatively gradually in an extended "edge" region to give the effectively larger radius found by "edge-sensitive" experiments.

It is easily seen that the nuclear "surface" *cannot* be sharp. Even if we consider a nuclear model where the nucleons move in an effective potential with a sharp edge, the nucleon wave functions still have an exponential attenuation in the classically forbidden region. Furthermore, since the effective potential is due to the presence of other nucleons in forming a "self-consistent nuclear box", and in view of the $1\text{–}3\times10^{-13}$ cm range of the basic nuclear forces, the effective potential and nucleon density must require a dropping-off region significantly larger than the range of the nuclear forces.

In α-decay theory, the effective value of R_0 is where the nuclear density is large enough to essentially overcome the Coulomb barrier effects. This is further complicated by the question of the position of the α particle's effective "surface," which must be some distance from its center. The usual addition[12] of 1.2 $\times10^{-13}$ cm for these effects could certainly be much too small.

Similarly, fast neutron scattering experiments are somewhat difficult of exact interpretation for a nucleus with a gradual falling off of nuclear density at the "surface." For neutrons of a few Mev energy particularly, there is probably strong interaction with the outer regions of the nucleus.[13] Similar remarks apply for meson scattering experiments.

The evaluation of nuclear radii for low-Z elements from the Coulomb energy difference of mirror nuclei leads to values of r_0 from 1.39 to 1.47×10^{-13} cm when a uniform model is employed. Since the Coulomb energies for mirror nuclei would seem to have about the same dependence on the nuclear density distribution as does the K-shell μ-meson binding, this would seem to constitute a serious disagreement with the results of the present experiment. However, further study of this matter has been made by Cooper and Henley[7] who find that various corrections should be applied to the mirror nuclei results. Briefly these fall in the following three catagories, all of which tend to reduce the Coulomb energy difference for mirror nuclei.

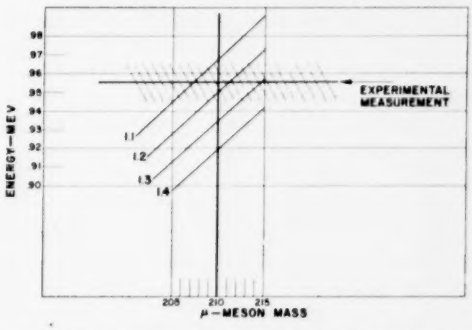

FIG. 19. The $2p\rightarrow1s$ transition energy in Ti as a function of meson mass and nuclear radius. The experimental values all fall within 1 percent of 0.955 Mev. The calculated energies are shown for various values of r_0 in units of 10^{-13} cm, assuming constant proton density inside the nucleus.

The first effect is associated with the Pauli exclusion principle which requires that the total nuclear wave function be antisymmetric in all of the protons. This leads to an excess of space-antisymmetric pairings of protons which means that they have a tendency to correlate their motions in such a way as to *increase* their average spacing. Furthermore, it is not the *average* Coulomb energy per proton that is measured, but the *change* in Coulomb energy when the last nucleon changes from a neutron to a proton. Thus the Coulomb energy difference involves the total increase in the number of antisymmetric pairings when $Z\rightarrow Z+1$. The second effect comes from a study of the predictions of the shell model[14] of Mayer and Haxel, Jensen, and Suess which

[12] See J. M. Blatt and V. W. Weisskopf, *Theoretical Nuclear Physics* (John Wiley and Sons, Inc., New York, 1952), Chap. 11, Eq. (2.19).

[13] R. Jastrow and J. Roberts, Phys. Rev. **85**, 757 (1952).

[14] See P. F. A. Klinkenberg, Revs. Modern Phys. **24**, 63 (1952).

identifies the transforming nucleon as being in a single-particle d state for the important region $Z=9$ to perhaps 20. The radial probability density for a d state gives an effective radius which is appreciably greater than the average over all of the protons, even for a square well potential. If a harmonic oscillator potential is used, the radius at which $E=V$ increases with increasing individual particle energy. Since the transforming nucleon is considered to occupy the highest filled individual-particle state, its wave packet tends to fill a larger volume than the other individual particle wave packets. This third effect is true even for the one-dimensional problem and is thus not directly related to the angular momentum of the state. Considering all of these three effects together, it seems that the mirror nuclei results can probably be brought into agreement with the results of the present experiment. It may be noted that Wilson[15] has reanalyzed the results for mirror nuclei using a gradual falling off of nuclear density at the surface, but without considering the special effects mentioned above.

If a gradual dropping off of nuclear density at the "surface" of the nucleus is assumed, it is still of interest to consider the variation $\rho(r)$ of the proton density inside this boundary region. Feenberg[16] particularly has emphasized the Coulomb repulsion effect and favored a nuclear model where the proton density is larger near the surface than at the center. This leads also to a quite different explanation[16] of the "magic" numbers and is in disagreement with the model more generally favored at present,[14] which essentially assumes a potential closer to that of the oscillator model. In conclusion we note that results for high-energy electron scattering by nuclei were presented by R. Hofstadter *et al.* at the 1953 Washington Meeting of the American Physical Society. Preliminary analysis of their results seemed to favor a model where $\rho(r)$ is a maximum at $r=0$ and drops off steadily at larger r. It seems likely that the most precise determination of the correct $\rho(r)$ *vs* r will come from combining the results of such electron scattering experiments, which suggest the shape of $\rho(r)$ *vs* r, with the μ-meson x-ray results, which give a precision evaluation of the scale factor r_0 for any assumed shape $\rho(r/r_0)$.

It is also possible to obtain information concerning nuclear size by using the results of ordinary (electron) x-ray spectroscopy, as has been pointed out by Schawlow and Townes.[17] The $2p_{\frac{1}{2}}$, $2p_{\frac{3}{2}}$ fine structure splitting for high-Z elements is affected by nuclear size to a very small, but measurable extent. The analysis[17] of available x-ray data gives $r_0 \approx 1.5\times10^{-13}$ cm, with much lower precision than the results of the μ-mesonic x-ray measurements. With improvements in the experimental accuracy of the (ordinary) x-ray measurements, and re-examination of the theoretical analysis to see that no significant higher-order effects (of quantum electrodynamics) have been neglected, the x-ray fine structure splitting should be capable of providing independent, precise information concerning nuclear size.

We wish to thank the many members of the Columbia Physics Department with whom we have discussed various aspects of the problem. Particular thanks are due Dr. Henley and Mr. Cooper, and Professor Wheeler for communication of the results of their calculation prior to publication. Mr. Samuel Koslov has given considerable valuable assistance in the later phases of the experimental measurements and in the calculations.

[15] R. R. Wilson, Phys. Rev. **88**, 350 (1952).

[16] E. Feenberg and K. C. Hammack, Phys. Rev. **75**, 1877 (1949). See also other papers by L. W. Nordheim and M. G. Mayer in the same issue (pp. 1968, 1969, and 1894).

[17] A. L. Schawlow and C. H. Townes, Science **115**, 284 (1952).

PHYSICAL REVIEW VOLUME 92, NUMBER 3 NOVEMBER 1, 1953

Mu-Mesonic Atoms and the Electromagnetic Radius of the Nucleus

L. N. COOPER AND E. M. HENLEY*
Department of Physics, Columbia University, New York, New York
(Received July 22, 1953)

An attempt is made to interpret recent experiments on the x-ray spectrum of μ^--mesonic atoms. In particular, an analysis is made of the $2p-1s$ transition energies, which are sensitive to the nuclear charge distribution. Agreement with experiment is obtained for a uniform sphere of nuclear charge of radius $R \approx 1.2\times10^{-13}A^{\frac{1}{3}}$ cm. Various effects such as nuclear polarization, electric quadrupole moment, screening by atomic electrons, and a meson-nucleon interaction of the order indicated by the charge exchange capture reaction are considered and do not alter this radius appreciably. However, an anomalous meson-nucleus interaction, though doubtful, could alter the estimated radius. It is shown that the small nuclear radius is not in disagreement with that determined by other electromagnetic measurements, including mirror nuclei experiments.

INTRODUCTION

THE discovery by Conversi, Pancini, and Piccioni[1] of the smallness of the μ^--nuclear interaction and the resulting realization that the μ meson was not the Yukawa particle, although originally a great disappointment to theoretical physicists, has led to an interesting and useful tool with which the nucleus can be probed.

It was soon realized[2,3] that a relativistic μ meson can be slowed down in condensed matter, captured in bound states about a nucleus, and can make transitions to the lowest bound states in a time short compared to that for meson decay or nuclear capture. Thus there seemed to be a strong possibility that μ-mesonic atoms could be produced. Such atoms are of great interest because an investigation of their spectra might yield information about the nuclear proton distribution. Furthermore, if spectra of sufficient accuracy could be obtained, the spin, magnetic moment, and mass of the μ meson could be determined independently of other measurements. This was suggested by Wheeler,[4] and a study of μ^--mesonic atomic spectra has been carried out by Fitch and Rainwater.[5]

When first captured by an atom the μ^- meson interacts with the atomic electrons and with the nucleus, cascading down to the lower orbits through radiative and electronic processes. The highest angular momentum states are preferred for statistical reasons, and there is a large probability that the meson will fall to a $2p$ state. This is enhanced by the absence of a metastable $2s$ level. In the mesonic atom the $2s$ level is above the $2p$ level because of the extension of the nucleus. Wheeler[4] has shown that for Z larger than 15 the probability of radiative transitions among the lowest orbits is overwhelmingly larger than that of electronic (such as Auger) transitions. Thus a $2p-1s$ radiative transition is expected. A transition to the $1s$ state is of particular interest because the $1s$ level is most sensitive to the nuclear charge distribution. (The higher levels progressively become more hydrogen-like.) The energy and intensity of the x-rays emitted in the $2p-1s$ transition make them easiest to observe, and it is these x-rays that Fitch and Rainwater have studied.

The use of the μ^- meson as a nuclear probe is possible because the mesonic orbits are much closer to the nucleus than the corresponding electron orbits. This is due to the meson-to-electron-mass ratio, which is about 210. For heavy elements, the average radius of the meson ground state may lie inside the nucleus. In the case of lead for example, the probability of finding the $1s$-state meson inside the nucleus is approximately one half. For the heavy elements therefore, the lowest meson energy levels and transition energies are very sensitive to the nuclear charge distribution.

The effect of the atomic electrons on the lowest meson energy levels can be calculated by considering the screening effect of the electrons as decreasing the effective nuclear charge. The p-level shift for a heavy element such as lead is about 0.005 Mev or 0.1 percent of the p-state energy, while for a lighter element such as copper the corresponding shift is about 0.002 Mev or 0.3 percent of the orbit energy. We can therefore neglect the interaction of the meson with the atomic electrons in calculating the expected energy of the radiation emitted in the lowest-level transitions of the meson, and can treat the meson and nucleus as an isolated system.

When the experiment is carried out for an element with several isotopes, the chief effect to be expected with the present resolution is a broadening of the observed spectrum lines.

There are two distinct interactions of the meson with a nucleus. One is the electromagnetic interaction, which, as Wheeler has shown,[4] is predominant, while the other—a specific nuclear interaction such as that leading to the charge-exchange-capture reaction—is much smaller.

The electromagnetic interaction itself can be divided into static and dynamic interactions. These latter give rise to such refinements in the spectrum as hyperfine

* Frank B. Jewett Fellow.
[1] Conversi, Pancini, and Piccioni, Phys. Rev. **71**, 209 (1947).
[2] Fermi, Teller, and Weisskopf, Phys. Rev. **71**, 314 (1947).
[3] E. Fermi and E. Teller, Phys. Rev. **72**, 399 (1947).
[4] J. A. Wheeler, Revs. Modern Phys. **21**, 133 (1949).
[5] V. L. Fitch and J. Rainwater, Phys. Rev. (preceding paper) Phys. Rev. **92**, 789 (1953).

structure, which are very small. For aluminum, with spin 5/2, the splitting effect due to the interaction with the nuclear magnetic moment is about 10 ev.[4] For lead, Pb^{207}, the corresponding number is about 3 kev.

In Sec. I it is shown that the energy levels of a μ^--mesonic atom can be obtained by considering the meson to move in the electric potential produced by a uniformly charged spherical nucleus. In addition, for light nuclei, the shift of the $2p-1s$ transition energy resulting from the extent of the nucleus is shown to depend only on the second moment of the charge distribution.

In Sec. II we consider the dependence of these energy levels on (1) meson properties, (2) the assumed nuclear ground-state charge distribution, (3) nuclear polarization effects, and (4) anomalous meson nuclear interactions.

In Sec. III the results of the μ^--meson experiment are compared with other mesurements of the nuclear radius. Electromagnetic radii, as measured by high-energy electron and proton scattering and by isotope shifts, are consistent with the present experiment. We show that mirror nuclei radius measurements cannot be made consistent with the above by charge-distribution variations alone. However, inclusion of the Coulomb exchange energy and angular momentum effects in the calculation of the energy change in mirror nuclei transitions removes the discrepancy.

I. ENERGY LEVELS OF THE MESONIC ATOM

The entire meson-nucleus interaction can be divided into two parts, one of which is electromagnetic in origin, while the other is a specific nuclear interaction. Because of the smallness of the nuclear term, it is possible to calculate the energy levels of the meson-nucleus system by considering only the electromagnetic interaction and treating the nuclear interaction as a perturbation.

The Schrödinger equation for the meson-nucleus system is then

$$H\Psi=(H^N+H^\mu+H^e)\Psi=W\Psi, \tag{1}$$

where H^N is the total nuclear Hamiltonian, H^μ is the free meson Hamiltonian, and H^e is the electromagnetic interaction of the meson and nucleus.

In this treatment the μ^- meson is taken to have a spin[5] of $\frac{1}{2}$ and to satisfy the Dirac equation; thus H^μ is

$$H^\mu=\boldsymbol{\alpha}\cdot\mathbf{p}+\beta\mu.$$

($\hbar=c=1$ is used throughout.) $\boldsymbol{\alpha}$ and β are the usual Dirac matrices, and μ is the meson mass.

In the electromagnetic interaction term the nucleus is not treated as a point charge, since for heavy elements the meson may spend a considerable portion of its time inside nuclear matter. For a nucleus with Z protons H^e is

$$H^e=\sum_{i=1}^{Z}\left(-\frac{e^2}{|\mathbf{r}-\mathbf{R}_i|}\right), \tag{2}$$

where $\mathbf{R}_i$ is the position vector of the ith proton and $\mathbf{r}$ is the position vector of the μ^- meson.

The wave function for the meson-nucleus system can be separated if we assume that the nucleus is unaffected by the presence of the meson. Such an assumption is a legitimate first approximation because the meson-nucleus interaction is small compared to the forces which bind the nucleus. With this assumption, Ψ becomes

$$\Psi(\mathbf{R}_1\cdots\mathbf{R}_i\cdots\mathbf{R}_Z,\mathbf{r})=\psi(\mathbf{R}_1\cdots\mathbf{R}_i\cdots\mathbf{R}_Z)\Phi(\mathbf{r}),$$

and H^e can be replaced by

$$\langle\psi_0|H^e|\psi_0\rangle\equiv V, \tag{3}$$

where $\psi(\mathbf{R}_1\cdots\mathbf{R}_Z)$ is the nuclear wave function (ψ_0 is the ground state) and $\phi(\mathbf{r})$ is the meson wave function. In this case Eq. (1) becomes

$$H^N\psi=E\psi, \tag{4a}$$

and

$$(H^\mu+V)\Phi=\epsilon\Phi. \tag{4b}$$

W is thus $W=E+\epsilon$, where E is the nuclear and ϵ the mesonic energy.

If the nuclear ground-state charge distribution is taken to be uniform

$$\begin{aligned}&\rho(\mathbf{R}_i)=\text{constant} && R_i<R\\ &\rho(\mathbf{R}_i)=0 && R_i>R,\end{aligned} \tag{5}$$

then the potential V becomes

$$\begin{aligned}V&=-\frac{Ze^2}{R}\left(\frac{3}{2}-\frac{1}{2}\frac{r^2}{R^2}\right) && r\leq R\\ &=-\frac{Ze^2}{r} && r\geq R,\end{aligned} \tag{6}$$

where R is the nuclear radius. Equation (4b) is then the Dirac equation for a charged particle in the potential of a uniform sphere of charge Ze. This can be expanded into large and small components because the meson nucleus system is not very relativistic. From Eq. (6), the minimum potential, $-3Ze^2/2R$, is seen to occur at the center of the nucleus and to decrease with Z. Even for a heavy element such as lead $|V|_{\max}$ is only approximately 25 Mev, which is much smaller than the meson rest mass of 107 Mev. The equation for the large components may be written as

$$\left[H_S-\frac{(\epsilon-V)^2}{2\mu}+\frac{1}{8\mu^2}\nabla^2+\frac{1}{2\mu^2}\frac{1}{r}\frac{dV}{dr}\mathbf{L}\cdot\mathbf{S}\right]\phi_L=\epsilon\phi_L, \tag{7}$$

[5] J. Tiomno and J. A. Wheeler, Revs. Modern Phys. **21**, 144 (1949).

where H_S is the Schrödinger Hamiltonian, $H_S=-\nabla^2/2\mu+V$, and the last term is the spin-orbit interaction. We have solved this equation, treating the relativistic terms as perturbations on the Schrödinger solution. This can be shown to give energies that are accurate to better than 1 percent. The eigenvalues of the Schrödinger equation are obtained by matching the logarithmic derivatives of the internal and external wave functions at the edge of the nucleus. The internal wave function is[7]

$$\phi_{\epsilon l}(\text{internal}) \sim \exp(-\beta^2\rho^2/2)(\beta\rho)^l \lim_{b\to\infty} F(\gamma, b, l+3/2; \rho^2/b). \quad (8a)$$

For $l=0$, this can be written simply as

$$\phi_{\epsilon 0}(\text{internal}) \sim \exp(-\beta^2\rho^2/2)\mathfrak{H}_\Gamma(\beta\rho). \quad (8b)$$

Here $\rho=(8\mu\epsilon)^{\frac{1}{2}}r$, $\beta^4=Ze^2/(64\mu\epsilon^2R^3)$, $\gamma=\Gamma-(l+1)$, $\Gamma=(3Ze^2/8\epsilon R-\frac{1}{4})/2\beta^2-\frac{1}{2}$, l is the angular momentum of the state of energy ϵ, F is the hypergeometric series,[7] and $\mathfrak{H}$ is that solution to the Hermite differential equation[7] which is zero at the origin. The external wave function is

$$\phi_{\epsilon l}(\text{external}) \sim \rho^{-1}W_{k,[l(l+1)+\frac{1}{4}]^{\frac{1}{2}}}(\rho), \quad (9)$$

where $k=Ze^2(\mu/2\epsilon)^{\frac{1}{2}}$ and W is the confluent hypergeometric function.[8]

The corrections to the nonrelativistic energy levels due to the Dirac terms in Eq. (7) are of the order of 2 percent for lead and copper. The essential nonrelativistic motion of the meson allows us to treat corrections such as those arising from polarization as perturbations on the nonrelativistic solutions.

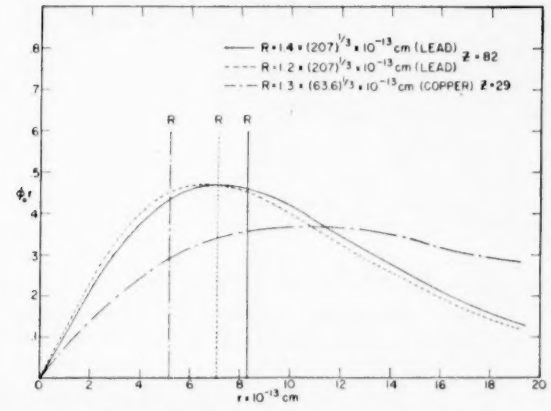

FIG. 1. Normalized, nonrelativistic 1s-state meson wave functions for copper and lead. The nuclear charge distribution is taken to be uniform and of radius $R=r_0A^{\frac{1}{3}}$.

[7] E. U. Condon and P. M. Morse, *Quantum Mechanics* (McGraw-Hill Book Company, Inc., New York, 1929), p. 79; H. Margenau and G. M. Murphy, *The Mathematics of Chemistry and Physics* (D. Van Nostrand and Company, New York, 1943), pp. 72, 76.

[8] E. T. Whittaker and G. N. Watson, *Modern Analysis* (MacMillan Company, New York, 1944), Chap. 16, especially p. 343.

TABLE I. Experimental and calculated $2p-1s$ transition energies. The meson mass is taken as $210m_e$.

Element	Z	Experimental $2p_{\frac{3}{2}}-1s_{\frac{1}{2}}$ energy Mev	Calculated r_0 ($R=r_0A^{\frac{1}{3}}$) to fit experiment ($\times10^{-13}$ cm)	Calculated $1s_{\frac{1}{2}}$ energy Mev	Calculated $2p_{\frac{3}{2}}-1s_{\frac{1}{2}}$ energy Mev	Calculated $2p_{\frac{1}{2}}-1s_{\frac{1}{2}}$ energy Mev
				$R=1.3\times10^{-13}\times A^{\frac{1}{3}}$ cm		
Aluminum	13	0.35				
Silicon	14	0.41				
Titanium	22	0.955	1.17	1.282	0.935	0.933
Copper	29	1.55	1.21	2.12	1.52	1.51
Zinc	30	1.60				
Antimony	51	3.50	1.22	5.22	3.41	3.37
Mercury	80	5.80				
Lead	82	6.02	1.17	10.11	5.48	5.30
Bismuth	83	6.02				

Fitch and Rainwater have solved the Dirac Eq. (4b) without expansion into large and small components and by other methods described in the preceding paper. For the elements we have treated, our calculated energy levels agree with theirs to within 1 percent. Their experimental and calculated results are repeated in Table I below. Our nonrelativistic wave functions for the 1s level of lead ($r_0=1.4$ and 1.2×10^{-13} cm) and copper ($r_0=1.3\times10^{-13}$ cm) are plotted in Fig. 1.

It is seen from Table I that for a meson mass of $210m_e$ and a nuclear radius larger or equal to $1.3\times10^{-13}A^{\frac{1}{3}}$ cm (as expected from other data[9]), the calculated $2p_{\frac{3}{2}}-1s_{\frac{1}{2}}$ transition energies are consistently smaller than those observed. A radius $R\approx1.2\times10^{-13}A^{\frac{1}{3}}$ cm, on the other hand, is consistent with the experimental data for all elements.

For light nuclei it is possible to treat the energy shifts due to both nuclear extension and relativistic effects as perturbations on the Schrödinger equation for a point charge. The correction due to nuclear extension $\Delta\epsilon_R$ is negligible for all but the 1s state. The corrections due to both effects may be computed as a power series expansion in $Z\alpha$ and $Z\alpha\mu R$, where α is the fine structure constant. For an arbitrary charge distribution the leading term in the expansion of $\Delta\epsilon_R$ is

$$\begin{aligned}\Delta\epsilon_R&=\langle\phi_0|V-V_p|\phi_0\rangle\\&=\frac{1}{\pi}(Z\alpha\mu)^2\int(V-V_p)d\mathbf{r}+\cdots\\&=-\frac{1}{6\pi}(Z\alpha\mu)^3\int\rho r^2d\mathbf{r}+\cdots,\end{aligned} \quad (10)$$

where the latter equality holds if

$$\lim_{r\to\infty} r^3(V-V_p)=0.$$

In Eq. (10) ϕ_0 is the nonrelativistic hydrogen-like wave function for the mesonic 1s level; V is defined by Eq.

[9] J. M. Blatt and V. F. Weisskopf, *Theoretical Nuclear Physics* (John Wiley and Sons, Inc., New York, 1952), pp. 14–15.

(3), V_p is the interaction energy of a point nucleus with the μ meson, $V_p=-Ze^2/r$, and ρ is the charge density corresponding to V, $\rho=-\nabla^2V$. For light nuclei, therefore, it is essentially only the second moment of the charge distribution which is determined by the x-ray transitions observed by Fitch and Rainwater. It is of interest to note that the integral in Eq. (10) determines the change in the cross section for the scattering by nuclei of high-energy electrons (less than $\sim$40 Mev) when the nucleus is an extended source rather than a point charge, as was shown by Feshbach.[10]

For a uniform charge distribution Eq. (10) gives

$$\Delta\epsilon_R=-\tfrac{2}{5}\mu(Z\alpha)^2(Z\alpha\mu R)^2. \tag{11}$$

The dependence of the leading term in $\Delta\epsilon_R$ on Z and R, as given by Eq. (11) is quite general. This can be seen from Eq. (10), since $\int\rho r^2d\tau$ is proportional to ZR^2. Hence $\Delta\epsilon_R$ is proportional to Z^4R^2, and it is only the coefficient [$\frac{2}{5}$ in Eq. (11)] which depends on the nuclear charge distribution.

II. CORRECTIONS TO ENERGY LEVELS

It is now necessary to consider the detailed dependence of the results of Sec. I on the assumptions that have been made.

A. Meson Properties

1. *Spin and Magnetic Moment*

The μ^- meson has been assumed to have a spin of one half. For a point particle spins of one or larger, or a large anomalous magnetic moment are inconsistent with cosmic-ray burst data.[11–13] An anomalous magnetic moment of about eight times the normal Dirac moment would be necessary to increase the $2p_{\frac{1}{2}}-1s_{\frac{1}{2}}$ transition energy by 0.5 Mev in lead. (Such an energy shift would lead to a radius of $1.3\times10^{-13}A^{\frac{1}{3}}$ cm from the experimental data.) The $2p_{\frac{1}{2}}-2p_{\frac{3}{2}}$ level splitting would then be 1.44 Mev and should have been observed. (Experimentally a 0.2-Mev splitting is believed to have been observed, corresponding to the normal Dirac moment.)

Spin zero is inconsistent with the decays of the pi meson and the mu meson, if the neutral decay products are assumed to be neutrinos. Even if the meson spin is assumed to be zero, however, the energy levels obtained in Sec. I remain substantially unaltered. The reason for this is that the spin interaction is small, its largest effect being to produce a fine structure in various orbital angular momentum states. The absence of the $2p$ fine structure would decrease the maximum calculated $2p-1s$ transition energy by a small amount.

[10] H. Feshbach, Phys. Rev. **84**, 1206 (1951).
[11] R. F. Christy and S. Kusaka, Phys. Rev. **59**, 414 (1941).
[12] R. E. Lapp, Phys. Rev. **64**, 255 (1943); **69**, 312 (1946).
[13] F. E. Driggers, Phys. Rev. **87**, 1080 (1952). Additional references are given here.

2. *Mass*

In the calculations reported in Table I the mass of the μ meson was taken to be $210m_e$, in agreement with the best measurements of this mass,[14,15] as well as a good fit of all the Fitch and Rainwater data. For a point nucleus, the hydrogen-like meson energy levels (and transition energies) are directly proportional to the mass of the meson. For a uniformly charged nucleus, however, the potential inside the nucleus is harmonic [see Eq. (6)]. Thus the meson spends some time in a potential for which the transition energies are inversely proportional to the square root of the mass.[16] The calculated $2p-1s$ transition energies then are not directly proportional to the meson mass. In particular, for heavy nuclei ($A\sim200$), where the probability of the meson being inside the nucleus is about one-half, the energy levels are quite insensitive to small variations in mass.

A perturbation procedure allows us to estimate the dependence of the energy levels on the meson mass as

$$\Delta\epsilon_{\mu k}=-(\epsilon_k-\bar{V}_k)\Delta\mu/\mu, \tag{12}$$

where ϵ_k is the energy for a meson of mass $210m_e$ in the state specified by the quantum number k, $\bar{V}_k=\langle\phi_k|V|\phi_k\rangle$, and $\Delta\mu$ is the change in meson mass. The term in parentheses in Eq. (12) represents the average kinetic energy of the meson in the state k.

For lead, with a nuclear radius $R=1.4A^{\frac{1}{3}}\times10^{-13}$ cm, a 5 percent *increase* in mass *increases* the $2p-1s$ transition energy by about 0.2 percent, or 8.0 kev. This small change in energy means that the average kinetic energies in the $2p$ and $1s$ states are almost equal; exact equality would lead to no change in the transition energy for a small variation in mass. For a radius of $1.3A^{\frac{1}{3}}\times10^{-13}$ cm, the increase in energy is approximately 14 kev. For a lighter nucleus, such as copper, on the other hand, a mass *increase* of only 0.7 percent *increases* the $2p-1s$ transition energy by a much as 10 kev. In this case, then, to fit the experimental transition energy with a radius, $r_0\approx1.3\times10^{-13}$ cm, the meson mass required would be 215–$216m_e$. A similar result is obtained for titanium, as shown in the accompanying paper by Fitch and Rainwater.

B. The Nuclear Ground State

In Part I the nuclear ground state proton charge distribution has been considered to be uniform and spherically symmetric.

1. *Discreteness of Charge Distribution*

In the above calculations the protons were replaced by a continuous distribution. This assumes implicitly

[14] Lederman, Booth, Byfield, and Kessler, Phys. Rev. **83**, 685 (1951).
[15] W. H. Barkas, University of California Radiation Laboratory Report UCRL-1285 (unpublished).
[16] L. I. Schiff, *Quantum Mechanics* (McGraw-Hill Book Company, Inc., New York, 1949), p. 61.

that the meson wavelength is much larger than the average wavelength of the nucleons. For heavy atoms, however, the wavelength of a meson in the $1s$ state is of the order of magnitude of nuclear dimensions. An estimate of the effect of a discrete nuclear charge distribution can be obtained by calculating the interaction of a meson with a static nucleon lattice. The protons are arranged symmetrically on spherical shells, the number of protons on a shell and the spacing of the shells being so chosen that the radial variation of the potential produced gives no energy level shifts from the uniform distribution. The shifts in energy levels can then be calculated for a single shell by perturbation theory to second order. (The first order is zero.) These are negligible for light nuclei because of the large average distance of the meson from the nucleus. Even for a heavy nucleus such as lead, the deviation from the energy levels calculated in Part I is less than 0.1 percent (10 kev) for the $1s$ state.

2. *Variations in the Ground-State Radial Charge Distribution*

We consider next variations in the radial distribution of the nuclear charge. Since the observed maximum $2p-1s$ transition energy determines only one parameter, it is not possible to specify completely the nuclear charge distribution from this data. For comparison with other experiments it was convenient to use as this parameter the radius of the uniform charge distribution which fits the observations. This defines an "effective electromagnetic radius," which we saw to be $1.2A^{\frac{1}{3}}\times10^{-13}$ cm.

For a given maximum charge density it is the uniform charge distribution which binds the $1s$ state meson most closely, and therefore gives the largest $2p_{\frac{1}{2}}-1s_{\frac{1}{2}}$ transition energy. This is so because the absolute value of the potential produced by a nonuniform charge distribution, with a fixed maximum density, is, from Gauss' law, always smaller than that of a uniform distribution with this maximum density. Thus any nuclear 'tail' or surface effect, without an increase in the maximum charge density, will decrease the $2p-1s$ transition energies.

Also the model with the proton density increased towards the edge of the nucleus as a result of Coulomb repulsion[17] will decrease the electromagnetic potential inside the nucleus and thus decrease the binding of the $1s$ state.

The deviations from a uniform charge distribution considered above, all decrease the calculated transition energy. The latter can be increased only by increasing the proton charge density at the center of the nucleus. Some evidence for such a distribution has recently been obtained by Hofstadter,[18] and analyzed by Schiff,[19] who finds a distribution compatible with $\rho(\mathbf{r})=Ze\exp(-r/a)/2a^3$. The potential V of such a distribution is [see Eq. (3)]

$$V_{\exp}=-\frac{Ze^2}{r}\left\{1-e^{-r/a}\left(1+\frac{r}{2a}\right)\right\}. \tag{13}$$

At the origin this potential is $V_{\exp}(r=0)=-Ze^2/2a$, whereas a uniform charge distribution gives $V_{\text{unif}}(r=0)=-3Ze^2/2R$. Therefore, unless $R/a>3$, the exponential distribution will *decrease* the calculated $2p-1s$ transition energies.[20] V_{unif} and $V_{\exp}$ are compared in Fig. 2 for $R/a=3$ and $R/a=4$.

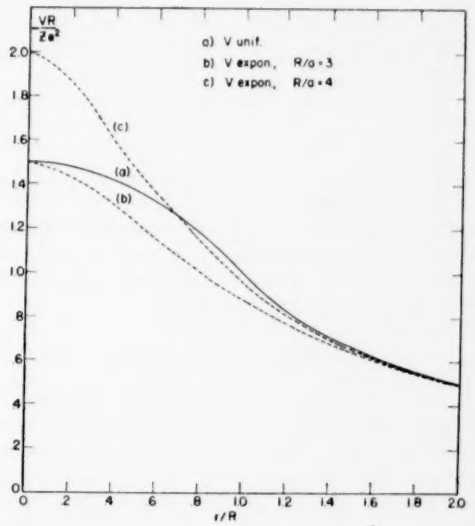

FIG. 2. Comparison of potentials produced by a uniform charge distribution of radius R and by an exponential charge distribution, $\rho\sim\exp(-r/a)$ for $R/a=3$ and 4.

3. *Quadrupole Moment*

There remains the possibility of asymmetries in the nuclear ground-state distribution. For nuclei with spins larger than one-half, such asymmetries generally give rise to quadrupole or higher moments. A nuclear quadrupole moment splits the $2p_{\frac{1}{2}}$ state into several levels. The magnitude of this level splitting has been calculated by Wheeler[21] in an adjoining paper by assuming the quadrupole to arise from a nucleus distorted into the shape of a prolate or oblate ellipsoid. For a uniformly distributed charge inside such a nucleus, Wheeler finds the potential energy V to be

[17] E. Feenberg, Phys. Rev. **59**, 593 (1941).
[18] Hofstadter, Fechter, and McIntyre, Phys. Rev. **91**, 439 (1953); also an article to be published.
[19] L. I. Schiff, Phys. Rev. (to be published).
[20] A nonrelativistic perturbation calculation on the $1s$-state energy level shows that for lead a must be of the order of 1.8×10^{-13} cm to correspond to a uniform charge radius of $1.2A^{\frac{1}{3}}\times10^{-13}$ cm. R/a is then approximately 3.9.
[21] J. A. Wheeler (following paper), Phys. Rev. **92**, 812 (1953).

(assuming the distortion from sphericity to be small):

$$V(r)=-\frac{Ze^2}{r}-\frac{1}{2}(3\cos^2\theta_{\mu I}-1)\frac{Qe^2}{2r^3}, \qquad r\gtrsim R;$$

$$V(r)=-\frac{Ze^2}{R}\left(\frac{3}{2}-\frac{1}{2}\frac{r^2}{R^2}\right)-\frac{1}{2}(3\cos^2\theta_{\mu I}-1)\frac{Qe^2r^3}{2R^5}, \quad r\lesssim R.$$

The quadrupole moment Q is $Q=2(c^2-a^2)/5$, where c and a are the major and minor axes of the ellipsoid, respectively; these axes are related to the spherical radius R by $R^3\approx a^2c$. The interaction term which arises from the quadrupole moment decreases rapidly inside the nucleus, so that the splitting is smaller than on the basis of a point-charge interaction. A simple estimate of the quadrupole splitting of the $2p_{\frac{3}{2}}$ level is obtained by Wheeler on the assumption of a nonrelativistic (hydrogen-like) point nucleus wave function.

In general, the quadrupole splitting is much smaller than the fine structure splitting. Exceptions to this rule occur for intermediate and heavy nuclei, where large quadrupole moments cause the splitting of the $2p_{\frac{3}{2}}$ level to be of the same order of magnitude as that from spin orbit coupling. In principle, the splitting can be made use of to measure the quadrupole moment, or if the latter is known, to obtain further information about the nuclear charge distribution.

C. Nuclear Polarization

In calculating the energy levels of the mesonic atom we assumed the nucleus to be unaffected by the presence of the meson. The electromagnetic term H^e was therefore averaged over the nuclear ground state, to compute a potential in which the meson was taken to move. We now include induced nuclear effects (polarization) on the meson level structure by treating $H'=H^e-\langle\psi_0|H^e|\psi_0\rangle$ as a perturbation on the meson-nucleus Hamiltonian, H^N+H_S.

The first-order correction, $W^{(1)}$, to the total energy of the meson-nucleus system, $W=E+\epsilon$, is zero for any meson state. It is in the second-order correction, $W^{(2)}$, that nuclear polarization effects appear. For a meson in the state k,

$$W^{(2)}=\sum_{\substack{N,\,m\\ N=0 \text{ with } m=k \\ \text{excluded}}}\frac{\langle\psi_0\phi_k|H'|\psi_N\phi_m\rangle\langle\psi_N\phi_m|H'|\psi_0\phi_k\rangle}{(E_0+\epsilon_k-E_N-\epsilon_m)}, \quad (14)$$

where N and m refer to the entire set of quantum numbers for a given state and $N=0$ and $m=0$ are those for the ground state. $H'=H^e-V$ can be expanded in spherical harmonics,

$$H'=-e^2\sum_{l=0}^{\infty}H_l'=-e^2\sum_{l=0}^{\infty}\sum_{i=1}^{Z}f_l(r,R_i)P_l(\cos\theta_i), \quad (15)$$

where for $l=0$

$$f_0(r,R_i)=1/R_i+V/Ze^2, \qquad r\leqslant R_i$$
$$=1/r+V/Ze^2, \qquad R_i\leqslant r\leqslant R$$
$$=0, \qquad R\leqslant r;$$

and for $l>0$

$$f_l(r,R_i)=r^l/R_i^{l+1}, \quad r\leqslant R_i$$
$$=R_i^l/r^{l+1}, \quad r\gtrsim R_i.$$

Here θ_i is the angle between the meson and ith nucleon position vectors, and P_l are the Legendre polynomials.

The orthogonality of Legendre polynomials with different values of l allows us to rewrite Eq. (14) as

$$W^{(2)}=e^4\sum_{l=0}^{\infty}W_l^{(2)},$$

where

$$W_l^{(2)}=\sum_{\substack{N,\,m\\ N=0 \text{ with } m=k \\ \text{excluded}}}\frac{\langle\psi_0\phi_k|H_l'|\psi_N\phi_m\rangle\langle\psi_N\phi_m|H_l'|\psi_0\phi_k\rangle}{(E_0+\epsilon_k-E_N-\epsilon_m)} \quad (16)$$

for a k-state meson.

The polarization effects are largest for a $1s$-state meson, for which they increase the binding energy. For a $2p$ state, where the average distance of the meson from the nucleus is much larger, the polarization effects are expected to be much smaller and may increase or decrease the binding energy.

$W_0^{(2)}$ can be interpreted as the system energy change resulting from a symmetric nuclear compression. In this term there are matrix elements which involve only changes in nuclear levels without any accompanying changes in meson levels (i.e. $N\neq 0$, $m=k$). In all higher-order terms (induced dipole, $l=1$; induced quadrupole, $l=2$; etc.) the nuclear transitions are always accompanied by meson transitions. In evaluating $W_l^{(2)}$ we perform closure over nuclear states; that is, the sum over nuclear states is performed by replacing the variable energy E_0-E_N by an average excitation energy.

For a $1s$ state meson, after the angular integrations have been performed, $W_l^{(2)}$ becomes

$$W_l^{(2)}=\frac{Z}{2l+1}\sum_m\int d\mathbf{R}_i\int_0^{\infty}r^2dr\int_0^{\infty}r'^2dr'|\psi_0|^2$$
$$\times R_0^*(r)R_{ml}(r)R_0(r')R_{ml}^*(r')f_l(R_i,r)$$
$$\times f_l(R_i,r')\frac{1}{(\langle E_0-E_N\rangle+\epsilon_0-\epsilon_m)}, \quad (17)$$

where R_{ml} is the meson radial function, m is now only the principal quantum number, and l is the orbital angular momentum quantum number.

The evaluation of $W_l^{(2)}$ can be further simplified if we perform closure over the meson as well as nucleon

states. Then, for the meson $1s$ state,

$$W_l^{(2)}=\frac{Z}{2l+1}\frac{1}{\langle E_0-E_N+\epsilon_0-\epsilon_m\rangle}\times\int|\phi_0|^2d\mathbf{r}\int|\psi_0|^2f_l^2(R_i,r)d\mathbf{R}_i. \quad (18)$$

For the light elements the leading terms in an expansion of $Z\alpha$ and $Z\alpha\mu R$ are

$$W_0^{(2)}=\frac{2}{35}\frac{Z^3\alpha^4\mu^2}{\langle E_0-E_N+\epsilon_0-\epsilon_m\rangle}(Z\alpha\mu R),$$
$$W_{l>0}^{(2)}=6\frac{Z^3\alpha^4\mu^2}{\langle E_0-E_N+\epsilon_0-\epsilon_m\rangle}(Z\alpha\mu R)\frac{1}{(2l+3)(2l+1)}. \quad (19)$$

From Eq. (19) it can be seen that for the light nuclei the s-state polarization effects increase with Z and R as Z^4R. For these nuclei the p-state effects are negligible in the approximation used. The ratio of the polarization to the $2p-1s$ transition energies therefore increase as Z^2R. For heavy elements the variation with Z and R of the polarization effects is not so simple, but the ratio of polarization to $2p-1s$ transition energy increases slowly with Z, and is largest when the maximum of $\phi_0^*\phi_0r^2$ lies approximately at the edge of the nucleus.

Equation (18) has been evaluated numerically for lead ($r_0=1.4\times10^{-13}$ cm) and copper ($r_0=1.3\times10^{-13}$ cm) for a uniformly charged nucleus. These results, along with those for aluminum, are listed in Table II. In this table the average nuclear energy denominator $\langle E_0-E_N\rangle$ is set equal to the mean nuclear excitation energy, as calculated from the statistical model (about 13 Mev). The average meson energy denominator, $\langle\epsilon_0-\epsilon_m\rangle$, is taken as somewhat above the minimum energy (the $2p-1s$ transition energy).

The closure approximation has the disadvantage of a great uncertainty in the choice of the proper energy denominator. However, it is possible to place an upper bound on the $1s$ state polarization effects for the heavy elements by using the minimum energy denominators consistent with the selection rules for the multipole considered. Since $W_0^{(2)}$ contains a term in which the meson makes no transition, $W_{00}^{(2)}$, and the minimum energy denominator in this case can be quite small, this term is evaluated separately (see Appendix A). The maximum polarization results for lead (Pb^{207} and Pb^{208}) are listed in Table III.

It is seen from Table II that for lead a reasonable estimate of the $1s$ state polarization effect is about 0.06 Mev (~1 percent of the $2p-1s$ transition energy). The maximum polarization energy shift is only about 3 percent (see Table III), and even this is not large enough to change the "effective electromagnetic radius" appreciably (less than $3\frac{1}{2}$ percent) from its calculated value of $1.2A^{\frac{1}{3}}\times10^{-13}$ cm. For the lighter elements Table II shows that the expected polarization effects are less than 1 percent of the $2p-1s$ transition energy. However, this produces a relatively larger change in the calculated radius, since for lighter nuclei the shift in the energy levels due to the total nuclear extension is itself quite small (about 2 percent for aluminum).

For the $2p$-state meson the polarization effects are much smaller than for the $1s$-state meson, and may be in the opposite direction (decrease the transition energy). These conclusions hold in the absence of resonances which could appear (for the $2p$ level) due to an excited nuclear state with energy of the order of the $2p-1s$ transition energy. However, any resonance effect is made extremely unlikely by the similarity of the observed transition energies for mercury, lead, and bismuth (see Table I).

TABLE II. Average polarization effects. The polarization energy $W^{(2)}=\sum_{l=0}^{\infty}W_l^{(2)}$ is computed for the $1s$ state meson by closure. $\langle E\rangle=\langle E_0-E_N+\epsilon_0-\epsilon_m\rangle$ is the average energy denominator. M is the matrix element computed from Eq. (18).

	Lead			Copper			Aluminum		
	M (Mev)^2	$\lvert\langle E\rangle\rvert$ (Mev)	$\lvert W\rvert=M/\langle E\rangle$ (Mev)	M (Mev)^2	$\lvert\langle E\rangle\rvert$ (Mev)	$\lvert W\rvert=M/\langle E\rangle$ (Mev)	M (Mev)^2	$\lvert\langle E\rangle\rvert$ (Mev)	$\lvert W\rvert=M/\langle E\rangle$ (Mev)
$W_0^{(2)}$	0.086	20.	0.0043	0.007	14.	0.0005	0.00081	13.	0.00006
$W_1^{(2)}$	0.466	20.	0.0233	0.085	14.	0.0061	0.00574	13.	0.00044
$W_2^{(2)}$	0.188	20.	0.0094	0.032	14.	0.0023	0.00243	13.	0.00019
$W_3^{(2)}$	0.099	20.	0.0049	0.015	14.	0.0011	0.00138	13.	0.00011
$W_4^{(2)}$	0.063	20.	0.0032	0.010	14.	0.0007	0.00086	13.	0.00007
$W_5^{(2)}$	0.042	20.	0.0021	0.007	14.	0.0001	0.00060	13.	0.00005
$W_6^{(2)}$	0.030	20.	0.0015	0.005	14.	0.0000	0.00044	13.	0.00003
$W_{7-\infty}^{(2)}$	0.190	20.	0.0095	0.033	14.	0.0023	0.00307	13.	0.00023
	$W^{(2)}=\sum_{l=0}^{\infty}W_l^{(2)}$ $=-0.058$ Mev			$W^{(2)}=\sum_{l=0}^{\infty}W_l^{(2)}$ $=-0.013$ Mev			$W^{(2)}=\sum_{l=0}^{\infty}W_l^{(2)}$ $=-0.0012$		
	$\frac{W^{(2)}}{W_{2p}-W_{1s}}=1.1\%$			$\frac{W^{(2)}}{W_{2p}-W_{1s}}=0.86\%$			$\frac{W^{(2)}}{W_{2p}-W_{1s}}=0.33\%$		

TABLE III. Maximum polarization effects for lead. Here $\langle E\rangle_{\min}=\langle E_0-E_N+\epsilon_0-\epsilon_m\rangle_{\min}$, where ϵ_m is the energy of the lowest meson excited state with angular momentum l and ϵ_0 is the $1s$ state energy for $r_0=1.4\times10^{-13}$ cm. $\langle E_0-E_N\rangle$ has been taken as 0.565 Mev for Pb^{207} and 2.62 Mev for Pb^{208} [M. H. L. Pryce, Proc. Phys. Soc. (London) **A65**, 773 (1952)]. Parity considerations would increase the estimate for $\langle E_0-E_N\rangle$.

Lead	207			208	
	M (Mev)^2	$\lvert\langle E\rangle\rvert_{\min}$ (Mev)	$\lvert W\rvert=M/\langle E\rangle_{\min}$ (Mev)	$\lvert\langle E\rangle\rvert_{\min}$ (Mev)	$\lvert W\rvert=M/\langle E\rangle_{\min}$ (Mev)
$W_{00}^{(2)}$	0.010	0.57	0.018	2.62	0.004
$W_0^{(2)}-W_{00}^{(2)}$	0.076	4.97	0.015	7.02	0.011
$W_1^{(2)}$	0.466	4.97	0.094	7.02	0.066
$W_2^{(2)}$	0.188	7.99	0.024	10.04	0.018
$W_3^{(2)}$	0.099	8.92	0.011	10.97	0.009
$W_4^{(2)}$	0.063	9.35	0.007	11.40	0.006
$W_5^{(2)}$	0.042	9.58	0.004	11.63	0.004
$W_6^{(2)}$	0.030	9.72	0.003	11.77	0.002
$W_{7-\infty}^{(2)}$	0.190	9.82	0.009	11.87	0.016
	$W_{\max}^{(2)}=\sum_{l=0}^{\infty}W_{l(\max)}^{(2)}$ $=-0.185$ Mev			$W_{\max}^{(2)}$ $=-0.136$ Mev	
	$\frac{W_{\max}^{(2)}}{W_{2p}-W_{1s}}=3.7\%$			$\frac{W_{\max}^{(2)}}{W_{2p}-W_{1s}}$ $=2.7\%$	

D. Specific Nuclear Interactions

Interactions between the μ^- meson and nucleus of non-electromagnetic origin so far have been neglected. One such reaction is the charge-exchange capture interaction $p+\mu^-\rightarrow n+\nu$. The strength of this interaction can be estimated from the coupling constant, which has been calculated to be of the order of that for β decay,[6,22] (i.e., $\sim 3\times 10^{-49}$ erg-cm^3). This is equivalent to a potential of less than 100 ev for any nucleus, and has a negligible effect on the computed energy levels.

Another possible meson-nucleon interaction is one that does not contribute to the charge-exchange reaction but causes scattering. This might be a pair interaction term, $H=g\int\psi^*\phi^*\phi\psi d\tau$, which causes potential like scattering and meson pair creation and annihilation. If such an anomalous effective interaction potential is small ($\sim$1 Mev) and has a range $\sim r_0$, then it will be difficult to distinguish its scattering from the Coulomb scattering due to the nuclear charge. The reason for this is that such an anomalous potential has approximately the same effect as a small change in the nuclear charge distribution. If the form of the interaction is that indicated above, however, it might be observed by direct pair creation experiments.

Thus, one possible explanation of the small radius obtained by Fitch and Rainwater is to postulate an attractive anomalous meson-nucleus interaction. The depth of an effective potential of radius R would have to be approximately 1 Mev for lead, to increase the calculated mesonic x-ray radius to $1.3\times 10^{-13}A^{\frac{1}{3}}$ cm. (The energy shift for any meson level is proportional to the depth of the potential and to the probability of finding the meson inside the nucleus; this probability is about one-half for the meson 1s state of lead.) There is presently little evidence for the anomalous interaction postulated above. The high-energy μ-meson anomalous scattering data of Amaldi[23] can be used to derive, in the Born approximation,[24] an equivalent potential. The data for lead and iron give an *upper* limit to the cross section per nucleon[23] of 4.5×10^{-29} cm^2. For lead and copper this gives a *maximum* potential of 0.8 and 0.4 Mev over the volume of the nuclei, and consequent $2p-1s$ transition energy shifts of about 0.4 and 0.03 Mev, respectively. However, the above limitations apply. Furthermore, Amaldi assumes spherically symmetric scattering to derive his maximum cross section. For lead, he observes only 13 large-angle scattering out of 73 000 total events, which suggests that a small proton contamination would be sufficient to materially alter the results. Thus, it is believed that such data cannot really be regarded as evidence for the existance of an anomalous scattering interaction.

[22] J. M. Kennedy, Phys. Rev. **87**, 953 (1952).
[23] E. Amaldi and G. Fidecaro, Phys. Rev. **81**, 339 (1951).
[24] N. F. Mott and H. S. W. Massey, *The Theory of Atomic Collisions* (Oxford University Press, London, 1949), p. 120.

III. CONSISTENCY OF SMALL ELECTROMAGNETIC RADIUS

This section considers whether the effective electromagnetic radius determined by the μ^--meson x-ray experiments is consistent with other measurements of the nuclear radius. These measurements can conveniently be separated into two groups. The first of these is sensitive to the nuclear charge distribution and consists chiefly of electron and proton scattering, isotope shifts of electron hyperfine structure, electron x-rays from heavy elements, and β-decay measurements. The second group depends upon a "nuclear force radius" and consists chiefly of neutron scattering, α-decay lifetime, and charged particle initiated nuclear reaction yield measurements.

A. Comparison with Experiments

1. *Electromagnetic Radius*

Measurements of both high-energy electron[25] and proton scattering[26] probe the nuclear proton distribution and have indicated an electromagnetic radius of the same order of magnitude as that determined by Fitch and Rainwater.

Isotope shifts of the electron hyperfine structure measure the change in proton charge distribution upon the addition of a neutron to the nucleus. The observed values of these shifts are approximately one-half those calculated on the basis of a constant nuclear density throughout a sphere of radius $R=1.5\times 10^{-13}A^{\frac{1}{3}}$ cm.[27] A possible explanation of this effect is an electromagnetic radius $R\approx 1.2\times 10^{-13}A^{\frac{1}{3}}$ cm,[27] although other explanations have also been proposed.[27,28]

Electron x-rays from heavy elements have been investigated by Schawlow and Townes[29] to deduce a nuclear charge distribution radius $R\approx 1.5\times 10^{-13}A^{\frac{1}{3}}$ cm. It is possible, however, that changes in the nuclear charge distribution may make this experiment agree with the μ-meson results.

β-decay data for mirror nuclei have been used to obtain an electromagnetic radius $R=1.4-1.5\times 10^{-13}A^{\frac{1}{3}}$ cm.[30] It will be shown in part B, however, that corrections to the usual calculations tend to reduce this estimate considerably.

2. *Nuclear Force Radius*

Fast neutron scattering experiments[31] have been analyzed on an optical model to give a nuclear radius

[25] Lyman, Hanson, and Scott, Phys. Rev. **84**, 626 (1951).
[26] Richardson, Ball, Leith, and Moyer, Phys. Rev. **83**, 859 (1951); K. M. Gatha and R. D. Riddell, Jr., Phys. Rev. **86**, 1035 (1952).
[27] M. F. Crawford and A. L. Schawlow, Phys. Rev. **76**, 1311 (1949).
[28] Wilets, Hill, and Ford, Phys. Rev. **91**, 1488 (1953).
[29] A. L. Schawlow and C. H. Townes, Science **115**, 284 (1952).
[30] J. M. Blatt and V. F. Weisskopf (see reference 9, Chap. VII, especially Sec. 2).
[31] Cook, Macmillan, Peterson, and Sewell, Phys. Rev. **75**, 7 (1949).

$R=1.3-1.4\times10^{-13}A^{\frac{1}{3}}$ cm.[32] It is essential to note that these measurements determine a "nuclear force radius" rather than a proton distribution radius. The sensitivity of the calculated radius to variations in the distribution of nuclear matter has not been investigated in detail.

Both α-decay lifetimes and the yield of charged particle initiated nuclear reactions indicate nuclear radii[9] $R=1.35-1.6\times10^{-13}A^{\frac{1}{3}}$ cm. These experiments measure chiefly the transparency of the Coulomb barrier which is superimposed on the nuclear force potential. They thus depend on the radius at which the repulsive Coulomb force becomes larger than the nuclear force but are uncertain because of the unknown size of the escaping or entering particles. It has been shown by Wheeler[33] that, on the basis of a strong coupling nuclear collective model, the α-decay radius is expected to be larger than that of the charge distribution because of the nuclear deformation.

B. Mirror Nuclei

The maximum β-decay energies for mirror nuclei, which specifically depend on the proton charge distribution, seem to require an electromagnetic radius $R=1.4-1.5\times10^{-13}A^{\frac{1}{3}}$ cm.

Since the mirror nuclei measurements are for $Z\leqslant21$, and the other electromagnetic experiments are more accurate for heavier elements, it might be argued that no real discrepancy exists, and that the electromagnetic radius increases for light elements. However, the following considerations indicate that such an assumption need not be made, and that a radius $R\approx1.2\times10^{-13}A^{\frac{1}{3}}$ cm can be made consistent with mirror nuclei experiments.

The difference in Coulomb energy of parent and daughter nuclei is calculated usually by assuming that a nucleon initially distributed uniformly over the nuclear sphere makes the transition. The Coulomb energy change, ΔE_c, for the reaction $A^{Z+1}\rightleftarrows A^{Z}$ is then

$$\Delta E_c=(6/5)(Ze^2/R). \tag{20}$$

In this, the nucleus is assumed to have the same initial and final radius. A simple calculation that allows for the proton sphere to change in the β-decay transition, due to the difference in Coulomb energy between the mirror nuclei, does not alter the above materially.

It will be shown below that it is impossible to make mirror nuclei and mesonic atom experiments consistent by merely changing the charge distribution, if it assumed that all protons have the same distribution and that the nuclear charge density is positive definite. (If a negative meson cloud existed which made the charge distribution vary in sign, then the two experiments could be made consistent with a charge distribution variation.) However, it will then be demonstrated that relaxation of the first condition above (all protons having the same charge distribution), together with angular momentum considerations, as well as the antisymmetrization of the nuclear-proton ground state wavefunction can make the two experiments agree.

For an arbitrary charge distribution, it is the difference of the electrostatic energy

$$\int\rho_1(\mathbf{r})U(\mathbf{r})d\mathbf{r} \tag{21}$$

between the nuclei Z and $Z\pm1$ that is determined by β-decay experiments. Here $U(\mathbf{r})$ is the potential determined by the charge distribution $\rho=Z\rho_1$ and is related to the previous V by $V=-eU$. As stated previously, it is the integral

$$\int(U-Ze/r)d\mathbf{r} \tag{22}$$

that is determined by both high-energy electron scattering (less than $\sim$40 Mev) and by the μ^--meson experiments for low Z. For a uniform charge distribution, where a radius $R\approx1.2\times10^{-13}A^{\frac{1}{3}}$ cm is needed to fit the mesonic x-ray data, the integral (21) is too large to fit the observed Coulomb energy change in β decay.

To determine if a charge distribution exists which decreases this discrepancy, the integral (21) was minimized, keeping Eq. (22) and the total charge constant. If dV/dr is continuous, a partial integration of (21) gives

$$(1/Z)\int(\nabla U)^2d\mathbf{r}.$$

The usual variation calculation then leads to a stationary value for

$$\nabla^2U=\text{constant}.\dagger$$

This corresponds to a uniform charge distribution. The resultant potential has been shown explicitly to give a smaller value for (21), under the auxiliary conditions, than a shell of charge or a charge distribution $\rho=A-Br$.

Thus the integral (21) is a minimum for a uniform charge distribution. This means that, under the assumptions made (including ρ positive definite) any nonuniform charge distribution increases the discrepancy between the meson-transition and β-decay results.

However, it is possible to construct nuclear models which, with the inclusion of (a) Coulomb exchange

[32] Fernbach, Serber, and Taylor, Phys. Rev. **75**, 1352 (1949).
[33] D. L. Hill and J. A. Wheeler, Phys. Rev. **89**, 1102 (1953).

† *Note added in proof.*—A similar result was obtained independently by Bitter and Feshbach (private communication). The restriction to positive definite ρ was not included explicitly in either proof so that the cutoff of ρ at $r=R$ had to be introduced *ad-hoc*. The restriction to positive ρ can be included explicitly by varying $s=(\rho)^{\frac{1}{2}}$, i.e., $s=s_0+\delta s$. The variational calculation then gives

$$\int_0^\infty s_0\delta s r^2(V_0+\gamma+\lambda r^2)dr=0.$$

Thus $V_0+\gamma+\lambda r^2=0$ only if s_0 (or $\rho_0)\neq0$. It can then easily be shown that

$$\begin{aligned}&\rho_0=\text{constant} &&\text{for } r<R\\ &\rho_0=0 &&\text{for } r>R\end{aligned}$$

is the minimum value.

energy and (b) angular momentum effects, reduce the above estimate of mirror nuclei radii. The difference in Coulomb energies for these nuclei is calculated below for a statistical model and a shell model.

In the Hartree approximation the Coulomb energy of a nucleus with Z protons is, after summing over spin coordinates,

$$E_c=\tfrac{1}{2}\sum_{i=1}^{Z}\sum_{j=1}^{Z}\int|\psi_i(\mathbf{R}_1)|^2|\psi_j(\mathbf{R}_2)|^2\frac{e^2}{R_{12}}d\mathbf{R}_1d\mathbf{R}_2$$

$$-\tfrac{1}{4}\sum_{i=1}^{Z}\sum_{j=1}^{Z}\int\psi_i^*(\mathbf{R}_1)\psi_j(\mathbf{R}_1)\psi_i(\mathbf{R}_2)$$

$$\times\psi_j^*(\mathbf{R}_2)\frac{e^2}{R_{12}}d\mathbf{R}_1d\mathbf{R}_2, \quad (23)$$

where ψ_i are the equivalent central potential proton wave functions. The first term in Eq. (23) is the direct Coulomb energy, while the second term is a Coulomb exchange energy arising from the antisymmetrization of the ground-state proton wavefunctions.[34]

Equation (23) is evaluated first for a nuclear statistical model. This yields a uniform charge distribution for the protons, so that the direct term gives the usual nuclear electrostatic energy. We obtain (if $A=2Z$)

$$E_c(Z)\approx\frac{3}{5}\frac{Z(Z-1)e^2}{R}-0.46\frac{Z^{4/3}e^2}{R}. \quad (24)$$

This result has been derived previously by Bethe and Bacher,[35] and Weizsacker.[36] The exchange term is significant for small values of Z, where mirror nuclei measurements are made. If the effective nuclear radius found from Eq. (24) is $R=r_0A^{\frac{1}{3}}$, then

$$r_0=r_0'(1-0.51Z^{-\frac{1}{3}}),$$

where r_0' is the radius calculated from the direct term alone. r_0 is smaller than r_0' and varies slowly with Z; for $Z=15$, r_0 is about 9 percent smaller than r_0'. Thus, the inclusion of the exchange term alone, reduces the radius of the uniform charge distribution deduced from β decay from an average of $1.45\times10^{-13}A^{\frac{1}{3}}$ cm to about $1.3\times10^{-13}A^{\frac{1}{3}}$ cm.

Equation (23) was also evaluated for a nuclear shell structure. For simplicity, an infinite square well potential was chosen. Here the protons are not distributed uniformly throughout the nucleus, and the nucleon which undergoes β decay will have a different charge distribution than the average of the other protons. The proton distribution therefore need not remain unchanged in the transition. In fact, for a nuclear shell model, as assumed here, the β-decay nucleon is usually in a higher angular momentum state than the other protons. The change in Coulomb energy for such a transition is less than is expected for a uniformly distributed particle, because the radial distribution of higher angular momentum states is weighted more heavily towards the periphery of the nuclear sphere, where the potential of the nuclear charge distribution is smallest in magnitude. An extreme of this model was considered by Bethe,[37] who assumed the extra nucleon to be free.

The radius of the square well R_w is chosen so that the resulting proton charge distribution produces an electric potential which satisfies the meson experiment; that is, the integral (22) gives the same value for this potential as when evaluated for a uniform charge distribution of radius $R=1.2\times10^{-13}A^{\frac{1}{3}}$ cm. The well parameter is assumed to remain constant in the reaction, since this parameter is determined by the nuclear forces which are assumed to be charge symmetric. The Coulomb energy change due to the addition of a proton to the above charge distribution is then calculated, and consists of two terms. The first, the direct term, will differ from that in Eq. (20) for the reasons discussed above, while the second term is the exchange energy. This was evaluated as in Condon and Shortley.[38] Calculations were performed for closed shell nuclei because a coupling scheme does not have to be specified here. Numerical results are presented in Table IV.

TABLE IV. Shell model calculation for mirror nuclei radii. $R=r_0A^{\frac{1}{3}}\times10^{-13}$ cm. $R_W=r_{0W}A^{\frac{1}{3}}\times10^{-13}$ cm is the radius of the infinite well such that the charge distribution produced by this well makes the integral $\int_0^\infty(V-V_p)r^2dr$ fit the μ^--meson experiment with an effective meson radius $R_M=r_{0M}A^{\frac{1}{3}}\times10^{-13}$ cm; $r_{0(D)}$ and $r_{0(D+E)}$ are those r_0 which, when substituted in Eq. (20), give the ΔE_c calculated on the infinite well model for the removal of a single proton above the closed shells. $r_{0(D)}$ includes only the direct term of Eq. (23) while $r_{0(D+E)}$ includes both direct and exchange terms. r_{0u} is the usual mirror nucleus radius adjusted so that Eq. (20) gives the observed maximum β-decay energy.

Z	r_{0W}	Effective meson radius r_{0M}	$r_{0(D)}$	Calculated effective mirror nuclei radius $r_{0(D+E)}$	Observed effective mirror nuclei radius r_{0u}
3↔2	1.78	1.2	1.29	1.53	···
9↔8	1.69	1.2	1.36	1.53	1.39
19↔18	1.55	1.2	1.20	1.25	1.47
21↔20	1.59	1.2	1.36	1.54	1.50
35↔34	1.38	1.2	···	···	···

For a nonclosed shell nucleus the same qualitative result is obtained, as shown by the following simple considerations. The Coulomb interaction of the single proton, which is involved in the transition, with the closed shells is of the same order of magnitude as calculated above for the single nucleon above a closed shell. The Coulomb interaction of this proton with other protons in the same shell is more difficult to estimate,

[34] E. Feenberg and G. Goertzel, Phys. Rev. **70**, 597 (1946) (additional references are listed here).
[35] H. A. Bethe and R. F. Bacher, Revs. Modern Phys. **8**, 162 (1936).
[36] C. F. von Weizsacker, Z. Physik **96**, 431 (1935).
[37] H. A. Bethe, Phys. Rev. **54**, 436 (1938).
[38] E. U. Condon and G. H. Shortley, *The Theory of Atomic Spectra* (Macmillan Company, New York, 1935), Chap. VI.

since this depends upon specific coupling assumptions. If we assume no coupling between single particle wave functions, then the exchange interaction becomes very large because the radial wave functions are identical, and this reduces the Coulomb energy considerably.

From Table IV and the qualitative discussion above, we see that, except for the $2s$ state, the inclusion of the Coulomb exchange term and angular momentum considerations are sufficient to explain the mirror nuclei data with a radius as small as that required by Fitch and Rainwater. This conclusion depends upon the nuclear model chosen; it is possible, of course, to construct models which minimize the above effects.

CONCLUSION

Experimental evidence obtained from the study of mesonic x-rays indicates a larger nuclear proton density than has heretofore been accepted. For a constant nuclear charge density, the measured $2p-1s$ transition energies can be understood in terms of a nuclear electromagnetic radius of about $R=1.2\times10^{-13}A^{\frac{1}{3}}$ cm.

With the usual nuclear radius ($1.35-1.5\times10^{-13}A^{\frac{1}{3}}$ cm) the experimental transition energies cannot be explained by nuclear polarization and other effects discussed, except for an anomalous meson-nucleus interaction; however, there is presently little evidence for such an interaction.

Comparison of the present results with previous electromagnetic radius measurements show general agreement, except for electron x-ray measurements. This agreement holds for mirror nuclei experiments, when calculations take into account Coulomb exchange energies and angular momentum considerations.

We wish to thank above all Professor R. Serber for many valuable discussions and Professor J. Rainwater and Dr. V. L. Fitch for communicating and discussing their results prior to publication. We also wish to thank Professor C. H. Townes and Dr. M. A. Ruderman for helpful discussion and Professor J. A. Wheeler for making available his calculations prior to publication.‡

‡ *Note added in proof.*—The authors are grateful to Professors L. L. Foldy and N. Kroll for pointing out to them that electrodynamic effects are not negligible. In particular, to lowest order in Z, the dominant term is caused by the polarization of the vacuum due to electron pairs. This gives a contribution [see for example R. Karplus and N. Kroll, Phys. Rev. **77**, 540 (1950)] in particular $D_F^{(2)}$ which increases the potential V by

$$\frac{2}{3\pi}\alpha V(r)[\ln(1/m_eR)-5/6].$$

There is presently no method for evaluating higher order Z corrections. The above increase in potential of somewhat less than $\frac{1}{2}$ percent for lead increases the $2p-1s$ transition energy by approximately 1 percent, which in turn leads to a 1 percent larger radius, R, for this element.

APPENDIX A

The term in $W_0^{(2)}$ which involves no meson transitions, $W_{00}^{(2)}$, is

$$W_{00}^{(2)}=\frac{1}{\langle E_0-E_N\rangle}\langle\phi_k(r)\phi_k(r')\times|\langle\psi_0|H_0'(r)H_0'(r')|\psi_0\rangle|\phi_k(r)\phi_k(r')\rangle, \quad \text{(A1)}$$

where closure over nucleon states has already been performed. The substitution

$$H_0'=\sum_{i=1}^{Z} f_0(r, R_i)P_0(\cos\theta_i),$$

according to Eq. (15), gives

$$W_{00}^{(2)}=\frac{1}{\langle E_0-E_N\rangle}\sum_{i=1}^{Z}\sum_{j=1}^{Z}\int d\mathbf{R}_1\cdots d\mathbf{R}_i\cdot d\mathbf{R}_j\cdots d\mathbf{R}_Z \times\int_0^\infty r'^2dr'\int_0^\infty r^2dr|\psi_0|^2|R_{00}(r')|^2|R_{00}(r)|^2 \times\left\{T(R_ir)T(R_jr')+\frac{V(r)V(r')}{Z^2e^4}\right\}, \quad \text{(A2)}$$

where

$$T(R_ir)=1/R_i \text{ for } r<R_i, \quad =1/r \text{ for } R_i<r.$$

In Eq. (A2) there are $Z(Z-1)$ terms with $i\neq j$, which are zero because the two expressions inside the brace cancel. For the remaining Z terms we obtain (for a uniform nuclear density to R)

$$W_{00}^{(2)}=\frac{Z}{\langle E_0-E_N\rangle}\left[\frac{3}{R^3}\int_0^R R_i^2dR_i\int_0^R|R_{00}(r)|^2r^2dr \times\int_0^R|R_{00}(r')|^2r'^2dr'T(R_ir)T(R_ir') -\left\{\frac{3}{R^3}\int_0^R R_i^2dR_i\int_0^R|R_{00}(r)|^2T(R_ir)r^2dr\right\}^2\right]. \quad \text{(A3)}$$

This equation has been integrated numerically to give the result reported in Table III.

Mu Meson as Nuclear Probe Particle[1]

JOHN A. WHEELER
Palmer Physical Laboratory, Princeton University, Princeton, New Jersey
(Received July 23, 1953)

The gamma ray ("Chang radiation") given out in the transition of a meson to the 1*s* ground state from a 2*p* orbit around a heavy nucleus of nonzero quadrupole moment is concluded to consist of several components of appreciable separation. Measurements of their energies should give information on (1) nuclear radius, (2) nuclear quadrupole moments, (3) the magnetic moment of the meson, (4) the nonuniformity of the nuclear charge distribution, and (5) nuclear polarizability and compressibility.

IN experiments in this laboratory, Chang has obtained evidence[2] for the emission of the order of three gamma rays on the average, in the energy interval 1 Mev to 5 or more Mev, for each negative meson stopped in lead. On the basis of theory,[3,4] these radiations are assigned in roughly comparable number to *nuclear* rearrangement radiation *following* the charge exchange reaction of the meson with the nucleus ($\mu^-+p\rightarrow n+\nu$), and to *mesonic* jumps between Bohr orbits roughly 7×10^{-8} sec *before* this reaction.[5]

The purpose of this note is to stress the value of more refined measurements of the energy and structure of the principal mesonic line in the Chang gamma radiation for our knowledge of (1) nuclear radii, (2) nuclear quadrupole moments, (3) the magnetic moment of the meson, (4) the nonuniformity of the nuclear charge distribution, and (5) nuclear polarizability and compressibility.

For probing the nuclear electric field the μ^- meson is an ideal test particle. Its specific interaction with the nucleus is exceedingly weak. To it, the nucleus appears as a transparent cloud of electricity. The degree of transparency is remarkable, in view of the density of nuclear matter, 1 or 2×10^5 tons/(mm).[3] Thus a meson moving in the K orbit of lead[4] spends roughly half its time within the nucleus, and in this period of $\sim4\times10^{-8}$ sec traverses about 5 meters of nuclear matter, or $\sim10^{17}$ g/cm^2.[6] This circumstance means that the major features of the nuclear electric field uniquely determine the mesonic energy level diagram. Conversely, these features can be determined by the position of the mesonic states.

Specifically, consider the $2p\rightarrow1s$ jump. The expected energy of this transition varies from 0.14 Mev for $_8$O, through 0.53 Mev for $_{16}$S, 1.6 Mev for $_{26}$Fe, to a value in the neighborhood of 5 Mev for $_{82}$Pb—the precise value for this and other heavy nuclei depending appreciably upon the nuclear radius. Otherwise stated, the energy of the resonance radiation in heavy elements depends upon the *density of electricity* in the nuclear interior, approaching in the idealized limit of nuclei large in comparison with the extension of the mesonic orbits the value characteristic of a harmonic oscillator,

$$E_{res}=\hbar e/\mu^{\frac{1}{2}}r_p^{3/2},$$

where $(4\pi/3)r_p^3$ is the volume occupied by one proton (and the neutrons associated with it). This gamma ray is favored for study both by convenient energy and by high relative probability of emission. Thus, of the mesons which get caught in an atomic field and tumble down from one Bohr orbit to another and finally reach the K level, the majority make this jump and send out the corresponding gamma "resonance radiation." For a nucleus with no quadrupole moment, this line is split by spin-orbit coupling into two components, the one due to $2p_{\frac{1}{2}}$ being half as strong as that which originates from $2p_{\frac{3}{2}}$. This stronger line is further split when there is a quadrupole moment.

The meson is the more tightly bound in the $2p$ state, the more of its time it spends within the nucleus; i.e., the more nearly its plane of motion parallels the directions in which the nucleus has a more than average amount of electric charge. The angle between the two directions is determined by the angle between the

[1] The author owes to Professor Rainwater the opportunity to let this note appear simultaneously with the important experimental results reported by Rainwater and Fitch in an accompanying paper [Phys. Rev. **92**, 789 (1953)]. The present note was written in October 1949 while the author was John Simon Guggenheim Memorial Fellow on leave of absence from Princeton, and was circulated privately. In the present text some small additions are made and a numerical error in the quadrupole splitting connected with the definition of the quadrupole moment is corrected. Thanks are expressed to Professor Leprince-Ringuet for the hospitality of the Laboratoire de Physique de l'École Polytéchnique, Paris. The work reported here is associated with the program of cosmic-ray and elementary particle research at Princeton University, supported under the joint program of the U. S. Atomic Energy Commission and the U. S. Office of Naval Research.

[2] W. Y. Chang, Revs. Modern Phys. **21**, 166 (1949); Phys. Rev. **75**, 1315 (1949).

[3] J. Tiomno and J. A. Wheeler, Revs. Modern Phys. **21**, 153 (1949).

[4] J. A. Wheeler, Revs. Modern Phys. **21**, 133 (1949).

[5] See Keuffel, Harrison, Godfrey, and Reynolds, Phys. Rev. **87**, 942 (1952) for measurements of this mean time for medium and heavy elements and references to such time measurements for lighter substances.

[6] The μ meson is not unique in this respect. The electron shows a comparable behavior. In fact, the nucleus is even somewhat more transparent to electrons than to μ mesons, because the energy release is smaller in the reaction, $e^-+p\rightarrow n+\nu$ (when it is energetically possible!) than in the corresponding mesonic charge exchange reaction, $\mu^-+p\rightarrow n+\nu$. But the *coupling constant* for the mesonic reaction is of the same order as that for the electronic charge exchange reaction. Of course, the K electron is much less useful than the K meson as a probe particle because the fraction of its time spent within the nucleus is roughly $[(\mu/m)^3=10^7]$-fold smaller.

angular momenta I of the nucleus and $j=\frac{1}{2}$ of the meson. When I is extremely large, the angle in question is the same in absolute value when $F=|\mathbf{F}|=|\mathbf{I}+\mathbf{j}|$ is equal to $I+\frac{1}{2}$ or $I-\frac{1}{2}$; and when $F=I+\frac{3}{2}$ or $I-\frac{3}{2}$. In this limit the quadrupole interaction splits $2p_{\frac{1}{2}}$ into two components of equal strength; but the values of I characteristic of actual nuclei give rise to three ($I=1$ or $\frac{3}{2}$) or four ($I>\frac{3}{2}$) components in the $2p_{\frac{1}{2}}$ level. With an electric quadrupole moment there is, of course, always associated a nuclear magnetic dipole moment and consequently a further displacement of the mesonic levels. However, this additional shift has already been shown[4] to be negligible (10 ev for Al^{27}) and is therefore disregarded here.

The energy of the two, four, or five components of the resonance radiation is determined by four quantities in the following order of importance (Fig. 1):

(1) A change in the *nuclear radius* of 10 percent alters the energy of all of the components of the lead line by about 0.4 Mev in 4.6 Mev (4.6 Mev is an approximate value calculated from a meson mass of $210m$ and the conventional nuclear radius, $R=1.4\times10^{-13}$ cm $A^{\frac{1}{3}}$; see reference 4; the experimental value is closer to 6 Mev, according to the accompanying report by Fitch and Rainwater). Consequently, a measurement of the center of gravity of the structure to an accuracy not out of reason, say 0.05 Mev, should determine the *effective* radius of the nucleus for *electric* interactions to 1 or 2 percent, a precision apparently better than that obtainable by the use of other probe particles.

(2) The *quadrupole moments* of many nuclei and the corresponding deviations of the nuclear electric fields from spherical symmetry produce percentagewise enormously greater effects in mesonic spectra than in electronic levels, owing to the greater fraction of the time spent by the meson within the nucleus.[6] For choice of elements for study of the splitting, one has to be guided by the known periodicities in the quadrupole moment as a function of mass and charge number:[7] the largest known moments are near Lu^{176} and Ta^{181}; there is possibly another maximum, with still larger moments, among the very heaviest nuclei.

A particularly appropriate case for discussion (Fig. 1) is that of $_{73}Ta^{181}$: heavy enough to pull the meson into close interaction with the nucleus; not heavy enough to have passed out of the region of large quadrupole moments; available in suitable physical form; quadrupole moment already measured via splitting of electronic energy levels. Some of the transuranic elements ought to show even greater quadrupole moments, and still larger splittings. Here no quantitative predictions can be made because of the unfortunate absence of quadrupole data for these most interesting of nuclei. Possibly the Chang radiation itself will turn out to give the most convenient means to determine nuclear spins and quadrupole moments in the transuranic region.

Especially instructive is a comparison of the quadrupole-induced line separation in the electronic and mesonic cases. If the nucleus were as small relative to the scale of meson orbits as it is compared to atomic dimensions, only the potential energy outside the nucleus,

$$V(r)=-(Ze^2/r)-[1.5\cos^2(\mu,I)-0.5](q/2)(e^2/r^3), \quad (1)$$

would count in either case; and one could get no more information about the quadrupole phenomenon from one measurement than from the other. Actually a meson

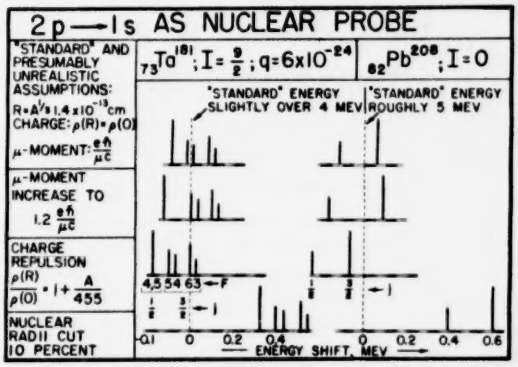
2p → 1s AS NUCLEAR PROBE
"STANDARD" AND PRESUMABLY UNREALISTIC ASSUMPTIONS:
R=A^{1/3}1.4x10^{-13}cm
CHARGE: ρ(R)=ρ(0)
μ-MOMENT: eħ/μc
μ-MOMENT INCREASE TO 1.2 eħ/μc
CHARGE REPULSION ρ(R)/ρ(0) = 1 + A/455
NUCLEAR RADII CUT 10 PERCENT
73Ta^181; I=9/2; q=6x10^-24
82Pb^208; I=0
"STANDARD" ENERGY SLIGHTLY OVER 4 MEV
"STANDARD" ENERGY ROUGHLY 5 MEV
4,5 5 4 6 3 F
1/2 3/2 1
-0.1 0 0.2 0.4 0 0.2 0.4 0.6
ENERGY SHIFT, MEV

FIG. 1. Fine structure of $2p\rightarrow1s$ lines of Ta and Pb as indicator of nuclear and mesonic properties. The second line shows the effect of a 20 percent anomaly in the magnetic moment of the meson; the third line shows the influence of nonuniformity of the charge density of the nucleus (40 percent greater at the center than at the surface for Ta, and 45 percent greater for Pb); the fourth line shows the effect of a 10 percent decrease in nuclear radius. All the numbers are approximate and illustrative only; they are estimates based on lowest relevant order of perturbation theory; details are given in the text. *Note*: Later information indicates that the spin of Ta^{181} is 7/2 rather than 9/2. The resulting change in the quadrupole splitting pattern is relatively small, as seen by inspection of the quadrupole splitting coefficients in Table I.

in the K orbit of Ta spends a significant fraction of its time inside the nucleus. There the quadrupole field is not only much smaller than what would be predicted from Eq. (1) but also depends in an important way on the distribution of the charge which is responsible for the quadrupole moment.

The level splittings plotted in Fig. 1 were calculated from the following picture[8] of the origin of quadrupole moments. One or more nucleons are considered—from the point of view of the individual particle model in its zeroth approximation—to be outside of closed shells and to be described by individual particle wave functions, not all of whose nodal surfaces are spherical. Each such particle exerts on the nuclear surface a non-

[7] The empirical data are summarized by W. Gordy, Phys. Rev. **76**, 139 (1949) and by Townes, Foley, and Low, Phys. Rev. **76**, 1415 (1949); theoretical discussions are given by D. Hill and J. A. Wheeler, Phys. Rev. **89**, 1132 (1953); and K. Ford, Phys. Rev. **90**, 29 (1953).

[8] J. Rainwater, Phys. Rev. **79**, 432 (1950); D. Hill and J. A. Wheeler, Phys. Rev. **89**, 1102 (1953).

uniform pressure, the magnitude of which is greatest in the directions normal to the largest number of nodal surfaces. As a consequence of such unbalanced pressures acting against the surface tension, the nucleus takes on an ellipsoidal form. The seat of the quadrupole moment is idealized as an ellipsoid with a uniform volume distribution of electric charge.

The potential energy of a meson in the field of such an ellipsoidal charge distribution, of radius R and quadrupole moment[9] q, is given by Eq. (1) outside the nucleus and inside by

$$V(r)=-(3Ze^2/2R)+(Ze^2r^2/2R^3) -[1.5\cos^2(\mu,I)-0.5](q/2)(e^2r^2/R^5). \quad (2)$$

The rapid falloff of the quadrupole field inside the nucleus cuts down the level splitting—relative to its value for a negligibly small nucleus of the same moment—by a form factor,

$$f_q\doteqdot 1/[1+0.1(RZ\mu e^2/\hbar^2)^2]^2 (\sim 1/2.4 \text{ for Ta}), \quad (3)$$

so that the width of the pattern produced by the quadrupole interaction has the order of magnitude,

$$\Delta E_{\text{quad}}=1 \text{ Mev}(q/10^{-24} \text{ cm}^2)(Z/237)^3 f_q. \quad (4)$$

One can look forward to an experimental determination of the form factor f_q in Eq. (4). For this purpose it is necessary to measure the quadrupole-induced splitting of the $2p_{\frac{3}{2}}$ level of a nucleus for which the quantity q is already known from the hyperfine structure of electronic levels. Then one will be in a position to check the theoretical formula (3) for f_q—or still better, to do a precise numerical integration of the Dirac equation and to compare the more accurate resulting value for f_q with experiment. In this way an observational test can be made of the view that the quadrupole moments of heavy nuclei arise in first approximation from an ellipsoidal deformation of a uniformly charged nuclear substance.

3. The *magnetic moment* of the meson has been assumed in the discussion so far to have the value, $2(e/2\mu c)\times(\hbar/2)$, appropriate for a particle whose probability amplitude function satisfies the Dirac equation. A value of the mesonic moment which is greater by the factor $(1+\epsilon)$ will produce a splitting between the $2p_{\frac{1}{2}}$ level and the center of gravity of the $2p_{\frac{3}{2}}$ pattern roughly equal to

$$\Delta E_{\text{spin}}=1 \text{ Mev}\times(1+2\epsilon)(Z/101)^4 f_s, \quad (5)$$

where the form factor f_s for a uniformly charged sphere of electricity has approximately the value

$$f_s\doteqdot 1/[1+0.2(RZ\mu e^2/\hbar^2)^2] (\sim 1/2.1 \text{ for Ta}). \quad (6)$$

Thus f_s is a quantity known within certain limits from existing determinations of nuclear radii and susceptible of more precise evaluation as in Item 1. Consequently a measurement of the spin splitting of the resonance line should give direct information about the magnetic moment of the μ meson.

4. The *distribution of charge* over the nucleus has been assumed uniform in the foregoing estimates. However, the charge density near the surface of a nucleus of mass number A is greater than the density at the center by a factor

$$(\rho_{\max}/\rho_{\min})=1+\delta \doteqdot 1+0.0022A \quad (=1.45 \text{ for Pb}), \quad (7)$$

according to early considerations[9] of Feenberg and Wigner. This effect does not significantly alter the quadrupole form factor f_q, and slightly decreases the spin-orbit coupling form factor, f_s. The principal effect of the nonuniformity in charge, however, is to raise the $1s$ level ($\sim$0.14 Mev for Pb). By overlooking this effect, one would deduce from the $2p-1s$ energy difference (Item 1) a nuclear radius about 3 percent too great. The appropriate correction can be calculated easily enough, of course, by adopting Feenberg and Wigner's theoretical expressions for the nonuniformity of charge. For an *experimental* means to determine independently the magnitude of the nonuniformity and the radius of the nucleus, it would be sufficient to know the positions—relative to the $2p$ triplet—not only of the $1s$ level, as already discussed, but also of the $2s$ state: the two mesonic states of zero angular momentum respond in different measure to the parameters R and $(\rho_{\max}/\rho_{\min})$. No calculations on this point are reported here as the transitions $2s\rightarrow 2p$ (energy for case of Pb estimated[4] to be of order of 1 Mev) are one state further removed from observation. Thus only a fraction of the captured mesons ever arrive at the $2s$ level, while the great majority pass through the $2p$ state on their way to the ground level.

The fine structure of the $2s\rightarrow 2p$ and $2p\rightarrow 1s$ lines will be expected to show a characteristic intensity pattern, assisting in identification of the components: (1) intensity *summed* over the components of $2p_{\frac{3}{2}}\rightarrow 1s$ very nearly twice the intensity of $2p_{\frac{1}{2}}\rightarrow 1s$ because the probability of *arrival* at any sublevel of $2p$ is approximately fixed by the statistical weight of that level; (2) intensity distribution *within* the components of $2p_{\frac{3}{2}}$ proportional to $2F+1$ for each component (details in Table I); (3) the small number of photons in each component of $2s\rightarrow 2p$, divided by the cube of the frequency of that component, proportional to the much larger number of photons in the corresponding com-

[9] Here the following symbols for the quadrupole moment are used: $q(\text{cm}^2)$ times $e=Q(\text{cm}^2\cdot\text{franklin})=\Sigma e_k(3z_k^2-r_k^2)=2\Sigma e_k r_k^2\times[1.5\cos^2(k,I)-0.5]=(2Ze/5)(c^2-a^2)=6ZeR_0\alpha/5$, where the last two expressions refer to the case of a uniform charge distribution bounded by the surface $R=R_0[1+\alpha P_2(\cos\theta)]$, with equatorial semi-axis $a=R_0(1-\alpha/2)$ and semi-axis of symmetry $c=R_0(1+\alpha)$.

E. Wigner, Bicentennial Symposium, University of Pennsylvania, 1940; E. Feenberg, Phys. Rev. **59**, 593 (1941). Smaller values for the coefficient of A in the redistribution formula of Eq. (7)—perhaps only half as great—are given by employing the later treatment of E. Feenberg, Rev. Mod. Phys. **19**, 239 (1947), as shown in detail in Table II of reference 11, as kindly pointed out by D. L. Hill.

ponent of $2p \rightarrow 1s$. This characteristic mesonic radiation is, of course, separate in time from the other half of the Chang radiation due to de-excitation of the residual nucleus *following* the charge exchange reaction. However, if the experimental time discrimination is not complete, the characteristic intensity pattern should distinguish the desired radiation from the de-excitation radiation, which will (a) normally in a heavy nucleus be divided among many lines and (b) not vary in energy monotonically with nuclear charge number.

5. The *polarizability* and *compressibility* of nuclear matter[10] can be deduced if one can determine the charge repulsion factor δ of Eq. (7), Item 4, and the swelling of a nucleus due to addition of a proton. This swelling effect has recently been called on by Wilets, Hill, and Ford[11] to explain some of the anomalies in the isotope shift of atomic spectral lines. The effect should be very much greater percentagewise in the case of the mesonic radiation. The experimentally relevant quantity is the shift in the center of gravity of the $2p \rightarrow 1s$ line as a result of changes in the number of neutrons and protons in the nucleus. Knowing the charge, one can, by calculation, determine what effective radius is required to fit the observations, thus determining the dependence of radius upon Z and A, and thereby permitting an estimate of the compressibility. However, in any such analysis one must allow for an important effect in the interpretation of the isotope effect first brought out by Wilets, Hill, and Ford. The presence of a nuclear quadrupole moment, described for instance by a deformation $R=R_0[1+\alpha P_2(\cos\theta)]$, increases the apparent extension of the nucleus—as regards its effect on the $1s$-level—by a fractional amount proportional to the *square* of α. This effect, moreover, is due to the intrinsic deformation of the nucleus—the deformation as seen by a nucleon which responds to the changing orientation of the nuclear boundary—and will therefore occur even in cases ($I=0$ or $I=\frac{1}{2}$) when the quadrupole moment as seen by an atomic electron averages out to zero. This deformation and the associated correction of the nuclear radius can be calculated or estimated from other information as described by Wilets, Hill, and Ford. It is the thus corrected radius which should serve as the starting point for an analysis of nuclear compressibility.

In conclusion, the spectroscopy of the characteristic mesonic gamma radiation, initiated by Chang and made into a science by Fitch and Rainwater, promises to teach interesting lessons about both the meson and the nucleus.

DETAILS

All the estimates reported in Fig. 1 and in the text have been made in the lowest relevant order of perturbation theory, using hydrogenic functions for the $2p$ state, employing for the $1s$ state of Pb a wave function found by numerical integration,[4] and estimating shifts of the $1s$ level of Ta, where necessary, by applying crude correction factors to the corresponding figures for lead. For any accurate analysis of experimental results, it is necessary to redo the calculations with wave functions determined by numerical integration of the wave equation in the appropriate field of force. Not to attempt this extensive task, but only to indicate how the present estimates were made, the following details are subjoined:

The shift in the $2p$ levels due to spin and quadrupole effects is given by

$$E_{sq}=[j(j+1)-l(l+1)-s(s+1)](\hbar^2/4\mu^2c^2)(dV/rdr)_{Av}$$
$$-(qe^2/2)[1.5\cos^2(\mu,j)-0.5]_{Av}$$
$$\times[1.5\cos^2(j,I)-0.5]_{Av}\begin{Bmatrix} r^2/R^5 \text{ for } r<R \\ 1/r^3 \text{ for } r>R \end{Bmatrix}_{Av}$$
$$=\begin{Bmatrix} 1 \text{ for } j=\frac{3}{2} \\ -2 \text{ for } j=\frac{1}{2} \end{Bmatrix}(\mu c^2/96)(Z/137)^4 f_s(x)$$
$$+\begin{Bmatrix} 1 \text{ for } j=\frac{3}{2} \\ 0 \text{ for } j=\frac{1}{2} \end{Bmatrix}[1.5\cos^2(j,I)-0.5]_{Av}$$
$$\times(\mu c^2/240)[q/(e^2/\mu c^2)^2][Z/(137)^2]^3 f_q(x)$$
$$=\begin{Bmatrix} \frac{1}{3} \text{ for } j=\frac{3}{2} \\ -\frac{2}{3} \text{ for } j=\frac{1}{2} \end{Bmatrix}1 \text{ Mev}(Z/101)^4 f_s$$
$$+\begin{Bmatrix} 1 \text{ for } j=\frac{3}{2} \\ 0 \text{ for } j=\frac{1}{2} \end{Bmatrix}[1.5\cos^2(j,I)-0.5]_{Av}0.5 \text{ Mev}$$
$$\times(q/10^{-24}\,\text{cm}^2)(Z/237)^3 f_q.$$

The evaluation is made with the hydrogenic wave function for the $2p$ state,

$$F_p=cr^2\exp(-Z\mu e^2 r/2\hbar^2),$$

normalized so that $\int F_p^2 dr=1$. Form factors dependent on the finite size of the nucleus are expressed in terms of the dimensionless variable, $x=RZ\mu e^2/\hbar^2$:

$$f_s(x)=\left\{x^{-3}\int_0^x x^4+\int_x^\infty x\right\}\exp(-x)dx$$
$$=24x^{-3}-(24x^{-3}+24x^{-2}+12x^{-1}+3)\exp(-x)$$
$$=1,\ 0.824,\ 0.564,\ 0.290 \text{ for } x=0,\ 1,\ 2,\ 3.5$$
$$\doteq 1/(1+0.2x^2)$$
$$=1,\ 0.833,\ 0.556,\ 0.290 \text{ for } x=0,\ 1,\ 2,\ 3.5;$$

[10] Reference 9 and W. J. Swiatecki, Proc. Phys. Soc. (London) **A63**, 1208 (1950).
[11] Wilets, Hill, and Ford, Phys. Rev. **91**, 1488 (1953).

and

$$f_q(x)=\left\{x^{-5}\int_0^x x^6+\int_x^\infty x\right\}\exp(-x)dx$$

$$=720x^{-5}-(720x^{-5}+720x^{-4}+360x^{-3}+120x^{-2}+30x^{-1}+5)\exp(-x)$$

$$=1,\ 0.796,\ 0.508,\ 0.341 \text{ for } x=0,\ 1,\ 2,\ 2.76$$

$$\doteq 1/(1+0.1x^2)^2$$

$$=1,\ 0.826,\ 0.510,\ 0.322 \text{ for } x=0,\ 1,\ 2,\ 2.76.$$

The factor $[1.5\cos^2(j,I)-0.5]_{Av}$ takes on very simple values in the case of a nuclear spin I, so large that it can be treated as infinite—a limit never attained in practice. Then the factor in question takes on the limiting value $+1$ for the pair of states characterized by the values, $F=I+\frac{3}{2}$ and $F=I-\frac{3}{2}$, of the quantum number F for sum of angular momentum of meson and nucleus. A similar degeneracy occurs for the only other states possible when $j=\frac{3}{2}$. Then $F=I+\frac{1}{2}$ or $I-\frac{1}{2}$ and the angular factor in question has the value -1. In this limit of large j, the state $j=\frac{3}{2}$ is therefore split up by interaction with the nuclear quadrupole moment symmetrically into two components. Their statistical weights are equal both to each other and to the statistical weight of the $j=\frac{1}{2}$ level, which is unaffected by the quadrupole interaction. In the contrary limit where the nuclear spin is 0 or $\frac{1}{2}$, there is, of course, no quadrupole splitting. For $I=1$ and $I=\frac{3}{2}$ there are three components. For every larger but still finite value of I there are four distinct components, $F=I+\frac{3}{2}$, $I+\frac{1}{2}$, $I-\frac{1}{2}$, $I-\frac{3}{2}$, with statistical weights $2F+1$ (compared to the weight $4I+2$ of the component $j=\frac{1}{2}$ of the Chang radiation), and with energies calculated by use of the formula of Casimir,

$$[1.5\cos^2(I,j)-0.5]_{Av}=\frac{1.5K(K+1)-2I(1+1)j(j+1)}{I(2I-1)j(2j-1)},$$

where $K=F(F+1)-I(I+1)-j(j+1)$.

TABLE I. Value of the factor $[1.5\cos^2(I,j)-0.5]_{Av}$ which appears in the formula for the quadrupole splitting of the $2p_{\frac{3}{2}}$ mesonic level. I=nuclear quantum number; F=resultant of I and of the angular momentum, $j=\frac{3}{2}$, of the meson.

I	$F=I+\frac{3}{2}$	$I+\frac{1}{2}$	$I-\frac{1}{2}$	$I-\frac{3}{2}$
0 or 1/2	no quadrupole splitting			
1	1	−4	5	no level
3/2	1	−3	1	5
2	1	−5/2	0	7/2
5/2	1	−11/5	−2/5	14/5
3	1	−10/5	−3/5	12/5
7/2	1	−13/7	−5/7	15/7
4	1	−49/28	−22/28	55/28
9/2	1	−10/6	−5/6	11/6
5	1	−24/15	−13/15	26/15
11/2	1	−85/55	−49/55	91/55
6	1	−33/22	−20/22	35/22
13/2	1	−19/13	−12/13	20/13
∞	1	−1	−1	1

The *shift* of levels due to a change δR in the radius R of a nucleus idealized as having a uniform charge density is

$$E_{\delta R}=(3Ze^2\delta R/2R^2)(1-r^2/R^2)_{Av}.$$

With a nonuniform charge density,

$$\rho=(3Ze/4\pi R^3)(1+R^{-2}r^2\delta)/(1+0.6\delta),$$

greater at the surface than at the center by the factor $(1+\delta)$, is associated an energy *increase* over the eigenvalues[4] for a uniform charge distribution, equal to

$$E_{\text{nonuniform}}=(Ze^2/R)[(1-r^2/R^2)^2]_{Av}(3\delta/20)/(1+0.6\delta).$$

The Formulation of the Kohn-Hulthén Variational Principle in Terms of the Scattering Operator Formalism*

HARRY E. MOSES
New York University, New York, New York
(Received April 22, 1953)

The Kohn-Hulthén variational principle is expressed in terms of the scattering operator formalism. It is shown that in terms of this formalism the principle can be expressed more abstractly and concisely than heretofore. Furthermore, certain ambiguities in the usual formulation of the principle have been removed.

1. INTRODUCTION

A VARIATIONAL principle has been devised by Hulthén for phase shifts in scattering problems.[1] The principle has been modified, and its applications have been extended by Kohn.[2] Both of these authors have set up the variational principle explicitly in terms of scattering phases. However, it is simpler to set up the variational principle in terms of the scattering operator formalism. In terms of this formalism the principle is more abstract and more general than in terms of the phase-shift representation. For example, the principle will be immediately applicable to the problem of the scattering of an electron by a heavy atom and, at least formally, to the problem of obtaining scattering operators in field theoretical problems.

It is also possible to give the variational principle an unambiguous and more concise form than has hitherto been done. The final form is given in Eq. (45a).

In order to discuss this more abstract formalism, we shall summarize the properties of the scattering operator, using essentially the concepts of Møller,[3] Friedrichs,[4] and Lippmann and Schwinger.[5]

2. THE SCATTERING OPERATOR

In scattering problems the Hamiltonian H of the system is broken up into two parts, one of which is called the unperturbed Hamiltonian H_0, and the other of which is called the perturbation ϵV. Thus

$$H=H_0+\epsilon V. \tag{1}$$

H_0 is so chosen as to have a continuous spectrum.

Let us denote the eigenvalues of H_0 by E. Generally the spectrum of H_0 is degenerate. We shall therefore introduce accessory dynamical variables which commute with H_0 and which together with H_0 form a complete set of commuting variables. We shall denote the eigenvalues of these accessory variables collectively by α. We shall then write the eigenfunctions of H_0 corresponding to the eigenvalues E and α as $\omega_0(E,\alpha)$, where

$$H_0\omega_0(E,\alpha)=E\omega_0(E,\alpha), \tag{2}$$

$$(\omega_0(E,\alpha),\omega_0(E',\alpha'))=\delta(E-E')\delta(\alpha,\alpha'); \tag{3}$$

the left-hand side of (3) means the Hermitian inner product, and $\delta(\alpha,\alpha')$ is a generalized δ function defined by

$$\int r(\alpha)\delta(\alpha,\alpha')d\alpha=r(\alpha') \text{ if } \alpha' \text{ is in } \mathfrak{s}$$
$$=0 \text{ otherwise}, \tag{4}$$

where $\mathfrak{s}$ is the range of integration. Integration over those variables included in α which lie in the discrete spectrum are to be replaced by summations.

It might be useful to indicate the nature of the variables α in order that they may be thought of in more concrete form. If one considers the scattering of a particle by a perturbing potential, one may take H_0 to be the kinetic energy of the particle, and ϵV may be considered as the scattering potential. In this case α might be chosen to be the polar angles which specify the direction of the momentum. One might also consider the scattering of an electron by an atom. H_0 would then be the sum of the kinetic energy operator of the electron and the Hamiltonian of the atom. In this case α would consist of the polar angles which give the direction of the electron's momentum, together with the variables which denote the state of the atom. For an example of a problem of this kind see Moses.[6]

We shall denote an arbitrary state Φ in the H_0 representation by $f(E,\alpha)$ and call it the "representer" in that representation; we write

$$\Phi\underset{E}{\leftrightarrow}f(E,\alpha)=(\omega_0(E,\alpha),\Phi), \tag{5}$$

or

$$\Phi=\int\int f(E,\alpha)\omega_0(E,\alpha)d\alpha dE. \tag{5a}$$

* This work was performed at Washington Square College of Arts and Science, New York University, and was supported in part by contract with the U. S. Air Force through sponsorship of the Geophysics Research Directorate of the Air Force Cambridge Research Center, Air Research and Development Command.

[1] L. Hulthén, quoted by N. F. Mott and H. S. W. Massey, *Theory of Atomic Collisions* (Oxford University Press, London, 1949), p. 128.

[2] W. Kohn, Phys. Rev. **74**, 1763–1772 (1948); **84**, 495–501 (1951).

[3] C. Møller, Kgl. Danske Videnskab. Selskab, Mat.-fys. Medd. **22**, 1–46 (1945).

[4] K. O. Friedrichs, Commun. Pure Appl. Math. **1**, 361–405 (1948).

[5] B. A. Lippmann and J. Schwinger, Phys. Rev. **79**, 469–480 (1950).

[6] H. E. Moses, Phys. Rev. **91**, 185–192 (1953).

An operator K in the H_0 representation will be written as K^E; it is defined by

$$K\Phi \underset{E}{\leftrightarrow} K^E f(E,\alpha). \tag{6}$$

In particular,

$$H_0{}^E = E, \tag{7}$$

as follows immediately from (2) and (5a). Sometimes it is convenient to write K^E as an integral operator with the kernel or "matrix" $K^E(E,\alpha|E',\alpha')$:

$$K^E f(E,\alpha) = \int\int K^E(E,\alpha|E',\alpha') f(E',\alpha') d\alpha' dE', \tag{8}$$

where

$$K^E(E,\alpha|E',\alpha') = (\omega_0(E,\alpha), K\omega_0(E',\alpha')). \tag{9}$$

For purposes of discussion of the scattering operator we are interested in eigenfunctions of H which correspond to eigenvalues lying in the same range and having the same degeneracy as the eigenvalues of H_0. We shall denote the eigenvalues of H by F. To describe such eigenfunctions of H we shall have to introduce operators which commute with H and which, together with H, form a complete set of commuting variables denoted collectively by β. The values of β have the same range as α. It is not generally possible to give β a direct physical meaning, but it is not necessary to do so for our purposes.

The eigenfunctions of H are not unique. We shall be interested in two different sets of eigenfunctions which we shall denote by $\omega^+(F,\beta)$ and $\omega^-(F,\beta)$; these we shall now characterize.

Let us denote the $\omega^\pm$ in the H_0 representation by $u_\pm$:

$$u_\pm(E,\alpha|F,\beta) = (\omega_0(E,\alpha), \omega^\pm(F,\beta)). \tag{10}$$

The eigenfunctions $\omega^\pm$ are characterized by the following equations for $u_\pm$:

$$u_\pm(E,\alpha|F,\beta) = \delta(E-F)\delta(\alpha,\beta) + \epsilon\gamma_\pm(F-E)T_\pm(E,\alpha|F,\beta), \tag{11}$$

where $\gamma_\pm(\zeta)$ is essentially $\delta_\mp(\zeta)$:

$$\gamma_\pm(\zeta) = \lim_{\xi\to+0} \frac{1}{\zeta \mp i\xi} = \pm i\pi\delta(\zeta) + P\frac{1}{\zeta}. \tag{12}$$

The letter P in (12) means that in integrations over integrands involving $1/\zeta$ as a factor, the Cauchy principal part is to be used. Also

$$T_\pm(E,\alpha|F,\beta) = \int\int V^E(E,\alpha|E',\alpha') u_\pm(E',\alpha'|F,\beta) d\alpha' dE' = V^E u_\pm(E,\alpha|F,\beta), \tag{13}$$

where the operator V^E operates on $u_\pm$ in so far as $u_\pm$ are functions of E,α.

The scattering operator and its inverse can be obtained in terms of the functions $u_\pm$ as follows: Consider solutions of $\Phi(t)$ of the Schrödinger equation:

$$i(\partial/\partial t)\Phi(t) = H\Phi(t) \quad (\hbar = 1). \tag{14}$$

If the limits

$$\lim_{t\to\pm\infty} e^{iH_0 t}\Phi(t) = \Phi_\pm \tag{15}$$

exist, then the scattering operator S is defined by

$$\Phi_+ = S\Phi_-. \tag{16}$$

If we consider the H_0 representer of $\Phi(t)$,

$$\Phi(t) \underset{E}{\leftrightarrow} f(E,\alpha;t),$$

we see that two possible solutions to the Schrödinger equation can be written:

$$f_\pm(E,\alpha;t) = \int\int u_\pm(E,\alpha|F,\beta) e^{-iFt} g(F,\beta) d\beta dF, \tag{17}$$

where $g(F,\beta)$ is a quadratically integrable function which was chosen to correspond to a choice of initial conditions on $f_\pm$ as seen below. Friedrichs[4] shows that f_- is characterized by

$$\lim_{t\to-\infty} e^{iEt} f_-(E,\alpha;t) = g(E,\alpha); \tag{18}$$

$$\lim_{t\to+\infty} e^{iEt} f_-(E,\alpha;t) = \int\int S^E(E,\alpha|E',\alpha') g(E'\alpha') d\alpha' dE', \tag{19}$$

where

$$S^E(E,\alpha|E',\alpha') = \delta(E-E')\delta(\alpha,\alpha') - 2\pi i\epsilon\delta(E-E')T_-(E',\alpha|E',\alpha'). \tag{20}$$

We can identify Eqs. (18) and (19) as being Eq. (15) in the H_0 representation. In particular, if we identify $g(E,\alpha)$ as the H_0 representer of Φ_- and $\int\int S^E(E,\alpha|E',\alpha') g(E',\alpha') d\alpha' dE'$ as the H_0 representer of Φ_+, we see that $S^E(E,\alpha|E',\alpha')$ is just the kernel of the integral operator which gives the scattering operator S in the H_0 representation.

In a smiliar way it can be shown that

$$\lim_{t\to+\infty} e^{iEt} f_+(E,\alpha;t) = g(E,\alpha), \tag{21}$$

$$\lim_{t\to-\infty} e^{iEt} f_+(E,\alpha;t) = \int\int \tilde{S}^E(E,\alpha|E',\alpha') g(E',\alpha') d\alpha' dE', \tag{22}$$

where

$$\tilde{S}^E(E,\alpha|E',\alpha') = \delta(E-E')\delta(\alpha,\alpha') + 2\pi i\epsilon\delta(E-E')T_+(E',\alpha|E',\alpha'). \tag{23}$$

It is clear that $\tilde{S}^E(E,\alpha|E',\alpha')$ is just the kernel of the integral operator which gives the inverse scattering operator S^{-1} in the H_0 representation.

In order to obtain the scattering operator we need only find $T_-(E,\alpha|E,\alpha')$. We shall formulate the variational principle for this function. It should be noted that $T_-(E,\alpha|E,\alpha')$ is the amplitude of the scattered wave in the **x** representation. It is easier to work in the H_0 representation than in the **x** representation because the Green's functions involved are simply γ_- functions; in the **x** representation they are considerably more complicated. It might also be mentioned that $\omega^{\pm}$ are the eigenstates $\psi_{\mp}$ of reference 5.

3. THE VARIATIONAL EXPRESSION

The Kohn-Hulthén variation principle is based upon variations of the following functional $A(\mathcal{T}_\pm)$:

$$A(\mathcal{T}_\pm)=I(\mathcal{T}_\pm)+\epsilon\mathcal{T}_-(F,\beta'|F,\beta), \tag{24}$$

where

$$I(\mathcal{T}_\pm)=\lim_{F'\to F}\int\int v_+^*(E,\alpha|F',\beta')(H^E-F)\times v_-(E,\alpha|F,\beta)d\alpha dE, \tag{25}$$

$$\begin{aligned} v_\pm(E,\alpha|F,\beta) &=\delta(E-F)\delta(\alpha,\beta)+\epsilon\gamma_\pm(F-E)\,\mathcal{T}_\pm(E,\alpha|F,\beta)\\ &=u_\pm(E,\alpha|F,\beta)+\epsilon\gamma_\pm(F-E)[\,\mathcal{T}_\pm(E,\alpha|F,\beta)\\ &\qquad -T_\pm(E,\alpha|F,\beta)]. \end{aligned} \tag{26}$$

The asterisk means the complex conjugate.

The functions $\mathcal{T}_\pm$ are to be regarded as trial functions for $T_\pm$. We shall prove later that variations of $A(\mathcal{T}_\pm)$ which result from variations of $\mathcal{T}_\pm$ about $T_\pm$ are zero. Hence $A(\mathcal{T}_\pm)$ is an insensitive functional of $\mathcal{T}_\pm$ in the vicinity of $\mathcal{T}_\pm=T_\pm$, and we can write

$$A(\mathcal{T}_\pm)\cong A(T_\pm), \tag{27}$$

where $\mathcal{T}_\pm$ approximates $T_\pm$. It will also be shown that

$$I(T_\pm)=0, \tag{28}$$

and that hence relation (27) can be written

$$\epsilon T_-(F,\beta'|F,\beta)\cong I(\mathcal{T}_\pm)+\epsilon\mathcal{T}_-(F,\beta'|F,\beta)=A(\mathcal{T}_\pm)$$

or, equivalently,

$$T_-(F,\beta'|F,\beta)\cong(1/\epsilon)A(\mathcal{T}_\pm). \tag{29}$$

Relation (29) is the form of the Kohn-Hulthén principle in terms of the scattering operator formalism. We use trial functions $\mathcal{T}_\pm$ in the right-hand side of (29) to obtain a more accurate expression for $T_-(F,\beta'|F,\beta)$.

It should be noted that in evaluating the expression (25) for $I(\mathcal{T}_\pm)$ one must take care not to interchange the limit and the integration processes prematurely. If one takes the limit before carrying out at least part of the integration, the integrand is not defined because one has the product of two symbolic functions $v_+^*v_-$ which have the same arguments in terms of the variables E and F. Products of symbolic functions having the same argument are generally not defined; however, if the symbolic functions have different arguments, their products can be defined. For example, $[\delta(x)]^2$ is not defined, but $\delta(x)\delta(y)$ is.

After some manipulation it is possible to break up the integrand into a sum in which terms involving products of symbolic functions are isolated. The integral over these products can be evaluated, and the limit $F'\to F$ is then taken. For the remaining terms it is proper to interchange the integration and limiting processes. The procedure will be illustrated in the proof of the variational procedure and in the discussion of some results.

In the usual version of the Kohn-Hulthén variational principle there is a serious ambiguity in the definition of $I(\mathcal{T}_\pm)$. In reference 2, for example, Kohn obtains two different values for $I(T_\pm)$ corresponding to the use of two different representations to evaluate this quantity. Of course, the value of $I(\mathcal{T}_\pm)$ ought to be independent of the representation. It should be noted, however, that the final results of reference 2 are correct.

4. PROOF OF THE KOHN-HULTHÉN VARIATIONAL PROCEDURE

We shall first prove Eq. (28). We have from the definition (25) of $I(\mathcal{T}_\pm)$ and definition (26) for $v_\pm$:

$$I(T_\pm)=\lim_{F'\to F}\int\int u_+^*(E,\alpha|F',\beta')(H^E-F)\times u_-(E,\alpha|F,\beta)d\alpha dE. \tag{30}$$

However, we remember that in the H_0 representation $u_-(E,\alpha|F,\beta)$ is an eigenfunction of H and H^E is the operator H. Hence, $H\omega^-(F,\beta)=F\omega^-(F,\beta)$ becomes

$$H^Eu_-(E,\alpha|F,\beta)=Fu_-(E,\alpha|F,\beta), \tag{31}$$

or

$$(H^E-F)u_-(E,\alpha|F,\beta)=0. \tag{32}$$

From this it follows that

$$I(T_\pm)=0. \tag{28}$$

We shall now show that variations of $A(\mathcal{T}_\pm)$ resulting from independent variations of $\mathcal{T}_\pm$ about $T_\pm$ vanish.

We denote this variation of $A(\mathcal{T}_\pm)$ by $\delta A(\mathcal{T}_\pm)$; then

$$\delta A(\mathcal{T}_\pm)=A(T_\pm+\delta T_\pm)-A(T_\pm). \tag{33}$$

Using (24), (25), (26) we have to the first order in $\delta T_\pm$

$$\begin{aligned} \delta A(\mathcal{T}_\pm)=\lim_{F'\to F}\epsilon\Big[&\int\int u_+^*(E,\alpha|F',\beta')(H^E-F)\\ &\times\gamma_-(F-E)\delta T_-(E,\alpha|F,\beta)d\alpha dE\\ &+\int\int\gamma_+^*(F'-E)\delta T_+(E,\alpha|F',\beta')\\ &\times(H^E-F)u_-(E,\alpha|F,\beta)d\alpha dE\Big]\\ &+\epsilon\delta T_-(F,\beta'|F,\beta). \end{aligned} \tag{34}$$

The second term in the right-hand side of Eq. (34) vanishes because of Eq. (32).

Let us designate the first integral on the right-hand side of (34) by $A'(T_\pm)$, which we now evaluate.

$$A'(T_\pm)=\lim_{F'\to F}\epsilon\int\int u_+^*(E,\alpha|F',\beta')(H^E-F)\times\gamma_-(F-E)\delta T_-(E,\alpha|F,\beta)d\alpha dE. \quad (35)$$

Since H is a Hermitian operator and since u_+ is an eigenfunction of H in the H_0 representation,

$$H^E u_+(E,\alpha|F',\beta')=F'u_+(E,\alpha|F',\beta'); \quad (36)$$

therefore we have

$$\begin{aligned}A'(T_\pm)&=\lim_{F'\to F}\epsilon\int\int[(H^{E*}-F)u_+^*(E,\alpha|F',\beta')]\times\gamma_-(F-E)\delta T_-(E,\alpha|F,\beta)d\alpha dE\\&=\lim_{F'\to F}\epsilon\int\int u_+^*(E,\alpha|F',\beta')(F'-F)\times\gamma_-(F-E)\delta T_-(E,\alpha|F,\beta)d\alpha dE. \quad (37)\end{aligned}$$

We note that

$$\begin{aligned}&(F'-F)\gamma_-(F-E)\\&\quad=[(F'-E)-(F-E)]\gamma_-(F-E)\\&\quad=(F'-E)\gamma_-(F-E)-(F-E)\gamma_-(F-E)\\&\quad=(F'-E)\gamma_-(F-E)-1. \quad (38)\end{aligned}$$

When (38) is used in (37) we have

$$\begin{aligned}A'(T_\pm)=\lim_{F'\to F}\epsilon\Big[&\int\int u_+^*(E,\alpha|F',\beta')(F'-E)\times\gamma_-(F-E)\delta T_-(E,\alpha|F,\beta)d\alpha dE\\&-\int\int u_+^*(E,\alpha|F',\beta')\times\delta T_-(E,\alpha|F,\beta)d\alpha dE\Big]. \quad (39)\end{aligned}$$

Now from (11) it follows that

$$(F-E)u_\pm(E,\alpha|F,\beta)=\epsilon T_\pm(E,\alpha|F,\beta). \quad (40)$$

Hence

$$\begin{aligned}A'(T_\pm)=\lim_{F'\to F}\epsilon\Big[&\epsilon\int\int T_+^*(E,\alpha|F',\beta')\times\gamma_-(F-E)\delta T_-(E,\alpha|F,\beta)d\alpha dE\\&-\int\int u_+^*(E,\alpha|F',\beta')\times\delta T_-(E,\alpha|F,\beta)d\alpha dE\Big]. \quad (41)\end{aligned}$$

Note that in the first of the integrals we no longer have products of symbolic functions, since $T_\pm$ and $\delta T_\mp$ are well-behaved functions. Only γ_- is a symbolic function.

In the second integral u_+^* is the only symbolic function. Hence, we can now interchange the limit and integration processes in both integrals. It was *not* possible to do this earlier. Then recognizing that $\gamma_-(\zeta)=\gamma_+^*(\zeta)$, we obtain from (41)

$$\begin{aligned}A'(T_\pm)=\epsilon\Big[&\epsilon\int\int\gamma_+^*(F-E)T_+^*(E,\alpha|F,\beta')\times\delta T_-(E,\alpha|F,\beta)d\alpha dE\\&-\int\int u_+^*(E,\alpha|F,\beta')\times\delta T_-(E,\alpha|F,\beta)d\alpha dE\Big]. \quad (42)\end{aligned}$$

Now from (11) it is seen that

$$\begin{aligned}&\epsilon\gamma_+^*(F-E)T_+^*(E,\alpha|F,\beta')\\&\qquad=u_+^*(E,\alpha|F,\beta')-\delta(E-F)\delta(\alpha,\beta').\end{aligned}$$

Hence,

$$\begin{aligned}A'(T_\pm)=\epsilon\Big[&\int\int u_+^*(E,\alpha|F,\beta')\delta T_-(E,\alpha|F,\beta)d\alpha dE\\&-\delta T_-(F,\beta'|F,\beta)-\int\int u_+^*(E,\alpha|F,\beta')\times\delta T_-(E,\alpha|F,\beta)d\alpha dE\Big]\\&=-\epsilon\delta T_-(F,\beta'|F,\beta). \quad (43)\end{aligned}$$

Finally, since

$$\delta A(\mathcal{T}_\pm)=A'(T_\pm)+\epsilon\delta T_-(F,\beta'|F,\beta),$$

we have from (43)

$$\delta A(\mathcal{T}_\pm)=0, \quad (44)$$

which completes the proof.

5. EXPLICIT FORM OF $A(\mathcal{T}_\pm)$

Although the form of $A(\mathcal{T}_\pm)$ given by Eqs. (24) through (26) is useful for proving the stationary properties of this functional, it is not very convenient for explicit calculation. One can substitute expressions (25) and (26) in (24) and obtain the following:

$$\begin{aligned}A(\mathcal{T}_\pm)=\epsilon V^E(F,\beta'|F,\beta)+\epsilon^2\Big\{&\int\int V^E(F,\beta'|E,\alpha)\times\gamma_-(F-E)\mathcal{T}_-(E,\alpha|F,\beta)d\alpha dE\\&+\int\int\mathcal{T}_+^*(E,\alpha|F,\beta')\gamma_-(F-E)V^E(E,\alpha|F,\beta)d\alpha dE\\&-\int\int\mathcal{T}_+^*(E,\alpha|F,\beta')\gamma_-(F-E)\mathcal{T}_-(E,\alpha|F,\beta)d\alpha dE\Big\}\\&+\epsilon^3\int\int\int\int\mathcal{T}_+^*(E,\alpha|F,\beta')\gamma_-(F-E)\\&\times V^E(E,\alpha|E',\alpha')\gamma_-(F-E')\\&\times\mathcal{T}_-(E',\alpha'|F,\beta)d\alpha dE d\alpha' dE'. \quad (45)\end{aligned}$$

Combining (29) and (45) we have as our final result for the variational principle,

$$T_-(F,\beta'|F,\beta)\cong V^E(F,\beta'|F,\beta)$$
$$+\epsilon\Big\{\int\int V^E(F,\beta'|E,\alpha)\gamma_-(F-E)\,\mathcal{T}_-(E,\alpha|F,\beta)d\alpha dE$$
$$+\int\int \mathcal{T}_+^*(E,\alpha|F,\beta')\gamma_-(F-E)V^E(E,\alpha|F,\beta)d\alpha dE$$
$$-\int\int \mathcal{T}_+^*(E,\alpha|F,\beta')\gamma_-(F-E)\,\mathcal{T}_-(E,\alpha|F,\beta)d\alpha dE\Big\}$$
$$+\epsilon^2\int\int\int\int \mathcal{T}_+^*(E,\alpha|F,\beta')\gamma_-(F-E)$$
$$\times V^E(E,\alpha|E',\alpha')\gamma_-(F-E')$$
$$\times\mathcal{T}_-(E',\alpha'|F,\beta)d\alpha dE d\alpha' dE'. \quad (45a)$$

The derivation of (45) is straightforward, though one must, as usual, take care in the use of the limit process involved in the definition of $I(\mathcal{T}_\pm)$.

We shall now indicate a few simple results. First of all we note that $T_\pm(E,\alpha|F,\beta)$ can be calculated by a perturbation procedure. Equations (11) through (13) can be combined to form an integral equation for either $u_\pm(E,\alpha|F,\beta)$ or $T_\pm(E,\alpha|F,\beta)$; this equation can be solved by iteration. First one uses the approximation $T_\pm\equiv 0$ and inserts this in Eq. (11) for $u_\pm(E,\alpha|F,\beta)$. With this value of $u_\pm$, one uses (13) to obtain better approximations for $T_\pm$; this procedure can be repeated to obtain any desired degree of accuracy. This method is equivalent to solving for $u_\pm$ or for $T_\pm$ by using a power series expansion in ϵ. Each iteration used to find $T_\pm$ is called a Born approximation for $T_\pm$. For example, the zeroeth Born approximation for $T_\pm(E,\alpha|F,\beta)$ is zero. The first, $V^E(E,\alpha|F,\beta)$, is obtained by using the first Born approximation for $u_\pm$, namely $u_\pm(E,\alpha|F,\beta)=\delta(E-F)\delta(\alpha,\beta)$, in (13).

Let us use the zeroeth Born approximation for $T_\pm$ as a trial function $\mathcal{T}_\pm$. That is, let us use as trial functions $\mathcal{T}_\pm=0$. Then we have from (45a)

$$T_-(F,\beta'|F,\beta)\cong V^E(F,\beta'|F,\beta). \quad (46)$$

This is just the first Born approximation to $T_-(F,\beta'|F,\beta)$ that would be obtained using the iteration scheme discussed above.

Let us take as trial functions $\mathcal{T}_\pm$ the first Born approximation to $T_\pm$, namely

$$\mathcal{T}_\pm(E,\alpha|F,\beta)=V^E(E,\alpha|F,\beta).$$

Substituting into (45a) and using the fact that V is a Hermitian operator, we have

$$T_-(F,\beta'|F,\beta)\cong V^E(F,\beta'|F,\beta)$$
$$+\epsilon\int\int V^E(F,\beta'|E,\alpha)\gamma_-(F-E)V^E(E,\alpha|F,\beta)d\alpha dE$$
$$+\epsilon^2\int\int\int\int V^E(F,\beta'|E,\alpha)\gamma_-(F-E)$$
$$\times V^E(E,\alpha|E',\alpha')\gamma_-(F-E')$$
$$\times V^E(E',\alpha'|F,\beta)d\alpha' dE' d\alpha dE. \quad (47)$$

This is just the third Born approximation to $T_-(F,\beta'|F,\beta)$ using the iteration procedure. Kohn[7] points out that if one uses for $\mathcal{T}_+$ the mth Born approximation to T_+ and for $\mathcal{T}_-$ the nth Born approximation to T_-, then the variational expression gives $T_-(F,\beta'|F,\beta)$ accurately to the $(m+n+1)$ approximation. It should be noted, however, that the variational expression in no way can be used as an iterative procedure to obtain T_-, since the Hulthén procedure gives an approximate function to $T_-(E,\alpha|F,\beta)$ only for $E=F$, whereas one needs trial functions which are defined for general values of E and F for an iterative method.

The author wishes to acknowledge helpful discussions with Mr. S. Schwebel.

[7] W. Kohn (private communication).

Space-Time Representation in Wave Mechanics

E. J. HELLUND AND M. K. BRACHMAN
Argonne National Laboratory, Lemont, Illinois
(Received May 29, 1953)

A Newtonian-like basis for describing the dynamical behavior of a system is presented. The nature of the correspondence with a Boltzmann type statistical mechanics is shown. Application of elementary transformation theory is used to effect the results.

INTRODUCTION

IT is well known that the classical equations of motion are satisfied "in the mean." Quantum theory defines the time rate of change of an observable Q averaged over the system by the canonical relation $\dot{Q}=-(i/h)\times[Q, H]$, where H is the Hamiltonian. This correspondence does not directly exhibit a detailed space-time development of the system. One can demonstrate, however, that it is possible to formulate quantum mechanics in such a way as to make explicit use of the concept of trajectories.[1] It is the purpose of the following work to develop such a basis. There is no over-all advantage in such a representation other than that it may possibly provide greater insight into special problems.[2]

TRANSFORMATION THEORY

Since in classical Newtonian mechanics variables are prescribed numerically at points in space-time, it is natural to anticipate the existence of an analogous representation in wave mechanics. Noncommutivity of canonically conjugate variables clearly suggests that the "points" in the latter representation be actually finite space-time regions (i.e., that space-time possess a cellular structure).[3] This does not imply that division of space-time into cells removes the basic differences existing between classical and quantum physics in the calculation of probabilities.[4] Briefly, the contribution of the theory to follow consists of the resolution of the velocity structure within a given cell and the determination of the proper kinematical relationships involving adjacent cells.

The subsequent analysis will be confined to the usual nonrelativistic Schrödinger mechanics of a single particle moving in a field specified by a potential $V(\mathbf{r})$. The generalization to many particles offers no difficulty.

The basis for the new representation is given by the orthonormal functions,

$$\psi(\mathbf{x}, x_0; \boldsymbol{\sigma}, \sigma_0; \mathbf{n}, n_0)$$
$$=\frac{1}{L^2}\exp\left\{\frac{2\pi i}{L}(n_1x_1+n_2x_2+n_3x_3+n_0x_0)\right\}$$
$$\text{for } (x_j-\sigma_jL)(x_j-\sigma_jL-L)<0, \quad j=0, 1, 2, 3;$$
$$=0 \text{ for } (x_j-\sigma_jL)(x_j-\sigma_jL-L)>0;$$
$$n_j=0, \pm1, \pm2, \cdots; \quad \sigma_j=0, \pm1, \pm2\cdots. \quad (1)$$

$\mathbf{x}\equiv x_1, x_2, x_3$ and x_0 denotes ct, where c is an arbitrarily determinable velocity. L is the cell size at "$\boldsymbol{\sigma}$."

It is clear that the functions form a complete set for any space-time domain finite or infinite in extent. The essential indeterminism in the representation lies in the finite widths of the energy-momentum spectra for a given cell. Finally, it is, of course, possible to use a representation in which the time extension of the cell is made infinitesimally small.

We begin with the Schrödinger equation for the representative $\Psi(\mathbf{x}, t)$,

$$\left[-\frac{\hbar^2}{2m}\left(\frac{\partial^2}{\partial x_1^2}+\frac{\partial^2}{\partial x_2^2}+\frac{\partial^2}{\partial x_3^2}\right)+V\right]\Psi=i\hbar\frac{\partial\Psi}{\partial t}$$
$$=i\hbar c\frac{\partial\Psi}{\partial x_0}. \quad (2)$$

One transforms to the equation for the new representation by multiplying by the complex conjugate of the functions given in Eq. (1) and integrating over 4-space. The kinetic energy operator and the total energy operator can subsequently be transformed by integrating by parts. The resulting surface terms again can be re-expressed in terms of the probability amplitudes,

$$\Xi(\boldsymbol{\sigma}, \sigma_0; \mathbf{n}, n_0),$$

for occupation of adjacent cells.[5] The resulting trans-

[1] R. P. Feynman, Revs. Modern Phys. **20**, 367 (1948). Feynman's approach differs fundamentally from that of the present paper.

[2] Compare the introductory remarks of reference 1.

[3] The commutators $[x_j, p_j]$ and $[E, t]$ do not vanish.

[4] J. von Neumann, *Mathematische Grundlagen der Quantenmechanik* (Dover Publications, New York, 1943), Chap. IV.

[5] Some care must be exercised in interpreting this step. Ψ and $\partial\Psi/\partial x$ are assumed to be continuous in the entire domain of integration including the cell boundaries. That is, one has

$$\left.\frac{\partial\Psi}{\partial x_j}\right|_{x_j=\sigma_jL+L}=\lim_{\epsilon\to0}\left.\frac{\partial\Psi}{\partial x_j}\right|_{x_j=\sigma_jL+L+\epsilon},$$

formation can be written more conveniently with the help of the following operators:

$$U_j(\sigma_j, \sigma_j') = -2\pi i\delta(\sigma_j, \sigma_j' - 1), \tag{3}$$

$$V = (n_1 n_2 n_3 | V | n_1' n_2' n_3'), \tag{4}$$

$$G_j(n_j, n_j') = n_j + n_j', \tag{5}$$

$$\left[\sum_{j=1}^{j=3} \frac{\hbar^2}{2mL^2}\{4\pi^2 n_j^2 + G_j(U_j + U_j^\dagger)\} + V + \frac{2\pi hc}{L} n_0 + \frac{hc}{2\pi}(U_0 + U_0^\dagger)\right]\Xi = 0, \tag{6}$$

where $U^\dagger$ denotes the Hermitean conjugate of U, and Kronacker delta functions are understood for indices not specifically noted.

$$1 = \prod_{j,k}^{j,k} \delta(n_j, n_j')\delta(\sigma_k, \sigma_k'). \tag{7}$$

The matrix V is diagonal in "σ," if velocity-independent.

In the event that an infinitesimal time extension of the cell is employed, Eq. (6) can be written as

$$\left[\sum_{j=1}^{j=3} \frac{\hbar^2}{2mL^2}\{4\pi n_j^2 + G_j(U_j + U_j^\dagger)\} + V\right]\Xi = ih\frac{\partial \Xi}{\partial t}. \tag{8}$$

Both Eq. (6) and Eq. (8) permit removal of the classical Hamiltonian. Since the two forms are mathematically equivalent, we shall just write the modified form of Eq. (8). The change basis is

$$\Xi \leftrightarrow \Xi \exp\left\{\frac{-2\pi^2 iht}{mL^2}\sum_{j=1}^{3} n_j^2 - \frac{i}{\hbar}V_{\text{diag}}t\right\}. \tag{9}$$

With all operators now undergoing a corresponding similarity transformation, we have

$$\left[\sum_{j=1}^{j=3} \frac{\hbar^2}{2mL^2} G_j(U_j + U_j^\dagger) + F\right]\Xi = ih\frac{\partial \Xi}{\partial t}, \tag{10}$$

where F denotes the equivalent (under the similarity transformation) of the off-diagonal part of V. "F" is, of course, proportional to the *classical force* for a slowly varying potential.

Equation (10) can be recognized as a Boltzmann-type continuity equation for ideal particles (i.e., there is no collision term). This follows from the easily established correspondences,[6]

$$\sum_{j=1}^{j=3} -\frac{hi}{2mL^2} G_j(U_j + U_j^\dagger) \leftrightarrow \sum_{j=1}^{j=3} v_j \frac{\partial}{\partial x_j}, \tag{11}$$

$$-\frac{i}{\hbar}F \leftrightarrow \sum_{j=1}^{j=3} X_j \frac{\partial}{\partial v_j}, \tag{12}$$

where v_j denotes the jth component of velocity and X_j denotes the jth force component per unit mass. The first term of Eq. (10) thus corresponds to the streaming term and the second to the acceleration term of the Boltzmann continuity equation.

The addition of a collision term with the aid of the correspondences exhibited in the streaming and acceleration terms would complete the quantum analog of the Boltzmann equation. The resultant interference of probability amplitudes or, equivalently, failure of the superposition principle introduces a finite particle size into the formalism.[7]

In spite of the close analogy with the classical statistical continuity equation, the present formalism, as previously noted, is not deterministic.[8]

DISCUSSION

Equation (6) can be taken as the basis for a space-time description of the system. The "path" of the particle could be obtained as that time sequence of which satisfied the corresponding variational problem. The simplest trial function would be that for which

and similarly for Ψ. The use of such a limit process is necessary in the presence of the Gibbs phenomenon. In addition, in order that $\partial\Psi/\partial x_j$ be expressible directly in terms of the occupation amplitudes of a given cell one must invoke the concept of summability. Specifically, one can use a theorem of Fatou on Abel's summability to complete the transformation of $\partial\Psi/\partial x_j$ as follows:

$$\left.\frac{\partial \Psi}{\partial x_j}\right|_{x_j = \sigma_j L + L} = \lim_{\substack{\epsilon \to 0 \\ a \to 1}} \sum_{n} \frac{2\pi i n_j}{L} a^{|n_j|} \times \exp\left[\frac{2\pi i}{L}\{n_1 x_1 + \cdots + n_j[(\sigma_j + 1)L + \epsilon]\}\right] \cdot \Xi(\sigma_1 \cdots \sigma_j + 1; n_1 \cdots n_0),$$

where

$$\Xi(\sigma_1 \cdots \sigma_j + 1; n_1 \cdots n_0) = \frac{1}{L_2}\int_{x_j = (\sigma_j + 1)L}^{x_j = (\sigma_j + 2)L} \cdots \int \Psi \times \exp\left\{\frac{-2\pi i}{L}(n_1 x_1 + \cdots + n_0 x_0)\right\} dx_1 dx_2 dx_3 dx_0.$$

The transformation is valid only in the sense that the limit exist. Simple isomorphism of the operators in the two representation can be shown to hold provided the transformations are defined subject to the limit process. A more detailed discussion of the concept of summability as employed in the preceding analysis can be found in the treatise by A. Zygmund, *Trigonometrical Series* (Monografje, Matematyczne Seminar Uniw. Warsaw, Poland, 1935), Chap. III and particularly Sec. 3.44.

[6] $(2\pi\hbar/L)G_j$ is a Hermitean velocity operator. Also, $(U_j + U_j^\dagger) \times (4\pi L)^{-1} \to \partial/\partial x_j$. The off-diagonal matrix elements of V, for a slowly varying potential, yield the representative product $\{X_j[i(n_j - n_j')]^{-1}\}_{j=1,2,3}$. The Hermitean matrix $[i(n_j - n_j')]^{-1}$ operating on Ξ is the analog of the classical operator $\partial/\partial v_j$. It is not the canonical conjugate of G_j, however, as the latter operator is diagonal in "σ," and therefore does *not* represent p_j/m.

[7] V. F. Weisskopf, Naturwiss. **23**, 669 (1935), (particularly p. 672); also Revs. Modern Phys. **21**, 305 (1949). A classical nonlinear electromagnetic field theory describing electrons of finite size has been proposed by M. Born and L. Infeld, Proc. Roy. Soc. (London) **144**, 425 (1934). Classical nonlinear meson fields have been discussed by L. I. Schiff, Phys. Rev. **84**, 1, 10 (1951).

[8] An exhaustive discussion of this aspect of the Schrödinger theory has been given by D. Bohm, Phys. Rev. **85**, 166, 180 (1952).

vanished everywhere except along a given path. Such a path obviously would not be stationary against the possibility of "branching."

Note should be taken of the differences between the one- and two-sided problems. The characteristic one-sided problem of the motion of a particle in a central force field must be solved subject to the proper boundary conditions at the origin. It is peculiar to the present representation that unless this is done, a Coulomb potential, for example, would possess infinite matrix elements. The proper boundary conditions require antisymmetry of Ξ at the origin in "n" space.

While only the operators explicit in the Hamiltonian have been formally exhibited in the new representation, all others can be evaluated similarly. In particular, the spin is simply expressible only in spherical geometry.

PHYSICAL REVIEW VOLUME 92, NUMBER 3 NOVEMBER 1, 1953

The Invariant Forms of the Nucleon-Nucleon Interaction*

DAVID FELDMAN
Department of Physics, University of Rochester, Rochester, New York
(Received July 28, 1953)

The invariant scattering matrix is used as a basis for the derivation of the possible forms of nucleon-nucleon interaction. The method has the particular advantage in that it allows for a systematic treatment of both exchange and nonexchange forces.

I.

RECENTLY, several authors[1] have shown that the most general form of the elastic scattering matrix M for two spin $\frac{1}{2}$ particles which is invariant under spatial rotations, spatial reflections, and time inversions can, in the center-of-momentum frame of reference S_0, be expressed as the sum of six types of terms, *viz.*,

$$M=A+B\boldsymbol{\sigma}_1\cdot\boldsymbol{\sigma}_2+C(\boldsymbol{\sigma}_1+\boldsymbol{\sigma}_2)\cdot\mathbf{l}+D(\boldsymbol{\sigma}_1-\boldsymbol{\sigma}_2)\cdot\mathbf{l}+E(\boldsymbol{\sigma}_1\cdot\mathbf{m})(\boldsymbol{\sigma}_2\cdot\mathbf{m})+F(\boldsymbol{\sigma}_1\cdot\mathbf{n})(\boldsymbol{\sigma}_2\cdot\mathbf{n}). \quad (1)$$

In terms of $\mathbf{k}_i$ and $\mathbf{k}_f$, the initial and final momenta, respectively, of particle 1, say, we can write $\mathbf{l}=\mathbf{k}_f\times\mathbf{k}_i$, $\mathbf{m}=\mathbf{k}_f-\mathbf{k}_i$, and $\mathbf{n}=\mathbf{k}_f+\mathbf{k}_i$. The functions A, $\cdots$, F depend on the scalars $k_i^2(=k_f^2)$ and $\mathbf{k}_i\cdot\mathbf{k}_f$, so that $A=A(k_i^2,\mathbf{k}_i\cdot\mathbf{k}_f)$, etc. For our purposes, it is more convenient to write instead $A=A(\mathbf{m},\mathbf{n})$ which is a fully equivalent way of expressing A since $\mathbf{m}\cdot\mathbf{n}=0$.[2]

It is the intent of this note to point out that one can now use Eq. (1) to derive directly the possible invariant forms of nucleon-nucleon interaction; a particular advantage of the method over the standard procedure of Wigner and Eisenbud[3] is that exchange forces can be treated on exactly the same footing as nonexchange forces.

Now, it is sufficient for our purposes to look for that nucleon-nucleon interaction which, in first Born approximation, will lead to M. This interaction, which, of course, will, in the first instance, be appropriate only for the frame of reference S_0, will generally be nonlocal in character. In the region of small energies, however, one can proceed, purely formally, as follows. Consider the term $A(\mathbf{m},\mathbf{n})$; having first abstracted a factor[4] $2\pi\delta(E_i-E_f)$, where E_i and E_f are the initial and final energies, respectively, we expand it in a Taylor series, regarding n as very small compared to M_n or M_p, the neutron or proton mass. Then,

$$A(\mathbf{m},\mathbf{n})=A_0(\mathbf{m})+n^2A_2(\mathbf{m})+\cdots. \quad (2a)$$

The term $A_0(\mathbf{m})$ will lead immediately to an ordinary static central force $\alpha_0(\mathbf{r})$, since one can write

$$A_0(\mathbf{m})=-i\int d\mathbf{r}\,\alpha_0(\mathbf{r})e^{-i\mathbf{m}\cdot\mathbf{r}}$$

$$=-i\int d\mathbf{r}e^{-i\mathbf{k}_f\cdot\mathbf{r}}\alpha_0(\mathbf{r})e^{i\mathbf{k}_i\cdot\mathbf{r}}. \quad (3)$$

We identify $\mathbf{r}$ with the relative coordinate of the two particles. If we adopt the convention that interactions which are more than linear in the relative momentum $\mathbf{p}=(1/i)\nabla_r$ are to be dropped, then the remaining terms on the right-hand side of (2a) contribute nothing. In this way, one finds that there are four interactions contributed by A, B, C, and E in (1) which can be expressed in terms of the forms

$$1,\ Q_{12}=\tfrac{1}{2}(1+\boldsymbol{\sigma}_1\cdot\boldsymbol{\sigma}_2),$$
$$S_{12}=3(\boldsymbol{\sigma}_1\cdot\mathbf{r})(\boldsymbol{\sigma}_2\cdot\mathbf{r})/r^2-\boldsymbol{\sigma}_1\cdot\boldsymbol{\sigma}_2,\quad(\boldsymbol{\sigma}_1+\boldsymbol{\sigma}_2)\cdot(\mathbf{r}\times\mathbf{p}), \quad (4a)$$

* This work was supported, in part, by the U. S. Atomic Energy Commission.

[1] L. Wolfenstein and J. Ashkin, Phys. Rev. **85**, 947 (1952); R. H. Dalitz, Proc. Phys. Soc. (London) **A65**, 175 (1952).

[2] It was previously stated [D. Feldman, Bull. Am. Phys. Soc. **28**, No. 4, 20 (1953)] that Eq. (1) would follow in a Lorentz-covariant theory without the need for the explicit assumption of time-inversion invariance. This conclusion, however, has since been found to have been based on a faulty argument.

[3] E. P. Wigner, Phys. Rev. **51**, 106 (1937); L. Eisenbud and E. P. Wigner, Proc. Nat. Acad. Sci. **27**, 281 (1941).

[4] For the sake of simplicity, we shall set $\hbar$, c, and the volume of the system equal to unity.

while D leads to

$$(\boldsymbol{\sigma}_1-\boldsymbol{\sigma}_2)\cdot(\mathbf{r}\times\mathbf{p}). \tag{4b}$$

F yields nothing in this case. Each term in (4a) and (4b) will appear multiplied by a real function[5] of r.

Instead of proceeding as in (2a), however, one can carry through the alternative expansion:

$$A(\mathbf{m},\mathbf{n})=A_0'(\mathbf{n})+m^2A_2'(\mathbf{n})+\cdots, \tag{2b}$$

where we have assumed $m\ll M_n, M_p$. The interaction which is deduced from $A_0'(\mathbf{n})$ will now be a static central force $\mathcal{A}_0'(\mathbf{r})$ multiplied by the space-exchange operator P, where the operator P has the property that $P\psi(\mathbf{R},\mathbf{r})=\psi(\mathbf{R},-\mathbf{r})$. We have denoted by $\mathbf{R}$ an absolute coordinate, which, together with the relative coordinate $\mathbf{r}$, specifies the positions of the two particles in space.[6] Upon applying (2b) to all the terms in (1), one derives a total of five interactions given by

$$P,\ Q_{12}P,\ S_{12}P,\ (\boldsymbol{\sigma}_1+\boldsymbol{\sigma}_2)\cdot(\mathbf{r}\times\mathbf{p})P, \tag{5a}$$

and

$$(\boldsymbol{\sigma}_1-\boldsymbol{\sigma}_2)\cdot(\mathbf{r}\times\mathbf{p})P; \tag{5b}$$

once again, each term in (5a) and (5b) will be multiplied by a real function of r. There are thus ten interactions in all, five with exchange and five without.

It is clear from the above development that an exchange force can always be written as an infinite series of non-exchange velocity-dependent forces,[7] and vice versa. It is equally evident, however, that it would be inconsistent to drop the exchange terms and keep non-exchange terms which are at most linear in $\mathbf{p}$.[8]

II.

Preparatory to generalizing the interactions (4a, b) and (5a, b) to an arbitrary Galilean frame of reference, we exhibit explicitly the two-particle character of our system by introducing the individual particle coordinates and momenta. Thus, let[6]

$$\mathbf{r}=\mathbf{r}_1-\mathbf{r}_2,\quad \mathbf{R}=\alpha\mathbf{r}_1+(1-\alpha)\mathbf{r}_2, \tag{6a}$$

where α is an arbitrary parameter; then

$$\mathbf{p}=(1-\alpha)\mathbf{p}_1-\alpha\mathbf{p}_2,\quad \mathbf{P}=\mathbf{p}_1+\mathbf{p}_2, \tag{6b}$$

with $\mathbf{p}_1=(1/i)\nabla_{r_1}$, $\mathbf{p}_2=(1/i)\nabla_{r_2}$, and $\mathbf{P}=(1/i)\nabla_R$. Furthermore, denoting the transformed wave function by $\phi(\mathbf{r}_1,\mathbf{r}_2)$, it also follows that

$$P=P_{12}(\alpha), \tag{6c}$$

where

$$P_{12}(\alpha)\phi(\mathbf{r}_1,\mathbf{r}_2)=\phi[\mathbf{r}_2+(2\alpha-1)(\mathbf{r}_1-\mathbf{r}_2),\ \mathbf{r}_1-(2\alpha-1)(\mathbf{r}_2-\mathbf{r}_1)]. \tag{6d}$$

The operator $P_{12}(\alpha)$ appears as that generalization of the space-exchange operator P which is appropriate under the coordinate transformation (6a). If $\alpha=\frac{1}{2}$, it reduces to the ordinary Majorana space-exchange operator P_{12} which simply replaces $\phi(\mathbf{r}_1,\mathbf{r}_2)$ by $\phi(\mathbf{r}_2,\mathbf{r}_1)$.

Now we note that, if $\phi_0(\mathbf{r}_1,\mathbf{r}_2,t)$ is the wave function of the two-particle system in the center-of-momentum system S_0, the wave function $\phi(\mathbf{r}_1,\mathbf{r}_2,t)$ in a frame of reference S moving with velocity v in the negative x-direction with respect to S_0 is given by[3]

$$\phi(\mathbf{r}_1,\mathbf{r}_2,t)=U\phi_0(\mathbf{r}_1,\mathbf{r}_2,t), \tag{7a}$$

where

$$U=\exp[i(M_1x_1+M_2x_2)v-\tfrac{1}{2}i(M_1+M_2)v^2t]; \tag{7b}$$

M_1 and M_2 are the masses of the two particles, respectively. It therefore follows that an interaction operator which is determined in S_0 will be valid in S if it commutes with $M_1x_1+M_2x_2$. It is clear that the spin operators, $\boldsymbol{\sigma}_1$ and $\boldsymbol{\sigma}_2$, and the relative coordinate $\mathbf{r}_1-\mathbf{r}_2$ satisfy this condition. In order that the relative momentum $(1-\alpha)\mathbf{p}_1-\alpha\mathbf{p}_2$ and the space-exchange operator $P_{12}(\alpha)$ shall be Galilean invariant, we must have $\alpha=M_1(M_1+M_2)^{-1}$. Under these circumstances, the relative momentum goes over into $M_1M_2(M_1+M_2)^{-1}\times(\mathbf{p}_1/M_1-\mathbf{p}_2/M_2)$ or the reduced mass times the velocity difference, and the space-exchange operator $P_{12}(\alpha)$ becomes $P_{12}[M_1(M_1+M_2)^{-1}]\equiv P_{12}'$, where

$$P_{12}'\phi(\mathbf{r}_1,\mathbf{r}_2)=\phi[\mathbf{r}_2+(M_1-M_2)(M_1+M_2)^{-1}(\mathbf{r}_1-\mathbf{r}_2),\ \mathbf{r}_1-(M_1-M_2)(M_1+M_2)^{-1}(\mathbf{r}_2-\mathbf{r}_1)]. \tag{8}$$

The ten types of interaction for the two-particle system (4a, b) and (5a, b) can accordingly be taken over for an arbitrary Galilean frame of reference provided one makes the following transcriptions:

$$\boldsymbol{\sigma}_1\to\boldsymbol{\sigma}_1,\quad \boldsymbol{\sigma}_2\to\boldsymbol{\sigma}_2,\quad \mathbf{r}\to\mathbf{r}_1-\mathbf{r}_2, \tag{9a}$$

$$\mathbf{p}\to\mu(\mathbf{v}_1-\mathbf{v}_2),\quad P\to P_{12}', \tag{9b}$$

where μ is the reduced mass of the two particles $M_1M_2(M_1+M_2)^{-1}$, $\mathbf{v}_1$ is the velocity operator of particle 1 and equal to $\mathbf{p}_1/M_1$ (a similar statement being made for $\mathbf{v}_2$), and P_{12}' is characterized by (8).

It is interesting that it is P_{12}' which appears here as a natural extension of P_{12}; the operator P_{12}' has been given previously by Breit and Wigner[9] and by Plesset[10] who constructed it heuristically. In the case that $M_1=M_2$, Eq. (9b) can be rewritten in the form

$$\mathbf{p}\to\tfrac{1}{2}(\mathbf{p}_1-\mathbf{p}_2),\quad P\to P_{12}; \tag{9c}$$

it is for this case only that it is the ordinary Majorana space-exchange operator which enters.

[5] The Hermitian character of the interactions will be insured by the unitarity of the scattering matrix.

[6] E. E. Salpeter and H. A. Bethe, Phys. Rev. **84**, 1232 (1951).

[7] See also J. A. Wheeler, Phys. Rev. **50**, 643 (1936).

[8] It is also interesting to note that the interactions which are derived by making the expansion (2a) [or (2b)] form a complete set in that any interaction which is invariant in the sense of Wigner and Eisenbud can be expressed in terms of them. By way of illustration, the invariant forms $i[(\mathbf{r}\cdot\mathbf{p})V-V(\mathbf{p}\cdot\mathbf{r})]$ and $p^2V-2p_jVp_j+Vp^2$, which do not appear explicitly in our formalism (V is a real function of r), can easily be shown to be equivalent to static central interactions.

[9] G. Breit and E. P. Wigner, Phys. Rev. **48**, 918 (1935).

[10] M. S. Plesset, Phys. Rev. **49**, 551 (1936).

III.

We conclude this note with a brief remark about the isotopic spin formalism. Let the proton-proton, neutron-neutron, and neutron-proton interactions be denoted by $V_{pp}^{(1)}$, $V_{nn}^{(2)}$, and $V_{np}^{(3)}$, which contain four, four, and ten types of terms, respectively, making a total of eighteen.[11] Assuming that $M_n=M_p$, and assigning isotopic spin $+1$ and -1 to the proton and neutron, respectively, the total interaction V_{12} for the nucleon-nucleon system, to be used with wave functions which are completely anti-symmetric in space, spin, and isotopic spin coordinates, can be written as follows:

$$V_{12}=\tfrac{1}{4}\{V_{12}^{(1)}(1+\tau_{1z})(1+\tau_{2z})+V_{12}^{(2)}(1-\tau_{1z})(1-\tau_{2z})$$
$$+V_{12}^{(3)}(1-\tau_{1z})(1+\tau_{2z})+V_{21}^{(3)}(1+\tau_{1z})(1-\tau_{2z})\}; \quad (10)$$

τ_1 and τ_2 are the standard isotopic spin matrices. In view of the important property that, for a completely antisymmetric wave function ϕ, one has

$$P_{12}Q_{12}T_{12}\phi=-\phi, \quad (11)$$

where $T_{12}=\frac{1}{2}(1+\tau_1\cdot\tau_2)$, it follows directly from (10) that V_{12} can be expressed as a sum of eighteen types of interactions given by the product of (4a) with

$$1,\ T_{12},\ (\tau_1+\tau_2)_z,\ \tau_{1z}\tau_{2z}, \quad (12a)$$

(4b) with

$$(\tau_1-\tau_2)_z, \quad (12b)$$

and, finally, the product of

$$(\sigma_1\times\sigma_2)\cdot(\mathbf{r}\times\mathbf{p}) \quad (4c)$$

with

$$(\tau_1\times\tau_2)_z; \quad (12c)$$

each term is multiplied by a real function of r, and it is to be understood that, for this case, the relative coordinate and momentum are given by $\mathbf{r}_1-\mathbf{r}_2$ and $\frac{1}{2}(\mathbf{p}_1-\mathbf{p}_2)$, respectively.

The number and types of interactions which are thus obtained are precisely those given by Wigner and Eisenbud. From our standpoint, however, the isotopic spin formalism has led to nothing new. It permits a more unified treatment of the nucleon-nucleon interaction and, in particular, a simpler representation of exchange forces.

If the neutron and proton masses are not equal to one another, the transition to the isotopic spin formalism can be carried through in a manner analogous to the case of equal masses only for the center-of-momentum system.[12] On transforming to an arbitrary Galilean frame of reference, however, the situation becomes quite complicated since the unitary transformation which carries the system from S_0 to S will depend on the nature of the two particles. Under these circumstances, one is better off avoiding the use of the isotopic spin formalism altogether.

[11] On account of the complete antisymmetry in space and spin variables of like-particle wave functions, the only types of interactions which enter in $V_{pp}^{(1)}$ and $V_{nn}^{(2)}$ are those contained in (4a).

[12] The kinetic-energy operator of the two-particle system will now depend on the isotopic spin.

Letters to the Editor

PUBLICATION of brief reports of important discoveries in physics may be secured by addressing them to this department. The closing date for this department is five weeks prior to the date of issue. No proof will be sent to the authors. The Board of Editors does not hold itself responsible for the opinions expressed by the correspondents. Communications should not exceed 600 words in length and should be submitted in duplicate.

Observation of Cyclotron Resonance in Germanium Crystals*

G. DRESSELHAUS, A. F. KIP, AND C. KITTEL
Department of Physics, University of California, Berkeley, California
(Received September 8, 1953)

WE have observed cyclotron or diamagnetic resonance in n- and p-type germanium crystals at 4°K at a frequency of 9050 Mc/sec. In cyclotron resonance absorption the conduction electrons or holes are curved in spiral orbits by the application of a static magnetic field; resonant absorption of energy from an rf electric field perpendicular to the static magnetic field occurs when the frequency of the electric field is equal to the frequency of rotation of the particle. This is the principle of the cyclotron an the simple magnetron. The angular rotation frequency in a crystal is

$$\omega_L=(eH)/(m^*c), \tag{1}$$

where m^* is the appropriate effective mass; thus the experiment determines the effective mass directly. Cyclotron resonance should not be confused with electron spin resonance. Cyclotron resonance arises from an electric dipole transition, whereas spin resonance arises from a magnetic dipole transition: the transition probabilities for the former are larger by a factor of the order of 10^{10} under the conditions of our experiment.

The theory of cyclotron resonance absorption goes back to Drude, Voigt, and Lorentz. The effect is important to the propagation of radio waves through the upper atmosphere.[1] The translation of the theory to solids has been discussed recently by Dingle[2] and by Shockley;[3] the latter who has pointed out that conditions in germanium are favorable for the observation of the effect. For a plane polarized E field the conductivity at frequency ω is related to the static conductivity σ_0 by the equation

$$\frac{\sigma}{\sigma_0}=\frac{1+i\omega\tau}{1+(\omega_L{}^2-\omega^2)\tau^2+2i\omega\tau}; \tag{2}$$

here τ is the collision or relaxation frequency of the electrons. It is desirable to have $\omega\tau>1$ to define the resonance; for this it is advantageous to work with pure crystals at low temperatures and high frequencies.

Cyclotron resonance was observed in a 38 ohm-cm n-type germanium crystal at a field of 370±5 oersteds, corresponding to an effective mass at 4°K of

$$m^*/m=0.11,$$

presumably for electrons. The static magnetic field was parallel to a 100 axis. The relaxation time is approximately 0.7×10^{-10} sec as estimated from the width of the resonance (~100 oersteds half-width at half-power). We note that Suhl and Pearson,[4] in an unsuccessful attempt to detect cyclotron resonance in n-Ge, were able to set a limit $m^*/m<0.3$; this is compatible with our measurements.

The relative intensity of the resonance depends on the rf power level. With our present equipment no signal from the specimen is detected at low rf power. As the power is increased the resonance line *suddenly* appears. Further increases in power make the specimen visible over a wider range of static magnetic field intensity. At the highest powers the resonance line is broadened. Similar effects were observed in p-type germanium. The resonance positions are essentially independent of power at the levels employed. The cavity was always filled with liquid helium. The dependence of the signal on power level is consistent with a large increase in carrier concentration caused by avalanche ionization of shallow traps (or perhaps donor impurity atoms) occurring as the electrons near resonance gain sufficient energy from the rf field to cause ionization. Threshold rf fields in the 1 to 10 v/cm range start the carrier multiplication.[5] The presence of ionization effects near resonance eliminates the possibility that paramagnetic impurities cause the resonance. The behavior of the resonance signals during thermal ionization on warming up above 4°K was easily distinguishable from the behavior during rf ionization.

Cyclotron resonance was also observed in a p-type germanium crystal having about 10^{14} acceptors/cm³. Two resonances were observed, one at 125±5 oersteds with a half-width of about 50 oersteds and another at 970±50 oersteds with a half-width of about 100 oersteds. Ionization was observed near each resonance. The order of magnitude of the intensities of the two lines are comparable. In all runs the field was explored up to 9000 oersteds. The hole resonances correspond to, at 4°K,

(a) $m^*/m=0.04$; $\tau\approx0.5\times10^{-10}$ sec,
(b) $m^*/m=0.30$; $\tau\approx2\times10^{-10}$ sec.

The field was applied parallel to 100, 110, and 111 axes in successive experiments. No shift in resonance positions with orientation was observed. The sample on the 100 run was different in size and shape from that used on the other runs, so that "cavity-type" false resonances may presumably be excluded.

We wish to express our gratitude to Dr. A. V. Siefert of Sylvania Electric Products, Inc., and to Mr. R. E. Davis of the Westinghouse Research Laboratories for supplying high-quality germanium crystals for the present program. We are indebted to Professor W. F. Giauque and Dr. D. N. Lyon for the provision of liquid helium, and also to the Shell Development Company for liquid helium. The x-ray orientations were kindly performed by Dr. J. Washburn.

* This work has been assisted in part by the U. S. Office of Naval Research.

[1] For a review see H. R. Mimno, Revs. Modern Phys. **9**, 1 (1937).
[2] R. B. Dingle, Proc. Roy. Soc. (London) **A212**, 38 (1952).
[3] W. Shockley, Phys. Rev. **90**, 491 (1953).
[4] H. Suhl and G. L. Pearson, Bull. Am. Phys. Soc. **28**, No. 4, 24 (1953).
[5] It appears that this picture will explain the resistance discontinuities in p-Ge in static electric fields at 4°K and below reported by A. N. Gerritsen, Physica **15**, 427 (1949); it is possible that ionization might also explain the increase in carrier concentration at low temperatures reported by C. S. Hung and J. R. Gliessman, Phys. Rev. **79**, 726 (1950).

The Structure of Liquid Helium

JAMES REEKIE AND T. S. HUTCHISON
Royal Military College of Canada, Kingston, Ontario, Canada
(Received July 16, 1953)

A STUDY has recently been completed in our laboratories of the angular intensity distribution of x radiation scattered by liquid helium. From this, following essentially the method of analysis described by Gingrich,[1] an atomic distribution function for the liquid has been evaluated. The experimental method has already been indicated elsewhere,[2] and in this note we wish briefly to present the qualitative results obtained.

While minor variations in intensity distribution may result as the temperature of the liquid helium is changed, these are at present considered to be within our observational accuracy. It is, therefore, certain that no large change occurs in the atomic distribution over the whole liquid range from 4°K to 1.27°K, nor can the λ-point transition be regarded as the result of any drastic re-ordering process.

Taking the intensity distribution at 2.06°K, just below the λ point, as typical of the present results, we obtain the atomic distribution shown in Fig. 1. This gives, as usual, the number of

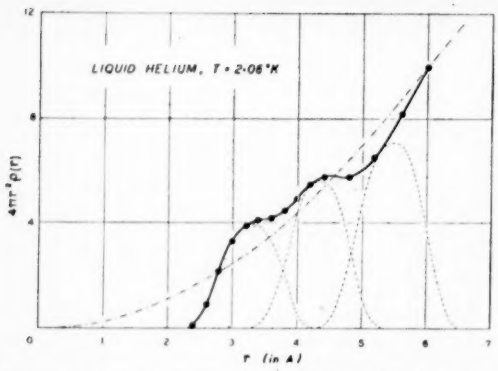

FIG. 1. The distribution function for liquid helium below the λ point.

atoms contained in any shell of radius r and thickness dr; the smooth dotted curve indicates the *mean* atomic density at the same temperature. Using Coulson and Rushbrooke's[3] criterion that $r\rho(r)$ has symmetric similarity about each value of r for which the distribution curve shows a maximum, the latter can then be reduced to its component shells. This is also shown in Fig. 1, from which the following distribution of helium atoms around any one atom may be deduced:

Distance, A	Number of atoms in shell
3.15	4
4.24	6
5.40	8

There may be some uncertainty about the accuracy of the atomic density deduced from our data for the third shell. However, from other considerations there appears to be little doubt that the distribution given is the correct one for liquid helium.

While bulk helium is certainly not possessed of any extensive long-range order, we believe that results of appreciable significance may follow from a consideration of the lattice structure which can be built up to conform to the above distribution. It is readily seen that a simple tetragonal lattice with an axial ratio c/a of $\sqrt{2}$ will approximately satisfy the atomic distribution found for helium, and such a structure with $a=3.15$A could form the unit cell. Early speculations relating to the atomic distribution in liquid helium, based as they were on the idea of order-disorder transitions, suggested that the actual structure might be developed from a face-centered cubic lattice.[4,5] It is instructive in the present case to consider how the tetragonal cell may be derived by a similar procedure. It will be clear that the distribution found can be made up by simply removing in a particular way eight of the twelve nearest neighbors in a face-centered array, all other atom points remaining occupied. Figure 2 shows a structure resulting from this process, and a striking feature of this array will be immediately evident. One set of (100) planes is appreciably more densely populated than any other plane. If the helium had long-range order, this plane would in fact be an exceedingly effective "slip plane."

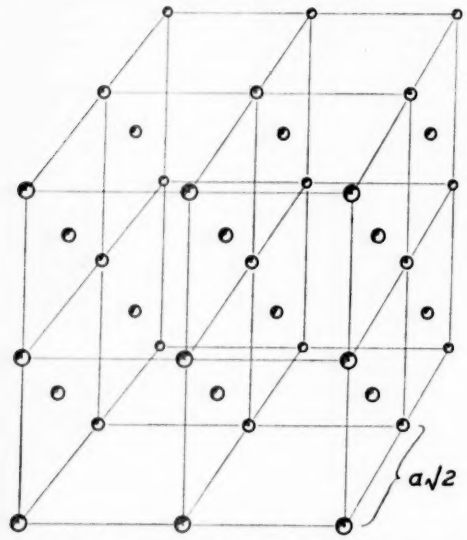

FIG. 2. Lattice configuration for liquid helium, showing preferential (100) planes.

One is tempted to consider, therefore, whether the helium II film (or the "superfluid" component of the liquid) does actually have such an ordered structure as shown in Fig. 2, and whether such order exists over a sufficient extent to permit of easy slip on the preferential (100) plane. The fact that the helium II film is effectively at a temperature of 0°K and has zero entropy[6] lends support to the necessity of its having *some* kind of order, and such physical order is in many ways a more satisfactory concept than an ordering in "momentum space." So long as no appreciable momentum interchange occurs between the preferential (100) planes, the formation of a helium II film on any surface in contact with the liquid, and its nonviscous flow on that surface, would naturally follow. On this view, viscosity would suddenly appear in any extended "superfluid" portion of the liquid, as soon as bulk helium II adjacent to that portion had reached a sufficient temperature that its ("normal") atoms possessed enough energy to destroy the "superfluid" structure. It is of interest to note that a simple calculation of the binding energy[7] between opposite pairs of atoms on the preferential (100) planes of the proposed lattice structure yields a value of about 2×10^{-16} erg. If this is equated to $kT/2$, a value of nearly 3°K is obtained for T. The onset of viscosity in the superfluid regions when the bulk liquid reached this temperature would, of course, be associated with the λ-point transition.

According to this picture, *both helium I and bulk helium II* would simply have the liquid-type distribution actually found; we should not expect present x-ray methods to show any structural change at the λ point.

Finally, we may remark that a calculation of the total energy at 0°K of such a structure as shown in Fig. 2, using the Slater-Kirkwood[7] potential function and London's curve for zero-point energy,[8] gives a binding energy of 15 calories per mole and a molar volume of 27 cc. These figures agree remarkably well with the experimental values deduced for helium II, and give further confidence in the correctness of the proposed structure. Full details of this work will be published elsewhere.

[1] N. S. Gingrich, Revs. Modern Phys. **15**, 90 (1943).
[2] Hutchison, Beaumont, and Reekie, Proc. Phys. Soc. (London) **A66**, 409 (1953).
[3] C. A. Coulson and G. S. Rushbrooke, Phys. Rev. **56**, 1216 (1939).
[4] H. Fröhlich, Physica **4**, 639 (1937).
[5] W. H. Keesom and K. W. Taconis, Physica **5**, 270 (1938).
[6] P. L. Kapitza, J. Phys. U.S.S.R. **5**, 59 (1941).
[7] J. C. Slater and J. G. Kirkwood, Phys. Rev. **37**, 832 (1931).
[8] F. London, Proc. Roy. Soc. (London) **A153**, 576 (1936).

Čerenkov Effect at Microwave Frequencies*

M. DANOS, S. GESCHWIND,† H. LASHINSKY, AND A. VAN TRIER‡
Columbia Radiation Laboratory, Columbia University, New York, New York
(Received September 8, 1953)

ČERENKOV radiation at microwave frequencies has been experimentally detected. Approximately 10^{-7} watt of Čerenkov radiation at a wavelength of 1.25 cm was obtained.

In the arrangement used (see Fig. 1), the radiation is excited by a flat electron beam which passes as closely as possible over

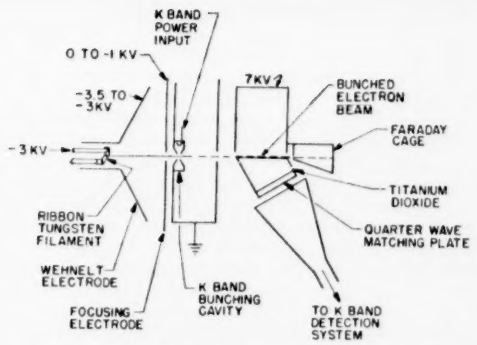

FIG. 1. Schematic diagram of experimental arrangement.

the surface[1] of a dielectric material after having been bunched at a K-band frequency. The radiation leaves the dielectric through a quarter-wave matching plate and is then picked up by a microwave horn and detected with a 1N26 crystal. The electron beam is 4 mm wide and approximately 0.3 mm high and passes over a 1.9-cm length of dielectric which is polycrystalline TiO_2.[2] The measured dielectric constant of this material at $\lambda = 1.25$ cm is 105. The beam voltage is 10 kv, the current 0.2 ma, and the bunching frequency 24 000 Mc/sec. The beam is bunched by passage through a klystron-like cavity. The K-band klystron which energizes this cavity is switched on and off at a 6-kc rate to facilitate the subsequent amplification of the signal. In addition, the electron beam is "chopped" at 20 cps, thereby providing a means of discriminating between the leakage power coming from the bunching cavity and radiation due to the electron beam. Radiation is detected by a crystal, the signal amplified and displayed on an oscilloscope.[3]

Because of the bunching of the beam, the radiation contains only the bunching frequency and its harmonics. At the present writing, only the fundamental has been examined.

To verify that the signal was indeed due to Čerenkov radiation, the distance between the electron beam and the dielectric was varied. The signal intensity decreased very rapidly as the distance between dielectric and electron beam was increased. This is to be expected for Čerenkov radiation.[4]

It was estimated that under the conditions of the present experiment a power in the order of 10^{-6} w can be expected.

We wish to thank Professor Townes for his help and encouragement during the course of the experiment.

* Work supported jointly by the U. S. Signal Corps and U. S. Office of Naval Research.
† Present address: Bell Telephone Laboratories, Murray Hill, New Jersey.
‡ Present address: Warande 182A, Schiedam, Holland.
[1] Mandelstam (unpublished) quoted, e.g., in reference 4.
[2] Supplied by Bell Telephone Laboratories, Murray Hill, New Jersey.
[3] Further details are given in Columbia Radiation Laboratory Quarterly Report, June 30, 1953 (unpublished).
[4] V. L. Ginsburg and J. M. Frank, Compt. rend. acad. sci. U.R.S.S. **56**, 699 (1947).

Capillarity in Helium II*

C. T. LANE AND R. V. DYBA
Sloane Physics Laboratory, Yale University, New Haven, Connecticut
(Received September 14, 1953)

IN the course of developing apparatus for experiments on the surface tension of He^3-He^4 mixtures, we have observed a rather interesting phenomenon connected with superfluid He^4. The method employed is the standard "capillary rise" technique using, however, parallel plates rather than the more usual capillary tube.

Figure 1 indicates one of the arrangements. Two optically flat glass plates GG are separated by two strips of aluminum foil SS thus forming a clear region about 20 mm long, 6 mm wide, and with a gap of 36 microns. These plates were suspended by two stainless steel wires, each 1 mm in diameter, from the top of the cryostat, and provision was made to raise or lower the plates from outside the cryostat. A cathetometer was employed to observe liquid levels and the light source was a low-power fluorescent lamp with heat-absorbing glass filters.

The procedure consisted in lowering the assembly until the bath level was at position a in Fig. 1 (i.e., both plates immersed) and measuring the height of the meniscus and the bath level as a function of time. Figure 2 shows two such typical runs, at 1.25°K and 2.15°K, respectively. As the bath level falls (due to evaporation) so does the meniscus, the difference in level at any time being the capillary rise. The vertical broken line in Fig. 2 indicates the point at which the bath level just falls below the gap between the two plates, i.e., to the right of this line only one plate is immersed (position b in Fig. 1). Nevertheless, the distance between meniscus and bath remains the same. This continues, as the bath level falls, until the immersed plate presents a certain minimum periphery to the bath, at which point the meniscus suddenly collapses and all liquid drains out of the space between the plates. The minimum periphery where this occurs was temperature dependent, being approximately 41 mm at 2.15°K and 21 mm at 1.25°K.

The above effect also occurred in reverse. Thus, as the plates were lowered into the bath no meniscus formed between them until this least periphery on the single plate was reached; thence the meniscus slowly rose between the plates (time of the order of 1 minute) until it reached its equilibrium height equal to the capillary rise appropriate to the temperature in question.

Clearly the mobile helium film (thickness $\sim 10^{-6}$ cm) is the agent which feeds the liquid via the surface of the lower plate into the volume between the plates. Actually, this process must involve a fairly complex balance since the meniscus loses liquid both by evaporation and also from the mobile film which forms there. Naturally, we checked to see whether this process occurs in He I; it does not.

In addition, if, with the meniscus between the plates, the latter are suddenly raised so that contact with the bath is broken, the meniscus then falls (in He II) and liquid drips from the sharp tip of the lower plate. But in He I the meniscus "stays put" for a considerable time and only slowly drops by evaporation (this is true also of water). This, of course, is a variation on one of the well-known beaker experiments of Daunt and Mendelssohn.

The above results appear to have some interesting practical implications. Thus it appears that, when the mobile film is constrained to flow through a narrow channel (as wide as 75 microns in some of our runs), bulk liquid is formed in this channel. A number of experiments[1-3] involving He II or superfluid He^3-He^4 solutions have made use of narrow channels in the form of capillary leaks and, up to now, it has always been supposed that only the film passes through such channels whereas, most probably, they held bulk liquid. The interpretation of such experiments is, therefore, open to some doubt. In view of the fact that the bulk

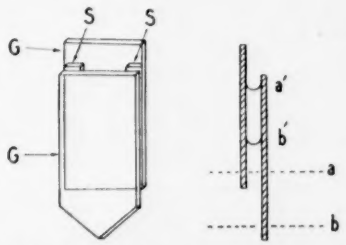

FIG. 1. Isometric view of the glass plates plus a vertical cross section through the center line.

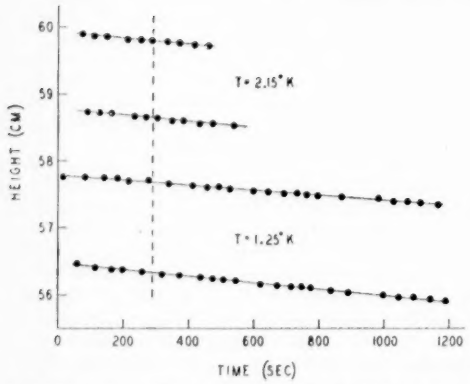

FIG. 2. Height of the meniscus (upper curve of each pair) and bath level as a function of time for 2.15°K and 1.25°K, respectively.

liquid only forms above a certain minimum periphery for the film, it would appear possible to design a superleak which would pass the film only.

* Assisted by the U. S. Office of Naval Research.
[1] J. B. Brown and K. Mendelssohn, Nature **160**, 670 (1947).
[2] Fairbank, Lynton, and Lane, Phys. Rev. **79**, 211 (1950).
[3] E. F. Hammel and A. F. Schuch, Phys. Rev. **87**, 154 (1952).

Detection of the Free Neutrino*

F. REINES AND C. L. COWAN, JR.
Los Alamos Scientific Laboratory, University of California, Los Alamos, New Mexico

(Received July 9, 1953; revised manuscript received September 14, 1953)

AN experiment[1] has been performed to detect the free neutrino. It appears probable that this aim has been accomplished although further confirmatory work is in progress. The cross section for the reaction employed,

$$\nu_- + p \rightarrow n + \beta^+, \tag{1}$$

has been calculated[2,3] from beta-decay theory to be given by the expression,

$$\sigma = \left(\frac{G^2}{2\pi}\right)\left(\frac{h}{mc}\right)^2\left(\frac{p}{mc}\right)^2\left(\frac{1}{v/c}\right), \tag{2}$$

where σ = cross section in barns; p, m, v = momentum, mass, and velocity of emitted positron (cgs units); c = velocity of light (cm/sec); $2\pi\hbar$ = Planck's constant (cgs units); and G^2 = dimensionless lumped β-coupling constant (= 55 from measurements of neutron and tritium β decay).[4] An estimate of the fission fragment neutrino spectrum has been made by Alvarez on the basis of the work of Way and Wigner.[5] From this information, we calculated the expected cross section to be $\sim 6\times 10^{-20}$ barn Consideration of the momentum balance shows that the positron takes off most of the available energy.

The delayed-coincidence technique employed made use of the positron to produce the first pulse and the γ's from the neutron captured in the Cd loaded scintillator solution for the second pulse.[1] The predicted first pulse spectrum due to the positron has a threshold at 1.02 Mev (assuming both annihilation gammas are collected), rises to a maximum at a few Mev, and falls towards zero with increasing energy, vanishing in the vicinity of 8 Mev. Neutron capture times in the vicinity of 5μsec were employed.

The detector was set up in the vicinity of the face of a Hanford reactor and was surrounded on all sides by a shield comprised of 4 to 6 feet of paraffin alternated with 4 to 8 inches of Pb. In order to minimize the effects of tube noise and to eliminate the counting of individual tube after-pulses, the 90 photomultipliers were divided into two banks of 45. The signal from each bank was amplified by a corresponding linear amplifier and fed to two independent pulse-height selecting gates, one of which was set to accept pulses characteristic of the positron signal and the other to accept those characteristic of the neutron-capture gammas. The output pulses from the two "positron" gates were then fed to a coincidence circuit with a resolving time of 0.3 microsecond, and those from the two "neutron" gates to a similar circuit. When a pulse appeared at the output of the "positron" coincidence circuit, an 18-channel time-delay analyzer (with 0.5-microsecond channel widths) was triggered. If a second pulse then appeared at the output of the "neutron" coincidence circuit within nine microseconds after this, a count was registered in the appropriate channel, recording in this manner the number of "delayed coincidences" obtained and the delay time for each. The amplitude of the first or "positron" pulse was simultaneously recorded for each delayed pair by delaying all signals from one of the banks in a third linear amplifier and then impressing them on a ten-channel pulse-height analyzer which was gated whenever a delayed coincidence was obtained. The expected delayed-coincidence rate, allowing for detector efficiencies and for gate settings, was 0.1–0.3 counts/minute. The apparatus was checked using a double-pulser designed for the purpose and by observing cosmic-ray μ-meson decay within the detector. The system was energy-calibrated using a Co^{60} source in the center of the detector as well as by the N^{16} activity in water piped from within the pile to around the detector.

An appreciable delayed-coincidence background ($\sim$5 counts/min) was observed which was independent of pile power. The function, delayed-pair rate per unit time *vs* delay time, which was obtained for many background delayed-pair counts, rises from zero at the origin to a maximum at about 3.5 microseconds and then tails exponentially characteristic of the Cd concentrations used, following closely the predicted function obtained in a Monte Carlo calculation for neutron capture in the detector. As the energy of the second pulse of each pair was also characteristic of the gamma radiation from neutron capture in Cd, it may be assumed that the second event of each pair was due to the presence of a neutron in the detector.

A covering GM blanket which reduced the μ-meson counting rate by 75 percent when turned on in anticoincidence reduced this delayed pair rate insignificantly. A six-foot thick water shield installed above the detector and capable of absorbing at least 30 percent of the cosmic-ray nucleonic component also failed to change the delayed-pair rate significantly. Subsequent work in an underground location in which the cosmic-ray background is greatly diminished indicates that the Hanford background is probably due to cosmic rays, for example, neutrons arising from μ^- capture in shield materials, stars which include neutrons and gamma rays energetic enough to create electron-positron pairs, showers, etc.

The change in delayed-coincidence counting rate when the pile went from full power to zero power was detected only for a first pulse gate setting of from 2 to 5 Mev. The accidental background obscured the pile signal below 2 Mev. Table I lists details of the

TABLE I. Listing of data.

Run	Pile status	Length of run (seconds)	Net delayed pair rate counts/min	Accidental background rate counts/min
1	up	4000	2.56	0.84
2	up	2000	2.46	3.54
3	up	4000	2.58	3.11
4	down	3000	2.20	0.45
5	down	2000	2.02	0.15
6	down	1000	2.19	0.13

various runs. Least-squares fits of the observed counting rates in the delayed-time channels lead to the following results:

Pile up (three runs totaling 10 000 seconds): 2.55±0.15 delayed counts/min.

Pile down (three runs totaling 6000 seconds): 2.14±0.13 delayed counts/min.

Difference due to the pile: 0.41±0.20 delayed count/min.

This difference is to be compared with the predicted $\sim\frac{1}{3}$ count/min due to neutrinos, using an effective cross section of $\sim 6\times 10^{-20}$ barn for the process. It is to be remarked that a small channel overlap in the time-delay analyzer would be reflected in an amplified percentage decrease (<0.12 count/min) in the pile difference number. Measurements of the number of fast neutrons leaking from the pile face made with nuclear emulsion plates, and consideration of thed etector shielding employed, rules out neutron-proton recoils as causing this difference.

A more detailed report is in preparation. It is difficult to acknowledge properly the many contributions to all phases of this experiment. We wish to thank our colleagues: E. C. Anderson, L. J. Brown, D. Carter, F. B. Harrison, F. N. Hayes, C. W. Johnstone, Lt. P. R. Powell (USN), R. L. Schuch, Capt. W. A. Walker (USA), M. P. Warren, T. J. White, and J. G. Winston for their devotion to the task. Dr. R. Sard of Washington University was most helpful in discussions relative to cosmic rays. The staff of the Hanford Engineering Works has been wonderfully cooperative during the Hanford phase of the work.

[a] Work performed under the auspices of the U. S. Atomic Energy Commission.

[1] F. Reines and C. L. Cowan, Jr., Phys. Rev. **90**, 492 (1953); Cowan, Reines, Harrison, Anderson, and Hayes, Phys. Rev. **90**, 493 (1953). Important changes from the detector described in this reference include the use of Dumont K1177 photomultiplier tubes and a sodium silicate-titanium dioxide reflecting surface.

[2] E. Konopinski and H. Primakoff (private communications).

[3] We find it convenient to label the neutrino accompanying β^- emission as ν_-, and that accompanying β^+ emission as ν_+.

[4] E. J. Konopinski and L. M. Langer, *Annual Review of Nuclear Science* (Annual Reviews, Inc., Stanford, California, 1953), Vol. 2, p. 261.

[5] L. W. Alvarez, University of California Radiation Laboratory Report UCRL-328, 1949 (unpublished); K. Way and E. P. Wigner, Phys. Rev. **73**, 1318 (1948). Work in progress at this laboratory tends to indicate that these predictions are high.

Nuclear Scattering of High-Energy Neutrons

T. B. TAYLOR

Department of Physics, Cornell University, Ithaca, New York and Los Alamos Scientific Laboratory, Los Alamos, New Mexico

(Received September 11, 1953)

THE so-called "optical model" of the nucleus has been reexamined in the light of recent measurements[1-3] of the total neutron cross sections of various nuclei for neutron energies ranging from 30 Mev to 400 Mev. Using the nuclear model and method of calculation described by Fernbach, Serber, and Taylor,[4] an attempt was made to fit the measured cross sections by adjusting the values of R, the nuclear radii K, the inverse mean free path for absorption of neutrons in nuclear matter, and V, the average potential encountered by a neutron inside the nucleus. Both K and V were allowed to depend upon the neutron energy, but were assumed to be the same for all nuclei. Calculations were made only for neutron energies greater than 50 Mev because of the feeling that below this energy the approximations which were used in solving the scattering problem would not be valid.

The ratio $\sigma_{\text{total}}/\pi R^2$ may conveniently be expressed as a function of k_1R, with k_1/K as a parameter, where k_1 is the increase in the magnitude of the propagation vector of a neutron upon entering the nucleus. It was observed that $\sigma_{\text{total}}/\pi R^2$ is a maximum for k_1R equal to 2.0, for all values of k_1/K. Hence k_1R_{lead} was taken to be equal to 2.0 at 85 Mev, the neutron energy at which the maximum in the experimental lead cross section occurs. It was then possible, by using the measured cross sections of Pb, Cd, Cu, Al, and C at 85 Mev, to find a value of k_1 and a set of nuclear radii which would correspond to any chosen value of k_1/K. A search was then made for values of K and k_1 as a function of energy, for several assumed values of k_1/K at 85 Mev, which would give good agreement between all the experimental and

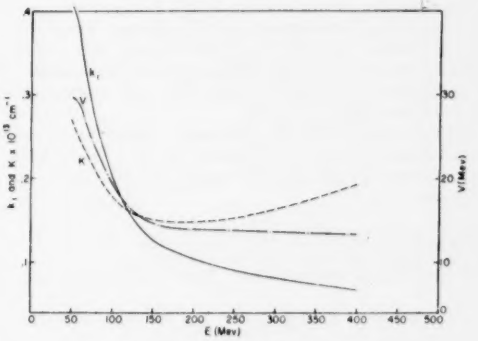

FIG. 1. Energy dependence of k_1, K, and V.

calculated cross section between 50 and 150 Mev, as well as at 400 Mev. By assuming a value of k_1/K of 1.25 at 85 Mev, it was possible to choose the energy dependence of K and k_1 in such a way that the calculated cross sections for all the nuclei considered agreed within quoted experimental errors with the observed cross sections in the neutron energy range of 65 to 400 Mev. The resulting curves of K and k_1 as a function of energy are shown in Fig. 1, together with the values of V corresponding to k_1. The nuclear radii which were obtained are given in Table I, and the calculated and observed cross sections are compared in Fig. 2.

TABLE I. Nuclear radii of C, Al, Cu, Cd, and Pb as determined from the best fit of their total neutron cross sections.

Nucleus	$R\times 10^{13}$ (cm)	$R\times 10^{13}/A^{\frac{1}{3}}$
C	3.52	1.54
Al	4.49	1.50
Cu	5.80	1.45
Cd	6.86	1.42
Pb	8.12	1.37

The value of K at 85 Mev may be changed by ±50 percent without causing serious disagreement between calculated and observed cross sections. Corresponding to this spread in K, however, there is possible a spread of only ±10 percent in k_1 and ±3 percent in the radius of any of the nuclei considered. There appears to be a definite minimum in K as a function of energy somewhere be-

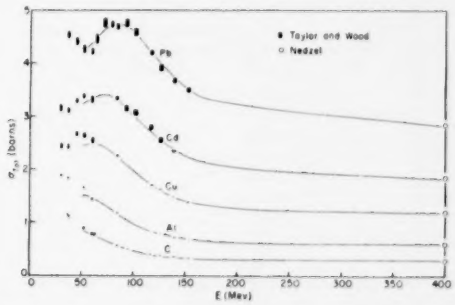

FIG. 2. Observed and calculated total neutron cross sections of Pb, Cd, Cu, Al, and C as functions of neutron energy.

tween 150 and 400 Mev, for all choices of K at 85 Mev. Since, according to this model, the neutron absorption cross section is independent of k_1, measured neutron absorption cross sections (cross sections for all inelastic processes) would provide a much better basis for determining K than an analysis of the total cross sections alone.

It is interesting that V decreases from the conventional 30 Mev at low energy to about 14 Mev above 180 Mev. The drop occurs moderately rapidly near the energy at which the repulsive core in p-p scattering becomes important. It is not necessary to let V go to zero or negative values.

A detailed account of this work will be published later. The author wishes to express his thanks to Professor H. A. Bethe for his continued interest in this work and for many helpful discussions.

[1] A. E. Taylor and E. Wood, Phil. Mag. **44**, 95 (1953).
[2] B. Ragent and W. I. Linlor, Phys. Rev. **91**, 440 (1953).
[3] V. Alexander Nedzel, Phys. Rev. **91**, 440 (1953).
[4] Fernbach, Serber, and Taylor, Phys. Rev. **75**, 1352 (1949).

π^+-p Scattering Near 260 Mev*

W. B. Fowler, R. M. Lea,† W. D. Shephard,‡ R. P. Shutt, A. M. Thorndike, and W. L. Whittemore
Brookhaven National Laboratory, Upton, New York
(Received September 9, 1953)

ELASTIC scattering of positive pions of 260-Mev average kinetic energy has been observed in a hydrogen-filled diffusion cloud chamber. The pions which were emitted from a carbon target at 32° to the 2.2-Bev proton beam in the Cosmotron were selected from particles of different momenta or negative sign by an analyzing magnet, and separated from protons of the same momentum by a 2.5-inch carbon absorber. They then entered the cloud chamber which has a sensitive length of 6 feet and width of 11 inches. A hydrogen pressure of 19 atmospheres was maintained. We are here reporting on data obtained from 1300 photographs. The pictures were scanned for scattering and $\pi-\mu$ decay events occurring in the gas, using a projected image which was distorted so that the 6 foot length was compressed to a length of 1.5 feet while the 11 inch width was retained. In this manner, a considerable amount of scanning time is saved and confusion due to background radiation occurring in random directions is reduced. Furthermore, since small angles are magnified 4 to 5 times in the distorted images, actual deflections somewhat smaller than 1° can easily be detected.

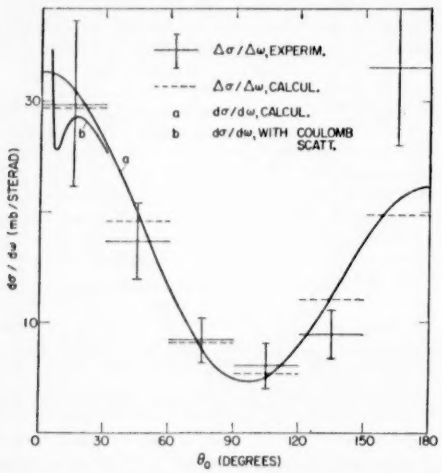

FIG. 1. Differential scattering distribution $\Delta\sigma/\Delta\omega$ for 260-Mev π^+-p scattering in center-of-mass system. Curve (a) was calculated making use of s- and p-wave phase shifts found by Fermi and Metropolis at 213 Mev. Curve (b) indicates the effect of Coulomb scattering.

292 $\pi-\mu$ decays were found, 281 of which showed deflections of less than 7.0°. From this cut-off angle one infers that over 90 percent of the pions had energies above 210 Mev. If all pions had 210-Mev energy, the angular distribution of $\pi-\mu$ deflections should be constant between 0 and 7.0°. The actual distribution begins to drop at 5°, indicating that some pions with energies as high as 330 Mev were present. From the shape of the $\pi-\mu$ distribution, one can infer that the average energy of the pions was 260 Mev. Adding a 15 percent correction to the number of $\pi-\mu$ decays observed for cases with deflections $<1°$, which were not counted, one finds by the previously described method[1] that 1280 ± 70 g/cm^2 of hydrogen were scanned. A direct measurement of the track length in a sample of pictures gave a path length consistent with that inferred from the $\pi-\mu$ count.

$116\pi^+-p$ elastic scattering events with scattering angles $>5°$ were found, resulting in a cross section of 150 ± 18 millibarns.[2] Their differential angular distribution in the center-of-mass system, shown in Fig. 1, appears to be nonisotropic and somewhat asymmetrical. Assuming charge independence, Fermi and Metropolis[3] have deduced s- and p-wave phase shift angles from π^-+p scattering up to 213 Mev. From their phase shifts of $\alpha_3=-63.6°$, $\alpha_{33}=42.9°$, and $\alpha_{31}=36.5°$, one would expect a cross section of 170 mb for π^+ at 213 Mev. It thus appears that the cross section remains high at our average energy, although a slight drop is indicated. Making use of the same phase shifts but normalizing to the cross section found here, curve (a) in Fig. 1 has been drawn and also averages have been indicated for the same intervals as used for the experimental data. Most experimental points agree with our statistical errors. The high experimental value above 150°, is substantiated by further experiments now in progress, may indicate a d-wave scattering component.

Curve (b) shows the result expected from interference with the Coulomb scattering[4] taking place mostly at angles $<30°$. Because of the large magnitude of the α_3, α_{33}, and α_{31} chosen here, the effect of Coulomb scattering is small at all angles of interest to us. Its effect on an admixture of d-wave scattering, however, could be great for angles $<30°$.

* Work performed under the auspices of the U. S. Atomic Energy Commission.
† Now at Yale University, New Haven, Connecticut.
‡ Now at Wesleyan University, Middletown, Connecticut.
[1] Fowler, Fowler, Shutt, Thorndike, and Whittemore, Phys. Rev. **91**, 135 (1953).
[2] Two additional scattering events were found which were probably inelastic.
[3] E. Fermi and N. Metropolis, Los Alamos Report LA-1492, 1952 (unpublished).
[4] L. Van Hove, Phys. Rev. **88**, 1358 (1952).

Time-Dependent Quadrupole Interaction in Angular Correlation of Nuclear Radiation. I. Cd^{111}*

P. B. Hemmig and R. M. Steffen
Department of Physics, Purdue University, Lafayette, Indiana
(Received September 10, 1953)

SEVERAL interactions of nuclear moments with extranuclear fields may be responsible for the attenuation of directional correlations of successive nuclear radiation:

(a) interaction of the magnetic moment μ of the intermediate nuclear state with a static magnetic field H;

(b) interaction of the electric quadrupole moment Q of the nucleus with a static electric field gradient $\partial^2V/\partial z^2$;

(c) interaction of μ with a randomly fluctuating field H (magnetic "relaxation" process);

(d) interaction of Q with a randomly fluctuating electric field gradient $\partial^2V/\partial z'^2$ (quadrupole "relaxation" mechanism).

The experimental verification of the static magnetic interaction (a) was made by the g determination of the 0.08μsec state of Cd^{111}.[1] The presence of the static quadrupole interaction (b) was indicated by the correlation measurements on single crystals of In,[2] and also by the results obtained with liquid sources.[3,4]

The influence of the randomly fluctuating interactions (c) and (d), such as must exist in liquids, on the angular correlation of nuclear radiations has been considered theoretically by Pound and Abragam,[5,6] but no direct experimental evidence for this interaction type has been given so far.

If the directional correlation is expressed in the form $W(\theta)=1+\sum_k G_k A_k P_k(\cos\theta)$, where $G_k=1$ corresponds to the undisturbed correlation, Abragam and Pound's model for the time-dependent quadrupole interaction in a liquid yields the following expression for the attenuation factors G_k:[6]

$$G_k=\frac{1}{1+\lambda_k\tau_N}\,\frac{1-e^{-\delta-\lambda_k\tau_N\delta}}{1-e^{-\delta}},$$

$$\lambda_k=\frac{3}{80}\left(\frac{eQ}{\hbar}\right)^2\left\langle\left(\frac{\partial^2 V}{\partial z'^2}\right)\right\rangle_{Av}\cdot\tau_c\frac{k(k+1)[4I(I+1)-k(k+1)-1]}{I^2(2I-1)^2}, \tag{1}$$

where $\delta=\tau_0/\tau_N$ is the ratio of the finite resolving time τ_0 of the coincidence analyzer to the lifetime τ_N of the intermediate nuclear state of angular momentum I. τ_c is closely related to the characteristic time which, in Debye's theory of dielectric dispersion in polar liquids, characterizes the time interval during which molecular orientation persists.[7] τ_c is connected with the macroscopic viscosity η of the liquid. A crude approximation for τ_c is[8]

$$\tau_c=4\pi\eta a^3/3kT, \tag{2}$$

where a is the molecular radius. Hence G_k depends on the viscosity η of the liquid source.

The influence of the viscosity on the directional correlation $W(\theta)=1+A_2G_2P_2(\cos\theta)$ of the Cd^{111} gamma rays was investigated by measuring A_2G_2 with sources of very dilute aqueous $InCl_3$ solution to which different amounts of glycerine were added (Fig. 1)

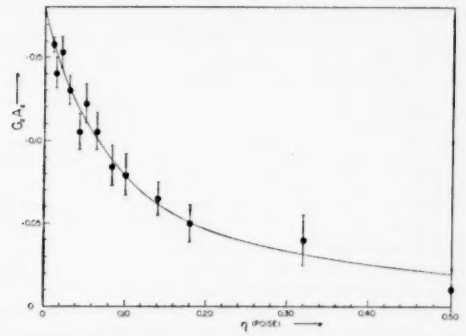

FIG. 1. Attenuation of the Cd^{111} gamma-gamma directional correlation in water-glycerine mixtures of different viscosity η. The solid line represents the theoretical curve for $A_2=-0.18$ and $\lambda_2=25\eta_{\text{poise}}$.

and also by changing the temperature of a 55 percent water-glycerine mixture. The resolving time of the coincidence analyzer was 0.125μsec ($\delta=1.0$).

That the observed attenuation is due mainly to the time-dependent quadrupole interaction and not to magnetic relaxation phenomena is indicated by the fact that the addition of paramagnetic ions (Fe^{+++}) to the liquid does not attenuate the correlation.[3]

Combining expressions (1) and (2), A_2G_2 can be expressed as a function of η, the coefficient A_2 for the unperturbed correlation and the quadrupole interaction term $eQ(\partial^2V/\partial z'^2)/h$ being left as parameters. A least-squares fit of the data yields -0.18 for A_2 and 500 Mc/sec for $eQ(\partial^2V/\partial z'^2)/h$, assuming 1.5×10^{-8} cm for a.

The value of A_2 agrees with the value $A_2=-0.17\pm0.01$ corresponding to the maximum anisotropy found with the single, crystal sources. As to the electric quadrupole interaction energy the value obtained here should not be considered more than a rough estimate, due to the crude approximation for τ_c and also due to the fact that $\partial^2V/\partial z'^2$ is probably not the same for the different water-glycerine mixtures. Nuclear magnetic resonance absorption experiments, however, show a remarkable constancy of the details of the molecular motion for different water-glycerine mixtures up to $\eta=1$ poise at least as far as the magnetic interaction is concerned.

Further experiments, to study the validity of the assumptions made above and to arrive at a better estimate of the quadrupole interaction, are in progress and will be reported later.

* Supported by the U. S. Atomic Energy Commission.

[1] H. Aeppli *et al.*, Helv. Phys. Acta **25**, 339 (1952).
[2] Albers-Schonberg, Hänni, Heer, Novel, and Scherrer, Phys. Rev. **90**, 322 (1953).
[3] R. M. Steffen, Phys. Rev. **90**, 1119 (1953).
[4] Albers-Schonberg, Heer, Novel, and Rüetschi, Phys. Rev. **91**, 199 (1953).
[5] R. V. Pound and A. Abragam, Phys. Rev. **90**, 993 (1953).
[6] A. Abragam and R. V. Pound, Phys. Rev. **91**, 936 (1953).
[7] P. Debye, *Polar Molecules* (Dover Publications, New York, 1945).
[8] Bloembergen, Purcell, and Pound, Phys. Rev. **73**, 679 (1948).

Isotopic Spin and New Unstable Particles

M. GELL-MANN
Department of Physics and Institute for Nuclear Studies, University of Chicago, Chicago, Illinois

(Received August 21, 1953)

PEASLEE[1] has considered the interesting possibility that the principle of charge independence, now believed to hold for nucleons and pions, may extend to the new unstable particles as well. In order to discuss this suggestion, let us suppose that both "ordinary particles" (nucleons and pions) and "new unstable particles" (V_1, V_4, τ, etc.) have interactions of three kinds:

(i) Interactions that rigorously conserve isotopic spin. (We assume these to be strong.)

(ii) Electromagnetic interactions. (Let us include mass-difference effects in this category.)

(iii) Other charge-dependent interactions, which we take to be very weak.

Peaslee inquires whether the quasi stability of the V_1^0 may be accounted for in this way if we assume it has isotopic spin 5/2. With respect to (i) the decay into pion and nucleon is absolutely forbidden. Interactions of type (iii) are supposed to be weak enough to account for the long observed lifetime of $\sim3\times10^{-10}$ second. However, he concludes that effects of type (ii) will cause transitions in a very much shorter time than this, since, for example, each electromagnetic interaction can change the isotopic spin of the system by one unit.

Recently Pais[2] has made the ingenious proposal that the new unstable particles differ from the ordinary ones in possessing one unit of "orbital isotopic angular momentum" and a negative "isotopic parity." If we then re-interpret (i) as referring to conservation of total isotopic angular momentum and isotopic parity, we see that as far as (i) is concerned, the decay of new unstable particles into ordinary ones is forbidden. Also, these particles will always be produced in even numbers, as Pais had suggested earlier.[3] Moreover, effects of type (ii) conserve isotopic parity, as Pais has introduced it, and so do not contribute to instability of the new particles.

In connection with the work of Peaslee and of Pais, the author would like to put forward an alternative hypothesis that he has considered for some time, and which, like that of Pais, overcomes the difficulty posed by electromagnetic interactions. Let us suppose that the new unstable particles are fermions with integral isotopic spin and bosons with half-integral isotopic spin. For example, the V_1 particles may form an isotopic triplet, consisting of V_1^+, V_1^0, and V_1^-. The τ^+ and V_4^0 may form an isotopic doublet, which we may call τ^+ and τ^0. To each of these particles there

would presumably correspond an antiparticle,[4] which we shall denote by means of square brackets.

In this scheme, (ii) is ineffective in causing decay because it can change isotopic spin only by integers, whereas in $V_1^0 \rightarrow \pi^- + p$, for example, the isotopic spin is 1 on the left and $\frac{1}{2}$ or $\frac{3}{2}$ on the right. Only interactions of type (iii), which do not respect isotopic spin at all, can lead to decay. Moreover, the new unstable particles again are produced only in even numbers.

There is no difficulty associated with stating a generalized Pauli principle for each kind of new unstable particle. For example, let us postulate that the wave function of a collection of V_1's must be totally antisymmetric in space, spin, and isotopic spin. If the wave function of two V_1's is antisymmetric in space and spin, as it would be for particles of identical charge, then the total isotopic spin must be 0 or 2, which includes $V_1^+V_1^+$, $V_1^-V_1^-$, and $V_1^0V_1^0$. If the total isotopic spin is 1, the wave function is to be symmetric in space and spin, which is all right since the charges are then not identical. Similarly, the postulate that the wave function of a collection of τ's must be totally symmetric in space, spin, and isotopic spin leads to no contradictions.

It should be noted that according to this scheme the conservation of the z component of isotopic spin is more stringent than conservation of charge.[5] To see this, let us remark that the τ^+ and τ^0 have z components equal to $+\frac{1}{2}$ and $-\frac{1}{2}$, respectively, like the proton and neutron. Correspondingly the antiparticles $[\tau^+]$ and $[\tau^0]$ have z components equal to $-\frac{1}{2}$ and $+\frac{1}{2}$, respectively, like the antiproton and antineutron. Thus we see that the reactions $\pi^- + p \rightarrow V_1^0 + \tau^0$ and $\pi^- + p \rightarrow V_1^- + \tau^+$ are allowed, while the reactions $\pi^- + p \rightarrow V_1^0 + [\tau^0]$ and $\pi^- + p \rightarrow V_1^+ + [\tau^+]$ are forbidden, although all four are allowed by conservation of charge. In order to produce anti-τ's it would be necessary to resort to a reaction like $\pi^- + p \rightarrow n + \tau^+ + [\tau^+]$ or $\pi^- + p \rightarrow n + \tau^0 + [\tau^0]$.

In a similar fashion, all reactions of the form nucleon+nucleon$\rightarrow$ $V_1 + V_1$ and all reactions of the form τ+nucleon$\rightarrow V_1 + \pi$ are forbidden, while reactions such as nucleon+nucleon$\rightarrow V_1 + \tau$+nucleon or $[\tau]$+nucleon$\rightarrow V_1 + \pi$ are allowed.

[1] D. C. Peaslee, Phys. Rev. **86**, 127 (1952).
[2] A. Pais (unpublished). The author is indebted to Professor Pais for the communication of his results prior to publication.
[3] A. Pais, Phys. Rev. **86**, 663 (1952).
[4] We postulate the principle of invariance under the operation of charge conjugation, which carries every particle into its antiparticle. In the case of charged particles, such as the electron and the π^+, it is obvious that the antiparticles are the positron and the π^-, respectively. A neutral particle, however, may or may not be identical with its antiparticle. Among neutral fermions, it is necessary that the neutron and the antineutron be distinct, while the question of whether the neutrino and antineutrino are distinct is one that must be settled by experiment. Among neutral bosons, the γ ray and π^0 are apparently identical with their respective antiparticles, but there is no reason to believe that this is a general rule. We suppose here that the τ^0 is a neutral boson which is not identical with its antiparticle. A model for such a situation is provided by picturing the τ particle as a complex of a nucleon and an anti-V_1, while the $[\tau]$ is pictured as the corresponding complex of antinucleon and V_1.
[5] Of course the conservation of charge is absolute, while the conservation of the z component of isotopic spin can be violated by interactions of type (iii). Such violations should, however, play no important role in production phenomena.

Differential p-p Elastic-Scattering Cross Section at 144, 271, and 429 Mev*

J. MARSHALL, L. MARSHALL, AND V. A. NEDZEL
Institute for Nuclear Studies, University of Chicago, Chicago, Illinois
(Received August 24, 1953)

THE differential p-p elastic-scattering cross section at 90 degrees barycentric angle has been determined at 144, 271, and 429 Mev and has been found to be constant with energy within experimental error. In addition, the differential elastic-scattering cross section for 429-Mev protons on liquid hydrogen has been measured as a function of angle by a scintillation counter technique which counts both incident and scattered protons, individually.

A beam of protons was scattered from a beryllium target in the 170-inch synchrocyclotron, was analyzed in the fringing field of the cyclotron magnet, and entered the experimental area through a collimator in the heavy shield. It was further monochromatized in an external magnet in the experimental area, and the proton energy was determined by range measurement. The energy of the collimated beam so obtained was varied by moving the beryllium target in the cyclotron azimuthally and at constant radius so that trajectories of the protons of desired energies would pass through the collimator. In a preliminary experiment similar to that of Oxley and co-workers,[1] these beams were subjected to a second scattering on a beryllium target and analyzed for left-right scattering asymmetry. No asymmetry was found; consequently these beams are considered unpolarized for practical purposes.

The apparatus to determine the differential cross section consisted first of a pair of scintillation counters (No. 1 and No. 2), the sensitive area of each of which consisted of a one-inch square diphenyl acetylene crystal. The incident beam of monochromatic protons passed successively through these two counters and was defined by them. The beam next encountered the scatterer, a container of liquid hydrogen. The container was a Styrofoam double-walled cylinder with axis vertical and perpendicular to the beam. The incident beam passed through the two-inch Styrofoam walls, then through four inches of liquid hydrogen, and emerged through two inches of Styrofoam.

The measurements were made according to two different schemes. From 90° to 54° barycentric angle both elastically scattered protons were detected simultaneously and in coincidence with the incident proton. Below 54° the less energetic proton begins to have too little energy to escape from the scatterer. Owing to the low intensity of the incident proton beam it was impractical to make measurements at smaller angles by decreasing the thickness of the scatterer.

Instead, a second scheme for detection of elastically scattered protons was used, relying on the fact that pion production is nearly always accompanied by a charged particle which is emitted close the the direction of the beam. When a pion is produced the associated nucleons have very little berycentric energy and, therefore, move almost with the center-of-mass velocity, consequently, almost in the direction of the beam. For example, in the reaction $p + p \rightarrow d + \pi^+$, the deuterons are emitted in a cone of a little less than 8° half-angle around the direction of the beam. According to the first method, two liquid scintillators were placed on opposite sides of the beam at angles variable and complementary in the barycentric system. One counter (No. 4) was $9\frac{1}{2}$ inches in diameter at a radius of 14 inches, and the other (No. 3) was $3\frac{1}{2}$ inches in diameter at 30 inch radius and defined the solid angle of the measurement.

The first two counters were connected in double coincidence (1, 2) to count the number of incident protons. All four counters (1, 2, 3, 4) were connected in quadrupole coincidence to count the scattered protons. At the beam intensity which was used to measure scattered protons, the counting losses in the double coincidence were measured to be 7 percent. This correction was avoided by the use of a monitor, a 5-inch diameter liquid scintillator placed below the beam to count protons from a lead scatterer in the beam several feet past the liquid hydrogen.

The monitor was connected in double coincidence (M, 2) with one of the first two counters. The counting rate in (M, 2) was $\frac{1}{16}$ of the counting rate in (1, 2), so that when the counting losses in (1, 2) were as great as 7 percent the counting losses in (M, 2) were negligible.

The ratio (M, 2)/(1, 2) was measured at low beam intensity, and the ratio (1, 2, 3, 4)/(M, 2) was measured at high beam intensity, with and without hydrogen. The cross section is proportional to the product of the ratios with hydrogen minus the product of the ratios without hydrogen.

The background (no hydrogen) count was 14 percent of the count with hydrogen at 429 Mev, 27 percent at 271 Mev, and 12 percent at 144 Mev. The electronics were adjusted for plateaus against delays of each counter and against counter voltages. These

plateaus were redetermined for each proton energy, to take into account new delays introduced to compensate for changes in time of travel for incident and scattered protons.

According to the second method, counter 3 was set at variable angle $(+\theta)$ at 30-inch radius from the scattering center to detect the elastically scattered protons, and counter 4 was placed to extend from $+5$ to -20 degrees to detect deuterons. Counters 1, 2, and 3 were connected in coincidence and counter 4 was connected in anticoincidence $(1, 2, 3, -4)$. Accordingly $(1, 2, 3, -4)$ measured all charged particles scattered at angle θ in coincidence with an incident proton, if no charged particle reached counter 4 simultaneously. So all events $p+p \rightarrow d+\pi^+$ were eliminated, even when the deuteron was subjected to Rutherford scattering in the target.

Furthermore, counter 4 extended over much more than the solid angle in which deuterons could emerge in order to eliminate most of the events in which a pion is accompanied by a free proton and neutron. This occurs in only about 1 out of 5 pion productions[2] at 350 Mev and is probably infrequent at 429 Mev also. A third possible process is $p+p \rightarrow \pi^0+p+p$, but this was improbable of detection because (*a*) it is about 8 times less probable than charged pion production,[3] (*b*) the decay gamma ray was detected with very low probability in counter 3, and (*c*) due to the virtual diproton state the two protons tended to emerge in the same solid angle as the deuterons, and so very probably trigger counter 4.

The ratio $(1, 2, 3, -4)/(M, 2)$ was measured at high beam intensity and the ratio $(M, 2)/(1, 2)$ was measured at low beam intensity, with and without hydrogen. The cross section is proportional to the product of the ratios with hydrogen minus the product of the ratios without hydrogen.

At 54° the cross section obtained by the first method was found to be equal within experimental error to that obtained by the second method. The results are summarized in Table I. There is

TABLE I. Differential elastic p-p scattering cross section at 429 Mev. Method *a* is detection of two scattered protons. Method *b* is detection of the more energetic scattered proton in anticoincidence with a second charged particle emitted at small angles.

Millibarns per steradian	Method	Barycentric angle
3.42 ±0.13	*a*	90°
3.51 ±0.23	*a*	80°
3.11 ±0.19	*a*	65°
2.84 ±0.12	*a*	54°
2.80 ±0.21	*b*	54°
3.18 ±0.21	*b*	43°
2.86 ±0.20	*b*	28°

no certain deviation from isotropy within the statistical errors of these results, but there is an indication of some decrease in cross section at smaller angles. A similar behavior is suggested by the corresponding data at 345 Mev,[4] although there also the trend is not much larger than the experimental errors.

The isotropic character of the present data at 429 Mev is in considerable disagreement with the shape of the elastic-scattering curve observed by Mott *et al.*, at 435 Mev.[5] On the other hand, the absolute value of the cross section in the neighborhood of 90° is in good agreement with their data.

It is interesting to compute the total p-p cross section at 429 Mev using the present data. Assuming isotropy and a differential scattering cross section of 3.3 mb/sterad one computes 20.7 mb for the total elastic scattering. To this must be added the π^0 production cross section, 0.45 mb,[3] and the π^+ production cross section. A measurement of the latter is being made by A. H. Rosenfeld of this laboratory, who privately reported a preliminary value of 3 mb. One finds 24.2 mb for the sum of these data. This is to be compared with, and agrees well with, the value 24±1 mb determined by transmission at the same energy.[6]

The cross sections reported in Table II for lower energies are much smaller than values reported by previous workers[7–10] al-

TABLE II. Differential elastic p-p scattering cross section at 90° barycentric angle.

Millibarns/steradian	Energy (Mev)
3.21 ±0.11	144 ±5
3.67 ±0.34	271 ±9
3.42 ±0.13	429 ±14

though in agreement with a new result, 3.5±0.4 mb/steradian for the energy interval 150 to 350 Mev, from the Berkeley group, written to us by Owen Chamberlain. Our work differs from previous counter experiments in that the incident protons are counted individually. Previous workers have used radioactive methods, Faraday cages, or ion chambers to determine the incident flux.

* Research supported by a joint program of the U. S. Office of Naval Research and the U. S. Atomic Energy Commission.

[1] Oxley, Cartwright, Rouvina, Baskir, Klein, Ring, and Skillman, Phys. Rev. **91**, 419 (1953).
[2] K. M. Watson and K. A. Brueckner, Phys. Rev. **83**, 1 (1951), see Fig. 6.
[3] Marshall, Marshall, Nedzel, and Warshaw, Phys. Rev. **88**, 632 (1952).
[4] Chamberlain, Segrè, and Wiegand, Phys. Rev. **83**, 923 (1951).
[5] Mott, Sutton, Fox, and Kane, Phys. Rev. **90**, 712 (1953).
[6] Marshall, Marshall, and Nedzel, Phys. Rev. **91**, 767 (1953).
[7] C. L. Oxley and R. D. Schamberger, Phys. Rev. **85**, 416 (1952).
[8] O. A. Towler, Phys. Rev. **84**, 1262 (1951).
[9] Birge, Kruse, and Ramsey, Phys. Rev. **83**, 274 (1951).
[10] Cassels, Pickavance, and Stafford, Proc. Roy. Soc. (London) **214**, 262 (1952).

The Attenuation Cross Sections of 37-Mev Pions in Hydrogen

C. E. ANGELL AND J. P. PERRY
University of Rochester, Rochester, New York
(Received September 17, 1953)

WE previously reported[1] 16.0±1.0 millibarns for the attenuation cross section of 37-Mev positive pions and 17.3±1.4 millibarns for negative pions in hydrogen. In arriving at these numbers we overlooked an important correction[2] due to the $\pi-\mu$ decays which occur between the second and third crystals of the telescope. Applying this correction and a further small correction due to a refinement in the calculation of our geometry, these numbers become $\sigma(\pi^+)=11.8\pm1.0$ millibarns and $\sigma(\pi^-)=12.9\pm1.7$ millibarns.[3] The π^+ value agrees with that obtained from our measured angular distribution.[4] The measurement of the π^- angular distribution at this energy is not yet completed.

[1] C. E. Angell and J. P. Perry, Phys. Rev. **90**, 724 (1953).
[2] S. L. Leonard and D. H. Stork, Bull. Am. Phys. Soc. **28**, No. 4, 19 (1953).
[3] These values represent the cross sections for scattering into the angular region ~50° to 80° in the laboratory system. [For the π^- mesons the charge-exchange scattering for the entire angular range (0° to 180°) is included.]
[4] C. E. Perry and J. P. Angell, Phys. Rev. **91**, 1289 (1953).

Neutron Total Cross Section for Bismuth and Uranium between 45 and 160 Mev*

W. I. LINLOR AND B. RAGENT
Radiation Laboratory, Department of Physics, University of California, Berkeley, California
(Received September 8, 1953)

NEUTRON total cross sections for bismuth and uranium have been measured in a good geometry transmission experiment, using a time-of-flight instrumentation.[1,2] The source of neutrons was the stripped deuteron beam of the 184-inch synchrocyclotron. The results are shown in Fig. 1. Uncertainties are shown in terms of standard deviations, due to counting statistics only, and to energy channel width.

The distribution of values indicates a "dip" in cross section in the vicinity of 60 Mev for the two elements, similar to results first obtained by Taylor and Wood for lead.[3–4]

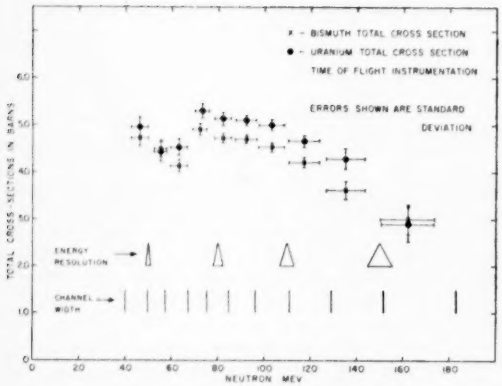
X - BISMUTH TOTAL CROSS SECTION
● - URANIUM TOTAL CROSS SECTION
TIME OF FLIGHT INSTRUMENTATION
ERRORS SHOWN ARE STANDARD DEVIATION
TOTAL CROSS SECTIONS IN BARNS
ENERGY RESOLUTION
CHANNEL WIDTH
NEUTRON MEV

FIG. 1. The variation with energy of the neutron total cross section for bismuth and uranium, measured by time-of-flight instrumentation. The errors shown are standard deviations based on total counts and on energy channel width.

Absolute values of the cross section may be in error by a constant estimated to be ± 0.2 barn because of beam intensity variations. Inasmuch as such a constant would be added to all the points for an element, it would not affect the variation of cross section with energy.

The energy scale was calibrated by time-of-flight of gamma rays. The time-of-flight of a neutron or photon could be measured with a probable error of $\pm 0.2\times 10^{-8}$ second, including the effect of neutron production time (this leads to a resolution of 5×10^{-11} second per meter at the flight distance of 43.7 meters). At 90 Mev the absolute value of the quoted energy seems to be in error by not more than ± 2 Mev.

We wish to thank Professor H. F. York for suggesting this technique and Professor L. W. Alverez, under whose guidance this work was carried out, for valuable suggestions; also James Vale, Lloyd Hauser, and the cyclotron crew for much cooperation. Thanks are due also Robert Silver and John Leahy whose help at times of runs was particularly welcome, and Vern Ogren and Don Paxson, both of whom rendered expert electronics assistance in many ways.

* This work was sponsored by the U. S. Atomic Energy Commission.
[1] University of California Radiation Laboratory Report UCRL-1952 (unpublished).
[2] W. I. Linlor and B. Ragent, Phys. Rev. **91**, 440 (1953).
[3] A. E. Taylor and E. Wood, Phys. Rev. **87**, 907 (1952).
[4] A. E. Taylor and E. Wood, Phil. Mag. **44**, 95 (1953).

The Giant Nuclear Dipole Resonance*

M. FERENTZ
Argonne National Laboratory, Lemont, Illinois
AND
M. GELL-MANN† AND D. PINES
Department of Physics, University of Illinois, Urbana, Illinois
(Received August 21, 1953)

WE have applied the collective description of nucleon interactions[1] to the investigation of the giant dipole resonance in heavy nuclei.[2] Our method follows closely that developed by Bohm and Pines[3] for the treatment of electron-electron interactions in metals. We start with a system of individual nucleons, interacting via short-range two-body forces, and investigate to what extent these forces lead to collective behavior. We find that the part of the nucleon-nucleon potential V_{ij} which is proportional to $\tau_x^i\tau_x^j$ can lead to an oscillation of the nucleus as a whole, similar to the dipole oscillation suggested by Goldhaber and Teller,[4] and investigated by Steinwedel and Jensen.[4] The excited level corresponding to this oscillation lies at an energy

$$\hbar\omega = W_0 A^{-\frac{1}{3}} \tag{1}$$

above the ground state, where a rough calculation indicates $W_0 \approx 80$ Mev, a result which is in agreement with the experimentally observed position of the giant resonance. We find the γ-ray width of this level to be proportional to $A^{\frac{4}{3}}$, and use the width to obtain the cross sections for absorption and scattering of γ rays in this region. Throughout we have neglected certain effects of the $(\tau_x^i\tau_x^j+\tau_y^i\tau_y^j)$ terms in the potential, which are known to give rise to an increase in the frequency of the oscillation, as can be seen from the sum rule calculations of Bethe and Levinger.[5] Preliminary results indicate that such corrections are not large. Surface effects are also neglected, an approximation which restricts the application of our method to heavy nuclei.

Our approach consists in concentrating our attention on the following portion of the nuclear Hamiltonian,

$$H_0 - \sum_i \frac{p_i^2}{2M} + \sum_{\mathbf{k}} \sum_{i\neq j} \frac{V_k}{2} \tau_x^i \tau_x^j e^{i\mathbf{k}\cdot(\mathbf{x}_i-\mathbf{x}_j)}, \tag{2}$$

where the V_k are the Fourier components in a box of nuclear dimensions of a nucleon-nucleon potential of range μ^{-1}. The potential V is formally repulsive since $\tau_x^i\tau_x^j$ appears in the complete Hamiltonian as part of an exchange operator, which we take to be that of Majorana. We perform a canonical transformation directly analogous to that applied by Bohm and Pines[3] in the electron case. We are then able to isolate a part of the Hamiltonian corresponding to harmonic oscillations of the quantities

$$\rho_{\mathbf{k}} = \Sigma_i \tau_x^i e^{-i\mathbf{k}\cdot\mathbf{x}_i} \quad (\mathbf{k}\neq 0), \tag{3}$$

which are the fluctuations in the difference between neutron and proton densities.

The lowest mode of oscillation $[k\approx\pi/R=(\pi/R_0)A^{-\frac{1}{3}}]$ is weakly coupled to the motions of individual nucleons, to the ordinary density fluctuations of the nucleus, and to the terms in the nuclear Hamiltonian that are omitted in (2). The higher modes are strongly coupled, appreciably damped, and thus unimportant. The frequency of the lowest mode is

$$\omega = \left(\frac{Ak^2V_k}{M}\right)^{\frac{1}{2}} = \left[\frac{3\pi^2 D_0}{MR_0^5\mu(\mu^2+k^2)}\right]^{\frac{1}{2}} A^{-\frac{1}{3}} = \frac{W_0}{\hbar}A^{-\frac{1}{3}}, \tag{4}$$

if V is chosen to be a Yukawa potential of depth D_0. The value of W_0 quoted above is obtained by fitting D_0 and μ to low-energy two-particle data.

We identify the giant dipole resonance with the first excited state of our lowest oscillator mode, and calculate the γ-ray width of this level by expressing the dipole moment operator in terms of the $\rho_{\mathbf{k}}$, (3). The matrix elements of the $\rho_{\mathbf{k}}$ are the well-known oscillator matrix elements. The result for the γ-ray width at resonance is

$$\Gamma_\gamma = \frac{1}{6}\frac{e^2}{\hbar c}\frac{\hbar^2\omega^2}{Mc^2}A = \frac{1}{6}\frac{e^2}{\hbar c}\frac{W_0^2}{Mc^2}A^{\frac{1}{3}} \tag{5}$$

for equal numbers of neutrons and protons. Γ_γ depends on V_k only through ω and is very much smaller than the total level width Γ. Inserting (5) in the Breit-Wigner formulae, one may obtain the γ-ray scattering and absorption cross sections in the neighborhood of resonance. Thus,

$$\sigma_{\text{scatt}}(\text{res.}) = \frac{\pi}{6}\left(\frac{e^2}{\hbar c}\right)^2\left(\frac{W_0}{\Gamma}\right)^2\left(\frac{\hbar}{Mc}\right)^2 A^{4/3}, \tag{6}$$

which, for example, ≈ 3 millibarns for Ta^{181}.

It is of interest to compare our results for the absorption cross section with the sum rules of Bethe and Levinger, (not including their exchange-force corrections). For the integrated absorption cross section, $\int\sigma dE$, we obtain $\frac{1}{2}\pi^2(e^2\hbar/Mc)A$, which is just their result, showing that our single dipole level "exhausts" the sum rule, just like the level of Goldhaber and Teller. On the other hand, we find for both the mean and harmonic mean energies for photon

absorption simply $\hbar\omega$, since there is but a single level. These results are in disagreement with those of Bethe and Levinger only because they neglect correlations in the gound state wave function of the nucleus. Such correlations are of great importance in our model, and seem to be necessary in order to explain the experimentally observed variation of the resonance energy with atomic number.

Details will be published in a forthcoming paper.

* Research supported in part by the Office of Naval Research, Office of Ordnance Research, U. S. Army, and the U. S. Atomic Energy Commission.
† Now at Institute for Nuclear Studies and Department of Physics, University of Chicago, Chicago, Illinois.
[1] M. Ferentz and D. Pines, Phys. Rev. **87**, 188 (1952) and M. Ferentz, Ph.D. Thesis, University of Pennsylvania, 1953 (unpublished).
[2] See, for instance, the review article by K. Strauch, Ann. Rev. Nuc. Sci. **2**, 105 (1953).
[3] D. Pines and D. Bohm, Phys. Rev. **85**, 338 (1952); D. Bohm and D. Pines, Phys. Rev. (to be published).
[4] M. Goldhaber and E. Teller, Phys. Rev. **74**, 1046 (1948); H. Steinwedel and J. H. D. Jensen, Z. Naturforsch. **5a**, 413 (1950).
[5] J. Levinger and H. Bethe, Phys. Rev. **78**, 115 (1950).

Nuclear Radii*

FRANCIS BITTER AND HERMAN FESHBACH
Department of Physics, Research Laboratory of Electronics and Laboratory of Nuclear Science, Massachusetts Institute of Technology, Cambridge, Massachusetts
(Received June 26, 1953; revised manuscript received September 8, 1953)

WE would like to point out that nuclear radii as predicted from isotope shift and high-energy electron scattering are in excellent agreement. Recent experiments on μ-mesonic x-rays corroborate these results.[1,2] These radii are considerably smaller than those usually quoted. However, they are in excellent agreement with those obtained from the most recent semi-empirical mass formula and may be reconciled with radii as obtained from the Coulomb energy difference in light nuclei.

Electron scattering experiments have been performed by Lyman, Hanson, and Scott[3] with electrons at 15.7 Mev, by Hammer, Raka, and Pidd[4] at 33 and 43 Mev, and by Hofstadter *et al.*[5] at 116 Mev, for a variety of elements. We shall analyze the first set of experiments. The second set gives similar results as far as nuclear radii are concerned. The third set does not show Ramsauer minima, again indicating a small radius. For the lower-energy experiments, according to theory[6] only one phase shift, η_0' is required. We have, therefore, evaluated the phase shift required to match the experimental data at each scattering. The resulting values should be constant. There are, however, a number of difficulties. For very light elements, and for small angles for all elements, the effect of nuclear size is small and would require experiments of great accuracy. For this reason the aluminum data are not useful for the present purpose. For large angles and for heavy elements the scattering is very small, again making the experiments difficult. Moreover, the theoretical uncertainties are greatest at large angles. The most consistent results are obtained for copper and silver, less consistent results for gold. (See Table I.)

TABLE I. Values of the phase shift η_0'.

ϑ	Copper	Silver	Gold
90°	0.0054	0.0213	0.141
120°	0.0052	0.0228	0.112
150°	0.005	0.0213	0.120

Employing the theoretical results,[6,7] we find that for a homogeneous charge distribution the copper and silver radii are $1.0\times10^{-13}A^{\frac{1}{3}}$ cm and $1.1\times10^{-13}A^{\frac{1}{3}}$ cm, respectively. The nuclear radius for gold is not well determined; but if an average phase shift of $\eta_0'=0.120$ is taken, the nuclear radius is $1.2\times10^{-13}A^{\frac{1}{3}}$ cm. These results are in agreement with those of Raka *et al.*, who obtain a radius of $(1.1\pm0.075)\times10^{-13}A^{\frac{1}{3}}$ cm for Sn and $(1.03)\times10^{-13}A^{\frac{1}{3}}$ cm for W.

The isotope-shift data in Fig. 1 has been summarized by Brix and Kopfermann.[8] We have replotted the data taking the nuclear radius as $1.1\times10^{-13}A^{\frac{1}{3}}$ cm. The agreement with the data is very much better than that obtained with $1.5\times10^{-13}A^{\frac{1}{3}}$ cm. It clearly would be of interest to do electron scattering experiments with the rare earths Ce, Sm, Eu, as well as with Rb, Xe, Ba, which show large deviations from the average line. It should be noted that the tacit assumption is made here that the isotope shift is a pure volume effect.

It is of interest to show that these radii may not be reconciled with the larger Coulomb energy radii of $1.47\times10^{-13}A^{\frac{1}{3}}$ cm commonly quoted,[3] for we shall show that no positive definite charge distribution exists which will give a smaller nuclear radius for scattering and a larger one for the nuclear Coulomb energy. The effective nuclear Coulomb radius R_N is defined by

$$\frac{1}{R_N}=\frac{5}{6Z^2e^2}\int\int\frac{\rho(\mathbf{r})\rho(\mathbf{r}_0)}{|\mathbf{r}-\mathbf{r}_0|}\frac{d\mathbf{r}}{4\pi}\frac{d\mathbf{r}_0}{4\pi}. \tag{1}$$

The scattering and isotope shift depend primarily upon the volume integral of the perturbing potential,[9]

$$\int\frac{\rho(\mathbf{r}_0)}{|\mathbf{r}-\mathbf{r}_0|}d\mathbf{r}_0-\frac{Ze}{r}.$$

It may be shown that this difference is proportional to

$$\int\rho(\mathbf{r})r^2d\mathbf{r}.$$

Hence, the scattering radius R_s is defined by

$$R_s^2=\frac{5}{3Ze}\int\rho(\mathbf{r})r^2(d\mathbf{r}/4\pi). \tag{2}$$

We now ask for what charge distribution the ratio R_s/R_N is stationary:

$$\frac{\delta(R_s/R_N)}{\delta\rho}=0,\quad \delta\int\rho d\mathbf{r}=0;$$

or

$$\frac{1}{R_s}\frac{\delta R_s}{\delta\rho}=\frac{1}{R_N}\frac{\delta R_N}{\delta\rho};\quad \delta\int\rho d\mathbf{r}=0. \tag{3}$$

From Eq. (2) we find

$$\frac{\delta R_s}{\delta\rho}=\frac{5}{6Ze}\frac{r^2}{R_s}, \tag{4}$$

while from Eq. (1) it follows that

$$\frac{\delta R_N}{\delta\rho}=-\frac{5}{3}\frac{R_N^3}{Z^2e^2}V, \tag{5}$$

where

$$V(\mathbf{r})=\int\frac{\rho(\mathbf{r}_0)}{|\mathbf{r}-\mathbf{r}_0|}d\mathbf{r}_0.$$

Inserting (4) and (5) into (3), we find that $V(\mathbf{r})\sim A-Br^3$, where A and B are constants. For positive definite charge density the constants correspond to a homogeneous charge distribution. We determine that the homogeneous charge distribution corresponds to a minimum for the ratio (R_s/R_N) by evaluating the ratio for an actual example. It is, of course, possible to obtain $R_s<R_N$ by relaxing the positive definite charge density condition and thus permitting regions of negative charge within the nucleus, as might be possible in a meson theory of the nucleus.

We turn now to other evidence for nuclear radii. Here it is interesting to note that the most recent determination of the semi-empirical mass formula by Green and Engler[9] give the Coulomb energy term as $0.750(Z^2/A^{\frac{1}{3}})$mMU. This corresponds to the relation $R_N=(1.23\times10^{-13})A^{\frac{1}{3}}$ cm, in agreement with our determination. The second source of evidence is obtained from mirror nuclei. These are light and, as Wigner has pointed out, correlation effects are important. In particular, the exchange Coulomb energy has the effect of reducing the Coulomb energy and therefore increasing the effective radius. Both Elton[10] and Cooper and Henley[1] have pointed out that the nucleon involved in the β transition

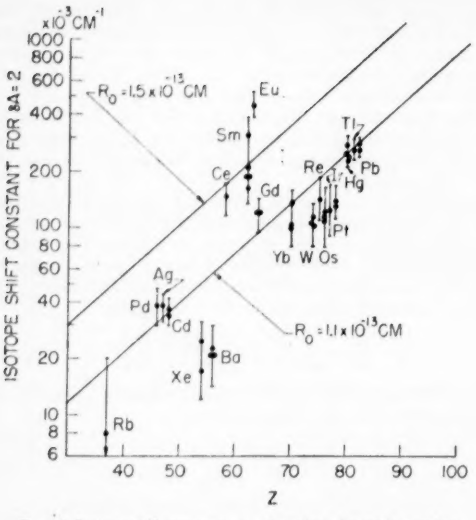

FIG. 1. Isotope shift constant as a function of atomic number.

between mirror nuclei is near the nuclear surface and will have a smaller than average Coulomb interaction. Cooper and Henley have tested these suggestions by a model and have shown it to be plausible that both of these effects are sufficient to reconcile the values of R_s and R_N. Finally, we have the evidence from nuclear reactions. It is perhaps not too surprising that these radii are large because the strong absorption properties of nuclear matter would tend to weight the surface regions more heavily. Actually, this may be seen by defining a radius in terms of an effective range theory.[11] Of course it no longer is possible to take the nucleus as having a uniform distribution, but rather a tail of some extension must be assumed.

* This work was assisted in part by the U. S. Army Signal Corps, the Air Materiel Command, and the U. S. Office of Naval Research; and in part by the joint program of the U. S. Office of Naval Research and the U. S. Atomic Energy Commission.

[1] L. N. Cooper and E. M. Henley, Phys. Rev. **91**, 480 (1953).
[2] V. L. Fitch and J. Rainwater (private communication).
[3] Lyman, Hanson, and Scott, Phys. Rev. **84**, 626 (1951).
[4] Hammer, Raka, and Pidd, Phys. Rev. **90**, 341 (1953).
[5] Hofstadter, Fechter, and McIntyre, Phys. Rev. **91**, 439 (1953).
[6] H. Feshbach, Phys. Rev. **84**, 1206 (1951).
[7] L. K. Acheson, Phys. Rev. **82**, 488 (1951).
[8] P. Brix and H. Kopfermann, Festschr. Akad. Wiss., Göttingen 17–49 (1951).
[9] A. E. S. Green and N. A. Engler, Phys. Rev. **91**, 40 (1953).
[10] L. R. B. Elton (private communication).
[11] J. Schwinger (private communication).

Charged Particles of Mass Intermediate between Proton and Deuteron

D. T. KING, NATHAN SEEMAN, AND MAURICE M. SHAPIRO
Nucleonics Division, Naval Research Laboratory, Washington, D. C.
(Received September 2, 1953)

OBSERVATIONS of singly charged unstable particles with mass intermediate between those of proton and deuteron have been described by Leighton[1] and by Levi-Setti.[2] Two examples of such heavy particles have been found in this laboratory. One was observed as a moderately fast product of a fundamental nucleon-nucleon collision.[3] The other came to rest, and apparently decayed with the emission of light meson, probably a pion. The mass estimates are in fair agreement, although different methods of mass determinations were appropriate for the two cases: measurements of ionization and multiple scattering for the fast particle, scattering and residual range for the slow one. Both events occurred in Ilford G.5 emulsions exposed in combination with C and Pb absorbers at an atmospheric depth of ~11 g/cm² and geomagnetic latitude 56°N. Table I summarizes the track data.

The track of our first example originates in a "fundamental" collision; i.e., there are no tracks attributable to evaporation particles or to a recoil nucleus. The star comprises a total of 5 tracks, all of grain density less than 2.5 times the "plateau" value, and one of these tracks is very probably due to a charged primary particle. The nature of the generating interaction suggests that the incident particle had at least several Bev of energy. With respect to the forward direction of the assumed primary, the particle of interest was emitted at an angle of ~120° in the laboratory system, and it left the emulsion at a distance of 18.6 mm from its origin. This considerable length of track, and the fact that its grain density lies well above the insensitive region of the ionization minimum, permit the mass determination, $2560\pm500m_e$. For velocity calibration, 34 tracks of protons and pions in the same emulsions, having comparable lengths and grain densities, were measured.

The primary track of our second example exhibits the increase in scattering and ionization characteristic of a charged particle coming to rest. The "constant saggita" method of multiple scattering measurement, which utilizes the range-energy relation for known particles, was applied to this track and to those of 18 calibration tracks of stopped protons. It can be shown that when the scattering cell size s is varied with residual range R according to the relation $s\sim R^{0.385}$, then the mean saggitas (second differences $\bar{D}$ and $\bar{D}_p$, respectively) for a singly charged particle of mass m and for the proton mass m_p are related by $m/m_p=(\bar{D}_p/\bar{D})^{2.37}$. Thus, using the $\bar{D}$ values in Table I, the mass $(2860\pm850)m_e$ is obtained. The sensitivity of mass to $\bar{D}$ leads to considerable error; nevertheless this method seems the best available for particles arrested in emulsion. Application of the alternative constant-cell method of scattering yields a mass value $2940m_e$ which agrees with the one above within experimental error. In arriving at the $\bar{D}$ values, cutoff was applied for large single scatters and correction was made for spurious scattering noise. Omitting the data for the last 800 microns and the last 200 microns of range, respectively, led to values $m=1.42m_p$ and $m=1.70m_p$. We have provisionally adopted the mean value $(1.56\pm0.45)m_p$.

As seen from Table I, the secondary of the slow heavy particle is very probably a pion. It is possible definitely to rule out a proton secondary. A similar example, involving a $\pi^\pm$ secondary, has been reported by Peters.[4]

Using the velocity of our meson secondary, we have computed the Q value and primary mass for each of two assumed decay schemes,[5]

$$V^\pm \rightarrow \text{neutron}+\pi^\pm+Q, \quad (1)$$

$$V^\pm \rightarrow V_1{}^0+\pi^\pm+Q'. \quad (2)$$

TABLE I. Summary of track data.

Fast particle	
Track length	18.6 mm
Multiple scattering (600μ cells)	$(0.068°\pm0.012°)/(100\mu)^{\frac{1}{2}}$
Grain density/plateau density	2.25 ± 0.07
$p\beta$	390 ± 70 Mev/c
Mass (in m_e)	2560 ± 500
Stopped particle	
(a) Primary	
Track length	3.7 mm
Scattering: mean saggita	0.34μ
Mean saggita, protons	0.41μ
Mass (in m_e)	2860 ± 850
(b) Secondary	
Track length	2.2 mm
Multiple scattering	$(0.17°\pm0.04°)/(100\mu)^{\frac{1}{2}}$
Grain density/plateau density	1.15 ± 0.07
$p\beta$	150 ± 35 Mev/c
Mass (in m_e)	330 ± 90

We find that for (1), $Q=(103_{-15}^{+20})$ Mev and the calculated mass is $2315m_e$; for (2), $Q'=(101_{-15}^{+20})$ Mev and the mass is $2650m_e$.

Support for scheme (2) is provided by recent cloud-chamber observations of cascade V-particle events in which a charged primary disintegrates into a V_1^0 and a light meson,[6,7]

$$V^-\rightarrow V_1^0+(\pi^- \text{ or } \mu^-)+Q. \quad (3)$$

Evidence thus exists for the emission of a V_1^0 as a neutral decay product of a charged heavy particle, whereas there is no corresponding evidence, so far as we know, for a secondary neutron. It seems reasonable, therefore, as a working hypothesis, to identify our scheme (2) with (3) of the Pasadena group.[7] The respective Q values, 101_{-15}^{+20} Mev (NRL) and 60 ± 15 (Pasadena) are not inconsistent.

As for the *charged* secondary, the cloud-chamber observations do not permit a choice between π and μ. However, under the foregoing hypothesis, we conclude that the charged secondary in the V-particle cascades is more likely to be a pion than a muon.

We are grateful to Mr. B. Stiller and Mr. F. W. O'Dell for their assistance, and to Mrs. N. T. Redfearn for much of the scanning.

[1] R. B. Leighton, Rochester Conference on High Energy Physics, December, 1952 (Interscience Publishers, New York, 1953); York, Leighton, and Bjornerud, Phys. Rev. **90**, 167 (1953).
[2] R. Levi-Setti, Royal Society Conference on Fundamental Particles, London, January, 1953 (unpublished); Bonetti, Levi-Setti, Panetti, and Tomasini, Nuovo cimento **10**, 345 (1953); and International Congress on Cosmic Radiation, Bagnères de Bigorre, July, 1953 (unpublished).
[3] King, Seeman, and Shapiro, International Congress on Cosmic Radiation, Bagnères de Bigarre, July, 1953 (unpublished).
[4] Peters, Lal, and Pal, International Congress on Cosmic Radiation, Bagnères de Bigarre, July, 1953 (unpublished).
[5] We have used the symbol V to denote the heavy particle.
[6] Armenteros, Barker, Butler, Cachon, and York, Phil. Mag. **43**, 597 (1952).
[7] Anderson, Cowan, Leighton, and van Lint, Bull. Am. Phys. Soc. **28**, No. 5, 17 (1953).

Intermediate Coupling and Nuclear Reactions

A. M. Lane
Department of Mathematical Physics, Birmingham University, Birmingham, England
(Received September 14, 1953)

PREVIOUS discussion of the shell model has centered around such "static" experimental quantities as magnetic moments, spins, etc. It is the purpose of this letter to point out that this discussion can be extended to include the "dynamical" quantities of the type found in nuclear reactions. These quantities include the reduced widths of energy levels for nucleon emission and the matrix elements of electromagnetic transitions. There is a considerable accumulation of such data[1] in light nuclei, most of which has never been seriously used to investigate nuclear structure.

If an extreme mode of coupling is assumed in nuclei (i.e., $L-S$ or $j-j$), then theoretical expressions for these dynamical quantities can be found very simply using the theory of fractional parentage.[2] For instance, consider the reduced width in $L-S$ coupling for a nucleon transition of the type:

compound nucleus $\lambda\rightarrow$residual nucleus p +nucleon;

i.e.,

$$l^n(\alpha TSL,J)\rightarrow l^{n-1}(\alpha_p T_p S_p L_p,J_p)+l; \quad (1)$$

i.e., the emission of one nucleon from a state λ of n equivalent nucleons to leave a residual nucleus of $(n-1)$ equivalent nucleons. The symbols α, T, S, L, J have their usual meaning. The reduced width[3] for this process can be shown to be

$$\gamma_{\lambda sl}^2=\gamma^2(l)n\langle\alpha\|\alpha_p\rangle^2U^2(L_pS_p\tfrac{1}{2},J_pS)U^2(SL_pJl,sL), \quad (2)$$

where the U functions are Recah functions[2] and where $\langle\alpha\|\alpha_p\rangle$ is an abbreviated notation for the total fractional parentage coefficient[2] appropriate to the two states of (1). α and α_p, as usual, denote symmetry characters. The symbol s denotes the values of the coupled spins of the nucleon and residual nucleus,[3] and $\gamma^2(l)$ is the reduced width for a single l nucleon in the potential well of the shell model (the value will be $\sim\hbar^2/Ma$, where M is the reduced mass of the nucleon and a is the radius of the well). In $j-j$ coupling, the reduced width for the transition

$$j^n(\alpha TJ)\rightarrow j^{n-1}(\alpha_p T_p J_p)+j \quad (3)$$

emerges as

$$\gamma_{\lambda sl}^2=\gamma^2(l)n\langle\alpha\|\alpha_p\rangle^2U^2(J_p\tfrac{1}{2}Jl,sj). \quad (4)$$

Formulas can be derived similarly for the values of the matrix elements of electromagnetic transitions in $L-S$ and $j-j$ coupling.

The formulas both for reduced widths and electromagnetic matrix elements have been extensively compared with experimental values in light nuclei. It is found that neither extreme coupling mode can fit the data, but there is strong suggestion that intermediate coupling can do so.

In order to test this conclusion, the mirror nuclei C^{13} and N^{13} have been examined in detail. The properties of these nuclei are well known[1] and altogether there are eleven useful independent data on the first four levels of these nuclei:

(1) the binding energies of the first-excited states in the two nuclei,

(2) the slow-neutron scattering length for C^{12} and the "effective range" of slow-neutron scattering,[4]

(3) the reduced widths of the first- and third-excited states in N^{13} (these are essentially "single-particle" levels, the first $(\frac{1}{2}+)$ being simply a $2s$ nucleon added to the C^{12} "core," and the third $(5/2+)$ being a $1d$ nucleon added similarly),

(4) the $E1$ and $M1$ transition widths from the first- and second-excited states of N^{13} to the ground state,

(5) the reduced widths of the ground- and second-excited states [the latter is observed in N^{13} from proton scattering in C^{12}, and the former is obtained for C^{13} from the yield of the (d,p) stripping reaction on C^{12}],

(6) the magnetic moment of C^{13}.

Of these data, the predicted values of (1), (2), and (3) are not sensitive to the mode of coupling in the shell model, but only to the potential well of the model. These six independent data can all be fitted with a certain choice of square well (depth 35 Mev, radius 4.05×10^{-13} cm). The predictions for the other data (4), (5), and (6) are all sensitive to the mode of coupling in the shell model, some of them being extremely so. Analysis shows that all the five data of (4), (5), and (6) are fitted extremely well by an intermediate coupling model with a value of the usual parameter a/K of about 4.5 (a being the strength of the spin-orbit coupling and K the exchange integral).[5]

Consequently every observable feature of the first four states of C^{13} and N^{13} is consistent with an intermediate coupling model of the nucleus. This appears to give by far the most consistent support for the model found hitherto. A complete account of this work will appear in a series of articles in the *Proceedings of the Physical Society (London)*,[6] and as part of a review article on nuclear reactions.[7]

[1] F. Azjenberg and T. Lauritsen, Revs. Modern Phys. **24**, 321 (1952).
[2] G. Racah, Phys. Rev. **63**, 367 (1943); H. A. Jahn and H. van Wieringen, Proc. Roy. Soc. (London) **A214**, 502 (1951); B. H. Flowers and A. R. Edmonds, Proc. Roy. Soc. (London) **A214**, 515 (1952).
[3] E. P. Wigner and L. Eisenbud, Phys. Rev. **72**, 29 (1947).
[4] R. G. Thomas, Phys. Rev. **88**, 1109 (1952).
[5] D. R. Inglis, Revs. Modern Phys. **25**, 390 (1953).
[6] A. M. Lane, Proc. Phys. Soc. (London) (to be published); A. M. Lane and L. A. Radicati, Proc. Phys. Soc. (London) (to be published).
[7] R. G. Thomas and A. M. Lane, Revs. Modern Phys. (to be published).

Periodic Ellipse of the Strong-Focusing Equation*

B. C. Carlson
Palmer Physical Laboratory, Princeton University, Princeton, New Jersey
(Received September 11, 1953)

THE equation of free betatron oscillations in the strong-focusing synchrotron is a Hill's equation of the form[1]

$$d^2x/d\theta^2+n(\theta)x=0, \quad (1)$$

where $n(\theta)$ can be taken (by including a scale factor in θ) to alternate between 1 in converging sectors and -1 in diverging

sectors. If each sector is of length $\Delta\theta=\nu$, then $n(\theta)$ is periodic with period 2ν. The amplitude x and slope $x'=dx/d\theta$ at $\theta+2\nu$ are linear functions of the amplitude and slope at θ,

$$\begin{pmatrix} x \\ x' \end{pmatrix}_{\theta+2\nu} = \begin{pmatrix} A_{11} & A_{12} \\ A_{21} & A_{22} \end{pmatrix} \begin{pmatrix} x \\ x' \end{pmatrix}_{\theta}. \tag{2}$$

The translation matrix $A=||A_{ij}(\theta)||$ has unit determinant, thus preserving density in phase space. The motion is stable if $|\frac{1}{2}\,\mathrm{Tr}A| = |\frac{1}{2}(A_{11}+A_{22})|<1$, in accordance with Floquet's theory of differential equations with periodic coefficients.

In the stable case, A can be written as the equivalence transform $A=S^{-1}(\theta)R(\beta)S(\theta)$ of an orthogonal matrix $R(\beta)$ representing a rotation through angle β, where $\cos\beta=\frac{1}{2}\,\mathrm{Tr}A$ is independent of θ. Multiplication of Eq. (2) on the left by S shows that A leaves invariant a quadratic form in x and x', corresponding for any given set of initial conditions to an ellipse (a hyperbola in the unstable case) with center at the origin of phase space. As θ increases by successive increments of 2ν, the point (x, x') advances clockwise around the perimeter. The radius vectors to two adjacent positions enclose a fraction $\beta/2\pi$ of the total area of the ellipse.

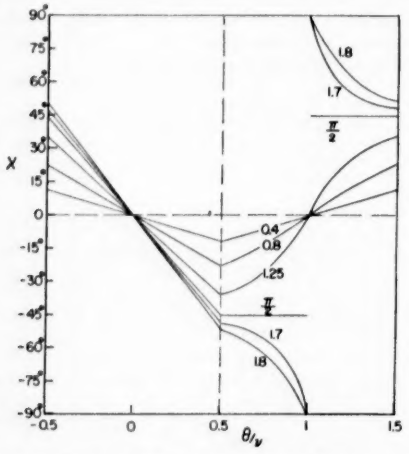

FIG. 1. The angle χ (defined modulo π) between the major axis of the ellipse and the x axis in phase space. The region $-0.5<\theta/\nu<0.5$ is a converging sector and $0.5<\theta/\nu<1.5$ is a diverging sector. The curves are labeled by values of ν, where 2ν is the period of $n(\theta)$.

Since the matrix elements A_{ij} are periodic functions of θ with period 2ν, the eccentricity and orientation of the ellipse will also have this period. The continuous history of a point in phase space, as distinguished from the preceding account of its positions at equal intervals of θ, therefore, can be described as motion on an ellipse whose shape and orientation change periodically with the period of $n(\theta)$. Its area, which is determined by the initial conditions, remains constant since Eq. (1) can be written in Hamiltonian form and satisfies Liouville's theorem.

The following parametrization of the unimodular group leads to a simple description of the periodic motion of the ellipse:

$$\begin{aligned} A_{11} &= \cos\beta - \sin\beta \sinh\psi \sin 2\chi, \\ A_{22} &= \cos\beta + \sin\beta \sinh\psi \sin 2\chi, \\ A_{12} &= \sin\beta(\sinh\psi \cos 2\chi + \cosh\psi), \\ A_{21} &= \sin\beta(\sinh\psi \cos 2\chi - \cosh\psi). \end{aligned} \tag{3}$$

Equations (3) correspond to writing the transformation (2) as a rotation of phase space viewed from rectangular axes that have been rotated and stretched. The ellipse left invariant by the transformation (2) is

$$e^{-\psi}(x\cos\chi+x'\sin\chi)^2+e^{\psi}(-x\sin\chi+x'\cos\chi)^2=I^2=\text{constant}. \tag{4}$$

If by definition $\psi\geq 0$, then the major axis makes an angle χ with the x axis; the semimajor and semiminor axes are of length $Ie^{\psi/2}$ and $Ie^{-\psi/2}$, respectively.

The dependence of ψ and χ on θ is easily obtained by writing down the translation matrix (a product of simple factors, one for each interval of θ in which $n(\theta)$ is constant) and solving Eqs. (3) for the parameters. One finds that $\cos\beta=\cos\nu\cosh\nu$ and that in a converging sector with center at the origin of θ (i.e., for $-\nu/2\leq\theta\leq\nu/2$),

$$\begin{aligned} \coth\psi &= \sin\nu \coth\nu, \\ \chi &= -\theta. \end{aligned} \tag{5}$$

Thus the ellipse rotates without change of shape in a converging sector. In a diverging sector ($\nu/2\leq\theta\leq 3\nu/2$),

$$\begin{aligned} \cosh\psi &= \sin\nu(\sin\beta)^{-1}\cosh 2(\theta-\nu), \\ \tan 2\chi &= \tan\nu(\sinh\nu)^{-1}\sinh 2(\theta-\nu). \end{aligned} \tag{6}$$

Equations (5) and (6) are plotted in Figs. 1 and 2 for various values of ν in the first stability region of Eq. (1). A transition

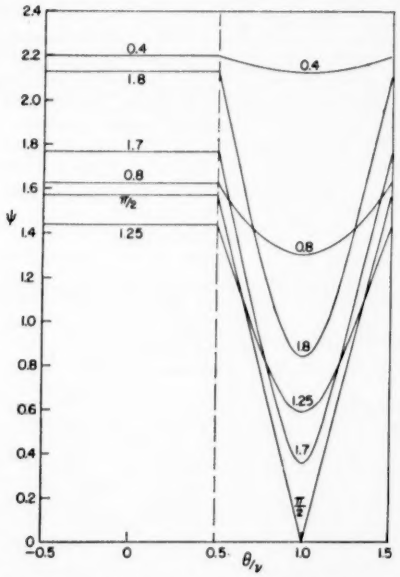

FIG. 2. ψ is the natural logarithm of the ratio of major to minor axis of the ellipse. See caption of Fig. 1 for the abscissa. The curves are labeled by values of ν.

occurs at $\nu=\pi/2$ between libration of the ellipse and end-over-end rotation. At the transition point the ellipse does not rotate at all in a diverging sector but simply degenerates at the center of the sector to a circle, for which χ is indeterminate. At the end of a diverging sector the ellipse returns, of course, to its shape and orientation at the beginning of a converging sector. The maximum excursion in x of any point on the ellipse occurs at the center of a converging sector, where χ vanishes and ψ is a maximum.

If $n(\theta)$ is an arbitrary periodic function instead of being piecewise constant, one cannot in general write down the explicit form of the translation matrix, but it is still possible to find the differential equations of motion of the ellipse. Differentiation with respect to θ of $Fx^2+2Hxx'+Gx'^2=\text{constant}$, and substitution of $-nx$ for x'' leads to a quadratic form in x and x' whose coefficients must vanish identically, since x and x' can be varied independently by varying the initial conditions. The resulting equations are $F'=2nH$, $G'=-2H$, and $H'=nG-F$, and they satisfy $FG-H^2$

=constant. In terms of ψ and χ, these equations become

$$(\chi'+1)2\sin 2\chi=\psi'(\coth\psi\cos 2\chi+1),$$
$$\psi'=(1-n)\sin 2\chi. \quad (7)$$

It can be verified readily that Eqs. (5) and (6) are a periodic solution of Eqs. (7) when n alternates between 1 and -1.

This work resulted from a conversation with Hartland S. Snyder, who suggested investigating the periodic motion of the invariant ellipse.

* This work was supported by the U. S. Atomic Energy Commission and the Higgins Scientific Trust Fund.

[1] Courant, Livingston, and Snyder, Phys. Rev. **88**, 1190 (1952).

PHYSICAL REVIEW VOLUME 92, NUMBER 3 NOVEMBER 1, 1953

Proceedings of the American Physical Society

Minutes of the 1953 Spring Meeting of the New York State Section at Schenectady, April 10 and 11, 1953

THE twenty-ninth meeting of the New York State Section convened at the General Electric Research Laboratory, The Knolls, Schenectady, on April 10 and 11, 1953. About 130 members and friends of the section registered for the two-day session.

Friday morning was devoted to tours of the laboratories, and to a relatively short session of two invited papers. Five invited papers were presented at the afternoon session. At the dinner meeting on Friday evening, Mr. James Stokley of the G. E. Research staff discussed "Calendars—Past, Present, and Future."

The closing session, again consisting of invited papers, followed the business meeting of the section on Saturday morning. The local committee, Messrs. Harold Way, Roger Powell, and Frank Studer, under the chairmanship of G. C. Baldwin, deserve commendation.

The principal item of business at the Saturday session was the election of officers. Resignation of H. Hoerlin from the executive committee produced an unanticipated third vacancy; it was ruled that this vacancy be filled by the candidate receiving the third highest number of votes in the balloting for executive committee membership. Officers and members of the executive committee for the next two years are as follows:

Chairman: L. P. Smith, *Cornell University*
Vice-Chairman: Harold E. Way, *Union College*
Secretary: L. W. Phillips, *University of Buffalo*
Treasurer: William I. Caldwell, *Taylor Instrument Company*
Executive Committee:
G. P. Smith, *Corning Glass Works*
G. C. Baldwin, *General Electric Research Laboratories*
R. J. Gladieux, *Kenmore High School*
G. W. Hazzard, *St. Lawrence University*
T. E. Renzema, *Clarkson College*

Titles of the invited papers presented at the various sessions are listed below.

L. W. Phillips, *Secretary*
New York State Section
The University of Buffalo
Buffalo 14, New York

Invited Papers

Electrical Conductivity of Metals at Low Temperatures. Milan Fiske, *General Electric Research Laboratory.*

Crystal Growth and Spirals, Etch-Figures and Holes. F. H. Horn, *General Electric Research Laboratory.*

Studies of the Biological Effects of High-Voltage X-Radiation. H. M. Rozendaal, *General Electric Research Laboratory*

Apparatus for Studies with Cathode Rays. E. J. Lawton, *General Electric Research Laboratory*

Biological Studies with High-Energy Cathode Rays. M. D. Bellamy, *General Electric Research Laboratory.*

Experimental Evidence for Inheritance of Radiation Effects. G. Heidenthal, *Russell Sage College*

Effects of High-Energy Radiation on Glass. S. D. Stookey, *Corning Glass Works*

Electroluminescence. W. W. Piper, *General Electric Research Laboratory*

Double-Crystal Neutron Spectrometer. V. C. Wilson, *General Electric Research Laboratory*

Neutron Velocity Spectrometer with Betatron Source. E. R. Gaerttner, *Knolls Atomic Power Laboratory.*

Čerenkov Radiation. J. Rich, *General Electric Research Laboratory*

Minutes of the Meeting Held at Rochester, New York, June 18–20, 1953

(Corresponding to the *Bulletin of the American Physical Society*, Volume 28, No. 4).

THE American Physical Society held its 1953 Summer Meeting in the East at Rochester, New York, on Thursday, Friday, and Saturday, June 18, 19, and 20. The host was the University of Rochester. The Secretary was unable to attend this meeting, but avails himself of a report made by Professor J. B. Platt. To quote: "The statistics are: a total of 363 persons registered, 281 from

outside Rochester. I am fairly sure that some physicists attended without registering, and that some outsiders escaped our census. The banquet was very pleasant. Dean Pegram was a gracious toastmaster, and Dr. W. A. Noyes had some profound and thought-provoking remarks to make about the training of scientists. Unfortunately the banquet was not well attended (92) but those who did attend made a most congenial group." What Professor Platt does not say is that the Department of Physics of the University of Rochester was largely responsible for the excellent program of invited papers, and (of course) entirely to be credited with the housing and management of the meeting.

The Council met on June 20. It elected twelve candidates to Fellowship and 121 to Membership; the names follow.

Elected to Fellowship: R. M. Badger, V. H. Benioff, C. D. Coryell, E. W. Cowen, M. A. Greenfield, A. W. Haeff, C. K. Jen, R. M. Karplus, C. B. Millikan, M. L. Sands, R. L. Walker, and D. M. Yost.

Elected to Membership: Betsy Ancker, Rodney D. Andrews, Jr., William Balas, •Richard L. Becker, Herbert E. Behrens, Chester M. Bennett, Edgar F. Bennett, Paul P. Bey, Francis L. Bouquet, Jr., Robert L. Brock, William D. Brooks, William H. Burke, Jr., Shih Kan Chen, •Tien Chi Chen, Ralph W. Christiansen, Philip J. Closmann, •Edward E. Conrad, George A. Craig, William R. Davis, David C. dePackh, James K. de Pagter, Hugh E. DeWitt, Edward E. Donaldson, •Stanley M. Edelman, Edward M. Elvejord, Charles E. Engelke, Georges Louis Farre, Herbert C. Field, Markus E. Fierz, Tomas E. Firle, Paul A. Flinn, Julian R. Frederick, Arthur J. Freeman, Archer H. Futch, Jr., Wilford R. Gardner, Theodore H. Geballe, Harold B. Goldberg, Bruce B. Goodman, Charles R. Gossett, Jack J. Grossman, Roy W. Gould, Joseph Guarracini, Richard A. Gudmundsen, George J. Habetler, Jacob M. Hammer, William E. Harding, John Charles Healy, Richard C. Heckman, William W. Henoch, •Alvin F. Hilderbrandt, Joseph H. Holloway, John E. Hove, •Dale H. Husemoller, James S. Hyde, Gerald W. Iler, Paul A. Janssens, Thomas L. Jenkins, James E. Johnson, William F. Jones, Farnham S. Jory, •John A. Kadyk, Alexander D. Kavadas, Edmund J. Kazanski, William A. Klemperer, Albert D. Krall, Philip Krupen, Osamu Kusumoto, Daniel A. Larson, Samuel C. Lawrence, Jr., Clarence E. Lee, Curt A. Levis, Chia-Chiao Lin, Walter E. Lockwood, Paul R. Malmberg, Enrico Mantica, James H. Marable, Miles J. Martin, Donald R. Maxson, David E. McConnell, George C. Messenger, Lucio Mezzetti, George A. Michael, Norman S. Namerow, Roger L. Nataf, Joseph L. Neuringer, John W. Noaks, Zachary M. O'Friel, •Kenneth H. Olsen, Richard A. Oriani, Gerald M. Padawer, Ralph J. Panos, Rudolph J. Parker, George C. Patterson, Donald Robbins, Robert L. Rutledge, Edward M. Saunders, Jacob M. Schmidt, George S. Scholl, •Robert B. Schwartz, Edward A. Scicchitano, John M. Sellen, Jr., Edward Sonder, George M. Stamps, Lyn H. Stauffer, Edward O. Stejskal, Shigeki Suwa, Morris Tanenbaum, Sheldon G. Turley, Paul W. Ussery, John M. Watkins, Warren Weaver, Honer E. Webb, •Murray Weinstein, •Tunis Wentink, Jr., James R. White, •John W. G. Wignall, Rollie B. Williams, Yeivin S. Yehudah, Gideon Yekutieli, Julius L. Yucker, Jr., Berthold Zarwyn, and Harold Zirin.

•—Student

Errata Pertaining to Papers B5, C3, C7, R10, and S5

B5, by E. M. Baroody. A footnote should be added, reading, "Sponsored by the U. S. Army Signal Corps and the U. S. Air Force."

C3, by Norman W. Lord. In line 15, "1.40 ev" should read "1.45 ev."

C7, by J. L. Stull and L. R. Bickford, Jr. In the next to the last line, "λ_{100}" should read "$\delta 1/1_{100}$."

R10, by Richard Schlegel. In line 11, "$\nu' = \nu_0(1-$" should read "$\nu' = \nu_0/(1-$."

S5, by Conyers Herring. In line 18, "T^q" should read "T^{-q}."

KARL K. DARROW, *Secretary*
American Physical Society
Columbia University
New York 27, N. Y.

PROGRAMME

THURSDAY MORNING AT 10:00

Upper Strong Auditorium

(H. W. FULBRIGHT presiding)

Nuclear Models

A1. The Cloudy Crystal Ball Model. V. F. WEISSKOPF, *M.I.T.* (30 min.)
A2. The Collective Model. J. A. WHEELER, *Princeton University.* (30 min.)
A3. The Shell Model. A. DE-SHALIT, *M.I.T.* (30 min.)
Discussion to be led by M. GOLDHABER, G. SCHARFF-GOLDHABER, E. B. PAUL, AND KEITH BOYER.

THURSDAY MORNING AT 10:00

Lower Strong Auditorium

(K. G. MCKAY presiding)

Secondary Electron Emission

B1. Theory of Secondary Emission. J. F. MARSHALL, *Bartol Research Foundation.* (30 min.)
B2. The Theory of Secondary Electron Production for a Screened Coulomb Interaction. A. VAN DER ZIEL, *University of Minnesota.* (30 min.)
B3. Auger Peaks in the Energy Spectra of Secondary Electrons from Various Materials. J. J. LANDER, *Bell Telephone Laboratories.* (30 min.)

Contributed Papers

B4. Average Energy of Electrons Emitted from Metals under High Energy Electron Bombardment. JOHN H. ANSON, KENNETH A. WRIGHT, AND JOHN G. TRUMP, *M.I.T.* —Measurements have been made of the average energy of the secondary electrons emitted from thick targets of C, Al, and Pb bombarded by 2 and 3 million volt electrons and of the ratio of secondary to primary electron current. The average secondary electron energy was determined as the difference between the incident electron energy and the sum of the calorimetrically determined heat energy in the target material and the calculated x-radiation. For 2-Mev primaries the secondary electron emission from Pb approaches 60 percent of the primary electron current and carries away nearly 30 percent of the incident energy. For Al the emission ratio is 15 percent and the energy ratio is 4 percent. The application of this information to phenomena at the anode end of high voltage acceleration tubes and to an instrument for electron dosage control will be discussed.

B5. The Role of the Surface Barrier in Secondary Emission from Metals. E. M. BARODY, *Battelle Memorial Institute.*—In secondary emission the transfer of momentum between the interacting primary and secondary electrons on the one hand and the metal as a whole on the other plays an essential part. In theoretical work this transfer has been introduced in various ways. According to Vyatskin,[1] the bulk of the observed emission is a nonclassical surface phenomenon caused by the potential energy rise at the metal surface. In the quantum-mechanical treatment of the problem, this leads to a momentum transfer which would not have been expected on classical grounds. We have made a study of Vyatskin's articles, particularly the earlier ones, which develop a theory based on Sommerfeld's model, and similar to Mitchell's 1934 theory of the surface photoelectric effect. This study has led to the conclusion that Vyatskin's effect exists in principle but that it is extremely small, making a negligible contribution to the total emission.

[1] A. Ya. Vyatskin, J. Exptl. Theoret. Phys., U.S.S.R., **9**, 826 (1939); **9**, 1049 (1939); **12**, 22 (1942); **20**, 547 (1950).

B6. Secondary Electron Emission from Diamond. J. B. JOHNSON,* *Bell Telephone Laboratories.*—Secondary electron emission was measured on a diamond which Ahearn[1] had previously studied as an α-particle counter. The clear cleavage plate, 0.2 mm thick and 7 mm on a side, was bombarded with short pulses of focused electrons for the secondary emission measurements. Charging effects were avoided by using small currents, low duty cycle, and heat when needed. The maximum δ varied in repeatable contours over the surface from 2 to 3.5. There was no clear correspondence of this pattern with the counting efficiency contours of Ahearn. Thus here the pattern is determined by the surface properties of the target, while the conductivity pattern is set by the volume properties. The average δ measured by defocused beam at room temperature had a maximum of 2.8 at 750 volts and was 1.7 at 5000 volts. At 750°C the yield was substantially reduced at and above 750 volts, as observed also with MgO.[2] This signifies that at the higher temperature the energy of the internal secondaries is more rapidly reduced below the escape level by the increased lattice vibrations.

* Now at Edison Laboratory, West Orange, New Jersey.
[1] A. J. Ahearn, Phys. Rev. **84**, 798 (1951).
[2] J. B. Johnson and K. G. McKay, "Secondary Emission of Crystalline MgO" (to be published).

THURSDAY MORNING AT 10:00

Biology Lecture Room

(J. H. HOLLOMON presiding)

Liquid State; Solid State Physics, I

C1. Proton Magnetic Resonance in Liquid Crystals. P. L. JAIN, H. A. MOSES, J. C. LEE, AND R. D. SPENCE, *Michigan State College.*—We have studied the proton resonance line in several liquid crystals. In the liquid phase of *p*-azoxyanisole, *p*-azoxyphenetole, and anisaldazine the line is narrow but on passing into the liquid crystal phase the line splits into three components whose separation is the order of one gauss between components. The separation between satellite lines increases as the temperature of the liquid crystal phase is lowered. The central component remains larger than the satellites throughout the liquid crystal phase of *p*-azoxyanisole and anisaldazine, while in the *p*-azoxyphenetole the central component gradually shrinks down to the level of the satellites as the temperature is reduced. In all three cases the sharp structure disappears in the solid state. The resonance lines of the liquid crystal phases of cholesteryl benzoate and sodium oleate and sodium stearate showed no structure.

C2. The Rotation of Microwave Polarization in Liquid Crystals in a Transverse Magnetic Field. GLEN A. MANN AND R. D. SPENCE, *Michigan State College.*—Previous experiments[1] on the effects of a magnetic field on the complex dielectric constant of liquid crystals at microwave frequencies indicate that such substances should be capable of producing a rotation of the plane of polarization in a circular wave guide placed in a transverse magnetic field. Investigations of this rotation are reported in this paper. The rotation appears to result from two sources—the difference of absorption coefficients and difference of phase shifts along and transverse to the direction of the magnetic field. The emergent wave is strongly polarized indicating that the effect of the differential absorption predominates. Although the rotation per wavelength is quite large even at small magnetic fields, the rotation possible is limited by certain saturation effects.

[1] E. Carr and R. D. Spence, Phys. Rev. **90**, 339A (1953).

C3. Nucleation of Ordered Phases in Cu_3Au. NORMAN W. LORD,* *Raytheon Manufacturing Company.*—Experimental data[1] covering the kinetics of ordering in Cu_3Au from 279 to 384°C is interpreted in accordance with nucleation theory. The ordering has been shown to proceed in two distinct stages. One can then associate different nucleation processes for each of them. The mechanism hypothesized for the complicated "coalescence" stage is consistent with available experimental evidence.[2] The earlier simple ordering stage has no observed incubation period and is assumed to follow the Becker theory. The second stage has an observed incubation period and only after this does it conform to the theory. The temperature dependence of the relaxation times for each stage are used to calculate the activation energy for the formation of growing nuclei. A value of 1.40 ev is used for the diffusion activation energy. The results are in qualitative agreement with Becker's sample theoretical calculations. The activation energy for the "coalescence" stage falls off much more rapidly with decreasing temperature than that for the first stage.

* The experimental work was done at Columbia University.
[1] N. W. Lord, Bull. Am. Phys. Soc. **28**, No. 2, 23 (1953).
[2] Jones and Sykes, Proc. Roy. Soc. (London) **166**, 376 (1938); Owen and Sim, Phil. Mag. **88**, 342 (1937).

C4. The Measurement of the Specific Heats of the Alkali Metals. H. PRESTON-THOMAS, T. M. DAUPHINEE, AND D. K. C. MACDONALD, *National Research Council, Canada.*—An apparatus of novel design has been constructed to measure the specific heats of some pure and alloyed alkali metals in the range from 15°K to 300°K; in particular Rb and Cs have never been measured. The range will later be extended to lower temperatures. We wished to reduce experimental errors to the order of 0.1 percent for the measurement of small anomalies and possible time-dependent effects; economy in the use of the scarcer metals was also important. These aims led to the following design: Eight cm^3 or less of the metal to be measured are cast in vacuum into the copper calorimeter and then sealed in under pure helium gas. Heat input is continuous during an experiment, the copper heating coil serving also as the thermometer. Adiabatic conditions are maintained and recorded automatically, manual adjustments being required only at intervals of several hours. All requisite data (power input, temperature, and time) appear on a single recorder chart, allowing for extraction or verification of results at any subsequent time. Measurements already completed on sodium show that the desired consistency has been achieved, while a series of test procedures suggests that systematic errors have been kept within the required limits.

C5. Thermoelectricity in Metals at Low Temperatures. D. K. C. MACDONALD AND W. B. PEARSON, *National Research Council, Canada.*—A wide range of experiments has been carried out to determine the absolute thermoelectric power down to ~4°K on the alkali and group IB metals both in the pure state and as dilute alloys. In all cases the temperature range extends at least to 70°K and in some cases to 300°K. Since these metals, and sodium and potassium in particular, are generally accepted to be good approximations to the theoretical model of an "ideal" metal, the data are particularly suitable for comparison with the modern theories of electron transport. Serious disagreement is found in both magnitude and temperature dependence, and it appears quite probable that the theory may be lacking in a number of respects. However, apart from the adequacy or otherwise of the fundamental theory, the results on the dilute alloys in particular appear to offer much useful information on both the "normal" and "abnormal" scattering of electrons in metals.

C6. An H-T Antiferromagnetic Boundary and Apparent Molecular Field for $MnBr_2 \cdot 4H_2O$. WARREN E. HENRY, *Naval Research Laboratory.*—The magnetization of manganous bromide tetrahydrate has been carried out at liquid helium temperatures and in magnetic fields up to 58 000 gauss. The general technique of measurement and analysis of data is the same as in previous work[1] with manganous chloride tetrahydrate. Thus one is enabled to make the following comparison:

	Néel temperature	Molecular field
$MnCl_2 \cdot 4H_2O$	~1.73°K	~14 000 gauss
$MnBr_2 \cdot 4H_2O$	~2.2 °K	~17 500 gauss

The Néel temperature is defined as the antiferromagnetic transition temperature in zero magnetic field. The field de-

pendence of the antiferromagnetic transition temperature was studied by carrying out moment measurements in a controlled, changing temperature and at fixed, constant magnetic fields. The critical temperature is reached when

$$(\partial M/\partial T)_H = 0.$$

Some values of $T_c(H)$ were thus obtained. By assuming that for $H > H_m$ no spontaneous antiferromagnetic ordering takes place at the absolute zero, one can set the limiting critical field equal to the molecular field. With these values of H_c and T_c, one can draw a curve and extrapolate to $H_c = 0$ to get the Néel temperature. Thus one obtains for $MnBr_2 \cdot 4H_2O$ an antiferromagnetic transition curve plotted in the H-T plane.

[1] W. E. Henry, Bull. Am. Phys. Soc. **28**, No. 3, 11 (1953); Phys. Rev. (to be published).

C7. Magnetostriction of Magnetite.* J. L. Stull and L. R. Bickford, Jr., *Alfred University.*—Magnetostriction measurements were made on circular wafers cut from natural and synthetic crystals and a synthetic polycrystalline specimen of Fe_3O_4. The strain gauge technique was used, with the data in the form of recorded curves of strain *vs* magnetic field. For measurements below room temperature (to 120°K) the strain gauges were calibrated by comparing results obtained for the thermal expansion of brass *vs* fused silica as measured by (1) strain gauges and (2) standard dilatometric techniques. At room temperature the magnetostriction is positive along [111] and [110], but negative along [100]. The magnetostriction is largest in magnitude along the body diagonal: $\lambda_{111} = 80 \times 10^{-6}$ for a synthetic crystal. In the temperature region in which the preferred direction of the spontaneous magnetization switches from [111] to [100] (*ca* 130°K) the structure of all the magnetostriction curves changes. In some cases λ_{100} changes sign. These results are correlated with other magnetic properties.

* Supported in part by the U. S. Office of Naval Research.

C8. Magnetic Resonance in Ferrimagnetic and Antiferromagnetic Systems.* L. R. Bickford, Jr., *Alfred University.*—The previously reported[1] microwave resonance absorption spectrum of Fe_3O_4 at 83°K has been re-analyzed, and the observed doubling of resonance peaks has been attributed to the separate contributions of the A and B spins (spins of magnetic ions on the tetrahedral A sites and octahedral B sites, respectively). Some implications of the analysis are (1) the exchange field H_E need not appear in the resonance equations;[2] (2) resonance peaks in cubic ferrite materials are unresolved doublets, with the line width and apparent g factor being partially dependent upon the magnitude of magnetic anisotropy; (3) the disappearance of resonance absorption at the Curie temperature of antiferromagnetics is a magnetic anisotropy effect; and (4) the Fe_3O_4 transition appears to be primarily a magnetic transition of a type which might be expected to occur in certain other ferrites and in antiferromagnetic materials.

* Supported in part by the U. S. Office of Naval Research.
[1] L. R. Bickford, Jr., Phys. Rev. **78**, 449 (1950).
[2] C. Kittel, Phys. Rev. **82**, 565 (1951).

C9. Phase Transitions in the $NaNbO_3$-$KNbO_3$ System.* G. Shirane,† R. E. Newnham, and R. Pepinsky, *The Pennsylvania State College.*—Phase transitions in $KNbO_3$ and $NaNbO_3$ have been examined by dielectric[1] and x-ray[2] measurements. The transitions in $KNbO_3$ are rather similar to those in $BaTiO_3$, the crystal being ferroelectric below 435°C. Though $NaNbO_3$ was also reported as ferroelectric,[1] Vousden[2] reported a nonpolar space-group for this crystal. Dielectric, optical, x-ray, and specific heat measurements have been carried out, in an exploration of the phase diagram of the $NaNbO_3$-$KNbO_3$ system, using both single crystal and ceramic specimens. No evidence for ferroelectricity is obtained for pure $NaNbO_3$ by dielectric and pyroelectric tests, but a ferroelectric phase appears upon addition of a small amount of $KNbO_3$. Dielectric properties and their relations to crystal structure are reported for the complete $NaNbO_3$-$KNbO_3$ system.

* Development supported by the Air Research and Development Command and the U. S. Office of Naval Research.
† On leave from Tokyo Institute of Technology, Tokyo, Japan.
[1] B. Matthias and J. Remeika, Phys. Rev. **82**, 727 (1951).
[2] E. A. Wood, Acta Cryst. **4**, 353 (1951).
[2] P. Vousden, Acta Cryst. **4**, 545 (1951).

C10. Study of the Transition in $LiNH_4C_4H_4O_6 \cdot H_2O$.* F. Jona and R. Pepinsky, *The Pennsylvania State College.*—Lithium ammonium tartrate monohydrate has been reported to be ferroelectric in the direction of the b axis below about 100°K.[1, 2] The behavior of the dielectric constant ϵ_b has been re-examined in the range from −190° to about +120°C and appears to be quite different from the behavior in other ferroelectric crystals. A Curie-Weiss law can be assumed only in a small temperature range above the Curie point. Another interpretation of this behavior is given. The dielectric constant ϵ_a shows a small anomaly at the Curie point, whereas ϵ_c is essentially independent of temperature. The dependence of the three dielectric constants on a dc biasing field has been investigated as a function of the temperature, and thermal expansion has been examined by dilatometric measurements. The effect of a partial substitution of hydrogen by deuterium on the dielectric properties has also been investigated.

* Development supported by Air Research and Development Command.
[1] B. T. Matthias and J. K. Hulm, Phys. Rev. **82**, 108 (1951).
[2] W. J. Merz, Phys. Rev. **82**, 562 (1951).

Thursday Afternoon at 2:00

Biology Lecture Room

(L. P. Smith presiding)

Solid State Physics, II

D1. Color Center Formation in Alkali Halides Containing $S^=$. E. Burstein and B. W. Henvis, *Naval Research Laboratory.*—The addition of $S^=$ to KCl and KBr enhances the formation of the F band and suppresses the formation of other trapped electron bands such as the R, M, and N bands. Since negative ion vacancies are introduced simultaneously with the divalent anions in order to maintain neutrality, the increased darkenability of alkali halide crystals containing $S^=$ is attributed to an increased concentration of negative ion vacancies and possibly to an increased trapping

of holes, presumably by $S^=$. The crystals also exhibit a marked increase in the bleachability of the F band which may be attributed to the absence of "hard F centers" and to the trapping of holes by $S^=$ to form centers, with bands in the ultraviolet, which allow ready recombination of the trapped holes with electrons. The presence of $S^=$ extends the ultraviolet absorption edge of KCl to about 2200A and that of KBr to about 2300A.

D2. Time-Dependent Spectra of Electroluminescent Zinc Sulfide. E. E. LOEBNER, *Sylvania Electric Products Inc.*—The brightness during electroluminescence has been investigated heretofore as a function of either time or wavelength only.[1] An AO Rapid Scanning Spectrograph makes a simultaneous measurement possible. The data can be represented as a surface in three-dimensional, brightness-wavelength-time space. Sections parallel to the brightness-time plane intersect the surface in monochromatic "waves of brightness." They exhibit generally sharp asymmetrical peaks and shallow minima. A relative phase shift with wavelength is apparent. A projection into the brightness-wavelength plane results in two spectral envelops of all the minima and maxima of brightness. This permits a separation into a permanent and fluctuating component of radiation. The former is insensitive to variations in magnitude and frequency of the exciting electric field, while the latter exhibits a sharp rise at the blue end, shifting toward the violet, with increasing frequency. A fine structure of about ten bands between 4000A and 5800A is apparently associated with the Stark effect. These data furnish new insight into the mechanism of electroluminescence, which promises to become a powerful tool in solid state physics.

[1] Destriau, Phil. Mag. **38**, 700 (1947); Waymouth *et al.*, Sylvania Technologist **5**, 54 (1952).

D3. Interpretation of Some Electroluminescent Effects. FRANK MATOSSI, *U. S. Naval Ordnance Laboratory.*—The consideration of electron transitions between valence band, conduction band, and traps as presented by Randall and Wilkins' theory of luminescent growth is extended to include terms which take into account emptying of traps by an electric field, the change of transition probabilities, and the draining off of electrons into surface traps. The result of the mathematical analysis corresponds to effects observed in a sulfide phosphor under the influence of a periodic electric field while continuously excited by ultraviolet radiation. These are a momentary illumination, an extinguishing effect, and the superposition of a ripple with twice the frequency of the field, whose amplitude decreases with increasing frequency. The draining effect is acting only as long as not all surface states are filled. At low frequencies, polarization and current effects have to be taken into account. These will be discussed in general terms, together with relevant observations.

D4. Efficiency of Conversion from Light to Electric Power by a Ge Grown Junction. RALPH P. RUTH AND JAMES W. MOYER, *Knolls Atomic Power Laboratory.**—The efficiency with which a Ge grown junction converts power received from incident light into maximum power in an external resistive load has been measured as a function of incident radiation intensity. The crystal used was a disk cut from an ingot with the junction parallel to the faces and close to the n face; the light was incident normal to the surface on the n side. The observed efficiency for white light increases approximately as the $\frac{3}{4}$ power of the incident intensity over an intensity range of three decades before leveling off at a maximum for an intensity of 0.1 watt cm^{-2}. The maximum efficiency, uncorrected for the quantum efficiency of the process or for the reflectivity of the Ge, is approximately $\frac{1}{2}$ percent. For infrared radiation beyond 0.9μ the efficiencies were slightly higher. An effective quantum conversion efficiency appreciably less than 100 percent was observed with the junction used. If this effect were not present power conversion efficiencies several times as large as those observed might be attained. The theory of the photovoltaic effect at a p-n junction has been developed to the point of qualitative agreement with the observed efficiency-intensity relationship.

* Operated by the General Electric Company for the U. S. Atomic Energy Commission.

D5. Diffusion of Lithium into Germanium and Silicon. C. S. FULLER AND J. A. DITZENBERGER, *Bell Telephone Laboratories.*—The diffusivity of lithium in p type single crystals of Ge and Si has been investigated in the range 300 to 1000°C by the method previously described.[1] Lithium is found to be a donor in Ge and Si. The equations, $D=13\times10^{-4}\exp(-10700/RT)$ and $D=94\times10^{-4}\exp(-18100/RT)$, are found to apply to the diffusion of Li in Ge and Si, respectively, where D is the diffusivity in cm^2/sec and $R=1.98$ calories. Li shows a maximum solubility of approximately 10^{18} cm^{-3} in both Ge and Si, assuming each Li atom supplies one electron to the conduction band. This maximum occurs at 500±25°C for Si. However, because of spontaneous precipitation of Li at room temperature in Ge, the temperature dependence of solubility for Li in Ge is less certain.

[1] C. S. Fuller, Phys. Rev. **86**, 136 (1952).

(Abstract withdrawn)

D7. Etch Pits in Plastically Deformed Germanium. C. J. GALLAGHER, *General Electric Research Laboratory.*—Following plastic flow in germanium, etch pits, with separations of a few microns at small strains, have been observed in (111) faces, aligned on slip lines which are traces of (111) planes. These show certain similarities to those found by Vogel, Pfann, Corey, and Thomas,[1] which were interpreted as sites of single dislocations at small angle grain boundaries. Similar pits have also been observed in (111) faces in material subjected to thermal shock where there is no external evidence of slip. On other faces the slip lines disappear as the etch proceeds, with no pits developed. The incubation time for plastic flow[2] follows the relation suggested by Seitz[3] $\tau=\tau_0 e^{Q/RT}$ ($\tau_0=3\times10^{-8}$ second, $Q=24\,000$ cal/mole). Thermoelectric measurements on high resistivity germanium bent at temperatures below 500°C show that the deformed region is always more p type, probably due to the introduction of electron trapping states associated with lattice defects. Minor-

ity carrier lifetimes in the same material are less than a few microseconds.

[1] Vogel, Pfann, Corey, and Thomas, Bull. Am. Phys. Soc. **28**, No. 2, 32 (1953).
[2] C. J. Gallagher, Phys. Rev. **88**, 721 (1952).
[3] F. Seitz, Phys. Rev. **88**, 722 (1952).

D8. Floating Zone Recrystallization. P. H. KECK, W. VAN HORN, J. SOLED, AND A. MACDONALD, *Signal Corps Engineering Laboratories.*—Equipment to carry out recrystallization and zone melting of silicon from a floating liquid zone[1] will be described and results obtained are discussed.

[1] P. H. Keck and M. J. E. Golay, Phys. Rev. **89**, 1297 (1953).

D9. Crystal Growth of Silicon by the Tip Fusion Process. P. H. KECK, S. B. LEVIN, J. BRODER, AND R. LIEBERMAN, *Signal Corps Engineering Laboratories.*—In this new method, which does not require a container for the melt, a seed crystal is supported on a pedestal in a gas tight chamber. The tip of the crystal is melted by radiation or induction heating and is maintained in the molten state while a stream of finely divided powder is slowly fed from above into the liquid tip. The growing crystal is lowered at such a rate that the molten zone remains of nearly constant size. The method is similar to the Verneuil process[1] in some respects but differs in others; in particular it is free from the limitations imposed by the use of a combustion flame. The tip fusion process can be carried out in vacuum or any desired gas atmosphere. It is very suitable for silicon and other high melting materials. Results obtained on silicon will be discussed.

[1] A. Verneuil, Compt. rend. **135**, 791 (1902).

D10. Crystal Habit of Silicon and Germanium. G. WOLFF, *Signal Corps Engineering Laboratories.*—A study of natural faces has been undertaken on silicon and germanium grown from the melt, from the gaseous phase and from solutions. The experimental results are compared with the theoretical expectations.

Invited Paper

D11. A New Method of Calculating Energy Bands in Crystal Lattices. WALTER KOHN, *Carnegie Institute of Technology.* (40 min.)

THURSDAY AFTERNOON AT 2:00
Lower Strong Auditorium
(DANIEL ALPERT presiding)

Electron Physics

E1. Electron Ejection from Metals by Positive Ions and Metastable Atoms of a Few Electron Volts. DAVID STERNBERG, *Columbia University.* (30 min.)

E2. Theory and Experiment Concerning Resonance Transitions and Auger Transitions Occurring as an Ion Approaches a Metal Surface. H. D. HAGSTRUM, *Bell Telephone Laboratories.* (30 min.)

Contributed Papers

E3. Electron Emission from Metals Under High Energy Positive Ion Bombardment. HENRY C. BOURNE, JR., ROBERT W. CLOUD, AND JOHN G. TRUMP, *M.I.T.*—Measurements were made of the electron yield from targets of aluminum, steel, magnesium, copper, gold, and lead when bombarded by ions from hydrogen, helium, nitrogen, xenon, and mercury. The ions, whose energy was varied over the range from 10 to 140 kilovolts, were produced by ionization of the residual gas in the anode electrode and emerged through a small opening into the essentially uniform accelerating field. A rapid initial rise of electro emission with ion energy was followed in all cases by a slow linear increase. The emission ratio varied from 2 to 20 and was maximum for nitrogen ions on steel. The dependence on extractive gradient at the bombarded metal surface was slight and no simple dependence on the nature of the ion or of the bombarded metal was observed. The significance of these measurements on a theory of high voltage breakdown in vacuum will be discussed.

E4. Vacuum Fluctuation Noise in Electron Streams.* J. WEBER, *University of Maryland.*—For a slightly damped oscillator, the mean squared noise voltage is given by[1]

$$\overline{V^2}=\frac{1}{C}\left[\frac{h\nu}{2}+\frac{h\nu}{\exp(h\nu/kt)-1}\right],$$

where C is the capacity. The first term represents the effect of the vacuum fluctuations and the second term represents the effect of the thermal fluctuations. This value is predicted to be the result of precise measurements of the mean squared electromotive force. It is well known that the use of electrons[2] as test charges does not in general lead to precise field measurements. Nonetheless a perturbation theory calculation shows that the noise induced in a small current electron stream which interacts weakly with a damped oscillator corresponds precisely to the value which would be calculated classically using the expression above. The transit angle was assumed to be small. Both the thermal and the vacuum fluctuations contribute to the electron stream noise.

* Supported by the U. S. Office of Naval Research.
[1] J. Weber, Phys. Rev. **90**, 977 (1953).
[2] W. Heitler, *The Quantum Theory of Radiation*, p. 78.

E5. Electrical Breakdown of Extremely Short Gaps. P. KISLIUK, *Bell Telephone Laboratories.*—Breakdown across short gaps (~1000A) has been shown to take place at voltages far below the minimum sparking potential. Arc voltages show that the discharge is in metal vapor,[1] and pressures of several atmospheres are developed. Breakdown fields are on the order of 3×10^6 volts/cm. The initiation time of these arcs is at most 3×10^{-9} seconds,[2] and each ion must produce many electrons. The number of electrons liberated by an ion approaching the cathode surface[3] is insufficient, so the field at the cathode must remain high enough to maintain the current by field emission. Ions are necessary to prevent space charge limitation of the current. Only 0.3 percent of the current at the cathode is carried by ions, so that heat and material transfer measurements can be explained in terms of the energy dissipated at the anode by electron impact, and the evaporation and condensation of metal on the electrode sur-

faces. Possible origins of the initiating ions when the initial $p\ d$ product is very low will be discussed.

[1] L. H. Germer and F. E. Haworth, J. Appl. Phys. **20**, 1085 (1949).
[2] L. H. Germer and J. L. Smith, J. Appl. Phys. **23**, 553 (1951).
[3] R. R. Newton, Phys. Rev. **73**, 1122 (1948).

E6. Probe Measurements in an Argon Discharge Containing Running Striations.* N. L. OLESON, *U. S. Naval Postgraduate School.*—A direct current discharge containing argon is known to have oscillations in tube voltage, current and light intensity.[1] In the present investigation a small cylindrical tungsten probe is inserted into the positive column of an argon discharge and held at a fixed potential with respect to the anode. The region adjacent to the probe is scanned by a photomultiplier (RCA, 931A). The voltage developed across a small resistance in series with the probe is fed through a preamplifier to one beam of a Du Mont 279 Oscilloscope, the output of the phototube to the other beam. This permits a study of probe current *versus* light intensity. Preliminary measurements with an argon discharge reveal a sharp burst of electrons prior to maximum light intensity and a maximum positive ion current near the maximum light intensity. A movable probe discharge tube has also been constructed and will be described.

* This work is supported by the U. S. Office of Naval Research.
[1] T. Donahue and G. H. Dieke, Phys. Rev. **81**, 248 (1951).

THURSDAY AFTERNOON AT 2:00

Upper Strong Auditorium

(J. S. FOSTER presiding)

Nuclear Masses; Radioactive Substances

F1. Some Mass-Spectrographic Studies of Nuclear Stability. H. E. DUCKWORTH, *McMaster University.* (30 min.)

Contributed Papers

F2. Atomic Masses for Ga, Ge, As, Se, and Br.* B. G. HOGG† AND H. E. DUCKWORTH, *McMaster University.*—New mass spectrographic measurements are combined with existing transmutation and microwave absorption data to give the following masses: Ga^{69}=68.9478±2 amu, Ge^{70}=69.9460±4 amu, Ge^{72}=71.9449±2 amu, Ge^{74}=73.9447±4 amu, Ge^{76}=75.9460±4 amu, As^{75}=74.9454±3 amu, Se^{74}=73.9460±4 amu, Se^{76}=75.9432±2 amu, Se^{77}=76.9442±2 amu, Se^{78}=77.9420±2 amu, Se^{80}=79.9421±6 amu, Se^{82}=81.9431±6 amu, Br^{79}=78.9435±4 amu, and Br^{81}=80.9425±5 amu. These constitute all the stable isotopes of these elements with the exception of Ga^{71} and Ge^{73}.

* Work supported by the Research and Development Command, U. S. Air Force, the National Research Council of Canada, and the Research Council of Ontario.
† National Research Council of Canada Fellow.

F3. Applications of the Wigner Semi-Empirical Mass Formula to Isobars.* J. T. MCCARTHY, *Western Reserve University.*—The success of most applications of semi-empirical mass formulas has been limited because of attempts to apply the formulas over wide regions of the periodic table. Discontinuities in binding energy arise near magic-number nuclei; these appear to indicate the formation of closed shells of protons and neutrons. In two recent publications[1] the Wigner formula has been shown to be fairly successful in regions where there are no discontinuities. In the present work the empirical parameter of this formula has been evaluated, by means of mass-spectrographic and distintegration-energy data, for several regions above A=36. In regions free from discontinuities the parameter appears to be a smooth function of A with few exceptions. Using these values of the parameter the energy available for double-beta decay between many isobars has been calculated. The limitations and degree of reliability of the formula will be discussed.

* Supported by the National Science Foundation.
[1] Collins, Nier, and Johnson, Phys. Rev. **86**, 408 (1952); R. E. Halsted, Phys. Rev. **88**, 666 (1952).

F4. K Capture in Na^{22}.* R. H. MILLER AND R. SHERR, *Princeton University.*—We have investigated the decay of Na^{22} using a $4\pi\beta$ proportional counter to detect the positrons and a NaI(Tl) scintillation counter for the γ-rays. Setting the two counters in coincidence the ratio of coincidences to γ-counts is equal to $\epsilon_\beta[\eta_1+(1-K)\eta_2]$, where ϵ_β is the β-counter efficiency; η_1 and η_2 are the fractions of the total γ-counts due to annihilation radiation and 1.28-Mev γ-rays, respectively, for a given setting of the bias of an integral discriminator which selects the γ-pulses for the coincidences; K is the percentage K capture. By varying the bias we obtain data which fit this expression fairly well, leading to a value for K of 9±2 percent and $\epsilon_\beta \approx 0.98$. Little change was observed for foils of zapon and aluminum covering the (massless) source up to 170 $\mu g/cm^2$. (Correction for the fluorescent yield of Na^{22} will increase K by a small amount.) The value of K calculated for an allowed transition (Feenberg and Trigg) is 10 percent (corrected for shielding).

* This work was supported in part by the U. S. Atomic Energy Commission and the Higgins Scientific Trust Fund.

F5. Radiations from As^{77} and Ge^{77}.* B. L. SARAF, J. VARMA, AND C. E. MANDEVILLE, *Bartol Research Foundation.*—As^{77} was grown from its germanium parent when GeO_2 was irradiated by slow neutrons in the Oak Ridge pile. Gamma-rays decaying with the 40-hr period were detected at 85 kev, 160 kev, 250 kev, 270 kev, and 520 kev, the relative intensities of the unconverted quantum radiations being 3, 1, 20, 0.04, and 6. Gamma-rays of lower energies may also be present. The continuous nuclear gamma-ray spectrum accompanying orbital electron capture in the 11-day Ge^{77} has an end point at 225±12 kev, yielding a value of 4.3 for log ft of the allowed electron capture transition which may be designated as $p_{1/2} \rightarrow p_{3/2}$, in agreement with the assignment of a spin of $\frac{1}{2}$ to Ge^{77} in accord with the shell model.

* Assisted by the joint program of the U. S. Office of Naval Research and the U. S. Atomic Energy Commission.

F6. Radioactivity of Sm^{153}. ROBERT KATZ AND MILFORD R. LEE, *Kansas State College.*—The radiations from 47.0-hr Sm^{153} have been studied in a variable-field, 180° focusing, beta-ray spectrometer-spectrograph. Three beta-ray spectra

of maximum energy and relative intensity 0.255-Mev, 9 percent; 0.685-Mev, 70 percent; 0.795-Mev, 21 percent have been found, and a fourth of maximum energy 0.62-Mev and relative intensity <2 percent has been postulated. Conversion electrons have been found of gamma-rays of energy 0.0691, 0.1027, and 0.548-Mev. A decay scheme in excellent agreement with nuclear shell theory is proposed in which spin and parity have been assigned to all levels. The discrepancy between the magnetic moment measurement and shell theory with regard to the ground state of Eu^{153} has been resolved in favor of the $d_{5/2}$ assignment of shell theory. No excited $h_{11/2}$ state has been found in Eu^{153}. This, together with the scarcity of odd proton isomers in the region $Z=50$ to 82 as compared to the relative abundance of odd neutron isomers in the same region,[1] may imply that the pairing energy for protons of high j is greater than that for neutrons.

[1] M. Goldhaber and R. D. Hill, Revs. Modern Phys. **24**, 179 (1952).

F7. Radioactivities of Thallium Isotopes.* INGMAR BERGSTRÖM AND R. D. HILL, *University of Illinois.*—A large number of the Tl activities can be produced from (d,n) and $(d,2n)$ reactions using ordinary Hg. Mercury has six stable isotopes with abundances ~10 per cent between $A=198$ and 204. It is therefore possible to produce every Tl isotope between 198 and 205 with 10-Mev deuterons. We have studied the K capture activities of Tl using beta-ray spectrographs which cover the electron energy region from about 15 kev to 800 kev. Thus far we have observed about 150 conversion (not γ-ray) lines, decaying with the lifetimes between 2 hours and 12 days. One isomeric transition of 260 kev (approximately 2 hours half-life) and of $M4$ character has been observed. This transition may be the 1.8 hr Tl^{198} activity already observed but further work is in progress to establish its mass number. The isomeric γ-ray is followed by a 282-kev γ-ray, probably due to a magnetic dipole transition. The ground state of Tl^{198} has been observed to decay with a half-life of about 4 hours. This has been shown by following the decay of the well-known 411-kev and 695-kev transitions of Hg^{198}. Many of the other γ-rays can be fitted into some of the already known level schemes of Hg.

* Assisted by joint program of the Atomic Energy Commission and the U. S. Office of Naval Research.

F8. Alpha-Gamma Angular Correlation in Ionium (Th^{230}). G. M. TEMMER AND J. M. WYCKOFF, *National Bureau of Standards.*—We have studied the angular correlation between the alpha-particles of Th^{230} leading to the first excited state of Ra^{226} and the subsequent 68-kev gamma-ray to the ground state. Rosenblum *et al.* have classified the latter as an $E2$ transition by comparison of L shell conversion measurements with theoretical calculations.[1] We measured coincidences of alpha-particles in a 0.001-inch terphenyl flake with gamma-pulses from a thin NaI(Tl) crystal.[2] The angle subtended by both detectors was ten degrees. Accidental coincidences accounted for at most five percent of the total coincidence rate. The angles between counters, the corresponding counting rates (counts/hour) and standard deviations follow (uncorrected except for accidentals): 84°, 4.65±0.71; 135°, 9.38±0.91; 180°, 3.53±0.60; 225°, 9.74±1.10. The correlation function which comes closest to these results is $\sin^2 2\theta$, corresponding to a 0-2-0 transition. This establishes another case of $J=2^+$ for the first excited state of an even-even nucleus.[3] The experiment is being refined to determine any slight deviations from the pure $\sin^2 2\theta$ correlation.[4]

[1] S. Rosenblum and M. Valadares, Compt. rend. **234**, 2359 (1952); Gellman, Griffith, and Stanley, Phys. Rev. **85**, 944 (1952).
[2] We are indebted to Dr. Paul Fields of the Argonne National Laboratory for supplying the electromagnetically separated source.
[3] M. Goldhaber and A. W. Sunyar, Phys. Rev. **83**, 906 (1951).
[4] A. Abraham and R. V. Pound, Phys. Rev. **89**, 1306 (1953).

F9. Indications of the Interaction of Electric Field Gradients and Nuclear Electric Quadrupole Moments in Angular Correlation. ROLF M. STEFFEN,* *Purdue University.*—It is well known that the Cd^{111} γ-directional correlation depends strongly on the chemical state and on the environment of the decaying In^{111} atom. This was explained hitherto by magnetic interaction. However, magnetic decoupling experiments with a magnetic field applied in the direction of the propagation of one γ-ray showed no tendency to restore the maximum directional correlation.[1, 2] This result seems to indicate that the attenuation of the Cd^{111} correlation in solid sources is due to the interaction between the crystalline grad E field and the electric quadrupole moment of the 0.247-Mev excited state of Cd^{111}. The largest anisotropy found for nonmetallic solids is exhibited by In_2O_3 and $In(OH)_3$. Both are cubic crystals with relatively small values of grad E at the position of the In, owing to the high symmetry of their space groups: T_h^7 and T_h^6, respectively. A further indication that the attenuation of the Cd^{111} correlation in the solid sources is caused by crystalline grad E field stems from the fact that, without exception, liquid In^{111} sources of very different character give the maximum correlation. During the progress of this work a convincing proof for the electric quadrupole interaction on the Cd^{111} correlation has been given by the results obtained with single crystals of Indium as sources.[3]

* Supported in part by the U. S. Atomic Energy Commission.
[1] Albers, Schonberg, Hänni, Heer, Novey, and Scherrer, Phys. Rev. **90**, 322 (1953).
[2] R. M. Steffen, Phys. Rev. **90**, 321 (1953).

FRIDAY MORNING AT 10:00

Lower Strong Auditorium

(L. W. PHILLIPS presiding)

Cryogenics

G1. The Hydrodynamics of Liquid Helium II. K. R. ATKINS, *University of Toronto.* (30 min.)

Contributed Papers

G2. A Theory of Liquid Helium. JOHN M. RICHARDSON, *Bureau of Mines.*—Our model is a system of identical bosons of spin O interacting with central forces within a container of volume V. We first define an effective Hamiltonian $\hat{H}$ dependent only upon the occupation numbers of the momentum states. $\hat{H}$ is defined so that the sum of $\exp[(\mu N-\hat{H})kT]$ over occupation numbers is equal to the correct grand partition function for the above model. We set up the correspond-

ing variational problem of pressure maximization, and in it we approximate the distribution function by a product of factors each referring to the occupancy of a momentum state. In H we neglect terms cubic and higher order in the occupation numbers. It is possible to express the variational problem in terms of the average occupation numbers. We assume that states of nonvanishing momentum are normally occupied, that is, their average occupation numbers are independent of the volume V. However, we admit the possibility that the state of vanishing momentum may be abnormally occupied, that is, the average occupation number may be proportional to the volume. When this possibility is favored by the variational principle, we interpret it to be the superfluid component. The quasi-continuum of normally occupied states constitutes the normal component. The results will be discussed in detail.

G3. On the Theory of Liquid He_3–He_4 Mixtures. LOUIS GOLDSTEIN, *Los Alamos Scientific Laboratory.*—The asymptotic model of Liquid He_3–He_4 mixtures has been investigated whereby the components are represented as ideal antisymmetric and symmetric fluids, respectively, whose atoms are constrained to move in a smoothed constant potential energy well. Complete miscibility is indicated at all temperatures. The isothermal energy of mixing is positive at low temperatures provided that the degeneracy of the antisymmetric component be small. The phase transition exhibited by the symmetric component is perturbed. While it is a smooth first-order phase change in absence of He_3, it becomes a third-order one in the presence of the latter. The constant pressure and volume heat capacities of the mixtures have sharp peaks along the transition line; their temperature derivatives have lambda-points along this line. The transition line is thus associated with a well-defined third-order phase change with the exception of its two limiting points. The one with vanishing He_3 concentration corresponds to a first-order phase change, while the other, with vanishing He_4 concentration, is not associated with any transition of finite order.

Optical Physics

G4. Recent Developments in the Infrared Spectroscopy of Gases at Very High Pressures. H. L. WELSH, *University of Toronto.* (30 min.)

Contributed Papers

G5. Intensity of Lyman-Alpha Line in Solar Spectrum.* WM. A. RENSE, *University of Colorado.*—Analysis of the Lyman-alpha emission line in the solar spectrum, recently photographed with a grazing-incidence concave grating spectrograph flown in an Aerobee rocket December 12, 1952, has been completed. The exposure was made at an average height of 81 km. From instrument constant an estimate of line intensity and line profile was made. The wavelength was computed to be 1215.5±1A. The line exhibits, at the altitude range of the rocket during the 28-second exposure, a narrow emission center with broad emission wings. The width is about 5A, but instrumental scattering may have masked the possible extension of the line into a faint continuum. The total intensity of the Lyman-alpha radiation at the earth, after atmospheric absorption is allowed for, is estimated to be 0.05 microwatts/cm^2. Solar activity was well above average on the day of the flight, and there are indications that Lyman-alpha intensity was correspondingly high at the time of the flight.

* The research reported in this paper has been sponsored by the Geophysics Research Directorate of the Air Force Cambridge Research and Development Center.

G6. Theory of Fine Structure Pressure Broadening of Spectral Lines.* MAKOTO TAKEO AND SHANG-YI CH'EN, *University of Oregon.*—The existence of the difference in behavior of the shift and the broadening of the absorption series lines of alkali atoms under different pressures of foreign gases has been well-established experimentally.[1] Presumably because of the lack of knowledge of intermolecular interaction, this fact is not yet accounted for theoretically. Assuming the limit of statistical approach, an extended picture of Thomas-Fermi atomic model to include optically excited states under hydrostatic pressure is proposed. Result shows a new force law involved for excited states in addition to Lennard-Jones' repulsion force under spherically symmetric assumption. Perturbation and variation method are applied to the Michels, de Boer, and Bijl's model[2] of compressed atom by expanding the infinite potential wall in terms of Dirac's δ-function to have an atomic wave function perturbed by pressure. Then the doublet separation is calculated to show linear dependence on relative density of nonpolarizable foreign gases. Differences of van der Waals' forces for $^3P_{2}$ and $^3P_{1}$ states will be attributed to the difference in charge distribution between them. An atom at $^3P_{1}$ state is spherically symmetric, while one at $^3P_{2}$ state has electric quadrupole moment. The fact will be discussed that the difference is never small in the fine structure pressure broadening.

* This work is supported by a research grant of the National Science Foundation.

[1] S. Y. Ch'en and D. A. Kohler, Phys. Rev. (to be published).
[2] Michels, de Boer, and Bijl, Physica 9, 981 (1937).

G7. The Recording of X-Ray Diffraction Patterns by a Scintillation Counter. J. C. M. BRENTANO AND I. LADANY, *Northwestern University.*—Counter techniques present the advantage over photographic recording that count rates are proportionate to intensities. The G-M counter generally used is, however, unfavorable for evaluating intensity distributions by sectional scanning because of the limited yield for x-ray photons and the count loss for high count rates. Either regions of low count rate are affected by statistical fluctuations or those of high count rate by systematic errors difficult to assess. Thalliated sodium iodide scintillation counters present high absorption and permit high counting rates. An effective way of reducing the background count was found in limiting the crystal size to the beam cross section. We could thus reduce the background to 0.3 count/sec. With molybdenum K α-radiation the photons are easily countable. Using a nuclear 162 unit with discriminator, proportionality between intensity and count rate was observed up to 36 000 counts/sec. Under comparative conditions count rates were over one order of magnitude higher than for G-M counters for cobalt radiation and sufficiently high to permit scanning with a powder rod. Apart from higher accuracy of scintillation counting use of molybdenum radiation permits simple instrumentation and suppresses differential absorption of mixed powders.

FRIDAY MORNING AT 9:30

Upper Strong Auditorium

(L. APKER presiding)

I1. The Darkening of Crystals of the Silver Halides by Light. F. SEITZ, *University of Illinois.* (40 min.)

I2. The Present Status of the Electronic Properties of Silver Chloride. L. P. SMITH, *Cornell University.* (40 min.)

I3. Low-Intensity Reciprocity Law Failure in Photographic Exposure and Its Dependence on a Two-Quantum Process. JULIAN WEBB, *Eastman Kodak Company.* (25 min.)

I4. Some Fundamental Approaches to the Problems of Photographic Sensitivity. FRANZ URBACH, *Eastman Kodak Company.* (25 min.)

FRIDAY MORNING AT 10:00

Biology Lecture Room

(G. SCHARFF-GOLDHABER presiding)

Interactions of High-Energy Protons; Nuclear Energy Levels

J1. Interactions of 2.2-Bev Protons in Nuclear Emulsions. L. W. SMITH, C. P. LEAVITT, A. M. SHAPIRO, C. E. SWARTZ, AND M. WIDGOFF, *Brookhaven National Laboratory.**—Four-hundred micron Ilford G-5 emulsions have been exposed in the monoenergetic internal proton beam at the Brookhaven Cosmotron. Convenient exposures of $\sim 3\times 10^4$ protons per cm^2 are obtained in one pulse by accelerating a fraction of the injector Van de Graff dc beam. Background is minimized by using a pneumatic plunger to propel the emulsions from behind the shadow of the back wall into the vacuum chamber and a few milliseconds later turning off the rf accelerating voltage allowing the beam to spiral in upon the plates. The proton energy is determined by a knowledge of the beam radius and rotation frequency or field value. The spread in projected and dip angles of the beam in the emulsion is a few tenths of a degree, and the protons on the average traverse several centimeters of emulsion. "Along the track" scanning of approximately ten meters of track yields a total interaction mean free path of 33 ± 6 cm (approximately 0.8 geometrical cross section) in agreement with area scanning and flux measurements. Approximately thirty percent of the total events are apparent scatterings consisting of a single outgoing minimum track with or without a short ($<10\mu$) recoil. Characteristics of the interactions will be discussed.

* Under the auspices of the U. S. Atomic Energy Commission.

J2. Stars Induced in Nuclear Emulsions by 2.2-Bev Protons. M. WIDGOFF, C. P. LEAVITT, A. M. SHAPIRO, L. W. SMITH, AND C. E. SWARTZ, *Brookhaven National Laboratory.** Ilford G-5 plates exposed in the 2.2-Bev proton beam inside the Cosmotron have been examined for stars. Only stars which have an incoming minimum track within $\pm 1°$ of beam direction have been considered. These stars constitute 85–90 percent of all stars found by area scanning. The star size distribution has been obtained for about 300 of these proton stars:

Number of outgoing tracks	3–6	7–10	11–14	15–18	>18.
Number of stars	103	82	68	35	6.

For 130 of these stars the outgoing tracks have been classified with regard to their ionization, and the angular distributions of the light ($<1.2\ g_{min}$) and gray (1.2–$3\ g_{min}$) tracks have been found. Fifty-five percent of these stars have at least one light outgoing track, and 77 percent have at least one gray outgoing track, the mean outgoing track numbers being 0.7 light, 1.3 gray, and 7.6 black. The angular distributions show marked forward peaks: for light tracks the forward to backward ratio is 16:1, for gray tracks 10:1. These results are preliminary, and further work on the analysis of these interactions is in progress.

* Under the auspices of the U. S. Atomic Energy Commission.

J3. Determination of Level Parameters for Low Energy Neutron Resonances. J. S. LEVIN, D. J. HUGHES, AND W. Y. KATO, *Brookhaven National Laboratory.**—Methods have been developed for obtaining σ_0 and Γ separately for neutron resonances below about 10 ev where the instrumental resolution is of the same order as the width of the resonance (broadened by the Doppler effect). In those cases where the resolution is somewhat greater than the level width a method involving the measurement of the areas above transmission dips of thick and thin samples can be used.[1] Where the resolution width is smaller than that of the resonance level methods have been worked out for correcting measured thin sample transmission curves for the effect of instrumental resolution. With a resolution of 0.09 ev full width at half-maximum, preliminary measurements using the area method give $\sigma_0=32\,000$ barns (isotopic), $\Gamma=0.14$ ev for the 5 ev resonance in Ag. For the same resonance the method of correcting the transmission dip for the resolution function gives $\sigma_0=29\,000$ barns, $\Gamma=0.20$ ev. These measurements will be discussed and results for other low energy resonances will be presented.

* Under auspices of the U. S. Atomic Energy Commission.

[1] Melkonian, Havens, and Rainwater, Bull. Am. Phys. Soc. **28**, No. 3, 26 (1953).

J4. Energy Levels in Thorium. D. J. HUGHES, W. Y. KATO, AND J. S. LEVIN, *Brookhaven National Laboratory.**—The nuclear energy levels in Th at excitation energy just above neutron binding have been measured by observation of neutron resonances with the Brookhaven fast chopper. This zero-spin nucleus constitutes a useful comparison with Ag, whose level density has already been measured.[1] In the neutron energy region 0–100 ev, where all resonances are re-

solved, the observed spacing is 25 ev, actually somewhat less than the value for Ag (44 ev). This spacing of levels of a single J value is about ten times larger than predicted by the usual statistical model, although this model is in good agreement with 1-Mev neutron cross sections for heavy elements. The neutron widths may be calculated if Γ_λ is assumed to be 0.1 ev; the reduced (to 1 ev) widths obtained about 0.3 mv are much narrower than the value (3 mv) expected from the observed spacing. There is one wide level at 70 ev, however, of unreduced width 30 mv, for which the large scattering is evidenced by the characteristic interference dip.

* Under auspices of the U. S. Atomic Energy Commission.
[2] Kato, Stafne, Levin, and Hughes, Bull. Am. Phys. Soc. **28**, No. 3, 26 (1953).

J5. Preliminary Results with the Indiana Heavy Particle Spectrometer.* V. K. RASMUSSEN, D. W. MILLER, B. M. CARMICHAEL, AND M. B. SAMPSON, *Indiana University.*—A point-focusing magnetic spectrometer with a mean radius of 20 inches has been constructed. This instrument, a copy of the 16-inch spectrometer at the California Institute of Technology,[1] is to be used with the external beam from the Indiana cyclotron. It is mounted so that it can be rotated around the focal point of the beam focusing and analyzing magnet pair. A target chamber with a sliding O-ring seal allows this rotation to be made without breaking the vacuum connection between the cyclotron and the spectrometer. All angles from a minimum of 10° to maxima of 45° counterclockwise and 145° clockwise are available. Preliminary observations of the scattering of 21.5-Mev α-particles by carbon have been made. The elastic group and the inelastic groups corresponding to the first three excited states of C^{12} have been found at several angles, and it is has been noted that their intensity changes quite rapidly with angle. Observation of groups corresponding to higher states of C^{12} is more difficult because of their reduced intensity and because of the continuum due to $C^{12*}\rightarrow Be^8+\alpha$; $Be^8\rightarrow 2\alpha$.

* Supported by the joint program of the U. S. Office of Naval Research and the U. S. Atomic Energy Commission.
[1] Snyder, Rubin, Fowler, and Lauritsen, Rev. Sci. Instr. **21**, 852 (1950).

J6. Gamma Rays from the Reaction $P^{31}(p\gamma)S^{32}$. H. E. GOVE AND E. B. PAUL, *Chalk River Laboratories.*—The gamma-rays from this reaction have been studied for proton energies between 1.03 and 2.1 Mev. The gamma-rays were detected in a NaI crystal 2 in. in diameter by 2 in. long and a 5819 photomultiplier. Fifteen resonances were observed in the energy range studied. Eleven of these below 1.65 Mev have been observed previously.[1] At three resonances the gamma-transitions to the ground and first excited states of S^{32} have been studied. At 1.17 and at 1.27 Mev the transitions to the first excited state exceed that to the ground state by at least a factor of 10. The angular distributions indicate $J=2\pm$ for both capturing states if the first excited state of S^{32} is assumed to be $2+$. At 1.90 Mev the transition to the first excited state is less than a seventh of that to the ground state and the angular distribution indicates $1-$ for this resonance.

[1] Grove, Cooper, and Harris, Phys. Rev. **80**, 107 (1950).

J7. Excitation Levels of Li^7 and F^{19} by Betatron Irradiation. J. GOLDEMBERG AND L. KATZ, *University of Saskatchewan.*—The neutron yield from Li^7 and F^{19} has been measured as a function of the operating energy of the University of Saskatchewan betatron. Counting statistics were held to one percent accuracy, and it is believed that the betatron energy was controlled to better than ±5 kev. The neutron yield curves were found to exhibit breaks which are interpreted as excitation levels in the nuclei irradiated. The breaks were found at: Levels of Li^7: 9.6, 10.8, 12.4, 14, 17.5 Mev. Levels of F^{19}: 11, 11.5, 11.9, 15.3 Mev. Good agreement was found with previously measured levels. The two elements were compared in the region 13 to 15 Mev, where it was clearly demonstrated that a break is present in Li^7 but not in F^{19}.

J8. Fine Structure in the $C^{13}(\gamma,n)C^{12}$ Neutron Yield. L. KATZ AND J. GOLDEMBERG, *University of Saskatchewan.*—The neutron yield resulting from the reaction $C^{13}(\gamma,n)C^{12}$ when carbon is irradiated in the University of Saskatchewan betatron has been examined as a function of the betatron operating energy. This curve was found to consist of a number of straight line portions. These discontinuities in the curve are attributed to photonuclear absorption by individual levels in C^{13}. Measurements of residual activity taken one year apart[1] and the neutron yield results are in excellent agreement with each other and with levels found in $B^{11}(p,n)C^{11}$ experiments. The breaks were found at 19.3, 19.7, 20.1, 20.5, 20.7, 21.1, 21.6, 22.4, and 22.8 Mev. Energies are measured relative to the threshold for this reaction at 18.7 Mev obtained from mass data.

[1] Haslam, Katz, Horsley, Cameron, and Montalbetti, Royal Society Canada, June Meeting, 1952.

Post-Deadline Papers, if Any

FRIDAY AFTERNOON AT 2:00

Upper Strong Auditorium

(J. A. WHEELER presiding)

M1. McGill, Fifty Years after Rutherford and Soddy. J. S. FOSTER, *McGill University.* (40 min.)

M2. The Double Scattering of Protons. C. L. OXLEY, *University of Rochester.* (30 min.)

Nuclear Physics

M3. Apparatus for Double Scattering of 240-Mev Protons. W. F. CARTWRIGHT, C. L. OXLEY, J. ROUVINA, E. BASKIR, D. KLEIN, J. RING, AND W. A. SKILLMAN, *University of Rochester.*—Apparatus has been developed to measure polarization effects in proton scattering by observing asymmetries in double scattering. The first scatter is from a target in the circulating cyclotron beam. Protons scattered at 27 degrees are collimated, selected roughly in

energy, and passed into the second scattering apparatus outside the cyclotron vacuum tank. This apparatus is rigidly mounted in a cylindrical can rotatable about an axis that can be made to coincide with the direction of protons from the first scatterer. The useful beam is defined by a cylindrical scintillation counter on the axis. The second scattering is a p-p scatter detected by quadruple coincidences between the beam defining counter, a two-counter telescope detecting the protons scattered in a range about 27 degrees, and a counter for the lower energy recoil. An exploratory crystal 15 inches behind the beam defining crystal is used in coincidence with it to align the beam with the mechanical axis. The polyethelene scatterer is replaced with carbon to evaluate backgrounds. The targets and beam defining counter are optically set on axis. A magnetic shield prevents appreciable distortions of the proton paths.

M4. On the Temperature Dependence of BF_3 Proportional Neutron Counters.* FRANK R. WOODS, EDGAR F. BENNETT, AND JOHN A. LOCKWOOD, *University of New Hampshire.*—A study of the temperature dependence of commercial BF_3 neutron counters has been made during the past year. The tubes were enclosed in a temperature controlled jacket separated from an independent temperature regulated moderator by a vacuum chamber. The voltage pulse-height distributions with a Ra-Be neutron source at a fixed distance were investigated for various tube temperatures and moderator temperatures. The shape of the voltage pulse-height distributions was not affected by changes in moderator temperature, but the integrated counting rate decreased slightly with increased moderator temperature. This could be accounted for by the change in energy of the neutrons incident on the tube. There was a large decrease in the average pulse height with increase in tube temperature, as in agreement with Goodwin and Iona.[1] On analysis this was found to be due to the increased formation of negative ions in the pulse. With a fixed discriminator setting the temperature dependence in some cases was as high as 0.3 percent °C.

* Supported by the Geophysical Research Division, Air Force Cambridge Research Center.
[1] A. Goodwin, Jr., and M. Iona, Phys. Rev. **88**, 168A (1952).

M5. A Fast-Neutron Spectrometer Using the $T(d,n)$ Alpha-Reaction. G. K. O'NEILL,* *Cornell University.*—A time-of-flight spectrometer has been developed which takes advantage of the D+T reaction mechanics to achieve a low background and good resolution. 110-kev deuterons from the Cornell cyclotron are brought out to a tritium-zirconium target. A thin stilbene crystal, shielded from scattered deuterons by a thin foil and from tritium betas by a magnetic field, detects the 3.5-Mev alpha-particle emitted in the reaction. The position of the crystal is so chosen that a photomultiplier viewing it delivers a timing pulse only when a neutron starts on a path free, for several meters, of all matter but air and the desired scattering material. Knowledge of the neutron's time-zero is limited only by the associated electronics and by variations in the path-length and energy of the alpha-particle. Contributions of the latter are calculated to be less than 10^{-9} second. The device does not require a pulsed source and wastes almost none of the available ion-beam. Experimental neutron-alpha coincidence curves as a function of neutron detector position and delay will be shown.

* U. S. Atomic Energy Commission Predoctoral Fellow.

M6. Quadrupole Focusing Lenses for Charged Particles. BRUCE CORK AND EMERY ZAJEC, *University of California, Berkeley.*—A set of four strong focusing magnetic quadrupole lenses has been constructed and operated. Each lens consists of four air-cooled electromagnets with pole tips having a hyperbolic cross section. The aperture of each lense is 2 in. in diameter, and the length is 4 in. Measurements of the magnetic field demonstrate that the hyperbolic cross section satisfies the requirements of a constant magnetic field gradient very well. The technique of deflecting a current carrying flexible wire has been used to measure the trajectory of charged particles through the system of lenses. It has been observed that the strong focusing requirements are satisfied. The system of lenses was then used to focus 0.5-Mev protons, 20-Mev deuterons, and 40-Mev alpha-particles. The parallel beam of 0.5-Mev protons was detected by observing the incandescence of a quartz plate while the protons were bombarding it. The focused beam was less than 1 mm in diameter. The astigmatic 20-Mev deuteron beam from the 60-inch cyclotron was increased in current density by a factor greater than 30.

M7. A High Yield Radio-Frequency Ion Source.* HAROLD P. EUBANK, *Brown University.*—An investigation of the operating characteristics of an rf ion source has been made with the ultimate purpose of obtaining sufficient ion current to render feasible the study of (n,p) reactions. To date the source has yielded up to 15 ma of ion current of which 80 to 90 percent consist of atomic ions. The dependence of the ion current upon the operating parameters of the source—pressure, rf power, and extracting voltage—has been measured throughout the available ranges. Although the density of ionization is found to increase steadily with both pressure and power, the ion current exhibits a clearly defined maximum within the range of each of the parameters employed. This is interpreted in terms of the potential distribution about the face of the exit canal which under proper conditions can yield considerable focusing of the ion beam prior to extraction.

* This work was supported in part by the U. S. Atomic Energy Commission.

M8. Bremsstrahlung and Electron Scattering Cross Sections in Au for 247-Mev Electrons and Positrons.* PHILIP C. FISHER, *University of Illinois.*—The absolute cross sections for gold for the top 40 percent of the bremsstrahlung spectrum have been measured for electrons and positrons of 247-Mev mean energy with the aid of a magnetic cloud chamber. With the possible exception of the top 2 percent of the spectrum, electrons and positrons give the same result. The Bethe-Heitler[1] spectrum is at least 8.7 ± 2.7 percent above the experimental spectrum. The Maximon, Bethe, and Davies[2] theory agrees with experiment. Scattering by electrons was also observed as a function of energy of the struck or lowest energy electron. For these particles having energies between 20 and 130 Mev, the scattering cross section ratios of experiment to theory are 0.96 ± 0.06 and 1.06 ± 0.08 for incident electrons and positrons, respectively.[3, 4] The cross-sectional ratio of electrons to positrons in the same energy interval is 1.31 ± 0.13 for experiment and 1.46 for theory. All errors are probable errors.

* Supported by the joint program of the U. S. Office of Naval Research and the U. S. Atomic Energy Commission.
[1] H. Bethe and W. Heitler, Proc. Roy. Soc. (London) **146**, 83 (1934).
[2] Maximon, Bethe, and Davies, Phys. Rev. **87**, 156 (1952).
[3] C. Moller, Ann. Physik **14**, 531 (1932).
[4] H. Bhabha, Proc. Roy. Soc. (London) **164**, 195 (1936).

FRIDAY AFTERNOON AT 2:00

Lower Strong Auditorium

(R. L. SPROULL presiding)

Field Emission

N1. New Methods of Field-Emission Microscopy. E. W. MUELLER, *Pennsylvania State College.* (30 min.)

N2. Field Emission from Oxygen on Tungsten. J. A. BECKER, *Bell Telephone Laboratories.* (30 min.)

N3. Field Emission and Chemisorption. ROBERT GOMER, *University of Chicago.* (30 min.)

N4. High Density Field-Emission Phenomena. W. P. DYKE, *Linfield College.* (30 min.)

Contributed Paper

N5. The Field Emission Microscope Investigation of Surface Reactions.* RALPH KLEIN, *Bureau of Mines.*—The field emission microscope[1] is a valuable tool for investigating surface reactions because events are revealed on a molecular scale, the state of the surfaces can be well defined, work functions can be easily measured, and differences of reaction on different crystal planes are readily observed. The reaction of carbon with oxygen on tungsten has been studied using this method. The average work functions over the emitting point show that the work function of a carbon-on-tungsten surface differs very little from that of clean tungsten, regardless of the amount of carbon present. Differences in the work functions of various oxgen-on-tungsten surfaces give an indication of relative surface coverages. Comparison of the pattern changes after heating an oxgen-carbon-on-tungsten surface with those of the surfaces oxgen-on-tungsten and carbon-on-tungsten suggests that the rate controlling step in the reaction is the breaking of the W—O bonds of the chemisorbed oxygen.

* This research is a part of the work being done at the Bureau of Mines supported by the Flight Research Laboratory, Wright Air Development Center.

[1] E. W. Müller, Physik. Z **37**, 838 (1936).

FRIDAY AFTERNOON AT 2:00

Biology Lecture Room

(J. B. PLATT presiding)

P1. Mechanism of Evaporation of Liquids. K. C. D. HICKMAN, *Eastman Kodak Company.* (45 min.)

FRIDAY EVENING AT 7:00

Hotel Seneca

(G. B. PEGRAM presiding)

Banquet of the American Physical Society

After-Dinner Speech

"How Are We Training Our Scientists?" W. A. NOYES, *University of Rochester*

SATURDAY MORNING AT 10:00

Upper Strong Auditorium

(H. D. SMYTH presiding)

Nuclear Reactors

Q1. Possible Designs for an Economical Power Reactor. J. J. GREBE, *Dow Chemical Company.* (30 min.)

Q2. Current Status of the Theory of Reactor Dynamics. W. K. ERGEN, *Oak Ridge National Laboratory.* (30 min.)

Q3. The Thermal Test Reactor of Knolls Atomic Power Laboratory. LEWI TONKS, *Knolls Atomic Power Laboratory.* (30 min.)

Q4. Experience with the NRX Reactor. W. B. LEWIS, *Chalk River Laboratories.* (30 min.)

SATURDAY MORNING AT 10:00

Biology Lecture Room

(P. G. BERGMANN presiding)

Cosmic Rays; Theoretical Physics

R1. Emulsion Cloud-Chamber Study of High Energy Radiation at Mountain Altitude.* J. Z. KLOSE, M. F. KAPLON, D. M. RITSON, AND W. L. WALKER, *University of Rochester.*—An emulsion cloud chamber consisting of 24 alternate 6 in. × 4 in. 3.13-mm Pb plates and 250μ Ilford G-5 emulsions was exposed for one month at Echo Lake, Colorado. Using techniques similar to those in previous studies,[1] high energy nuclear interactions and electronic showers were detected and studied. From the analysis of the nuclear showers (median energy $\sim 10^{13}$ ev) an absorption mean free path in atmosphere of the high energy interacting component is derived. The value obtained, $\lambda_A \sim 120$ g/cm^2, is appreciably longer than the geometric mean free path. The flux and zenith angle distribution of the electronic showers will be discussed.

* Supported by U. S. Air Force, Air Research Development Command.
[1] M. F. Kaplon and D. M. Ritson, Phys. Rev. **88**, 386 (1952).

R2. Interactions of Heavy Primaries of the Cosmic Radiation.* M. F. KAPLON, J. H. NOON, AND D. M. RITSON, *University of Rochester.*—In tracing 300 heavy primaries 90 interactions were found with nuclei of a photographic emulsion "block." The emulsion "block" was composed of 92 400-micron stripped emulsions (6 in. × 4 in.) piled above each other. The block had been flown for six hours at White Sands (41° geomagnetic). Eight of the 90 interactions found appeared to be with the hydrogen of the emulsion. These can be used for charge calibration. Out of the 90 interactions 22 fragments with $Z=3$, 4, or 5 were found to emerge, confirming previously published values.[1] Thus it does not seem possible to account for an apparently observed primary flux of these nuclei[2] in terms of secondaries produced in the atmosphere. A detailed discussion of mean free paths and mechanism of the interactions will be presented at the meeting.

* Supported by U. S. Air Force, Air Research Development Command.
[1] H. L. Bradt and B. Peters, Phys. Rev. **80**, 943 (1950).
[2] Dainton, Fowler, and Kent, Phil. Mag. **43**, 729 (1952).

R3. Total Cross Sections for Positive Pions in Hydrogen. STANLEY L. LEONARD AND DONALD H. STORK, *University of California, Berkeley.*—The total cross section for positive pions scattered at angles greater than 35° in liquid hydrogen has been measured for pions of energies 33, 45, 56, and 69 Mev. Pions were identified by pulse height and $H\rho$. The measured cross section at 33 Mev is 7.9±2.2 mb. A "liquid hydrogen in−liquid hydrogen out" subtraction was performed, and the pion flux has been corrected for muon contamination. In addition, a correction has been made for those pions which decayed after passing through the pulse-height counters and give rise to muons of such low energy that they reached the end of their range in the target. These pion decays were indistinguishable from true attenuation events. This correction amounted to about 9 mb at 33 Mev. Low energy muons resulting from pion decays ahead of the pulse-height crystals were readily distinguished from the pions by the pulse-height analysis. Analysis of data leading to values for the cross section at 45, 56, and 69 Mev is now in progress and these results will also be presented.

R4. Tamm-Dancoff Theory of Pion Photoproduction.* MARC ROSS, *Cornell University.*—The differential cross sections for the production of positive and neutral π-mesons by 311-Mev photons on protons have been calculated. The electromagnetic interaction is treated in perturbation theory. Matrix elements are evaluated between definite initial and final states. The wave functions for the final (meson plus nucleon) states are solutions of integral equations derived in the Tamm-Dancoff approximation using PS, PS meson theory.[1] The $s_{\frac{1}{2}}$ $I_{\frac{1}{2}}$ and $p_{\frac{3}{2}}$ $I_{\frac{1}{2}}$ states are treated in Born approximation to avoid divergence difficulties. The initial state (nucleon system) is treated in perturbation theory. The coupling constant is fixed at $G^2/4\pi=17.5$ to yield an attractive scattering phase shift of 50° for the $p_{\frac{3}{2}}$ $I_{\frac{3}{2}}$ state at 160 Mev (−33° for $s_{\frac{1}{2}}$ $I_{\frac{3}{2}}$). The shape and magnitude of the π^0 production are in good agreement with experiment. The total cross section for π^+ production is about $\frac{2}{3}$ experiment; the angular distribution is peaked just slightly beyond 90°. The π^+ production would be in better agreement with experiment if the s state matrix elements were moderately increased; at present, however, an adequate treatment for the s states is not available. Inclusion of Pauli type anomalous moments in the electromagnetic interaction is considered. The resulting cross sections are too large.

* Sponsored by National Science Foundation.
[1] Dyson, Schweber, and Visscher, Phys. Rev. **90**, 372 (A) (1953).

R5. Phenomenological Analysis of Meson-Nucleon Scattering. A. E. WOODRUFF, *University of Rochester.*—The potential model for the S wave in pion-nucleon scattering first suggested by Marshak[1] has been extended to include the $I=\frac{1}{2}$ S state. The existing data for both $I=\frac{3}{2}$ and $I=\frac{1}{2}$ S phase shifts between 0 and 135 Mev can be roughly fitted by an attractive potential with a repulsive core for the $I=\frac{3}{2}$ S state and a purely attractive well for the $I=\frac{1}{2}$ S state. Since both experiment and theory indicate that the most important P phase shift is that for the $I=\frac{3}{2}$, $J=\frac{3}{2}$ state, the three total cross section on hydrogen (π^+ elastic, π^- elastic, π^- charge exchange) can be used to calculate the three phase shifts α_1, α_3, and α_{33}. The values of α_1 and α_3 which are thereby obtained from the recent measurements at Chicago,[2] Rochester,[3] and Columbia[4] fit the model for the S phase shifts, while the α_{33} phase shift follows a p^3 law. Calculations of the α_{33} phase shift using the integral equation of Dyson[5] performed by B. P. Nigam will also be presented and compared with the data, together with further investigations of the model.

[1] R. E. Marshak, Phys. Rev. **88**, 1208 (1952).
[2] Weaver, Lord, and Orear, Bull. Am. Phys. Soc. **28**, No. 3, 42 (1953).
[3] Barnes, Angell, and Perry, private communication.
[4] Bodansky, Sachs, and Steinberger, preprint.
[5] Third Annual Rochester Conference Proceedings, December, 1952, p. 77.

R6. Effects of Certain Three-Body Nuclear Interactions in H^3 and He^3.† A. W. SOLBRIG, JR., *Vanderbilt University** (introduced by Ingram Bloch).—This limited, theoretical study is phenomenological and nonrelativistic. Effects of interactions on wave functions, magnetic dipole moments, and binding energies are obtained by first-order perturbation methods. The interactions satisfy well-known requirements of invariance, contain no power of momentum higher than the first, involve no dependence on charge, and introduce only P state in a first-order calculation. They con-

tain spin-orbit interactions and may give rise to interaction moments. Each interaction contains a scalar radial function of positions f. The unperturbed potential corresponds to pairwise Hooke's law forces between nucleons. The first-order energy perturbation is shown to vanish for all the interactions. It is shown, without further specialization of the f, that no one of fifty-eight of the seventy-five interactions yields observed magnetic moments. No definite conclusion is obtained for eleven of the remaining seventeen interactions, for calculations with plausible f appear difficult. Each of the remaining six interactions yields observed magnetic moments with plausible f.

† Work performed, in part, under U. S. Atomic Energy Commission Predoctoral Fellowship.
* Now at Los Alamos Scientific Laboratory, Los Alamos, New Mexico.

R7. Implications of Lorentz Invariance for the Scattering of Spin 1/2 Particles.* DAVID FELDMAN, *University of Rochester*.—The most general matrix element M for the scattering of spin ½ particles which is invariant under the group of Lorentz transformations (including spatial reflections) can be expressed as the sum of ten types of terms (these may be classified as S, V, T, PV, PS with or without exchange); further considerations of charge conjugation and time inversion lead to nothing new. For the purpose of effecting a transition to the nonrelativistic limit as well as for convenience in investigating polarization effects at all energies, it is useful to transform the free-particle Dirac spinors into a two-component form using the method of Foldy and Wouthuysen. Under these circumstances, M assumes a structure which is identical with that which has already been given previously by several authors[1] who, in their derivations, restricted themselves from the very beginning to the nonrelativistic domain and who had to assume explicitly the invariance of the S matrix with respect to time inversion. The various theorems on polarization effects[1] that follow from the structure of M hence all stem directly from the requirements of Lorentz invariance. Similar considerations are being made to determine the consequences for the nonrelativistic two-nucleon potentials.

* This work was supported in part by the U. S. Atomic Energy Commission.
[1] L. Wolfenstein and J. Ashkin, Phys. Rev. **85**, 947 (1952); R. H. Dalitz, Proc. Phys. Soc. (London) **A65**, 175 (1952).

R8. "Fusion" Theory of Bosons and Nonlocal Field. SATOSI WATANABE, *U. S. Naval Postgraduate School*.—The nonlocal nature of boson fields is attributed to the internal structure of bosons as suggested by de Broglie-Heisenberg's depiction[1] of these particles as combinations (fusion) of spinor particles. A mathematical formalism is developed to implement such correlation of the nonlocal theory for bosons to the fusion theory. As an illustration, the case will be examined in which the resulting nonlocal equations turn out to be identical with those of Yukawa,[2] except for one new equation,

$$[x_\mu[x^\mu, U]]-\lambda^3 U+(1/64)\lambda^4\{P_\mu\{P^\mu, U\}\}=0,$$

replacing the one in Yukawa's theory which differs from this by the absence of the third term. The curved brackets here mean an anticommutator, and $\hbar=1$.

[1] L. de Broglie, Compt. rend. **198**, 135 (1934) and subsequent papers; W. Heisenberg, Z. Naturforsch. **5a**, 251 (1950) and subsequent papers.
[2] H. Yukawa, Phys. Rev. **77**, 219 (1950); **80**, 1047 (1950).

R9. Grand Canonical Ensembles, Laplace Transform, and the Darwin-Fowler Contour Integrals.* PETER G. BERGMANN AND EZRA NEWMAN, *Syracuse University*.—Let the Hamiltonian of a thermodynamic system depend on some parameter (s) such as volume or number of particles. Then the mean of the partial derivative of the Hamiltonian with respect to such a strain parameter represents the associated stress. If we combine ordinary (petit) canonical ensembles with different values of the strain parameter, weighting each ensemble with an appropriate exponential factor, then this Laplace transformation leads to the grand canonical ensemble. This transition interchanges, in a certain sense, the respective roles of strain and stress. A return to the petit ensemble is possible, by means of an inverse Laplace transformation, the integration to be carried out in the complex plane. The well-known Darwin-Fowler method for obtaining partition functions for fixed particle numbers is precisely such an inverse Laplace transformation. We are attempting to apply these methods to nonequilibrium situations.

* Supported by Office of Scientific Research, U. S. Air Force.

R10. Inertia as a Consequence of Wave Properties. RICHARD SCHLEGEL, *Michigan State College*.—Masses are usually determined by their gravitational or inertial effects. In principle, however, the individual mass value of a group of similar particles may be determined from deBroglie wavelength observations. We consider the deBroglie equation (1) as an empirical equation relating velocity, wavelength, Planck's constant h, and a mass parameter m. This equation, with the Lorentz transformations (2) and assumption of a frequency $\nu=E/h$ (3), associated with energy E, yields $E=mc^2$ (by inverting usual derivation of deBroglie's equation). Also, from the Lorentz transformations, $\nu'=\nu_0\ (1-v^2/c^2)^{\frac{1}{2}}$, (4), where ν_0 is frequency of some point process at rest and ν' the frequency for an observer with relative velocity v. Equation (4) and $E=h\nu=mc^2$ give $m'=m_0/(1-v^2/c^2)^{\frac{1}{2}}$, (5), which has then been derived from equations for wave properties, (1), (2), and (3), with no assumption of momentum conservation or other inertial properties. From (5), and energy change defined as $\int_0^s F\cdot ds$ for arbitrary force F and displacement s, we readily get Newton's second law. We thereby may present inertia as a consequence of wave properties rather than as a primitive concept. Equation (5) is seen as resting on the frequency change (4) resulting from the Lorentz transformation.

R11. Description of Quantum States through Distributions of Observable Values. NORBERT WIENER AND ARMAND SIEGEL, *M.I.T.*—Quantum-mechanical states may be characterized by distributions of the allowable values of observables over differential space,[1] a generalized form of Hilbert space. Mean values are then calculated by use of a weighting factor; this is equivalent to the assignment of measure to sets of points in Hilbert space. We use the ensemble of idealized complex Brownian motion functions[2] $X(\alpha,x)$, where x is analogous to the time in the experimentally observed Brownian motion, X is the (complex) displacement, and α is a parameter identifying an individual function of the set of all such Brownian motions, and thus identifying points in differential space. The wave function $\phi(x)$ is transformed to a function of α by the formal Stieltjes integral $\psi(\alpha)=\int\langle dX\rangle(\alpha,x)\phi(x)\cdot x(\alpha)$. The value of x belonging to the point α is then determined by an infinite sequence of dichotomies or polychotomies of the range of integration, by an algorithm that will be given. Since the time variation of $\psi(\alpha)$ is given by a point transformation of α, the method is closely related to the Gibbsian method of statistical mechanics.

[1] N. Wiener, J. Math. and Phys. **2**, 131 (1923).
[2] N. Wiener, Acta Math. **55**, 117–258 (1930); Paley and Wiener, *Fourier Transforms in the Complex Domain* (Am. Math. Soc., 1934), Chapter 9.

SATURDAY MORNING AT 10:00

Lower Strong Auditorium

(S. MROZOWSKI presiding)

Solid State Physics, III

S1. Current-Voltage Characteristics of Cadmium Sulfide Crystals Using Ohmic Contacts. R. W. SMITH AND A. ROSE, *RCA Laboratories Division.*—Cadmium sulfide crystals can be made with a wide range of resistivities and photosensitivities. The electrode material making contact to these crystals determines in large part the current-voltage characteristics observed. Electrodes of silver, copper, gold, platinum, and graphite usually give rectifying contacts. Cadmium sulfide is an *n* type semiconductor. It has now been found that indium and gallium make low resistance, ohmic contacts to cadmium sulfide crystals throughout their resistivity range from 10 to 10^{13} ohm-cm. Using one indium and one silver electrode on low resistivity cadmium sulfide crystals large area rectifiers have been made. Current densities of over one amp/sq cm in the forward direction with a few volts applied and a front to back current ratio of 10^7 were observed. The ohmic contacts appear to be completely free from the photovoltaic effects observed with rectifying contacts. The ohmic contacts permit efficient photoconductive performance at low voltages. Quantum gains of 10^4 (corresponding to over 10 amperes per lumen) have been obtained with only 10 volts applied across a crystal 10^{-2} cm thick. The ohmic contacts enable significant currents (over 10^{-3} ampere per sq cm) to be passed through thin insulating crystals in the dark. The dependence of these currents on ac and dc voltages suggests that they are space-charge-limited currents due to injected carriers from the cathode.

S2. Space-Charge-Limited Currents in Insulators. A. ROSE AND R. W. SMITH, *RCA Laboratories.*—A trap-free insulator should be able to pass relatively large space-charge-limited currents if one electrode supplies a reservoir of free charge carriers. Such currents should increase as the square of the applied voltage. Current-voltage curves of this form have been reported through thin layers of amorphous selenium illuminated by strongly absorbed light at one electrode. These currents, however, are orders of magnitude lower than would be expected for any reasonable value of carrier mobility. Shallow traps can account both for the low magnitudes of current and for the retention of the square law dependence on voltage. Currents of a space-charge-limited nature, drawn through thin crystals of CdS in the dark, are reported in a companion paper.[1] These currents by contrast have been observed to increase nearly exponentially with applied voltage. Such an exponential rise may be derived from the assumption of traps distributed continuously in energy. The magnitude of these currents was used to estimate a volume density of traps of the order of 10^{13} cm^{-3}. The use of space-charge-limited currents should be a powerful tool for measuring the perfection of crystals since the ease of making observations improves as the trap density becomes vanishingly small.

[1] R. W. Smith and A. Rose, Abstract No. S1.

S3. Some Noise Observations on CdS Crystal Photoconductors. CARL SHULMAN, R. W. SMITH, AND A. ROSE. *RCA Laboratories.*—Cadmium sulfide crystals with indium or gallium electrodes show noise powers which are orders of magnitude less than those measured in CdS with silver electrodes. Furthermore, crystals have been found in which the noise spectrum is observed to flatten off at low frequencies. However, for most crystals the noise power is proportional to the incident light intensity and to the square of the voltage across the crystal. It is suggested therefore that, to a first approximation, the noise can be understood in terms of a photomultiplier model[1] in which the noise current is given by the expression $i^2=2eGI\Delta f$, where G is the gain of the crystal or the ratio of photocurrent to photon current. G may be greater or less than unity and is proportional to the applied voltage and carrier life time. Δf is understood not to exceed the speed of response of the crystal. Values of G determined from noise measurements check order of magnitude of actual measured gains.

[1] B. Davydov and B. Gurevich, J. Phys. (U.S.S.R.) **7**, 138 (1943).

S4. The Seebeck Effect in Germanium. T. H. GEBALLE, *Bell Telephone Laboratories.*—The Seebeck effect in germanium has been investigated by previous workers.[1] In this investigation, the Seebeck and Hall effects have been measured from liquid hydrogen temperatures to the intrinsic region for a series of *n* and *p* type single crystals. It has been shown[2] quite generally that in a thermoelectric circuit the Seebeck voltage per degree Q is equal to the entropy convected through the circuit per unit current. When the usual band scheme is assumed, the entropy convected by unit current is simply $\Delta E_F/T$ plus a term involving kinetic energy transported by electrons. ΔE_F is the distance of the Fermi level from the band edge. ΔE_F determined from Seebeck voltage agrees with ΔE_F determined from Hall voltage in order of magnitude down to about 200°K. As the temperature is lowered still further, the Seebeck voltage becomes increasingly too large, reaching a maximum just above the hydrogen boiling point. It appears that an additional mechanism other than electron transport of entropy must be considered in order to relate the observed data. This is considered in the next paper by C. Herring.

[1] H. P. R. Frederikse, Phys. Rev. **86**, 647 (1952); Lark-Horovitz, Middleton, Miller, Scanlon, and Wallerstein, Phys. Rev. **69**, 259 (1946); V. A. Johnson and K. Lark-Horovitz, Bull. Am. Phys. Soc. **28**, No. 2, 32 (1953).

[2] C. Herring, Phys. Rev. **59**, 889 (1941); C. Herring and M. H Nichols, Revs. Modern Phys. **21**, 185 (1949).

S5. Theory of Thermoelectric Power of Semiconductors. CONYERS HERRING, *Institute for Advanced Study and Bell Telephone Laboratories.*—The usual theory of thermoelectric power cannot explain the marked rise in the numerical magnitude of this quantity observed by Geballe for high resistivity germanium specimens at moderately low temperatures. It is proposed that this rise is due to the existence of appreciable assymmetry in the distribution of phonons in lattice momentum, this assymmetry occurring whenever the processes restoring randomness of phonon motions become sufficiently slow. The effect may be described either as a drag exerted on the electrons or holes by the thermal conduction phonon current, or, equivalently, as a contribution to the Peltier heat flow in an isothermal specimen, due to phonons dragged along by the electric current. Over a considerable range of temperatures T and carrier concentrations n the additional thermoelectric power ΔQ should be independent of n and roughly proportional to T^q, where q is in the neighborhood of 2.5. However, at very low T or at very large n, ΔQ should decrease toward zero, because at low T

the phonon distribution becomes governed by boundary scattering and because for large n a saturation effect should occur. The absolute magnitude of the effect can be roughly predicted from thermal conductivity data.

S6. Measurement of Charge Multiplication in Germanium and Sicilon p-n Junctions. K. B. McAfee and K. G. McKay, *Bell Telephone Laboratories.*—Previous measurements[1] have shown that carriers injected into narrow p-n junctions biased at greater than the critical field strength do not multiply in crossing such barriers. Present measurements describe the effect of extending the portion of the characteristic studied into the precritical region. Three separate methods of injection of carriers were employed. These were (1) photo injection; (2) injection by α-particles; and (3) injection by transistor action. The results show definite charge multiplication by a factor of almost 20 as the critical voltage is approached. Very similar results are obtained in comparing the three injection methods. α-particle bombardment sets the time scale of the multiplication process at less than 0.02 microsecond in both germanium and silicon. Both electrons and holes show approximately the same multiplication at equal field strengths. Examination of the results using the Townsend β-mechanism as a model and assuming that holes and electrons have very similar ionization coefficients yields resonable values for the ionization rates for holes and electrons at room temperature. It is concluded that both electrons and holes ionize in germanium and silicon junctions, at field strengths of approximately 10^5 and 2×10^5 volts/cm, respectively, a fact casting some doubt on the applicability of the Zener theory.

[1] McAfee, Ryder, Shockley, and Sparks, Phys. Rev. **83**, 650 (1951).

S7. Theory of Low Temperature "Breakdown" Effect in Germanium. N. Sclar, E. Burstein, and J. W. Davisson, *Naval Research Laboratory.*—The field dependent electrical breakdown in germanium[1] is attributed to the impact ionization of neutral impurities by free charge carriers. Debeye's data[2] on the Hall mobility of electrons shows that lattice vibration scattering is dominant from 300°K down to 11°K for samples with resistivities greater than about 2 ohm-cm. The critical field for the onset of breakdown is accordingly calculated by setting the rate at which the charge carriers lose energy to the lattice vibrations equal to the rate at which they gain energy from the field and requiring their kinetic energy to be equal to the ionization energy (ΔE) of the impurities. This gives

$$E=[2(\Delta E)c(m^*/kT)^{\frac{1}{2}}]/lq,$$

where c is the velocity of sound and l is the mean free path which varies as $1/T$. For n type germanium at 4.2°K, the results give E_{calc}=7.1 volts/cm with E_{obs}=6.4 volts/cm. Ryder obtains a discontinuity at $E\approx12$ volts/cm in the $E-J$ characteristic at 20°K which Conwell[3] attributes to an increase in mobility. It is suggested that this discontinuity may be due to impact ionization, for which the present theory gives E_{calc}=16 volts/cm.

[1] Sclar, Burstein, Turner, and Davisson, Bull. Am. Phys. Soc. **28**, No. 2, 17 (1953).
[2] E. M. Conwell, Proc. Inst. Radio Engrs. **40**, 1327 (1952).

S8. Faraday Rotation in Germanium. H. Suhl and G. L. Pearson, *Bell Telephone Laboratories, Inc.*—Measurements of Faraday rotation in germanium were made in the 1.25-cm band, at 77°K and magnetic field strengths to 16 kilooersteds. In an electron gas with collision frequency small compared with signal frequency, the rotation *versus* field curve rises to a maximum, then reverses rather steeply (at cyclotron resonance), and gradually returns to zero. Similar behavior would occur in germanium, if the energy-momentum surfaces were sufficiently simple and if the collision frequency was low enough. The ellipsoidal surfaces of Shockley' should give one, or two, such resonances, depending on sample orientation. From the corresponding field values, the effective masses can be computed. At 77°K, the mean free path is too small to give resonance, but information can still be gained by curve-fitting. Consider for simplicity a single effective mass m^* only. If m^* equalled m, we should have obtained resonance. The collision frequency equals the reciprocal mobility times e/m^*. Hence, the smaller m^*, the less the curves resemble the resonance curve. They reach an asymptotic form without reversal in rotation as m^*/m decreases to values less than the ratio: (collision frequency with $m^*=m$)/(signal frequency). Our measurements on n type place us close to this region, indicating $m^*<0.3m$ in at least one orientation.

[1] W. Shockley, Phys. Rev. (to be published).

S9. Temperature Dependence of Electron Mobility in AgCl.* Frederick C. Brown, *Reed College.*—Improved crystal counter techniques[1] have been used to measure the absolute values of drift mobility for electrons in AgCl from liquid nitrogen to dry ice temperatures. Measurements were made on single crystals grown from the melt which were relatively free from impurities and in which the electrons had long drift paths. A fast amplifying system was employed that could be used with a rise time less than 0.015 microsecond when necessary. The shape of the conduction pulses for energy released by beta-particles is shown to be useful in indicating the saturation condition required for the mobility determination. Preliminary results on a limited number of samples as well as consideration of the data of Haynes and Shockley[2] indicate a $T^{-3/2}$ dependence on temperature as predicted by electron interaction with acoustical modes of vibration at the lower temperatures.

* Supported by grants from the Research Corporation and the National Science Foundation.
[1] R. Hofstadter, Nucleonics **4**, No. 5, 29 (1949).
[2] J. R. Haynes and W. Shockley, Phys. Rev. **82**, 935 (1951).

Author Index to Papers Presented at the Rochester Meeting

Anson, John H., Kenneth A. Wright, and John G. Trump—B4
Atkins, K. R.—G1
Baroody, E. M.—B5
Becker, J. A.—N2
Bergmann, Peter G. and Ezra Newman—R9
Bergström, Ingmar and R. D. Hill—F7
Bickford, L. R., Jr.—C8
Bourne, Henry C., Jr., Robert W. Cloud, and John G. Trump—E3
Brentano, J. C. M. and I. Ladany—G7
Brown, Frederick C.—S9
Burstein, E. and B. W. Henvis—D1
Cartwright, W. F., C. L. Oxley, J. Rouvina, E. Baskir, D. Klein, J. Ring, and W. A. Skillman—M3
Cork, Bruce and Emery Zajec—M6
De-Shalit, A.—A3
Duckworth, H. E.—F1
Dyke, W. P.—N4
Ergen, W. K.—Q2
Eubank, Harold P.—M7
Feldman, David—R7
Fisher, Philip C.—M8
Foster, J. S.—M1
Fuller, C. S. and J. A. Ditzenberger—D5
Gallagher, C. J.—D7
Geballe, T. H.—S4
Goldemberg, J. and L. Katz—J7
Goldstein, Louis—G3
Gomer, Robert—N3
Gove, H. E. and E. B. Paul—J6
Grebe, J. J.—Q1
Hagstrum, H. D.—E2
Herring, Conyers—S5
Henry, Warren E.—C6
Hickman, K. C. D.—P1
Hogg, B. G. and H. E. Duckworth—F2
Hughes, D. J., W. Y. Kato, and J. S. Levin—J4
Jain, P. L., H. A. Moses, J. C. Lee, and R. D. Spence—C1
Johnson, J. B.—B6
Jona, F. and R. Pepinsky—C10
Kaplon, M. F., J. H. Noon, and D. M. Ritson—R2
Katz, L. and J. Goldemberg—J8
Katz, Robert and Milford R. Lee—F6
Keck, P. H., S. B. Levin, J. Broder, and R. Lieberman—D9
Keck, P. H., W. Van Horn, J. Soled, and A. MacDonald—D8
Kisliuk, P.—E5
Klein, Ralph—N5
Klose, J. Z., M. F. Kaplon, D. M. Ritson, and W. L. Walker—R1
Kohn, Walter—D11
Lander, J. J.—B3
Leonard, Stanley L. and Donald H. Stork—R3
Levin, J. S., D. J. Hughes, and W. Y. Kato—J3
Lewis, W. B.—Q4
Loebner, E. E.—D2
Lord, Norman W.—C3
MacDonald, D. K. C. and W. B. Pearson—C5
Mann, Glen A. and R. D. Spence—C2
Marshall, J. F.—B1
Matossi, Frank—D3
McAfee, K. B. and K. G. McKay—S6
McCarthy, J. T.—F3
Miller, R. H., and R. Sherr—F4
Mueller, E. W.—N1
Oleson, N. L.—E6
O'Neill, G. K.—M5
Oxley, C. L.—M2
Preston-Thomas, H., T. M. Dauphinee, and D. K. C. MacDonald—C4
Rasmussen, V. K., D. W. Miller, B. M. Carmichael, and M. B. Sampson—J5
Rense, Wm. A.—G5
Richardson, John M.—G2
Rose, A. and R. W. Smith—S2
Ross, Marc—R4
Ruth, Ralph P. and James W. Moyer—D4
Saraf, B. L., J. Varma, and C. E. Mandeville—F5
Schlegel, Richard—R10
Sclar, N., E. Burstein, and J. W. Davisson—S7
Seitz, F.—I1
Shirane, G., R. E. Newnham, and R. Pepinsky—C9
Shulman, Carl, R. W. Smith, and A. Rose—S3
Smith, L. P.—I2
Smith, L. W., C. P. Leavitt, A. M. Shapiro, C. E. Swartz, and M. Widgoff—J1
Smith, R. W. and A. Rose—S1
Solbrig, A. W., Jr.—R6
Steffen, Rolf M.—F9
Sternberg, David—E1
Stull, J. L. and L. R. Bickford, Jr.—C7
Suhl, H. and G. L. Pearson—S8
Takeo, Makoto and Shang-Yi Ch'en—G6
Temmer, G. M. and J. M. Wyckoff—F8
Tonks, Lewi—Q3
Urbach, Franz—I4
Van der Ziel, A.—B2
Watanabe, Satosi—R8
Webb, Julian—I3
Weber, J.—E4
Weisskopf, V. F.—A1
Welsh, H. L.—G4
Wheeler, J. A.—A2
Widgoff, M., C. P. Leavitt, A. M. Shapiro, L. W. Smith, and C. E. Swartz—J2
Wiener, Norbert and Armand Siegel—R11
Wolff, G.—D10
Woodruff, A. E.—R5
Woods, Frank R., Edgar F. Bennett, and John A. Lockwood—M4

CONTENTS—Continued

Letters to the Editor:

Observation of Cyclotron Resonance in Germanium Crystals . . . G. Dresselhaus, A. F. Kip, and C. Kittel 827

Structure of Liquid Helium . . . James Reekie and T. S. Hutchison 827

Corrosive Effect at Microwave Frequencies . . . M. Dunn, S. Gershenfeld, H. Leshinsky, and A. von Trier 828

Capillarity in Helium II . . . C. T. Lane and E. V. Dyke 829

Detection of the Free Neutrino . . . F. Reines and C. L. Cowan, Jr. 830

Nuclear Scattering of High-Energy Neutrons . . . T. B. Taylor 831

π^+-p Scattering Near 240 Mev . . . W. B. Fowler, R. M. Lea, W. D. Shephard, R. P. Shutt, A. M. Thorndike, and W. L. Whittemore 832

Time-Dependent Quadrupole Interaction in Angular Correlation of Nuclear Radiation. I Cd^{111} . . . P. B. Heaney and R. M. Steffen 832

Isotopic Spin and New Unstable Particles . . . M. Gell-Mann 833

Differential p-p Elastic Scattering Cross Section at 184, 271, and 429 Mev . . . J. Marshall, L. Marshall, and V. A. Nedzel 834

Attenuation Cross Sections of 37-Mev Pions in Hydrogen . . . C. E. Angell and J. P. Perry 835

Neutron Total Cross Section for Bismuth and Uranium between 45 and 160 Mev . . . W. I. Linlor and B. Ragent 835

Giant Nuclear Dipole Resonance . . . M. Fowler, M. Gell-Mann, and D. Place 836

Nuclear Radii . . . Francis Bitter and Herman Feshbach 837

Charged Particles of Mass Intermediate between Proton and Deuteron . . . D. T. King, Nathan Seeman, and Maurice M. Shapiro 838

Intermediate Coupling and Nuclear Reactions . . . A. M. Lane 839

Periodic Effects of the Strong Focusing Equations . . . R. C. Carlson 839

Proceedings of the American Physical Society:

Minutes of the 1953 Spring Meeting of the New York State Section at Schenectady, April 10 and 11, 1953 . . . 841

Minutes of the Meeting held at Rochester, New York, June 18–20, 1953 (Corresponding to the *Bulletin of the American Physical Society*, Volume 28, No. 4) . . . 841

CONTENTS

THE PHYSICAL REVIEW SECOND SERIES, VOLUME 92, NO. 3 NOVEMBER 1, 1953

Nonparticipation of He^3 in the Superfluidity of He^4 . . . Lester Goldman and James R. Arnold 557
Exchange Coupling in $CuK_2Cl_4 \cdot 2H_2O$ by Paramagnetic Resonance Absorption . . . Kazuo Ono, Hidetaro Abe, and Junji Shimada 551
Spin-Wave Theory of Antiferromagnetism for Simple Cubic Lattices . . . M. E. Schafroth 553
Photoelectric Studies of Iron . . . Alvin B. Cardwell 554
Solid-State Absorption Spectra of Mg and MgO . . . John R. Townsend 555
Intermediate State of a Hollow Superconducting Tin Cylinder . . . J. Gittleman 561
Transition into the Intermediate State of Hollow Superconducting Cylinders . . . B. Serin, J. Gittleman, and E. A. Lynton 565
Evaluation of Lattice Sums for Cubic Crystals . . . J. Hove and J. A. Krumhansl 569
Internal Friction of Rock Salt Single Crystals . . . D. R. Frankl 573
Electrical Properties of Black Phosphorus . . . Robert W. Keyes 580
Annealing of Bombardment Damage in a Diamond-Type Lattice: Theoretical . . . R. C. Fletcher and W. L. Brown 586
Annealing of Bombardment Damage in Germanium: Experimental . . . W. L. Brown, R. C. Fletcher, and K. A. Wright 591
Bleaching Properties of *F*-Centers in KBr at 5°K . . . Jordan J. Markham, Raul T. Platt, Jr., and Irving L. Mador 597
Augmented Plane Wave Method for the Periodic Potential Problem . . . J. C. Slater 603
Collective Description of Electron Interactions: III. Coulomb Interactions in a Degenerate Electron Gas . . . David Bohm and David Pines 609
Collective Description of Electron Interactions: IV. Electron Interaction in Metals . . . David Pines 626
Quenching of Mercury Resonance Radiation (2537A) by Nitrogen . . . C. G. Maitland 637
Hyperfine Structures of Silver and Gold by the Atomic Beam Magnetic Resonance Method . . . Günter Wessel and Hin Low 641
Zeeman Effect of the Cr Ground State . . . P. Brix, J. T. Risinger, H. Low, and G. Wessel 647
7.66-Mev State in C^{12} . . . D. N. F. Dunbar, R. E. Pixley, W. A. Wenzel, and W. Whaling 649
Reaction $C^{12}(\gamma,3p)Li^9$ . . . Daryl Reagan 651
Total Neutron Cross Section of Phosphorus . . . K. F. Hansen, R. M. Kiehn, and Clark Goodman 653
Inelastic Scattering of Fast Neutrons in Carbon and Lead . . . B. G. Whitmore 654
Slow Neutron Resonances in Holmium, Thulium, and Lutetium . . . H. L. Poole, Jr., H. H. Landon, and V. L. Sailor 656
Alpha-Alpha Scattering from 12.88 to 21.82 Mev . . . F. E. Steigert and M. B. Sampson 660
Inelastic Scattering of Protons and Deuterons from F^{19} and F^{21} . . . C. K. Bockelman, C. P. Browne, W. W. Buechner, and A. Sperduto 665
Evaluation of the Interaction Effect in n-p Capture . . . N. Austern 670
Capture Gamma Rays from the Proton Bombardment of Be^9 . . . W. F. Hornyak and T. Coor 673
Drift Mobilities in Semiconductors. I. Germanium . . . M. B. Prince 681
K-Auger Electrons, Positrons, and Conversion Electrons of Zn^{65} Above 5 kev . . . J. F. Perkins and S. K. Haynes 687
Alpha Spectra of Cm^{245}, Cm^{243}, and Cm^{244} . . . Frank Asaro, S. G. Thompson, and I. Perlman 694
Slow Neutron Velocity Spectrometer Studies. V. Re, Ta, Rh, Cr, Ge . . . E. Melkonian, W. W. Havens, Jr., and L. J. Rainwater 702
Thermal Neutron Absorption Cross Sections of Boron and Gold . . . E. S. Carter, H. Palevsky, V. W. Myers, and D. J. Hughes 716
Summary of *K*-Meson Data . . . L. Leprince-Ringuet and B. Rossi 722
Neutron-Proton Scattering near 180° at 90 Mev . . . W. Selove, K. Strauch, and F. Titus 726
Search for *V* Particles Produced by 450-Mev Protons . . . A. H. Rosenfeld and S. B. Treiman 727
Interaction of Negative Pions with Mercury . . . Nathan Sugarman and Agnes Heiber 730
Ionization Loss at Relativistic Velocities in Nuclear Emulsion . . . Bertram Schiller and Maurice M. Shapiro 735
Stopping Cross Section of Gases for Protons, 30–600 kev . . . H. K. Reynolds, D. N. F. Dunbar, W. A. Wenzel, and W. Whaling 743
Characteristics of Neutral Meson Production in the Proton Bombardment of Carbon Nuclei . . . Walker E. Crandall and Burton J. Moyer 749
Decay of Gallium 67 . . . W. E. Meyerhof, L. G. Mann, and H. J. West, Jr. 758
Lattice-Space Quantization of a Nonlinear Field Theory . . . L. I. Schiff 765
Production of Neutral Mesons by 340-Mev Protons on Hydrogen . . . J. W. Mather and E. A. Martinelli 769
Studies of X-Rays from Mu-Mesonic Atoms . . . Val L. Fitch and James Rainwater 789
Mu-Mesonic Atoms and the Electromagnetic Radius of the Nucleus . . . L. N. Cooper and E. M. Henley 801
Mu Meson as Nuclear Probe Particle . . . John A. Wheeler 812
Formulation of the Kohn-Hohlde Variational Principle in Terms of the Scattering Operator Formalism . . . Harry E. Moses 817
Space-Time Representation in Wave Mechanics . . . E. J. Hellund and M. K. Brachman 822
Invariant Forms of the Nucleon-Nucleon Interaction . . . David Feldman 824

(continued on cover three)

LANCASTER PRESS, INC., LANCASTER, PA.